Catalysts and Process Design for Living Aqueous Polymerization to Ultra High Molecular Weight Polyethylene Nanocrystals

Dissertation

zur Erlangung des akademischen Grades eines

Doktors der Naturwissenschaften (Dr.rer.nat.)

vorgelegt von

Manuel Schnitte

aus Konstanz

an der

Universität Konstanz

Mathematisch-Naturwissenschaftliche Sektion

Fachbereich Chemie

Konstanz, 2021

Tag der mündlichen Prüfung: 12.03.2021

1. Referent:	Prof. Dr. Stefan Mecking
2. Referent:	Prof. Dr. Rainer Winter
3. Referent:	Prof. Dr. Alexander Wittemann
Prüfungsvorsitz:	Prof. Dr. Alexander Wittemann

„Also wenn wir jetzt über eine Paste reden,
meinen wir nicht eine typische Paste,
wie man sich im eigentlichen Sinne eine Paste vorstellen würde.
Aber schon so eine Art Paste,
also ein Material mit pastösen Eigenschaften.“ *

- Fazit unseres ersten Fachgruppentreffens zum Thema
„3D-Druck von neuartigen Pasten“

* „Das Schönste, was wir erleben können, ist das Geheimnisvolle.
Es ist das Grundgefühl, das an der Wiege von wahrer Kunst und Wissenschaft steht.
Wer es nicht kennt und sich nicht mehr wundern,
nicht mehr staunen kann, der ist sozusagen tot und sein Auge ist erloschen."

- Albert Einstein (1952)

Die vorliegende Dissertation entstand in der Zeit von Januar 2016 bis Juni 2020 unter der Leitung von Herrn Prof. Dr. Stefan Mecking am Fachbereich Chemie der Universität Konstanz.

Danksagung - Acknowledgement

Mein größter Dank gilt Prof. Dr. Stefan Mecking für die Aufnahme in seine Arbeitsgruppe und die Betreuung dieser Arbeit. Er vertraute mir ein herausforderndes, spannendes und zugleich vielseitiges Thema an und zeigte stetig Interesse an meinen Arbeiten. Dabei gab er mir zahlreiche hilfreiche Anmerkungen, ließ mir aber auch viele Freiheiten und ermöglichte mir die Freude an der Forschung zu entdecken und meine Ergebnisse auf zahlreichen Konferenzen vorzustellen.

Für die Übernahme der Zweitbetreuung und des Zweitgutachtens möchte ich mich bei Prof. Dr. Rainer Winter bedanken. Zudem danke ich ihm und seiner Arbeitsgruppe, dass ich ihre analytischen Geräte nutzen durfte, als auch für die tolle gemeinsame Zeit auf Ebene L7.

Weiterer Dank gilt Prof. Dr. Alexander Wittemann für die Übernahme des Drittgutachtens, des Prüfungsvorsitzes und für hilfreiche Diskussionen.

Ein ganz besonderer Dank gilt Dr. Inaqui Göttker gen. Schnetmann für eine umfangreiche Einführung in die Nickelchemie, zahlreiche Hilfestellungen und Anmerkungen und eine sehr gute Laborpartnerschaft. Dr. Philip Kenyon danke ich für die Einarbeitung auf dem Gebiet der wässrigen, katalytischen Polymerisation. Florian Wimmer danke ich für die gemeinsame Bewältigung der Polymeranalytik und eine hervorragende, freundschaftliche Zusammenarbeit. Ebenso danke ich ihm, Manuel Häußler und Marcel Eck für die Unterstützung beim 3D-Druck. Manuel Häußler danke ich zudem für die Durchführung von Zugversuchen. Annika Sickinger danke ich für SEM Aufnahmen und für eine großartige Bürotischnachbarschaft. Sonja Stadler danke ich für das Überlassen von **2^{Ant}-CF_3/Pyr** und Eva Schiebel für das Messen und Auswerten von Röntgenkristallstrukturen. Bei Dr. Verena Goldbach bedanke ich mich für ihre Unterstützung bei zahlreichen Reaktorexperimenten und für viele schöne Momente innerhalb und außerhalb der Universität.

Bei Dr. Marina Krumova bedanke ich mich für ihre Unterstützung bei TEM und AFM Aufnahmen. Bei Lars Bolk bedanke ich mich für die Lehre in der Kunst der GPC Analytik, sowie für zahlreiche gemeinsame Stunden vor aufgeschraubten Geräten und Computern. Bei ihm und Robin Kirsten möchte ich mich generell bedanken, dass sie „den Laden am Laufen halten“. Gleiches gilt auch für Gisela Berner in allen organisatorischen Belangen (hier sind auch Susan Kyncl, Ulrike Mandausch und Christina Hipper-Meier zu nennen).

Larissa Casper, Dr. Markus Maier und Dr. Michael Linseis (AG Winter) danke ich für Unterstützung bei zahlreichen cyclovoltammetrischen Experimenten. Bei Rose Rosenberg (AG Cölfen) bedanke ich mich für die Durchführung und Auswertung von AUC Experimenten. Des

Weiteren danke ich Anke Friemel und Ulrich Haunz für die Hilfe und technische Unterstützung bei NMR Messungen und für die Durchführung von Hochtemperatur-NMR Experimenten.

Meinen Mitarbeiterinnen und Mitarbeitern, sowie Bachelor-Anwärterinnen und Bachelor-Anwärtern Raphael Steimbach, Kai Riedmiller, Larissa Casper, Simon Cardinal, Anne Staiger, Janine Scholliers und Sophia Lipinski danke ich für ihren Beitrag zum Gelingen dieser Arbeit. Gleiches gilt auch für meine wissenschaftlichen Hilfskräfte Philipp Schoch und Katrin Zoller für ihre Unterstützungen bei Labortätigkeiten.

Der gesamten AG Mecking (gegenwärtige und ehemalige Mitglieder) danke ich für eine großartige gemeinsame Zeit auf diversen Ausflügen, Festen, Konferenzen und im ganz normalen universitären Alltag. Das gilt besonders für „die Nickels“, mein Büro L722 und meine Labor-WG in L717.

Ich danke dem Sonderforschungsbereich (SFB) 1214 „Anisotropic Particles as Building Blocks: Tailoring Shape, Interactions and Structures“ für die finanzielle Unterstützung während der Promotion in allen Belangen. Besonders sind hier Stephan Siroky und Desiree Bruttel zu nennen, die sich stets mit größter Bemühung allen koordinativen Fragen angenommen haben. Beim SFB 1214 Forschungsrat, dessen Mitglied ich als Vertreter der wissenschaftlichen Mitarbeiter sein durfte, bedanke ich mich für die produktive Zusammenarbeit. Bei der IRTG, ihren Mitgliedern und besonders bei meinen SFB-Mitstreitern Christina Rank, Annika Sickinger und Dr. Julian Ruiz bedanke ich mich für die tolle gemeinsame Zeit und den guten wissenschaftlichen Austausch, den wir stets während allen Treffen, Posterdays und Retreats hatten.

Ein großer Dank gebührt zudem meinen Freunden in Konstanz, der Gruppe „Flucht um 6“, der Reisegruppe „Zipfle-Schnibach“, dem 11-Uhr-Mittagstisch, der „Strong by Zumba“-Sportgruppe, meinem Semester WS-10/11 und allen sonstigen Wegbegleitern für viele schöne Momente in meiner universitären Zeit.

Ich bedanke mich bei Annika Sickinger, Florian Wimmer, Natalie Schunck, Lukas Odenwald, Anne Staiger und Eva Schiebel für das kritische Korrekturlesen dieser Arbeit und für ihre Anmerkungen.

Ganz besonders danke ich zum Schluss meiner Familie, langjährigen Freunden und meinem Freund Nikolai, die mich immerwährend und geduldig in allen Phasen des Studiums und der Promotion unterstützt haben. Ohne euren Rückhalt wäre es mit der Chemie vermutlich erheblich schlechter gelaufen. Danke!

Publications and Communications

Parts of this thesis have been published.

Journal Publications

- Schnitte, M.; Lipinski, S.; Schiebel, E.; Mecking, S. *Organometallics* **2020**, *39*, 13-17. *"Pentafluorophenyl Groups as Remote Substituents in Ni(II) Polymerization Catalysis"*
- Schnitte, M.; Scholliers, J. S.; Riedmiller, K.; Mecking, S. *Angew. Chem. Int. Ed.* **2020**, *59*, 3258-3263. *"Remote Perfluoroalkyl Substituents are Key to Living Aqueous Ethylene Polymerization"*
- Schnitte, M.; Staiger, A.; Casper, L. A.; Mecking, S. *Nat. Commun.* **2019**, *10*, 2592. *"Uniform shape monodisperse single chain nanocrystals by living aqueous catalytic polymerization"*

Poster Presentations

- Schnitte, M.; Staiger, A.; Mecking, S. at the *5th Blue Sky Conference on Catalytic Olefin Polymerization*, Naples and Sorrento, Italy, June 2019. *"Single-chain Polyethylene Nanocrystals by Living Polymerization in Aqueous Media"*
- Schnitte, M.; Staiger, A.; Mecking, S. at the *52nd Annual German Catalysis Meeting*, Weimar, Germany, March 2019. *"Single-chain Polyethylene Nanocrystals by Living Polymerization in Aqueous Media"*
- Schnitte, M.; Staiger A.; Cardinal, S.; Mecking, S. at the *SFB 1214 Symposium "Anisotropic Particles"*, Konstanz, Germany, September 2018. *"Anisotropic Polymer Nanocrystals by Living Ethylene Polymerization in Aqueous Media"*
- Schnitte, M.; Casper, L. A.; Mecking, S. at the *51st Annual German Catalysis Meeting*, Weimar, Germany, March 2018. *"Advanced Catalysts and Process Design for Polyethylene Nanocrystal Synthesis"*
- Schnitte, M.; Godin, A.; Riedmiller, K.; Krumova, M.; Göttker-Schnetmann, I.; Mecking, S. at the *253rd ACS National Meeting and Exposition*, San Francisco, California, USA, April 2017. *"Single Chain Polyethylene Nanocrystals"*
- Schnitte, M.; Godin, A.; Riedmiller, K.; Krumova, M.; Göttker-Schnetmann, I.; Mecking, S. at the *50th Annual German Catalysis Meeting*, Weimar, Germany, March 2017. *"Catalytic Insertion Polymerization in Aqueous Media for Nanocrystal Synthesis"*

- Schnitte, M.; Godin, A.; Kenyon, P.; Krumova, M.; Göttker-Schnetmann, I.; Mecking, S. at the *Macromolecular Colloquium*, Freiburg, Germany, February 2017.
  "Single Chain Polyethylene Nanocrystals"

Oral Presentations

- Schnitte, M.; Staiger, A.; Mecking, S. at the *5th Blue Sky Conference on Catalytic Olefin Polymerization*, Naples and Sorrento, Italy, June 2019.
  "Single-chain Polyethylene Nanocrystals by Living Polymerization in Aqueous Media"

Publications Related to this Work

- Mecking, S.; Schnitte, M. *Acc. Chem. Res.* **2020**, *53*, 2738-2752. *"Neutral Nickel(II) Catalysts: From Hyperbranched Oligomers to Nanocrystal-Based Materials"*

Parts of this thesis have been reproduced and reprinted with permission.

Schnitte, M.; Staiger, A.; Casper, L. A.; Mecking, S. Uniform shape monodisperse single chain nanocrystals by living aqueous catalytic polymerization. *Nature Communications* **2019**, *10*, 2592. (DOI: 10.1038/s41467-019-10692-1)
Open Access, CC BY 4.0 license, Copyright 2019 The Authors, published by Springer Nature.
(*chapter 3*)

Schnitte, M.; Scholliers, J. S.; Riedmiller, K.; Mecking, S. Remote Perfluoroalkyl Substituents are Key to Living Aqueous Ethylene Polymerization. *Angewandte Chemie International Edition* **2020**, 59, 3258-3263. (DOI: 10.1002/anie.201913117)
Open Access, CC BY-NC 4.0 license, Copyright 2020 The Authors, published by Wiley-VCH Verlag GmbH & Co. KGaA.
(*chapter 4*)

Schnitte, M.; Lipinski, S.; Schiebel, E.; Mecking, S. Pentafluorophenyl Groups as Remote Substituents in Ni(II) Polymerization Catalysis. *Organometallics* **2020**, *39*, 13-17.
(DOI: 10.1021/acs.organomet.9b00784)
Copyright 2020 American Chemical Society.
(*chapter 5*)

Zusammenfassung - Abstract

Polyolefine sind eine wichtige Klasse von Kunstoffen, die sich durch vielseitige Anwendungsmöglichkeiten auszeichnet und durch katalytische Polymerisation von Olefinen mit frühen Übergangsmetallen gewonnen werden kann. Die verwendeten Katalysatoren erlauben eine präzise Einstellung der Molekulargewichte und Mikrostrukturen der erhaltenen Polymere, was die resultierenden Materialeigenschaften maßgeblich beeinflusst. Im besonderen Fall von Polyethylen, dem wichtigsten Polyolefin, kann das katalytische Kettenwachstum gegenüber anderen Reaktionen begünstigt und sog. Ultrahochmolekulares Polyethylen (ultra high molecular weight polyethylene, UHMWPE) erzeugt werden. Dieses Material besitzt außergewöhnliche Eigenschaften (z.B. eine hohe Abriebfestigkeit und Stärke), lässt sich aber aufgrund zahlreicher, bereits bei der Herstellung gebildeter Verschlaufungen der Polymerketten nur schwer verarbeiten (die Viskosität der Polymerschmelze ist stark erhöht). Abhilfe könnte die Herstellung und Verwendung von UHMWPE in Form einer wässrigen Polymerdispersion schaffen. Polymerdispersionen zeichnen sich durch eine generell einfache Handhabung aus und liefern das Material als nanoskalige Partikel. Durch gezielte Anordnung dieser Nanopartikel könnten Materialien mit neuartigen Eigenschaften zugänglich gemacht werden, insbesondere im spannenden Fall von anisotropen, nicht-sphärischen Partikelformen. Allerdings erfordert diese Strategie sehr einheitliche Nanopartikel, um entsprechend definierte Materialeigenschaften erhalten zu können. Im Sinne einer katalytischen Polymerisation wäre ein hochkontrolliertes Kettenwachstum und ein gleichzeitiges, gezielt ablaufendes Partikelwachstum unter wässrigen Bedingungen notwendig. Bis heute konnte kein katalytisches Verfahren entwickelt werden, das diesen Ansprüchen genügt.

Die vorliegende Arbeit beschreibt das Konzept einer katalytischen, lebenden Polymerisation von Ethylen in Wasser unter Bildung einer Polymerdispersion. Aufgrund ihrer äußerst hohen Empfindlichkeit gegenüber Wasser lassen sich klassische Katalysatoren früher Übergangsmetalle hierzu nicht verwenden. Dem gegenüber zeigen sich weniger oxophile, späte Übergangsmetall-Katalysatoren deutlich toleranter und eignen sich z.B. für die Copolymerisation von Ethylen und polaren Comonomeren. Diese neigen aber zur sog. β-Hydrid-Eliminierung (BHE), dem Schlüsselschritt zu Kettenübertragung und Verzweigungsbildung, was die Herstellung von linearem, hochmolekularem Polyethylen deutlich erschwert.

N-Terphenyl Salicylaldiminato Nickel(II)-Komplexe eignen sich zur Polymerisation von Ethylen in wässriger Tensidlösung. Dabei findet die Polymerisation innerhalb kompartimentierter Bereiche, den Tensid-Mizellen, statt. Das gebildete Polyethylen wird in

Form von nanoskaligen, isolierten Einkristallen erhalten, die sich durch eine ungewöhnliche, anisotrope Form auszeichnen. Ein sehr hoher Grad an struktureller Ordnung innerhalb dieser Nanokristalle entsteht durch eine schnelle und geordnete Ablagerung der gebildeten Polymerkette auf dem wachsenden Kristall. BHE kann hierbei durch Verwendung von elektronenziehenden Gruppen (z.B. $-CF_3$) in bestimmten Positionen des Liganden unterdrückt werden, womit die Bildung von linearem, hochmolekularem Polyethylen signifikant gefördert wird.

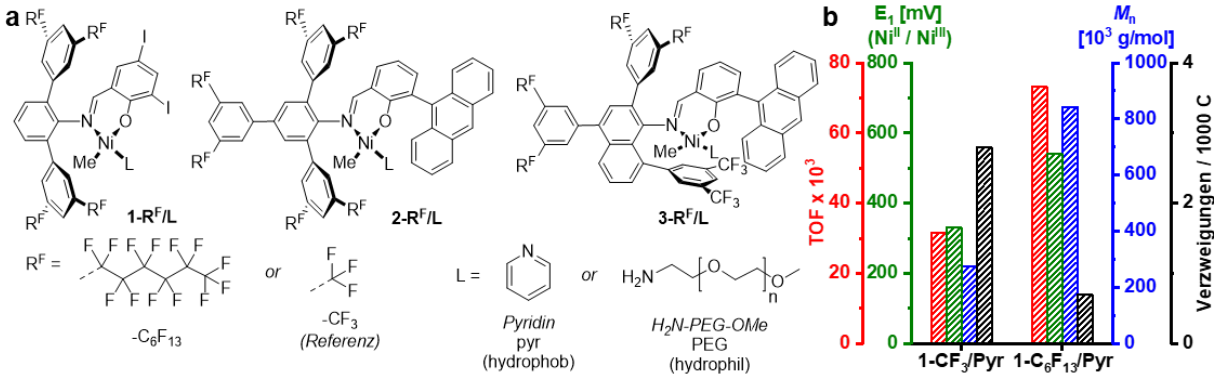

Abbildung 1. a) Auswahl der in der vorliegenden Arbeit untersuchten Katalysatoren. Verglichen zu den Referenzsystemen (R^F = $-CF_3$) sind die neuartigen Katalysatoren mit langen Perfluoroalkylketten substituiert (z.B. R^F = $-C_6F_{13}$). Der koordinierte labile Ligand L unterscheidet sich für lipophile Vorstufen (L = pyr) und hydrophile Vorstufen (L = PEG), geeignet für wässrige Polymerisationen. b) Vergleich experimenteller Daten aus Polymerisationsexperimenten (in Toluol) und aus elektrochemischen Messungen (Cyclovoltammetrie). TOF = Katalysatorwechselzahl, E_1 = Peakpotential, M_n = Molekulargewicht.

Um diesen Effekt noch weiter zu verstärken, wurden in der vorliegenden Arbeit stark elektronenziehende, lange Perfluoroalkylketten (z.B. $-C_6F_{13}$) in den entscheidenden Positionen verschiedener etablierter Katalysatorstrukturen eingefügt (siehe Abbildung 1, a). Alle dadurch erhaltenen Katalysatoren wurden zur Polymerisation von Ethylen in Toluol unter verschiedenen Bedingungen getestet. Hierbei zeigten sie hohe Aktivitäten und erzeugten weniger verzweigte Polyethylene mit höheren Molekulargewichten als die entsprechenden CF_3-substituierten Referenzsysteme (siehe Abbildung 1, b). Dies deutete auf eine effektive Unterdrückung von BHE durch die C_6F_{13}-Substitution hin. Dieser Effekt wurde durch elektrochemische Untersuchungen an den entsprechenden Katalysatorvorstufen näher untersucht. Hier zeigte sich, dass die Elektronendichte am Nickel-Zentrum durch die Perfluoroalkyl-Substituenten in der Ligandstruktur stark abgesenkt wird (durch Unterdrückung bestimmter Wechselwirkungen zwischen dem Liganden und dem Metallatom). Die engen Molkulargewichtsverteilungen der in Reaktorexperimenten erhaltenen Polymere deuteten zudem auf einen kontrollierten Kettenwachstumsprozess hin.

Polymerisationsexperimente in wässriger Tensidlösung zeigten, dass eine lebende Polymerisation mit diesen neuartigen Katalysatoren erzielt wurde. Dies ging aus einer linearen Beziehung zwischen den erhaltenen Molekulargewichten und dem Umsatz (bzw. der Reaktionszeit) und sehr engen Molekulargewichtsverteilungen hervor (siehe Abbildung 2, a). Entsprechende Berechnungen ergaben, dass ein Nickel-Zentrum nur eine Polymerkette erzeugt und keine Kettenübertragung stattfand. Durch Optimierung verschiedener Paramater in einem automatisierten Reaktoraufbau konnte das Verfahren weiter verbessert werden. Durch nun ermöglichte Katalysatorlebenszeiten von über 4 Stunden wurden kolloidal stabile Dispersionen von UHMWPE-Nanokristallen (M_n > 3 x 10^6 g/mol) gebildet. Aufgrund des wohldefinierten Bildungsmechanismus dieser Kristalle enthielten diese keinerlei Verschlaufungen. Dies konnte durch Untersuchungen der thermischen Eigenschaften (DSC) des erhaltenen Polymers weiter bestätigt werden. Mithilfe von elektronenmikroskopischen Untersuchungen (TEM) an Dispersionen, die nach unterschiedlichen Polymerisationszeiten erhalten wurden, konnte der Partikel-bildungsprozess weiter aufgeklärt werden. Mit steigender Größe wurden zuerst hexagonale, flache Partikel erhalten, die sich dann zu rautenförmigen Plättchen entwickelten (siehe Abbildung 2, b).

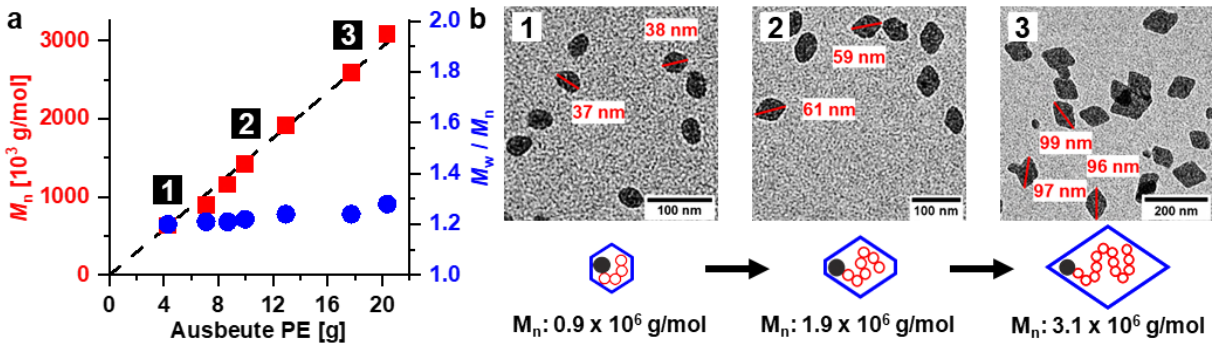

Abbildung 2. a) Molekulargewichte und entsprechende Polydispersitätsindices verschiedener Polyethylene, erhalten aus wässrigen Polymerisationen nach unterschiedlichen Reaktionszeiten bzw. -umsätzen. b) Dazugehörige TEM-Aufnahmen zeigen die Veränderung von Partikelgröße und -form mit zunehmendem Molekulargewicht. Diese Korrelation ergibt sich aus Kristallisation einer einzelnen wachsenden, lebend polymerisierten Kette.

Zudem wurden eine insgesamt sehr einheitliche Partikelform und eine enge, monodisperse Partikelgrößenverteilung in allen Fällen festgestellt. Durch einen direkten Vergleich der durchschnittlichen Masse eines Partikels und des chromatographisch bestimmten mittleren Molekulargewichts des gebildeten Polyethylens ergab sich, dass jeder einzelne Partikel durch Kristallisation einer einzigen Polymerkette gebildet wurde. Da diese Polymerkette von einem Nickel-Zentrum in einer lebenden Polymerisation erzeugt wird, korrelierten auch Partikelgröße und -form direkt mit dem Umsatz bzw. der Reaktionszeit. Die in der lebenden Polymerisation

erhaltene enge Molekulargewichtsverteilung des UHMWPEs spiegelte sich dabei direkt in der ebenfalls engen Partikelgrößenverteilung der Nanokristalle wider.

Die TEM-Aufnahmen der Partikel zeigten bereits eine hohe Neigung zur Bildung gleichmäßiger Schichten, begünstigt durch ihre einheitlichen Formen und Größen. Dabei konnte eine Nahordnung benachbarter Partikel beobachtet werden, die durch einfaches Eintrocknen einer verdünnten Dispersion bei Raumtemperatur erzeugt wurde (siehe Abbildung 3, a). Aufgrund dieser vielversprechenden Beobachtungen wurden die neuartigen UHMWPE-Dispersionen in verschiedenen Ansätzen zur Herstellung partikelbasierter Materialien getestet. Das Polymer sollte hier direkt in Form der Dispersion, ausgefällt als Pulver und in Form einer wässrigen Paste genutzt werden.

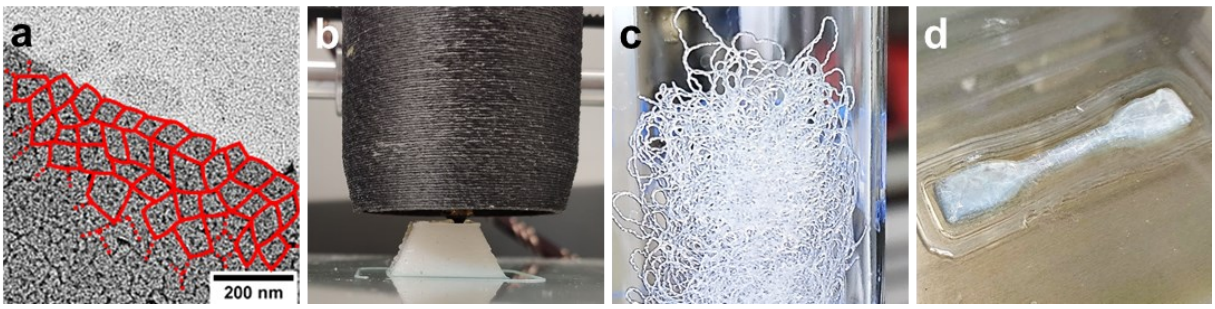

Abbildung 3. Verschiedene Ansätze zur Herstellung partikelbasierter Materialien. a) Bildung gleichmäßiger Schichtstrukturen mit Nahordnung zwischen benachbarten Partikeln. b) 3D-Druck von Polyethylen als Granulat. c) Herstellung von UHMWPE-Fäden durch „Dispersionsfaserspinnen“ von UHMWPE-Nanokristalldispersionen. d) 3D-Druck von UHMWPE-Pasten, erhalten durch Verdickung der hergestellten Dispersionen.

Der einzigartige Charakter der UHMWPE-Nanokristalle blieb beim Ausfällen erhalten und sollte ein leichteres Verarbeiten im geschmolzenen Zustand ermöglichen. Dazu wurde der 3D-Druck von kommerziellem Polyethylen als Granulat versucht und verschiedene Objekte konnten hergestellt werden, deren Qualität mit den Ergebnissen klassischer 3D-Filamentdrucker vergleichbar war (siehe Abbildung 3, b). Erste Experimente mit UHMWPE-Pulver zeigten hier vielversprechende Extrusionseigenschaften des nicht-verschlauften Materials.

Geeignet für sehr anspruchsvolle Anwendungen, wird UHMWPE u.a. zu ultrastarken Fäden verarbeitet. Ausgehend von der Dispersion sollten solche Fäden durch sog. „Dispersionsfaserspinnen“ erzeugt werden, wobei die Dispersion in einem sehr einfachen Aufbau direkt und gleichmäßig in ein Fällbad geleitet wurde (siehe Abbildung 3, c). Die isolierten Fäden zeigten zunächst eine limitierte mechanische Stabilität. Diese konnte jedoch durch Behandlung mit Wärme und der damit einhergehenden Kettendiffusion zwischen benachbarten Nanokristallen in der Fadenstruktur weiter verbessert werden.

Um die Integrität der anisotropen Nanokristalle und die damit einhergehenden Eigenschaften zu erhalten und trotzdem die Vorteile des 3D-Drucks nutzen zu können, wurden die UHMWPE-Dispersionen im 3D-Druck von Pasten verwendet (siehe Abbildung 3, d). Dazu wurde die Dispersion, z.B. durch Entfernen des Dispersionsmediums, stark verdickt und eine wässrige Paste erzeugt. Erste Experimente demonstrierten den vielseitigen Charakter des 3D-Pastendrucks, der direkt auf diese UHMWPE-Pasten angewendet werden konnte.

Insgesamt deuten die hier angewendeten verschiedenen Verarbeitungstechniken auf ein großes Potential hin, die erhaltenen Dispersionen mit ihren einheitlichen UHMWPE-Nanokristallen in alternativen Verfahren zur Herstellung von Materialien mit völlig neuartigen Eigenschaften zu nutzen.

Table of Contents

List of Abbreviations

Abbreviations of the 'International System of Units' (SI-Units), chemical formulae, and abbreviations of chemical groups (Me, Et, etc.) in accordance to the IUPAC (International Union of Pure and Applied Chemistry) nomenclature are not mentioned.

Equipment and Methods

ADMET	acyclic diene metathesis (polymerization)
AFM	atomic force microscopy
AUC	analytical ultracentrifugation
CDSA	crystallization-driven self-assembly
DFT	density functional theory
DLS	dynamic light scattering
DSC	differential scanning calorimetry
FDM	fused deposition modeling
GPC	gel permeation chromatography
MD	molecular dynamics (simulation)
MIVM	multi-inlet vortex mixer
NMR	nuclear magnetic resonance
ROMP	ring-opening metathesis polymerization
SAXS	small angle x-ray scattering
SEM	scanning electron microscopy
SLS	selective laser sintering
TEM	transmission electron microscopy

NMR Spectroscopy

δ	chemical shift in ppm
br.	broad
COSY	correlation spectroscopy
d	doublet
dd	doublet of doublets
hept	heptet/septet
HMBC	heteronuclear multiple bond correlation
HSQC	heteronuclear single quantum coherence

$^{n}J_{XY}$	coupling constant of atom X and Y over n bonds
m	multiplet
ppm	parts per million
q	quartet
quint.	quintet
s	singlet
t	triplet
v	virtual (multiplet)

Compounds

acac	acetylacetone
COE	cyclooctene
dba	dibenzylideneacetone
DCM	dichloromethane
DMF	dimethylformamide
DMSO	dimethyl sulfoxide
H_2N-PEG-OMe	α-methoxy-ω-amino poly(ethylene glycol)
HDPE	high density polyethylene
LDPE	low density polyethylene
LLDPE	linear low density polyethylene
MAO	methylaluminoxane
PE	polyethylene
PEG	polyethylene glycol
pTsOH	*para*-toluenesulfonic acid
Pyr	pyridine
SDS	sodium dodecyl sulfate
THF	tetrahydrofuran
TPPTS	trisodium 3,3',3-phosphinetriyltribenzenesulfonate
tmeda	N,N,N′,N′-tetramethylethane-1,2-diamine
UHMWPE	ultra high molecular weight polyethylene
X^Y	X^Y-coordinating ligand

Other Abbreviations

a.u.	arbitrary unit
BHE	β-hydride elimination

cat.	catalyst(s)
d_h	hydrodynamic diameter
equiv.	equivalent(s)
h	hour(s)
MWD	molecular weight distribution
M_n	number average molecular weight
M_w	weight average molecular weight
M_p	peak molecular weight
M_z	Z average molecular weight
M_v	viscosity average molecular weight
M_w/M_n	molecular weight distribution
min	minute(s)
n.d.	not determined
quant.	quantitative
ref.	reference(s)
r.t.	room temperature
T_m	melting temperature
TO	turnover(s)
TOF	turnover frequency
TON	turnover number
vs.	versus
wt-%	percentage by weight (solids content)

Index of Complexes

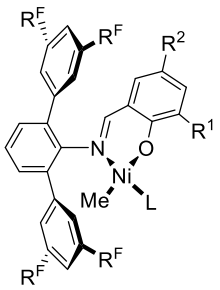

1^{I}-R^{F}/L: R^{F} = CF_3, C_4F_9, C_6F_{13} *or* C_8F_{17}
R^1 = R^2 = I

1^{Ant}-R^{F}/L: R^{F} = CF_3 *or* C_6F_{13}
R^1 = anthryl, R^2 = H

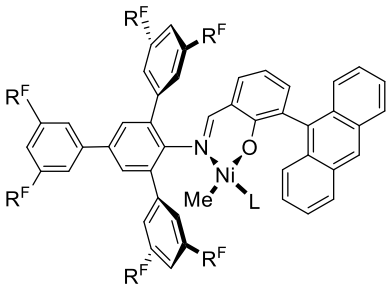

2^{Ant}-R^{F}/L: R^{F} = CF_3 *or* C_6F_{13}

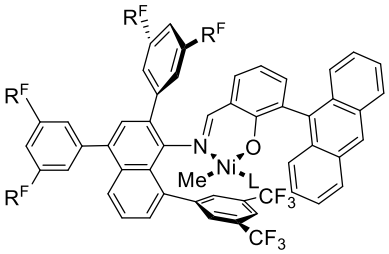

3^{Ant}-R^{F}/L: R^{F} = CF_3 *or* C_6F_{13}

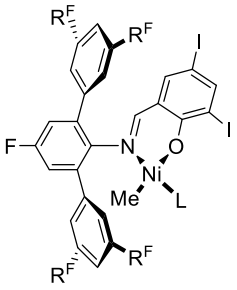

4^{I}-R^{F}/L: R^{F} = C_6F_5

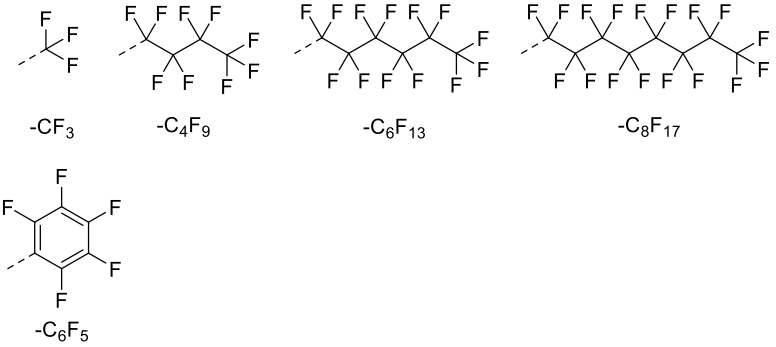

-CF_3 -C_4F_9 -C_6F_{13} -C_8F_{17} -C_6F_5

L =  *or* 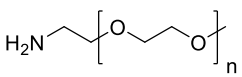 *or* 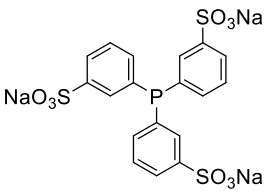

Pyridine
Pyr

H_2N-PEG-OMe
PEG

TPPTS

1 General Introduction

History and advances of our modern society are strongly based on the development of technology and materials.[1] Inspired by nature, where simple molecules are connected to highly functional macromolecular structures (e.g. polysaccharides or polypeptides), polymers have dramatically grown in importance during the 20th century.[2,3] However, the widespread and excessive use of plastics in daily consumables, respectively, the increase in solid waste generation and simultaneous lack in (utilization of) appropriate recycling technologies, has become subject of serious discussion.[4,5] Nevertheless, the increase in annual polymer demand (resins and fibers) from 90 million tons in 1985 to 381 million tons in 2015 reflects their imperative role in modern technology.[6]

Polyolefins are widely used for a broad range of different applications (>300 grades of different polyolefins are commercially available) and represent about 50% by weight of all commodity polymers.[7] Polyethylene is the simplest polyolefin, based on repeating methylene units, and accounts for at least one third of the annual plastics production.[6,8] Its physical properties (e.g. density or melting temperature) are mainly determined by the macromolecular chain architecture (e.g. molecular weight, distribution thereof, branch density, etc.), typically controlled by the polymerization method (see Figure 1.1).[9] The polyethylenes formed are typically divided into different commodity classes ranging from LDPE (low density polyethylene, used for soft materials, e.g. foils and packaging) and LLDPE (linear low density polyethylene) over HDPE (high density polyethylene) to UHMWPE (ultra high molecular weight polyethylene, used for tough and abrasive-resistant high-performance materials, e.g. medical implants).

LDPE is produced by free-radical polymerization at high ethylene pressures (> 1000 bar) and elevated temperatures (> 100 °C), resulting in formation of a highly branched microstructure (numerous short chain branches, and also long chain branches), that disturbs crystallization.[10]

Hence, LDPE shows low melting temperatures, low densities and limited mechanical strength, making it suitable for fabrication of soft materials. By contrast, catalytic insertion polymerization offers precise microstructure control during the polymerization process and allows for fabrication of almost perfectly linear polymer chains under mild reaction conditions. Nowadays, HDPE is produced by Ziegler-Natta and Phillips type early transition metal catalysts (in gas phase or in liquid hydrocarbons) and offers high crystallinity, high density and mechanical strength, suitable for more demanding applications.[11-14] By catalytic copolymerization of ethylene with α-olefins, a defined amount of short chain branches can be incorporated into the linear polymer chain to yield LLDPE with tunable crystallization and melting properties.

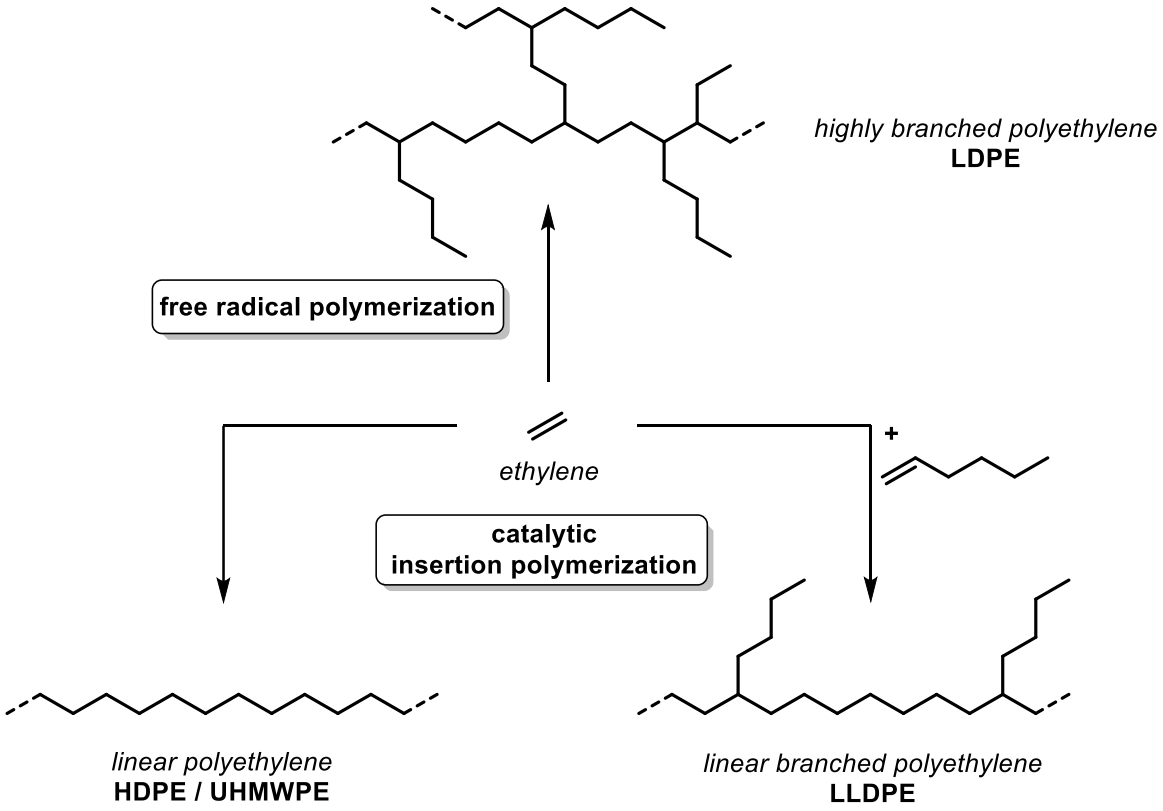

Figure 1.1. Overview of different polyethylene classes and their microstructures. Whereas LDPE is formed by free-radical polymerization, linear HDPE, UHMWPE and LLDPE are synthesized by catalytic insertion (co)polymerization.

The field of applications of polymeric materials is greatly enhanced by aqueous polymer colloids (polymer latices), produced in ten millions of tons per year and used for e.g. coatings or adhesives.[15-17] Their properties, emerging from the nanostructured character, can substantially differ from the respective bulk material.[18] Beside particle sizes and particle size distributions, the particle shape is of major importance with regard to formation of superstructures or films.[19]

The special case of anisotropic particle shapes can unlock totally unknown direction-dependent properties.[20,21] However, gaining direct influence on the particle shape during the polymerization and particle formation process is challenging, as traditional emulsion polymerization techniques mostly rely on free-radical polymerization methods with very limited control over the chain growth mechanism (and the design of polymer microstructure, respectively).[17,22] While controlled radical polymerization techniques enable the synthesis of polymers with narrow molecular weight distributions, catalytic insertion polymerization goes beyond, allowing precise chain microstructure tuning (e.g. branching or stereoselectivity). However, the compatibility of organometallic catalysts with aqueous systems is very limited.

Chapter 1.1 will introduce the concept of an aqueous catalytic insertion polymerization enabling the synthesis of crystalline high molecular weight polyethylene in the form of stable polymer dispersions. With a detailed mechanistic understanding in hand, chain growth can be promoted to an extent that UHMWPE, a material with extraordinary properties, can be formed (*chapter 1.2*). This is obtained in the unusual morphology of nanoscale single crystals of anisotropic shape created by direct crystallization of the growing chain (*chapter 1.3*). The yet unmet challenge here is to create a highly controlled chain growth process with an equally controlled particle growth to generate uniformly shaped UHMWPE nanocrystals, which are desired as building blocks for materials with well-defined properties.

1.1 Aqueous catalytic polymerization

The industrial fabrication of aqueous polymer dispersions by emulsion polymerization requires water-tolerant techniques and employs free-radical polymerization exclusively.[15,16] The control over molecular weights could be enhanced by the development of aqueous controlled free-radical polymerization methods.[23-25] Concerning aqueous free-radical polymerization of polyethylene[26], particle shapes beyond spheres[27,28] or the generation of stable dispersions in the absence of any organic surfactants[29-31] have been reported. The ill-defined microstructure control does, however, not allow to use crystallization as major structure forming principle for the generation of nanoparticles. Considering all available polymerization methods, catalytic techniques ideally address the necessity of microstructure control and profit from readily accessible and simple monomer feedstocks (e.g. ethylene or propylene).

Nowadays, traditional early transition metal catalysts are used in the form of microscopic catalyst grains for heterogeneous gas-phase olefin polymerization (Unipol process, Union Carbide; introduced in the late 1970's).[9,32] Gas-phase processes have several economic advantages (large scale, absence of liquids, etc.) and are highly flexible regarding catalyst type and (co)monomer feedstock. Polyethylene is generated on the grains' surface, leading to particles with shape and size distributions highly depending on the properties of the initial catalyst particles. In contrast to homogeneous approaches, the environment around every individual active center cannot be precisely influenced, leading to slightly heterogenous polymer structures.[33,34] This issue can be addressed by using homogeneous metallocene catalysts enabling precise polymer microstructure control with regard to e.g. stereoselective incorporation of monomer building blocks.[35-37] While a fundamental knowledge about the nature of active centers in heterogenous catalysts is still subject of current research[38-41], the basic mechanism of chain growth during insertion polymerization of olefins is well understood (proposed by Cossée and Arlmann, see Figure 1.2).[42-44]

Despite the great performance of early transition metal catalysts in olefin polymerization, their oxophilic nature strongly limits their use in alternative solvents. However, direct synthetic pathways to aqueous dispersions of catalytically produced materials are sought, but require a different catalyst design.

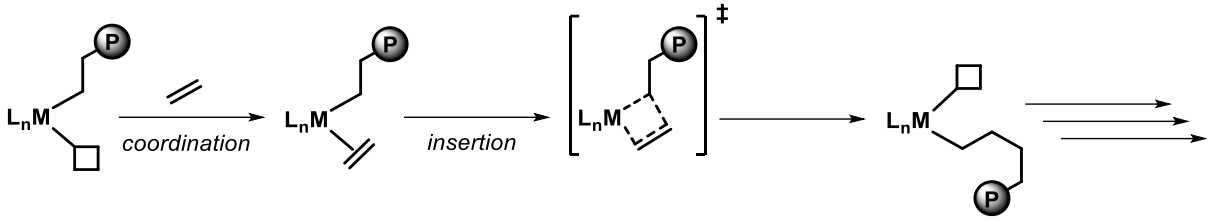

Figure 1.2. Insertion chain growth mechanism for catalytic polymerization as suggested by Cossée and Arlmann.[42-44] Chain growth occurs at the metal center, when an ethylene molecule coordinates to an empty site and inserts into the metal-polymeryl bond (catalyst activation not shown). M = metal species (e.g. Ti), L = other coordinated species (chelating ligand or solid support), P = polymer chain.

1.1.1 Late transition metal polymerization catalysis

Towards the end of the last century, catalysts with yet unmet properties and beyond the classical metallocene structure were introduced.[45,46] These post-metallocenes became increasingly common in industry.[8] Such processes mainly focused on early transition metal catalysts that are highly active and selective, but sensitive to polar compounds due to their oxophilic nature. To extend the range of accessible polymers (e.g. from catalytic copolymerization with polar comonomers) catalysts based on less oxophilic late transition metals were intensively investigated.[47-49]

However, this was a challenging endeavor as late transition polymerization catalysts show a high affinity to undergo β-hydride elimination (BHE), which competes with chain growth and leads to branch formation and chain transfer (see Figure 1.3 for mechanistic overview).[50] In detail, a species with β-agostic interactions[51] is formed after every insertion step. This allows for subsequent BHE yielding a metal hydride species with a coordinated alkene (intermediate cis/trans-isomerization steps are necessary in some cases).[52-54] This process is completely reversible. If the alkene rotates prior to reinsertion, a secondary metal-polymeryl species is formed and a methyl branch in the polymer backbone is generated, if ethylene coordinates and chain growth continues from that state (Figure 1.3, center). Longer side chains are formed by an identical mechanism with the respective number of BHEs, alkene rotations and subsequent reinsertions occurring (so-called 'chain walking'), prior to ethylene insertion and chain growth. Instead of undergoing reinsertion, the alkene can also be replaced by ethylene and a new chain is started (chain transfer; Figure 1.3, top). While experimental observations suggest that chain transfer occurs via associative displacement of the coordinated alkene with ethylene,[55] theoretical calculations are also indicative for a direct β-hydrogen transfer from the alkyl chain to the monomer.[56] A recent DFT study discussing nickel salicylaldiminato catalysts shows evidence for chain transfer occurring via coordination and direct insertion of an incoming

ethylene molecule via a five-coordinated intermediate.[53] While the detailed mechanism of chain transfer seems to be highly dependent on catalyst type and reaction conditions, the consequence is identical in all cases: chain transfer directly competes with chain growth and limits molecular weights of polymers formed.

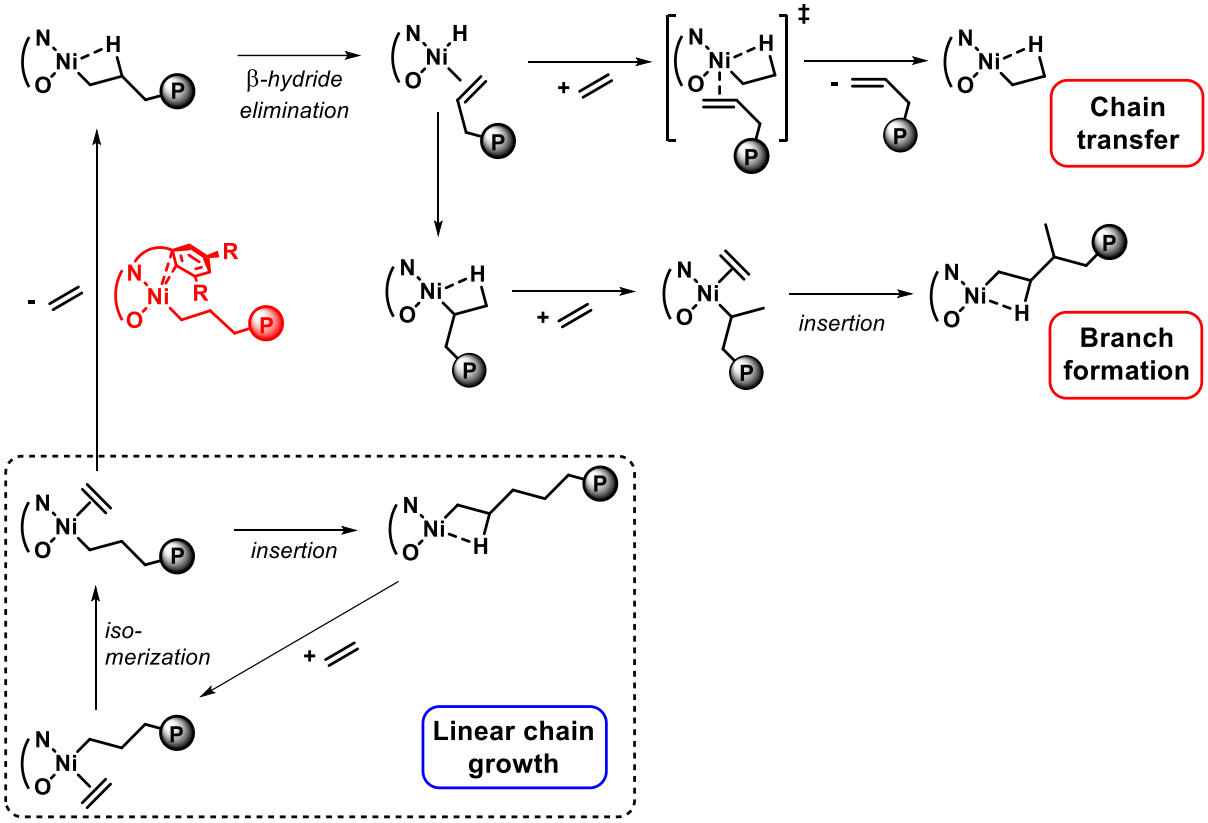

Figure 1.3. Mechanistic overview of catalytic ethylene polymerization with (*N*-terphenyl) Ni(II) salicylaldiminato catalysts.[53] Linear chain growth and β-hydride elimination (BHE) shown, leading to chain transfer and branch formation. An η^2-interaction of distal aryl rings in the ligand backbone with the active center, strongly dependent on the nature of remote substituents -R, promotes ethylene displacement and subsequent BHE (red structure, *vide infra*). N^O = (*N*-terphenyl) salicylaldiminato ligand, P = polymer chain.

This tendency of undergoing chain transfer is used as key feature in the Shell Higher Olefin Process (SHOP) to generate α-olefins by ethylene oligomerization using neutral Ni(II) complexes with chelating κ^2-(*P,O*) ligands (developed by Keim, Figure 1.4).[57,58] This process was designed to directly address the market demand for detergents and provides high quality products based on ethylene as easily available feedstock.[59] A nickel hydride species, formed by activation of the precatalyst, performs ethylene insertion and subsequent chain propagation.[60] After a limited number of ethylene molecules have been inserted, the active species undergoes BHE and chain transfer yielding the initial nickel hydride and the desired α-olefin oligomers in a Schulz-Flory chain length distribution.[61]

The development of the SHOP process demonstrated the capabilities of nickel catalysts in performing ethylene insertion chain growth on an industrial scale with, however, molecular weights far below the ones accessible by early transition metal catalysts. On the other hand, they were successfully applied in polar solvents such as ethanol, a promising perspective for new, more tolerant polymerization catalysts. By intensive ligand modifications to strongly promote chain growth over chain termination, Klabunde and Ostoja-Starzewski reported formation of high molecular weight polyethylene with κ²-(*P,O)* ligand Ni(II) catalyst systems (Figure 1.4).[62-64] A basic relation between the ligand framework and the properties of polyethylenes formed was reported.

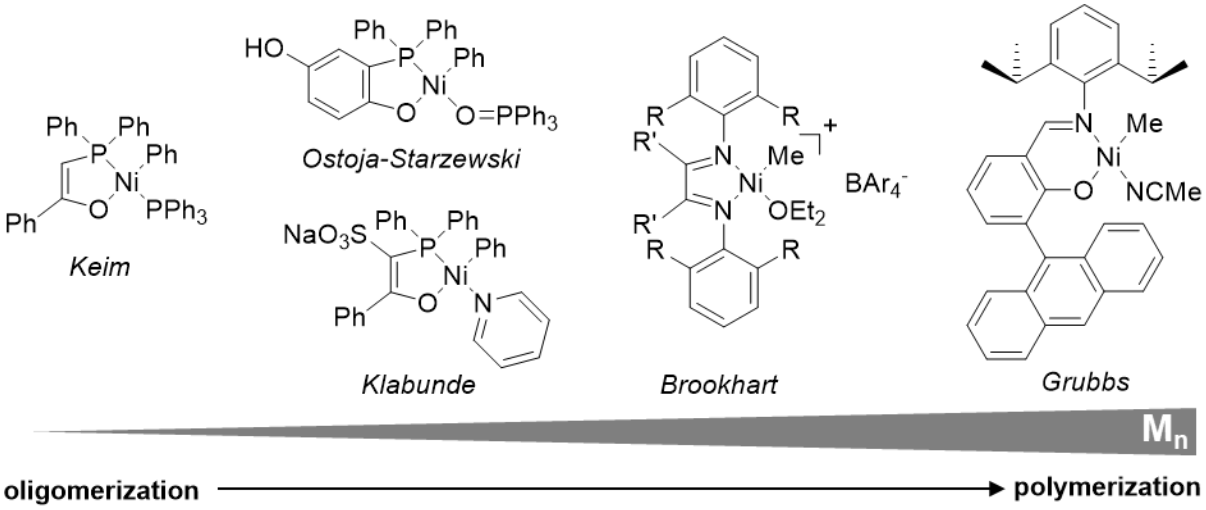

Figure 1.4. Evolution of nickel catalysts for ethylene oligo- and polymerization.[65]

Later, Brookhart and coworkers presented a series of Ni(II) and Pd(II) based cationic α-diimine catalysts (Figure 1.4).[66] These catalysts showed high rates of chain walking and produced branched high molecular weight polyethylenes of $M_n > 10^5$ g/mol.[55,67] They required activation of the initial nickel dimethyl species with strong acids bearing weakly-coordinating anions (or activation by alkylation of an initial nickel dibromide species with MAO).[68] Branching could be strongly controlled by the ligand structure and polymerization conditions (e.g. branch contents were found to increase with polymerization temperature).[69] By increasing the steric bulk in the α-diimine ligand backbone, branching could be effectively suppressed, while an increased steric bulk in the axial position of the active center led to a substantial increase in molecular weights (by blocking the axial approach of ethylene to initiate chain transfer).[55,69,70] Brookhart, Daugulis and coworkers recently revealed the impact of different ligand backbone conformations on chain growth, switching from catalytic production of oligomers to UHMWPE under otherwise identical conditions.[71] Further development of those α-diimine catalyst systems[72] enabled

copolymerization with polar comonomers (e.g. acrylates)[73-79], living polymerizations[80-82], chain transfer polymerizations[83,84], synthesis of (functionalized) UHMWPE[85-87], α-olefin homo-polymerization[88-90] or addressed the yet unmet challenge of copolymerizing internal olefins.[90-92]

Inspired by Brookhart's findings and the robust heteroatomic κ²-(*P,O*) SHOP catalysts, Grubbs and coworkers (and simultaneously Johnson at DuPont) introduced a new class of neutral nickel salicylaldiminato complexes based on κ²-(*N,O*) ligands (Figure 1.4).[93-95] Initial experiments described the formation of high molecular weight polyethylene of $M_n > 10^5$ g/mol and linearities of ~ 20-50 branches per 1000 carbon atoms.[93] Molecular weights and polymer microstructures were strongly affected by the substituents in 3,5-position of the former salicylaldehyde. Further, a scavenger (e.g. $[Ni(COD)_2]$ or $B(C_6F_5)_3$) was required to remove the phosphine ligand during catalyst activation, unless the substituent in 3-position was bulky enough to force dissociation of the phosphine.[54,94] The bulkiness further hampered formation of an inactive bis-chelated species (two salicylaldiminato units coordinated to one nickel center) and demonstrated the importance of sterics on catalyst stability and activity.[94,96] While enhanced activities were observed at elevated temperatures, molecular weights decreased and branch contents increased due to an accelerated rate of BHE. By applying a more labile ligand (e.g. acetonitrile, instead of a phosphine), these catalysts could be employed as true single component systems without any cocatalyst or scavenger needed.[94] They were also active in copolymerization with functional comonomers or α-olefins, and in polymerization of norbornene.[97-100] Selected examples were able to incorporate radicals, or to polymerize ethylene and acrylates in a dual radical/catalytic pathway (migratory insertion polymerization of acrylates was found to be challenging, however[101,102]).[103-105]

After initial studies with Ni(II) salicylaldiminato catalysts revealed the role of sterics and electronic influences on the active center,[106] this group reported in 2004 a new generation of catalyst types bearing a *N*-terphenyl substitution with remarkable properties (Figure 1.5, left).[107,108] The rate of BHE and subsequent reactions could be precisely tuned by the electronic character of groups in selected positions of the terphenyl moiety's outer phenyl rings, far away from the active metal center (Figure 1.5, center). When electron-donating groups (e.g. $-CH_3$, $-OCH_3$) were present, hyperbranched oligomers were formed.[107,109] By strong contrast, linear and high molecular weight polyethylene was produced, when electron-withdrawing groups were placed in those remote positions (e.g. $-CF_3$, $-NO_2$, $-SF_5$).[107,110,111] Surprisingly, the productivity of the respective catalyst system was not significantly altered by this remote substituent effect and steric aspects played only a minor role.[109] Experimental data suggested that the polymer's

microstructure is mainly dependent on the electronic character of the substituents, rather than on their position.[112,113]

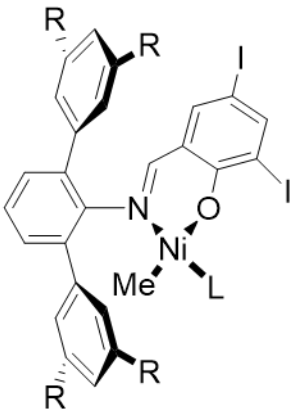

R	M_n [10^3 g/mol]	branches/ 1000 C
$-CH_3$	2	80
$-CF_3$	175	3
$-NO_2$	215	2
$-SF_5$	303	1

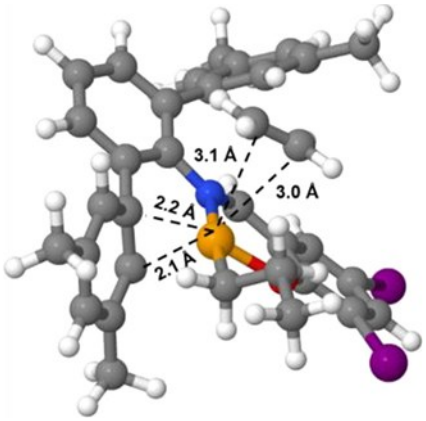

Figure 1.5. *Left:* structure of *N*-terphenyl Ni(II) salicylaldiminato catalysts with remote substituents R influencing the outcome of catalytic polymerization (L = labile ligand, pyridine). *Center:* molecular weights and branch contents of polyethylenes produced with respective catalysts bearing different remote substituents R under otherwise identical conditions (40 bar ethylene pressure, 30 °C reaction temperature, in toluene).[110,111] *Right:* 3D transition state geometry of a nickel-polymeryl species (R = CH_3, after ethylene displacement) with η^2-interactions between the metal center and distal aryl rings highlighted (see also Figure 1.3, red structure).[53] Adapted with permission from the American Chemical Society (*J. Am. Chem. Soc.* **2018**, *140*, 1305–1312, Copyright 2018).

Recent DFT studies revealed a weak interaction between the distal phenyl rings and the nickel center to be responsible for the observed effect by promoting decoordination of ethylene and subsequent BHE (Figure 1.5, right).[53] Electron-withdrawing substituents in remote positions weaken these interactions leading to a removal of electron density from the metal center, as shown by electrochemical measurements and solid-state X-ray crystal analysis. An interaction between fluorine atoms of the remote substituent and the growing chain[114], as suggested for early transition metal catalysts[115-117], is clearly not operative, as evident from experiments with catalysts bearing electron-withdrawing non-fluorinated NO_2 groups in remote positions.[110] A study of Ma and coworkers, where fluorine atoms were placed in selected positions of the outer phenyl rings, suggested a Ni-F interaction in some cases with, however, no significant impact on the polymer microstructure.[112] Several examples for catalyst systems using weak interactions between neighboring groups and the active center to influence the polymer microstructure were recently presented.[53,118-124]

In contrast to *N*-terphenyl Ni(II) salicylaldiminato systems, catalysts bearing functionalized *N*-naphthyl moieties, as introduced by the groups of Brookhart and Daugulis, strongly focus on steric aspects (Figure 1.6).[125,126] By placing phenyl rings in 2- and 8-postion of the naphthyl moiety and an 9-anthryl functionality at the 3-position of the salicylaldehyde, a highly efficient shielding

of the active center was achieved. The catalyst was able to perform BHE and subsequent branch formation, but no chain transfer as axial coordination of ethylene and dissociation of the polymeryl-olefin in an associative exchange mechanism was hindered. In direct consequence, highly efficient chain walking catalysts were created that were capable of producing branched UHMWPE in a living polymerization in toluene and in coordinating solvents (e.g. THF, diethyl ether).[125] Recently, the same groups reported a new catalyst structure bearing two substituted naphthyl moieties for more extensive axial shielding (see Figure 1.6, right), enabling formation of UHMWPE exceeding $M_n > 4 \times 10^6$ g/mol ($M_w/M_n = 1.2$).[127]

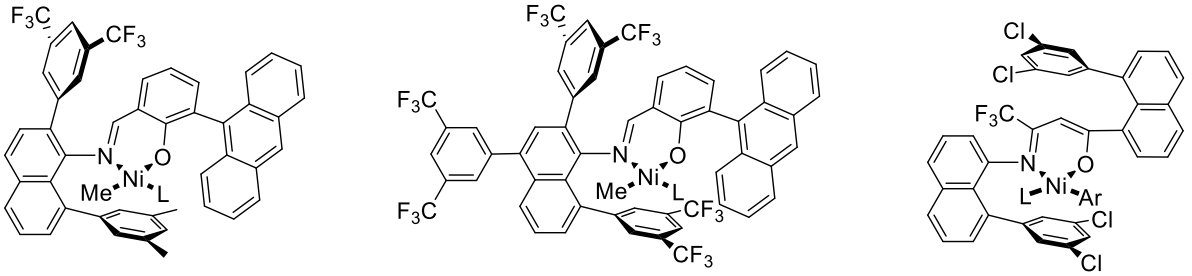

$M_n = 1.3 \times 10^6$ g/mol
$M_w/M_n = 2.4$
in toluene
Brookhart, Daugulis (2015)

$M_n = 1.1 \times 10^6$ g/mol
$M_w/M_n = 1.2$
in THF
Mecking (2018)

$M_n = 4.1 \times 10^6$ g/mol
$M_w/M_n = 1.2$
in toluene
Brookhart, Daugulis (2020)

Figure 1.6. Chemical structures of different *N*-naphthyl type salicylaldiminato Ni(II) catalysts providing access to UHMWPE in different solvents (L = labile ligand).[125-127]

In addition to the chelating salicylaldimine, also the labile ligand, coordinated to the metal center in the precatalyst, has a remarkable influence on the polymerization outcome. While highly labile ligands (e.g. L = tmeda) afford very active catalysts, their counterparts with strongly coordinating ligands (e.g. L = 2,6-lutidine) are polymerization inactive and do not decompose for hours even when exposed to air.[128-130] These ancillary ligands (or a coordinating solvent) can also alter polymer microstructures and molecular weights by re-coordination during polymerization to form a 'dormant state' that can provide additional pathways for cis/trans-isomerization and subsequent BHE.[131]

Beside the examples described here, many other important types of late transition metal catalysts for generation of high molecular weight polyolefins were developed during the last decades (e.g. Drent type catalysts[132-134], anilinotropone systems[135-138] or binuclear/bimetallic catalysts[139-147]). They all were conducive to establish a picture of nickel catalysts providing access to a broad variety of different polymer structures and molecular weights. Several examples of such catalysts producing UHMWPE were recently reported.[85-87,111,125-127,148-151]

1.1.2 Catalytic polymerization in biphasic systems

Water as reaction medium offers several advantages such as non-toxicity, natural abundance and non-inflammability, just to name a few.[152] Several industrial biphasic aqueous processes have been implemented to effectively separate (and recycle) catalysts and products, with SHOP or hydroformylation reactions being prominent representatives.[59,153-156] Catalytic polymerizations of olefins in aqueous media afford a broad variety of different polymer types but are restricted to tolerant late transition metal catalyst systems.[157,158] First suspension polymerizations in water with α-diimine catalysts[159-161] or SHOP-type κ^2-(*P,O*) catalysts[160,162,163] generated polyethylene of comparable properties to polymers produced in organic media. The even more tolerant, neutral salicylaldiminato catalysts remained mostly unaffected from addition of small amounts polar and protic compounds to the reaction mixture.[94] Hence, they were intensively tested in polymerizations in polar media and alternative solvents, such as carbon dioxide.[164,165] Experiments in mixtures of water and acetone, toluene or pentane provided high molecular weight polyethylene in a suspension polymerization.[162] While the presence of water significantly reduced catalyst lifetimes (*vide infra*), a direct impact on chain transfer or branch formation was not observed.

Concerning the aqueous reaction environment, a direct polymerization to stable polyethylene dispersions would be highly desirable. Hence, several catalytic polymerization techniques in aqueous emulsion were developed.[22] Stable polyethylene dispersions (particle sizes of ~ 300 nm) were obtained when the complex, dissolved in a small amount of hydrocarbon, was emulsified by ultrasound in an aqueous surfactant solution and the resulting reaction mixture subsequently pressurized with ethylene.[166] These particles exhibited an unique lamella structure, as every submicron droplet crystallized individually and independently.[167]

Enhanced catalytic activities in the formation of high molecular weight polyethylenes were observed when binuclear catalysts were used.[128] Copolymerization of ethylene with 1-butene and norbornene (and polymerization of the respective homopolymers) under aqueous conditions afforded high molecular weight (co)polymers with precisely tunable microstructures (and crystallinities).[168,169] Catalytic ethylene emulsion polymerization and subsequent free-radical polymerization of styrene or butyl acrylate afforded colloidally stable multi-phase latices.[170] Organic/inorganic nanocomposite particles were obtained by polymerization in the presence of functionalized silica particles.[171]

In a recent approach, initial catalyst emulsions were prepared by using a multi-inlet vortex mixer (MIVM).[130] The MIVM allowed for rapid mixing in the turbulent regime and was

previously employed to e.g. form conjugated polymer nanocomposites.[172,173] The hydrophobic catalyst precursor was dissolved in a polar organic solvent and rapidly mixed with an aqueous surfactant solution, followed by ethylene pressurization, which led to immediate polyethylene formation within the droplets. The obtained dispersions consisted of (minimally-)entangled, high molecular weight polyethylene in the form of multi-lamellar platelets. A set of several solvents and catalysts was benchmarked and demonstrated the MIVM technique to be promising in the formation of sub-micron particles.

1.1.3 Water-soluble catalysts and nanocrystal formation

The synthesis of very small polyethylene nanoparticles (< 50 nm) requires a highly dispersed state of the catalyst in the initial the reaction mixture. This was achieved by starting from catalyst microemulsions[174], or with hydrophilic catalyst precursors.[175] Such hydrophilic Ni(II) *N*-terphenyl salicylaldiminato catalysts, which were rendered water-soluble by the labile ligand (L), were prepared and used for aqueous ethylene polymerization experiments (see Figure 1.7).[176,177]

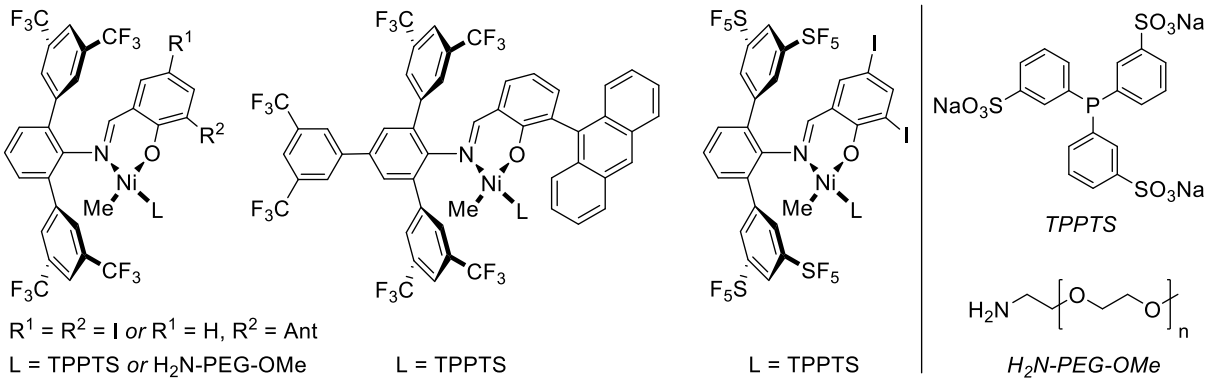

Figure 1.7. *Left:* chemical structures of water-soluble Ni(II) salicylaldiminato catalysts used for generation of polyethylene nanocrystals.[177] *Center:* catalyst capable of producing 'ideal polyethylene nanocrystals'.[178] *Right:* pentafluorosulfanyl-substituted catalyst yielding UHMWPE dispersions.[111]

Immediate dissolution of the catalyst precursor when water and surfactant were added at room temperature were indicative for formation of a homogenous catalyst solution. This is decisive for a subsequent undisturbed particle growth process, without any agglomerated active species being present. Upon pressurization the labile ligand is displaced by ethylene, forming the active species that is hydrophobic and effectively stabilized by adsorbed surfactant (see Figure 1.9).[178,179] The growing chain immediately nucleates and deposits in a highly ordered fashion on the crystal's growth front leaving no opportunity for any disorder (the rate of crystallization is much faster than chain growth).[178] Thus, highly ordered polyethylene particles

are formed, which are in fact single crystals (see *chapter 1.3* for details on the nanocrystals' structure).[180] DLS studies revealed a very small particle size of ~ 10 nm, evident for a particle formation mechanism where the active sites do not interfere with each other and can generate single particles (which consisted of several chains, however).

By optimizing the catalyst's structure (Figure 1.7, center) and process parameters, polymerization in aqueous surfactant solution at 10-15 °C afforded 'ideal polyethylene nanocrystals' with crystallinities of $\chi > 90$ % (according to DSC; $M_n > 4 \times 10^5$ g/mol, $M_w/M_n = 1.4$; < 0.7 branches per 1000 carbon atoms).[178] The particle shapes were found to be hexagonal platelet-like, evolving to lozenge shaped platelets with increasing lateral sizes (see Figure 1.9 and *chapter 1.3*).[179,180]

However, polymerization activities were quickly ceasing within 1 hour reaction time, pointing to significant catalyst deactivation. NMR studies with the respective dmso-coordinated catalyst precursors in DMSO/D_2O mixtures suggested bimolecular reductive coupling between two nickel alkyl species to be the dominant deactivation pathway, while hydrolysis[181] of nickel alkyls with D2O was negligible under these conditions (see Figure 1.8 for reaction schemes).[182]

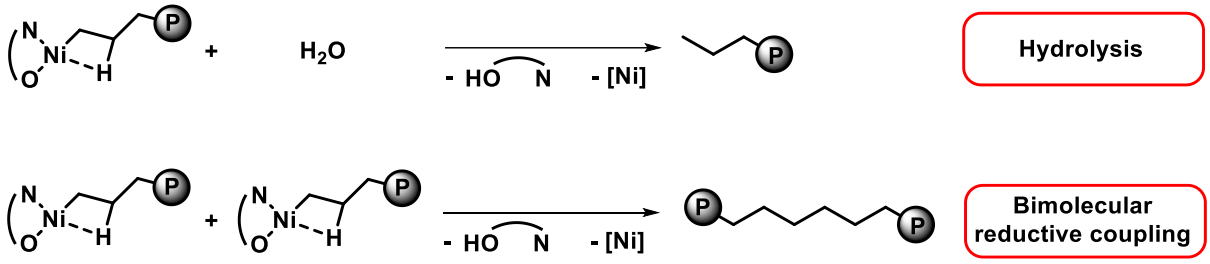

Figure 1.8. Hydrolysis and bimolecular reductive coupling as possible side reactions in aqueous catalytic ethylene polymerization (immediate decomposition of eventually formed bis-chelated nickel species in water is assumed).[179,181,182] N∩O = salicylaldiminato ligand, P = polymer chain.

By strong contrast, short-time polymerization experiments with ^{13}C-labled catalyst precursors and subsequent polymer end group analysis by NMR spectroscopy revealed that bimolecular reductive coupling is only relevant in early polymerization stages, while hydrolysis is clearly the dominant deactivation pathway under true pressure reactor conditions in H_2O.[179] During hydrolysis, the catalyst decomposes and saturated polymer chain ends are formed, prohibiting re-insertion and continued growth. As a direct consequence, every hydrolysis reaction reduces the amount of active species and broadens molecular weight and particle size distributions (formation of 'dead chain ends/particles'). In identical polymerization experiments performed in D_2O, reduced catalytic activities were retained for more than 24 hours (the reason for the reduced polymerization rate in D_2O compared to H_2O remained unclear).[179] A

pronounced isotope effect affecting the autodissociation behavior of D_2O vs. H_2O was assumed to be responsible for the enhanced catalyst lifetimes.

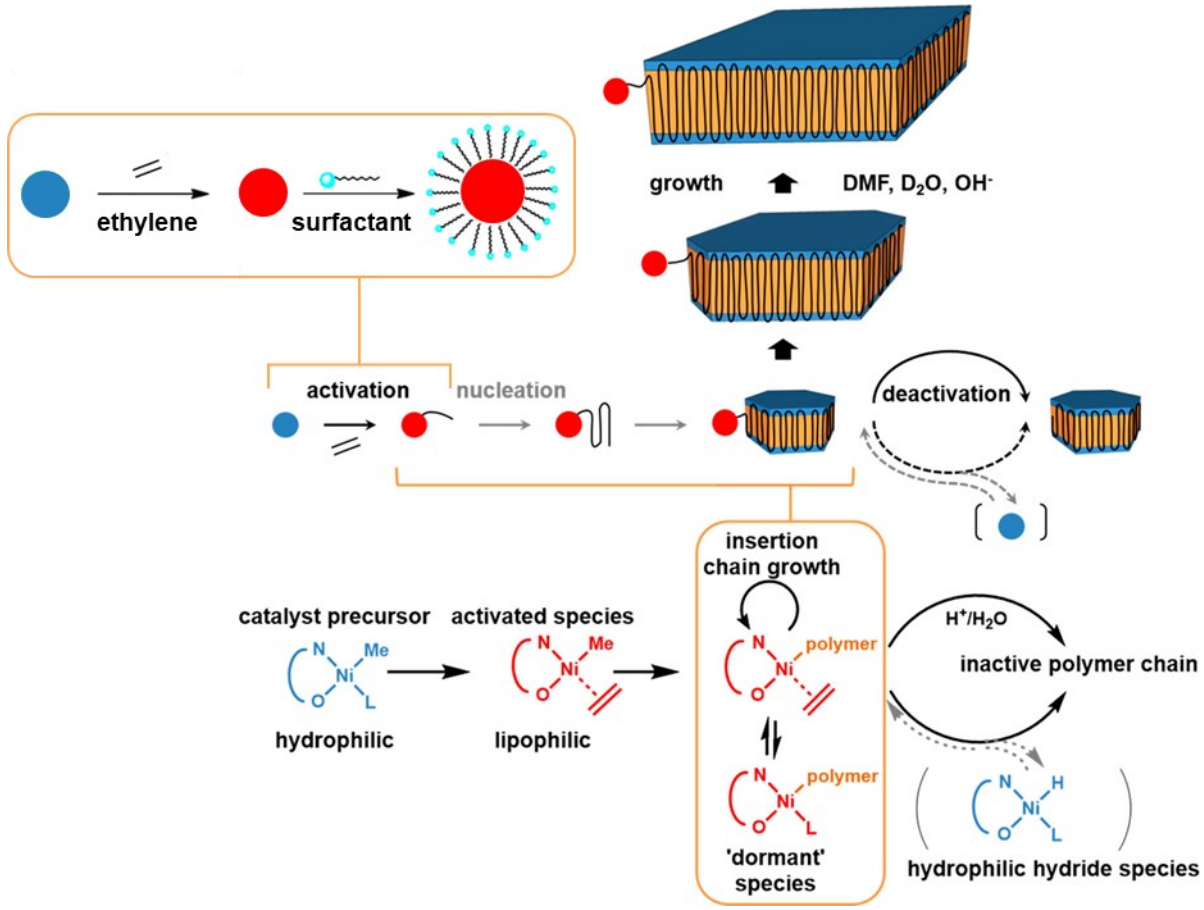

Figure 1.9. Particle formation mechanism in aqueous catalytic ethylene polymerization including catalyst activation, chain/particle growth and deactivation (hydrolysis).[179] Adapted with permission from the American Chemical Society (*Macromolecules* **2016**, *49*, 8825–8837; Copyright 2016, CC BY license).

To investigate the role of species formed from $2H_2O \rightleftarrows H_3O^+ + OH^-$, the pH of the reaction mixture was varied.[179] While the catalyst immediately decomposed under acidic conditions, catalytic activities and lifetimes were strongly enhanced in basic media (pH = 12.5; addition of cesium hydroxide) yielding 7 wt-% polyethylene dispersions of linear, high molecular weight polyethylene ($M_n > 7 \times 10^5$ g/mol; $M_w/M_n = 1.2$; < 1 branch per 1000 carbon atoms). Accordingly, acidic protonolysis of the active species was identified as main deactivation pathway (see Figure 1.9 for mechanistic overview). Other than that, chain growth was found to be mostly unaffected by chain transfer and termination under basic conditions (ca. 2 chain transfers events per nickel center in 60 minutes). Addition of basic, weakly coordinating compounds (like DMF) significantly increased catalyst lifetimes by reversible coordination to the active species (at an expense of polymerization rate, however).[179] Generally, the precursor complexes were not significantly sensitive to water as experiments with 30 minutes pre-exposure to an aqueous

surfactant solution prior to ethylene pressurization did not show any differences in reactivity.[179] When the surfactant was added to an aqueous solution of catalyst precursor after 30 minutes pre-exposure, very large lozenge-shaped particles were obtained after short reaction times indicating aggregation of nickel species before polymerization.[179]

To further promote chain growth over chain transfer and branch formation, highly electron-withdrawing pentafluorosulfanyl (-SF_5) groups were placed in remote positions of the catalyst structure (Figure 1.7, right).[111] This enabled generation of narrow dispersed UHMWPE (M_n = 1.4 x 10^6 g/mol, M_w/M_n = 1.2) in the form of aqueous dispersions. DSC studies revealed a very low entangled and highly crystalline structure (χ > 75 %) of the polymer formed.

Concerning palladium catalysts, polymerization of ethylene in water was tested with water-soluble κ^2-(*P,O*)-phosphinesulfonato catalyst systems exhibiting overall performances lower than those of the nickel systems described herein.[183,184] However, generation of anisotropic lentil-shaped particles in a new aqueous polymerization approach was recently presented by Guironnet and coworkers.[185]

The finely dispersed character, the high functional group tolerance of the catalysts employed, and the relatively high polymer solids content accessible make the polyethylene nanocrystal dispersions interesting candidates as material precursors. Nanocomposite particles of polyethylenes with various microstructures were obtained by using catalyst precursors with different remote substituents in a two-step polymerization approach.[186] The particles created during the first step acted as seed to subsequently form multi-phase particles in the second step. Polymerization in water and in presence of graphene yielded conductive graphene-polyethylene composites.[187] The small size of the nanocrystals allowed for homogenous distribution of graphene within the polymer matrix, enabling high conductivities and enhanced material properties. A direct and covalent functionalization of the polyethylene nanocrystals was achieved by copolymerization with carbohydrate-comonomers in water, and led to formation of self-stabilizing particles with the functional groups located on the particle surfaces.[188]

1.2 Ultra high molecular weight polyethylene (UHMWPE)

The extraordinary high chain length of ultra high molecular weight polyethylene (UHMWPE, typically referred to $M_n > 10^6$ g/mol) leads to outstanding physical and mechanical properties, when compared to lower molecular weight HDPE (e.g. in wear resistance or mechanical strength; see Figure 1.10).[9,189] Most notable are its extreme toughness, abrasion resistance, lubricity and chemical inertness. These characteristics make it an excellent engineering material for industrial applications, such as pickers for textile machineries or siding for ships (> 90 % of UHMWPE produced is used by industries).[190] UHMWPE is also applied in orthopedics as bearing material in artificial joints (~ 3 million joint replacement procedures are conducted per year, most of them incorporate UHMWPE), or is fabricated to ultrastrong fibers for bulletproof wests, sails and ropes.[190-194]

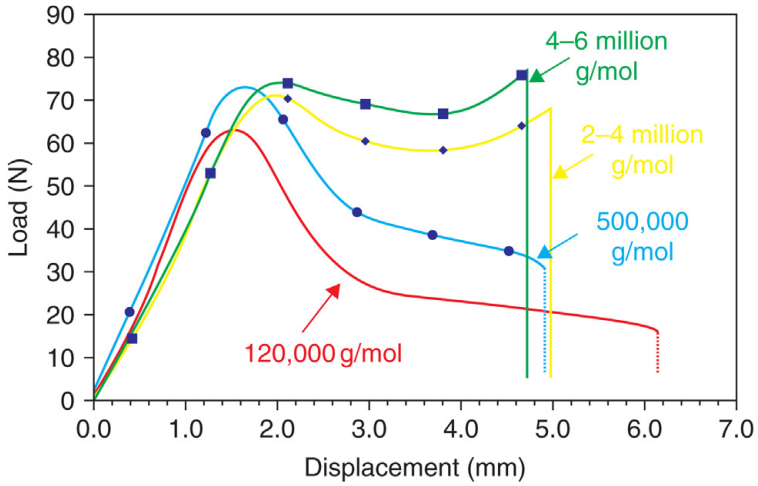

Figure 1.10. Small punch test of polyethylenes differing in their molecular weights (conducted at room temperature and a rate of 0.5 mm/min).[195] The biaxial drawing behavior of polyethylene is strongly molecular weight dependent. Reprinted with permission from Elsevier (Kurtz, S. M. in *UHMWPE Biomaterials Handbook* **2016**, Copyright 2016).

Caused by the high chain lengths, several individual polymer chains can be part of several crystalline lamellae, connecting them as tie molecules (Figure 1.11). Formation of chain entanglements between adjacent chain segments further increases those physical bindings. Molecular modeling and rheological measurements of bulk material suggest the presence of several entanglements per individual polymer chain (molecular weight of ~1200 g/mol between single entanglements).[196,197] Hence, considering the high molecular weight of UHMWPE, chain dynamics are strongly affected by entanglements leading to highly viscous polymer melts (according to $\eta_0 \sim M^{3.4}$; η_0: melt viscosity, M: molar mass)[198]. An increase in molecular weight by a factor of 10 accounts for an increase in zero shear viscosity of a factor 1000.[199] By contrast,

UHMWPE without any entanglements shows similar melt-processability as HDPE.[200] As UHMWPE exhibits a rather complex structural behavior and mechanical properties, molecular modeling is used to understand and predict e.g. its elasticity behavior or chain conformations.[201,202]

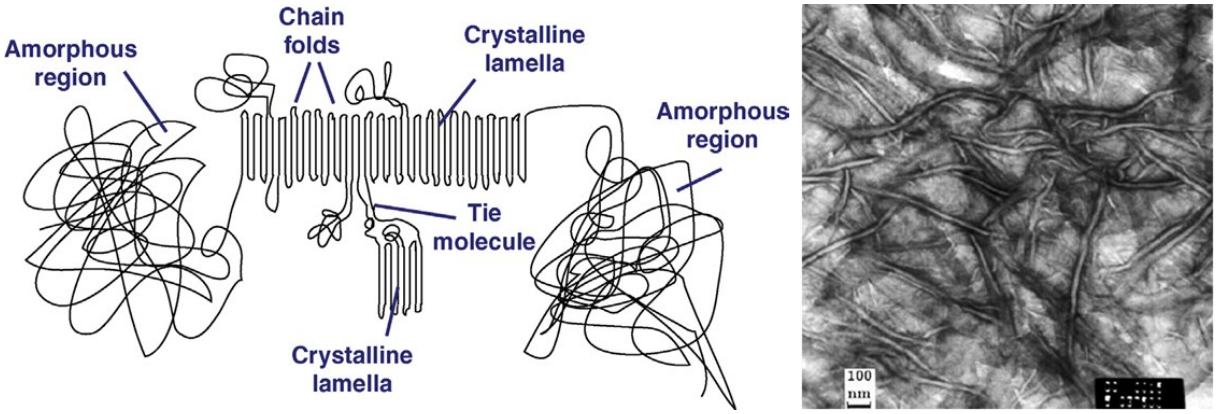

Figure 1.11. *Left:* illustration of a single UHWMPE chain in bulk, that can be part of several different morphologies (conformations involving adjacent chains, e.g. entanglements, not shown).[190] *Right:* TEM micrograph of UHMWPE showing amorphous and crystalline regions (lamellae).[190] Reprinted with permission from Elsevier (Kurtz, S. M. in *UHMWPE Biomaterials Handbook* **2016**, Copyright 2016).

1.2.1 Synthesis and processing of UHMWPE

Synthesis of UHMWPE requires catalysts performing very high rates of chain propagation relative to chain termination, allowing for the generation of the desired chain lengths.[81,203,204] Phenoxy-imine (FI) type titanium catalysts are promising candidatesforn producing UHMWPE.[205-207] Key here is a metal-fluorine interaction, which enables a living polymerization of olefins that provides very high molecular weight polymers with narrow molecular weight distributions.[115-117] Such catalysts are especially used for generation of disentangled UHMWPE through polymerization in diluted solution (*vide infra*).

Polymerization of UHMWPE on an industrial scale was commercialized by Ruhrchemie (later known as Ticona, Hoechst and now Celanese) in the 1950's.[195] Nowadays, most processes rely on classical Ziegler-Natta catalyst systems in a slurry phase process.[208] But also homogenous metallocenes are used by lower capacity manufacturers. Design of such processes is highly challenging as chain termination, e.g. in presence of an excess of aluminum alkyls via chain transfer, must be avoided. The solvent must be highly efficient in heat and mass transfer and impurities in the obtained polymer must be very limited (with respect to medical applications). The various grades of UHMWPE produced are usually classified by their average molecular weights and purities (e.g GUR resins by Celanese[209] or MG resins by DSM).[195]

The high melt viscosity of the very long entangled polymer chains (*vide supra*) makes processing difficult and requires well-designed methods. UHMWPE is usually obtained as powder (Figure 1.12, left) and requires consolidation/compaction below the melting point by careful combination of pressure, temperature and time prior to further processing (Figure 1.12, center).[210,211] During consolidation, the UHMWPE chain segments in adjacent particles start to intermingle ('intergranular diffusion'), promoted by the high pressures and temperatures.[195,212] Nevertheless, the original granular and crystalline structure stays intact and substantially influences the properties of the consolidated material by formation of grain boundaries and defects.[213,214] Further machining consists of milling and turning operations to obtain the desired 3D object and finish surfaces (Figure 1.12, right). Medical applications require subsequent sterilization by gamma irradiation or by treatment with ethylene oxide.[215]

Figure 1.12. Typical processing steps to manufacture UHMWPE components.[195] *Left:* UHMWPE resin powder. *Center:* semi-finished rods that have been consolidated from the resin powder. *Right:* machining of the UHMWPE rods on a lathe. Reprinted with permission from Elsevier (Kurtz, S. M. in *UHMWPE Biomaterials Handbook* **2016**, Copyright 2016).

UHMWPE rods in sizes between 20 mm and several centimeters can be obtained by ram extrusion of powder (Figure 1.13).[195] The UHMWPE powder is fed into a heated extruder equipped with a reciprocating ram. The back pressure of the already molten material and the ram maintain a constant pressure on the material. Beyond the outlet, the rods are gradually cooled down allowing for overall production rates of several millimeters per rod per minute. Isotactic pressing of such rods at elevated temperatures and pressures results in the formation of extended-chain crystallite morphologies, exhibiting thick lamellae structures and high crystallinities (commercialized as Hylamer by DuPont).[216] This high-pressure crystallization process can increase the crystallinity of polyethylene to up to 99 %.[217,218] Compression molding of UHMWPE between two heated plates yields sheets with lateral dimensions up to several meters and thicknesses of 30 – 80 mm.[195,219] The processing time can take up to 24 hours and the obtained sheets are usually directly cut into their final shape.

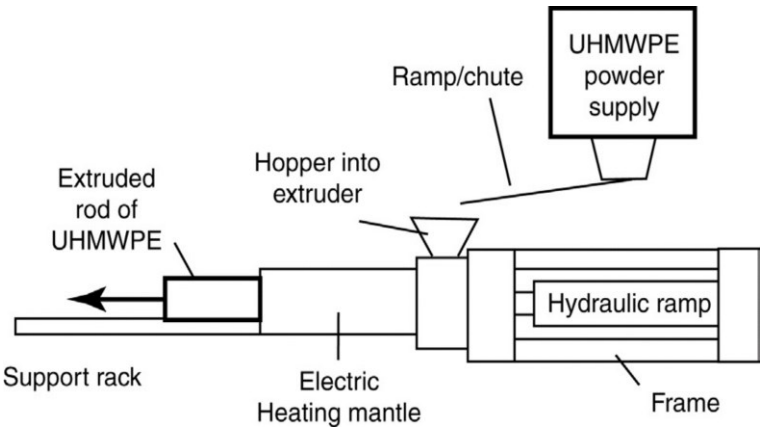

Figure 1.13. Schematic illustration of a ram extruder.[195] Reprinted with permission from Elsevier (Kurtz, S. M. in *UHMWPE Biomaterials Handbook* **2016**, Copyright 2016).

A large share of UHMWPE is fabricated to fibers. They can be woven or knitted into outstandingly strong ropes, nets or textiles (e.g. for bulletproof wests, sailing and commercial fishing; see Figure 1.14).[193] UHMWPE fibers are produced by so-called 'gel-spinning', whereby a UHMWPE solution is extruded through a spinneret and drawn in hot state to orient the polymer chains parallel to the fiber direction (see *chapter 7.2.2* for detailed description of the gel-spinning process, and Figure 1.14). This uniaxial orientation dramatically contributes to their high modulus and strength, which is substantially higher than that found for UHMWPE bulk material.[220] Such fibers are commercialized by DSM as Dyneema® (and by Honeywell as Spectra®), in different linear densities, colors and purities.[221,222]

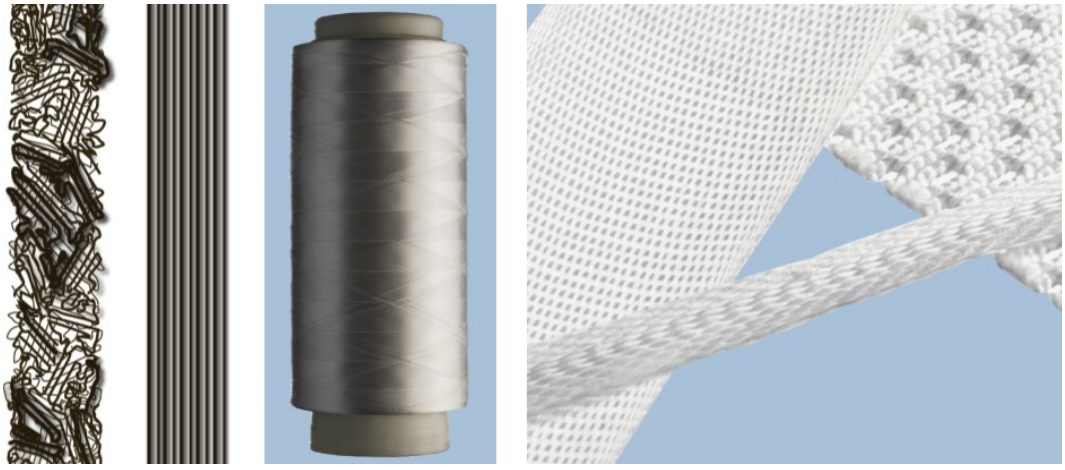

Figure 1.14. *Left:* macromolecular orientation of UHMWPE chains prior and after drawing to obtain high modulus properties.[193] *Center:* braided UHMWPE sutures (Dyneema® Purity).[193] *Left:* two-dimensional weaves made of UHMWPE (Dyneema® Purity fibers).[193] Adapted with permission from Elsevier (Siskey, R. *et al.* in *UHMWPE Biomaterials Handbook* **2016**, Copyright 2016).

The anisotropic material structure in UHMWPE fibers creates a very beneficial strength-to-volume ratio (Figure 1.15). The oriented and straight polymer chain conformation results in high

levels of crystallinities and tensile strengths, while elongation at break remains low.[193,223] Accordingly, UHMWPE fibers are very fatigue resistant and, however, sensitive to creep and relaxation under long-term strain/stress.[223] Considering the chemical inertness of polyethylene, UHMWPE fibers are very useful for medical applications.

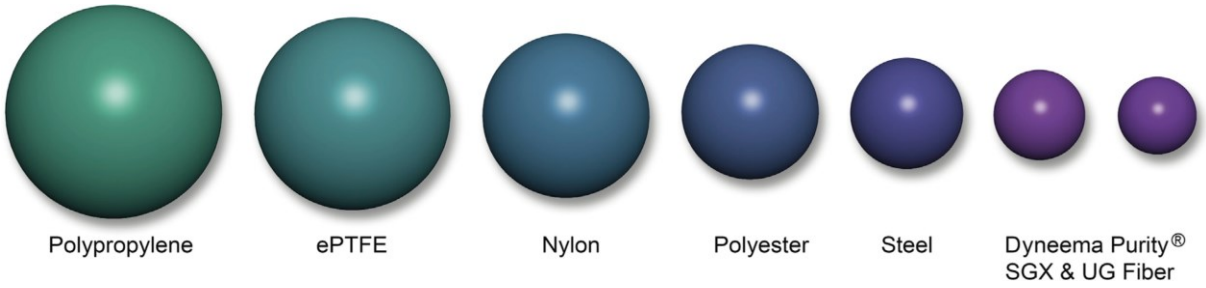

Figure 1.15. Reduction of fiber profiles of different materials.[193] Fibers of these materials in the given diameter would have an identical strength (Dyneema Purity® fibers consist of UHMWPE). Reprinted with permission from Elsevier (Siskey, R. *et al.* in *UHMWPE Biomaterials Handbook* **2016**, Copyright 2016).

Composites of UHMWPE to enhance its properties are usually obtained by blending with other materials prior to consolidation. In the special case of UHMWPE, two forms (bulk and fiber) with very different properties are available and allow for generation of homocomposites (also known as 'self-reinforced' composites). Both, sintering of several bundled oriented fibers, and reinforcement of a powder-matrix with fibers have been investigated.[224,225] It was hypothesized, that the identical chemical composition and crystallization behavior of both materials strongly promotes their compatibility, with the fibers keeping their original and unique molecular orientation during processing.[220,226] Accordingly, strongly improved material strength and creep resistance were reported, when 8 wt-% fibers were embedded in a UHMWPE matrix.[226]

Beside self-reinforcement, UHMWPE composites with different filler materials were developed for aerospace, industrial and biomedical applications.[227] Carbon fiber reinforced UHMWPE was introduced in the 1970's and considered for orthopedic implants (with, however, catastrophic results in clinical studies).[228] By contrast, modern carbon composites (with carbon nanotubes or graphene) represent promising materials due to their mechanical and direction-depended properties.[229-233] Furthermore, composites of UHMWPE with ceramics, glass, metals, clay or natural fillers have been developed.[227] As example for the latter case, UHWMPE was reinforced with hydroxyapatite nanoparticles for bone replacements.[234,235]

Cross-linking of polymer chains by radiation (gamma and electron beam) is conducted to further increase wear and oxidative resistance of UHMWPE.[236] Ionizing radiation cleaves C-H and C-C bonds, leading to cross-linking via free-radical recombination. The emerging structure

can be further influenced by the irradiation temperature.[237] Mainly two different processes are used: (1) annealing and irradiation, and (2) melting during/after irradiation.[238,239] Thermal treatment is necessary as the generated free radicals can be trapped in the crystalline domains. Heating above the melting point eliminates crystalline parts and substantially increases chain mobility to support radical recombination. However, the polymer microstructure is heavily altered and nascent crystalline properties, emerging from the polymerization process, are lost. Irradiation below the melting point (annealing) is much less effective but preserves the crystalline structure of the polymer and most of its microstructure, desired for cross-linking of nascent powders.

The applications of UHMWPE presented herein establish a picture of a very versatile material with unusual properties and challenging processing methods. Processes that would yield UHWMPE in an easier to handle form (e.g. disentangled state) are highly desired. The various approaches in blending UHMWPE with other materials to enhance its capabilities further require access to a highly dispersed form.

1.2.2 Disentangled UHMWPE

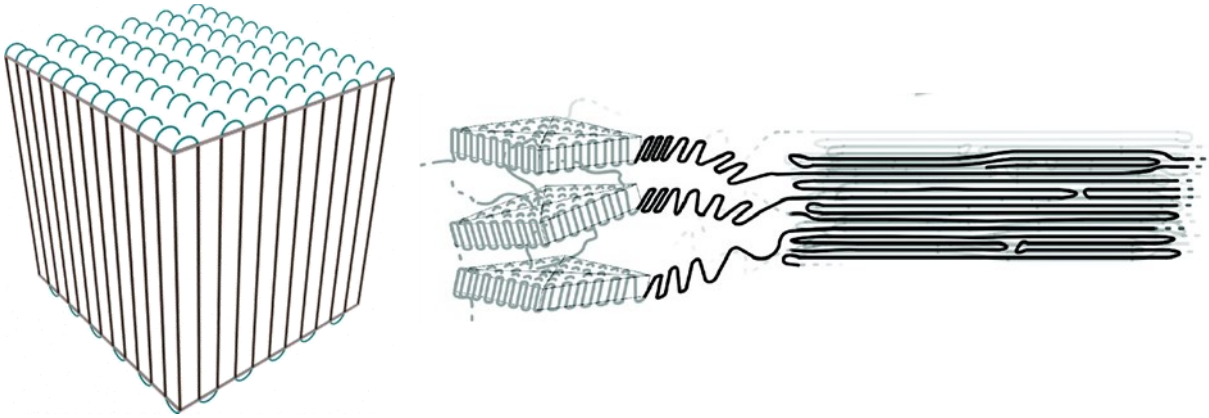

Figure 1.16. *Left:* Model of an ideally disentangled UHWMPE lamellae (amorphous regions consist of tight back loops, only).[216] *Right:* Concept of drawing disentangled UHMWPE single crystals to oriented high modulus structures.[240] Adapted with permission from Elsevier (Bellare, R. *et al.* in *UHMWPE Biomaterials Handbook* **2016**, Copyright 2016) and the American Chemical Society (*Macromolecules* **2011**, *44*, 5558–5568, Copyright 2011).

The major limiting factors in accessible mechanical properties of UHMWPE fibers are the maximum levels of chain extension and uniaxial alignment, achievable during gel-spinning and drawing.[241] This is not substantially influenced by shape, size or order of the crystalline entities, but highly dependent on the degree of chain entanglements.[242] The drawability of two UHMWPE samples of similar molecular weights, but with distinct levels of entanglements, differ

substantially: the disentangled sample can be drawn up to 150 times, the entangled sample only 7 times (M_w ~ 4 x 10^6 g/mol, at 125 °C).[243-245] Draw ratios of > 50 would be required to generate maximum levels of stiffness and tensile strength, desired for ultrahigh modulus and ultrahigh strength fibers.[246] The deformation of disentangled UHMWPE below the melting point results in continuous increase in crystallinity, enabling solvent-free solid-state drawing techniques.[240]

Disentangled UHMWPE can be obtained by slow crystallization from a highly diluted solution.[247,248] The long molecules, far away from each other, do not interfere and formation of entanglements of two individual chains upon crystallization is excluded through their spatial remoteness. Under ideal conditions, nanosized crystals composed of single polymer chains can be generated. However, this crystallization from dilute solution requires very low polymer volume fractions (< 0.05) and is highly time consuming.[199,249] Solutions of higher polymer contents (~10 wt-%) can provide low-entangled UHMWPE as used for the gel-spinning process towards high modulus fibers.[250] The presence of a few entanglements deteriorate mechanical properties in a tolerable range. An additional supportive macromolecular process known as 'reeling in' further reduces entanglements during crystallization.[242] The degree of entanglements can also be tuned by the solvent quality, as this strongly influences the polymer coil radius in solution. Using a rather poor solvent (e.g. vegetable oil) reduces the chance of entanglement formation upon cooling, as the individual chains will collapse more.[241] This 'chain contraction' reduces the probability of two individual polymer chains overlapping with each other during crystallization.

As a direct synthesis approach, disentangled UHMWPE can be generated by catalytic polymerization in highly diluted solutions.[251,252] Low reaction temperatures are highly important here to ensure fast crystallization of the growing chain, leaving no opportunity to form entanglements.[199] Rastogi and coworkers reported that entanglements are mainly formed in early polymerization stages, prior to nucleation.[253] After nucleation has occurred, the fast crystallization of the forming chains directly on the crystal surface hampers entanglement formation.

Melting of disentangled UHWMPE leads to formation of a homogenous melt with entanglements between individual chains quickly forming (Figure 1.17, top).[252] When disentangled crystals are rapidly heated above the melting temperature, chains will immediately undergo the so-called 'chain explosion' (also 'melt explosion') and form random coils facilitating subsequent formation of entanglements.[254] By contrast, slow heating generates a long-lived heterogenous melt state with only a few entanglements forming in initial melt stages (Figure 1.17,

bottom).[252] Hereby, the term 'heterogenous' describes an unequal distribution of entanglements between formerly crystalline and amorphous regions. In this state, chain dynamics are strongly constrained. Such slow melting experiments can be used to prove the disentangled nature of a random polyethylene sample, as the melting behavior is substantially different.[255] While the melting temperature of UHMWPE crystals is theoretically predicted to be ~ 131 – 136 °C, much higher values of > 141 °C are usually observed that are lost on second heating cycles (~ 135 °C).[244] Rastogi and coworkers demonstrated, that this increase in first melting points vanishes for disentangled UHMWPE when slow heating rates (≤ 1 K/min) are used.[244,255]

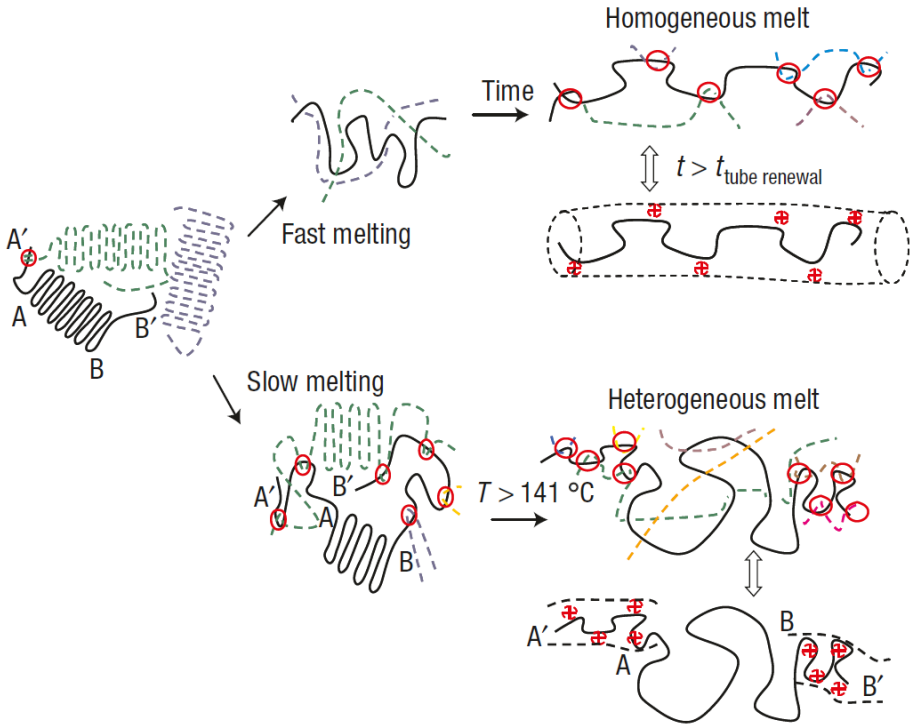

Figure 1.17. Melting of crystallized, disentangled UHMWPE with different heating rates.[252] Fast heating leads to simultaneous movement of all chain sections and immediate formation of entanglements, equally distributed along the polymer chains (homogenous melt, *top*). Slow heating leads to slow detachment of chain segments (A'-A and B'-B of the black chain) from the crystal surface that can entangle with neighbored chain parts (green and blue chains). When the melting point is reached (T > 141 °C), part A-B also melts but remains disentangled as most of the chain ends are 'trapped' in previously formed entanglements, leading to a heterogenous entanglement distribution along the chain (heterogeneous melt, *bottom*). Reprinted with permission from Springer Nature (*Nat. Mater.* **2005**, 4, 635–641, Copyright 2005).

Considering finely dispersed forms of disentangled UHMWPE, bulk precipitation of nascent polymer during polymerization could be inhibited by addition of LLDPE to the reaction mixture.[256] Co-crystallization of forming polymer and dissolved LLDPE created a brush structure on the chain fold surface, prohibiting aggregation by steric stabilization. However, this concept is restricted to organic solvents (toluene) and the co-crystallization altered the UHMWPE's

crystalline structure. Additionally, the polymer was found to be still minimally entangled. Indeed, aqueous catalytic polymerization allows for the synthesis of UHMWPE particles with well-defined crystalline structures.[111] As particle growth occurs in isolated surfactant micelles, formation of tie chains between individual lamellae can be excluded. A robust aqueous catalytic procedure that guarantees highly controlled chain growth, and, on the same level, a controlled particle growth would be highly desirable in terms of producing uniformly shaped disentangled UHMWPE nanocrystals. Such a living polymerization would provide very narrow dispersed UHMWPE chains with beneficial impact on abrasive wear of fabricated materials.[257]

1.3 Nanoparticle formation by crystallization as structure forming principle

The properties of semicrystalline polymers are strongly influenced by their morphology, making them versatile components in a broad range of applications for commercial thermoplastics.[258-260] The structure and crystallization of polyethylene, an important synthetic material, was studied intensively and is well understood.[261-263] Initial reports, where polymer chains were crystallized from diluted solutions to nanoparticles, revealed that the macromolecules form lamellar structures. However, the found lamella thicknesses were much smaller than the length of an extended chain. This led to the assumption that the polymer chains in the particles' structure fold back and forth, forming lamellae with the chains situated approximately perpendicular to the lamella surface (Figure 1.18).[264,265]

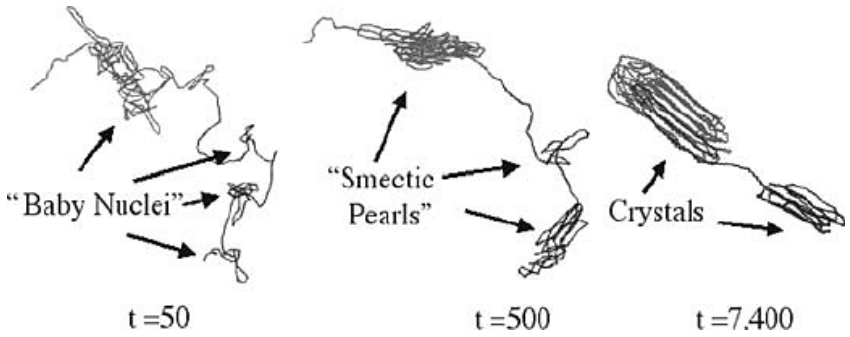

Figure 1.18. MD simulation showing a 'birth of a lamella' at different stages (time in 10^{-10} s).[266] Reprinted with permission form Springer (Muthukumar, M. in *Progress in Understanding of Polymer Crystallization* **2007**, Copyright 2007).

The crystallization process is decisive for the properties and stature of many nanostructured materials, irrespective of a polymeric or inorganic nature. The shapes and sizes of many anisotropic particles are directly influenced by the way the building blocks organize to generate

a solid and by the subsequent crystal growth.[20,267] These initial steps of particle nucleation are still poorly understood, in spite of intensive scientific work.[268] In the special case of polyethylene nanocrystals, insertion chain growth and polymer crystallization, two very different mechanisms, have to work 'hand in hand' to form the desired nanocrystals. Their anisotropic shape directly emerges from the way the polyethylene chains organize during this process, which makes crystallization the structure forming principle here (see *chapter 1.3.1*). This concept is not restricted to crystallization of nascent chains. Large and ordered, anisotropic particles can be generated by organization of polymeric building blocks in a 'living crystallization-driven self-assembly' (see *chapter 1.3.2*).

1.3.1 Polyethylene nanocrystals

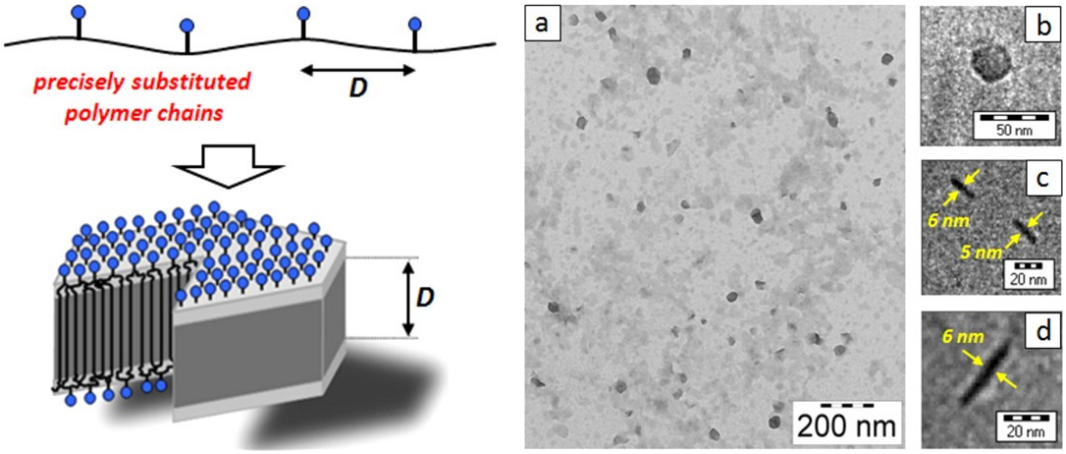

Figure 1.19. Schematic representation of a self-stabilized nanocrystal from precisely, long-spaced carboxy-substituted polymer chains (*left*) and cryo-TEM images (*right*, carboxy groups placed on every 45th carbon atom).[269] Adapted with permission from the American Chemical Society (*ACS Macro Lett.* **2013**, *2*, 125–127; Copyright 2013).

The aqueous polymerization with Ni(II) salicylaldiminato catalysts (*chapter 1.1.3*) can produce polyethylene in an unusual form of finely dispersed, anisotropic nanocrystals. In this process, the growing chain is directly folded and deposited on the crystal growth front, leaving no opportunity to form any disorder with tight loops and no (or only little) entanglement formation.

Direct synthesis of strictly linear polyethylene in aqueous emulsion can be achieved by ring-opening metathesis polymerization (ROMP) of *trans*-cyclooctene, followed by hydrogenation to generate fully saturated chains in the form of hexagonal particles.[270] Similar functionalized and self-stabilizing crystals can be obtained by placing functional groups in regular distance on the polyethylene backbone (synthesized by acyclic diene metathesis polymerization, ADMET; see

Figure 1.19).[269] The length of the spacing methylene sequences determines the nanocrystals' thickness. Recently, the group of Winey and this group reported the synthesis of periodic polyethylene sulfonates (methylene spacers of 23 carbon atoms), forming gyroid structures which are highly desired with regard to ion conduction in single-ion conducting polymers.[271] Identical polymers with methylene spacers of 48 carbon atoms formed self-stabilized, anisotropic nanoparticles with crystalline cores in water.[272] Catalytically prepared copolymers of ethylene and acrylic acid were found to also form self-stabilizing particles, however, with less defined structure.[273]

Remarkably, formation of such polyethylene-like nanostructures does not require folding of single polymer chains into lamellae. The synthetic pathway of 'chain doubling', presented by this group, provides access to long and well-defined α,ω-difunctional chains, namely telechelic polyethylene[274-276] composed of precisely 48 carbon atoms with symmetric end functionalities.[277] These telechelic molecules performed self-assembly in aqueous solution to form hexagonal platelets (Figure 1.20, left), very similar to nanocrystals composed of pure polyethylene. MD simulations revealed that both, the length of the polyethylene segment and the nature of the functional groups are influencing the particles' order (shorter chain analogues did not form particles), and were indicative for the presence of a stretched/extended chain crystallized core structure (Figure 1.20, right).[278]

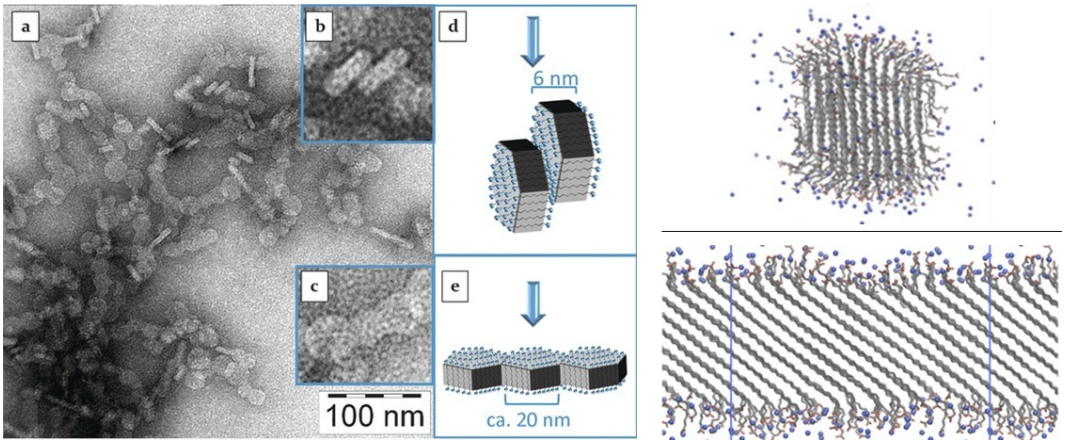

Figure 1.20. *Left:* TEM images of nanocrystals formed by self-assembly of telechelic polyethylene dicarboxylates (consisting of 48 carbon atoms).[277] *Right:* MD simulation snapshots of such nanocrystals (top) and a lamellar layer (bottom) indicating a titled chain structure.[278] Adapted with permission from Wiley-VCH (*Angew. Chem. Int. Ed.* **2017**, *56*, 7589–7594; Copyright 2017) and the American Chemical Society (*Macromolecules* **2019**, 52, 6142–6148; Copyright 2019).

Generation of long methylene sequences by subsequent self-metathesis reactions results in strictly linear polyethylene, beneficial for crystallization. In contrast, polyethylene formed in insertion polymerization can contain little branching that must be incorporated into the crystal

structure.[279] Larger irregularities can cause formation of amorphous regions and disrupt crystallinity.[280] Indeed, virtually 'perfect' linear polyethylene (< 0.7 branches per 1000 carbon atoms) can be generated in aqueous catalytic polymerizations at low temperatures (see Figure 1.21).[111,178] DSC and SAXS measurements revealed an unusually high crystallinity of $\chi > 90$ %.[178] These 'ideal polyethylene nanocrystals' consisted of single crystalline lamellae, sandwiched between two amorphous layers. It was assumed, that the amorphous layers contain only tight loops, as indicated by their thin nature and solid state NMR measurements.[178,281] Annealing experiments, directly performed on aqueous dispersions or on submicron films (*vide infra*), showed a growth of the individual lamellae in thickness.[282-284] This lamella thickening, carefully studied via cryo-TEM, AFM and SAXS, was found to proceed without altering the amorphous regions and was strongly dependent on the applied annealing temperature. This concept of polymer chains slipping through each other strongly supported the idea of a disentangled nature, as entanglements would impede chain motion. The kinetic melting behavior of precipitated nanocrystals was used to further demonstrate the disentangled nature, even for molecular weights exceeding $M_n > 10^6$ g/mol .[111,130]

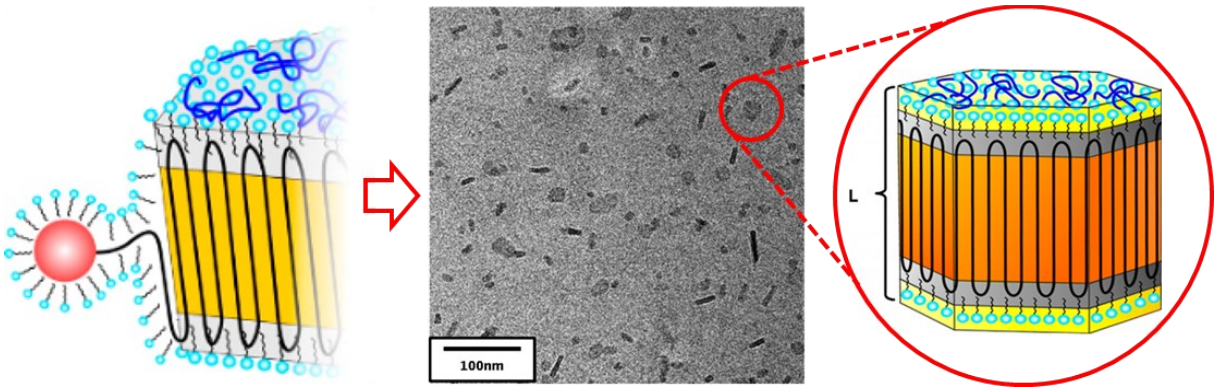

Figure 1.21. Formation of 'ideal polyethylene nanocrystals' in aqueous catalytic polymerization. The active center forms the polymer chain that is directly deposited in a highly ordered fashion on the crystal growth front (*left*). The obtained nanocrystals (*center*, cryo-TEM) consist of a single lamellae, sandwiched between thin amorphous layers (*right*). Adapted with permission from the American Chemical Society (*J. Am. Chem. Soc.* **2013**, *135*, 11645–11650; Copyright 2013).

To investigate the evolution of particle size and shape over the course of a polymerization experiment, a customized automated sampling chamber was connected to a pressure reactor and enabled the drawing of samples from an ongoing experiment in defined intervals.[179] These experiments revealed that the emerging chain immediately crystallizes and that the particles are generated in the very first seconds of the polymerization. Particle shapes evolved with increasing size from single-lamella hexagonal platelets (~ 30 nm lateral size) to truncated lozenge shaped platelets (> 60 nm lateral size; see Figure 1.22, top and Figure 1.9). For diameters of > 100 nm

usually lozenge shaped particles were obtained (only in D_2O or in presence of DMF; see *chapter 1.1.3*).[179] These shapes are known for polyethylene crystals, representing their lozenge habit and are also observed for polyethylene single crystals made by crystallization from melt or solution.[285-288] The observed evolution of shape with the particle size results from an anisotropic growth rate, with the faster growing {100} faces disappearing (see Figure 1.22, bottom).[180,289] Particle thicknesses increased during the first minutes to ~ 7 nm (measured by AFM and TEM) but did not change during the further polymerization experiment. Therefore, the particle growth exclusively occurred in lateral dimensions. The particle thickness was found to be mostly dependent on the reaction temperature with smaller thicknesses obtained at stronger undercoolings (in accordance to the Gibbs-Thomson equation[290]).[291] The observed thickening within the first minutes was stated to be caused by post-crystallization reorganization and not by the chain deposition mechanism itself.[179]

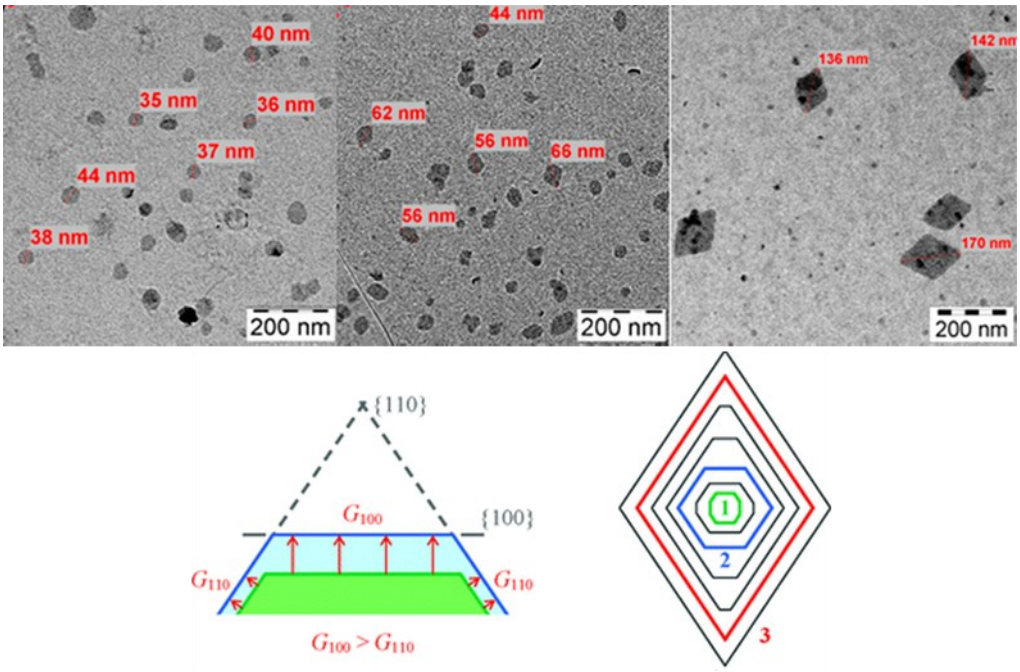

Figure 1.22. Evolution of polyethylene nanocrystal particle shapes and sizes during aqueous catalytic polymerization. *Top:* TEM images reveal the particle shapes to develop from predominantly hexagonal platelets (left) through truncated lozenges (middle) to predominantly lozenges (right) with increasing particle size.[179] *Bottom:* Schematic growth process of polyethylene nanocrystals.[180] The faces {100} of hexagons slowly disappear as they grow faster than the {110} face, resulting in formation of a lozenge shape. Adapted with permission from the American Chemical Society (*Macromolecules* **2016**, *49*, 8825–8837; Copyright 2016, CC BY license and *Nano Lett.* **2007**, *7*, 2024–2029; Copyright 2007).

Polyethylene nanocrystals were also used for the formation of ultrathin crystalline polymer films, being of practical interest considering their unique properties, which are substantially different from those of the bulk material.[292-294] Dropwise application of an aqueous polyethylene

nanocrystal solution on a glass slide and subsequent drying at room temperature afforded transparent polyethylene films of 1 µm thickness.[294] Ultrathin films were obtained by spin coating, yielding continuously covered substrates with an equal film thickness of ~ 50 nm. AFM and TEM measurements revealed a homogenous topography existing over hundreds of micrometers.[284] The approach differs substantially from traditional routes as the material is already in a highly ordered crystalline state when transferred to the substrate and does not require further thermal treatment. This facilitates formation of highly ordered films under conditions where organic solvents and elevated temperatures are undesired.

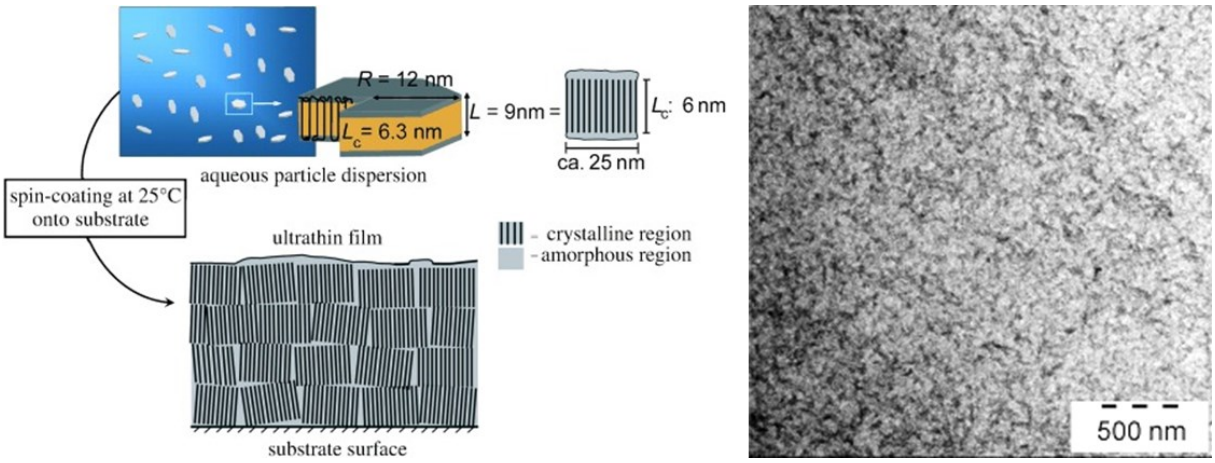

Figure 1.23. Preparation and structure of ultrathin films made of polyethylene nanocrystals (*left*).[294] TEM images (*right*) reveal a homogenous topography. Reprinted with permission from Wiley-VCH (*Angew. Chem. Int. Ed.* **2008**, *47*, 4509–4511; Copyright 2008).

1.3.2 Particle formation by living crystallization-driven self-assembly (CDSA)

Amphiphilic molecules (e.g. surfactants or block copolymers) are capable of forming a broad variety of nanostructures by self-assembly.[295] Intense investigations have revealed the generation of hierarchical colloid materials on larger length scales (e.g. by use of nanocrystals[296] or nanorods[297]). However, methods employing anisotropic amphiphilic building blocks derived from soft matter were lacking. In 2015, Manners, Winnik and coworkers presented an approach for the generation of tailored, functional, hierarchical structures on the multi-micrometer length scale.[298] These were built by assembling triblock co-micelles obtained by living crystallization-driven self-assembly (CDSA).[299,300] In this technique, micelle structures of copolymers are formed by crystallization and grow epitaxially upon the addition of polymer (see Figure 1.24, left). This process, very analogous to chain growth in a living polymerization, creates micelles

with a very narrow size dispersity. By subsequent addition of different compatible copolymers, co-micelles composed of different building blocks were formed. These triblock co-micelles were then assembled into superstructures by solvent variations showing side-by-side or end-to-end inter-micellar associations (see Figure 1.24, right). The process can be further influenced by the co-micelle architecture in terms of sequences, block lengths or chemical composition, allowing for the generation of very different micrometer scale colloids (e.g. networks, cylindrical brushes, or strands).

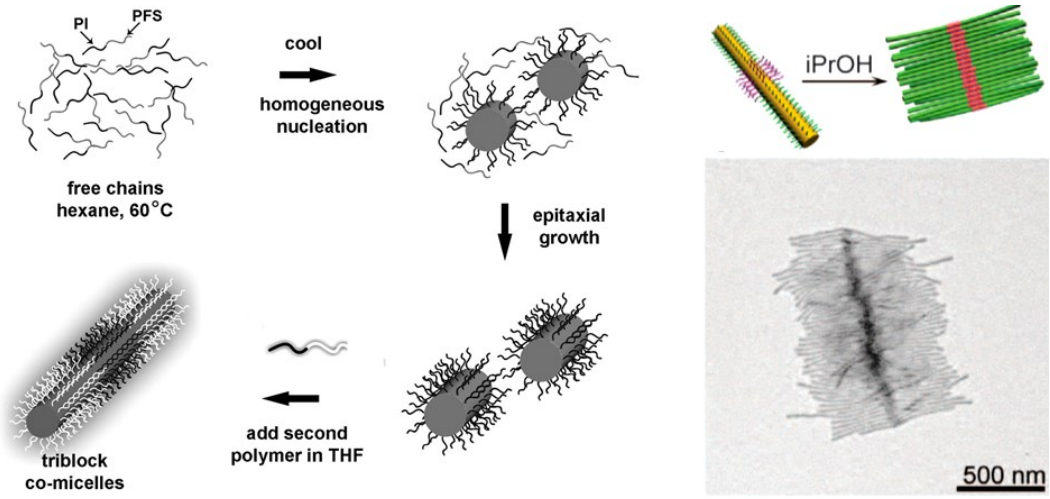

Figure 1.24. *Left:* Concept to generate triblock co-micelles by living CDSA (PFS = polyferrocenylsilane, PI = polyisoprene).[299] *Right:* Assembly of such triblock co-micelles to hierarchical superstructures ('1D supermicelles') via side-by-side stacking.[298] Adapted with permission from the AAAS (*Science* **2007**, *317*, 644–647; Copyright 2007; and *Science* **2015**, *347*, 1329–1332; Copyright 2015).

Sequencing of different micellar structures was used to build up hollow and planar 2D architectures.[301] Rectangular platelet micelles were formed by growth of platelet-forming block-copolymers (long crystallizable core-forming block, short corona-forming block) on cylindrical micelle seeds. Selective corona cross-linking and treatment with THF removed the previous core seed, yielding rectangular platelets with perforated channels in the center (Figure 1.25, a). As the formed platelets were highly sensitive to small variations in the copolymers block lengths, an alternative approach without the need of a corona-forming block was sought. Inspired by the use of electrostatic forces to stabilize colloids in dispersions, the coronal chain segments were replaced by charged groups (e.g. phosphonium iodide).[302] Addition of such molecularly dissolved (unimeric) polymers to cylindric micelle seeds afforded highly uniform rectangular platelet micelles. Moreover, this seeded growth approach was characterized by a morphological memory effect, whereby the nature of the initially introduced seeds influenced further growth and led to very different accessible 2D particle shapes (e.g. rectangular, quasi-hexagonal, or diamond platelets; Figure 1.25, b).

So far, polymer synthesis and chain assembly in solution were totally separated steps. By combining polymerization-induced self-assembly[303] with CDSA, nanoparticles were generated by synchronous polymerization, crystallization and self-assembly.[304] Along with the aqueous catalytic formation of polyethylene nanocrystals, significantly higher solid contents (up to 25 wt-% vs. ~ 1 wt-% via post-polymerization manipulation) were accessible. The diblock copolymers were generated by sequential living anionic polymerization without any isolation or purification steps. TEM images showed the formation of ordered micelles upon addition of the second monomer in a different solvent and revealed a highly monodisperse cylindric form with controllable micelle lengths (Figure 1.25, c).

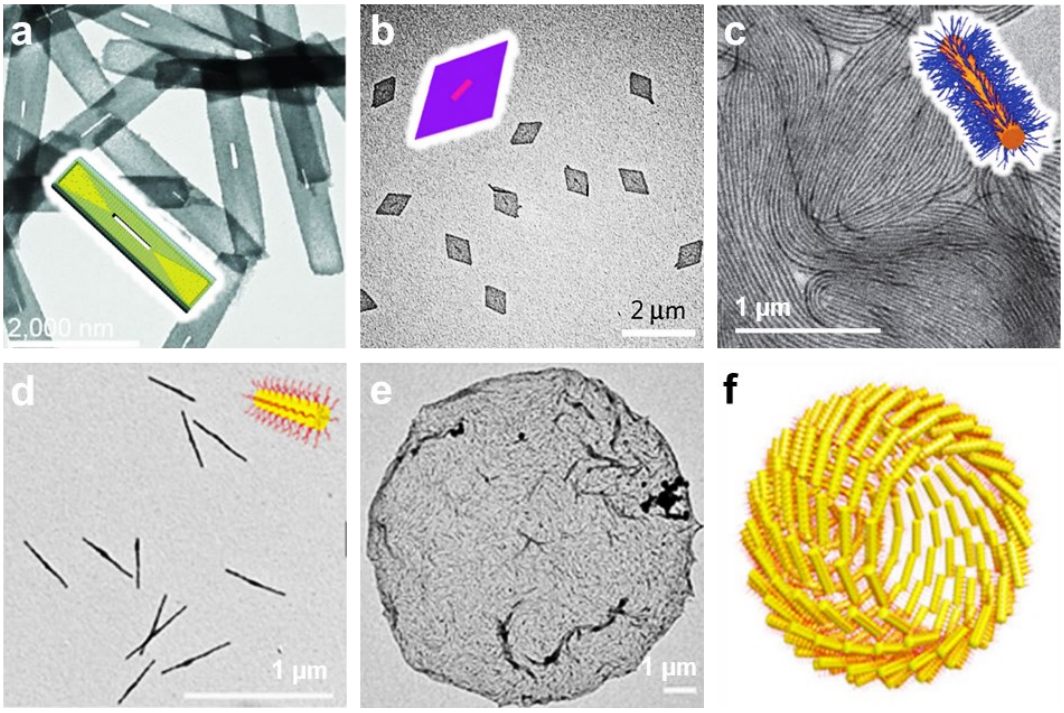

Figure 1.25. TEM images and structures of different assemblies formed by CDSA. a) Rectangular platelet micelles with hollow centers formed by living CDSA, subsequent cross-linking and selective core removal.[301] b) Uniform diamond platelets formed by growth of charged polymers on cylindric micelle seeds.[302] c) Cylindric micelles prepared by polymerization-induced CDSA.[304] d) – f) Cylindric micelles (d) used to generate large colloidosomes (e) by organization (f) at water-oil-interfaces.[305] Adapted with permission from the AAAS (*Science* **2016**, *352*, 697–701; Copyright 2016) and Springer Nature (*Nat. Mater.* **2017**, *16*, 481–488; Copyright 2017 and *Nat. Chem.* **2017**, *9*, 785–792; Copyright 2017 and *Nat. Commun.* **2017**, *8*, 426; Copyright 2017).

Addressing the formation of hierarchical 3D structures, diblock copolymers with appropriate wettability and chemical reactivity were used for living CDSA and the formed cylindric micelles (Figure 1.25, d) organized at the interfaces of a water-in-oil Pickering emulsion.[304] Afterwards, the droplets were cross-linked and colloidsomes[306] in the form of

semipermeable microcapsules were obtained (Figure 1.25, e-f). They exhibited an unusual membrane structure and their surfaces could be further modified and functionalized.

Living CDSA often employs copolymers containing poly(ferrocenyldimethylsilane) (PFS) as crystallizable, core-forming block. However, considering the use of such particles with their unique properties and shapes as nanocarriers for drug delivery, compatibility with aqueous and systems is desired. Furthermore, application in biological systems requires biodegradable polymer blocks. Manners and coworkers demonstrated the synthesis of copolymers with a crystallizable polycarbonate block and a water-soluble poly(ethylene oxide) block, and their living CDSA towards low-dispersity fiber-like micelles and block co-micelles in controlled lengths (~ 40-1500 nm).[307] Such short fiber-like micelles did not show any detectable cytotoxicity to both, primary and cancerous cells, under physiological aqueous conditions. Recently, formation of biodegradable block co-micelles of poly(lactide) block copolymers via living CDSA has been reported and the influence of hydrogen bonds on particle size uniformity was revealed.[308]

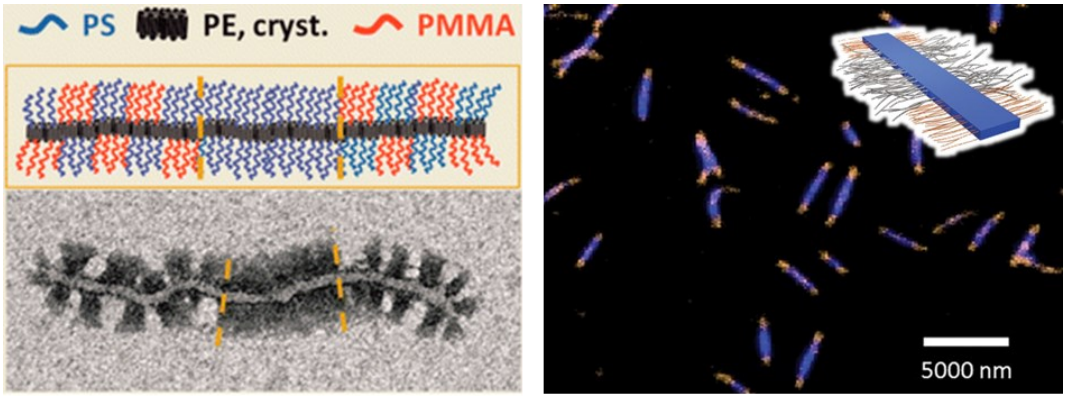

Figure 1.26. *Left:* Worm-like micelles with crystallized polyethylene core obtained by sequential CDSA.[309] *Right:* Laser scanning confocal microscopy image of uniform segmented, conjugated nanofibers with a crystalline core (blue emission) and two terminal segments with coronas exhibiting different emission properties (orange emission).[310] Adapted with permission from the American Chemical Society (*J. Am. Chem. Soc.* **2012**, *134*, 14217–14225; Copyright 2012) and the AAAS (Science **2018**, *360*, 897–900; Copyright 2018).

Beside anisotropic particle shapes, also the corona's stature and chemistry were varied for different micelle faces by using triblock copolymers. Schmalz and coworkers focused on a simple block design made of common olefinic monomers with linear polyethylene, the paragon molecule in polymer crystallization, as crystallizable core block.[311] By cooling of a homogenous polymer solution different micelle shapes, depending on the solubility of polyethylene in the respective solvent, were obtained.[312] In case of worm-like micelles, the morphology of the patch-like corona could be precisely influenced by the solvent quality for the corona-forming

polystyrene and poly(methyl methacrylate) blocks. Unique one-dimensional array structures with nearly alternating PS and PMMA patches were observed under certain conditions. Formation of identical structures via a living CDSA approach was later reported (see Figure 1.26, left).[309] Such triblock terpolymers were also used to form micelles as patchy building blocks for multi-micrometer hierarchical assemblies.[313] By incorporation of conjugated polymer blocks, continuous and segmented conducting and optically active nanowires were generated and are promising materials for the application in electronical and/or optical devices (e.g. photodetector materials or photovoltaics; see Figure 1.26, right).[310,314-317]

Living CDSA represents a totally different 'seeded growth' approach that is comparable to the principles of a living polymerization, both exhibiting a highly controlled growth process and providing access to narrow particle size distributions. While this technique originates from crystallization of very special metalloblock copolymers (polyferrocenylsilane), its scope has been greatly extended to simple saturated, conjugated[318], or biodegradable copolymers[319,320]. Nanostructures in a broad variety of sizes (up to micrometers), anisotropic shapes and functionalities are accessible, demonstrating the capabilities of crystallization as a structure forming principle. Such micellar materials show promising applications in drug delivery vehicles, directing templates, composite reinforcement, stabilizers, nanoelectronics and -optics, and many more.[321-324]

2 Objectives

Assembly of anisotropic shape nanoparticles holds potential to form superstructures and materials with yet unmet properties. However, routes to anisotropic polymer particle dispersions of high solids content are lacking. Polyethylene, an important synthetic material, can be obtained in the unusual form of nanoscale platelet-like single crystals by aqueous catalytic polymerization with Ni(II) salicylaldiminato catalysts. Generation of such nanocrystals with uniform shapes and sizes is highly desirable, considering formation of materials with well-defined properties by their assembly. Indeed, this would require a strictly living chain growth and, simultaneously, a living particle growth in absence of any termination reactions.

This work reports the concept of a living catalytic polymerization of ethylene in aqueous surfactant solution, achieved by careful catalyst and process design. Based on recent insights, how the ligand and reaction environment influence chain growth, perfluoroalkyl-substituted catalysts were targeted as promising candidates (*chapter 3*). Simultaneous optimization of an automatized pressure reactor setup and of the reaction parameters with focus on particle size dispersity, catalyst performance, etc. was conducted (*chapter 6*). Chain growth was promoted to an extent that highly uniform UHMWPE nanocrystals were formed in absence of chain entanglements. Remarkably, every particle consisted of one single polymer chain that is generated by one catalyst species ('single-chain particles'). By placing perfluoroalkyl-substituents in various chelating motifs, a rather general beneficial impact of such groups on catalytic properties could be identified (*chapter 4*). This is not limited to fully saturated fluorocarbons but was also found for very common aromatic pentafluorophenyl groups (*chapter 5*). Towards the aim of particle-based materials, the formed UHMWPE dispersions were tested as precursors for 3D printing techniques and fiber formation procedures (*chapter 7*).

3 Uniform Shape Monodisperse Single Chain Nanocrystals by Living Aqueous Catalytic Polymerization

3.1 Introduction

A key to nanoparticle-based materials is the ability to access nanoparticles with uniform shapes and sizes. For inorganic nanoparticles, this is a solved problem by and large. Metal or metal oxide nanoparticles with dimensions as low as a few nanometers can be generated in a variety of shapes in high quality, which allows for their further assembly.[325-330] By strong contrast, routes to polymer nanoparticles with a uniform shape beyond spheres are lacking.

For the particular important and challenging size regime of only a few nanometers to a few tens of nanometers, single-chain particles composed of uniform chains are a straightforward theoretical concept to achieve a uniform particle size (or, more precisely, volume). Single-chain particles have been much studied, and the field continues to expand.[331-334] They are commonly prepared by a post-polymerization collapse or assembly from solutions of separately synthesized chains. Although a shape control is recognized as one of the major potentials of single-chain nanoparticles, this has rarely been achieved.[335-339]

This chapter will present a different approach, namely direct polymerization to single-chain uniform-shape monodisperse nanocrystals (Figure 3.1). This is demonstrated for polyethylene, the largest and most important synthetic polymer material.

Parts of *chapter 3* are published in *Nat. Commun.* **2019**, *10*, 2592.

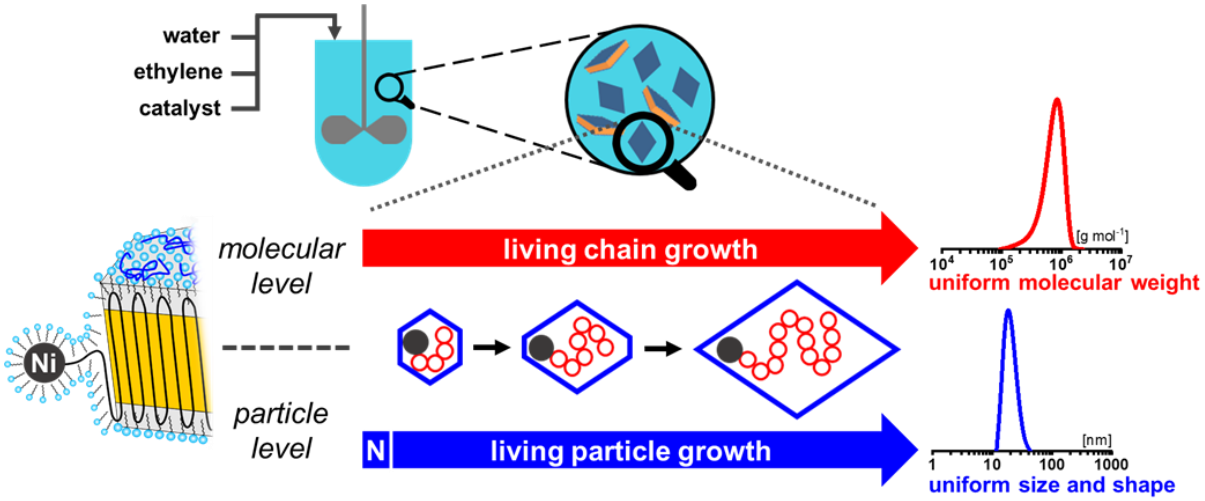

Figure 3.1. Concept to obtain uniform size and shape particles by controlled polymerization on a molecular, as well as on a particle level. An effective nucleation (N) ensures that particles contain only one active site and start to grow virtually at the same time. Due to the living character of polymerization, all particles continue to grow for the entire duration of the experiment, to yield particles each composed of a chain of identical length. As the growing chains are immediately deposited on the growing single-crystal particle during this process, particle shape evolves uniformly over time during polymerization.

3.2 Results and discussion

3.2.1 Catalyst design

This approach poses several challenges. To generate single-chain particles rather than larger aggregates, an efficient compartmentalization is required. Water as a medium offers itself, in being a polar medium that allows for an efficient colloidal stabilization of particles, and a non-solvent for most polymers. However, this requires well-designed polymerization methods.

Traditional insertion polymerization catalysts are extremely sensitive to traces of water. This can be overcome by less oxophilic late transition metal catalysts. With state-of-the-art catalysts, based on *N*-terphenyl salicylaldiminato Ni(II) complexes, ultra high molecular weight polyethylene can be generated in aqueous polymerizations.[111,185] This is formed as nanocrystals with an unusually high degree of order that arises from the immediate deposition of the growing chain on the crystal growth front.[178]

Based on recent insights how the ligand environment of the active site controls chain growth and chain transfer[53], and how active sites are terminated by water[179], the perfluoro-substituted motifs **1**^{I}-**R**^{F}/**L** were targeted (Figure 3.2; for details on synthesis and characterization of all catalyst precursors, see *Experimental Section*). This choice is based on the argument that

perfluoro groups are highly electron withdrawing[340], which suppresses specific chain transfer pathways, and due to their hydrophobicity[341] possibly hinder an access of water to the active sites. The major, yet unmet challenge toward the concept pursued here is to achieve a living nature of aqueous ethylene polymerization. This requires a strict suppression of chain transfer reactions as well as termination.

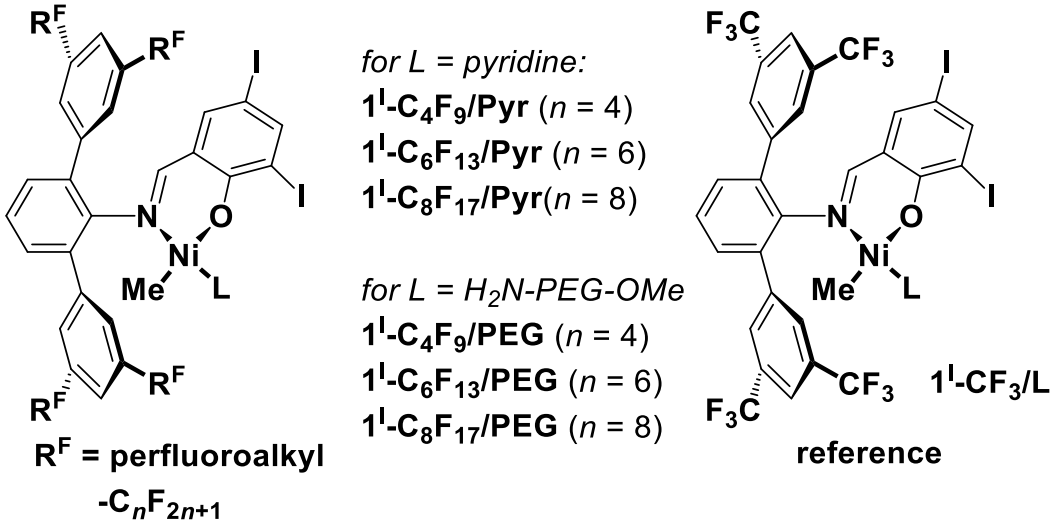

Figure 3.2. Catalysts precursors studied. Compared to the known reference system (*right*), the novel catalysts reported here feature perfluoroalkyl chains of variable length in the remote positions of the *N*-terphenyl moiety (*left*). The coordinated labile ligand L renders the catalyst precusors lipophilic (L = Pyr), or, for aqueous polymerizations, hydrophilic (L = H_2N-PEG-OMe).

Pressure reactor studies of ethylene polymerization in toluene as a reaction medium with the perfluoro-substituted complexes **1^{I}-R^{F}/Pyr** revealed these to be precursors to highly active catalysts (see Table 3.1 and *Experimental Section*, *chapter 3.4.7*). Compared with the benchmark catalyst precursor **1^{I}-CF$_3$/Pyr**, with electron-withdrawing trifluoromethyl remote substituents, catalyst activities (16 x 10^3 TO h^{-1} vs. 761 x 10^3 TO h^{-1}, entries 3 and 9, Table 3.1 and Figure 3.3, magenta curve) and molecular weights (27×10^3 g mol^{-1} vs. 308×10^3 g mol^{-1}, entries 2 and 8, Table 3.1 and Figure 3.3, blue curve) are substantially increased. More than 400.000 moles of ethylene can be polymerized per mole of catalyst precursor per hour. At the same time, the number of branches in the polymer is decreased to less than one branch per 1000 carbons, which is desirable to facilitate crystallization (*vide infra*). Notably, narrow molecular weight distributions as low as $M_w/M_n < 1.3$, indicative of a living polymerization, are observed in some cases.

Table 3.1. Ethylene polymerization results in toluene.

entry (cond.)	precatalyst	T [°C]	yield PE [g]	TOF[a]	M_n[b] x 10^3 [g mol^{-1}]	M_w/ M_n[b]	T_m[c] [°C]	crystallinity[c] [%]	branches/ 1000 C[d]
1[A]	1^I-CF_3/Pyr	30	2.21	31.5	275	1.5	133	48	2.8
2[B]	1^I-CF_3/Pyr	50	2.87	136.4	27	1.7	121	47	9.1
3[C]	1^I-CF_3/Pyr	70	0.17	16.2	8	2.0	114	47	14.0[e]
4[A]	1^I-C_4F_9/Pyr	30	3.60	51.4	489	1.5	133	58	0.8
5[B]	1^I-C_4F_9/Pyr	50	6.43	305.6	305	1.3	131	49	2.2
6[D]	1^I-C_6F_{13}/Pyr	15	5.26	6.3	1190	1.3	136	49	n.d.
7[A]	1^I-C_6F_{13}/Pyr	30	5.13	73.2	844	1.5	134	56	0.7
8[B]	1^I-C_6F_{13}/Pyr	50	8.17	388.4	308	1.4	131	46	1.9
9[C]	1^I-C_6F_{13}/Pyr	70	8.00	760.6	33	1.6	125	50	6.5
10[A]	1^I-C_8F_{17}/Pyr	30	3.52	50.2	515	1.5	135	60	0.7
11[B]	1^I-C_8F_{17}/Pyr	50	3.83	182.1	218	1.5	132	46	1.7

Polymerization conditions: (A) 5 µmol precatalyst, 30 min reaction time, (B) 3 µmol precatalyst, 15 min reaction time, (C) 3 µmol precatalyst, 7.5 min reaction time, (D) 5 µmol precatalyst, 5 h reaction time; all experiments performed in 100 mL of toluene with 40 bar ethylene pressure. [a] given in 10^3 x mol [C_2H_4] x mol^{-1} [Ni] x h^{-1}. [b] Determined by GPC at 160 °C in 1,2,4-trichlorobenzene. [c] Determined by DSC with 10 K min^{-1} heating rate (data from second heating cycle). [d] Determined by ^{13}C NMR spectroscopy. [e] Including 2.3 ethyl branches.

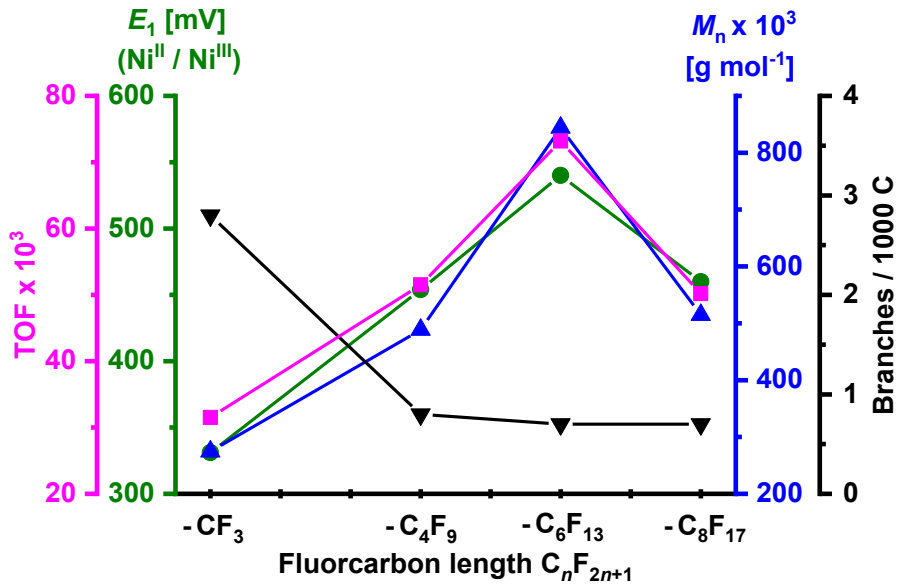

Figure 3.3. Comparison of the experimental data from polymerization experiments with different catalyst precursors. Catalytic activity (TOF, *magenta curve*), forward peak potential determined via cyclic voltammetry of pyridine precatalysts (E_1, *green curve*), molecular weight (M_n, *blue curve*) and branching values (*black curve*) of formed polyethylenes and fluorocarbon chain length in precatalysts' structures (**1^I-R^F/Pyr**) given. Experimental data from experiments at 30 °C in toluene (entries 1, 4, 7, 10; Table 3.1)

Both chain transfer, which limits molecular weights and broadens molecular weight distributions, and branch formation proceed through ß-hydrogen elimination (BHE) as an underlying reaction step. Correspondingly, an increase in molecular weight goes along with a reduction of branching, both desirable features. The pathway to BHE is known to be suppressed by electron-withdrawing substituents.[53] Cyclic voltammetry studies on the catalyst precursor of the oxidation and reduction transitions for the Ni(II)/Ni(III) pair showed that compared with the established trifluoromethyl substitution, indeed the electron density at the metal is lowered significantly in the perfluoroalkyl complexes (Figure 3.3, green curve), and this correlates qualitatively with the observed catalytic properties. The origin of the lower potential for $n = 8$ vs. $n = 6$ remains unclear at this point.

3.2.2 Aqueous polymerization and particles

Due to their superior performance, perfluorohexyl substituents ($-C_6F_{13}$) were used in the further studies of aqueous polymerizations. For polymerizations in aqueous systems, hydrophilic catalyst precursors with a weakly coordinating amino-polyethylene glycol ligand were generated (**1^I-R^F/PEG**). A space of various experimental parameters was optimized in pressure reactor experiments with regard to a uniform nature of the formed particles and catalyst performance, among others surfactant type and concentration, pH, reaction temperature, and sonication (see *Experimental Section* and *chapter 6* for comprehensive data). Other than **1^I-CF_3/PEG**, the perfluorinated catalyst precursors **1^I-C_4F_9/PEG**, **1^I-C_6F_{13}/PEG** and **1^I-C_8F_{17}/PEG** do not form homogenous molecular solutions, and a small amount of hydrophobic organic solvent (0.2–0.5 vol-%) is required to obtain a highly dispersed system. From a range of solvents, mesitylene evolved as the solvent of choice (see *chapter 6.2.2* for details). This enabled very narrowly distributed sub-100-nm particle sizes (see *Appendix* for dynamic light scattering (DLS) traces of PE dispersions). We attribute this to an undesired agglomeration of the catalyst precursor molecules via their very hydrophobic portions in the aqueous system in the absence of the small organic solvent volume.

Under the identified reaction conditions, catalytic activity was retained for more than 4 hours. Experiments conducted with different reaction times provided detailed insights into the chain and particle growth process (Table 3.2). For all experiments, stable and transparent to slightly opaque PE dispersions were obtained.

Table 3.2. Ethylene polymerization results of precatalyst **1^{I}-C_6F_{13}/PEG** in aqueous surfactant solution.

entry (cond.)	time [h]	yield PE [g]	TON[a]	M_n[b] x 10^3 [g mol^{-1}]	M_w/ M_n[b]	chains/ [Ni]	T_m[c] [°C]	cryst.[c] [%]	particle size (DLS)[d] [nm]	particle size (TEM)[e] [nm]	chains/ particle
1^{A}	0.5	4.29	20.4	631	1.2	0.9	142/136	66/41	18	23.6 ± 1.6	1.2 ± 0.3
2^{A}	1	7.09	33.7	896	1.2	1.1	143/135	64/43	20	28.9 ± 2.2	1.2 ± 0.3
3^{A}	2	8.67	41.2	1154	1.2	1.0	142/135	66/43	23	33.6 ± 2.3	1.3 ± 0.3
4^{A}	4	9.95	47.3	1421	1.2	0.9	143/136	64/42	24	36.8 ± 2.8	1.2 ± 0.3
5^{B}	1	12.94	61.5	1912	1.2	0.9	143/134	60/37	32	46.0 ± 6.1	1.4 ± 0.3
6^{B}	2	17.72	84.2	2588	1.2	0.9	144/135	62/39	36	53.9 ± 9.1	1.5 ± 0.4
7^{B}	4	20.37	96.1	3084	1.3	0.9	143/135	64/43	42	64.4 ± 12.3	1.7 ± 0.4

Polymerization conditions: (A) 7.5 µmol precatalyst, 40 bar ethylene pressure, 6.0 g of sodium dodecyl sulfate, 1.5 g of cesium hydroxide, 0.75 mL of mesitylene, in 150 mL of water, 15 °C reaction temperature; (B) 7.5 µmol precatalyst, 40 bar ethylene pressure, 12.0 g of sodium dodecyl sulfate, 3.0 g of cesium hydroxide, 1.5 mL of mesitylene, in 300 mL water, 15 °C reaction temperature; the catalyst solution was ultrasonicated prior to pressurization with ethylene under all conditions. [a] Given in 10^3 x mol [C_2H_4] x mol^{-1} [Ni]. [b] Determined by GPC at 160 °C in 1,2,4-trichlorobenzene. [c] Determined by DSC on nascent polymer powder, isolated by precipitation from the nanocrystal dispersion in methanol, measured with 10 K min^{-1} heating rate, first and second heating cycle reported. [d] Volume mean given. [e] Lateral particle size determined from TEM statistics (equivalent diameter and standard deviation reported, for details see *Experimental Section*).

Remarkably, this aqueous catalytic polymerization is truly living in nature, as evidenced by (1) a linear relationship between yields and molecular weights (Figure 3.4); (2) very narrow molecular weight distributions of $M_w/M_n = 1.1–1.2$; and (3) chains to Ni ratios of unity. As a given nickel center grows a single chain over the entire reaction time, linear narrowly distributed UHMWPE with $M_n > 10^6$ g/mol ($M_w/M_n = 1.2$; see Figure 3.5) can be produced (Table 3.2, entry 4). Even molecular weights in excess of $M_n > 3 \times 10^6$ g/mol are accessible (Table 3.2, entry 7). DSC studies of isolated polymers indicate a non-entangled nature of the formed UHMWPE, as concluded from a high first-cycle melting temperature of > 140 °C, which is not observed for slow heating rates in all cases.[255] The polymer microstructure is virtually devoid of any branches (< 0.7 branches per 1000 carbons) as revealed by ^{13}C NMR analysis, in accordance with the observed melting properties. The aqueous polymerization procedure yields the UHMWPE efficiently with high particle number densities (up to 13 wt-%, corresponding to $N = 10^{19}$ particles L^{-1}), precisely tunable by surfactant content and catalyst loading. This compares favorably to the state-of-the-art systems of high concentration single-chain nanoparticle dispersions[342,343] and differs from many post-polymerization procedures, which yield only low particle concentrations.

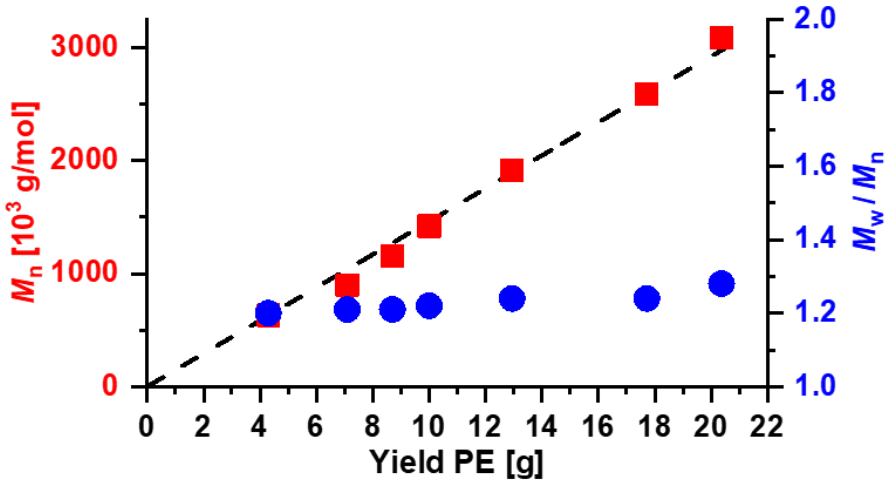

Figure 3.4. Molecular weights and polydispersity indices of the polyethylenes formed versus yields (aqueous polymerization experiments with reaction times varying from 0.5 to 4 h; Table 3.2).

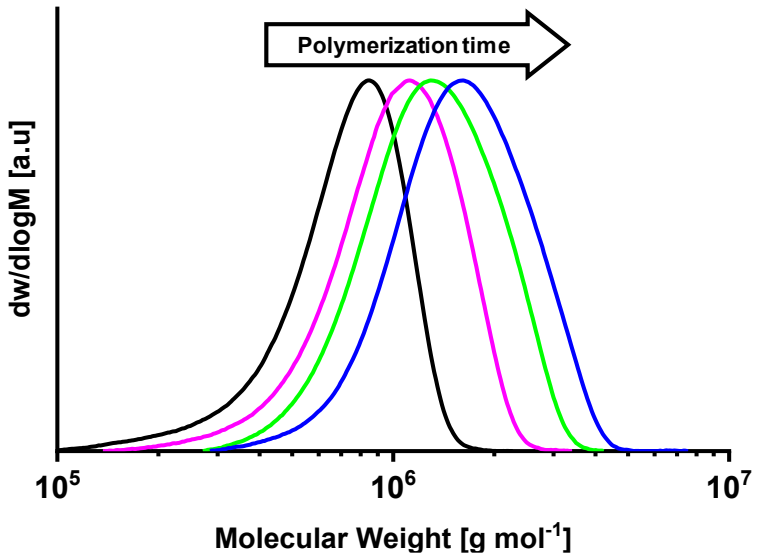

Figure 3.5. GPC traces of narrow distributed UHMWPEs obtained in aqueous polymerization after different reactions times. 0.5 hours reaction time (*black*), 1 h reaction time (*magenta*), 2 h reaction time (*green*), 4 h reaction time (*blue*). Data from Table 3.2, entries 1–4.

Transmission electron microscopy (TEM) reveals that the particle shape evolves from truncated lozenges to lozenges (due to a preferred deposition on the {110} crystalline growth front). A uniform shape and size-distribution and a non-aggregated nature of the particles is observed in all cases (see Figure 3.6, a-d). The aforementioned very narrow size distributions from DLS are further underlined by TEM statistical data and AUC experiments (see Figure 3.7 and *Experimental Section*).

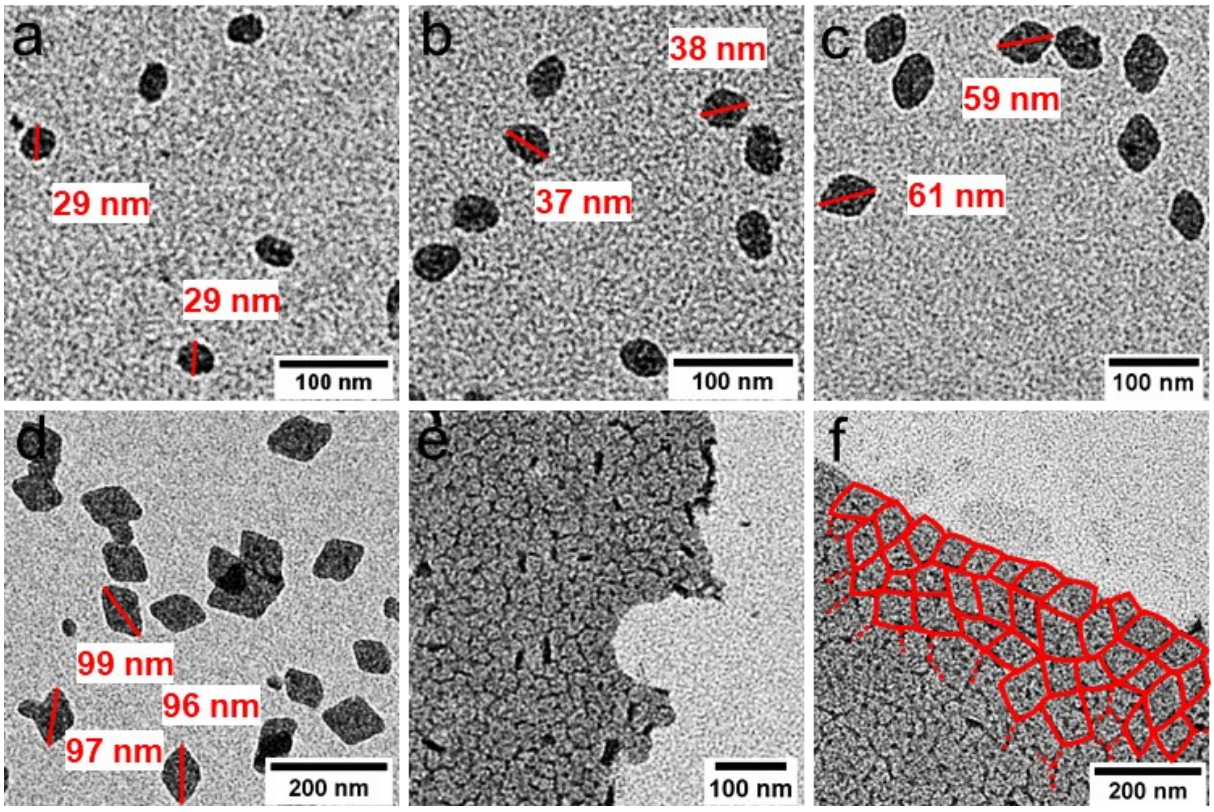

Figure 3.6. TEM images of UHMWPE nanocrystals. a–d) Nanocrystals obtained from aqueous polymerization after different reaction times showing the evolution of size and shape (entries 1 (a), 3 (b), 5 (c), and 7 (d), Table 3.2). e-f) layered structures with short-range order formed by drying of uniform particle dispersions with different sizes (entries 2 (e) and 7 (f), Table 3.2), particle boundaries marked in red. For full set of original TEM images, see *Appendix*.

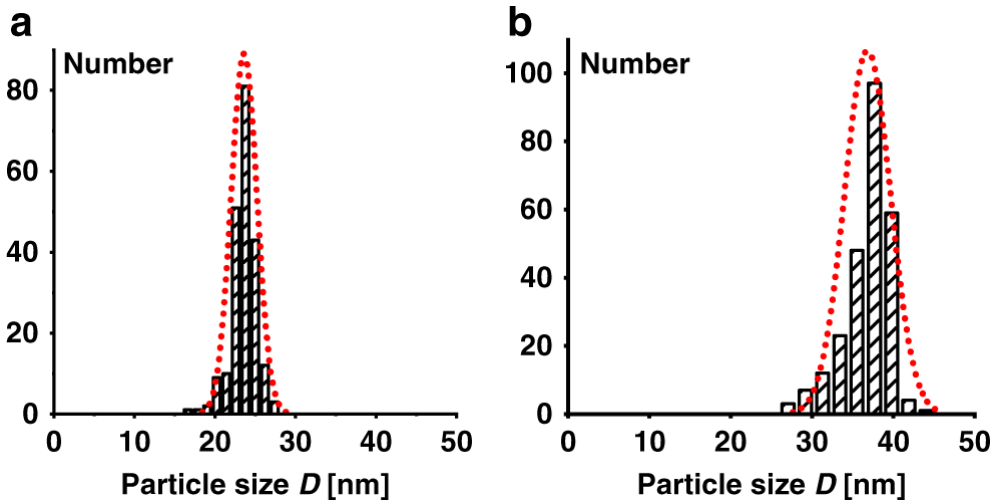

Figure 3.7. Histograms of particle sizes (equivalent diameter *D*) based on TEM statistics from polyethylene dispersions obtained. a) After 30 min reaction time (entry 1, Table 3.2). b) after 4 h reaction time (entry 4, Table 3.2). The dotted lines are calculated normal distribution curves.

A comparison of the average mass of a particle (see *Experimental Section* for detailed size analysis from TEM and AFM data) with the molecular weight of the formed polymer shows the particles to be composed of a single chain (Table 3.2, 'chains/particle' column). That is, a given particle is grown by one active Ni(II) site, and the final particle size and morphology are determined by the time available for growth, given by the duration of the polymerization experiment.

Concerning the potential of these anisotropic particles for assembly, samples that were dried without any additional manipulations (e.g. patterned surface, spin coating, etc.) to enable the particles to arrange, show a preferred orientation of adjacent particles (see Figure 3.6 and *Appendix*).

For anisotropic inorganic particles, like gold nanorods, micron scale highly ordered assemblies can be achieved in some cases.[344,345] These evolved from extensive studies and consequent careful choice of suitable preparative routes, aspect ratios, and assembly conditions.[346,347] While the above assemblies of the herein reported particles do not fully match the extensively optimized assemblies of inorganic nanoparticles, they appear promising. A direct comparison with anisotropic polymeric materials is difficult, since there are only few reports available. Recently, several examples (e.g., rod-like) were reported and show assemblies in comparable quality to those presented here.[298,304,348]

3.3 Conclusion

Anisotropic polymer nanoparticles with a uniform shape and size are accessible by aqueous catalytic polymerization. The key to this is a truly living catalytic polymerization that retains its living character for hours and up to very high molecular weights, providing single-chain nanocrystals of ultra high molecular weight polyethylene. This is enabled by advanced catalysts with highly hydrophobic perfluoroalkyl substituents, and a robust polymerization procedure that allows for a homogeneous non-aggregated solution of the catalyst precursors in the initial reaction mixture, despite their highly hydrophobic portions. Preliminary observations indicate the particles' ability to assemble. This concept, demonstrated for polyethylenes as an important synthetic material, paves the way for particle-based materials.

3.4 Experimental section

3.4.1 Materials and general considerations

All manipulations involving air- and/or moisture-sensitive substances were carried out under inert atmosphere using standard Schlenk and glovebox techniques. Solvents were dried and degassed using standard laboratory techniques. Pentane, diethyl ether, toluene and dichloromethane were dried and freed from oxygen by passing over columns with *BASF R3-11* catalyst and molecular sieves. Heptane was distilled over calcium hydride. Dioxane and benzene, purchased from *Merck*, were distilled over sodium. Pyridine, purchased from *Merck*, was destilled from potassium hydroxide. Mesitylene, purchased from *sigma-aldrich*, was distilled under nitrogen (first fraction of 10 % discarded). Water was deoxygenated by distillation under a constant nitrogen stream. Ethylene 3.5 was purchased from *Air Liquide* and used as obtained. 1,3-Dibromobenze and [Pd(dba)$_2$] were purchased from *TCI chemicals* and used as obtained. Copper powder, sodium dodecyl sulfate pellets, 4,4'-di-tert-butyl-2,2'-dipyridyl, methanol, *p*-toluene sulfonic acid were purchased from *sigma-aldrich* and used as obtained (liquids were dried over molecular sieves). Perfluorobutyliodide and perfluorooctyliodide, purchased from *Apollo Scientific*, were degassed and dried over molecular sieves. Perfluorohexyliodide, purchased from *fluorochem*, were degassed and dried over molecular sieves. Bis(pinacolato)diboron, purchased from *Activate Scientific*, was used as obtained. 2,6-Dibromoaniline, cesium fluoride, 3,5-diiodosalicylaldehyde and hexafluorobenzene, purchased from *abcr*, were used as obtained (liquids were dried over molecular sieves). Triphenylphosphine, purchased from *acros*, was used as obtained. [(tmeda)NiMe$_2$], purchased from *MCat*, was stored at -30 °C prior to use.[349] Sodium sulfate and sodium chloride, purchased from *Fisher Scientific*, were used as obtained. H_2N-PEG-OMe, purchased from *Iris Biotech*, was stored at -30 °C prior to use. Molecular sieves (4 Å, 0.4 nm, Type 514) were purchased from *Carl Roth*. NMR solvents, purchased from *Eurisotop*, were purged with nitrogen and dried over molecular sieves. The reference catalysts (**1^{I}-CF$_3$/L**) and [Ir(COE)$_2$Cl]$_2$ were synthesized according to reported procedures.[108,177,350]

NMR spectra were recorded on a *Bruker Avance III 400* with a BBFO plus probe with Z-gradient, *Bruker Avance III HD 400* with a TBO probe with Z-gradient or a *Bruker Avance III 600*. Chemical shifts were referenced to the signal of the solvent (residual proton signal for ^{1}H spectra, carbon signal for ^{13}C spectra). Multiplicities are reported as follows: s (singlet), doublet

(d), triplet (t), quartet (q), quintet (quint.), pentet (p), virtual multiplet (v), multiplet (m), broad (br.) and combination thereof. The NMR assignments were confirmed by common 2D NMR experiments (^{1}H,^{1}H-gCOSY; ^{1}H,^{13}C-gHSQC and ^{1}H,^{13}C-gHMBC). *MestReNova* software by *Mestrelab Research S.L.* was used for data evaluation. High temperature NMR spectroscopy of polymers was carried out at 130 °C in $C_2D_2Cl_4$ with 0.5 wt-% $Cr(acac)_3$ as relaxation agent. ^{13}C NMR spectra of polymers were referenced to the carbon signal of the solvent (74.4 ppm). The total integral of all polyethylene signals was set to 1000 C and the branch content determined from the values for the α-methyl signal (37.6 ppm) and the methyl signal (20.1 ppm). Elemental analysis was carried out on an *Elementar vario MICRO cube* instrument at the Department of Chemistry at the University of Konstanz. Molecular weights of synthesized polyethylenes were determined by high temperature gel permeation chromatography (GPC). A *Polymer Laboratories 220* instrument (software: *Cirrus Multi Offline GPC/SEC* software, version 3.3) equipped with *PLgel Olexis* columns at 160 °C in 1,2,4-trichlorobenzene (1.0 mL minute^{-1} flow rate) with refractive index (concentration signal), viscosity and light scattering detection (15° and 90°) was used. High molecular weights (> 100,000 g/mol) were determined using the triple detection method calibrated with narrow polystyrene standards. Lower molecular weights (< 100,000 g/mol) were determined by linear calibration versus polyethylene standards with concentration detection (refractive index) only. Differential scanning calorimetry (DSC) measurements of polymers were carried out on a *Netzsch DSC 204 F1* instrument (software: *Netzsch Proteus Thermal Analysis*, version 6.1.0) with a heating/cooling rate of 10 K/min. Additional measurements to investigate the polymer chain disentanglement were done with a heating/cooling rate of 1 K/min (only first heating cycle reported). Dynamic light scattering (DLS) was performed on diluted polyethylene dispersions using a *Malvern Zetasizer Nano-ZS ZEN 3600* instrument (633 nm) in backscattering mode (173°) at 25 °C. The data was analyzed to yield particle size distributions and polydispersity indices (PDIs; dimensionless number between 0 and 1; 1 being highly polydisperse; determined from gradient of cumulants analysis) using the *Malvern Zetasizer Software*, version 7.12. Transmission electron microscopy (TEM) images were recorded on a *Zeiss Libra 120 EF-TEM* instrument. Polyethylene dispersion samples were dialyzed versus demineralized water using *Spectra/Por Dialysis Membranes* 2, MWCO 12 – 14 kD and TEM samples prepared by drop casting (diluted to 0.01 wt-%), directly on the grid. The decrease of surfactant content during dialysis was monitored by tensiometry measurements. TEM images were analyzed using *iTEM* and *ImageJ/Fiji*[351-353] software. Atomic force microscopy (AFM) was performed on a *JPK NanoWizard* instrument. Samples were prepared from dialyzed dispersions

by drop casting and spin coating on a flat silicon waver. Tensiometry measurements were carried out on a *Krüss Process Tensiometer K100* (software: *Krüss Laboratory Desktop Software*, version 3.3) equipped with a platinum plate. Analytical ultracentrifuge (AUC) experiments were conducted on instruments of Prof. Helmut Cölfen's research group, using a *XLI* device from *Beckman Coulter* with interference optics (*vide infra*). Electrochemical measurements were performed on instruments of Prof. Rainer Winter's research group (*vide infra*).

3.4.2 Ligand synthesis

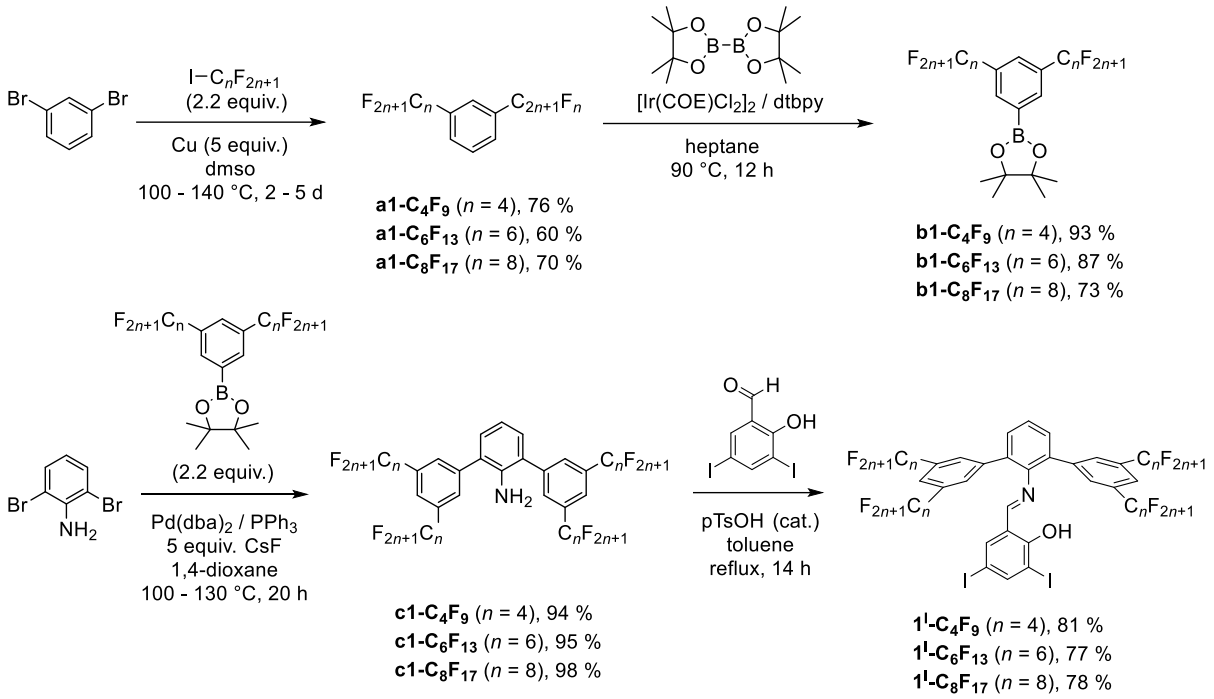

Scheme 3.1. Synthesis scheme of salicylaldimine ligands with perfluoroalkyl substitution. Starting with the synthesis of 1,3-di(perfluoroalkyl)benzene, followed by selective borylation and Suzuki coupling with 2,6-dibromobenzene to produce the respective terphenylamines. The salicylaldimine was obtained by acid catalyzed condensation with 3,5-diiodosalicylaldehyde.

Synthesis of 1,3-di(perfluoroalkyl)benzenes (a1-R^F)

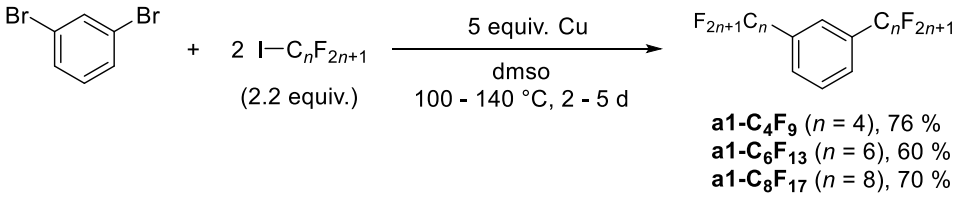

Scheme 3.2. Synthesis of 1,3-di(perfluoroalkyl)benzenes (**a1-R^F**). The compounds were obtained by copper-promoted Ullmann coupling of 1,3-dibromobenzene with the appropriate linear perfluoroalkyliodide.

General procedure: Compounds **a1-R^F** were synthesized according to a modified literature procedure.[354] 1,3-dibromobenzene (1 equiv.), copper powder (5 equiv.) and perfluoroalkyliodide (2.2 equiv.) were added to 250 mL of dmso. The reaction mixture was sealed and stirred for 2-5 days at 100 – 140 °C under exclusion of light. The resulting red suspension was allowed to cool to room temperature, poured into 400 mL of water and stirred for 15 minutes. The red

precipitates (inorganic salts) were filtered off and washed with diethyl ether (2 x 150 mL). The aqueous filtrate was extracted with diethyl ether (3 x 100 mL). The combined organic phases were washed with water (2 x 100 mL), brine (100 mL) and dried over sodium sulfate. After removing the solvent under reduced pressure, the product was obtained as yellow oil.

1,3-Di(perfluorobutyl)benzene (**a1-C_4F_9**)

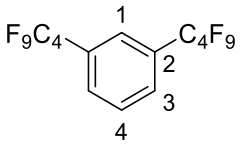

M = 514.2 g/mol

a1-C_4F_9, yield: 76 %

Compound **a1-C_4F_9** was synthesized according to the above general procedure using 7.75 g 1,3-dibromobenzene (32.8 mmol, 1 equiv.), 10.42 g copper powder (164 mmol, 5 equiv.) and 24.98 g perfluorobutyliodide (72.2 mmol, 2.2 equiv.). The reaction mixture was kept at 100 °C for 2 days. Yield: 76 %, 28.2 g, 54.8 mmol.

^{1}H NMR (400 MHz, $CDCl_3$, 300 K): δ (ppm) = 7.87 – 7.79 (m, 3H, *H-1*, *H-3*), 7.70 (t, $^3J_{HH}$ = 7.6 Hz, *H-4*).

^{19}F{^{1}H} NMR (376 MHz, $CDCl_3$, 300 K): δ (ppm) = -81.1 (tt, J_{FF} = 10 Hz, J_{FF} = 3 Hz, 6F, -CF_3), -111.4 (t, $^3J_{FF}$ = 14 Hz, 4F, $C_{arom}CF_2$), -122.8 (m, 4F, CF_2), -125.6 (m, 4F, CF_2).

^{13}C{^{1}H} NMR (101 MHz, $CDCl_3$, 300 K): δ (ppm) = 130.6 (t, $^3J_{CF}$ = 7 Hz, *C-3*), 130.1 (t, $^2J_{CF}$ = 25 Hz, *C-2*), 129.5 (s, *C-4*), 125.7 (quint., $^3J_{CF}$ = 7 Hz, *C-1*) , 125-107 (-C_4F_9, *broad due to multiple* $^XJ_{CF}$ *couplings)*

1,3-Di(perfluorohexyl)benzene (**a1-C_6F_{13}**)

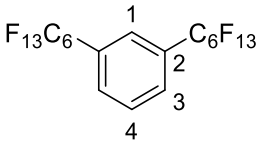

M = 714.2 g/mol

a1-C_6F_{13}, yield: 60 %

Compound **a1-C_6F_{13}** was synthesized according to the above general procedure using 7.61 g 1,3-dibromobenzene (32.3 mmol, 1 equiv.), 10.26 g copper powder (161.5 mmol, 5 equiv.) and 31.71 g perfluorohexyliodide (71.1 mol, 2.2 equiv.). The reaction mixture was kept at 140 °C for 5 days. Yield: 60 %, 13.5 g, 18.9 mmol.

^{1}H NMR (400 MHz, $CDCl_3$ / C_6F_6, 300 K): δ (ppm) = 7.85 – 7.79 (m, 3H, *H-1, H-3*), 7.68 (t, $^3J_{HH}$ = 3.5 Hz, *H-4*).

^{19}F{^{1}H} NMR (376 MHz, $CDCl_3$ / C_6F_6, 300 K): δ (ppm) = -81.7 (tt, J_{FF} = 10 Hz, J_{FF} = 3 Hz, 6F, *CF_3*), -111.8 (t, J_{FF} = 15 Hz, 4F, C_{arom}*CF_2*), -121.9 (m, 4F, *CF_2*), -122.4 (m, 4F, *CF_2*), -123.3 (m, 4F, *CF_2*), -126.8 (m, 4F, *CF_2*).

^{13}C{^{1}H} NMR (101 MHz, $CDCl_3$, 300 K): δ (ppm) = 130.6 (t, $^{4}J_{CF}$ = 6 Hz, *C-3*), 130.5 (t, $^{3}J_{CF}$ = 25 Hz, *C-2*), 129.5 (s, *C-4*), 125.8 (t, $^{4}J_{CF}$ = 6 Hz, *C-1*), 120-150 (*-C_6F_{13}, broad due to multiple $^{X}J_{CF}$ couplings*)

1,3-Di(perfluorooctyl)benzene (**a1-C_8F_{17}**)

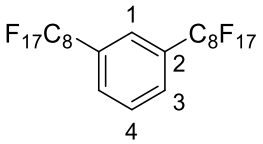

M = 914.2 g/mol

a1-C_8F_{17}, yield: 70 %

Compound **a1-C_8F_{17}** was synthesized according to the above general procedure using 1.42 g 1,3-dibromobenzene (6 mmol, 1 equiv.), 1.97 g copper powder (30 mmol, 5 equiv.) and 7.21 g perfluorooctyliodide (13.2 mmol, 2.2 equiv.). The reaction mixture was kept at 140 °C for 5 days. Yield: 70 %, 3.84 g, 4.2 mmol.

^{1}H NMR (400 MHz, $CDCl_3$ / C_6F_6, 300 K): δ (ppm) = 7.88-7.78 (m, 2H, *H-1, H-3*), 7.71 (t, $^{3}J_{HH}$ = 7.9 Hz, 1H, *H-4*).

^{19}F{^{1}H} NMR (376 MHz, $CDCl_3$ / C_6F_6, 300 K): δ (ppm) = -81.2 (m, 6F, *CF_3*), -111.5 (t, 4F, C_{arom}*CF_2*), -121.4 (m, 4F, *CF_2*), -122.2 (m, 12F, *CF_2*), -123.0 (m, 4F, *CF_2*), -126.4 (m, 4F, *CF_2*).

^{13}C{^{1}H} NMR (101 MHz, $CDCl_3$ / C_6F_6, 300 K): δ (ppm) = 130.6 (m, *C-3*), 129.5 (s, *C-4*), 130.3 (t, $^{2}J_{CF}$ = 25 Hz, *C-2*), 125.8 (m, *C-1*).

Synthesis of 3,5-di(perfluoroalkyl)phenylboronic acid pinacol esters (b1-R^F)

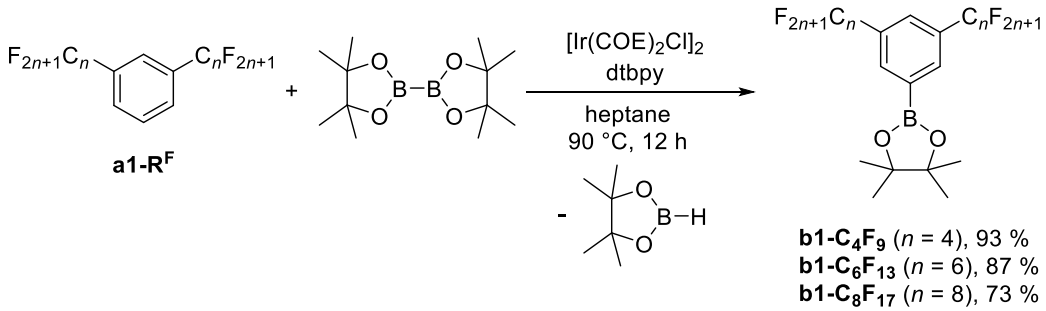

Scheme 3.3. Synthesis of 3,5-di(perfluoroalkyl)phenylboronic acid pinacol esters (**b1-R^F**). The selective borylation was performed via iridium-catalyzed reaction with bis(pinacolato)diboron.

General procedure: The synthesis was conducted according to a modified literature procedure.[355] $[Ir(COE)_2Cl]_2$ (0.005 - 0.01 equiv.) and 4,4'-di-tert-butyl-2,2'-dipyridyl (0.01 - 0.02 equiv.) were stirred for 5 minutes in 5 mL of heptane to give a dark blue catalyst suspension. This was transferred to a mixture of 1,3-di(perfluoroalkyl)benzene (**a1-R^F**, 1 equiv.) and

bis(pinacolato)biboron (1 equiv.) in 150 mL of heptane and stirred for 12 hours at 90 °C to give an orange solution. The reaction mixture was allowed to cool to room temperature, extracted with brine (2 x 150 mL) and dried over sodium sulfate. After removing the solvent in vacuum, the product was obtained as yellow oil. This was kept under vacuum for several hours to remove residues of pinacolborane.

3,5-Di(perfluorobuty)lphenylboronic acid pinacol ester (**b1-C_4F_9**)

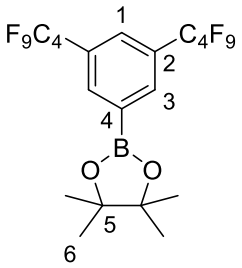

M = 640.1 g/mol

b1-C_4F_9, yield: 93 %

Compound **b1-C_4F_9** was synthesized according to the above general procedure using 25.7 g 1,3-di(perfluorobutyl)benzene (**a1-C_4F_9**, 50 mmol, 1 equiv.), 12.7 g bis(pinacolato)diboron (50 mmol, 1 equiv.), 0.180 g $[Ir(COE)_2Cl]_2$ (0.005 equiv.) and 0.125 g 4,4'-di-tert-butyl-2,2'-dipyridyl (0.01 equiv.). Yield: 93 %, 29.8 g, 47 mmol.

^{1}H NMR (400 MHz, $CDCl_3$, 300 K): δ (ppm) = 8.23 (s, 2H, *H-3*), 7.87 (s, 1H, *H-1*), 1.37 (s, 12H, *H-6*).

^{19}F{^{1}H} NMR (376 MHz, $CDCl_3$, 300 K): δ (ppm) = -81.4 (tt, J_{FF} = 10 Hz, J_{FF} = 3 Hz, 6F, CF_3), -111.5 (m, 4F, $C_{arom}CF_2$), -122.7 (m, 4F, CF_2), -125.9 (m, 4F, CF_2).

^{13}C{^{1}H} NMR (101 MHz, $CDCl_3$, 300 K): δ (ppm) = 136.7 (t, $^3J_{CF}$ = 6 Hz, *C-3*), 131.6 (br. m, *C-4*), 129.6 (t, $^3J_{CF}$ = 25 Hz, *C-2*), 128.0 (quint., $^3J_{CF}$ = 6 Hz, *C-1*), 123-106 (*-C_4F_9, broad due to multiple $^XJ_{CF}$ couplings),* 85.1 (s, *C-5*), 24.9 (s, *C-6*).

3,5-Di(perfluorohexyl)phenylboronic acid pinacol ester (**b1-C_6F_{13}**)

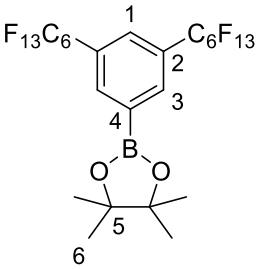

M = 840.2 g/mol

b1-C_6F_{13}, yield: 87 %

Compound **b1-C_6F_{13}** was synthesized according to the above general procedure using 10.1 g 1,3-di(perfluorohexyl)benzene (**a1-C_6F_{13},** 14.1 mmol, 1 equiv.), 3.6 g bis(pinacolato)diboron (14.1 mmol, 1 equiv.), 63 mg $[Ir(COE)_2Cl]_2$ (0.005 equiv.) and 50 mg 4,4'-i-tert-butyl-2,2'-dipyridyl (0.01 equiv.). Yield: 87 %, 10.4 g, 47 mmol.

^{1}H NMR (400 MHz, $CDCl_3$, 300 K): δ (ppm) = 8.22 (s, 2H, *H-3*), 7.86 (s, 1H, *H-1*), 1.37 (s, 12H, *H-6*).

^{19}F{^{1}H} NMR (376 MHz, $CDCl_3$, 300 K): δ (ppm) = -80.9 (tt, J_{FF} = 10 Hz, J_{FF} = 2 Hz, 6F, CF_3), -111.0 (t, J_{FF} = 14 Hz, 4F, $C_{arom}CF_2$), -121.3 to -121.8 (m, 8F, CF_2), -122.9 (m, 4F, CF_2), -126.2 (m, 4F, CF_2).

^{13}C{^{1}H} NMR (101 MHz, $CDCl_3$, 300 K): δ (ppm) = 136.6 (m, *C-3*), 129.5 (t, $^3J_{CF}$ = 25 Hz, *C-2*), 128.0 (m, *C-1*), 122-104 (*-C_6F_{13}, broad due to multiple $^XJ_{CF}$ couplings*), 85.0 (s, *C-5*), 25.0 (s, *C-6*), *C-4 was not detected, as expected for quaternary carbons with attached boryl groups.*

3,5-Di(perfluorooctyl)phenylboronic acid pinacol ester (**b1-C_8F_{17}**)

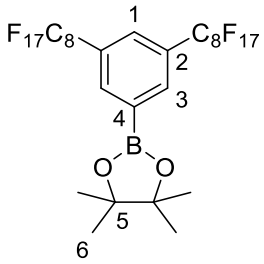

M = 1040.2 g/mol

b1-C_8F_{17}, yield: 73 %

Compound **b1-C_8F_{17}** was synthesized according to the above general procedure using 3.16 g 1,3-di(perfluorooctyl)benzene (**a1-C_8F_{17}**, 3.45 mmol, 1 equiv.), 0.88 g bis(pinacolato)diboron (3.45 mmol, 1 equiv.), 31 mg $[Ir(COE)_2Cl]_2$ (0.01 equiv.) and 25 mg 4,4'-di-tert-butyl-2,2'-dipyridyl (0.02 equiv.). Yield: 73 %, 2.5 g, 47 mmol.

^{1}H NMR (400 MHz, $CDCl_3$, 300 K): δ (ppm) = 8.23 (s, 2H, *H-3*), 7.86 (s, 1H, *H-1*), 1.37 (s, 12H, *H-6*).

^{19}F{^{1}H} NMR (376 MHz, $CDCl_3$, 300 K): δ (ppm) = -80.9 (tt, J_{FF} = 11 Hz, J_{FF} = 2 Hz, 6F, CF_3), -111.1 (t, J_{FF} = 14 Hz, 4F, $C_{arom}CF_2$), -121.2 (m, 4F, CF_2), -121.5 to -122.3 (m, 12F, CF_2), -122.8 (m, 4F, CF_2), -126.2 (m, 4F, CF_2).

^{13}C{^{1}H} NMR (101 MHz, $CDCl_3$, 300 K): δ (ppm) = 136.6 (t, $^3J_{CF}$ = 6 Hz, *C-3*), 129.5 (t, $^3J_{CF}$ = 25 Hz, *C-2*), 128.0 (m, *C-1*), 119-104 (*-C_8F_{17}, broad due to multiple $^XJ_{CF}$ couplings),* 85.0 (s, *C-5*), 25.0 (s, *C-6*), *C-4 was not detected, as expected for quaternary carbons with attached boryl groups.*

Synthesis of 3,3′,5,5′-tetra(perfluoroalkyl)terphenyl amines (c1-R^F)

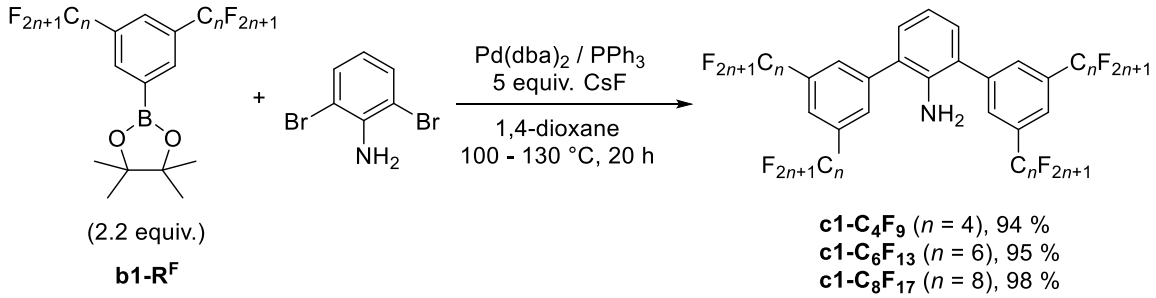

Scheme 3.4. Synthesis of 3,3',5,5'-tetra(perfluoroalkyl)terphenyl amines (**c1-R^F**). The terphenylamines were obtained from palladium catalyzed Suzuki coupling of boronic esters with 2,6-dibromoaniline.

General procedure: [Pd(dba)$_2$] and triphenylphosphine were stirred for 5 minutes in 10 mL of dioxane to give an orange catalyst solution. This was added to a mixture of 3,5-di(perfluoroalkyl)phenylboronic acid pinacol ester (**b1-R^F**, 2.2 equiv.), 2,6-dibromoaniline (1 equiv.) and cesium fluoride (5 equiv.) in 300 mL of dioxane. The dark orange reaction mixture was heated to 130 °C for 2 hours and stirred at 100 °C overnight to give a green suspension. The solvent was removed under reduced pressure, and the residue (dark sticky oil and inorganic salts) was washed with warm water (2 x 250 mL) and warm methanol (2 x 250 mL). The dark residue was diluted in diethyl ether and filtrated over a plug of Celite to remove palladium black impurities. After drying over sodium sulfate, the solvent was removed under reduced pressure to give the product as a brownish wax. The products were used for the next step (condensation) without further purification as they showed only minor impurities in the NMR spectra. Pure products could be obtained by column chromatography on silica using pentane/triethylamine [1:0.005] (for n = 6 and 8) or pentane/diethyl ether/trimethylamine [1:0.05:0.005] (for n = 4) as eluent.

3,3',5,5'-Tetra(perfluorobutyl)terphenyl amine (**c1-C_4F_9**)

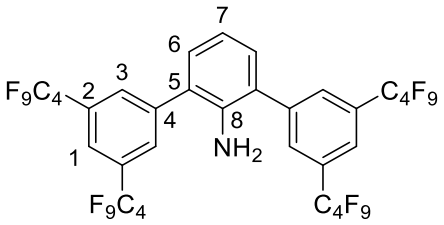

M = 1117.4 g/mol

c1-C_4F_9, yield: 94 %

Compound **c1-C_4F_9** was synthesized according to the above general procedure using 10.0 g 3,5-diperfluorobutyllphenylboronic acid pinacol ester (**b1-C_4F_9**, 15.6 mmol, 2.2 equiv.), 1.78 g 2,6-dibromoaniline (7.1 mmol, 1 equiv.), 5.36 g cesium fluoride (35.3 mmol, 5 equiv.), 0.208 g

$Pd(dba)_2$ (0.36 mmol, 0.05 equiv.) and 0.209 g triphenylphosphine (0.8 mmol, 0.11 equiv.). Yield: 94 %, 7.46 g, 6.7 mmol.

^{1}H NMR (400 MHz, $CDCl_3$, 300 K): δ (ppm) = 7.99 (s, 4H, *H-3*), 7.82 (s, 2H, *H-1*), 7.19 (d, $^3J_{HH}$ = 7.6 Hz, 2H, *H-6*), 7.00 (t, $^3J_{HH}$ = 7.6 Hz, 1H, *H-7*), 3.68 (s, 2H, NH_2).

^{19}F{^{1}H} NMR (376 MHz, $CDCl_3$, 300 K): δ (ppm) = -81.1 (tt, J_{FF} = 10 Hz, J_{FF} = 3 Hz, 12F, CF_3), -111.3 (t, J_{FF} = 12 Hz, 8F, $C_{arom}CF_2$), -122.6 (m, 8F, CF_2), -125.6 (m, 8F, CF_2).

^{13}C{^{1}H} NMR (101 MHz, $CDCl_3$, 300 K): δ (ppm) = 141.2 (s, *C-8*), 140.6 (s, *C-4*), 131.6 (m, *C-3*), 131.4 (s, *C-6*), 131.0 (t, $^2J_{CF}$ = 25 Hz, *C-2*), 125.5 (s, *C-5*), 124.7 (m, *C-1*), 121-105 (-C_4F_9, *broad due to multiple* $^XJ_{CF}$ *couplings*), 119.5 (s, *C-7*).

3,3',5,5'-Tetra(perfluorohexl)terphenyl amine (**c1-C_6F_{13}**)

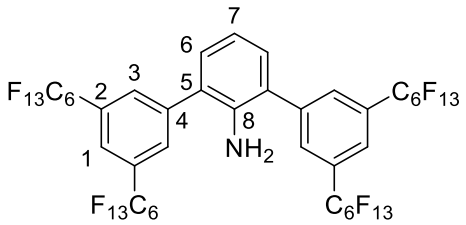

M = 1517.5 g/mol

c1-C_6F_{13}, yield: 95 %

Compound **c1-C_6F_{13}** was synthesized according to the above general procedure using 13.41 g 3,5-diperfluorohexylphenylboronic acid pinacol ester (**b1-C_6F_{13}**, 15.7 mmol, 2.2 equiv.), 1.82 g 2,6-dibromoaniline (7.25 mmol, 1 equiv.), 5.51 g cesium fluoride (36.3 mmol, 5 equiv.), 0.208 g $Pd(dba)_2$ (0.36 mmol, 0.05 equiv.) and 0.209 g triphenylphosphine (0.8 mmol, 0.11 equiv.). Yield: 97 %, 10.67 g, 7 mmol.

^{1}H NMR (400 MHz, $CDCl_3$ / C_6F_6, 300 K): δ (ppm) = 8.00 (s, 4H, *H-3*), 7.83 (s, 2H, *H-1*), 7.20 (d, $^3J_{HH}$ = 7.7 Hz, 2H, *H-6*), 6.99 (t, $^3J_{HH}$ = 7.7 Hz, 1H, *H-7*), 3.68 (s, 2H, NH_2).

^{19}F{^{1}H} NMR (376 MHz, $CDCl_3$ / C_6F_6, 300 K): δ (ppm) = -81.1 (tt, J_{FF} = 10 Hz, J_{FF} = 3 Hz, 12F, CF_3), -111.2 (t, J_{FF} = 12 Hz, 8F, $C_{arom}CF_2$), -121.5 (m, 8F, CF_2), -121.9 (m, 8F, CF_2), -123.0 (m, 8F, CF_2), -126.4 (m, 8F, CF_2).

^{13}C{^{1}H} NMR (101 MHz, $CDCl_3$ / C_6F_6, 300 K): δ (ppm) = 141.2 (s, *C-8*), 140.7 (s, *C-4*), 131.6 (m, *C-3*), 131.3 (s, *C-6*), 131.1 (t, $^2J_{CF}$ = 25 Hz, *C-2*), 125.5 (s, *C-5*), 124.8 (m, *C-1*), 120-105 (-C_6F_{13}, *broad due to multiple* $^XJ_{CF}$ *couplings*), 119.5 (s, *C-7*).

3,3',5,5'-Tetra(perfluorooctyl)terphenyl amine (**c1-C_8F_{17}**)

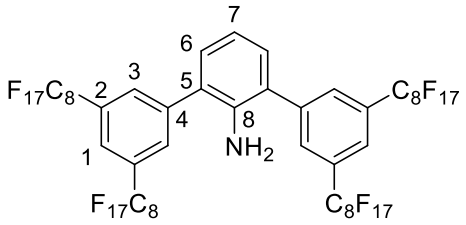

M = 1917.5 g/mol

c1-C_8F_{17}, yield: 98 %

Compound **c1-C_8F_{17}** was synthesized according to the above general procedure using 10.4 g 3,5-diperfluoroocylphenylboronic acid pinacol ester (**b1-C_8F_{17}**, 10 mmol, 2.2 equiv.), 1.09 g 2,6-dibromoaniline (4.35 mmol, 1 equiv.), 3.04 g cesium fluoride (20 mmol, 4.6 equiv.), 0.127 g $Pd(dba)_2$ (0.22 mmol, 0.05 equiv.) and 0.126 g triphenylphosphine (0.48 mmol, 0.11 equiv.). Yield: 98 %, 8.16 g, 4.3 mmol.

^{1}H NMR (400 MHz, $CDCl_3$ / C_6F_6, 300 K): δ (ppm) = 8.03 (s, 4H, *H-3*), 7.85 (s, 2H, *H-1*), 7.22 (d, $^3J_{HH}$ = 7.6 Hz, 2H, *H-6*), 7.00 (t, $^3J_{HH}$ = 7.6 Hz, 1H, *H-7*), 3.73 (s, 2H, NH_2).

^{19}F{^{1}H} NMR (376 MHz, $CDCl_3$ / C_6F_6, 300 K): δ (ppm) = -80.9 (tt, J_{FF} = 10 Hz, J_{FF} = 2 Hz, 12F, CF_3), -111.1 (t, J_{FF} = 14 Hz, 8F, $C_{arom}CF_2$), -121.2 (m, 8F, CF_2), -121.6 to -122.3 (m, 24F, CF_2), -122.8 (m, 8F, CF_2), -126.2 (m, 8F, CF_2).

^{13}C{^{1}H} NMR (101 MHz, $CDCl_3$ / C_6F_6, 300 K): δ (ppm) = 141.4 (s, *C-8*), 140.8 (s, *C-4*), 131.7 (m, *C-3*), 131.4 (s, *C-6*), 131.3 (t, $^2J_{CF}$ = 25 Hz, *C-2*), 125.7 (s, *C-5*), 124.7 (m, *C-1*), 121-105 (-C_8F_{17}, *broad due to multiple $^XJ_{CF}$ couplings*), 119.5 (s, *C-7*).

Synthesis of 3,5-diiodo-N-[2,6-bis(3,5-diperfluoroalkyphenyl)phenyl]-salicylaldimines (1^I-R^F)

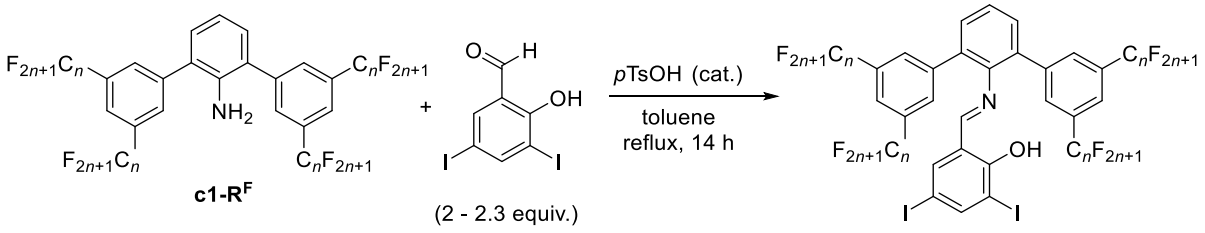

1^I-C_4F_9 (*n* = 4), 81 %
1^I-C_6F_{13} (*n* = 6), 77 %
1^I-C_8F_{17} (*n* = 8), 78 %

Scheme 3.5. Synthesis of 3,5-diiodo-*N*-[2,6-bis(3,5-diperfluoroalkyphenyl)phenyl]-salicylaldimines (**1^I-R^F**). Highly pure salicylaldimines were obtained from acid catalyzed condensation of terphenyl-amines with 3,5-diiodosalicylaldhyde, followed by column chromatography (pentane as eluent).

General procedure: Terphenylamine (**c1-R^F**, 1 equiv.), 3,5-diiodosalicylaldehyde (2.0 – 2.3 equiv.) and 50 mg *p*-toluene sulfonic acid hydrate (*p*TsOH) were added to 200 – 250 mL of toluene. The flask was equipped with a Soxhlet apparatus filled with dried molecular sieves to allow an azeotropic water removal during the reaction. The reaction mixture was heated to

intense reflux (heating bath temperature >160 °C) for 14 hours. Note, that a complete dissolution of the terphenylamine is essential for conversion to the desired product. The reaction mixture was allowed to cool down to room temperature, and the solvent was removed under reduced pressure. After purification via column chromatography on silica with pentane as eluent (yellow band), the product was obtained as a yellow sticky oil. Precipitation from a saturated pentane solution at -78 °C and careful removal of the supernatant gave the pure product as a yellow powder that was dried under vacuum overnight.

3,5-Diiodo-N-[2,6-bis(3,5-diperfluorobutylphenyl)phenyl]-salicylaldimine (**d1-C_4F_9**)

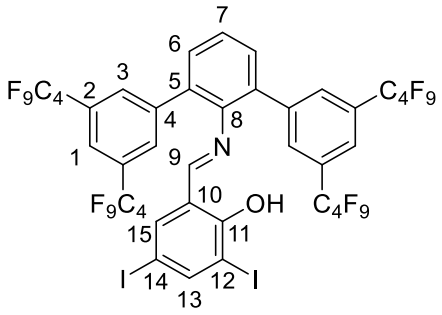

M = 1473.3 g/mol

1^I-C_4F_9, yield: 81 %

Compound **1^I-C_4F_9** was obtained following the general procedure with 7.46 g 3,3',5,5'-tetra(perfluorobutyl)terphenyl amine (**c1-C_4F_9**, 6.7 mmol, 1 equiv.), 5.0 g 3,5-diiodosalicylaldehyde (13.4 mmol, 2 equiv.) and 50 mg *p*TsOH in 250 mL of toluene. Yield: 81 %, 8.0 g, 5.4 mmol.

^{1}H NMR (400 MHz, $CDCl_3$, 300 K): δ (ppm) = 12.65 (s, 1H, O*H*), 8.01 (d, $^4J_{HH}$ = 2.0 Hz, *H-13*), 7.78 (br s, 4H, *H-3, H-9*), 7.75 (s, 2H, *H-1*), 7.52 (m, 3H, *H-6*, *H-7*), 7.04 (d, $^4J_{HH}$ = 2.1 Hz, *H-15*).

^{19}F{^{1}H} NMR (376 MHz, $CDCl_3$, 300 K): δ (ppm) = -80.9 (tt, J_{FF} = 11 Hz, J_{FF} = 3 Hz, 12F, CF_3), -111.3 (t, J_{FF} = 14 Hz, 8F, $C_{arom}CF_2$), -122.7 (m, 8F, CF_2), -125.5 (m, 8F, CF_2).

^{13}C{^{1}H} NMR (101 MHz, $CDCl_3$, 300 K): δ (ppm) = 168.3 (s, *C-9*), 159.8 (s, *C-11*), 150.4 (s, *C-13*), 144.7 (s, *C-8*), 140.6 (s, *C-4*), 140.3 (s, *C-15*), 132.3 (s, *C-5*), 131.8 (m, *C-3*, *C-6*), 130.6 (t, $^2J_{CF}$ = 25 Hz, *C-2*), 127.3 (s, *C-7*), 124.7 (m, *C-1*), 119-105 (-C_4F_9, *broad due to multiple* $^XJ_{CF}$ *couplings*), 119.3 (s, *C-10*), 86.7 (s, *C-12*), 79.8 (s, *C-14*).

Elemental analysis (%) for $C_{41}H_{13}F_{36}I_2NO$: Found (Calculated)
C 33.63 (33.42); H 1.49 (0.89); N 1.19 (0.95)

3,5-Diiodo-N-[2,6-bis(3,5-diperfluorohexylphenyl)phenyl]-salicylaldimine (**1^{I}-C$_6$F$_{13}$**)

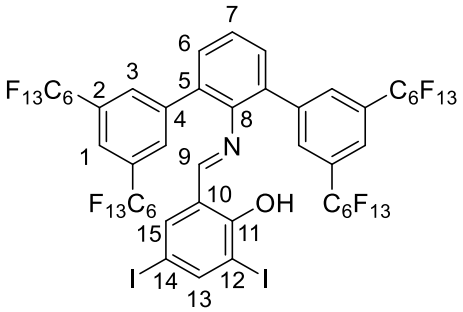

M = 1873.4 g/mol

1^{I}-C$_6$F$_{13}$, yield: 77 %

Compound **1^{I}-C$_6$F$_{13}$** was obtained following the general procedure with 8.8 g 3,3',5,5'-tetra(perfluorohexl)terphenyl amine (**c1-C$_6$F$_{13}$**, 5.6 mmol, 1 equiv.), 4.2 g 3,5-diiodosalicylaldehyde (11.2 mmol, 2 equiv.) and 50 mg *p*TsOH in 250 mL of toluene. Yield: 77 %, 8.1 g, 4.3 mmol.

^{1}H NMR (400 MHz, $CDCl_3$, 300 K): δ (ppm) = 12.68 (s, 1H, O*H*), 8.00 (d, $^{4}J_{HH}$ = 2.0 Hz, *H-13*), 7.79 (br s, 4H, *H-3, H-9*), 7.75 (s, 2H, *H-1*), 7.52 (m, 3H, *H-6*, *H-7*), 7.04 (d, $^{4}J_{HH}$ = 2.0 Hz, *H-15*).

^{19}F{^{1}H} NMR (376 MHz, $CDCl_3$ / C_6F_6, 300 K): δ (ppm) = -80.8 (tt, J_{FF} = 10 Hz, J_{FF} = 3 Hz, 12F, CF_3), -111.3 (t, J_{FF} = 12 Hz, 8F, $C_{arom}CF_2$), -121.5 (m, 8F, CF_2), -121.7 (m, 8F, CF_2), -122.7 (m, 8F, CF_2), -126.1 (m, 8F, CF_2).

^{13}C{^{1}H} NMR (101 MHz, $CDCl_3$, 300 K): δ (ppm) = 168.2 (s, *C-9*), 159.9 (s, *C-11*), 150.5 (s, *C-13*), 144.7 (s, *C-8*), 140.6 (s, *C-4*), 140.2 (s, *C-15*), 132.3 (s, *C-5*), 131.8 (m, *C-3*, *C-6*), 130.7 (t, $^{2}J_{CF}$ = 25 Hz, *C-2*), 127.4 (s, *C-7*), 124.7 (quint., $^{3}J_{CF}$ = 6.6 Hz, *C-1*), 122-105 (*-C_6F_{13}, broad due to multiple $^{X}J_{CF}$ couplings*), 119.3 (s, *C-10*), 86.7 (s, *C-12*), 79.8 (s, *C-14*).

Elemental analysis (%) for $C_{49}H_{13}F_{52}I_2NO$: Found (Calculated)
C 31.76 (31.42); H 1.10 (0.70); N 0.75 (0.79)

3,5-Diiodo-N-[2,6-bis(3,5-diperfluorooctylphenyl)phenyl]-salicylaldimine (**1^{I}-C$_8$F$_{17}$**)

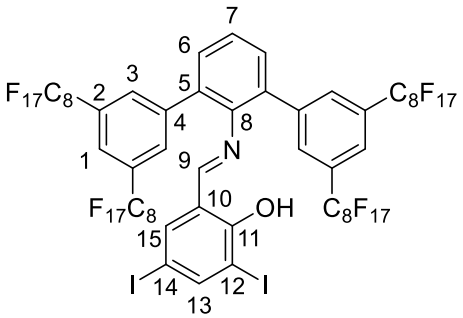

M = 2273.4 g/mol

1^{I}-C$_8$F$_{17}$, yield: 81 %

Compound **1^{I}-C$_8$F$_{17}$** was obtained following the general procedure with 4.39 g 3,3',5,5'-tetra(perfluorooctyl)terphenyl amine (**c1-C$_8$F$_{17}$**, 2.3 mmol, 1 equiv.), 1.94 g 3,5-diiodosalicylaldehyde (5.2 mmol, 2.3 equiv.) and 50 mg *p*TsOH in 200 mL of toluene. Yield: 81 %, 4.1 g, 1.79 mmol.

^{1}H NMR (400 MHz, $CDCl_3$, 300 K): δ (ppm) = 12.68 (s, 1H, O*H*), 8.00 (d, $^{4}J_{HH}$ = 2.0 Hz, *H-13*), 7.79 (br s, 4H, *H-3, H-9*), 7.75 (s, 2H, *H-1*), 7.52 (m, 3H, *H-6*, *H-7*), 7.04 (d, $^{4}J_{HH}$ = 2.0 Hz, *H-15*).

^{19}F{^{1}H} NMR (376 MHz, $CDCl_3$ / C_6F_6, 300 K): δ (ppm) = -80.9 (tt, J_{FF} = 10 Hz, J_{FF} = 2 Hz, 12F, CF_3), -111.1 (t, J_{FF} = 14 Hz, 8F, $C_{arom}CF_2$), -121.2 (m, 8F, CF_2), -121.6 to -122.3 (m, 24F, CF_2), -122.8 (m, 8F, CF_2), -126.2 (m, 8F, CF_2).

^{13}C{^{1}H} NMR (101 MHz, $CDCl_3$, 300 K): δ (ppm) = 168.2 (s, *C-9*), 159.9 (s, *C-11*), 150.5 (s, *C-13*), 144.7 (s, *C-8*), 140.6 (s, *C-4*), 140.2 (s, *C-15*), 132.3 (s, *C*-5), 131.8 (m, *C-3*, *C-6*), 130.7 (t, $^{2}J_{CF}$ = 25 Hz, *C*-2), 127.4 (s, *C-7*), 124.7 (quint., $^{3}J_{CF}$ = 6.6 Hz, *C-1*), 122-105 (-C_8F_{17}, *broad due to multiple* $^{X}J_{CF}$ *couplings*), 119.3 (s, *C-10*), 86.7 (s, *C-12*), 79.8 (s, *C-14*).

Elemental analysis (%) for $C_{57}H_{13}F_{68}I_2NO$: Found (Calculated)
C 29.88 (30.11); H 1.10 (0.58); N 0.58 (0.62)

3.4.3 Synthesis of complexes

Synthesis of κ²-(N,O)-salicylaldiminato nickelI(II) methyl pyridine complexes (1^{I}-R^{F}/Pyr)

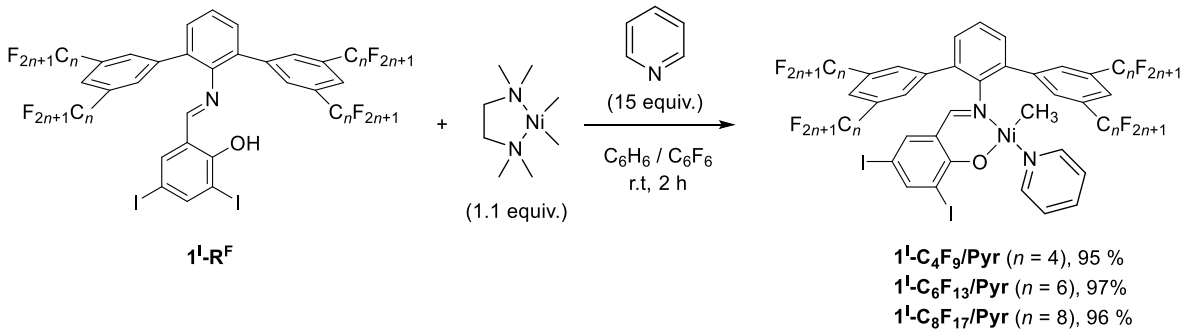

Scheme 3.6. Synthesis of κ²-(*N,O*)-salicylaldiminato nickel(II) methyl pyridine complexes (**1^{I}-R^{F}/Pyr**). The labile ligand (pyridine) was added to a mixture of nickel precursor and salicylaldimine to generate the respective nickel complex bearing different fluorocarbon substituents.

General procedure: To [(tmeda)NiMe₂] (1.1 equiv.) and the respective salicylaldimine (**1^{I}-R^{F}**, 1 equiv.), a solution of pyridine (15 equiv.) in 4.5 - 7 mL of benzene/hexafluorobenzene was added. Gas evolution (methane) was observed and the reaction mixture turned orange to red. The reactants were stirred for 2 hours at room temperature. The formed nickel black was removed via centrifugation. The red solution was frozen in liquid nitrogen und the solvent removed by freeze drying to give the desired product as a red powder.

{3,5-Diiodo-N-[2,6-bis(3,5-diperfluorobutylphenyl)phenyl]salicylaldiminato-κ² N,O}methyl-pyridinenickel(II) (**1^{I}-C_4F_9/Pyr**)

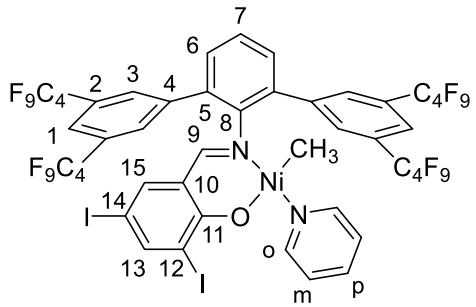

M = 1625.1 g/mol

1^{I}-C_4F_9 / Pyr, yield: 95 %

Complex **1^{I}-C_4F_9/Pyr** was synthesized following the general procedure for Ni(II) methyl pyridine complexes using 147 mg salicylaldimine **1^{I}-C_4F_9** (100 µmol, 1 equiv.), 23 mg [(tmeda)NiMe₂] (110 µmol, 1.1 equiv.) and 119 mg pyridine (1.5 mmol, 15 equiv.) in 6 mL of benzene. Yield: 95 %, 95 µmol, 154 mg.

^{1}H NMR (400 MHz, C_6D_6, 300 K): δ (ppm) = 8.38 (d, $^3J_{HH}$ = 5.6 Hz, 2H, *o-Pyr*), 8.27 (s, 4H, *H-3*), 8.03 (m, 3H, *H-1*, *H-13*), 7.06 (m, 3H, *H-6*, *H-7*), 6.73 (m, 2H, *H-15*, *p-Pyr*), 6.57 (s, 1H, *H-9*), 6.46 (t, $^3J_{HH}$ = 6.8 Hz, 2H, *m-Pyr*), -0.74 (s, 3H, Ni-CH_3).

^{19}F{^{1}H} NMR (376 MHz, C_6D_6, 300 K): δ (ppm) = -80.9 (t, J_{FF} = 10 Hz, 12F, CF_3), -110.9 (m, 8F, $C_{arom}CF_2$), -122.4 (m, 8F, CF_2), -125.4 (m, 8F, CF_2).

^{13}C{^{1}H} NMR (101 MHz, C_6D_6, 300 K): δ (ppm) = 167.8 (s, *C-9*), 164.1 (s, *C-11*), 151.2 (br. s, *o-Pyr*), 150.5 (s, *C-8*), 150.0 (s, *C-13*), 141.6 (s, *C-4*, *C-15*), 136.6 (br. s., *p-Pyr*), 132.6 (t, $^3J_{CF}$ = 5 Hz, *C-3*), 131.5 (s, *C-5*), 131.2 (s, *C-6*), 130.5 (t, $^2J_{CF}$ = 25 Hz, *C-2*), 127.1 (s, *C-7*), 124.6 (m, *C-1*), 123.2 (br. s, *m-Pyr*), 122-105 (-C_4F_9, *broad due to multiple* $^XJ_{CF}$ *couplings*), 119.6 (s, *C-10*), 96.8 (s, *C-12*), 72.4 (s, *C-14*), -7.7 (s, Ni-CH_3).

Elemental analysis (%) for $C_{47}H_{20}F_{36}I_2N_2NiO$: Found (Calculated):
C 35.05 (34.74); H 1.82 (1.24); N 2.23 (1.72)

{3,5-Diiodo-N-[2,6-bis(3,5-diperfluorohexylphenyl)phenyl]salicylaldiminato-κ²-N,O}methyl-pyridinenickel(II) (**1^I-C_6F_{13}/Pyr**)

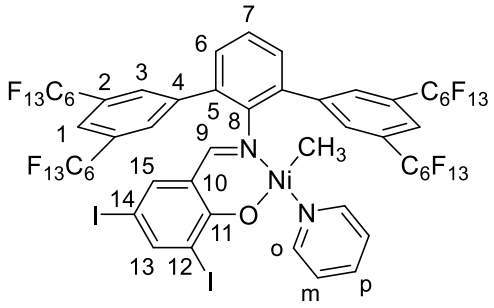

M = 2041.2 g/mol

1^I-C_6F_{13} / Pyr, yield: 97 %

Complex **1^I-C_6F_{13}/Pyr** was synthesized following the general procedure for Ni(II) methyl pyridine complexes using 281 mg salicylaldimine **1^I-C_6F_{13}** (150 µmol, 1 equiv.), 34 mg [(tmeda)$NiMe_2$] (165 µmol, 1.1 equiv.) and 178 mg pyridine (2.3 mmol, 15 equiv.) in 7 mL of benzene. Yield: 97 %, 146 µmol, 297 mg.

^{1}H NMR (400 MHz, C_6D_6/C_6F_6, 300 K): δ (ppm) = 8.38 (d, $^3J_{HH}$ = 4.7 Hz, 2H, *o-Pyr*), 8.20 (s, 4H, *H-3*), 7.95 (m, 2H, *H-1*), 7.94 (d, 1H, $^4J_{HH}$ = 2.2 Hz, *H-13*), 6.97 (m, 3H, *H-6*, *H-7*), 6.70-6.58 (m, 2H, *H-15*, *p-Pyr*), 6.49 (s, 1H, *H-9*), 6.40 (t, $^3J_{HH}$ = 6.8 Hz, 2H, *m-Pyr*), -0.82 (s, 3H, Ni-CH_3).

^{19}F{^{1}H} NMR (376 MHz, C_6D_6/C_6F_6, 300 K): δ (ppm) = -81.5 (t, J_{FF} = 10 Hz, 12F, CF_3), -111.2 (m, 8F, $C_{arom}CF_2$), -121.6 (m, 16F, CF_2), -122.9 (m, 8F, CF_2), -126.4 (m, 8F, CF_2).

^{13}C{^{1}H} NMR (101 MHz, C_6D_6/C_6F_6, 300 K): δ (ppm) = 168.0 (s, *C-9*), 164.3 (s, *C-11*), 151.5 (br. s, *o-Pyr*), 150.8 (s, *C-8*), 150.3 (s, *C-13*), 141.8 (s, *C-4*), 141.7 (s, *C-15*), 133.8 (br. s., *m-Pyr*), 132.8 (t, $^3J_{CF}$ = 5 Hz, *C-3*), 131.5 (s, *C-5*), 131.2 (s, *C-6*), 130.9 (t, $^2J_{CF}$ = 25 Hz, *C-2*), 127.3 (s, *C-7*), 124.9 (m, *C-1*), 123.4 (br. s, *p-Pyr*), 122-105 (-C_6F_{13}, *broad due to multiple* $^XJ_{CF}$ *couplings*), 119.8 (s, *C-10*), 96.7 (s, *C-12*), 72.1 (s, *C-14*), -8.0 (s, Ni-CH_3).

Elemental analysis (%) for $C_{55}H_{20}F_{52}I_2N_2NiO$: Found (Calculated)
C 32.49 (32.62); H 1.32 (1.00); N 1.38 (1.56)

{3,5-Diiodo-N-[2,6-bis(3,5-diperfluorooctylphenyl)phenyl]salicylaldiminato- κ²-N,O}methyl-pyridinenickel(II) (**1^{I}-C$_8$F$_{17}$/Pyr**)

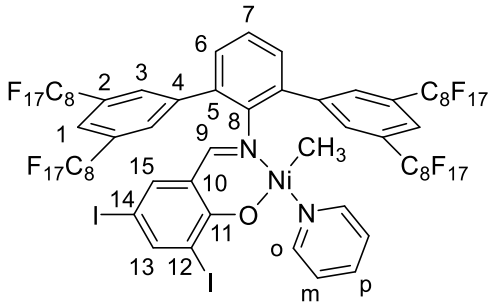

M = 2441.3 g/mol

1^{I}-C$_8$F$_{17}$ / Pyr, yield: 96 %

Complex **1^{I}-C$_8$F$_{17}$/Pyr** was synthesized following the general procedure for Ni(II) methyl pyridine complexes using 341 mg salicylaldimine **1^{I}-C$_8$F$_{17}$** (150 µmol, 1 equiv.), 34 mg [(tmeda)NiMe$_2$] (165 µmol, 1.1 equiv.) and 178 mg pyridine (2.3 mmol, 15 equiv.) in 5 mL of benzene and 1 mL of hexafluorobenzene. Yield: 96 %, 144 µmol, 369 mg.

^{1}H NMR (400 MHz, C_6D_6/C_6F_6, 300 K): δ (ppm) = 8.35 (d, $^{3}J_{HH}$ = 4.9 Hz, 2H, *o-Pyr*), 8.24 (s, 4H, *H-3*), 8.01 (m, 2H, *H-1*), 7.89 (d, 1H, $^{4}J_{HH}$ = 2.2 Hz, *H-13*), 7.05 (m, 3H, *H-6*, *H-7*), 6.76 (t, $^{3}J_{HH}$ = 7.7 Hz, 1H, *p-Pyr*), 6.65 (d, $^{4}J_{HH}$ = 2.2 Hz, 1H, *H-15*), 6.54 (s, 1H, H-9), 6.49 (t, $^{3}J_{HH}$ = 6.5 Hz, 2H, *m-Pyr*), -0.84 (s, 3H, Ni-CH_3).

^{19}F{^{1}H} NMR (376 MHz, C_6D_6/C_6F_6, 300 K): δ (ppm) = -81.4 (t, J_{FF} = 10 Hz, J_{FF} = 2 Hz, 12F, CF_3), -111.0 (t, J_{FF} = 14 Hz, 8F, $C_{arom}CF_2$), -121.0 to -122.5 (m, 32F, CF_2), -122.9 (m, 8F, CF_2), -126.4 (m, 8F, CF_2).

^{13}C{^{1}H} NMR (101 MHz, C_6D_6/C_6F_6, 300 K): δ (ppm) = 167.9 (s, *C-9*), 164.2 (s, *C-11*), 151.4 (s, *o-Pyr*), 150.7 (s, *C-8*), 150.3 (s, *C-13*), 141.7 (m, *C-4*, *C-15*), 133.3 (s, *m-Pyr*), 132.8 (t, $^{3}J_{CF}$ = 5 Hz, *C-3*), 131.3 (s, *C-5, C-6)*, 130.7 (t, $^{2}J_{CF}$ = 25 Hz, *C-2*), 127.2 (s, *C-7*), 124.9 (m, *C-1*), 123.3 (s, *p-Pyr*), 122-105 (-C_8F_{17}, *broad due to multiple $^{X}J_{CF}$ couplings*), 119.7 (s, *C-10*), 96.7 (s, *C-12*), 72.1 (s, *C-14*), -7.9 (s, Ni-CH_3).

Elemental analysis (%) for $C_{63}H_{20}F_{68}I_2N_2NiO$: Found (Calculated):
C 31.74 (31.20); H 1.59 (0.83); N 1.48 (1.16)

Synthesis of κ²-(N,O)-salicylaldiminato nickelI(II) methyl [α-methoxy-ω-amino poly(ethylene glycol)] complexes (1^{I}-R^{F}/PEG)

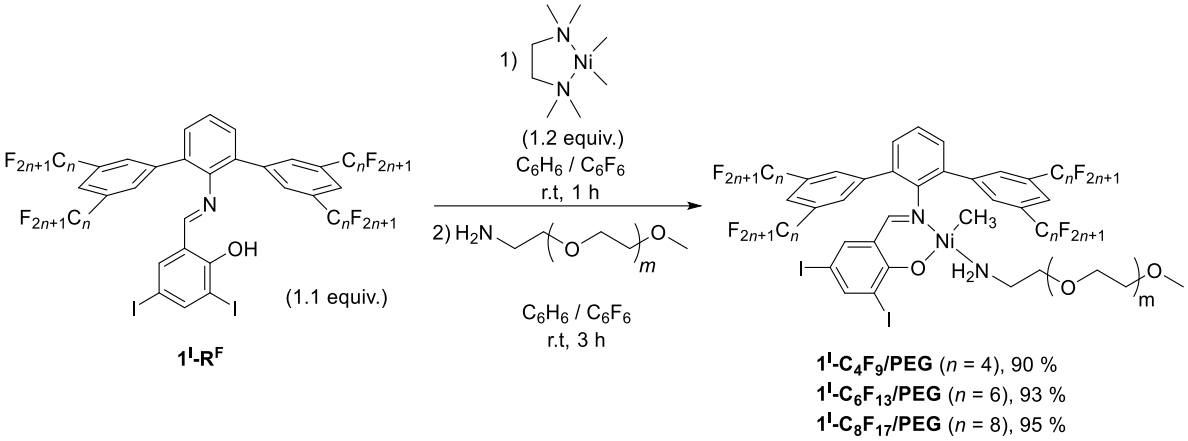

Scheme 3.7. Synthesis of κ²-(*N,O*)-salicylaldiminato nickel(II) methyl [α-methoxy-ω-amino poly(ethylene glycol)] complexes (**1^{I}-R^{F}/PEG**). The labile ligand (α-methoxy-ω-amino poly[ethylene glycol]) was added to a reacted mixture of nickel precursor and salicylaldimine to generate the respective nickel complex bearing different fluorocarbon substituents.

General procedure: To solid [(tmeda)$NiMe_2$] (1.2 equiv.) a solution of the respective salicylaldimine (**1^{I}-R^{F}**, 1.1 equiv.) in a mixture of benzene/hexafluorobenzene or neat benzene was added, and stirred for 1 hour at room temperature. During the addition, gas evolution (methane) was observed and an orange to red solution (slightly turbid) was obtained. α-Methoxy-ω-amino poly(ethylene glycol) (1.0 equiv.; *H_2N-PEG-OMe*; M_w = 1981 g mol^{-1}, unless noted otherwise) in 1 ml of benzene was added and the reaction mixture was stirred for further 3 hours at room temperature (the solution cleared up). After filtration through a syringe filter to remove nickel black, the solvent was removed under vacuum. The orange residue was washed with portions of pentane (3-5 times, 7.5 mL each) until the filtrate remained almost colorless (slightly orange). After drying under vacuum, the desired product was obtained as an orange powder.

{3,5-Diiodo-N-[2,6-bis(3,5-diperfluorobutylphenyl)phenyl]salicylaldiminato- κ²-N,O}methyl[α-methoxy-ω-amino poly(ethylene glycol)]lnickel(II) (**1^{I}-C_4F_9/PEG**)

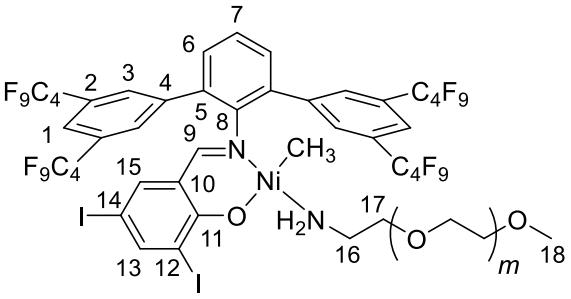

M = 3527 g/mol

1^{I}-C_4F_9/PEG, yield: 90 %

Complex **1^{I}-C_4F_9/PEG** was synthesized following the general procedure for Ni(II) methyl [α-methoxy-ω-amino poly(ethylene glycol] complexes using 193 mg salicylaldimine **1^{I}-C_4F_9** (131 µmol, 1.05 equiv.), 28 mg [(tmeda)NiMe₂] (138 µmol, 1.1 equiv.) and 248 mg [α-Methoxy-ω-amino poly(ethylene glycol] (125 µmol, 1 equiv.) in 6 mL of benzene. Yield: 90 %, 113 µmol, 399 mg.

^{1}H NMR (400 MHz, C_6D_6, 300 K): δ (ppm) = 8.11 (s, 4H, *H-3*), 7.96 (d, 1H, $^4J_{HH}$ = 2.2 Hz, *H-13*), 7.90 (s, 2H, *H-1*), 6.95 (m, 3H, *H-6*, *H-7*), 6.63 (d, 1H, $^4J_{HH}$ = 2.2 Hz, *H-15*), 6.47 (s, 1H, *H-9*), 3.78-3.18 (m, 233H, *H*-PEG), 3.14 (s, 3H, *H-18*), 3.05 (t, 2H, $^3J_{HH}$ = 4.9 Hz, *H-17*), 2.50 (m, 2H, *H-16*), 1.06 (t, 2H, $^3J_{HH}$ = 7.1 Hz, -NH_2), -1.19 (s, 3H, Ni-CH_3).

^{19}F{^{1}H} NMR (376 MHz, C_6D_6, 300 K): δ (ppm) = -80.9 (t, J_{FF} = 10 Hz, 12F, CF_3), -110.9 (m, 8F, $C_{arom}CF_2$), -122.4 (m, 8F, CF_2), -125.4 (m, 8F, CF_2).

^{13}C{^{1}H} NMR (101 MHz, C_6D_6, 300 K): δ (ppm) = 167.3 (s, *C-9*), 163.1 (s, *C-11*), 150.3 (s, *C-8*), 149.7 (s, *C-13*), 141.6 (s, *C-15*), 141.5 (s, *C-4*), 133.2 (s, *C-5*), 132.5 (t, $^3J_{CF}$ = 5 Hz, *C-3*), 131.2 (s, *C-6*), 130.4 (t, $^2J_{CF}$ = 25 Hz, *C-2*), 127.1 (s, *C-7*), 124.6 (m, *C-1*), 122-105 (-C_4F_9, *broad due to multiple* $^XJ_{CF}$ *couplings*), 119.8 (s, *C-10*), 96.8 (s, *C-12*), 72.5-70.1 (m, *C*-PEG, *C-14*, *C-17*), 58.7 (s, *C-18*), 43.2 (s, *C-16*), -13.3 (s, Ni-CH_3).

Elemental analysis (%) for $C_{131}H_{196}F_{36}I_2N_2NiO_{45}$: Found (Calculated)
C 46.51 (44.76); H 6.19 (5.62); N 0.90 (0.80)

{3,5-Diiodo-N-[2,6-bis(3,5-diperfluorohexylphenyl)phenyl]salicylaldiminato- κ²-N,O}methyl[α-methoxy-ω-amino poly(ethylene glycol)]lnickel(II) (**1^{I}-C_6F_{13}/PEG**)

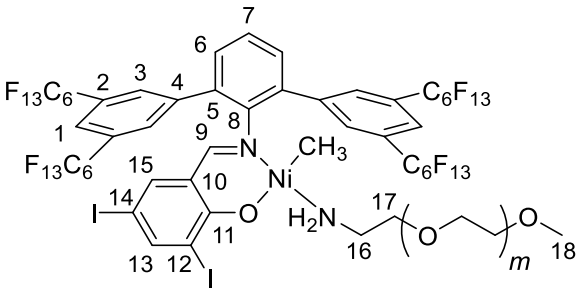

M = 3927 g/mol

1^{I}-C_6F_{13}/PEG, yield: 93 %

Complex **1^{I}-C_6F_{13}/PEG** was synthesized following the general procedure for Ni(II) methyl [α-methoxy-ω-amino poly(ethylene glycol] complexes using 296 mg salicylaldimine **1^{I}-C_6F_{13}** (158

μmol, 1.05 equiv.), 34 mg [(tmeda)NiMe$_2$] (165 μmol, 1.1 equiv.) and 297 mg [α-Methoxy-ω-amino poly(ethylene glycol] (150 μmol, 1 equiv.) in a mixture of 10 mL of benzene and 3 mL of hexafluorobenzene. Yield: 93 %, 140 μmol, 550 mg.

The analogue complex with M(H_2N-PEG-OMe) = 5516 g mol^{-1} was also prepared by an identical procedure.

^{1}H NMR (400 MHz, C_6D_6, 300 K): δ (ppm) = 8.14 (s, 4H, *H-3*), 7.97 (d, 1H, $^4J_{HH}$ = 2.2 Hz, *H-13*), 7.93 (s, 2H, *H-1*), 6.96 (m, 3H, *H-6*, *H-7*), 6.65 (d, 1H, $^4J_{HH}$ = 2.2 Hz, *H-15*), 6.50 (s, 1H, *H-9*), 3.78-3.19 (m, 230H, *H*-PEG), 3.14 (s, 3H, *H-18*), 3.07 (t, 2H, $^3J_{HH}$ = 4.9 Hz, *H-17*), 2.52 (m, 2H, *H-16*), 1.06 (t, 2H, $^3J_{HH}$ = 7.0 Hz, -*NH*$_2$), -1.16 (s, 3H, Ni-*CH*$_3$).

^{19}F{^{1}H} NMR (376 MHz, C_6D_6, 300 K): δ (ppm) = -80.9 (t, J_{FF} = 10 Hz, 12F, *CF*$_3$), -110.8 (t, 8F, J_{FF} = 14 Hz, C_{arom}*CF*$_2$), -121.4 (m, 16F, *CF*$_2$), -122.6 (m, 8F, *CF*$_2$), -126.0 (m, 8F, *CF*$_2$).

^{13}C{^{1}H} NMR (101 MHz, C_6D_6, 300 K): δ (ppm) = 167.2 (s, *C-9*), 163.1 (s, *C-11*), 150.2 (s, *C-8*), 149.8 (s, *C-13*), 141.6 (s, *C-15*), 141.5 (s, *C-4*), 133.2 (s, *C-5*), 132.5 (t, $^3J_{CF}$ = 5 Hz, *C-3*), 131.3 (s, *C-6*), 130.5 (t, $^2J_{CF}$ = 25 Hz, *C-2*), 127.1 (s, *C-7*), 124.7 (m, *C-1*), 122-105 (-*C*$_6$*F*$_{13}$, *broad due to multiple* $^XJ_{CF}$ *couplings*), 119.8 (s, *C-10*), 96.8 (s, *C-12*), 72.5-70.1 (m, *C*-PEG, *C-14, C-17*), 58.7 (s, *C-18*), 43.2 (s, *C-16*), -13.3 (s, Ni-*CH*$_3$).

Elemental analysis (%) for $C_{139}H_{196}F_{52}I_2N_2NiO_{45}$: Found (Calculated)
C 43.31 (42.64); H 5.20 (5.05); N 0.82 (0.72)

{3,5-Diiodo-N-[2,6-bis(3,5-diperfluorooctylphenyl)phenyl]salicylaldiminato- κ^2-N,O}methyl[α-methoxy-ω-amino poly(ethylene glycol)]lnickel(II) (**1^I-C$_8$F$_{17}$/PEG**)

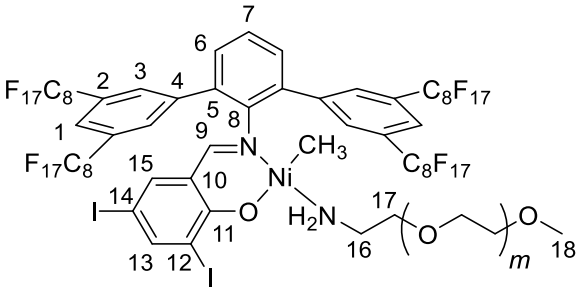

M = 4327 g/mol

1^I-C$_8$F$_{17}$ / PEG, yield: 95 %

Complex **1^I-C$_8$F$_{17}$/PEG** was synthesized following the general procedure for Ni(II) methyl [α-methoxy-ω-amino poly(ethylene glycol] complexes using 239 mg salicylaldimine **1^I-C$_8$F$_{17}$** (105 μmol, 1.05 equiv.), 23 mg [(tmeda)NiMe$_2$] (110 μmol, 1.1 equiv.) and 196 mg [α-Methoxy-ω-amino poly(ethylene glycol] (100 μmol, 1 equiv.) in a mixture of 6 mL of benzene and 3 mL of hexafluorobenzene. Yield: 95 %, 95 μmol, 411 mg

^{1}H NMR (400 MHz, C_6D_6/C_6F_6, 300 K): δ (ppm) = 8.17 (s, 4H, *H-3*), 7.99 (d, 1H, $^4J_{HH}$ = 2.2 Hz, *H-13*), 7.96 (s, 2H, *H-1*), 6.98 (m, 3H, *H-6*, *H-7*), 6.66 (d, 1H, $^4J_{HH}$ = 2.2 Hz, *H-15*), 6.51 (s, 1H, *H-9*), 3.73-3.19 (m, 218H, *H*-PEG), 3.14 (s, 3H, *H-18*), 3.09 (t, 2H, $^3J_{HH}$ = 4.9 Hz, *H-17*), 2.54 (m, 2H, *H-16*), 1.08 (t, 2H, $^3J_{HH}$ = 7.2 Hz, -*NH*$_2$), -1.14 (s, 3H, Ni-*CH*$_3$).

$^{19}F\{^1H\}$ NMR (376 MHz, C_6D_6/C_6F_6, 300 K): δ (ppm) = -81.4 (t, J_{FF} = 10 Hz, J_{FF} = 2 Hz, 12F, CF_3), -111.0 (t, J_{FF} = 14 Hz, 8F, $C_{arom}CF_2$), -121.1 to -122.2 (m, 32F, CF_2), -122.9 (m, 8F, CF_2), -126.4 (m, 8F, CF_2).

$^{13}C\{^1H\}$ NMR (101 MHz, C_6D_6/C_6F_6, 300 K): δ (ppm) = 167.4 (s, *C-9*), 163.3 (s, *C-11*), 150.5 (s, *C-8*), 149.9 (s, *C-13*), 141.7 (m, *C-15*, *C-4*), 133.4 (s, *C-5*), 132.7 (t, $^3J_{CF}$ = 6 Hz, *C-3*), 131.4 (s, *C-6*), 130.7 (t, $^2J_{CF}$ = 25 Hz, *C-2*), 127.1 (s, *C-7*), 124.8 (m, *C-1*), 122-105 (*-C_8F_{17}, broad due to multiple $^XJ_{CF}$ couplings*), 119.9 (s, *C-10*), 96.8 (s, *C-12*), 72.5, 72.2, 71.5-70.7, 70.4 (m, *C*-PEG, *C-14, C-17*), 58.7 (s, *C-18*), 43.3 (s, *C-16*), -13.3 (s, Ni-CH_3).

Elemental analysis (%) for $C_{147}H_{196}F_{68}I_2N_2NiO_{45}$: Found (Calculated)
C 41.40 (40.91); H 5.13 (4.58); N 0.80 (0.65)

3.4.4 Cyclic voltammetry of complexes (1^{I}-R^{F}/Pyr)

All electrochemical measurements were carried out with a computer-controlled BAS potentiostat, connected to a custom-built cyclindrical one-compartment cell (Prof. Rainer Winter's research group). The experiments were performed in a glovebox under inert atmosphere. A spiral-shaped Pt wire and an Ag wire, sealed into glass capillaries, were used as counter and reference electrodes and introduced at opposite sides of the cell. A platinum electrode was used as working electrode and introduced through the top port of the cell. Prior to all experiments, the working electrode was polished with 1 µm and 0.25 µm diamond paste (purchased from Buehler-Wirtz). The complex was dissolved in approximately 6 mL of dichloromethane mixed with NBu_4^+ PF_6^- (0.1 M) as supporting electrolyte. Referencing was performed by addition of decamethylferrocene (Cp^*_2Fe) as internal standard to the analyte solution, after all data of interest had been acquired, and another set of scans was recorded. Final referencing was performed against the ferrocene/ferrocenium couple with $E_{1/2}(Cp^*_2Fe)$ = - 550mV vs. $Cp_2Fe^{0/+}$. Electrochemical data were acquired with a standard sweep rate of 400 mV s^{-1}. A 10 Hz noise filter was applied to enhance the signal quality. For complex **1^{I}-C_8F_{17}/Pyr** the measurement was performed in presence of the reference only, as precipitation of decomposition products (presumably ligand) at the electrode surface hindered multiple high-quality measurements.

All cyclic voltammetry measurements of complexes **1^{I}-R^{F}/Pyr** showed oxidation and reduction transitions for the Ni(II)/Ni(III) pair. Only partial reversibility was observed, in line with an expected rapid decomposition of the formed Ni(III) species. Additional measurements of the free salicylaldehydes performed under otherwise identical conditions did not show redox transitions in the region of the corresponding pyridine precatalysts, suggesting metal centered oxidation and reduction processes.

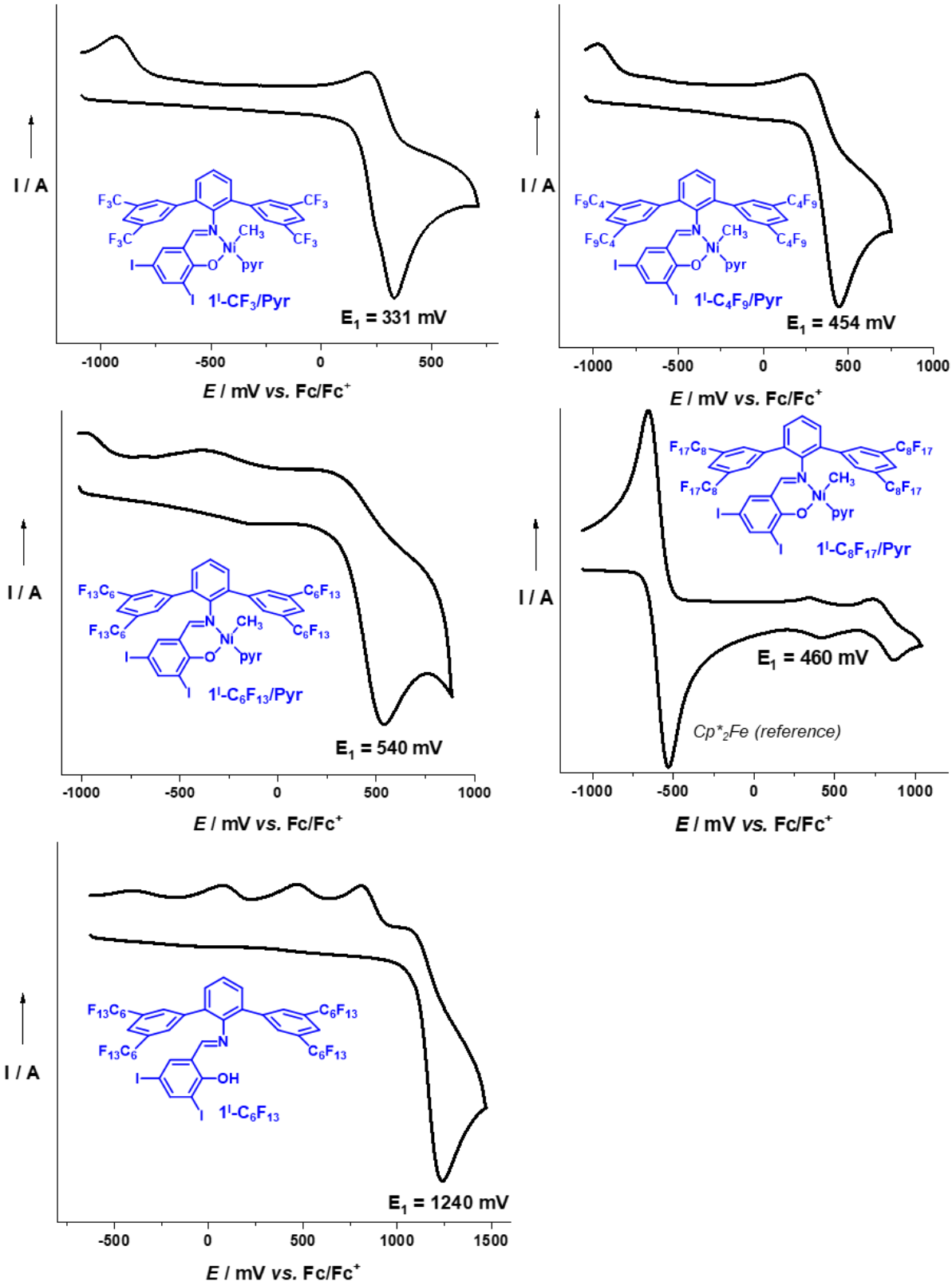

Figure 3.8. Cyclic voltammograms of complexes $\mathbf{1^{I}\text{-}R^{F}/Pyr}$, and salicylaldimine $\mathbf{1^{I}\text{-}C_6F_{13}}$.

3.4.5 Crystallographic data

Growing high quality crystals from compounds that contain huge portions of fluorinated alkyls is challenging as they show a high affinity to form oils and waxes when saturated solutions are cooled down or the solvent is evaporated. For the catalyst type herein described, layering a saturated solution of complex with an unpolar non-solvent (e.g. pentane) is the usual strategy of choice.[108] However, the perfluoroalkyl-substituted complexes showed to be soluble in a broad variety of different solvents, including alkanes. Layering with very polar solvents lead to catalyst decomposition within hours, usually needed to grow crystals. Hence, crystallization and subsequent X-ray diffraction analysis could not be performed. However, in the case of **1^{I}-C_8F_{17}/Pyr**, the bis-chelated decomposition product **[(1^{I}-C_8F_{17})$_2$Ni]** (Figure 3.9) could be crystallized, and the κ^2-*(N,O)* binding motif and the ligand backbone connectivity was confirmed. From 8 perfluorooctyl substituents present in such a molecule (64 perfluorinated carbons in total), just one group was highly disordered and could not be sufficiently modeled. Instead, the first two perfluorinated carbon atoms, connected to the aryl system, were modeled and the remaining C_6F_{13}-chain removed from the structure using the SQUEEZE routine.[356] Solvent accessible voids were calculated, where the former highly disordered chain was situated, and a solvent mask for the respective group applied. Although the resulting model is not fully consistent with the present structure, good modeled ellipsoids were found for the non-disordered rest of the structure with good confidence about molecular connectivity.

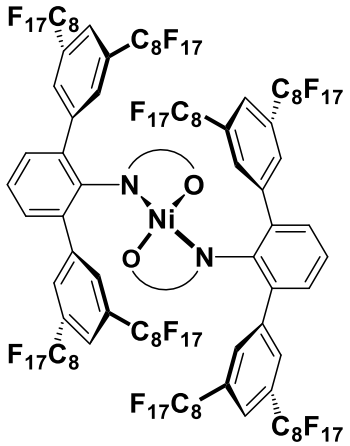

Figure 3.9. Schematic structure on the bis-chelated decomposition product **[(1^{I}-C_8F_{17})$_2$Ni]** that could be crystallized and analyzed via X-Ray diffraction.

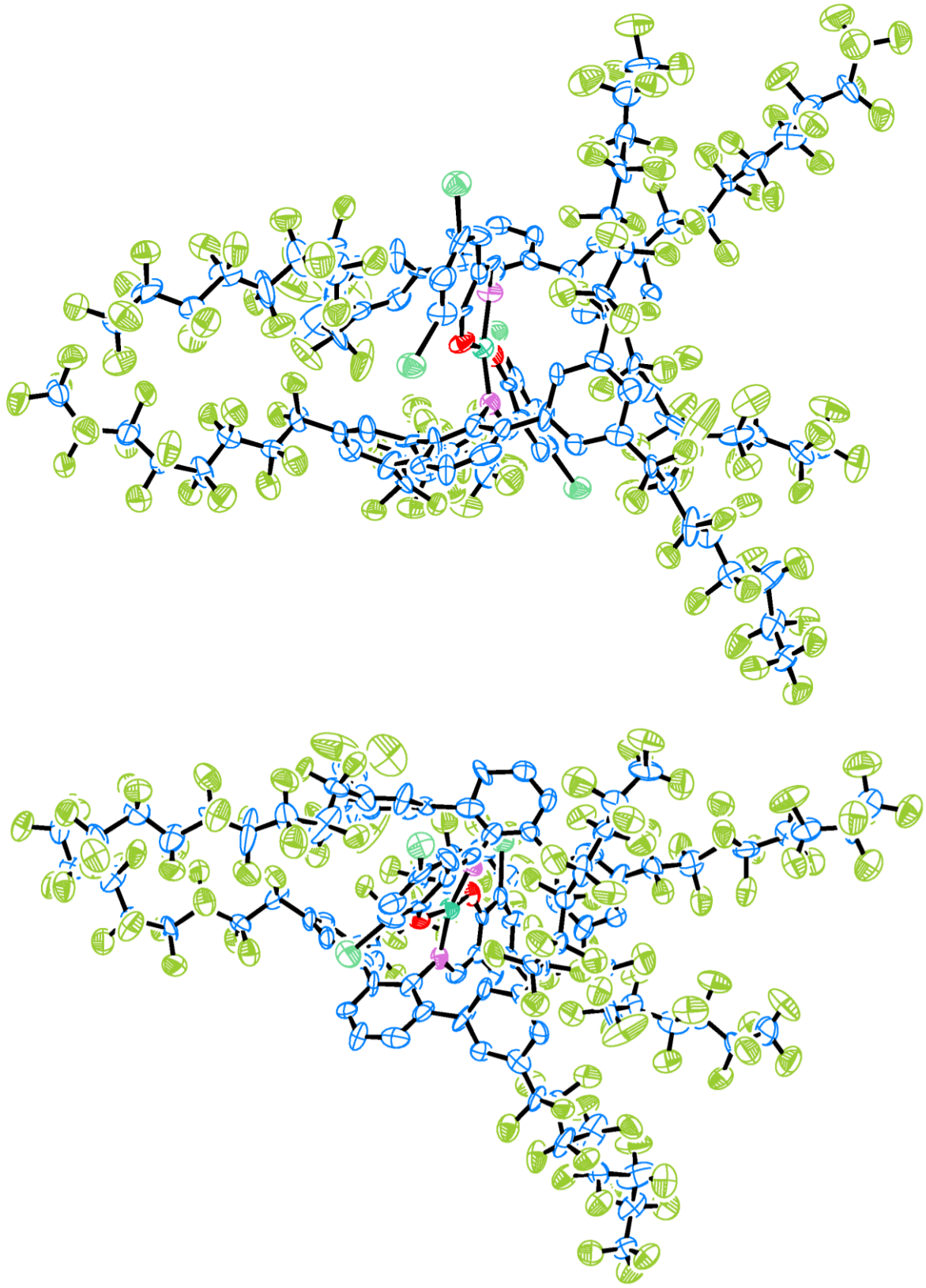

Figure 3.10. ORTEP plots (50 % probability ellipsoids, hydrogens are omitted for clarity) of structures determined by X-ray diffraction of **[(1^{I}-C_8F_{17})$_2$Ni]** from different perspectives.

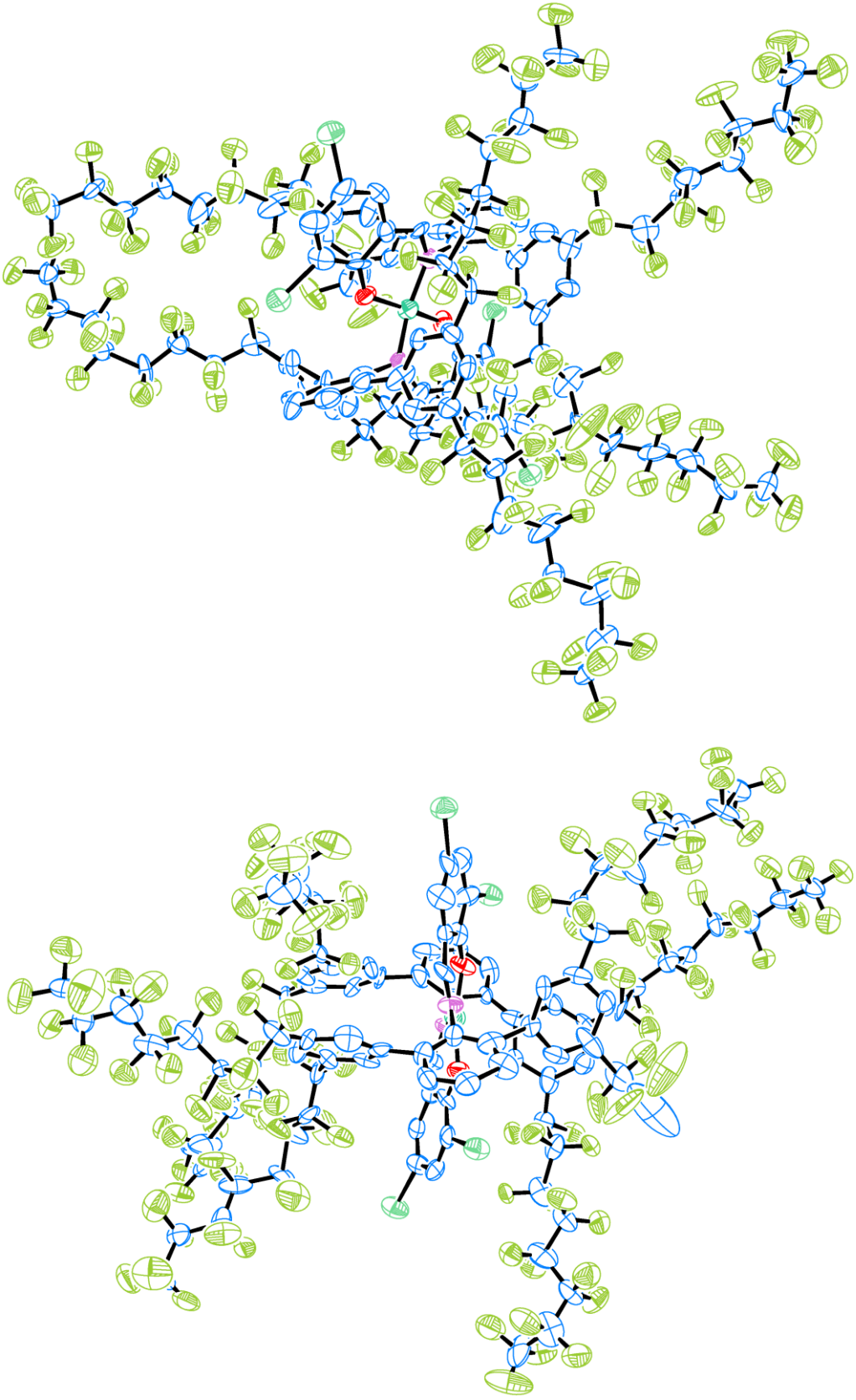

Figure 3.11. ORTEP plots (50 % probability ellipsoids, hydrogens are omitted for clarity) of the structure determined by X-ray diffraction of **[(1^{1}-C_8F_{17})$_2$Ni]** from different perspectives.

Crystal data and structure refinement for complex **[(1^I-C_8F_{17})$_2$Ni]:**

Identification code	CCDC 2009678
Empirical formula	$C_{216}H_{48}F_{246}I_8N_4Ni_2O_4$
Formula weight	8569.20
Temperature/K	100
Crystal system	triclinic
Space group	P-1
a/Å	18.2793(12)
b/Å	20.0082(11)
c/Å	23.0705(11)
α/°	73.636(4)
β/°	70.192(4)
γ/°	65.728(5)
Volume/Å^3	7136.3(8)
Z	1
ρ_{calc} g/cm^3	1.994
μ/mm^{-1}	1.210
F(000)	4098.0
Crystal size/mm^3	0.4 × 0.167 × 0.05
Radiation	Mo K_α (λ = 0.71073)
2Θ range for data collection/°	5.078 to 53.84
Index ranges	-23 ≤ h ≤ 23, -25 ≤ k ≤ 25, -29 ≤ l ≤ 27
Reflections collected	71493
Independent reflections	30300 [R_{int} = 0.2036, R_{sigma} = 0.3303]
Data/restraints/parameters	30300/0/2131
Goodness-of-fit on F^2	1.022
Final R indexes [I>=2σ (I)]	R1 = 0.1379, wR2 = 0.3490
Final R indexes [all data]	R1 = 0.3292, wR2 = 0.4433
Largest diff. peak/hole / e Å^{-3}	2.01 / -1.43

Experimental:

Single crystals of **[(1^I-C_8F_{17})$_2$Ni]** were obtained by layering a pentane solution with benzene. A suitable crystal was selected and placed on a STOE IPDS 2T diffractometer. The crystal was kept at 100 K during data collection. The structure was solved with ShelXT[357] (Intrinsic Phasing) structure solution program in Olex2 (v.1.2)[358] and refined with the ShelXL[359] (Least Squares minimization) refinement package. One highly disordered fluorocarbon chain segment (C_6F_{13} group) was removed from the model using the SQUEEZE routine. The resulting solvent accessible voids were removed by using the created solvent mask.[360] Graphical representations were created in ORTEP-3 (v.2014.1)[361] for Windows.

3.4.6 Polymerization procedures

Polymerization experiments in toluene

All ethylene polymerizations in toluene were conducted in a *Büchi miniclave* reactor with a 280 mL vessel. The reactor was equipped with a mechanical stirrer, a heating and cooling jacket connected to a thermostat, a thermocouple dipping into the polymerization mixture and a nitrogen/vacuum supply. Prior to all polymerization experiments, the reactor was evacuated and heated up (thermostat temperature: 90 °C). When the reactor temperature was > 60 °C, the reactor was flushed with nitrogen and evacuated three times. The reactor was brought 5 °C below the desired reaction temperature. The reactor was then filled with 100 mL of toluene via cannula transfer and the solution stirred with 500 rpm. The catalyst was dissolved in 5 mL of toluene and transferred into the reactor via syringe. Immediately after addition, the stirring rate was increased to 1000 rpm and the reactor pressurized to the desired pressure. During the pressurization procedure the temperature was adjusted to the desired reaction temperature. All experiments were conducted at constant pressure over the entire polymerization experiment with the ethylene feed controlled and monitored by *Bronkhorst* mass flow meters. After the stated reaction time, the ethylene flow was stopped and the reactor carefully vented. The reactor content was poured into 300 mL of methanol and stirred for 30 minutes. The precipitated polymer was filtrated, washed with methanol and dried in a vacuum oven (60 °C, 30 mbar) overnight.

Polymerization experiments aqueous surfactant solution

All ethylene polymerizations in water were conducted in a *Büchi ecoclave* reactor with a 600 mL vessel (see *chapter 6.2.1* for further details on the reactor setup). The reactor was equipped with a heating and cooling jacket connected to a thermostat, a mechanical stirrer, a nitrogen/vacuum supply, and an ultrasonotrode (*Hielscher UIP250*) and a thermocouple couple both dipping into the reaction mixture. A *Bronkhorst* MassFlow apparatus consisting of two flow meters (up to 20 g L^{-1} and 200 g L^{-1} ethylene), a pressure meter and a compressed air-driven badger valve was used to work under constant ethylene pressure. All gas valves and devices were connected to a *HiTec Zang LabBox* and operated by *HiTec Zang LabVision®* software (ver. 2.13). The software allowed for a precise process visualization, control and recording of all relevant parameters in one single process flow chart. The integration of *HiText™* programming language

enabled the construction of several automation scripts (e.g. for pressurization, temperature control, venting, etc.). Prior to all polymerization experiments, the reactor was evacuated and heated up (thermostat temperature: 90 °C) using a custom *HiText*™ program. When the reactor temperature was > 60 °C, the reactor was flushed with nitrogen, evacuated three times and automatically cooled down to 13 °C. The desired amount of surfactant (sodium dodecyl sulfate) and base (cesium hydroxide) and a magnetic stirrer bar were put into a Schlenk flask, and the flask was transferred into a glovebox. After addition of lipophilic solvent (e.g. mesitylene) and catalyst, the flask was sealed, brought outside the glovebox and water was added under vigorous stirring via cannula transfer. The clear orange solution (after 3-5 minutes of stirring) was then transferred to the reactor and stirred at 500 rpm. The polymerization experiment was started using a custom *HiText*™ program with a graphical interface to adjust ultrasound application power and duration, reaction time and reaction temperature control. The reaction mixture was then automatically treated with ultrasound (usually for 4 minutes with 120 Watt power) and the solution temperature monitored to stay around 15 °C. Immediately afterwards, the stirring rate was increased to 1000 rpm and the reactor pressurized stepwise to 40 bar ethylene pressure within 30 seconds. The ethylene flow was then controlled and recorded by the mass flow meter to ensure a constant pressure over the entire polymerization experiment. The reaction temperature was automatically adjusted to 15 °C. After the desired reaction time, the pressure was automatically released stepwise. Below 15 bar residual pressure, the reactor was vented manually into a beaker to collect migrating dispersion due to foaming. The entire dispersion was weighed, filtered over cotton wool and the solids content determined by precipitation of a 50 g aliquot of dispersion in 300 mL of methanol. After stirring for 30 minutes, the precipitated bulk polymer was filtered and washed thoroughly with water and methanol, and dried in a vacuum oven (60 °C, 30 mbar) overnight.

3.4.7 Additional polymerization experiments in toluene at lower ethylene pressures

Table 3.3. Polymerization experiments in toluene at 10 bar ethylene pressure with catalysts **1^{I}/Pyr**.

entry	precatalyst	T [°C]	yield PE [g]	TOF[a] x 10^3	M_n[b] x 10^3 [g mol^{-1}]	M_w/ M_n[b]	T_m[c] [°C]	crystallinity[c] [%]	branches/ 1000 C[d]
1	1^{I}-CF_3/Pyr	50	2.03	21.7	22.6	2.6	120	52	9
2	1^{I}-CF_3/Pyr	70	4.25	45.5	6.0	2.0	112	58	15
3	1^{I}-CF_3/Pyr	90	3.16	33.8	2.4	2.8	98	-	36
4	1^{I}-C_4F_9/Pyr	50	8.05	86.1	156.1	2.2	128	54	3
5	1^{I}-C_4F_9/Pyr	70	8.08	86.4	19.3	2.6	121	59	9
6	1^{I}-C_4F_9/Pyr	90	5.64	60.3	6.1	2.3	110	53	21
7	1^{I}-C_6F_{13}/Pyr	50	9.46	101.2	221.6	1.9	128	54	2
8	1^{I}-C_6F_{13}/Pyr	70	10.68	114.2	47.8	2.0	121	61	7
9	1^{I}-C_6F_{13}/Pyr	90	7.50	80.2	7.0	2.0	112	56	18
10	1^{I}-C_8F_{17}/Pyr	50	7.60	81.3	175.3	2.2	128	53	2
11	1^{I}-C_8F_{17}/Pyr	70	7.21	77.1	23.7	2.1	123	53	7
12	1^{I}-C_8F_{17}/Pyr	90	4.65	50.0	6.4	2.3	114	54	17

Polymerization conditions: 5 µmol precatalyst, 40 min reaction time, in 100 mL of toluene, 10 bar ethylene pressure. [a] Given in 10^3 x mol $[C_2H_4]$ x mol^{-1} [Ni] x h^{-1}. [b] Determined by GPC at 160 °C in 1,2,4-trichlorobenzene. [c] Determined by DSC with 10 K min^{-1} heating rate (data from second heating cycle). [d] Determined by ^{13}C NMR spectroscopy.

To investigate the influence of the present ethylene concentration on the observed dependencies between catalytic activities, polymer properties and perfluoroalkyl chain lengths in structures of catalysts **1^{I}-R^{F}/Pyr**, additional polymerization experiments in toluene were conducted at a reduced ethylene pressure of 10 bar.

Remarkably, identical tendencies for longer perfluoroalkyl chains were found, with **1^{I}-C_6F_{13}/Pyr** being clearly superior in terms of activities and molecular weights, as they were present in experiments at 40 bar ethylene pressure (Figure 3.12; see Table 3.1 for comprehensive polymerization data at 40 bar ethylene pressure). These findings underline the general beneficial electronical impact of long perfluoroalkyl groups in remote position on the active center, that is found for different solvents, temperatures and ethylene pressures (see also *chapter 4*).

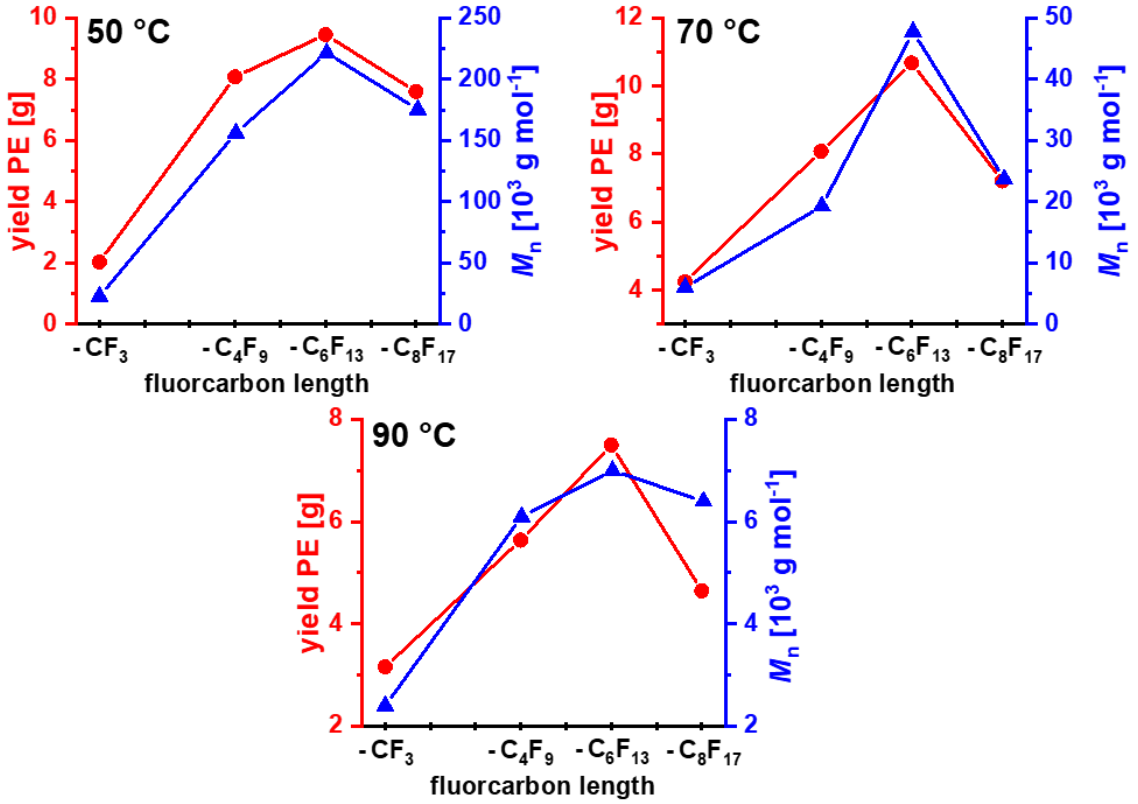

Figure 3.12. Polymer yield and molecular weight in dependence of the fluorocarbon chain length in the catalyst structure. Data from polymerizations in toluene at different temperatures (Table 3.3).

3.4.8 Influence of the fluorocarbon chain length in the catalyst structure in aqueous polymerizations

The length of the perfluorinated alkyl chain in the catalyst structure was found to have a strong impact on the catalytic properties of the active nickel center, as studied in detail in toluene as a reaction medium with lipophilic catalyst precursors (pyridine as labile ligand; see Figure 3.2 and *chapter 3.4.7*). These trends were also confirmed for hydrophilic analogues in aqueous system (Table 3.4).

Also, in aqueous systems, yields and molecular weights generally increased with increasing length of the fluorocarbon group in the catalyst structure (see Figure 3.13). This shows that these trends are independent of the solvent nature, and are based on a direct electronic influence caused by the fluorocarbon groups on the active nickel center. The experiments further underline catalyst **1-C_6F_{13}/PEG** to be the catalyst of choice.

Table 3.4. Results of aqueous polymerization experiments performed with catalysts bearing different fluorocarbon chain lengths.

entry	catalyst	yield PE[a] [g]	M_n[b] [10^3 g mol^{-1}]	M_w / M_n[b]	chains/ [Ni]	T_m[c] [°C] (crystallinity [%])	particle size[d] [nm]
1	1^I-CF_3/PEG	0.28	206	1.5	0.2	137 (69) / 133 (54)	16 (0.36)
2	1^I-C_4F_9/PEG	2.18	324	1.2	0.9	141 (79) / 136 (58)	18 (0.30)
3	1^I-C_6F_{13}/PEG	4.53	626	1.2	1.0	139 (79) / 135 (55)	23 (0.17)
4	1^I-C_8F_{17}/PEG	3.76	503	1.1	1.0	141 (73) / 136 (52)	24 (0.48)

Polymerization conditions: 40 bar ethylene pressure, 15 °C reaction temperature, 6.0 g sodium dodecyl sulfate, 1.5 g cesium hydroxide, 0.1 mL hexafluorobenzene, 7.5 µmol catalyst loading, 30 minutes reaction time, in 150 mL water. [a] Determined via precipitation in methanol. [b] Determined via GPC at 160 °C in 1,2,4-trichlorobenzene. [c] Determined by DSC (10 K min^{-1} heating rate), reported as [first heating / second heating]. [d] Volume average size from DLS (particle size polydispersity index)

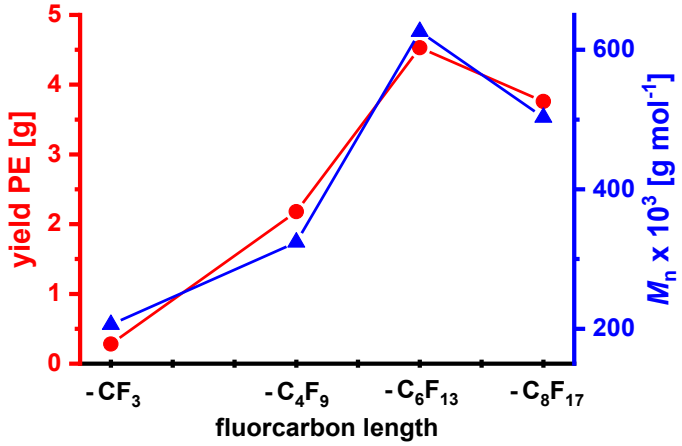

Figure 3.13. Polymer yield and molecular weight in dependence of the fluorocarbon chain length in the catalyst for aqueous system (data from Table 3.4).

An influence of the hydrophobic perfluoroalkyl on the dissociation rate of the labile amino-PEG ligand in aqueous system was also found. This is evident from low chains-per-nickel ratios for catalyst **1^I-CF_3/PEG** (entry 1, Table 3.4) as the labile ligand seems to bind strongly to the metal center and hinders a sufficient activation. This was not observed for catalysts **1^I-C_4F_9/PEG**, **1^I-C_6F_{13}/PEG** and **1^I-C_8F_{17}/PEG** with their hydrophobic perfluoroalkyl groups that force the highly hydrophilic labile ligand in close proximity to dissociate as revealed by chains-per-nickel rations close to unity (entry 2-4, Table 3.4). The catalyst was further modified by changing the length of the PEG-unit of the labile coordinated ligand molecule (1981 g mol^{-1} vs. 5516 g mol^{-1}). Catalysts bearing longer PEG-units generally showed a slightly higher activity, presumably due to an increased water-solubility of the labile ligand resulting in an enhanced dissociation rate (entries 1-3 vs. entries 4-6, Table 6.3). Other than this, an essentially similar behavior was observed.

3.4.9 Particle size statistics of PE nanocrystal dispersions

For particle size and volume statistics, lateral dimensions and the corresponding basal plane surface area were accessed by TEM imaging and particle thickness (*H*) was determined by AFM. Only isolated particles clearly oriented flat on the grid surface were considered for TEM analysis. The particles of different samples have a hexagonal, truncated-lozenge or lozenge shape, respectively, depending on the progress of morphology evolution as given by the duration of the polymerization experiment. The limited electron contrast of organic polymers results in a limited resolution of the edges, particularly relevant for particles with (lateral) sizes of ca. < 30 nm. To circumvent subjective errors of a manual analysis of particle dimensions and surface areas, an ellipsoidal fit of the particles employing analysis of TEM images via ImageJ/Fiji[351-353] software was used. This fit was verified to yield accurate areas even for lozenge shaped particles (*vide infra*). The TEM analysis routine provided values for the full-axis lengths *A* and *B* over all analyzed particles. The equivalent diameter *D* (diameter of a circle with same surface area as the fitted ellipse) was calculated according to equation 1 and used as characteristic parameter for comparison of lateral particle sizes of different samples.

$$D = 2\sqrt{0.25\,A\,B} \quad (1)$$

The average volume of a particle $V_{\mathbf{part}}$ was calculated according to equation 2, employing the average thickness (*H*) from AFM (*vide infra*).

$$V_{\mathrm{part}} = \frac{1}{6}\pi\,A\,B\,H \quad (2)$$

The average mass of one particle $m_{\mathbf{part}}$ was determined by multiplication of $V_{\mathbf{part}}$ with the density ρ_{PE} (equation 3). The density was assumed to be ρ_{PE} = 0.94 g cm^{-1} [362] for these type of nanocrystals (density of bulk UHMWPE). The mass of one polymer chain $m_{\mathbf{chain}}$ was calculated according to equation 4 using the mass-average molecular weight M_W. The chains per particle ratio $N_{\mathbf{chain}}/N_{\mathbf{part}}$ can then be determined by equation 5. The resulting data is summarized in Table 3.5 and Table 3.6.

$$m_{\mathrm{part}} = V_{\mathrm{part}} \cdot \rho_{\mathrm{PE}} \quad (3)$$

$$m_{\mathrm{chain}} = \frac{M_{\mathrm{W}}}{N_A} \text{ with } N_A = 6.022 \cdot 10^{23}\,mol^{-1} \quad (4)$$

$$\frac{N_{\mathrm{chain}}}{N_{\mathrm{part}}} = \frac{m_{\mathrm{part}}}{m_{\mathrm{chain}}} = \frac{V_{\mathrm{part}}\ \rho_{\mathrm{PE}}\ N_A}{M_{\mathrm{W}}} \quad (5)$$

Table 3.5. Statistical particle size data determined via ellipse fit method of TEM pictures. Values *A* and *B* are full-axis lengths of calculated ellipses (standard deviation reported). *D* is the average lateral particle size, calculated as mean value of *A* and *B* per particle (standard deviation reported).

entry in Table 3.2	number of particles	*A* [nm]	*B* [nm]	*D* [nm]
1	213	26.0 ± 2.3	22.0 ± 1.7	23.6 ± 1.6
2	238	33.1 ± 3.1	25.3 ± 2.3	28.9 ± 2.2
3	147	38.5 ± 3.6	29.3 ± 2.1	33.6 ± 2.3
4	255	41.9 ± 3.9	32.4 ± 2.7	36.8 ± 2.8
5	325	54.2 ± 7.7	39.2 ± 5.3	46.0 ± 6.1
6	140	63.6 ± 11.4	45.7 ± 7.5	53.9 ± 9.1
7	158	77.0 ± 15.3	53.9 ± 10.2	64.4 ± 12.3

Table 3.6. Values used to calculate the respective chain per particle ratio for data entries in Table 3.2. The particle height *H* was determined via AFM measurements (*vide infra*). Particle volume V_{part}, molecular weight M_w and the resulting chains per particle ratios are reported with estimated measured errors/error propagation analysis (*vide infra*).

entry in Table 3.2	*H* [nm]	V_{part} [10^{-24} m^3]	M_w [10^3 g mol^{-1}]	chains/ particles
1	5.2 ± 0.6[a]	1.6 ± 0.3	760 ± 76	1.2 ± 0.3
2	5.2 ± 0.6	2.3 ± 0.5	1087 ± 109	1.2 ± 0.3
3	5.3 ± 0.6 [a]	3.1 ± 0.6	1402 ± 140	1.3 ± 0.3
4	5.3 ± 0.6	3.8 ± 0.5	1735 ± 174	1.2 ± 0.3
5	5.3 ± 0.6 [a]	5.9 ± 1.2	2371 ± 237	1.4 ± 0.3
6	5.6 ± 0.7 [a]	8.5 ± 1.7	3202 ± 320	1.5 ± 0.4
7	5.6 ± 0.7	12.2 ± 2.4	3952 ± 395	1.7 ± 0.4

[a]Data of measured samples in similar particle size regime was used as the particles thickness do not change significantly during the particle growth process.

The validity of the automated ellipse fit was verified by comparison to manual analysis. This was performed for the case of lozenge particles, as the deviation from an ellipse is the largest for this particle shape (compared to hexagons and truncated lozenges), and as these are the largest type of particles such that the limited resolution of the particle edges weighs in least. Lozenge particles were analyzed by measuring all four side lengths and the short diagonal (Figure 3.14). An exemplary TEM image and the identical pictures with either the marked triangles or the automatically fitted ellipses are shown in Figure 3.15.

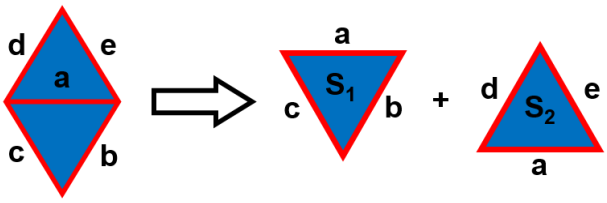

Figure 3.14. Schematic segmentation of a lozenge-shaped particle into two triangles with surface areas S_1 and S_2.

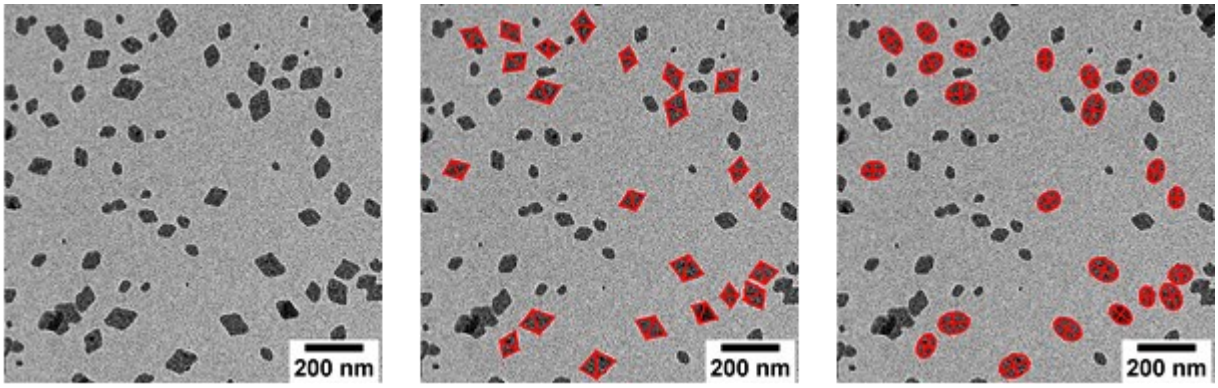

Figure 3.15. TEM image of sample with mixed-size lozenge particles. *Left*: without analysis. *Center*: with measured triangle side lengths for surface area determination. *Right*: with fitted ellipses for surface area determination.

The triangles' surface areas S_1 and S_2 is given by equations 6 and 7 and the overall lozenge surface area S_Δ is their sum, equation 8 (standard deviation over 50 particles reported).

$$S_1 = \sqrt{x(x-a)(x-b)(x-c)} \quad with\ x = \frac{a+b+c}{2} \quad (6)$$

$$S_2 = \sqrt{x(x-a)(x-d)(x-e)} \quad with\ x = \frac{a+d+e}{2} \quad (7)$$

$$S_\Delta = S_1 + S_2 = 3932 \pm 928\ \mathrm{nm}^2 \quad (8)$$

With the fitted full-axis lengths A and B determined by the automated ellipse fit, the surface area S_O is given by equation 9 (with standard deviation over 50 particles reported).

$$S_O = 0.25\ \pi\ A\ B = 4373 \pm 1027\ \mathrm{nm}^2 \quad (9)$$

Both methods gave similar results for an identical set of particles with only 10 % difference. This shows that the ellipse-fit routine is not only suited for surface determination of hexagonal/round particles but can also describe lozenge-shaped exemplars with satisfactory accuracy. In addition, the statistical distribution is identically expressed in both cases (Figure 3.16).

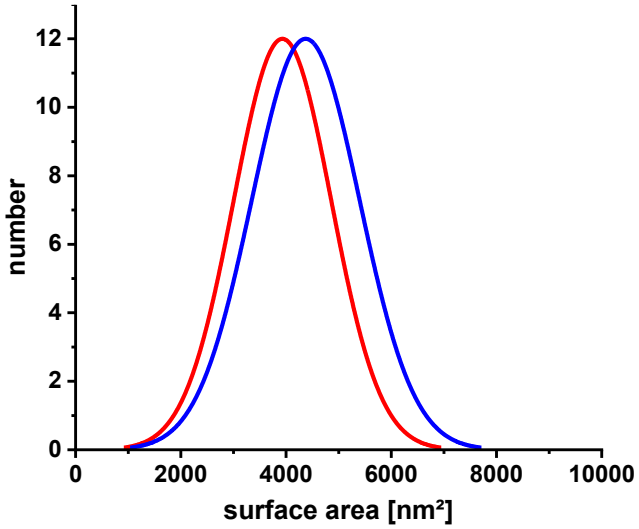

Figure 3.16. Particle surface area distribution of same set of particles. Either automatically determined by an ellipse-fit routine (*blue curve*) or manually measured with the triangle dissection (*red curve*).

Considering the propagation of systematic errors, we estimated the measurement error of the molecular weight determined by GPC ΔM_W to be ± 10 %, the error of the particle volume determined by TEM statistics ΔV_{part} to be ± 20 % and the particle density error $\Delta \rho_{PE}$ to be ± 10 %. Application of a Gaussian error propagation approach to equation 5 yields the error in determination of the chain per particle ratio by equation 10. Results for V_{part}, M_w and the chain-per-particle ratios are listed in Table 3.6

$$\Delta N_{C/P} = \sqrt{\left(\frac{\partial N_{C/P}}{\partial M_W}\right)^2 \Delta {M_W}^2 + \left(\frac{\partial N_{C/P}}{\partial V_{part}}\right)^2 \Delta {V_{part}}^2 + \left(\frac{\partial N_{C/P}}{\partial \rho_{PE}}\right)^2 \Delta {\rho_{PE}}^2}$$

$$= \sqrt{\left(-\frac{V_{part}\ \rho_{PE}\ N_A}{{M_W}^2}\right)^2 \Delta {M_W}^2 + \left(\frac{\rho_{PE}\ N_A}{M_W}\right)^2 \Delta {V_{part}}^2 + \left(\frac{V_{part}\ N_A}{M_W}\right)^2 \Delta {\rho_{PE}}^2} \quad (10)$$

$$with\ \Delta M_W = 0.1\ M_W\ , \Delta V_{part} = 0.2\ V_{part}\ , \Delta \rho_{PE} = 0.1\ \rho_{PE}$$

3.4.10 AFM measurements

Atomic force microscopy (AFM) measurements to determine the particles height were performed on samples generated by spin coating of dialyzed dispersions on silicon wafers using intermittent contact mode with silicon cantilevers.

Table 3.7. Values for particle heights *H* determined via AFM measurements.

entry in Table 3.2	**number of particles**	***H* [nm]**
2	31	5.2 ± 0.6
4	29	5.3 ± 0.6
7	36	5.6 ± 0.7

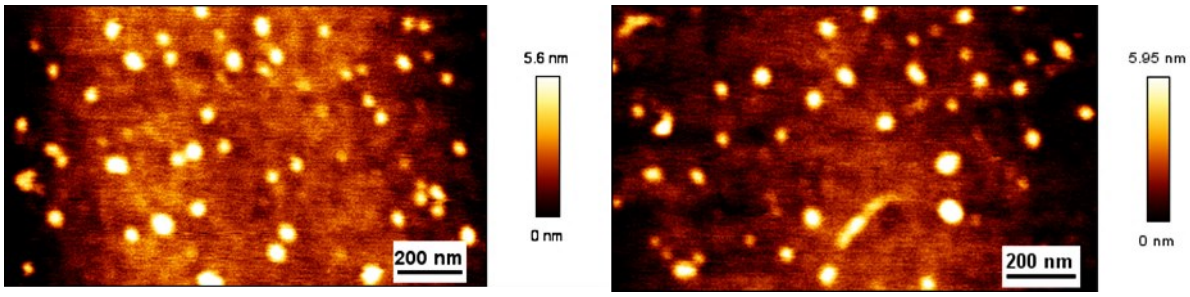

Figure 3.17. AFM image sections of dispersion sample obtained in aqueous polymerization (Table 3.2, entry 3).

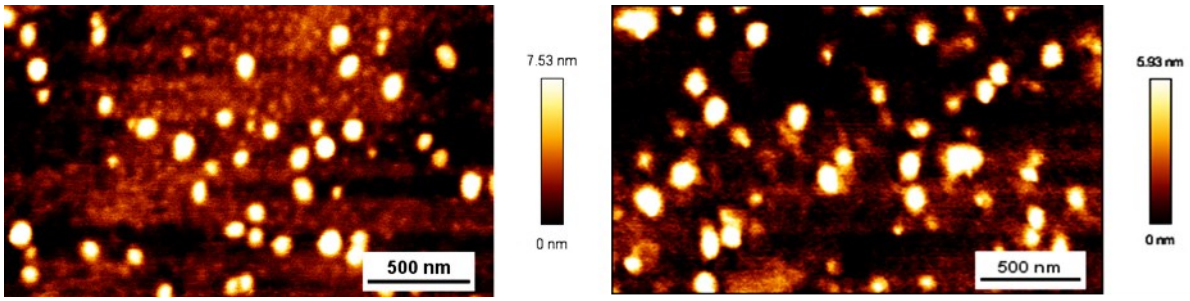

Figure 3.18. AFM image sections of dispersion sample obtained in aqueous polymerization (Table 3.2, entry 7).

3.4.11 AUC measurements

AUC analysis of lozenge-shaped particles (entry 7, Table 3.2) was performed to determine the particle size (hydrodynamic diameter d_h) and the distribution thereof by solvent variation analysis und spherical particle shape approximation (Figure 3.22). The analyte was diluted 1:40 with H_2O and D_2O and both samples measured (~ 0.2 wt-% PE). While in pure H_2O sedimentation occurred (s = 13.1 x 10^{-13} s; Figure 3.20), flotation was observed in D_2O/H_2O (97.6 vol-%; s = -42.4 x 10^{-13} s; Figure 3.21).

The spherical hydrodynamic diameter d_h was determined to be 33.0 ± 1.36 nm, slightly lower than found in DLS measurements whereby a spherical particle is assumed as well. The sedimentation coefficient distribution and the resulting particle size distribution reflected the narrowly dispersed, uniform character of the formed particles as also evident from DLS measurements and TEM statistical data.

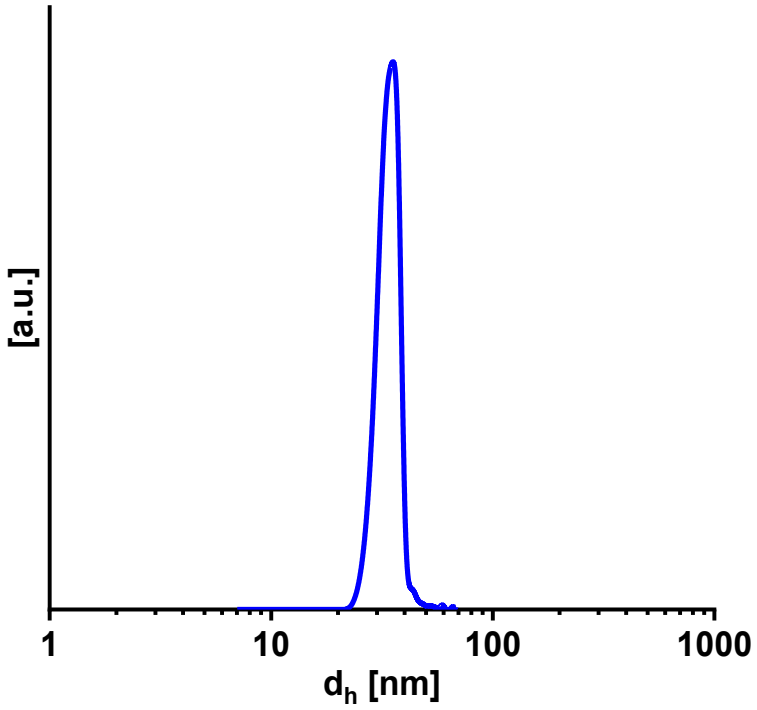

Figure 3.19. Particle size distribution (d_h, spherical particle shape assumed) determined from AUC measurements in H_2O (analyte: entry 7, Table 3.2).

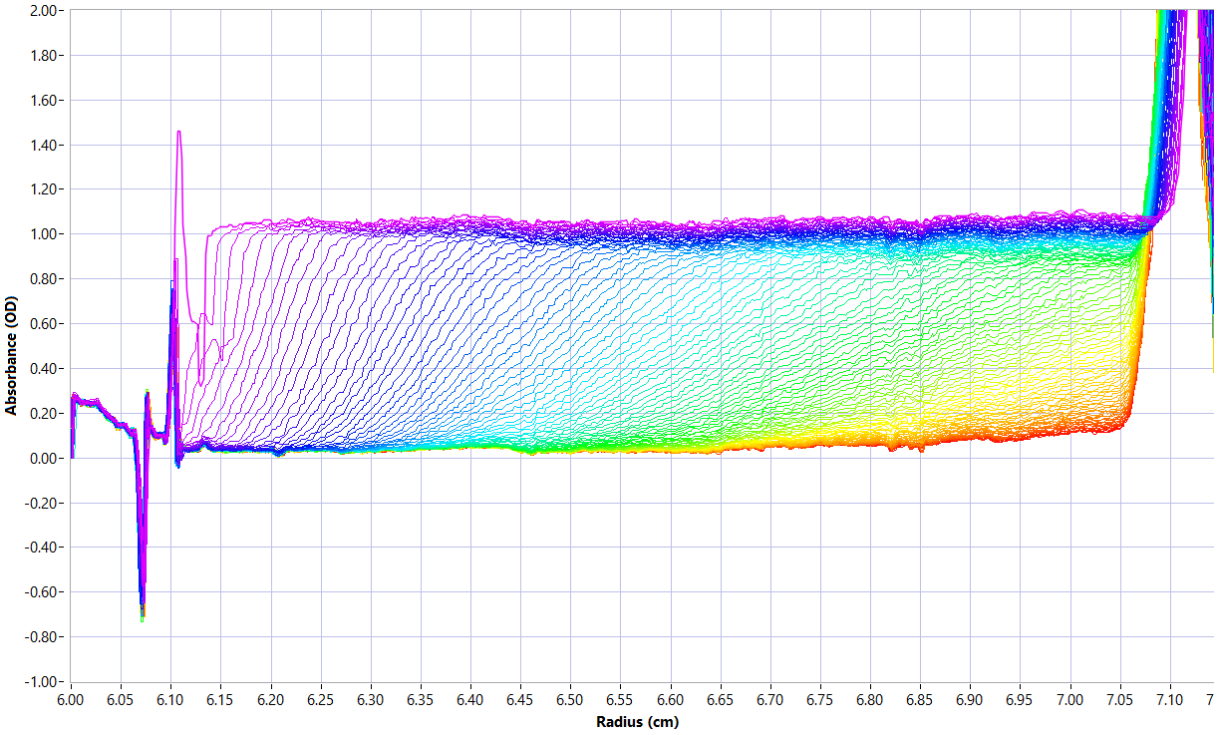

Figure 3.20. Absorbance profiles measured during AUC in H_2O (analyte: entry 7, Table 3.2, 30000 rpm, 280 nm, 20 °C, 120 scans).

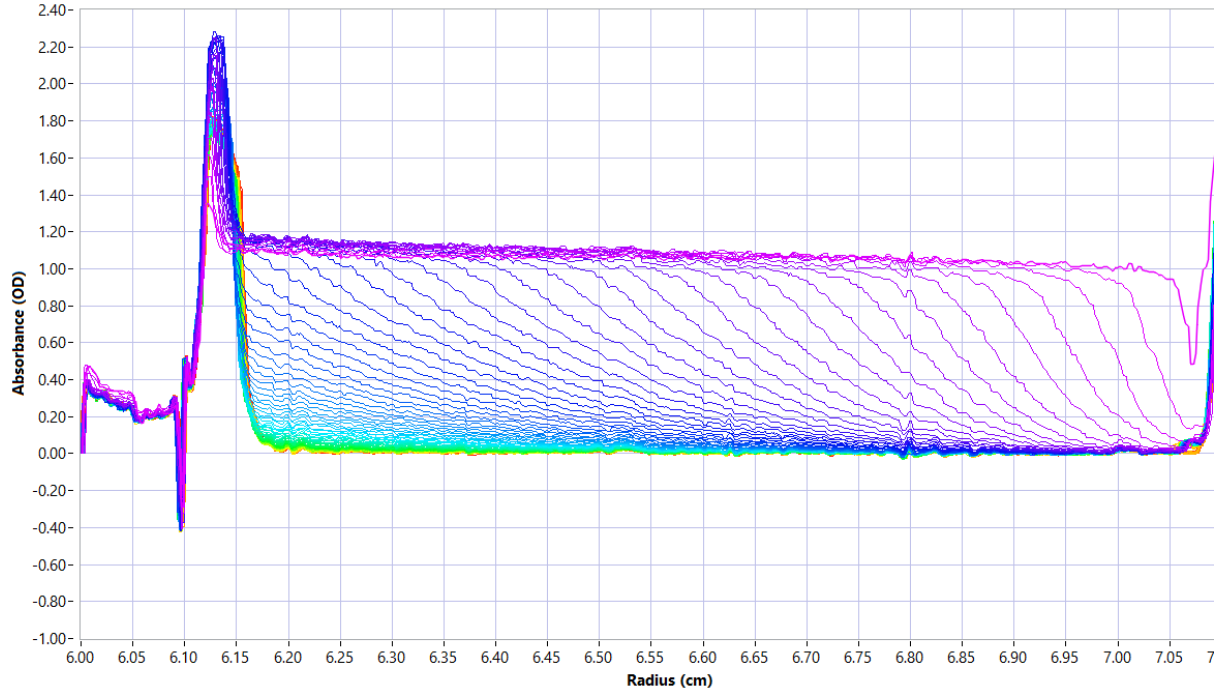

Figure 3.21. Absorbance profiles measured during AUC in 97.6 vol-% D_2O/H_2O (analyte: entry 7, Table 3.2, 30000 rpm, 280 nm, 20°C, 121 scans).

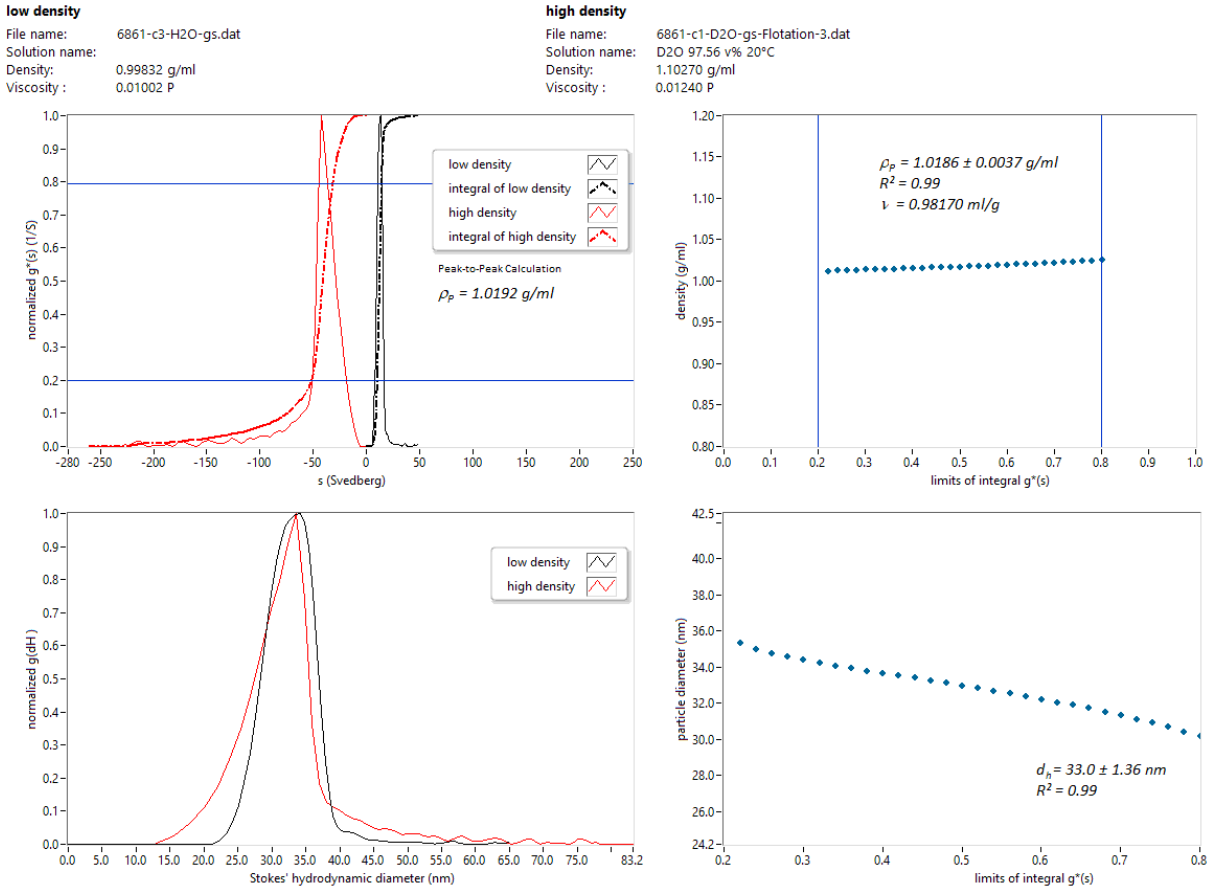

Figure 3.22. Determination of particle density ρ_P and hydrodynamic diameter d_h from AUC measurements in H_2O and H_2O/D_2O by solvent variation analysis (analyte: entry 7, Table 3.2).

3.5 Appendix

3.5.1 TEM Images of polyethylene nanocrystals

Exemplary TEM sections used for statistical calculations

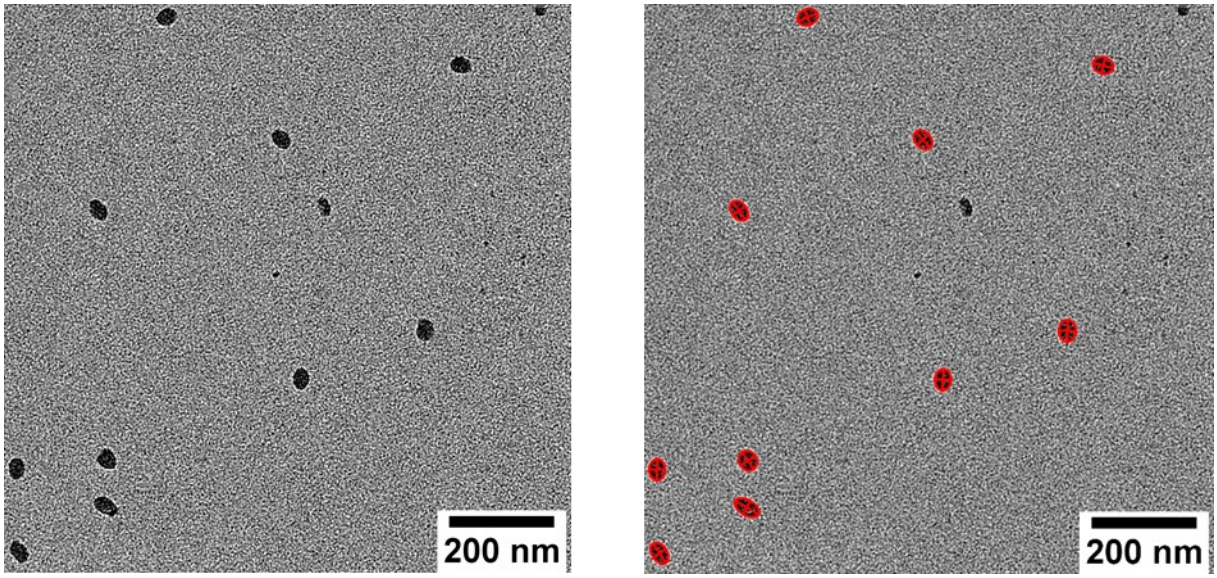

Figure 3.23. TEM image of polyethylene dispersion (entry 3, Table 3.2); applied ellipse fit shown (*right*).

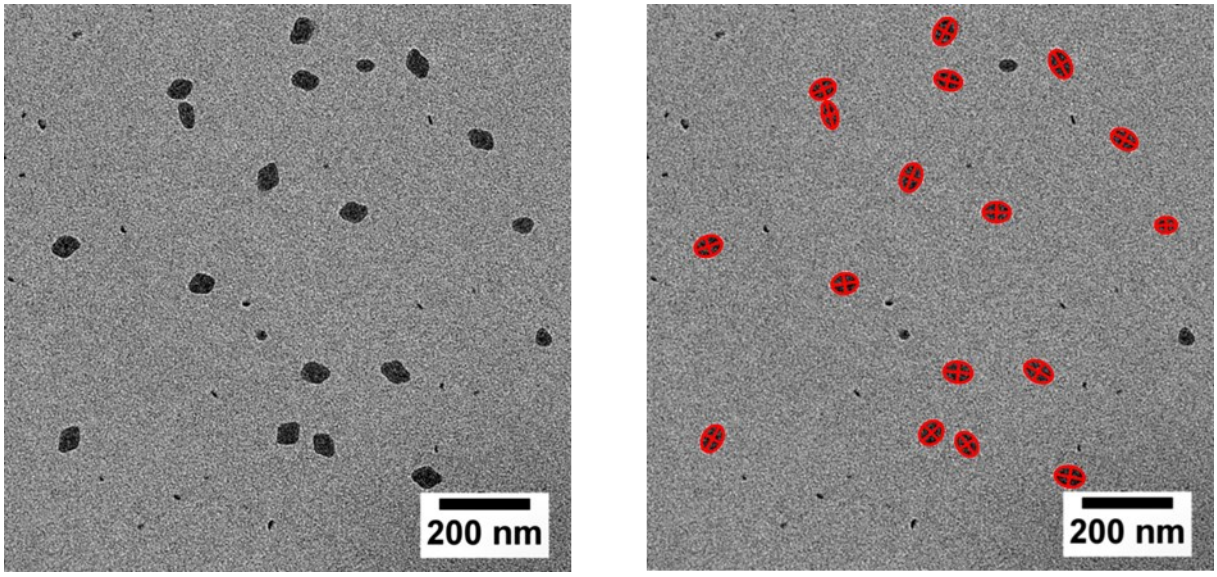

Figure 3.24. TEM image of polyethylene dispersion (entry 6, Table 3.2); applied ellipse fit shown (*right*).

TEM overview images of assembled particles

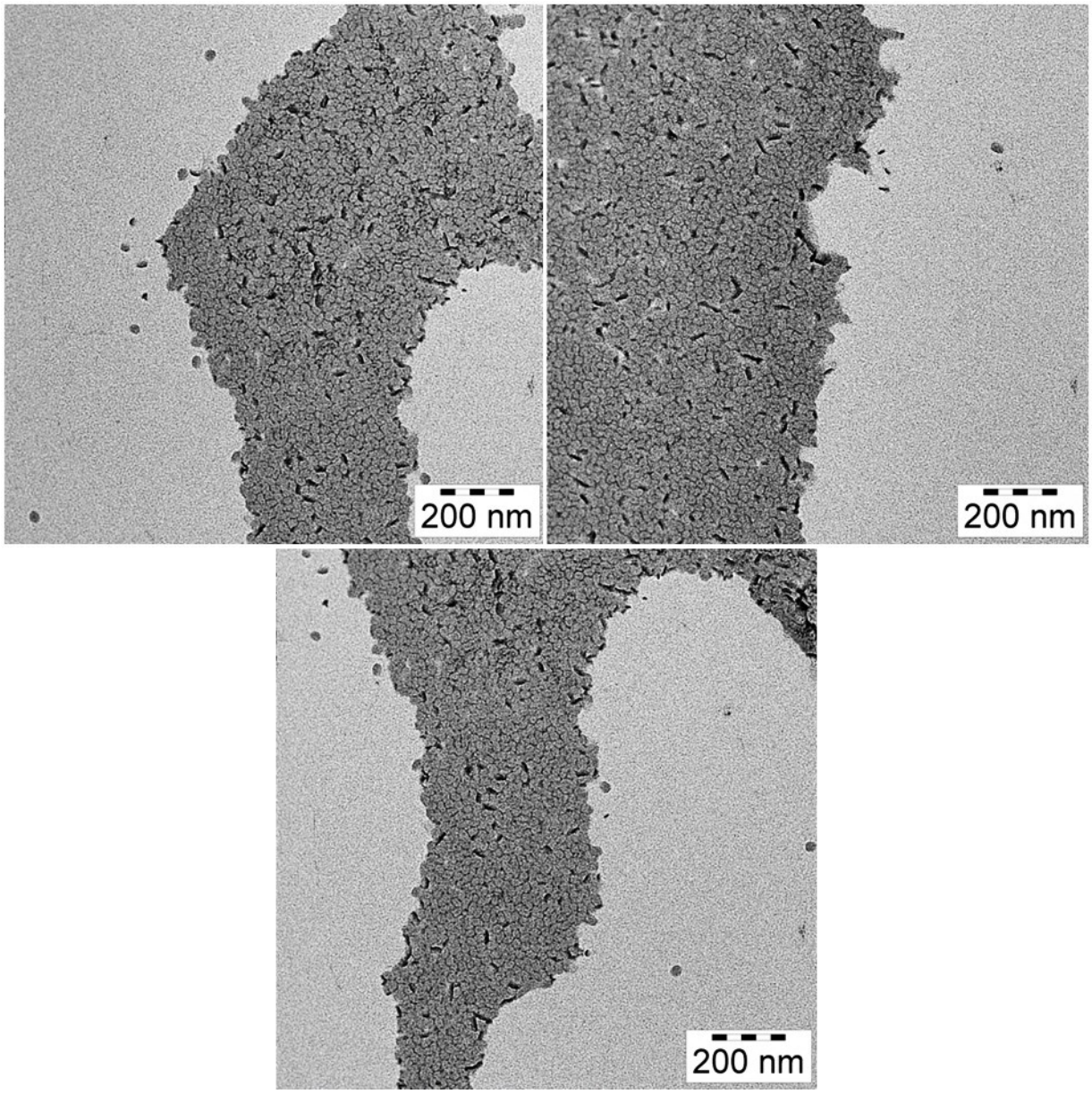

Figure 3.25. Assemblies of nanoparticles obtained in aqueous polymerization (entry 2, Table 3.2) to layers by drop casting of dialyzed dispersion. Dark structures are particles standing perpendicular to the electron beam.

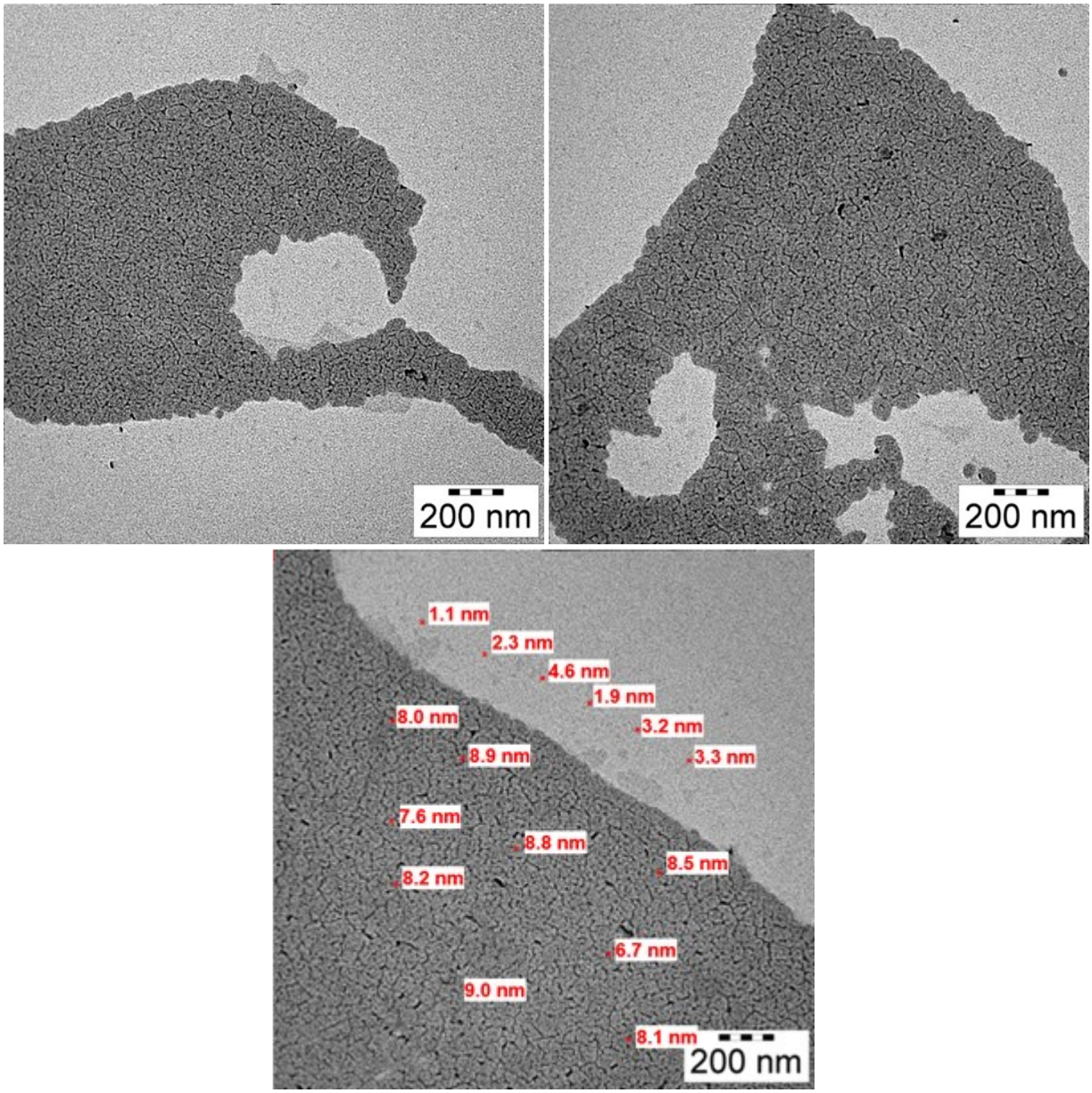

Figure 3.26. Assemblies of nanoparticles obtained in aqueous polymerization (entry 7, Table 3.2) to layers by drop casting of dialyzed dispersion. *Top:* Overview images of different assemblies. *Bottom:* Specimen thickness measurements (red) of typical particle layers determined via TEM. The thickness map was obtained from two acquired images, elastic and global bright-field image (without energy filtering/slit). The mean free path length of carbon was used for all measurements. The average layer thickness was around 6 nm, respectively, around the typical particle thickness as expected for monolayers.

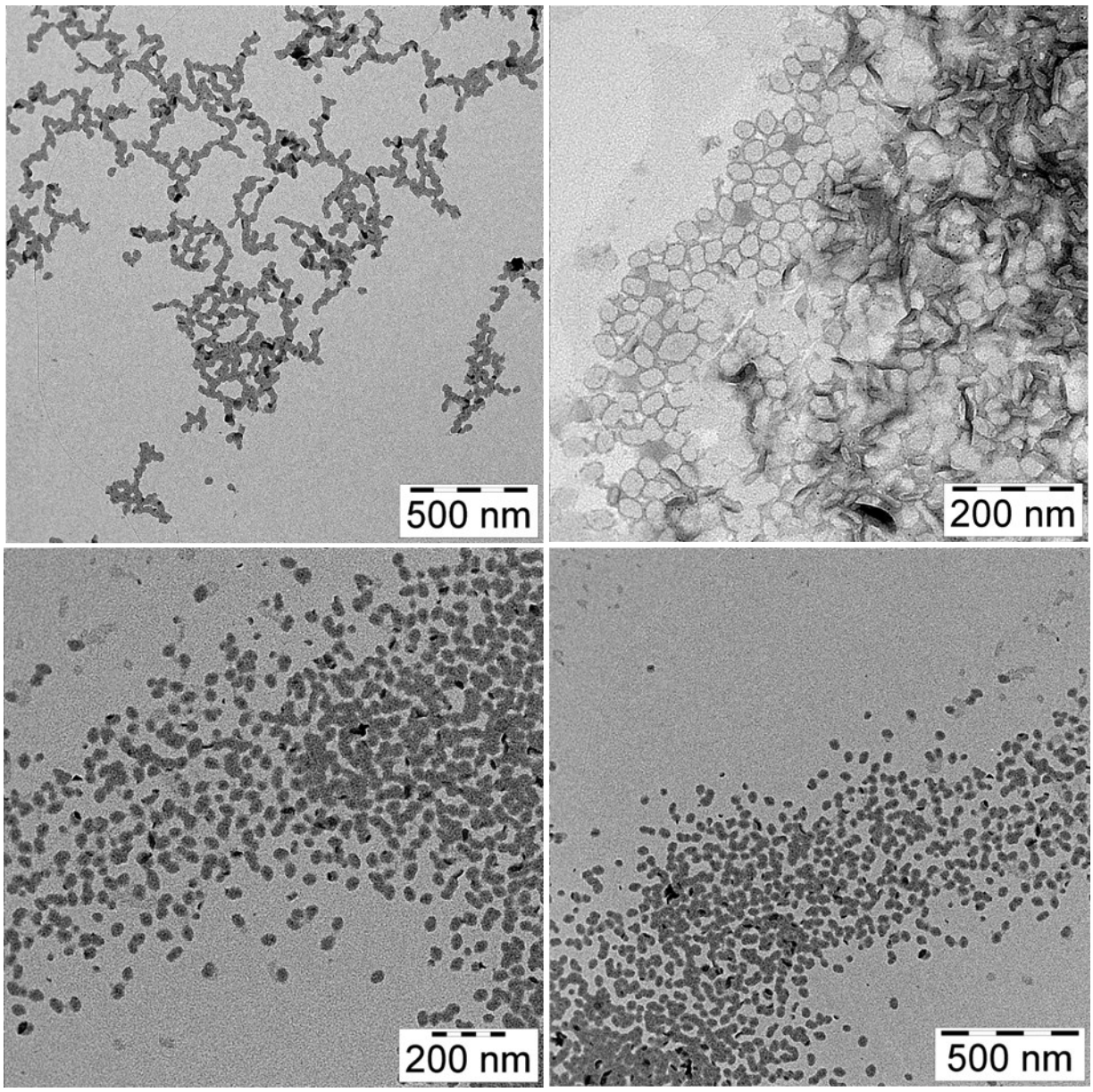

Figure 3.27. Assemblies of nanoparticles obtained in aqueous polymerization (entry 4, Table 3.2) to layers by drop casting of dialyzed dispersion. *Top, left*: Low concentrated dispersion was used. No formation of closed layers, but of dendritic structures was observed. *Top, right*: Higher concentrated dispersion was used. Typically ordered particles were found at the droplet rim together with multilayered structures (black). *Bottom*: Assemblies obtained from slow drying experiments at lower temperature (5-6 °C). A fluent transition between isolated single particles, small assemblies and layers was observed.

Particle shape analysis

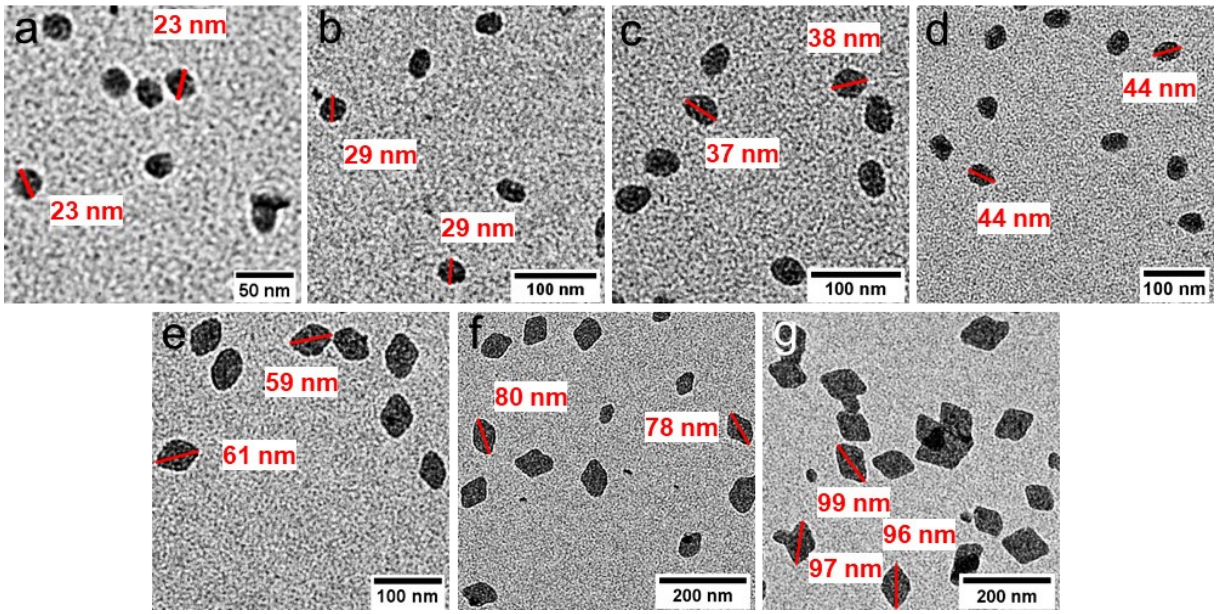

Figure 3.28. TEM images of UHMWPE nanocrystals obtained from aqueous polymerization after different reaction times showing the evolution of size and shape (entries 1-7 (a-g), Table 3.6).

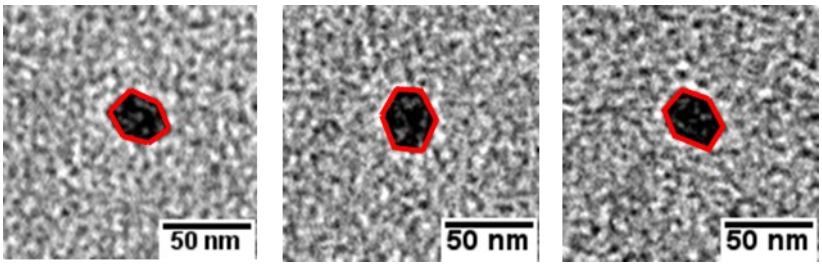

Figure 3.29. Close-up of hexagonal shaped particles obtained in aqueous polymerization (Table 3.2, entry 2).

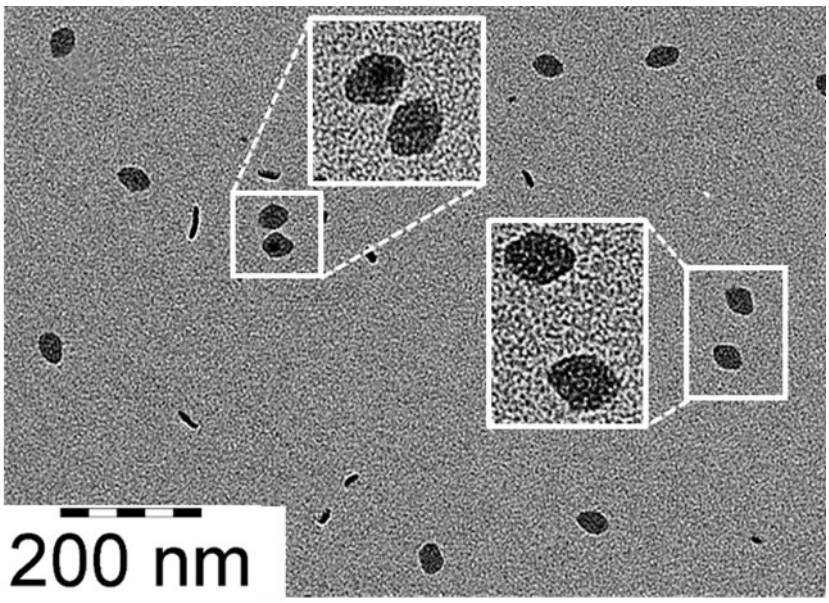

Figure 3.30. Close-up of truncated lozenge shaped particles obtained in aqueous polymerization (Table 3.2, entry 4). The differences in crystal face growth from hexagonal particles to truncated lozenges are usually identifiable for particles with lateral egde-to-edge sizes >40 nm (particles shown have ~45 nm).

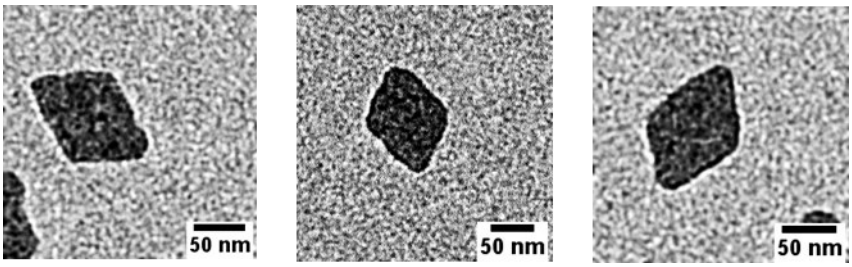

Figure 3.31. Close-up of lozenge shaped particles obtained in aqueous polymerization.

3.5.2 NMR spectra of complexes

NMR spectra of κ²-(N,O)-salicylaldiminato nickel(II) methyl complexes (1^{I}-R^{F}/Pyr)

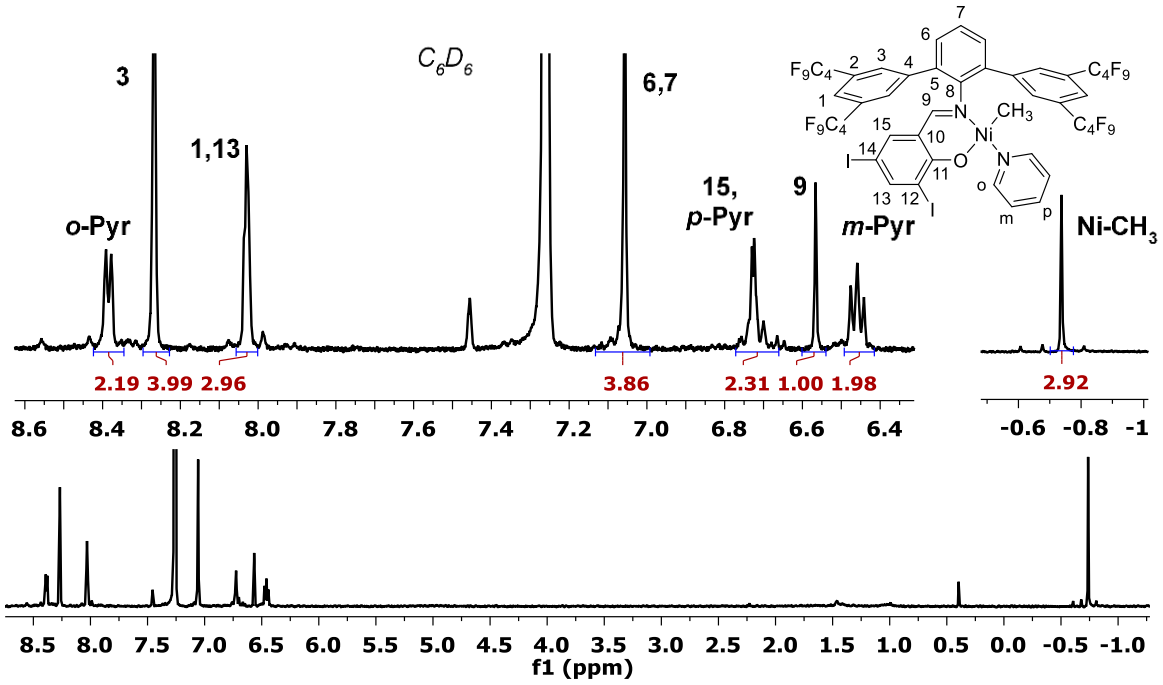

Figure 3.32. ^{1}H NMR spectrum (400 MHz, C_6D_6, 300 K) of complex **1^{I}-C_4F_9/Pyr**.

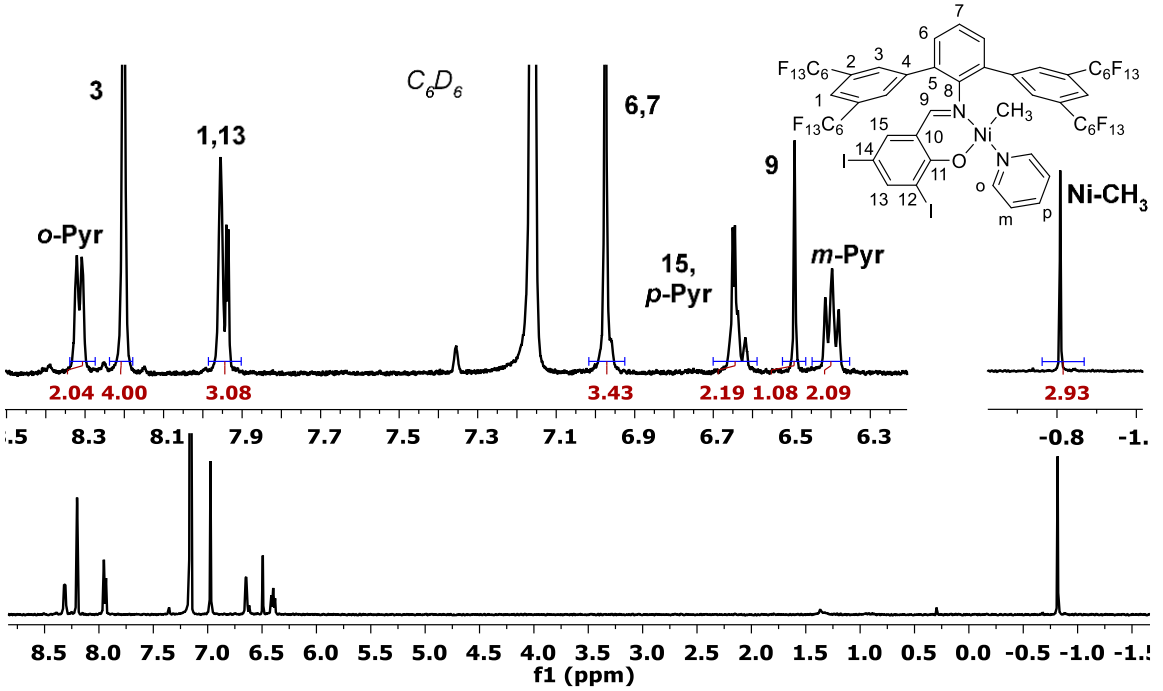

Figure 3.33. ^{1}H NMR spectrum (400 MHz, C_6D_6/C_6F_6, 300 K) of complex **1^{I}-C_6F_{13}/Pyr**.

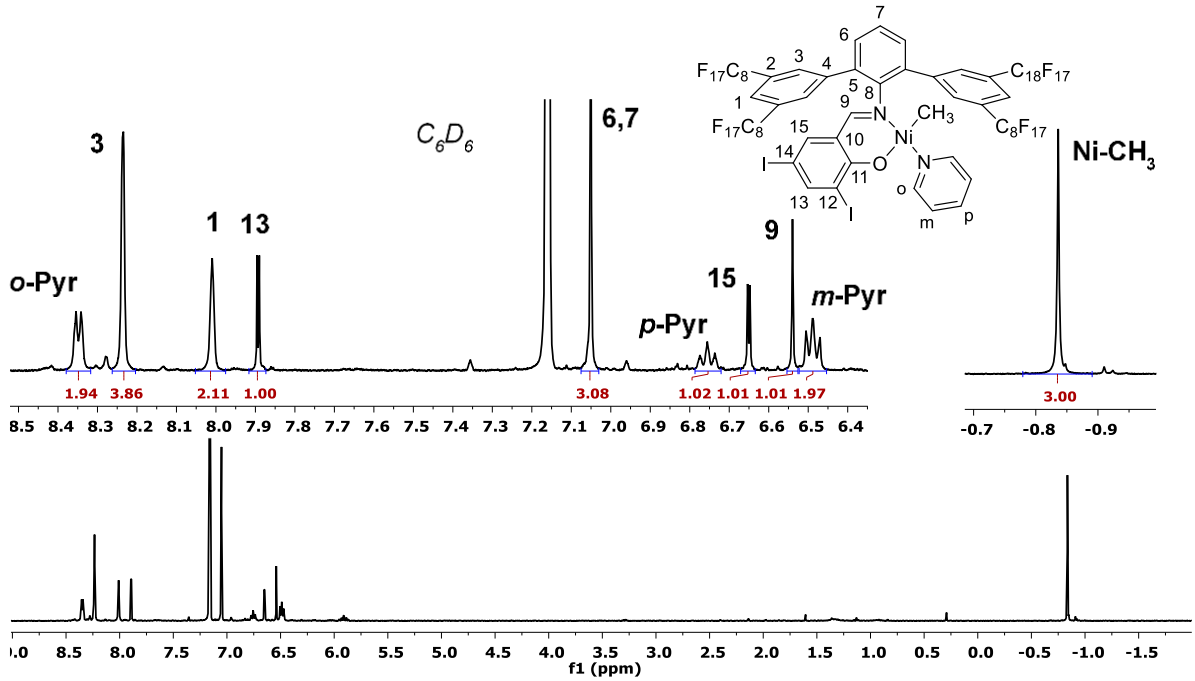

Figure 3.34. ^{1}H NMR spectrum (400 MHz, C_6D_6/C_6F_6, 300 K) of complex **1^{I}-C$_8$F$_{17}$/Pyr**.

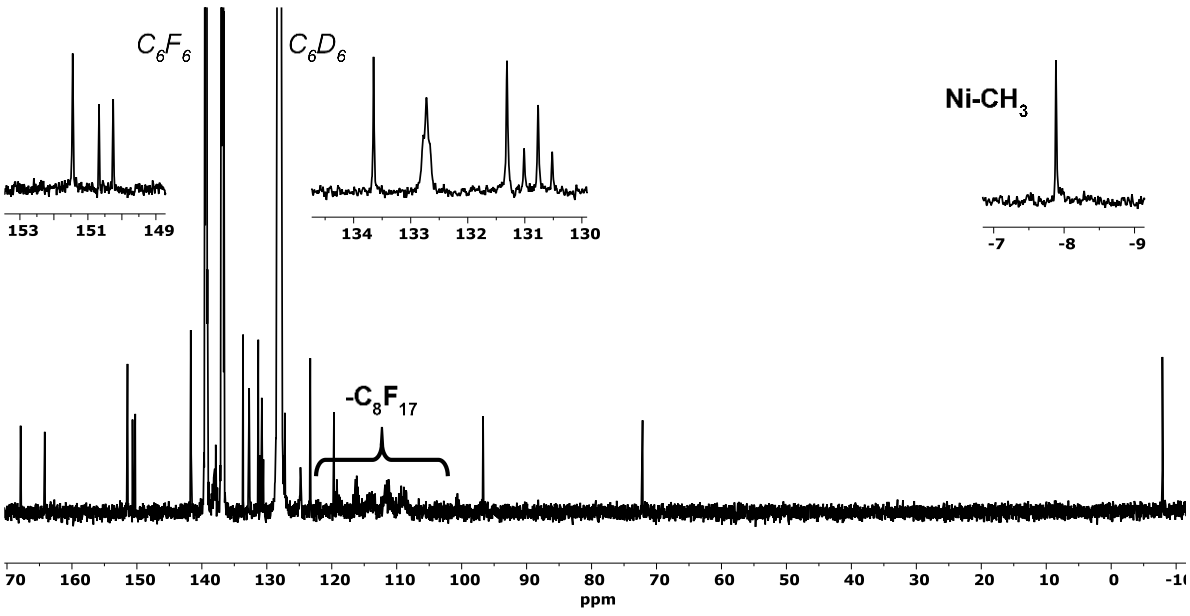

Figure 3.35. ^{13}C{^{1}H} NMR spectrum (400 MHz, C_6D_6/C_6F_6, 300 K) of complex **1^{I}-C$_8$F$_{17}$/Pyr**.

NMR spectra of κ²-(N,O)-salicylaldiminato nickel(II) methyl [α-methoxy-ω-amino poly(ethylene glycol] complexes (1^{I}-R^{F}/PEG)

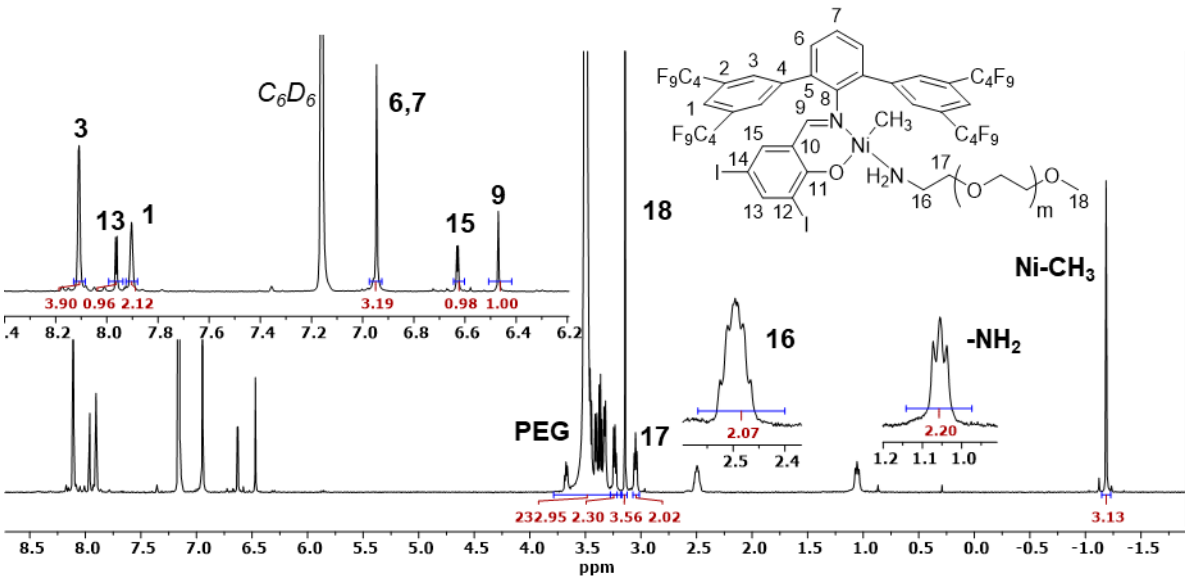

Figure 3.36. ^{1}H NMR spectrum (400 MHz, C_6D_6, 300 K) of complex **1^{I}-C_4F_9/PEG**.

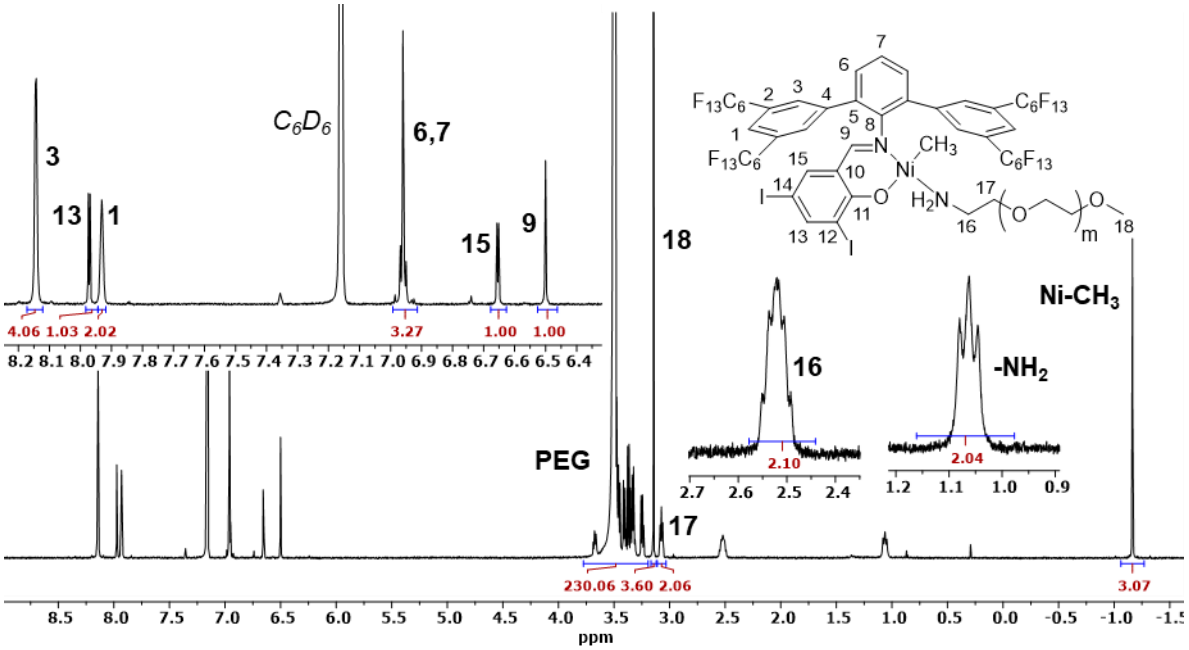

Figure 3.37. ^{1}H NMR spectrum (400 MHz, C_6D_6, 300 K) of complex **1^{I}-C_6F_{13}/PEG**.

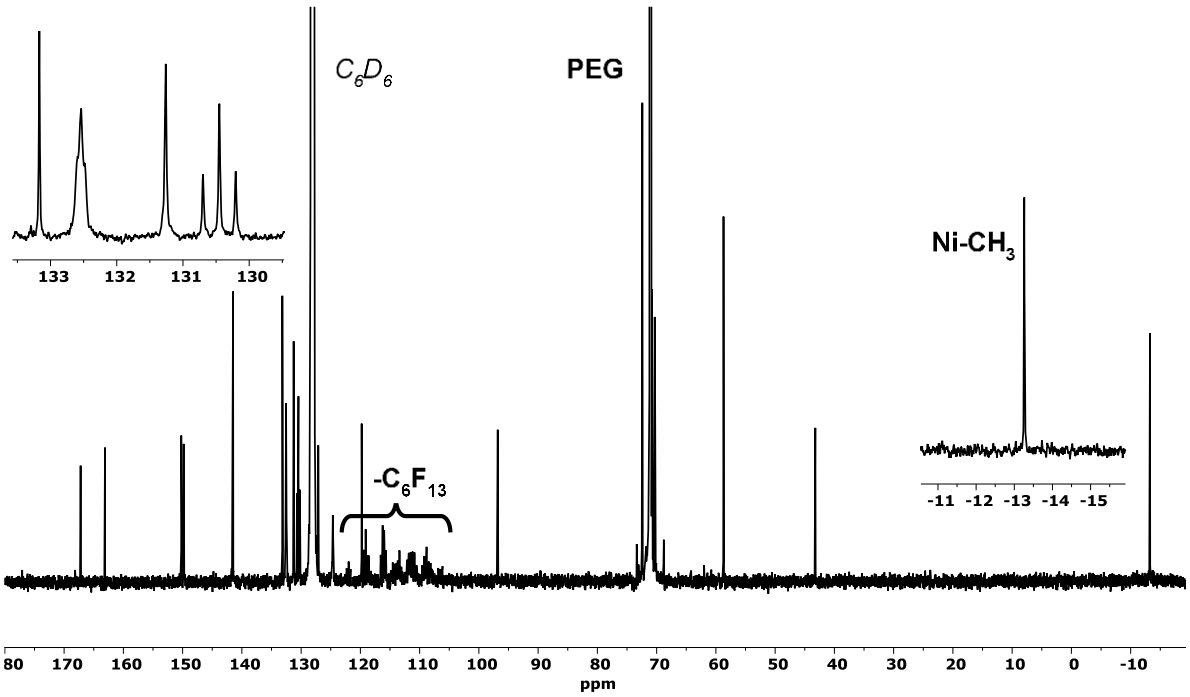

Figure 3.38. $^{13}C\{^{1}H\}$ NMR spectrum (400 MHz, C_6D_6, 300 K) of complex **1^{I}-C$_6$F$_{13}$/PEG**.

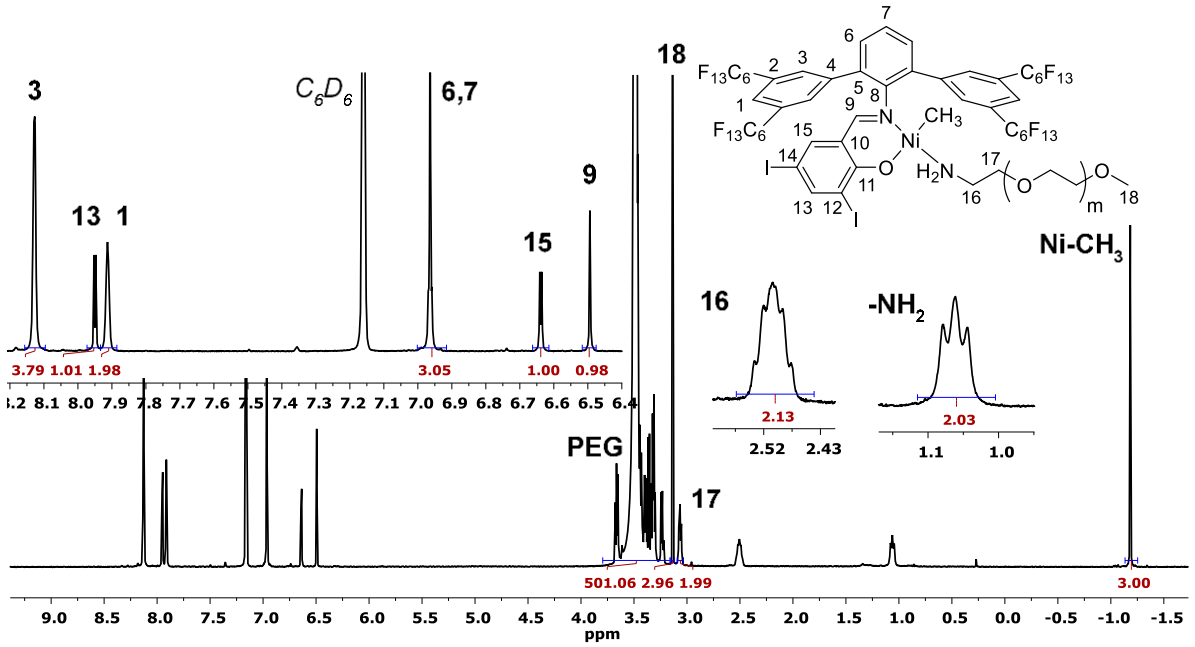

Figure 3.39. ^{1}H NMR spectrum (400 MHz, C_6D_6, 300 K) of complex **1^{I}-C$_6$F$_{13}$/PEG** with M(H_2N-PEG-OMe) = 5516 g mol^{-1}.

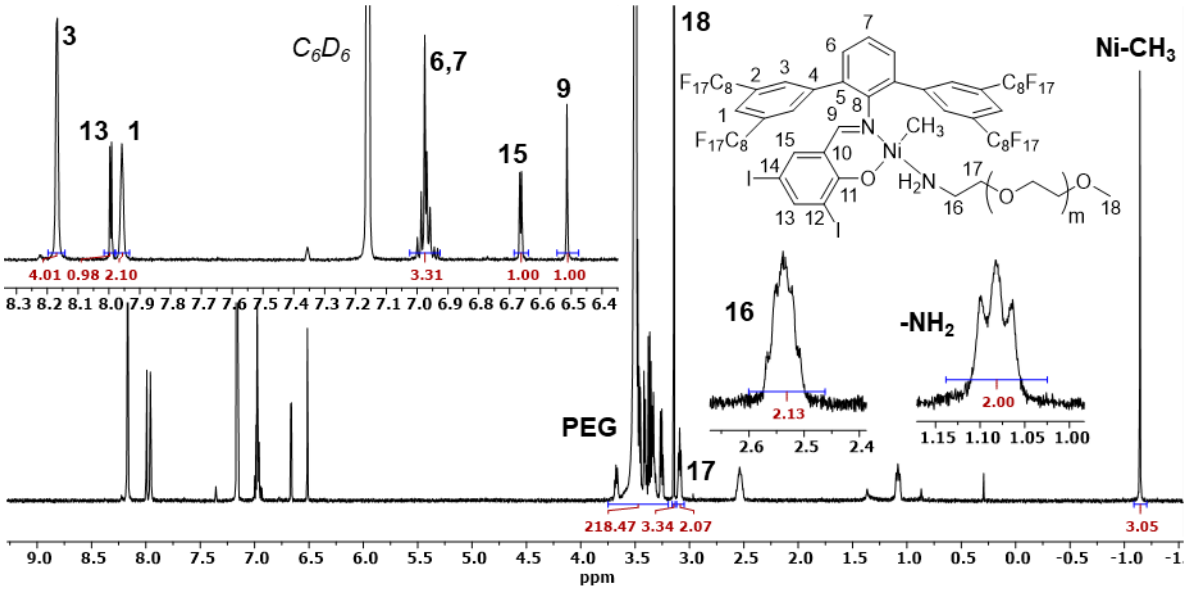

Figure 3.40. ^{1}H NMR spectrum (400 MHz, C_6D_6, 300 K) of complex **1^{I}-C$_8$F$_{17}$/PEG**.

3.5.3 Selected GPC traces of synthesized polyethylenes

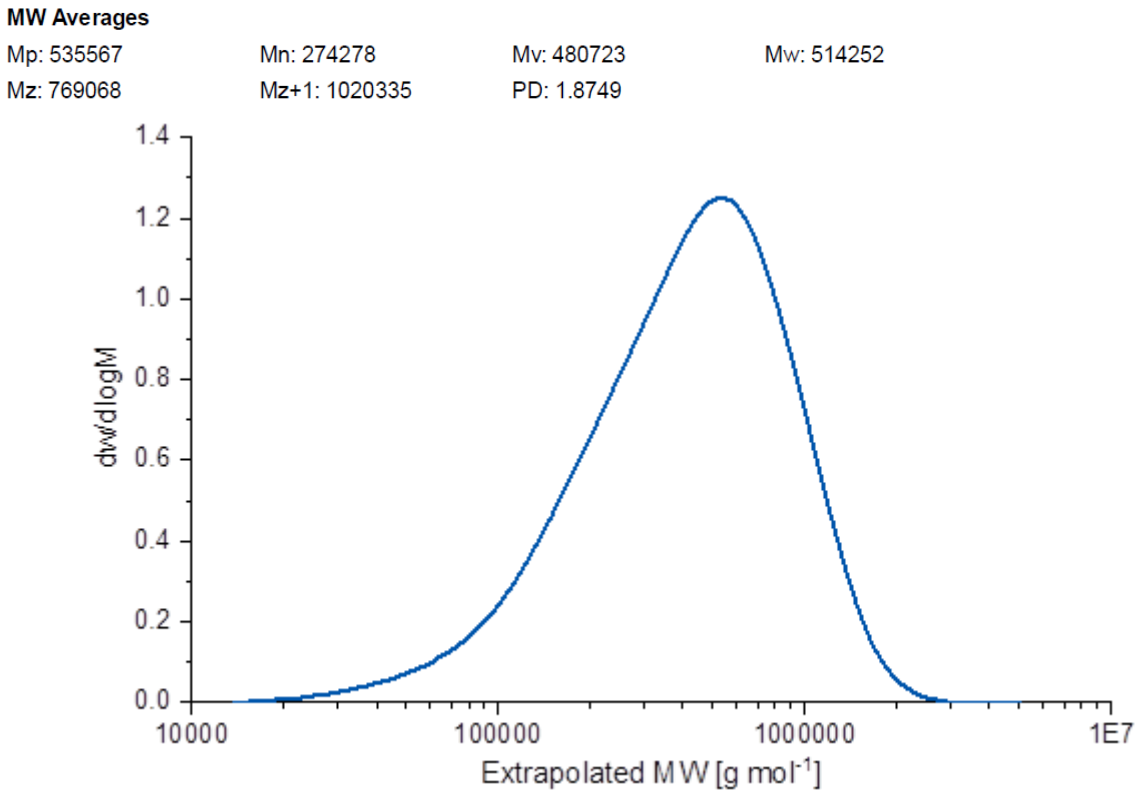

Figure 3.41. GPC trace of polyethylene obtained from polymerization in toluene (Table 3.1, entry 1).

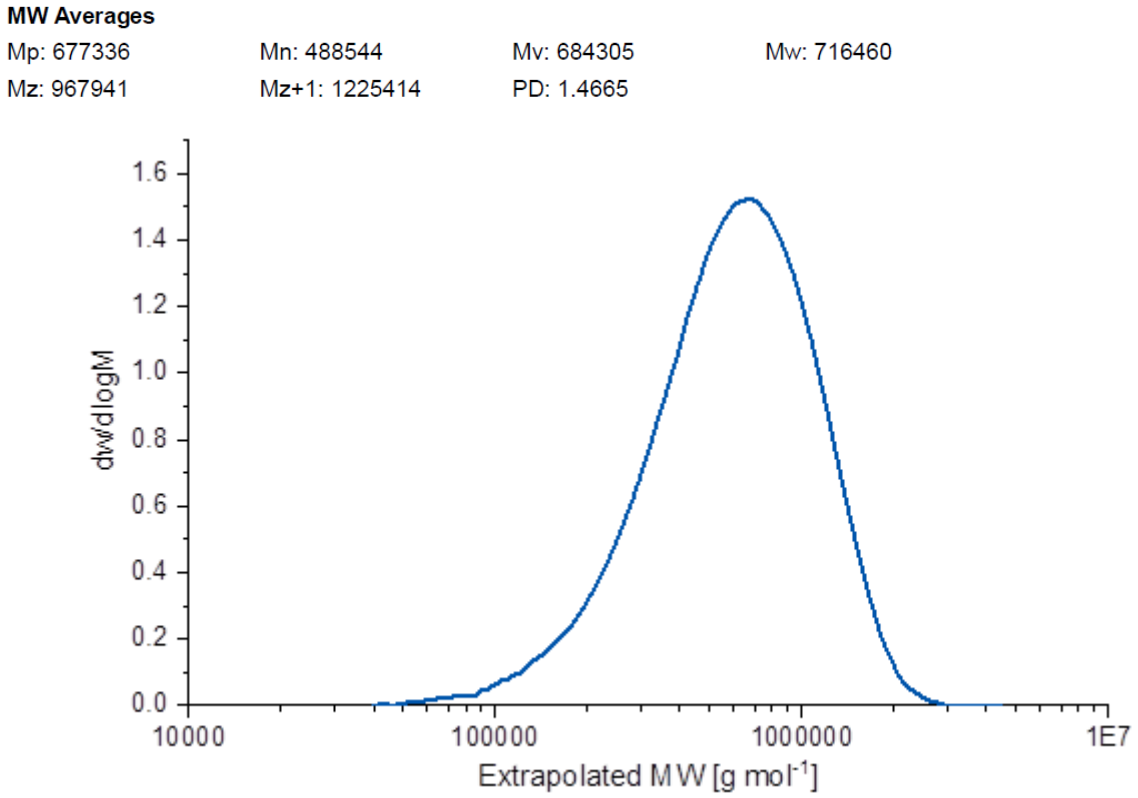

Figure 3.42. GPC trace of polyethylene obtained from polymerization in toluene (Table 3.1, entry 4).

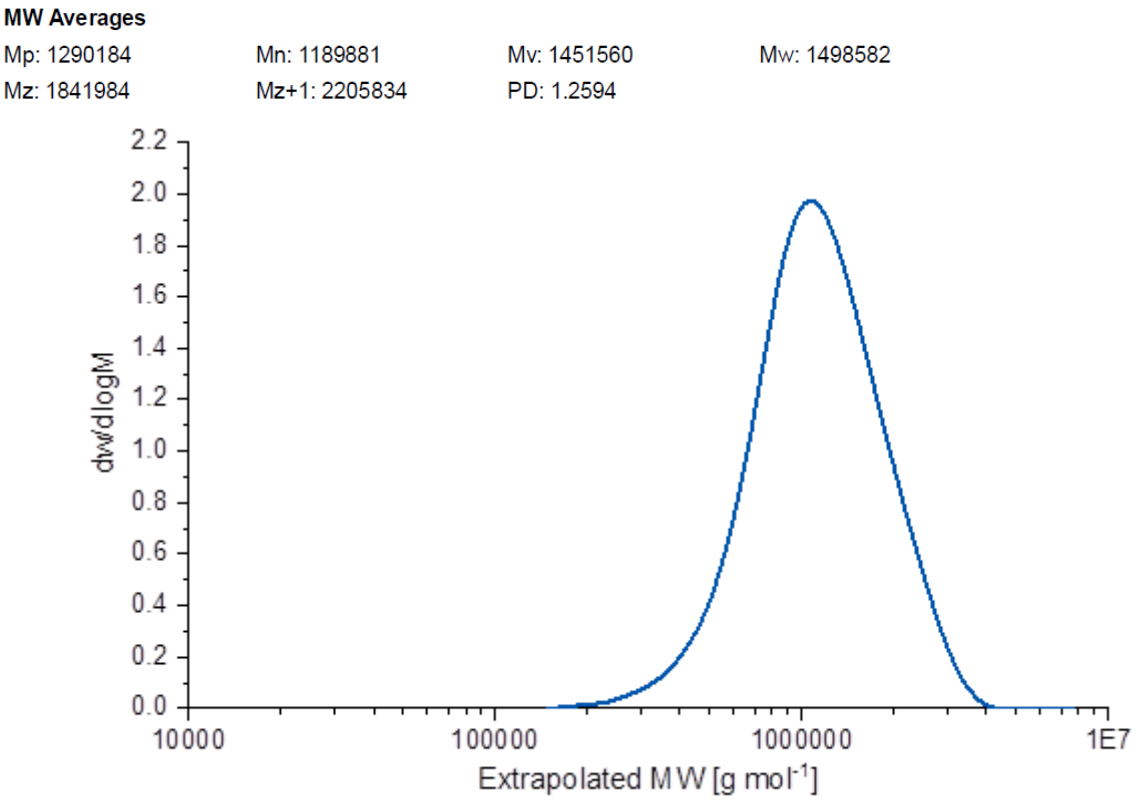

Figure 3.43. GPC trace of polyethylene obtained from polymerization in toluene (Table 3.1, entry 6).

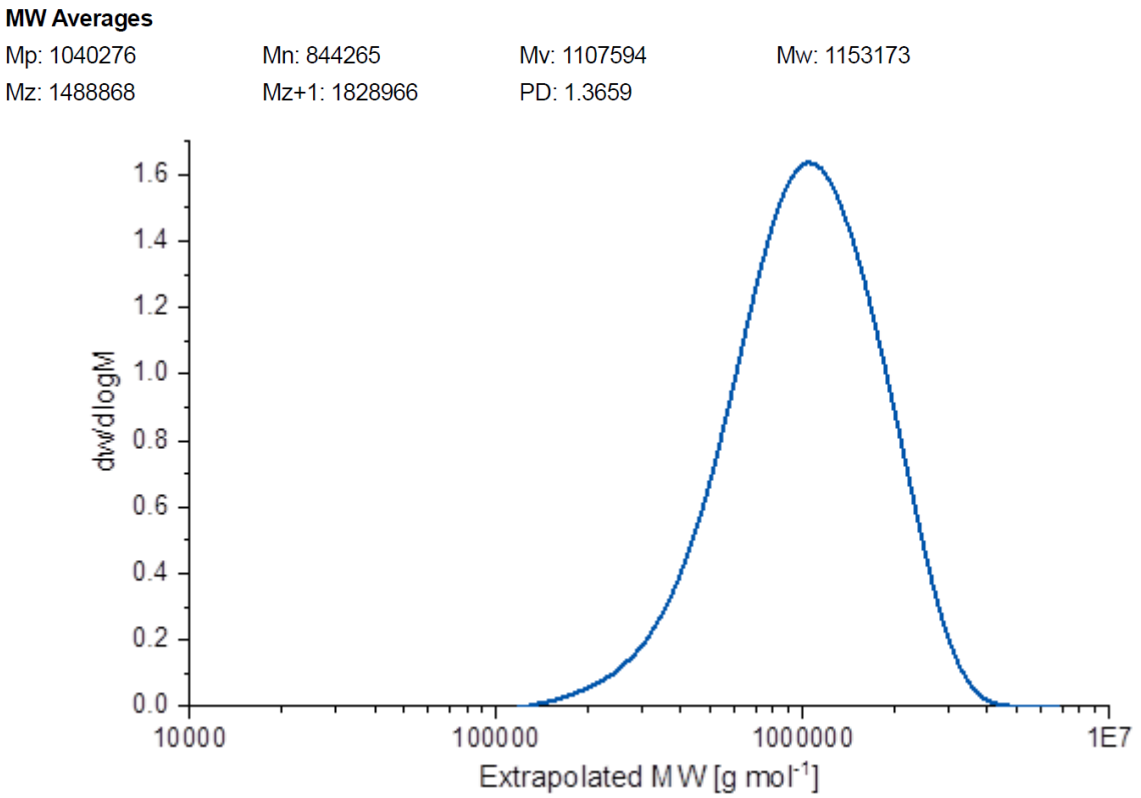

Figure 3.44. GPC trace of polyethylene obtained from polymerization in toluene (Table 3.1, entry 7).

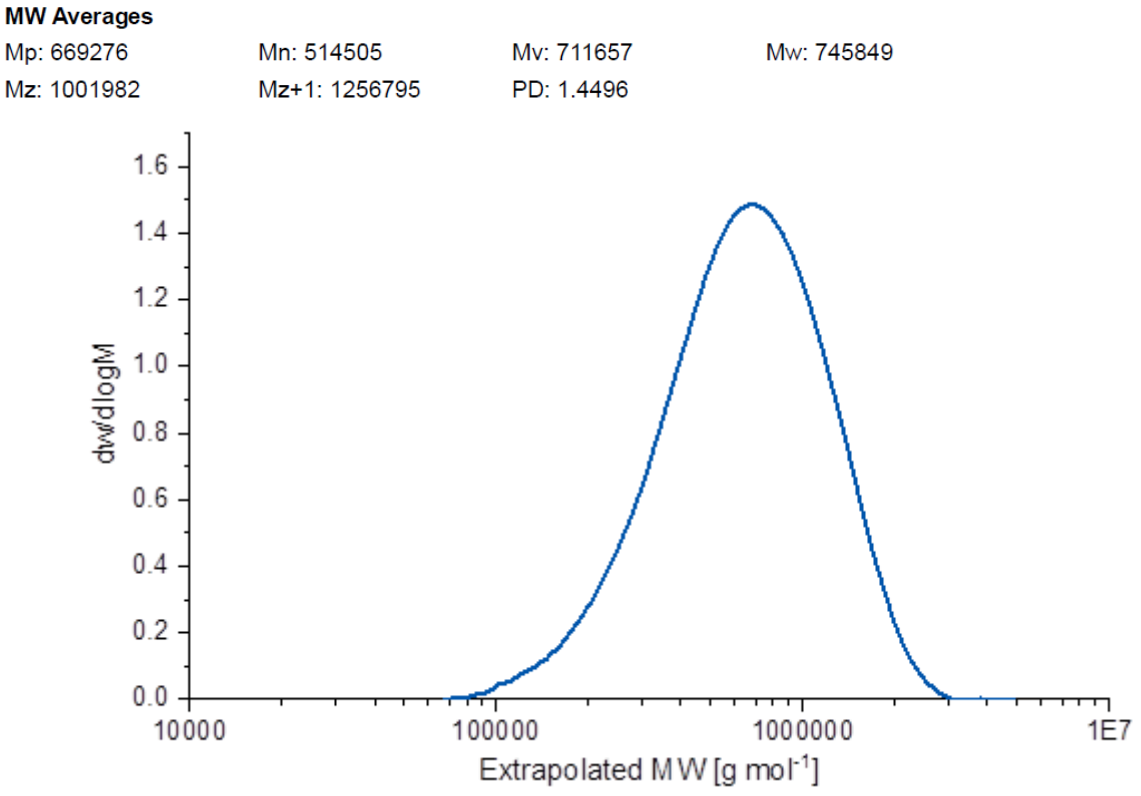

Figure 3.45. GPC trace of polyethylene obtained from polymerization in toluene (Table 3.1, entry 11).

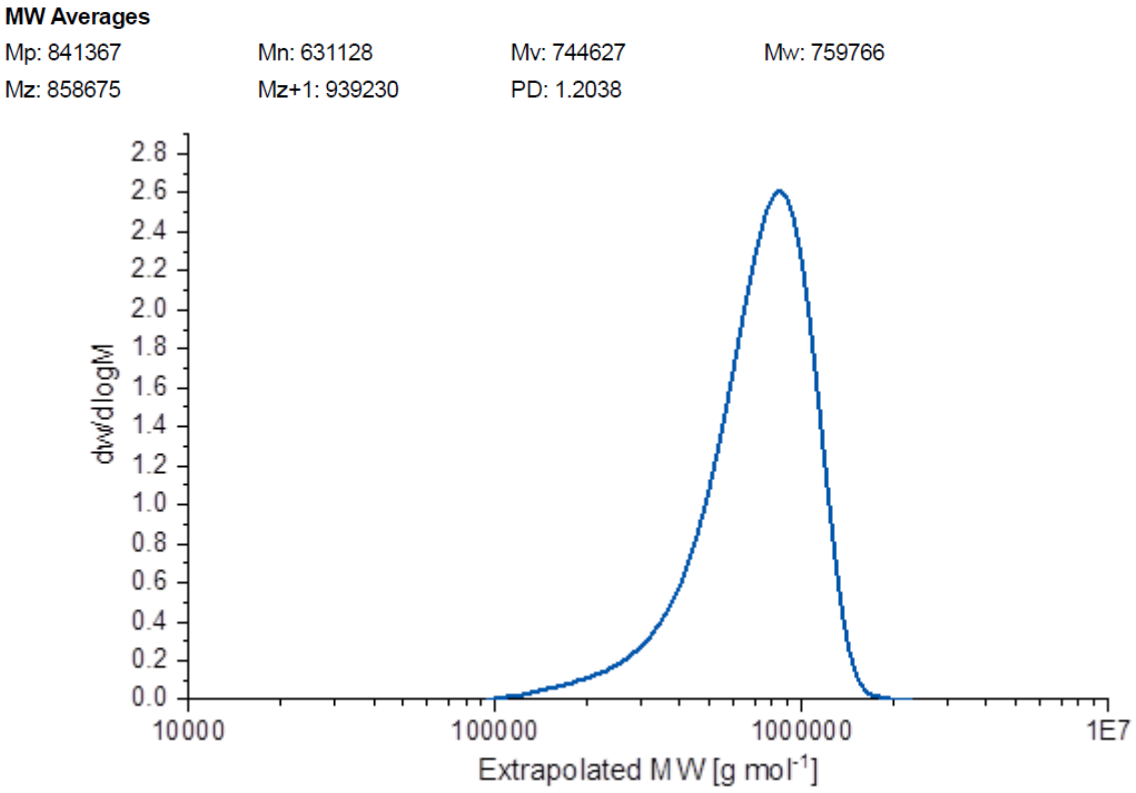

Figure 3.46. GPC trace of polyethylene obtained in aqueous polymerization (Table 3.2, entry 1).

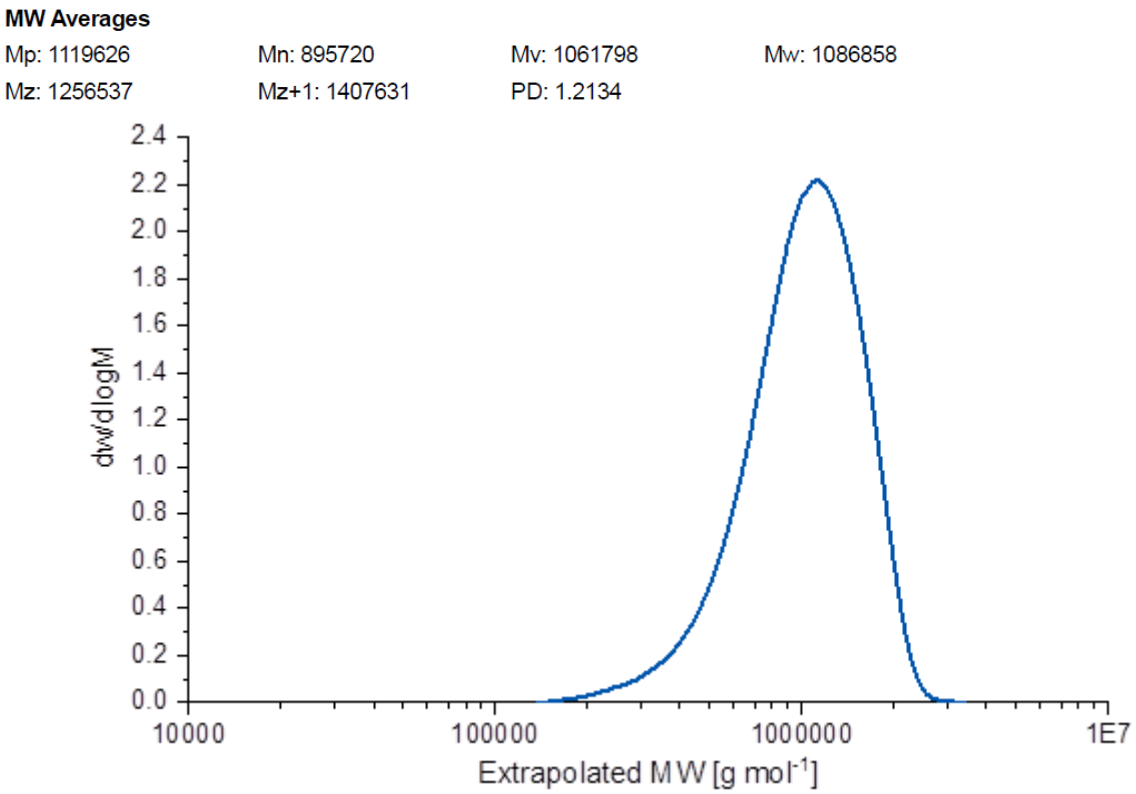

Figure 3.47. GPC trace of polyethylene obtained in aqueous polymerization (Table 3.2, entry 2).

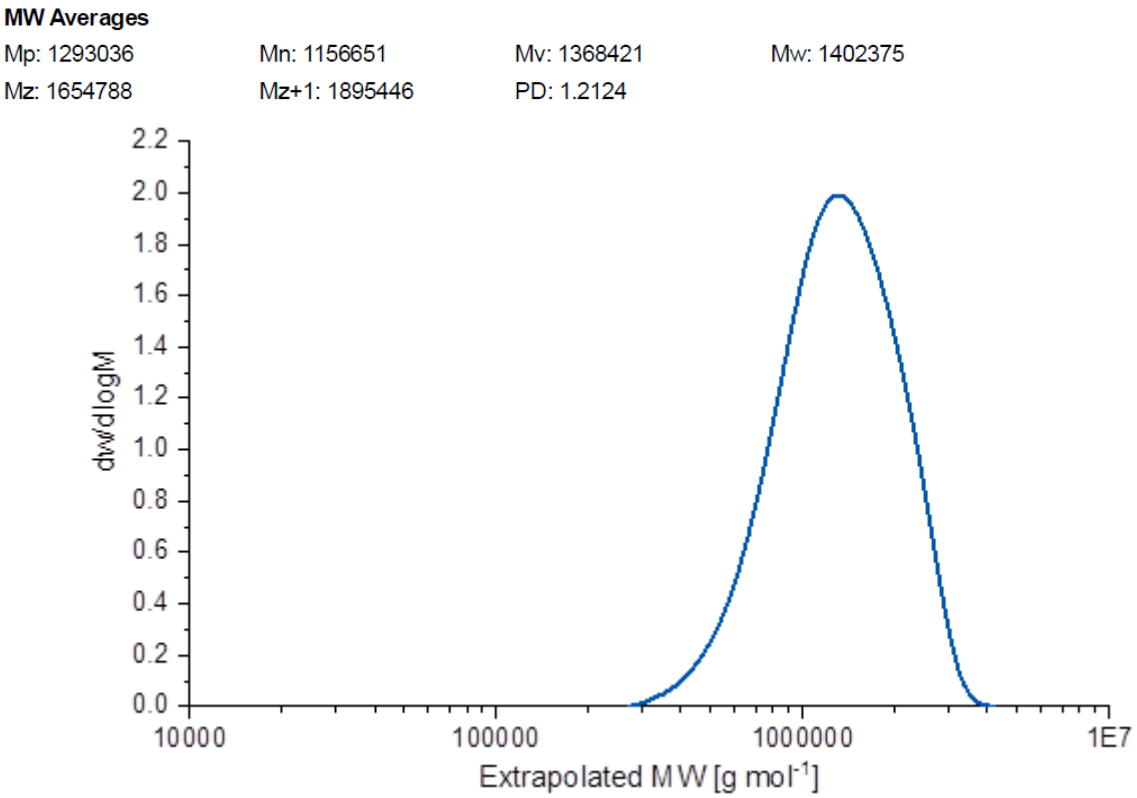

Figure 3.48. GPC trace of polyethylene obtained in aqueous polymerization (Table 3.2, entry 3).

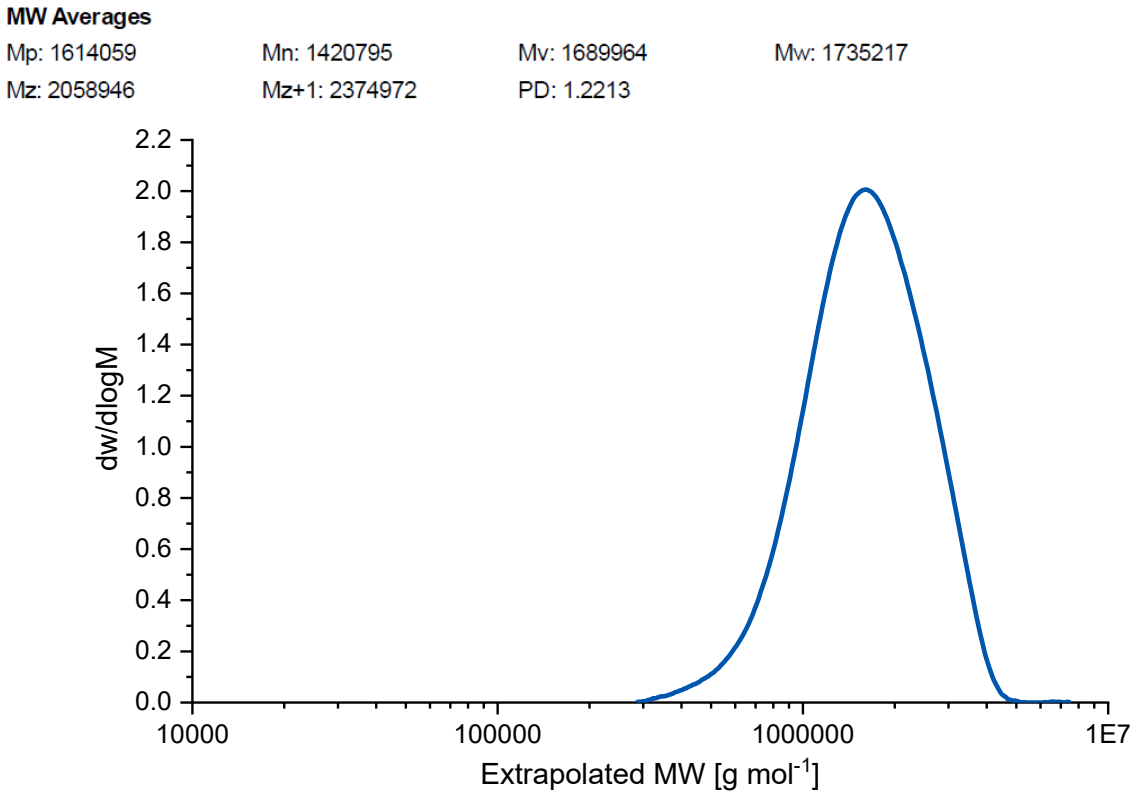

Figure 3.49. GPC trace of polyethylene obtained in aqueous polymerization (Table 3.2, entry 4).

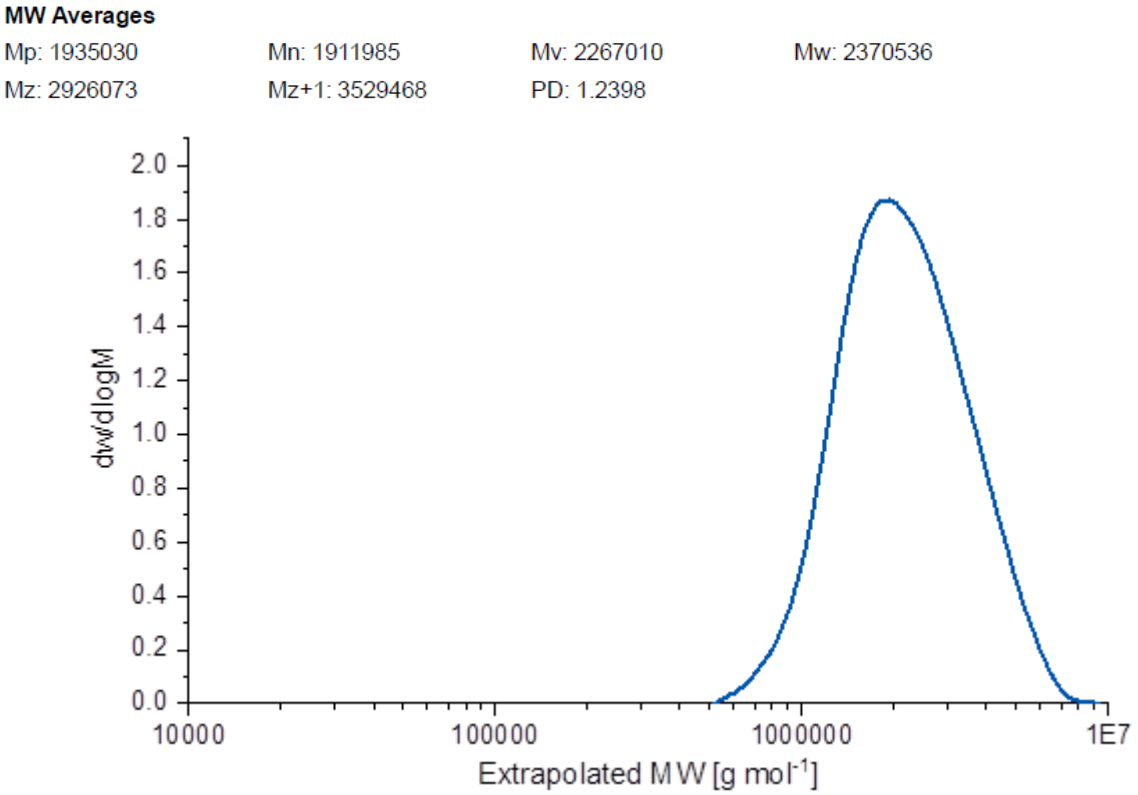

Figure 3.50. GPC trace of polyethylene obtained in aqueous polymerization (Table 3.2, entry 5).

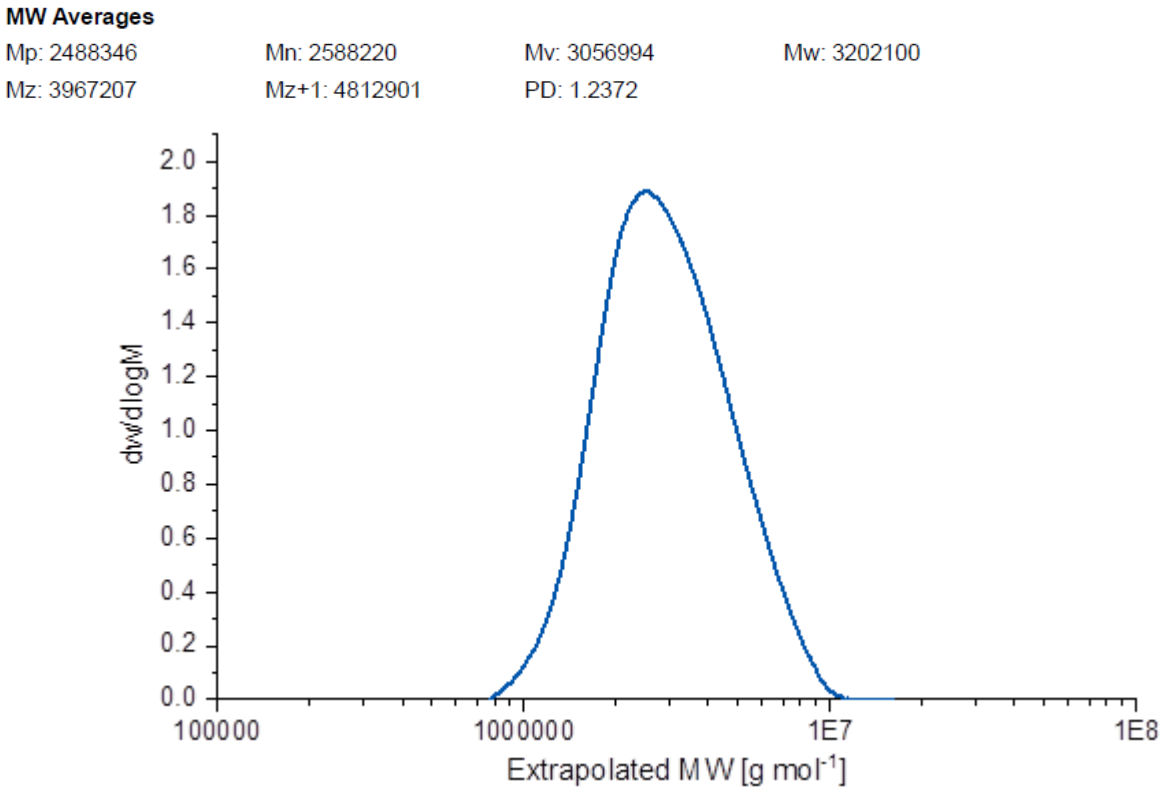

Figure 3.51. GPC trace of polyethylene obtained in aqueous polymerization (Table 3.2, entry 6).

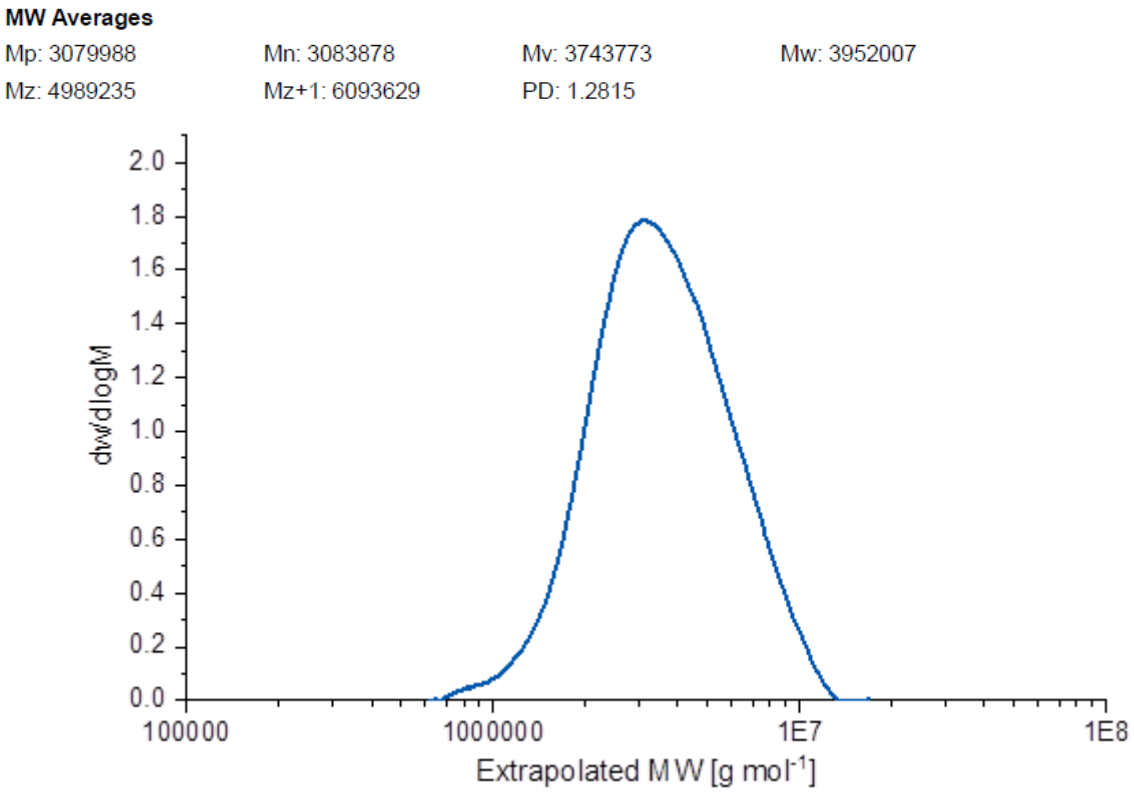

Figure 3.52. GPC trace of polyethylene obtained in aqueous polymerization (Table 3.2, entry 7).

3.5.4 Selected DSC traces of polyethylenes obtained in aqueous polymerization

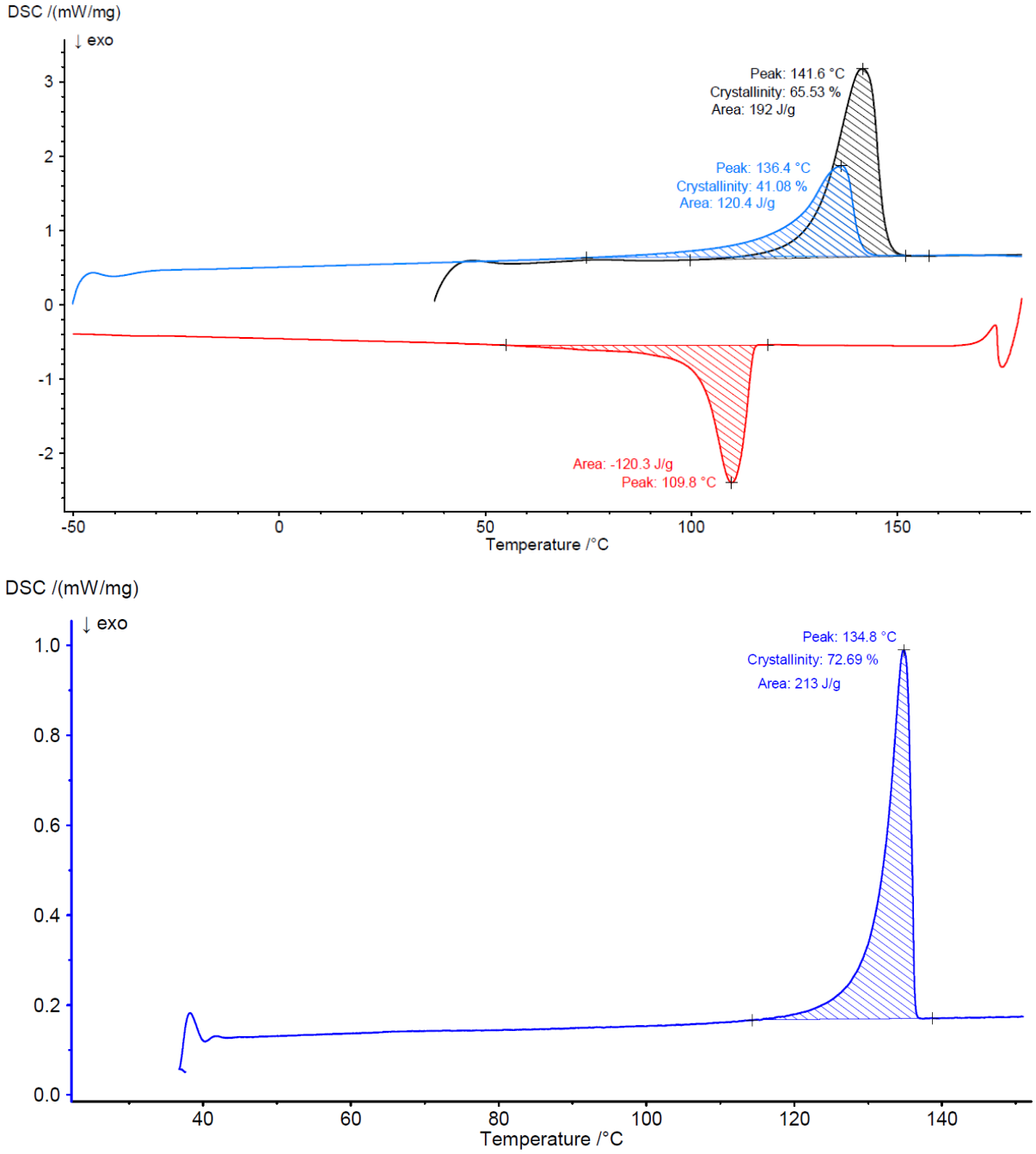

Figure 3.53. DSC traces of polyethylene obtained by aqueous polymerization (Table 3.2, entry 1). *Top*: measured with 10 K min^{-1} heating rate (black curve: 1st heating, red curve: 1st cooling, blue curve: 2nd heating). *Bottom*: measured with 1 K min^{-1} (only first heating shown).

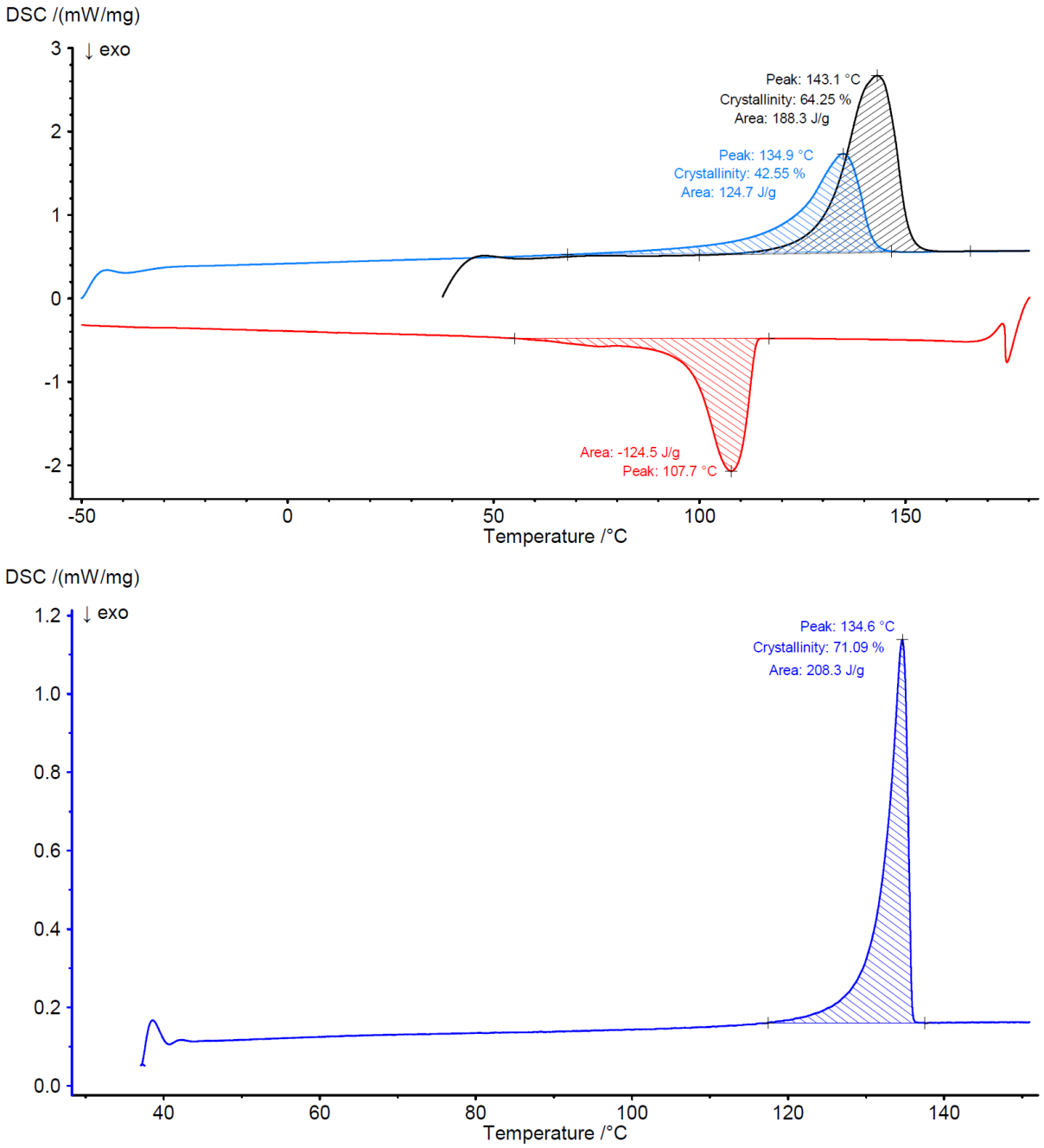

Figure 3.54. DSC traces of polyethylene obtained by aqueous polymerization (Table 3.2, entry 2). *Top*: measured with 10 K min^{-1} heating rate (black curve: 1st heating, red curve: 1st cooling, blue curve: 2nd heating). *Bottom*: measured with 1 K min^{-1} (only first heating shown).

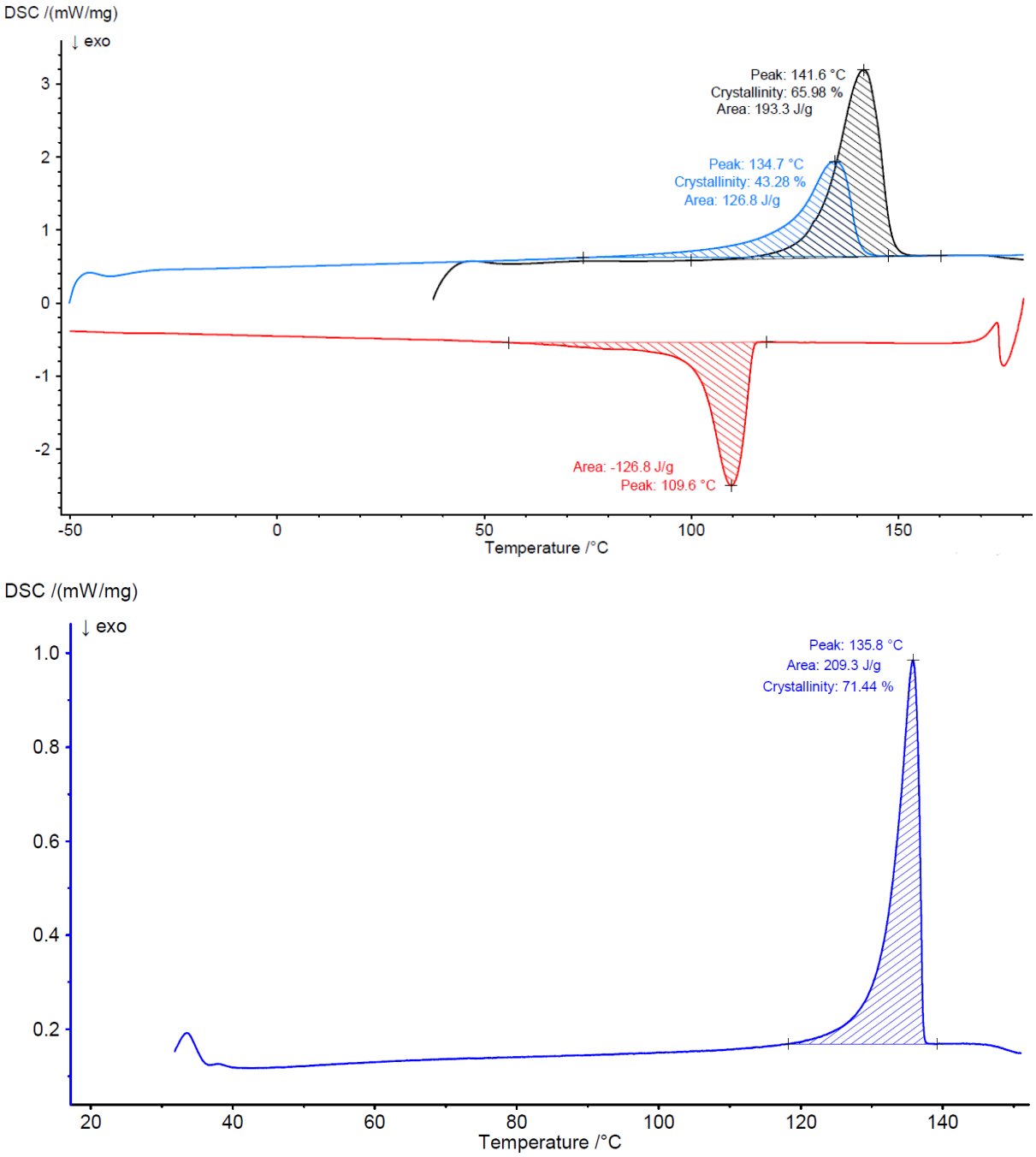

Figure 3.55. DSC traces of polyethylene obtained by aqueous polymerization (Table 3.2, entry 3). *Top*: measured with 10 K min^{-1} heating rate (black curve: 1st heating, red curve: 1st cooling, blue curve: 2nd heating). *Bottom*: measured with 1 K min^{-1} (only first heating shown).

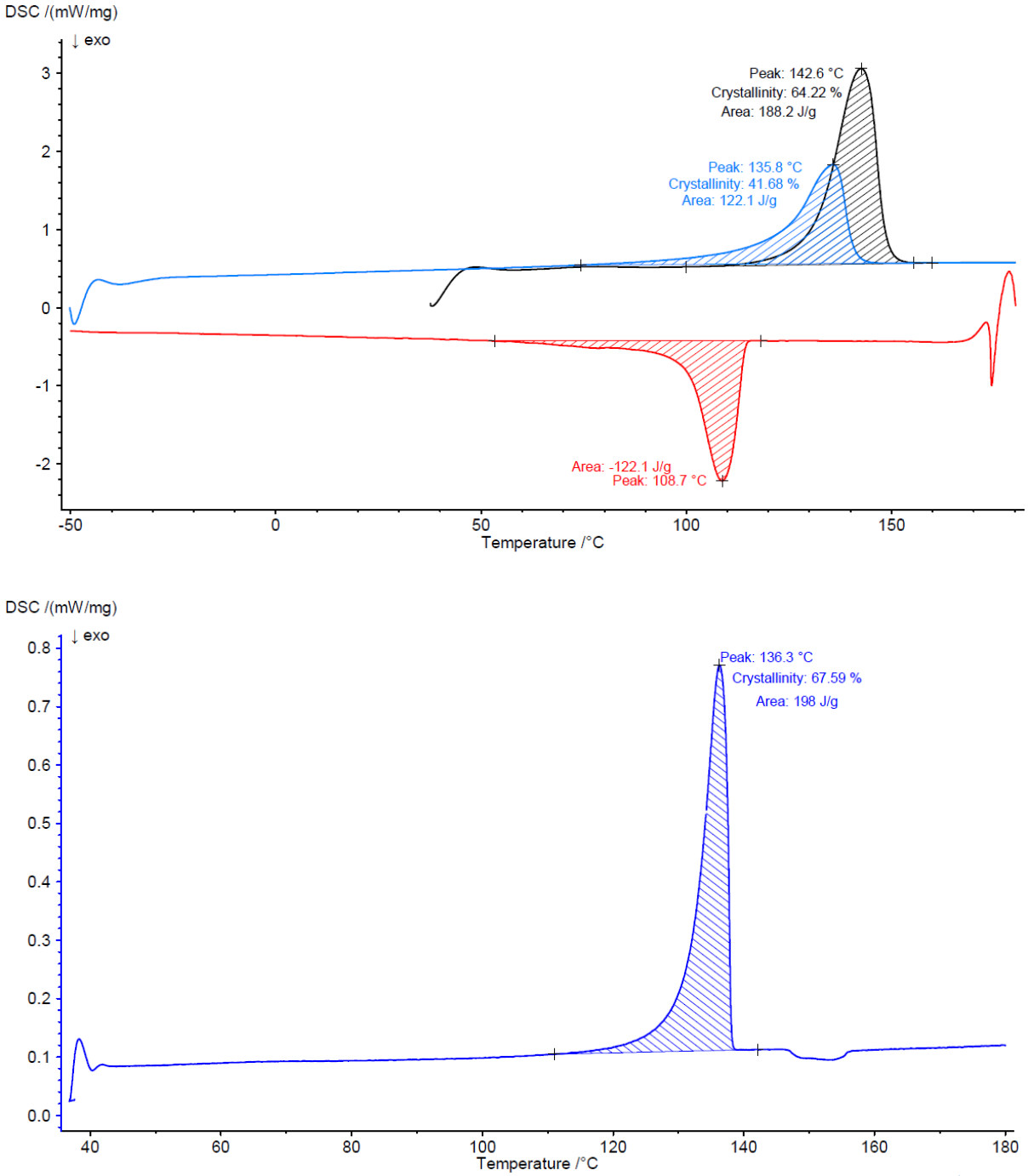

Figure 3.56. DSC traces of polyethylene obtained by aqueous polymerization (Table 3.2, entry 4). *Top*: measured with 10 K min^{-1} heating rate (black curve: 1st heating, red curve: 1st cooling, blue curve: 2nd heating). *Bottom*: measured with 1 K min^{-1} (only first heating shown).

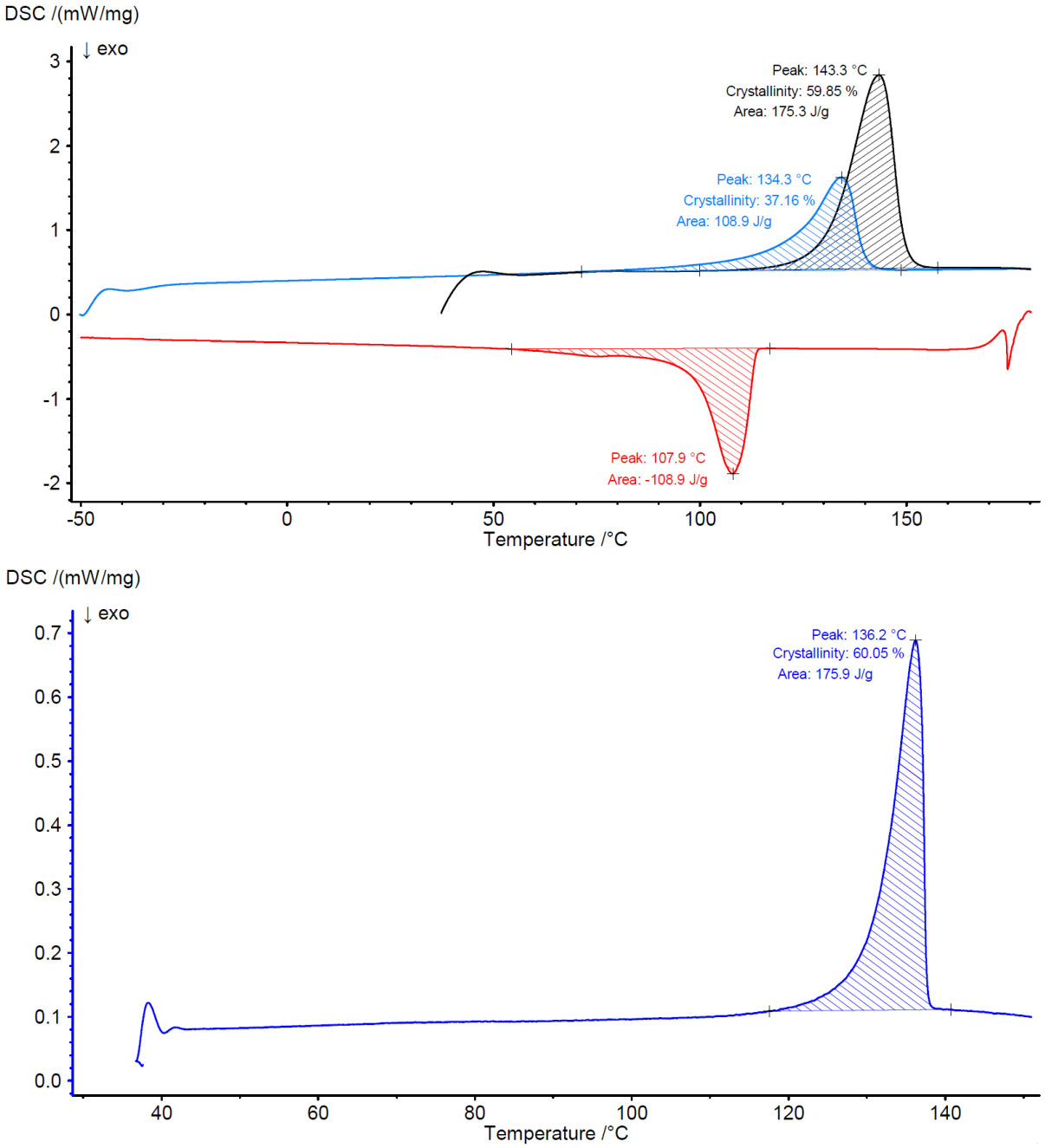

Figure 3.57. DSC traces of polyethylene obtained by aqueous polymerization (Table 3.2, entry 5). Top: measured with 10 K min^{-1} heating rate (black curve: 1st heating, red curve: 1st cooling, blue curve: 2nd heating). *Bottom*: measured with 1 K min^{-1} (only first heating shown).

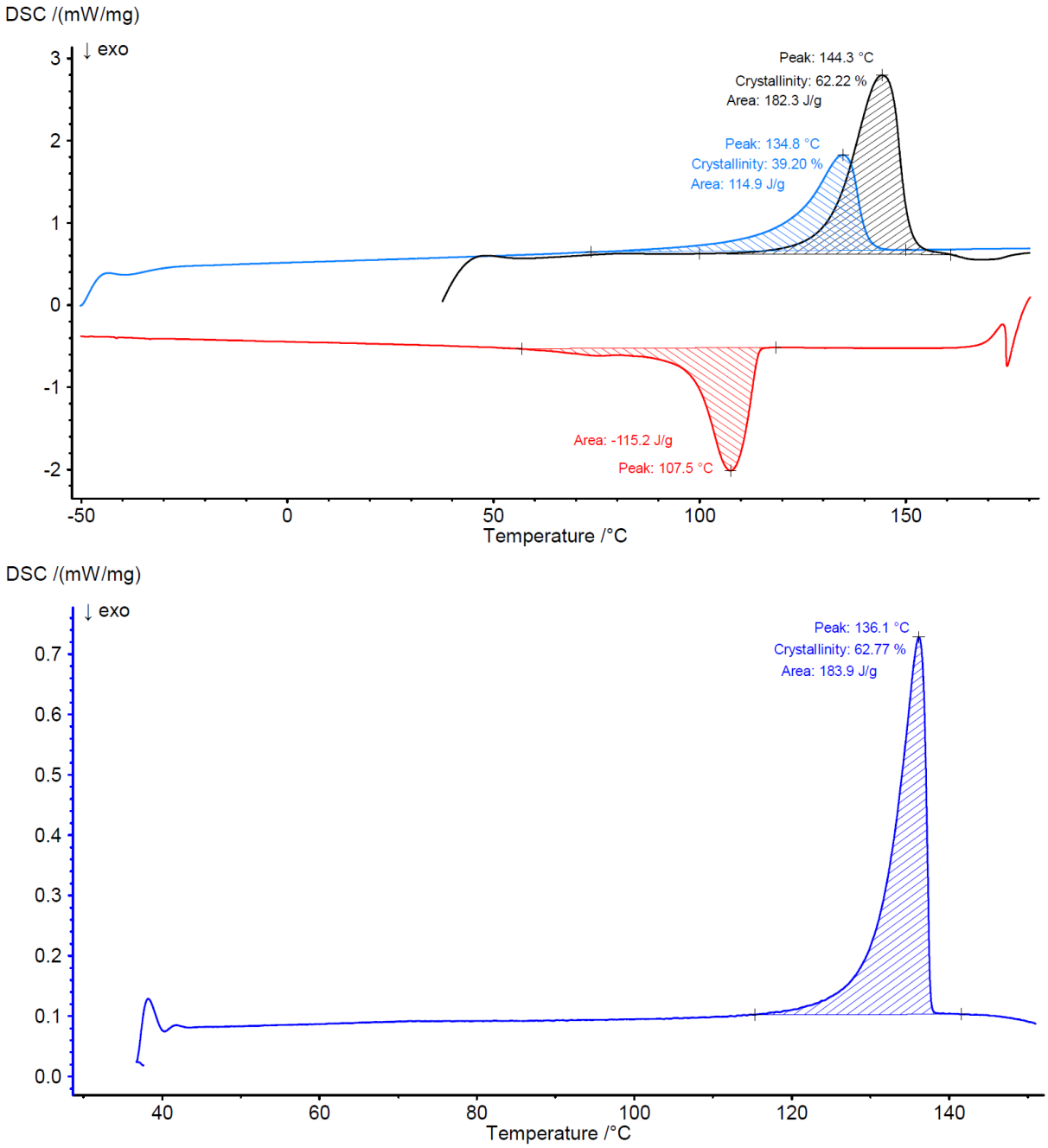

Figure 3.58. DSC traces of polyethylene obtained by aqueous polymerization (Table 3.2, entry 6). *Top*: measured with 10 K min^{-1} heating rate (black curve: 1st heating, red curve: 1st cooling, blue curve: 2nd heating). *Bottom*: measured with 1 K min^{-1} (only first heating shown).

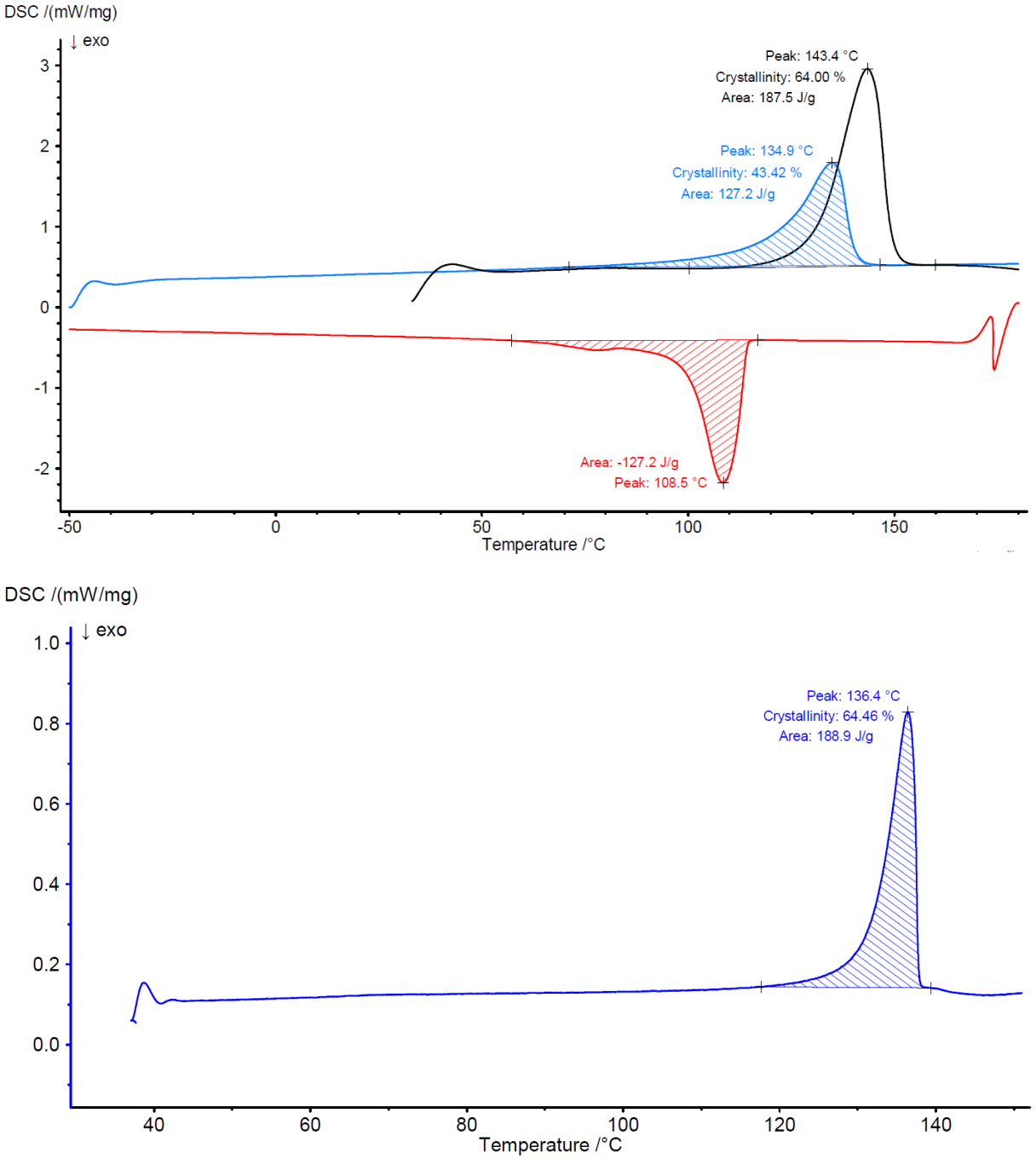

Figure 3.59. DSC traces of polyethylene obtained by aqueous polymerization (Table 3.2, entry 7). *Top*: measured with 10 K min^{-1} heating rate (black curve: 1st heating, red curve: 1st cooling, blue curve: 2nd heating). *Bottom*: measured with 1 K min^{-1} (only first heating shown).

3.5.5 DLS Data of nanocrystal dispersions

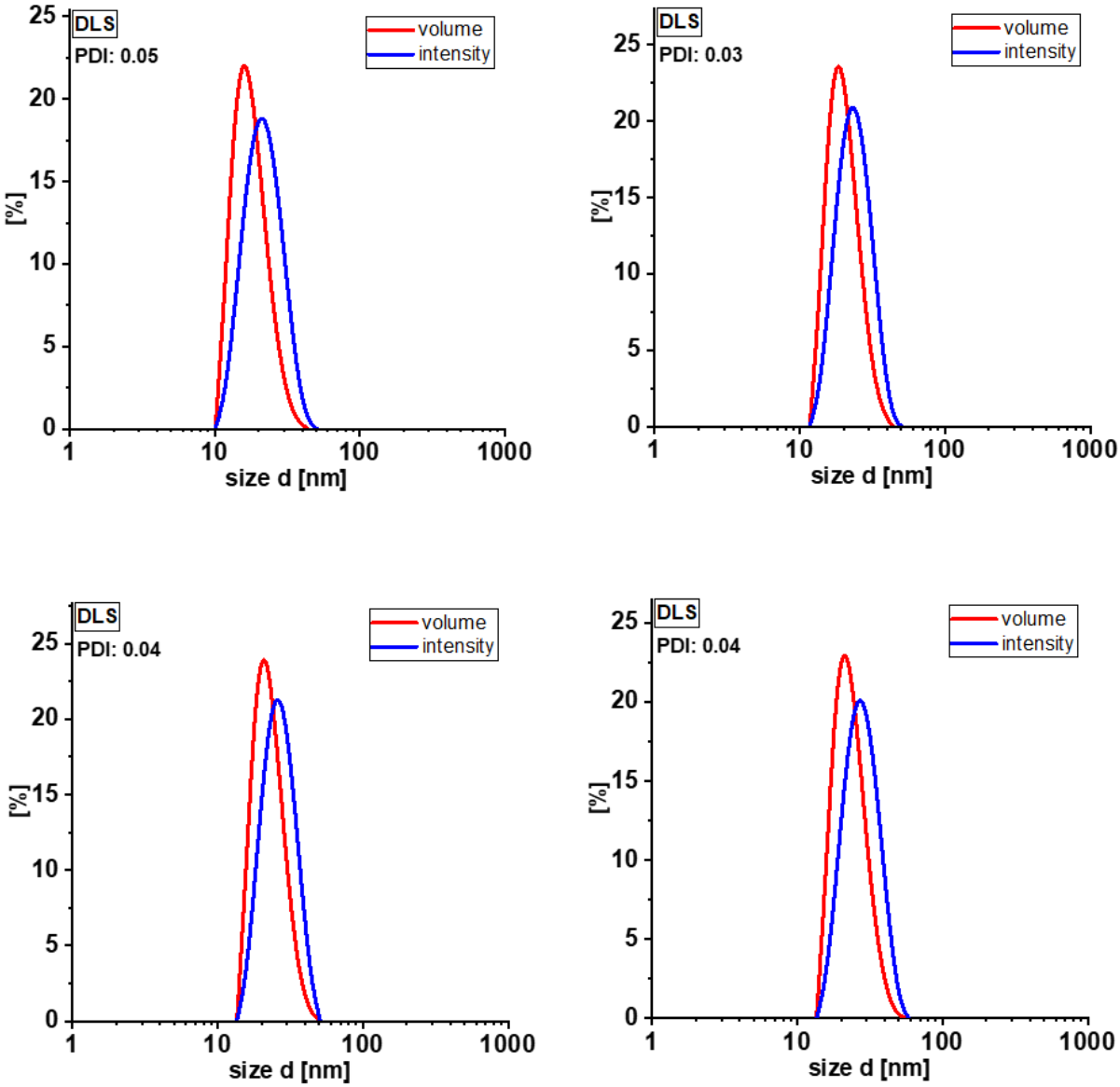

Figure 3.60. DLS traces of polyethylene dispersions (Table 3.2). Volume- and intensity-based distributions shown. PDI according to *Malvern Zetasizer* software. *Top, left*: entry 1 | *top, right*: entry 2 | *bottom, left*: entry 3 | *bottom, right*: entry 4.

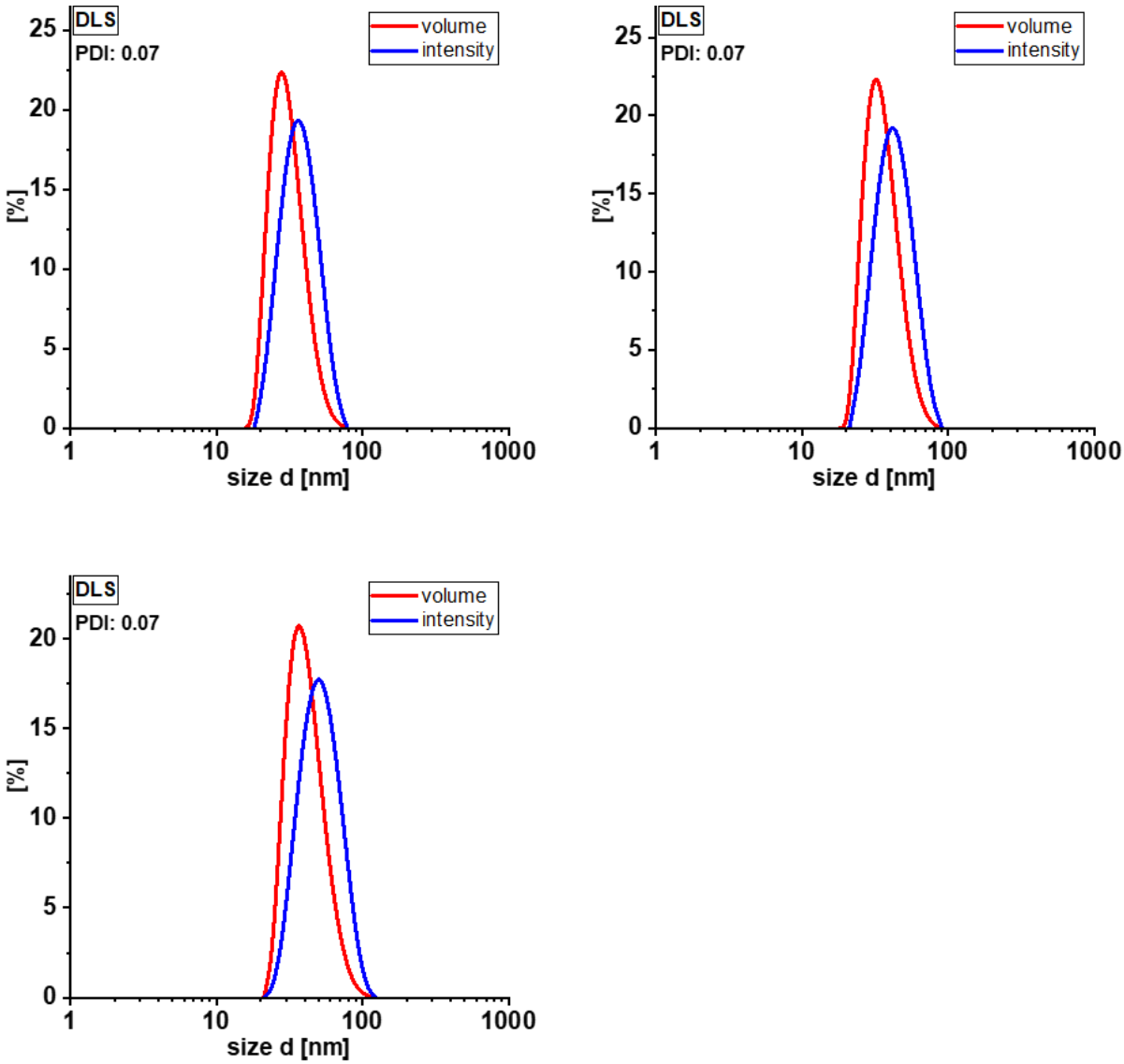

Figure 3.61. DLS traces of polyethylene dispersions (Table 3.2). Volume- and intensity-based distributions shown. PDI according to *Malvern Zetasizer* software. *Top, left*: entry 5 | *top, right*: entry 6 | *bottom*: entry 7.

3.5.6 Selected NMR spectra of synthesized polyethylenes

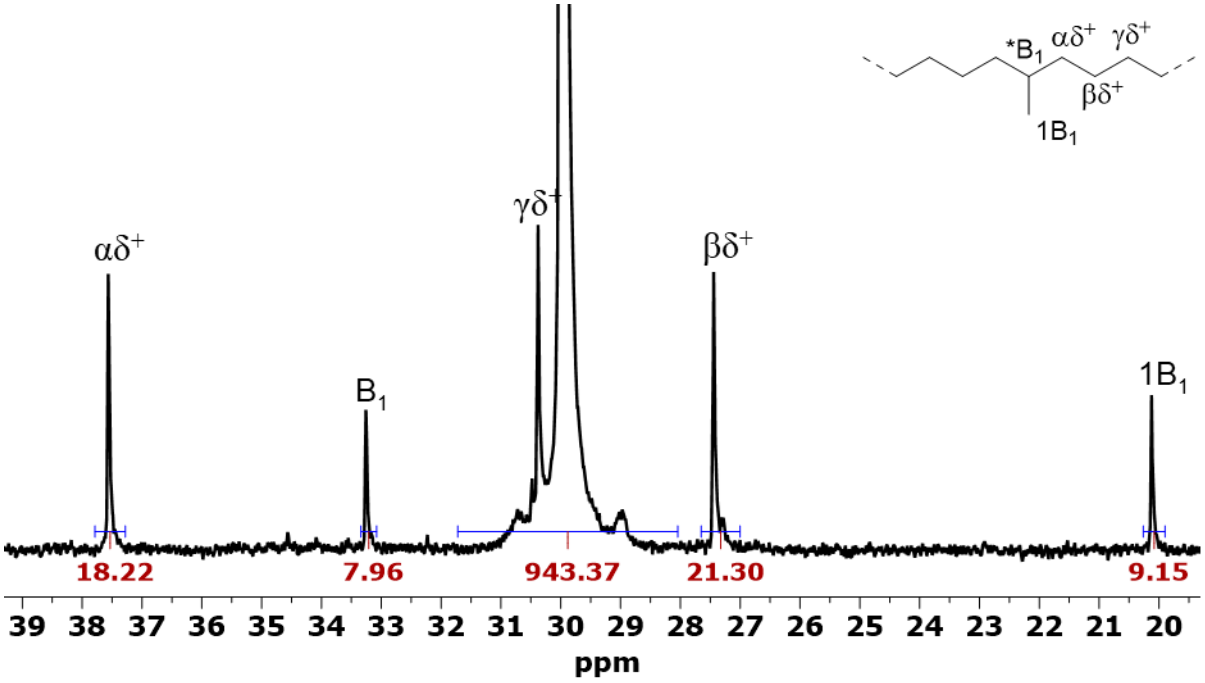

Figure 3.62. ^{13}C NMR spectrum (151 MHz, $C_2D_2Cl_4$, 388 K) of polyethylene obtained from polymerization in toluene (Table 3.1, entry 1).

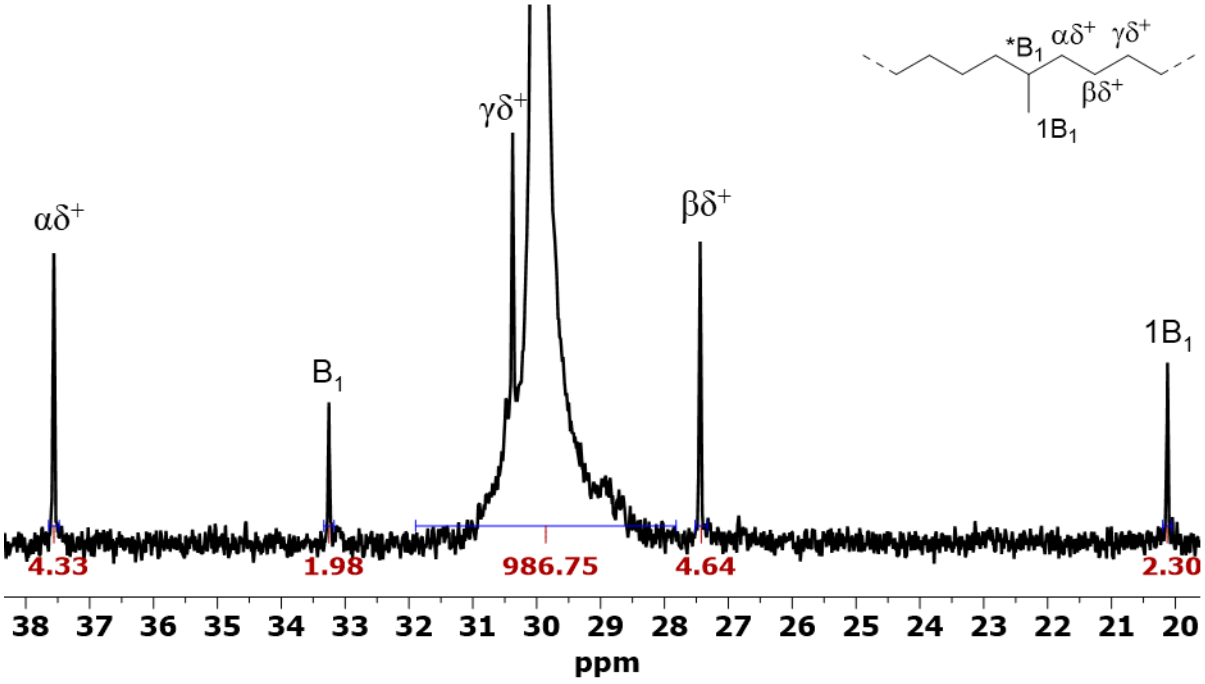

Figure 3.63. ^{13}C NMR spectrum (151 MHz, $C_2D_2Cl_4$, 388 K) of polyethylene obtained from polymerization in toluene (Table 3.1, entry 5).

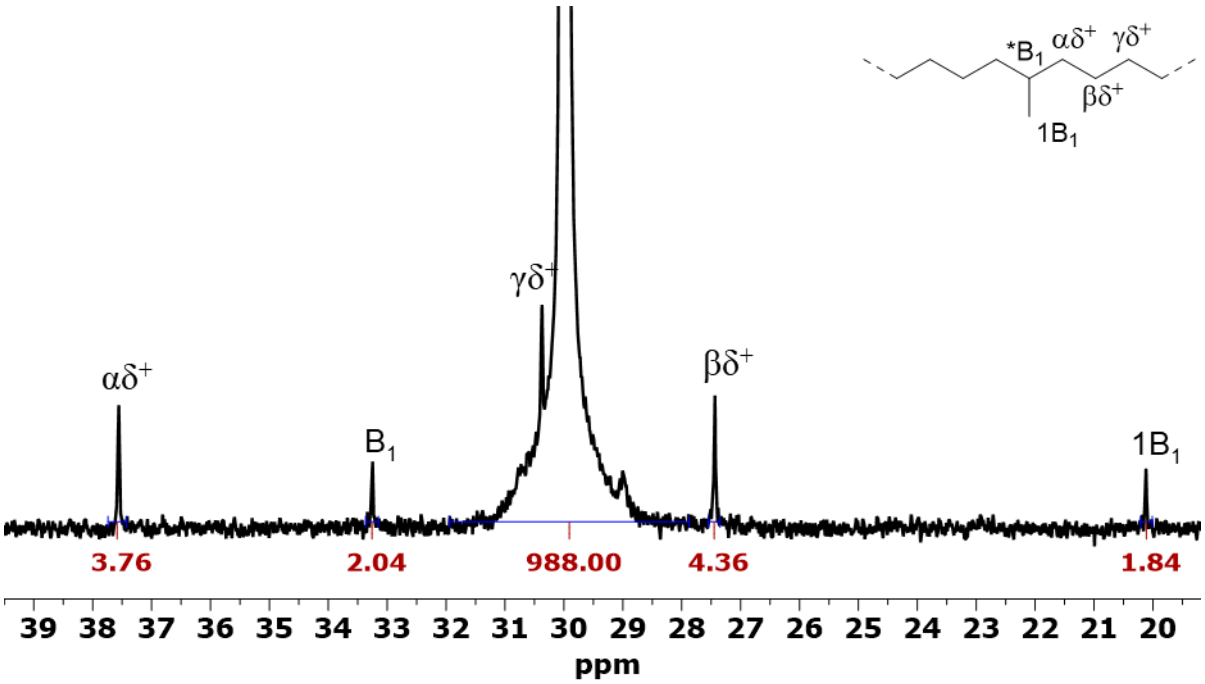

Figure 3.64. ^{13}C NMR spectrum (151 MHz, $C_2D_2Cl_4$, 388 K) of polyethylene obtained from polymerization in toluene (Table 3.1, entry 8).

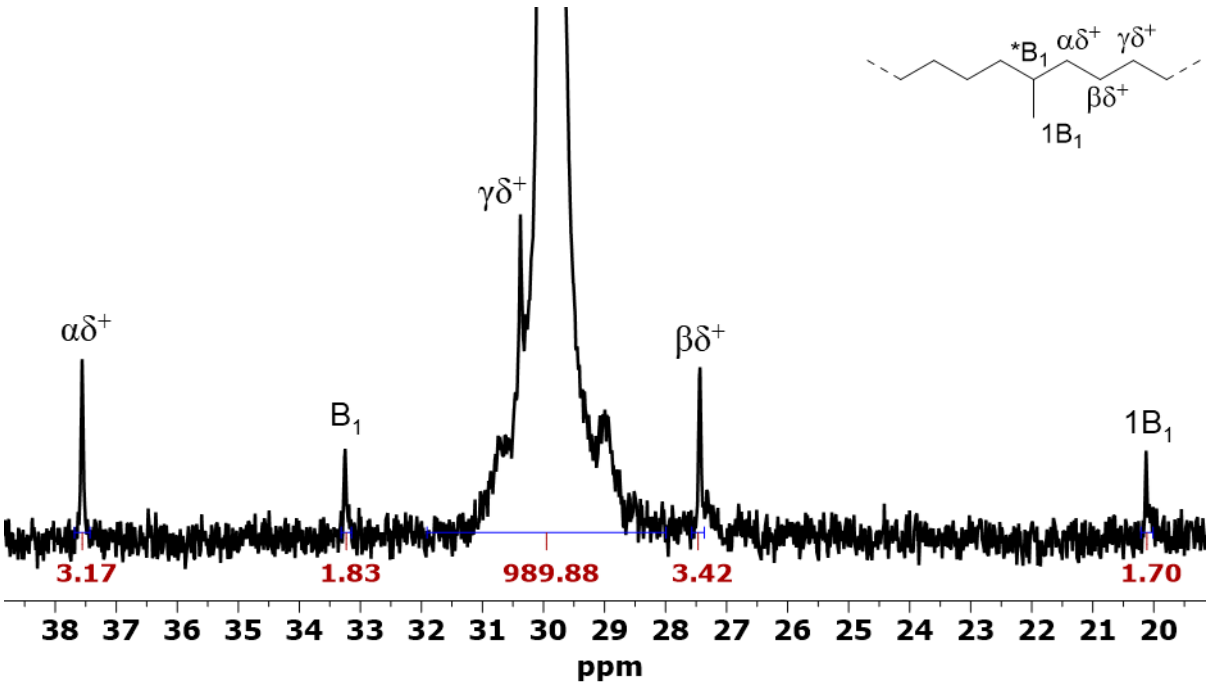

Figure 3.65. ^{13}C NMR spectrum (151 MHz, $C_2D_2Cl_4$, 388 K) of polyethylene obtained from polymerization in toluene (Table 3.1, entry 12).

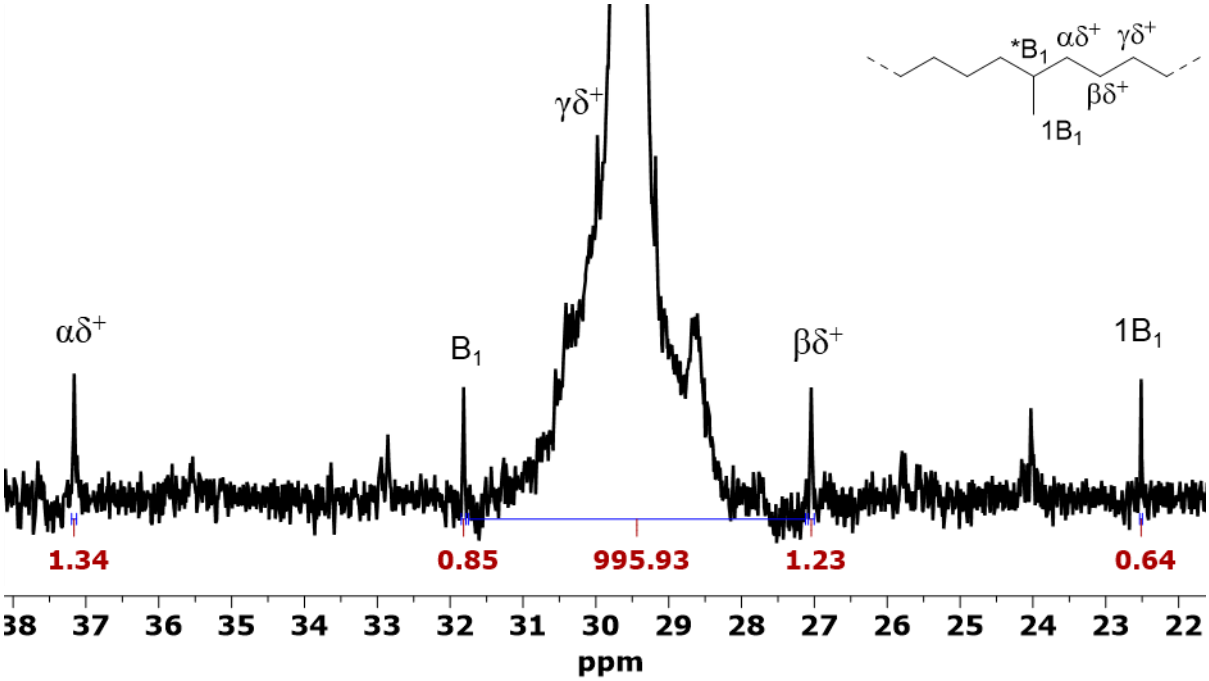

Figure 3.66. ^{13}C NMR spectrum (151 MHz, $C_2D_2Cl_4$, 388 K) of polyethylene obtained from polymerization in toluene (Table 3.2, entry 4).

4 Remote Perfluoroalkyl Substituents are Key to Living Aqueous Ethylene Polymerization

4.1 Introduction

The properties of molecular catalysts are often controlled by substituents chosen to the purpose. Perfluorinated alkyls – $(CF_2)_nCF_3$ – are well-established groups to adjust the solubility of homogeneous catalysts.[341] They can enhance catalysts' lipophilicity and allow for reactions under very apolar conditions or with very apolar substrates. This enables e.g. catalysis in supercritical carbon dioxide as an alternative and an environmentally friendly solvent[164,363,364], applications in biphasic mixtures for efficient catalyst recovery[365] or selective reagent separation[366,367], and catalyst heterogenization and new delivery methods.[368,369] Strategies to make a catalyst 'fluorous' are versatile and perfluorinated groups can also be placed in the structure of a catalyst precursor to enhance its activation and reactivity via its miscibility in different phases.[354,370] Fluorous catalysts in general show a versatile solubility behavior and are not limited to applications in equally fluorous solvents, that are often not desired due to their costs and environmental persistence.[371-373]

Parts of *chapter 4* are published in *Angew. Chem. Int. Ed.* **2020**, *59*, 3258-3263.

In contrast to their extensive utilization for solubility, examples where perfluorinated alkyl groups control the active metal center's catalytic reactivity are rare.[374-376] Although their synthetic chemistry is well established their potential is largely unexplored in this regard.

This chapter reports a case study showing how perfluoroalkyl substituents enhance catalyst performance. As a catalyst system, which is both mechanistically instructive to unravel the role of the perfluoroalkyl substituents as well as practically useful, neutral Ni(II) polymerization catalysts were studied.[49,377]

4.2 Results and Discussion

4.2.1 Influence of long perfluoroalkyl substituents in remote positions

Perfluoroalkyl (e.g. *n*-C_6F_{13}) substituted *N*-terphenyl salicylaldiminato Ni(II) catalysts (Figure 4.1) were demonstrated to be uniquely capable of a truly living polymerization of ethylene under aqueous conditions (*chapter 3*). In this process narrow distributed ultra high molecular weight strictly linear polyethylene (UHMWPE) is generated, in the unusual form of monodisperse uniform-shape nanocrystals.

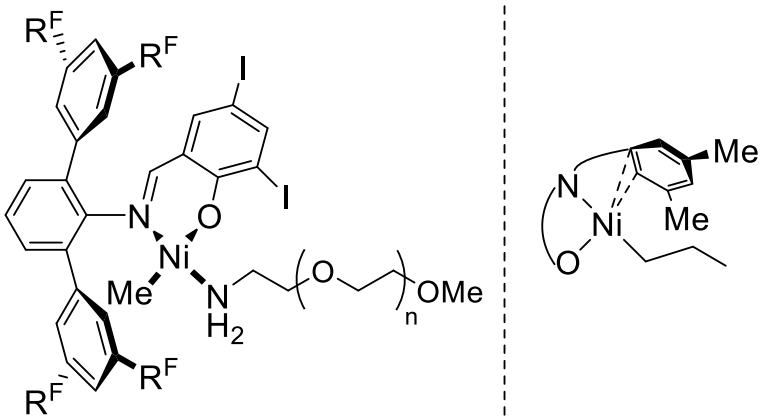

Figure 4.1. Catalyst precursor with C_6F_{13}-substituents in remote positions (R^F) capable of truly living ethylene polymerization in aqueous media (*left*). Interaction promoting chain transfer and branch formation in the case of electron-donating substituents, exemplified by methyl substituents (*right*).[53]

The strong influence of substituents in these remote positions of the chelating ligand, distant from the active center, can be related to a weak interaction between the distal aryl rings and the metal atom (Figure 4.1, right), that promotes decoordination of ethylene and favors β-hydride elimination (BHE).[53] BHE is the key step in chain transfer and branch formation. This

weak interaction is promoted by electron-donating groups, which afford hyperbranched ethylene oligomers. In contrast, with electron-withdrawing trifluoromethyl groups linear polyethylene is formed under otherwise identical conditions.[107,108] Note that a H-F interaction with the growing chain, what has been suggested for early[115,116] and late transition metal catalysts[114], is clearly not operative.[110]

To understand their role in catalysis, we investigated the influence of long perfluoroalkyl substituents (linear C_6F_{13} groups) in different established salicylaldiminato Ni(II) motifs under a set of conditions. We targeted the *N*-(quar)terphenyl based types **1**$^{\mathbf{Ant}}$-$\mathbf{R}^{\mathbf{F}}$/**L** and **2**$^{\mathbf{Ant}}$-$\mathbf{R}^{\mathbf{F}}$/**L** (Figure 4.2), known to be active in aqueous and non-aqueous ethylene polymerization towards linear high-molecular-weight polyethylene.[108,111,177,178] We also modified *N*-naphthyl type catalyst **3**$^{\mathbf{Ant}}$-$\mathbf{R}^{\mathbf{F}}$/**L** (Figure 4.2), capable of a controlled/living ethylene polymerization in a variety of solvents, and introduced C_6F_{13}-substituents in selected positions.[125,126] Anthryl moieties were placed in close proximity to the nickel center to shield the axial site and impede chain transfer reactions.[55,94,107]

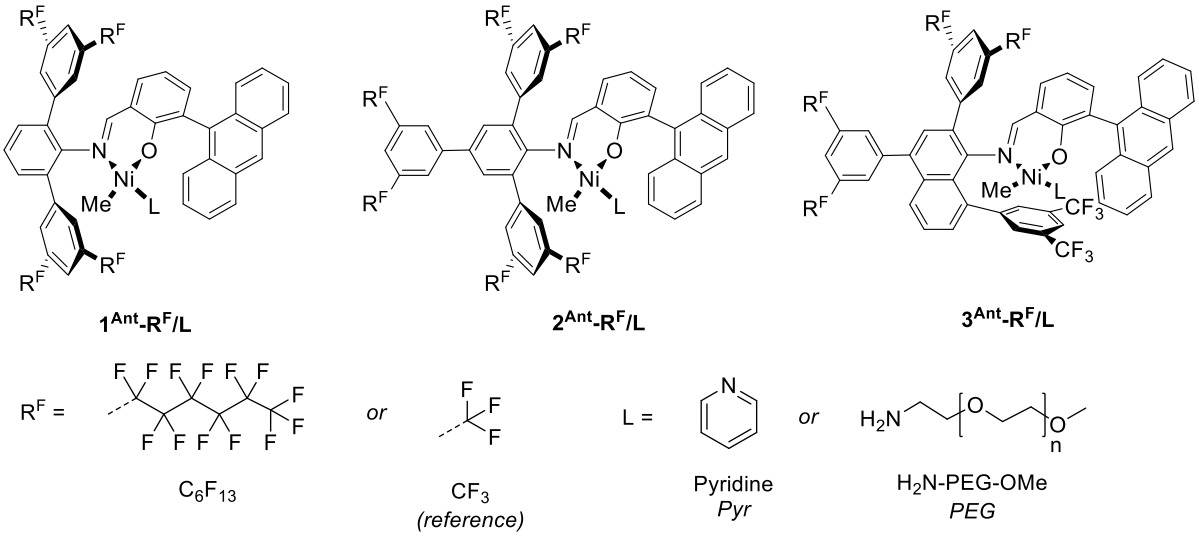

Figure 4.2. Catalyst precursors studied in this work. Compared to the reference systems (R^F = CF_3), the novel catalysts are substituted with linear long perfluoroalkyl groups (R^F = C_6F_{13}) in remote positions. The coordinated labile ligand L differs for lipophilic precursors (L = Pyr) and hydrophilic precursors (L = PEG), suitable for aqueous polymerizations.

The synthesis of the respective salicylaldimines was straightforward according to known procedures, slightly modified to handle the highly lipophilic intermediate products (see *Experimental Section* for details of synthesis and characterization of all catalyst precursors). As a key step, a copper-promoted Ullmann coupling of 1,3-diiodobenzene and perfluorohexyl iodide provided access to the 1,3-(diperfluorohexyl)phenyl structure motif incorporated in the aforementioned catalyst structures. Lipophilic precatalysts were obtained by reaction of

salicylaldimines with [(tmeda)$NiMe_2$] in the presence of pyridine as labile ligand. Hydrophilic analogues, suitable for aqueous polymerizations, were obtained in the presence of α-methoxy-ω-amino poly(ethylene glycol) (H_2N-PEG-OMe, see Figure 4.2).

Ethylene polymerization studies in heptane were carried out at different temperatures (30-50 °C), with C_6F_{13}-substituted catalyst precursors and the analogous CF_3 complexes to identify effects of perfluoroalkyl substituent under lipophilic conditions (Table 4.1).

Table 4.1. Ethylene polymerization experiments in heptane.

entry (cond.)	precatalyst	E_1[a] [mV]	T [°C]	yield PE [g]	TOF[b]	M_n[c] x 10^3 [g mol^{-1}]	M_w/M_n[c]	chains/ [Ni]	T_m[d] [°C] (cryst. [%])	branches/ 1000 C[e]
1	1^{Ant}-CF_3/Pyr	254	30	0.68	14.6	167	1.9	0.8	134 (53)	2.3
2	1^{Ant}-C_6F_{13}/Pyr	560	30	1.66	35.3	504	1.6	0.7	133 (49)	< 1.0
3	1^{Ant}-CF_3/Pyr	254	50	2.28	48.8	80	3.3	5.7	124 (47)	12.4
4	1^{Ant}-C_6F_{13}/Pyr	560	50	5.68	121.4	82	2.9	13.8	124 (50)	8.4
5	2^{Amt}-CF_3/Pyr	329	30	0.99	21.2	91	2.4	2.2	136 (57)	4.7
6	2^{Ant}-C_6F_{13}/Pyr	445	30	1.33	28.4	294	1.6	0.9	133 (55)	2.9
7	2^{Ant}-CF_3/Pyr	329	50	2.68	57.3	82	4.6	6.6	125 (51)	17.8
8	2^{Ant}-C_6F_{13}/Pyr	445	50	5.23	111.8	77	2.5	13.6	123 (49)	13.4
9	3^{Ant}-CF_3/Pyr	357	50	1.40	50.0	618	1.2	0.8	135 (47)	3.7
10	3^{Ant}-C_6F_{13}/Pyr	395	50	1.24	44.2	683	1.2	0.6	135 (46)	< 1.0

Polymerization conditions: 5 µmol catalyst loading, 20 minutes reaction time, 40 bar ethylene pressure, in 100 mL heptane. [a] Determined via cyclic voltammetry. [b] Given in 10^3 x mol [C_2H_4] x mol^{-1} [Ni] x h^{-1}. [c] Determined via GPC at 160 °C. [d] Determined via DSC (heating rate: 10 K/min), 2nd heating cycle reported. [e] Determined via selective detection of methyl and methylene IR-bands during GPC measurements (versus standards with known degree of branching), see *Experimental Section* for details.

All catalysts studied were active in ethylene polymerization and a significant effect of perfluoroalkyl chain length on catalytic performance and polymer properties was observed. Compared to their CF_3 analogues, the C_6F_{13}-substitued catalysts **1^{Ant}-C_6F_{13}/Pyr** and **2^{Ant}-C_6F_{13}/Pyr** showed higher activities (15 x 10^3 TO h^{-1} vs. 35 x 10^3 TO h^{-1}, entries 1 and 2, Table 4.1) and produced narrower distributed polyethylene of higher molecular weights (167 x 10^3 g mol^{-1} vs. 504 g mol^{-1}, entries 1 and 2, Table 4.1) with less branches (2.3 vs. < 1.0 branches per 1000 carbon atoms, entries 1 and 2, Table 4.1) at 30 °C reaction temperature. Chain transfer (which limits molecular weight and broadens molecular weight distribution) and branch formation proceed through BHE. The above data indicates a very effective suppression of these pathways by the C_6F_{13}-substitution.

Similar trends of activity and branching were observed at a higher reaction temperature of 50 °C comparing CF_3- and C_6F_{13}-substitued catalyst types **1^{Ant}-R^F/Pyr** and **2^{Ant}-R^F/Pyr.**

In case of catalyst type **3^{Ant}-R^F/Pyr**, the C_6F_{13}-substituted derivative again produced polyethylene with lower branches. Other than this, no significant differences were observed. Both catalysts perform a highly controlled polymerization as indicated by chains per nickel ratios close to unity and narrow molecular weight distributions of M_w/M_n = 1.2.

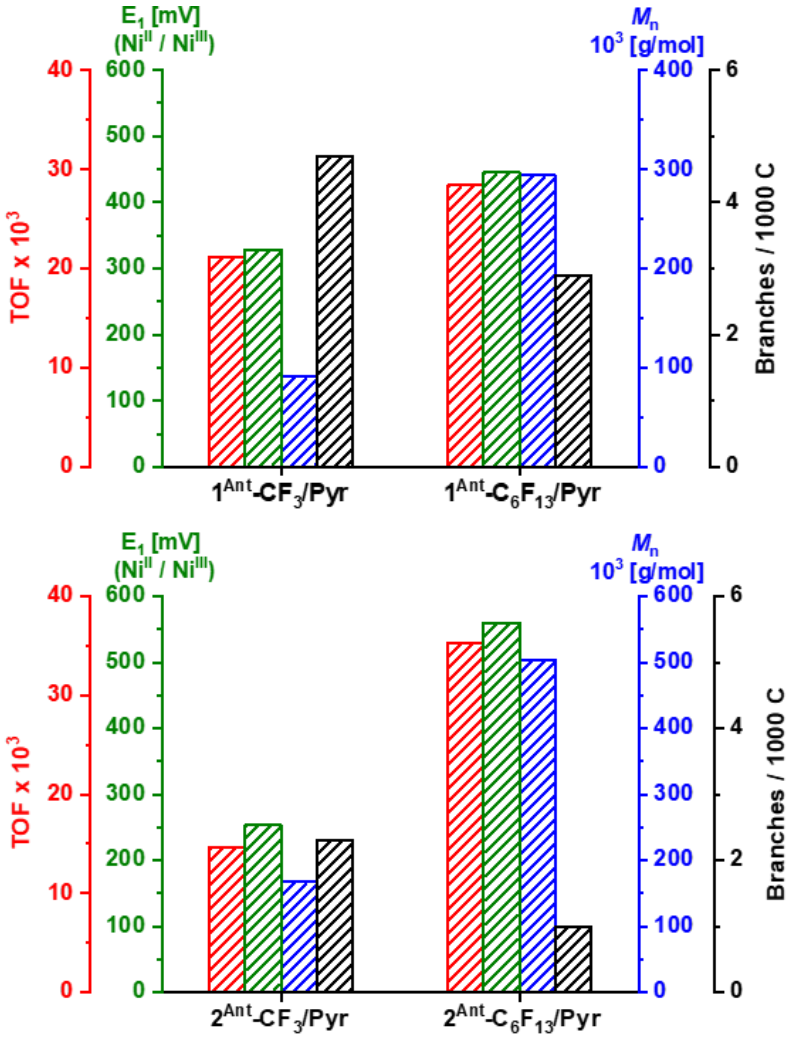

Figure 4.3. Comparison of experimental polymerization data with cyclic voltammetry data for different catalyst precursors (**1^{Ant}-R^F/Pyr**, *top* and **2^{Ant}-R^F/Pyr,** *bottom*). Catalytic activity (TOF, *red curve*), forward peak potential determined via cyclic voltammetry (E_1, *green curve*), molecular weight (*blue curve*) and branching values (*black curve*) of polyethylenes formed versus different catalyst precursors given. Experimental data from experiments at 30 °C in heptane (entries 1, 2, 5, and 6, Table 4.1).

The observed increase in polymerization rate and molecular weights vs. the CF_3 reference, together with a decrease in branching indicated a significant influence of the perfluoroalkyl substituents in remote positions of the catalyst structures on the active nickel center. To further illuminate the origin of this effect, cyclic voltammetry experiments were performed on all

pyridine precatalysts. The observed oxidation and reduction transitions for the Ni(II)/Ni(III) pair showed that, compared to the reference trifluoromethyl catalysts, the electron density at the metal center is significantly lower in the C_6F_{13}-substituted complexes as evidenced by an increase in measured forward peak potentials (column E1, Table 4.1) found for all catalyst types studied. This remarkable decrease in electron density (e.g. 211 mV [R^F = CF_3] vs. 541 mV [R^F = C_6F_{13}], catalyst **1^{Ant}-R^F/Pyr**, Table 4.1) correlates qualitatively with the observed catalytic and polymer properties in case of catalyst types **1^{Ant}-R^F/Pyr** and **2^{Ant}-R^F/Pyr** (see Figure 4.3). Note, that this effect on polymer microstructure may be enhanced further by the higher steric demand[109] of perfluoroalkyl vs. trifluoromethyl substituents.

In case of catalyst types **3^{Ant}-R^F/Pyr**, only a small difference in forward peak potentials was observed (357 mV [R^F = CF_3] vs. 395 mV [R^F = C_6F_{13}], entries 9 and 10, Table 4.1). This lower effect of the substitution pattern compared to the other two types of catalysts is expected, given that only one of the aryl substituents in *ortho*-position of the *N*-phenyl is altered, and the phenyl ring closest to the nickel center (8-position of the naphthylamine moiety, see Figure 4.2) was not modified. This electrochemical data agrees well with the similar catalytic properties observed for **3^{Ant}-C$_6$F$_{13}$/Pyr** and **3^{Ant}-CF$_3$/Pyr** (Table 4.1), the C_6F_{13}-substitution lead to a slight decrease in branching only while catalytic activity and molecular weight are similar to the CF_3 analog.

To probe for any pronounced solvent effects, e.g. through interactions with the active site or via the solvent quality for the polymer product formed, we performed polymerization experiments in toluene as a somewhat more polar and aromatic solvent (see *Experimental Section* for comprehensive experimental and analytical data of polymerization experiments in toluene with all catalyst precursors at different temperatures). In summary, we observed the same trends for catalysts **1^{Ant}-R^F/Pyr** and **2^{Ant}-R^F/Pyr** as outlined above with a superior role of catalysts with long perfluoroalkyl substituents. Namely, compared to the CF_3 reference (1) increased molecular weights (240 x 10^3 g mol^{-1} vs. 623 x 10^3 g mol^{-1}, entries 1 and 2, Table 4.6); (2) slightly increased catalytic activities (61 x 10^3 TO h^{-1} vs. 73 x 10^3 TO h^{-1}, entries 1 and 2, Table 4.6); and (3) decreased degrees of branching (1.7 vs. 1.1 branches per 1000 carbon atoms, entries 1 and 2, Table 4.6) were found. In line with the above polymerizations in heptane and cyclic voltammetry experiments, no significant impact of the longer perfluoroalkyl substituents in catalysts **3^{Ant}-R^F/Pyr** was observed. **3^{Ant}-C$_6$F$_{13}$/Pyr** produced polyethylene with slightly lower activity and, accordingly, with slightly lower molecular weights.

4.2.2 Living polymerization in aqueous surfactant solution

The high functional group tolerance of late transition metal catalysts allows their use even in polar protic environments.[74,378] During polymerization in aqueous surfactant solution with Ni(II) salicylaldiminato catalysts, the polyethylene is formed in the very unusual form of nanoscale single crystals.[177] They are characterized by a high degree of order, that arises from the unique particle growth mechanism, where the active center's growing chain is directly deposited on the crystal growth front, leaving no opportunity for any disorder.[178,179] This allows for effective generation of anisotropic polymer nanoparticles, that are otherwise difficult to access.[304,348]

Table 4.2. Ethylene polymerization experiments in aqueous surfactant solution.

entry	precatalyst	yield PE [g]	TON[a]	M_n[b] x 10^3 [g mol^{-1}]	M_w/ M_n[b]	chains/ [Ni]	T_m[c] [°C] (cryst. [%])	br./ 1000 C[d]	d_h (Vol.) [nm][e]
1	1^{Ant}-CF_3/PEG	5.87	27.9	484	2.0	1.6	142 (55) / 135 (36) 134	1.6	22 (0.05)
2	1^{Ant}-C_6F_{13}/PEG	9.61	45.7	866	1.3	1.5	143 (73) / 135 (48) 133	< 1.0	25 (0.08)
3	2^{Ant}-CF_3/PEG	4.78	22.7	408	1.8	1.6	140 (66) / 135 (48) 134	< 1.0	23 (0.07)
4	2^{Ant}-C_6F_{13}/PEG	10.65	50.6	885	1.4	1.6	140 (64) / 133 (41) 133	< 1.0	31 (0.12)
5	3^{Ant}-CF_3/PEG	1.64	7.8	486	1.6	0.5	138 (63) / 135 (51) 134	2.6	16 (0.14)
6	3^{Ant}-C_6F_{13}/PEG	9.39	44.6	1609	1.2	0.8	142 (65) / 136 (41) 137	< 1.0	21 (0.17)

Polymerization conditions: 7.5 µmol catalyst loading, 40 bar ethylene pressure, 4 hours reaction time, 15 °C reaction temperature, 6.0 g sodium dodecyl sulfate, 1.5 g cesium hydroxide, 0.75 mL mesitylene, in 150 mL degassed water, ultrasound applied prior to ethylene pressurization. [a] Given in 10^3 x mol [C_2H_4] x mol^{-1} [Ni]. [b] Determined via GPC at 160 °C. [c] Determined via DSC, reported as [1st heating cycle (crystallinity) \ 2nd heating cycle (crystallinity)] with 10 K/min heating rate, second line: 1st heating cycle with 1 K/min heating rate. [d] Branching per 1000 carbon atoms determined via selective detection of methyl and methylene IR-bands during GPC measurements (calibrated versus samples with known degree of branching), see *Experimental Section* for details. [e] Determined via DLS (volume mean and PDI reported).

All hydrophilic catalyst precursors of types $\mathbf{1^{Ant}}$-$\mathbf{R^F}$, $\mathbf{2^{Ant}}$-$\mathbf{R^F}$ and $\mathbf{3^{Ant}}$-$\mathbf{R^F}$ (with H_2N-PEG-OMe as labile ligand) were active for several hours under established reaction conditions in water (Table 4.2). Remarkably, all C_6F_{13}-substituted catalysts studied are clearly superior in aqueous polymerization compared to their CF_3 analogues, in terms of catalytic activity and properties of the produced polyethylenes. In case of catalysts $\mathbf{1^{Ant}}$-$\mathbf{C_6F_{13}}$/**PEG** and $\mathbf{2^{Ant}}$-$\mathbf{C_6F_{13}}$/**PEG**, the perfluoroalkyl substitution led to a comparable substantial increase in catalytic activities (e.g.

23 x 10^3 TO vs. 51 x 10^3 TO, entries 3 and 4, Table 4.2), molecular weights (408 x 10^3 g mol^{-1} vs. 885 x 10^3 g/mol, entries 3 and 4, Table 4.2) and decreased polydispersities (1.8 vs. 1.4, entries 3 and 4, Table 4.2) and branch contents (1.6 vs. < 1.0 branches per 1000 carbon atoms, entries 1 and 2, Table 4.2) vs. the trifluoromethyl reference. Under optimized reaction conditions (10 °C reaction temperature, high surfactant loading, see also *chapter 6*), both catalysts **1^{Ant}-C_6F_{13}/PEG** and **2^{Ant}-C_6F_{13}/PEG** are capable of a truly living ethylene polymerization in water, as evidenced by (1) linear relationships between yields and molecular weights; (2) narrow molecular weight distributions of M_w/M_n < 1.3; and (3) chain per nickel ratios close to unity (see the *Experimental Section*, Table 4.3 and Table 4.4 for comprehensive experimental and analytical data, and Figure 4.4). Even linear and narrow distributed UHWMPE with M_n = 2.0 x 10^6 g mol^{-1} is accessible at extended reaction times, as one nickel center grows one polymer chain over the entire polymerization experiment.

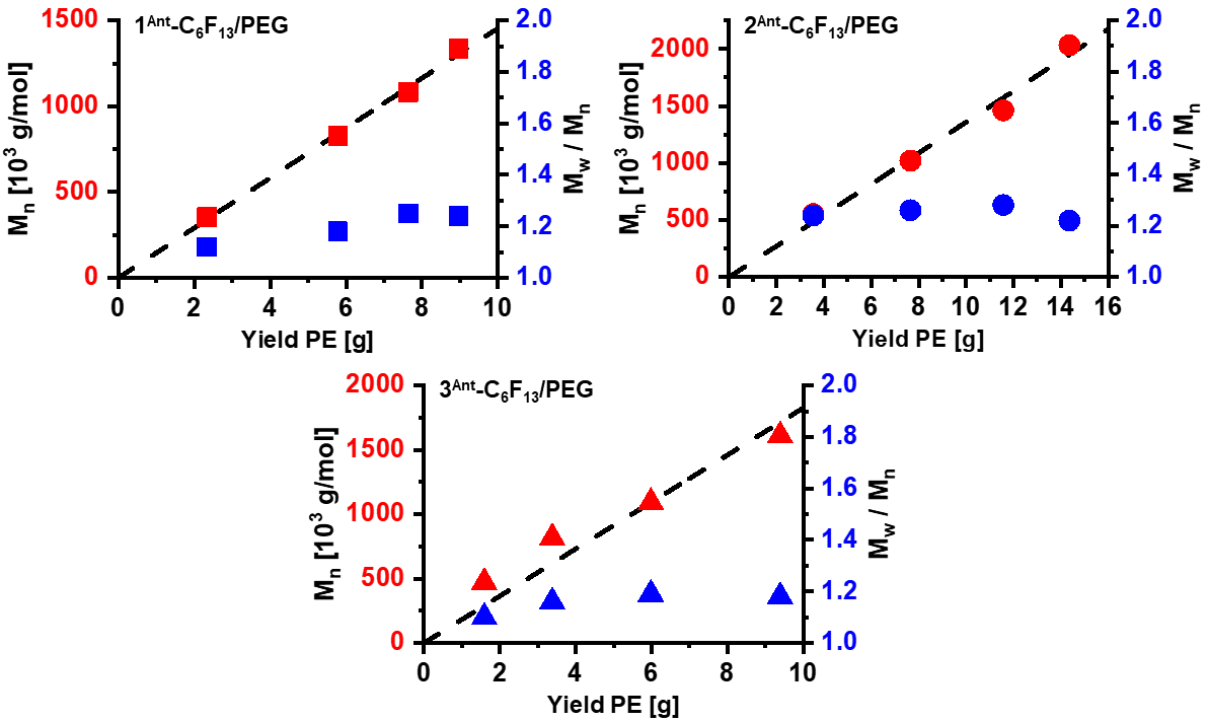

Figure 4.4. Molecular weights and polydispersity indices of polyethylenes formed versus yields from different aqueous polymerizations with different catalyst precursors (see *Experimental Section*, Table 4.3, Table 4.4 and Table 4.5)

Likewise, catalyst **3^{Ant}-C_6F_{13}/PEG** stands out as the first reported *N*-naphthyl type nickel(II) salicylaldiminato catalyst with adequate activities in water and accessible molecular weights of M_n = 1.6 x 10^6 g mol^{-1} with very narrow distributions of M_w/M_n = 1.1, that is formed in a strictly living polymerization (see the *Experimental Section*, Table 4.5 for comprehensive experimental and analytical data, and Figure 4.4). Different from the non-aqueous polymerization with

catalyst motif **3^{Ant}-R^{F}/L**, in the aqueous polymerization the CF_3 analogue is much less active (45×10^3 TO h^{-1} vs. 8×10^3 TO h^{-1}, entries 5 and 6, Table 4.2) and less controlled compared to the perfluoroalkyl complex. As polymerizations under aprotic conditions and insights from cyclic voltammetry experiments did not suggest a significant electronic influence of the long perfluoroalkyl groups on the active center for this catalyst type **3^{Ant}-R^{F}**, we tentatively address this different behavior in the aqueous system to the highly hydrophobic groups on the salicylaldiminato ligand. Possibly, the four C_6F_{13}-substituents create a highly apolar environment around the metal center that promotes rapid dissociation of the hydrophilic polar labile H_2N-PEG-OMe ligand into the aqueous solution and allows for an effective catalyst activation. ^{1}H NMR spectra of catalysts **3^{Ant}-R^{F}/PEG** point to a very strong binding of the labile ligand to the nickel center, as indicated by a hindered rotation (diastereotopic character) of the amino functionality and the protons in α- and β-positions (see *Experimental Section*, Figure 4.19, Figure 4.21 and Figure 4.24), that might prohibit an effective activation in case of the catalyst with exclusively trifluoromethyl substituents.

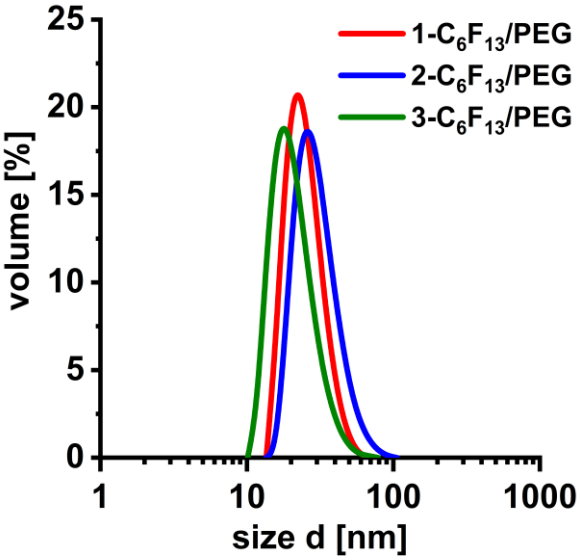

Figure 4.5. DLS traces of polyethylene dispersions obtained from aqueous polymerization with different catalyst precursors (entries 2,4 and 6, Table 4.2).

Considering the particle formation process, the generation of very small (< 100 nm) particles requires a high degree of dispersion of the catalyst precursor[185], and under ideal conditions an entire particle is grown by a single active site (see *chapter 3*). With the catalysts studied here, stable dispersions with a single well-defined particle population were obtained as observed by DLS (Figure 4.5). Even these highly fluorinated catalysts (e.g. 36 perfluorinated carbon atoms in chemical structure of **2^{Ant}-C$_6$F$_{13}$/PEG**) are able to form small uniform particles under aqueous

conditions, which are composed of completely disentangled polyethylene chains as evidenced by high melting points in the first heating cycle, that are not observed for slow heating rates.[255]

4.3 Conclusion

In summary, we present a clear case demonstrating the utility of perfluoroalkyl substituents to control catalytic properties. This demonstrates their potential for catalysis beyond the established use for achieving solubility in very apolar and fluorous media. The C_6F_{13} groups in the catalyst motifs studied substantially increased catalyst activity and molecular weight of the polymer product, and reduced branching. This establishes the mechanistic picture of a reduced electron density on the active metal sites – also supported by cyclic voltammetry on the catalyst precursors – when compared to the more commonly used trifluoromethyl groups. For the catalytic chain growth polymerization studied here, this favors chain growth and disfavors β-hydride elimination which is the key step of chain transfer and branching pathways. This occurs to an extent that enables truly living polymerizations even in aqueous systems. Perfluoroalkyl groups are similarly or slightly more electron withdrawing compared to CF_3 groups.[340,379] This accounts for their beneficial impact observed here. Further, longer substituents in the remote positions of the *ortho*-terphenyl motif also reduce BHE[109], possibly by hindering conformations suitable for an aryl-nickel interaction.

4.4 Experimental Section

4.4.1 Materials and general considerations

All manipulations involving air- and/or moisture-sensitive substances were carried out under inert atmosphere using standard Schlenk and glovebox techniques. Solvents were dried and degassed using standard laboratory techniques. Pentane, diethyl ether, toluene and dichloromethane were dried and freed from oxygen by passing over columns with *BASF R3-11* catalyst and molecular sieves. Heptane was distilled over calcium hydride. Tetrahydrofuran, purchased from *VWR*, was distilled over sodium/benzophenone. Dioxane and benzene, purchased from *Merck*, were distilled over sodium. Pyridine, purchased from *Merck*, was distilled from potassium hydroxide. Mesitylene, purchased from *sigma-aldrich*, was distilled under nitrogen (first fraction of 10 % discarded). Water was deoxygenated by distillation under a constant nitrogen stream. Ethylene 3.5 was purchased from *Air Liquide* and used as obtained. 1,3-Dibromobenze and [Pd(dba)$_2$] were purchased from *TCI chemicals* and used as obtained. 1-Napthylamine, trimethylsilylchloride, trimethyl borate, zirconium(IV) chloride, potassium hydroxide, N-bromosuccinimide, sodium dodecyl sulfate pellets, copper powder, 4,4'-di-tert-butyl-2,2'-dipyridyl and p-toluene sulfonic acid were purchased from *sigma-aldrich* and used as obtained (liquids were dried over molecular sieves). Perfluorohexyliodide, purchased from *fluorochem*, was degassed and dried over molecular sieves. Bis(pinacolato)diboron, purchased from *Activate Scientific*, was used as obtained. 2,6-Dibromoaniline, cesium fluoride, hexafluorobenzene and 3,5-diiodosalicylaldehyde, purchased from *abcr*, were used as obtained (liquids were dried over molecular sieves). Triphenylphosphine and *n*-buthyllithium (1.6 M in hexane), purchased from acros, were used as obtained. [(tmeda)NiMe$_2$], purchased from *MCat*, was stored at -30 °C prior to use.[349] Sodium sulfate and sodium chloride, purchased from Fisher Scientific, were used as obtained. H$_2$N-PEG-OMe, purchased from *Iris Biotech*, was stored at - 30 °C prior to use. Molecular sieves (4 Å, 0.4 nm, Type 514) were purchased from *Carl Roth*. Deuterated solvents for NMR spectroscopy, purchased from *Eurisotop*, were purged with nitrogen and dried over molecular sieves. 3-(9-anthryl)salicylaldehyde and [Ir(COE)$_2$Cl]$_2$ were synthesized according to reported procedures.[108,350]

NMR spectra were recorded on a *Bruker Avance III 400* instrument with a BBFO plus probe with Z-gradient, *Bruker Avance III HD 400* with a TBO probe with Z-gradient or a *Bruker Avance III 600*. Chemical shifts were referenced to the signal of the solvent (residual proton signal for

^{1}H spectra, carbon signal for ^{13}C spectra). Multiplicities are reported as follows: s (singlet), doublet (d), triplet (t), quartet (q), quintet (quint.), pentet (p), virtual multiplet (v), multiplet (m), broad (br.) and combination thereof. The NMR assignments were confirmed by common 2D NMR experiments (^{1}H,^{1}H-gCOSY; ^{1}H,^{13}C-gHSQC and ^{1}H,^{13}C-gHMBC). *MestReNova* software by *Mestrelab Research S.L.* was used for data evaluation. High temperature NMR spectroscopy of polymers was carried out at 130 °C in $C_2D_2Cl_4$ with 0.5 wt-% $Cr(acac)_3$ as relaxation agent. ^{13}C NMR spectra of polymers were referenced to the carbon signal of the solvent (74.4 ppm). The total integral of all polyethylene signals was set to 1000 C and the branch content determined from the values for the α-position signal (37.6 ppm) and the methyl signal (20.1 ppm). Elemental analysis was carried out on an *Elementar vario MICRO* cube instrument at the Department of Chemistry at the University of Konstanz. Molecular weights of synthesized polyethylenes were determined by high temperature gel permeation chromatography (GPC) in 1,2,4-trichlorobenzene or 1,2-dichlorobenzene at 160 °C. A standard flow rate of 1 mL/min was used, whereas a reduced flow rate of 0.5 mL/min was used for samples with expected $M_n > 5 \times 10^5$ g/mol to avoid sample shearing on the columns. Measurements in 1,2,4-trichlorobenzene were carried out on a *Polymer Laboratories 220* instrument equipped with *PLgel Olexis* columns (3 x 30 cm), a refractive index detector (concentration signal), a viscometer (*Viskotek 210 Differential Viscometer*) and light scattering detector (*Agilent PD2040*). Molecular weights were determined via a triple detection method versus narrow polystyrene standards (software: *Cirrus Multi Offline GPC/SEC* software, version 3.3). Measurements in 1,2-dichlorobenzene were performed on a *Polymer Char GPC-IR* instrument equipped with *PSS Polefin Linear XL* columns (3 x 30 cm, additional guard column), an infrared detector (*IR5 MCT*, concentration signal) and a viscometer. Molecular weights were determined via universal calibration versus narrow polystyrene standards (software: *PSS WinGPC*, version 8.32). The infrared detector was equipped with interference filters of different wavelengths that enabled the selective and simultaneous measurements of methyl and methylene band intensities and allowed for determination of the methyl branch content from GPC measurements (calibrated versus samples with known degree of branching, determined via high temperature ^{13}C-NMR experiments, *vide infra*). Selected samples were measured on both instruments to ensure identical results for molecular weight determination. Chains per nickel numbers were calculated using M_n (determined via GPC) and TON (turnover number). We estimated the measurement error of the molecular weight determined by GPC to be ± 10 % (see *Experimental Section*, *chapter 3* for further details). Differential scanning calorimetry (DSC) measurements of polymers were carried out on a

Netzsch DSC 204 F1 instrument (software: *Netzsch Proteus Thermal Analysis*, version 6.1.0) with a heating/cooling rate of 10 K/min. Additional measurements to investigate the polymer chain disentanglement of samples from aqueous polymerizations were performed with a heating/cooling rate of 1 K min^{-1} (only first heating cycle reported). Dynamic light scattering (DLS) was performed on diluted polyethylene dispersions (1 droplet dispersion in 2 mL water) using a *Malvern Zetasizer Nano-ZS ZEN 3600* instrument (633 nm) in backscattering mode (173°) at 25 °C. The data was analyzed to yield particle size distributions and polydispersity indices (PDIs; dimensionless number between 0 and 1; 1 being highly polydisperse; determined from gradient of cumulants analysis) using the *Malvern Zetasizer Software*, version 7.12. Electrochemical measurements were performed on instruments of Prof. Rainer Winter's research group (*vide infra*).

4.4.2 Polymerization procedures

Polymerization experiments in heptane and toluene

All ethylene polymerizations in toluene were conducted in a *Büchi miniclave* reactor with a 280 mL vessel. The reactor was equipped with a mechanical stirrer, a heating and cooling jacket connected to a thermostat, a thermocouple dipping into the polymerization mixture and a nitrogen/vacuum supply. Prior to all polymerization experiments, the reactor was evacuated and heated up (thermostat temperature: 90 °C). When the reactor temperature was > 60 °C, the reactor was flushed with nitrogen and evacuated three times. The reactor was brought 3 °C below the desired reaction temperature.

Heptane: The catalyst was dissolved in 100 mL heptane und the red solution canula transferred into the reactor.

Toluene: The reactor was then filled with 100 mL of toluene via cannula transfer and the solution stirred with 500 rpm. The catalyst was dissolved in 5 mL of toluene and transferred into the reactor via syringe.

Immediately after addition, the stirring rate was increased to 1000 rpm and the reactor was pressurized to the desired pressure. During the pressurization procedure the temperature was adjusted to the desired reaction temperature. All experiments were conducted at constant pressure over the entire polymerization experiment with the ethylene feed controlled and monitored by two *Bronkhorst* mass flow meters (up to 15 g h^{-1} and 150 g h^{-1}, respectively). After the desired reaction time, the ethylene flow was stopped and the reactor carefully vented. The reactor content was poured into 300 mL of methanol and stirred for 30 minutes. The precipitated polymer was filtrated, washed with methanol and dried in a vacuum oven (60 °C, 30 mbar) overnight.

Polymerization in aqueous surfactant solution

All ethylene polymerizations in water were conducted in a *Büchi ecoclave* reactor with a 600 mL vessel (see also *chapter 6.2.1* for details on reactor setup). The reactor was equipped with a heating and cooling jacket connected to a thermostat, a mechanical stirrer, a nitrogen/vacuum supply, and an ultrasonotrode (*Hielscher UIP250*) and a thermocouple couple both dipping into the reaction mixture. A *Bronkhorst* MassFlow apparatus consisting of two flow meters (up to 20 g h^{-1} and 200 g h^{-1} ethylene), a pressure meter and a compressed air-driven badger valve was

used to work under constant ethylene pressure. All gas valves and devices were connected to a *HiTec Zang LabBox* and operated by *HiTec Zang LabVision*® software (ver. 2.13). The software allowed for a precise process visualization, control and recording of all relevant parameters in one single process flow chart. The integration of *HiText*™ programming language enabled the construction of several automation scripts (e.g. for pressurization, temperature control, venting, etc.). Prior to all polymerization experiments, the reactor was evacuated and heated up (thermostat temperature: 90 °C) using a custom *HiText*™ script. When the reactor temperature was > 60 °C, the reactor was flushed with nitrogen, evacuated three times and automatically cooled down to 2 °C below the desired polymerization temperature. The desired amount of surfactant (e.g. sodium dodecyl sulfate) and base (e.g. cesium hydroxide) and a magnetic stirrer bar were placed in a Schlenk flask, and the flask was transferred into a glovebox. After addition of lipophilic solvent (e.g. mesitylene) and catalyst, the flask was sealed, brought outside the glovebox and water was added under vigorous stirring via cannula transfer. The clear orange solution (after 3-5 minutes of stirring) was then transferred to the reactor and stirred at 500 rpm. The polymerization experiment was started using a custom *HiText*™ program with a graphical interface to adjust ultrasound application power and duration, reaction time and reaction temperature control. The reaction mixture was then automatically treated with ultrasound (usually for 2 minutes with 120 Watt power) and the solution temperature monitored to stay around 15 °C or 10 °C. Immediately afterwards, the stirring rate was increased to 1000 rpm and the reactor pressurized stepwise to 40 bar ethylene pressure within 30 seconds. The ethylene flow was then controlled and recorded by the mass flow meter and a constant pressure kept over the entire polymerization experiment. The reaction temperature was automatically adjusted to 15 °C or 10 °C. After the desired reaction time, the pressure was automatically released stepwise. Below 15 bar residual pressure, the reactor was vented manually into a beaker to collect migrating dispersion due to foaming. The entire dispersion was weighed, filtered over cotton wool and the solids content determined by precipitation of a 50 g aliquot of dispersion in 300 mL of methanol. After stirring for 30 minutes, the precipitated bulk polymer was filtered and washed thoroughly with water and methanol, and dried in a vacuum oven (60 °C, 30 mbar) overnight.

4.4.3 Ligand synthesis

Synthesis of 3-(9-anthryl)-N-[2,6-bis(3,5-diperfluorohexylphenyl)phenyl]-salicylaldimine (1^{Ant}-C_6F_{13})

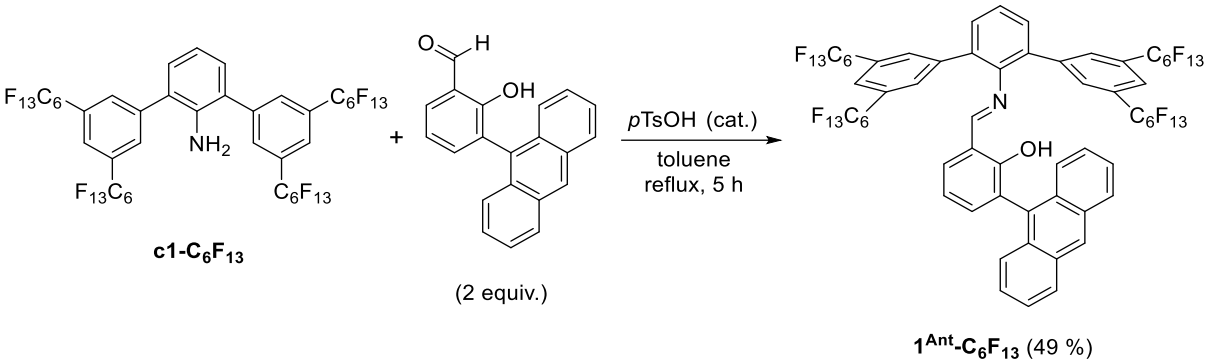

Scheme 4.1. Synthesis of 3-anthryl-*N*-[2,6-bis(3,5-diperfluorohexylphenyl)phenyl]-salicylaldimine (**1^{Ant}-C_6F_{13}**) by acid-catalyzed condensation reaction with 3-(9-anthryl)salicylaldehyde.

5.5 g 3,3',5,5'-Tetra(perfluorohexl)terphenyl amine (**c1-C_6F_{13}**, see *chapter 3*, 3.6 mmol, 1 equiv.), 2.38 g 3-(9-anthryl)salicylaldehyde (7.2 mmol, 2 equiv.) and 25 mg *p*TsOH were added to 200 mL toluene. The flask was equipped with a Soxhlet apparatus filled with dried molecular sieve to allow an azeotropic water removal during the reaction. The reaction mixture was heated to intense reflux (heating bath temperature >160 °C) for 5 hours. Note, that a complete dissolution of the terphenylamine is essential for conversion to the desired product. The reaction mixture was allowed to cool to room temperature, and the solvent removed under reduced pressure. The dark residue was purified by column chromatography on silica using pentane/diethyl ether (99:1) as eluent (yellow band). The product was obtained as a yellow solid. Yield: 49 %, 1.8 mmol, 3.23 g.

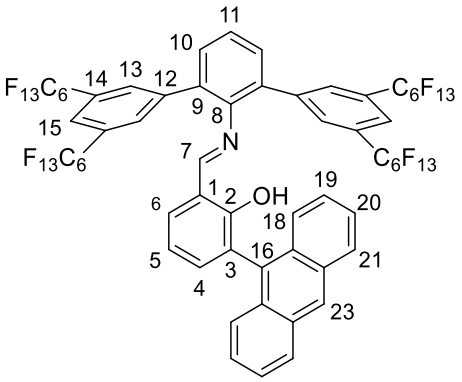

M = 1797.8 g/mol

1^{Ant}-C_6F_{13}, yield: 49 %

^{1}H NMR (400 MHz, $CDCl_3$, 300 K): δ (ppm) = 11.82 (s, 1H, *OH*), 8.48 (s, 1H, *H-23*), 8.20 (s, 1H, *H-7*), 8.01 (d, 2H, $^3J_{HH}$ = 8.4 Hz, *H-21*), 7.80 (s, 4H, *H-13*), 7.70 (s, 2H, *H-15*), 7.53-7.40 (m, 7H, *H-10*,

H-11, *H-18*, *H-20*), 7.35 (dd, 1H, $^{3}J_{HH}$ = 7.1 Hz, $^{4}J_{HH}$ = 2.0 Hz, *H-4*), 7.25-7.29 (m, 2H, *H-19*), 7.05-6.97 (m, 2H, *H-5*, *H-6*).

^{19}F{^{1}H} NMR (376 MHz, $CDCl_3$, 300 K): δ (ppm) = -80.9 (tt, J_{FF} = 10 Hz, J_{FF} = 3 Hz, 12F, CF_3), -111.0 (t, J_{FF} = 14 Hz, 8F, $C_{arom}CF_2$), -121.4 (quint., J_{FF} = 14 Hz, 8F, CF_2), -121.8 (m, 8F, CF_2), -122.8 (m, 8F, CF_2), -126.2 (m, 8F, CF_2).

^{13}C{^{1}H} NMR (101 MHz, $CDCl_3$, 300 K): δ (ppm) = 170.7 (s, *C-7*), 159.4 (s, *C-2*), 145.6 (s, *C-8*), 140.9 (s, *C-12*), 137.9 (s, *C-4*), 132.3 (s, *C-6 and C-16*), 132.1 (s, *C-9*), 131.9 (t, $^{3}J_{CF}$ = 5 Hz, *C-13*), 131.8 (s, *C-10*), 131.5 (s, *C-22*), 130.5 (s, *C-17*), 130.4 (t, $^{2}J_{CF}$ = 25 Hz, *C-14*), 128.4 (s, *C-21*), 127.4 (s, *C-3*), 127.2 (s, *C-23*), 126.8 (s, *C-11*), 126.2 (s, *C-18*), 125.5 (s, *C-19*), 125.2 (s, *C-20*), 124.5 (s, *C-15*), 122-105 (-C_6F_{13}, *broad due to multiple* $^{X}J_{CF}$ *couplings*), 119.3 (s, *C-5*), 118.1 (s, *C-1*).

Elemental analysis (%) for $C_{63}H_{23}F_{52}NO$: Found (Calculated)
C 42.08 (42.09); H 1.79 (1.29); N 0.78 (0.97)

Synthesis of 3-(9-anthryl)-N-[2,4,6-tris(3,5-diperfluorohexylphenyl)phenyl]-salicylaldimine (2^{Ant}-C_6F_{13})

3,3',3",5,5',5"-hexa(perfluorohexyl)quarterphenyl amine (**c2-C_6F_{13}**)

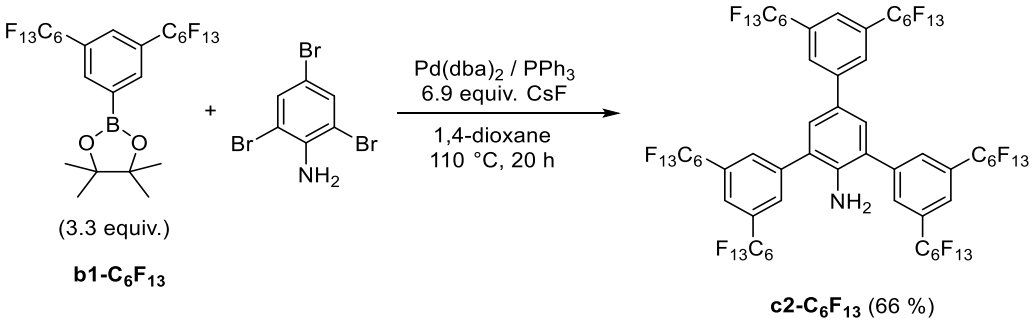

Scheme 4.2. Synthesis of 3,3',3",5,5',5"-hexa(perfluorohexyl)quarterphenyl amine (**c2-C_6F_{13}**). The quarterphenylamine was obtained from palladium-catalyzed Suzuki coupling of the boronic acid ester with 2,4,6-tribromoaniline.

0.308 g $Pd(dba)_2$ (0.5 mmol, 0.05 equiv.) and 0.290 g triphenylphosphine (1.1 mmol, 0.11 equiv.) were stirred in 12 mL dioxane to give an orange catalyst solution. This was added to a mixture of 27.7 g 3,5-di(perfluorohexylphenyl)boronic acid pinacol ester (**b1-C_6F_{13}**, see *chapter 3*, 33.0 mmol, 3.3 equiv.), 3.3 g 2,4,6-tribromoaniline (10.0 mmol, 1 equiv.) and 10.5 g cesium fluoride (69.0 mmol, 6.9 equiv.) in 300 mL dioxane. The dark orange reaction mixture was stirred at 110 °C overnight to give a green suspension (precipitation of inorganic salts). The solvent was removed under reduced pressure and the crude product (dark sticky oil) washed with warm water (2 x 200 mL) and warm methanol (4 x 100 mL). After column chromatography on silica

using pentane/triethylamine [1:0.005] as eluent, compound **c2-C_6F_{13}** was obtained as dark yellow oil. Yield: 66 %, 14.7 g, 6.6 mmol.

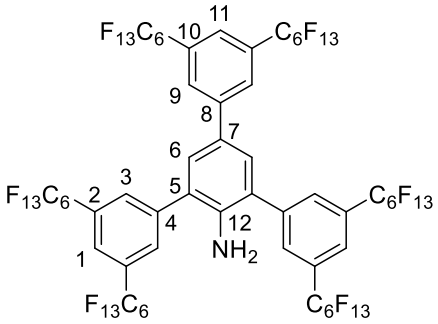

M = 2229.7 g/mol

c2-C_6F_{13}, yield: 66 %

^{1}H NMR (400 MHz, $CDCl_3$ / C_6F_6, 303 K): δ (ppm) = 8.07 (s, 4H, *H-3*), 7.97 (s, 2H, *H-9*), 7.91 (s, 2H, *H-1*), 7.76 (s, 1H, *H-11*), 7.44 (s, 2H, *H-6*), 3.90 (s, 2H, N*H*$_2$).

^{19}F{^{1}H} NMR (376 MHz, $CDCl_3$ / C_6F_6, 300 K): δ (ppm) = -81.4 (m, 18F, *CF_3*), -111.4 (m, 12F, C_{arom}*CF_2*), -121.4 to -122.3 (m, 24F, *CF_2*), -132.3 (m, 12F, *CF_2*), -126.6 (m, 12F, *CF_2*).

^{13}C{^{1}H} NMR (101 MHz, $CDCl_3$ / C_6F_6, 300 K): δ (ppm) = 142.1 (s, *C-12*), 141.7 (s, *C-8*), 140.6 (s, *C-4*), 132.0 – 131.8 (m, *C-3*, *C-2*, *C-10*), 130.1 (s, *C-6*), 129.1 (s, *C-7*), 128.5 (m, *C-9*), 126.4 (s, *C-5*), 125.4 (m, *C-1*), 125 – 105 (-*C_6F_{13}*, *broad due to multiple $^XJ_{CF}$ couplings*), 124.1 (m, *C-11*).

3-(9-anthryl)-N-[2,4,6-tris(3,5-diperfluorohexylphenyl)phenyl]-salicylaldimine (**1^{Ant}-C_6F_{13}**)

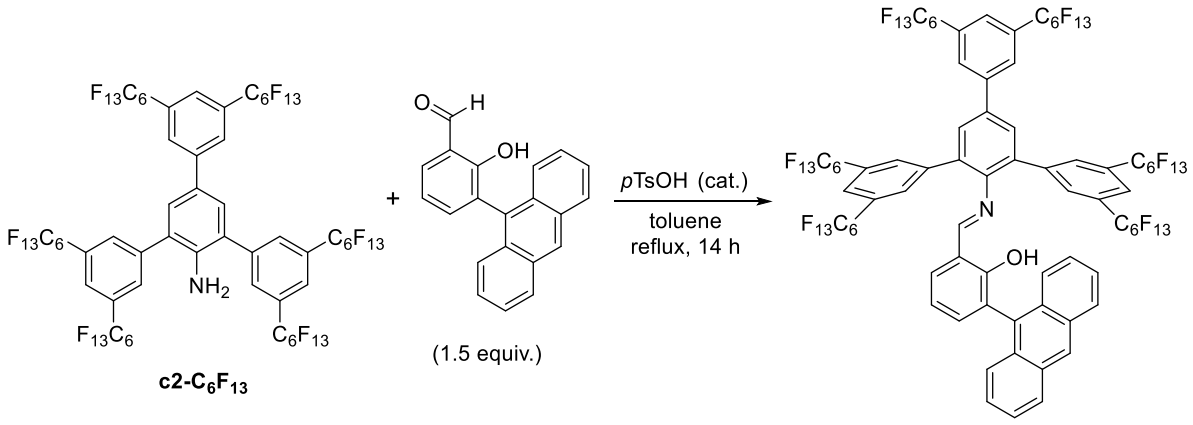

c2-C_6F_{13} (1.5 equiv.)

2^{Ant}-C_6F_{13} (91 %)

Scheme 4.3. 3-(9-anthryl)-*N*-[2,4,6-tris(3,5-diperfluorohexylphenyl)phenyl]-salicylaldimine (**1^{Ant}-C_6F_{13}**) was obtained from acid catalyzed condensation of the respective quarterphenylamine **c2-C_6F_{13}** with 3-(9-anthryl)salicylaldehyde.

3.61 g 3,3',3'',5,5',5''-hexa(perfluorohexyl)quarterphenyl amine (**c2-C_6F_{13}**, 1.62 mmol, 1 equiv.), 2.43 g 3-(9-anthryl)salicylaldehyde (2.43 mmol, 1.5 equiv.) and 50 mg *p*TsOH were added to 300 mL toluene. The flask was equipped with a Soxhlet apparatus filled with molecular sieve to allow an azeotropic water removal during the reaction. The reaction mixture was heated to

intensive reflux (heating bath temperature >160 °C) for 14 hours. Note, that a complete dissolution of the amine is essential for conversion to the desired product. After removing the solvent under reduced pressure, the residue was purified by column chromatography using pentane/diethyl ether (99:1) as eluent (yellow band). The product was obtained as yellow solid. Yield: 91 %, 1.47 mmol, 3.67 g.

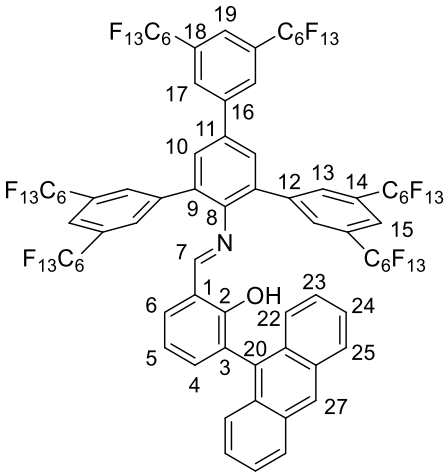

M = 2510.0 g/mol

2^{Ant}-C_6F_{13}, yield: 91 %

^{1}H NMR (400 MHz, C_6D_6 / C_6F_6, 300 K): δ (ppm) = 11.51 (s, 1H, *OH*), 8.14, (s, 1H, *H-27*), 8.12 (s, 2H, *H-17*), 8.04 (s, 1H, *H-19*), 7.88 (s, 6H, *H-13*, *H-15*), 7.80 (d, 2H, $^3J_{HH}$ = 8.3 Hz, *H-25*), 7.65 (s, 1H, *H-7*), 7.59 (d, 2H, $^3J_{HH}$ = 8.7 Hz, *H-22*), 7.54 (s, 2H, *H-10*), 7.40-7.29 (m, 4H, *H-23*, *H-24*),7.14 (m, 1H, *H-4*), 6.79 (dd, 1H, $^3J_{HH}$ = 7.9 Hz, $^4J_{HH}$ = 1.7 Hz, *H-6*), 6.70 (t, 1H, $^3J_{HH}$ = 7.6 Hz, *H-5*).

^{19}F{^{1}H} NMR (376 MHz, C_6D_6 / C_6F_6, 300 K): δ (ppm) = -81.7 (t, J_{FF} = 10 Hz, 12F, CF_3), -81.8 (t, J_{FF} = 6 Hz, 6F, CF_3), -111.4 (t, J_{FF} = 15 Hz, 8F, $C_{arom}CF_2$), -111.5 (t, J_{FF} = 15 Hz, 4F, $C_{arom}CF_2$), -121.6 (m, 12F, CF_2), -122.0 (m, 12F, CF_2), -123.2 (m, 12F, CF_2), -126.7 (m, 12F, CF_2).

^{13}C{^{1}H} NMR (101 MHz, C_6D_6 / C_6F_6, 300 K): δ (ppm) = 171.3 (s, *C-7*), 160.2 (s, *C-2*), 146.9 (s, C-8), 142.1 (s, *C-16*), 140.9 (s, *C-12*), 138.9 (s, *C-4*), 138.0 (s, *C-11*), 133.5 (s, C-9), 132.4 (t, $^3J_{CF}$ = 5.2 Hz, *C-13*), 132.2 – 131.7 (m, *C-6, C-18*, *C-26*), 131.2 (t,$^2J_{CF}$ = 25 Hz, *C-14*), 130.9 (s, *C-21*), 130.3 (s, *C-10*), 129.4 (t, $^3J_{CF}$ = 4.8 Hz, *C-17*), 128.8 (s, *C-25*), 128.3 (s, *C-3*), 128.1 (s, *C-20*), 127.4 (s, *C-27*), 126.4 (s, *C-22*), 126.5-125.3 (m, *C-15, C-19, C-23, C-24*), 122-106 (-C_6F_{13}, *broad due to multiple* $^XJ_{CF}$ *couplings*), 119.6 (s, *C-5*), 118.4 (s, *C-1*).

Elemental analysis (%) for $C_{81}H_{25}F_{78}NO$: Found (Calculated)
C 39.10 (38.76); H 1.00 (1.77); N 0.56 (0.56)

Synthesis of 3-(9-anthryl)-N-{2,4-bis[(3,5-(bis)perfluorohexyl)phenyl]-9-[(3,5-bistrifluoromethyl)phenyl]-naphthalen-1-amine}-salicylaldimine (3^{Ant}-C_6F_{13})

8-[3,5-bis(trifluoromethyl)phenyl]naphthalen-1-amine (**a3**)

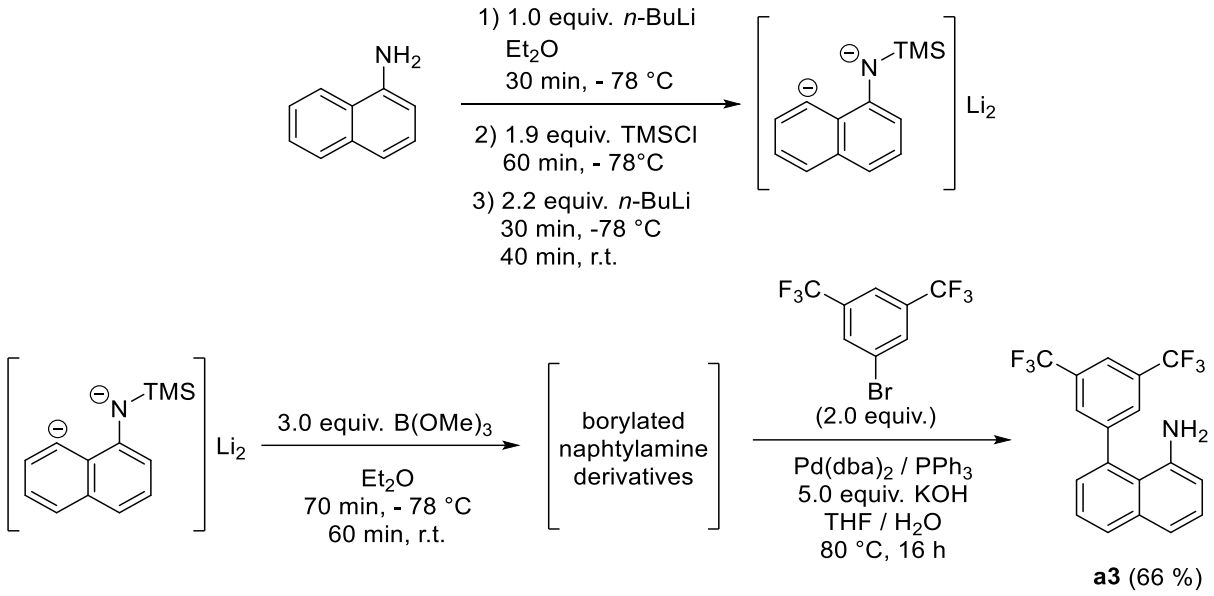

Scheme 4.4. One-pot multi-step synthesis of 8-[3,5-bis(trifluoromethyl)phenyl]naphthalen-1-amine (**a3**).[125] After lithiation and borylation of naphthylamine, the desired product can be obtained by palladium-catalyzed Suzuki coupling.

Compound **a3** was synthesized and characterized according to a modified literature procedure.[125] A solution of 1-naphthylamine (6.0 g, 42.0 mmol, 1.0 equiv.) in diethyl ether (100 mL) was cooled to -78 °C. *n*-Buthyllithium (1.6 M in hexane, 16.8 mL, 42.0 mmol, 1.0 equiv.) was added dropwise. After 30 minutes, trimethylchlorosilane (TMSCl, 5.8 mL, 98.0 mmol, 1.9 equiv.) was added dropwise and the mixture was stirred for 60 min. A sample was taken (0.5 mL), the solvents were removed under reduced pressure and the residue dissolved in MeOD-d_4 to verify conversion to the desired product via ^{1}H-NMR spectroscopy.

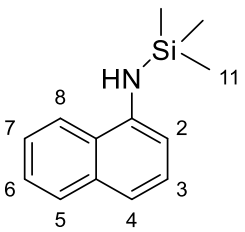

^{1}H NMR (400 MHz, MeOD, 300 K): δ (ppm) = 7.97 (m, 1H, *H-8*), 7.73 (m, 1H, *H-5*), 7.40 (dt, $^3J_{HH}$ = 6.4 Hz, $^4J_{HH}$ = 3.5 Hz, 2H, *H-6*, *H-7*), 7.22 (m, 2H, *H-3*, *H-4*), 6.82 (dd, $^3J_{HH}$ = 4.8 Hz, $^4J_{HH}$ = 3.8 Hz, 1H, *H-2*), 0.11 (s, 9H, *H-11*).

A second portion of *n*-buthyllithium (1.6 M in hexane, 39.0 mL, 46.0 mmol, 2.2 equiv.) was added dropwise and the reaction stirred for 30 min at -78 °C before allowing the reaction mixture to warm up to room temperature. After stirring for 40 minutes, the mixture was cooled to -78 °C again and a sample (0.5 mL) was taken. The solvent was removed under reduced pressure and the white residue was dissolved in MeOD-d_4 to verify formation of the desired lithiated product via ^{1}H-NMR spectroscopy.

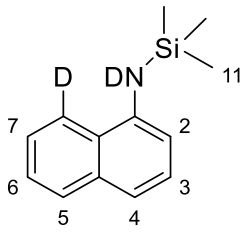

^{1}H NMR (400 MHz, MeOD, 300 K): δ (ppm) = 7.73 (m, 1H, *H-5*), 7.39 (m, 2H, *H-6*, *H-7*), 7.22 (m, 2H, *H-3*, *H-4*), 6.81 (dd, $^3J_{HH}$ = 5.1 Hz, $^4J_{HH}$ = 3.5 Hz, 1H, *H-2*), 0.11 (s, 9H, *H-11*).

Trimethylborate (14.2 mL, 125.0 mmol, 3.0 equiv.) was then added dropwise at -78 °C. After stirring for 70 minutes, the reaction mixture was allowed to warm to room temperature and stirred for another 60 min. The solvent was removed under reduced pressure, yielding the borylated intermediate product as a white precipitate, which was used for the following reaction without further purification. The intermediate product and KOH (11.8 g, 210.0 mmol, 5.0 equiv.) were dissolved in THF (80 mL). To this mixture, 1-bromo-3,5-bis(trifluoromethyl)benzene (14.4 mL, 84.0 mmol, 2.0 equiv.) and water (20 mL) were added carefully. A prepared orange catalyst solution of $Pd(dba)_2$ (480.0 mg, 0.8 mmol, 0.02 equiv.) and PPh_3 (468.0 mg, 1.8 mmol, 0.04 equiv.) in 15 mL THF was added. The mixture was stirred at 80 °C for 16 h. After cooling to room temperature, the phases were separated, and the aqueous phase extracted with THF (3 x 100 mL). The combined organic phases were washed with 0.5 M NaOH (2 x 100 mL), dried over Na_2SO_4 and concentrated under reduced pressure. The brown oil was purified by column chromatography on silica (eluent: petroleum ether/ethyl acetate, 5:1, R_F = 0.4) giving the pure compound **a3** as a dark red oil. Yield: 66 %, 26 mmol, 9.6 g. The product was characterized via ^{1}H-,^{13}C-, and ^{19}F-NMR spectroscopy in accordance to literature.[125,380]

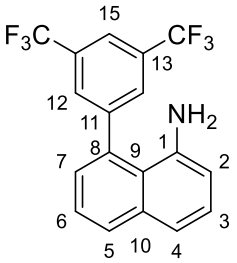

M = 355.3 g/mol

a3, yield: 66 %

^{1}H NMR (400 MHz, $CDCl_3$, 300 K): δ (ppm) = 7.96 (s, 2H, *H-12*), 7.94 (s, 1H, *H-15*), 7.87 (dd, $^{3}J_{HH}$ = 8.31 Hz, $^{4}J_{HH}$ = 1.45 Hz, 1H, *H-5*), 7.43 (m, 2H, *H-4*, *H-6*), 7.35 (dd, $^{3}J_{HH}$ = 7.75 Hz, $^{4}J_{HH}$ = 1.52 Hz, 1H, H-3), 7.35 (dd, $^{3}J_{HH}$ = 7.29 Hz, $^{3}J_{HH}$ = 1.55 Hz, 1H, H-7), 6.73 (d, 1H, H-2), 3.42 (s, 2H, N*H*$_2$).

^{13}C{^{1}H} NMR (101 MHz, $CDCl_3$, 300 K): δ (ppm) = 145.2 (s, *C-11*), 142.9 (s, *C-1*), 136.1 (s, *C-10*), 135.2 (s, *C-8*), 130.9 (q, $^{2}J_{CF}$ = 34 Hz, *C-13*), 130.2 (s, *C-5*), 129.7 (s, *C-12*), 129.2 (s, *C-7*), 127.2 (s, *C-3*), 124.8 (s, *C-6*), 122.1 (q, $^{1}J_{CF}$ = 274 Hz, *C-14*), 121.2 (m, *C-15*), 120.3 (s, C-9), 119.9 (s, *C-4*), 112.5 (s, *C-2*).

^{19}F{^{1}H} NMR (376 MHz, $CDCl_3$, 300 K): δ (ppm) = -65.6 (s, 6F, -C*F*$_3$).

2,4-dibromo-8-[3,5-bis(trifluoromethyl)phenyl]naphthalen-1-amine (**b3**)

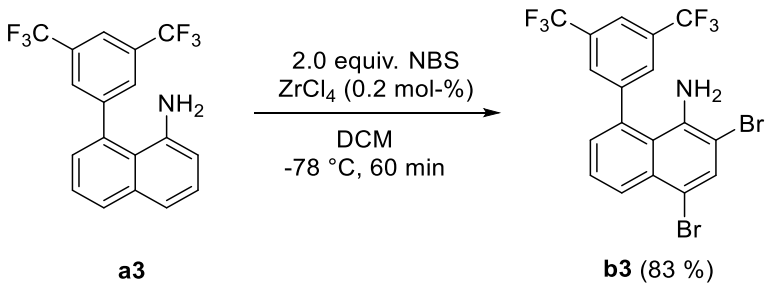

a3 **b3** (83 %)

Scheme 4.5. Selective bromination of 8-[3,5-bis(trifluoromethyl)phenyl]naphthalen-1-amine (**a3**) to obtain 2,4-dibromo-8-[3,5-bis(trifluoromethyl)phenyl]naphthalen-1-amine (**b3**).

Compound **b3** was synthesized and characterized according to a modified literature procedure.[125] *N*-Bromo-succinimide (5.1 g, 28.8 mmol, 2.0 equiv.) was dissolved in DCM (40 mL) and cooled to -78 °C. $ZrCl_4$ (66.3 mg, 0.03 mmol, 0.02 equiv.) was dissolved in DCM (30 mL) and added to the solution of *N*-Bromo-succinimide. The resulting mixture was added slowly to a solution of **a3** (5.2 g, 14.4 mmol, 1.0 equiv.) in DCM (180 ml) and stirred for 60 min at -78 °C. Aqueous $NaHCO_3$ solution (300 mL) was then added and the mixture subsequently treated with air while warming up to room temperature. The phases were separated and the aqueous phase was extracted with DCM (3 x 150 mL). The combined organic phases were washed with saturated aqueous NaCl solution (3 x 100 mL), dried over Na_2SO_4 and concentrated in vacuum. The crude product was purified by column chromatography on silica (petroleum ether/ethyl acetate, 20:1, 1 vol% triethylamine, R_F = 0.42) yielding the compound **b3** as a brown sticky oil. Yield: 83 %,

12 mmol, 6.21 g. The product was characterized via ^{1}H-,^{13}C-, and ^{19}F-NMR spectroscopy in accordance to literature.[125]

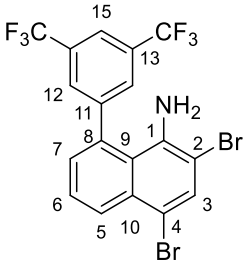

M = 513.0 g/mol

b3, yield: 83 %

^{1}H NMR (400 MHz, $CDCl_3$, 300 K): δ (ppm) = 8.33 (dd, $^{3}J_{HH}$ = 8.34 Hz, $^{4}J_{HH}$ = 3.10 Hz, 1H, *H-5*), 7.97 (s, 1H, *H-15*), 7.91 (s, 3H, *H-3*, *H-12*), 7.58 (m, 1H, *H-6*), 7.26 (dd, $^{3}J_{HH}$ = 6.16 Hz, $^{4}J_{HH}$ = 3.10 Hz, 1H, *H-7*), 4.08 (s, 2H, N*H*$_2$).

^{13}C{^{1}H} NMR (101 MHz, $CDCl_3$, 300 K): δ (ppm) = 144.5 (s, *C-11*), 140.1 (s, *C-1*), 135.4 (s, *C-8*), 134.0 (s, *C-3*), 132.8 (s, *C-10*), 131.8 (q, $^{1}J_{CF}$ = 270 Hz, *C-13*), 130.9 (s, *C-7*), 129.6 (m, C-12), 126.5 (s, *C-6*), 124.6 (s, *C-14*), 121.9 (m, *C-15*), 121.3 (s, *C-9*), 120.3 (s, *C-10*), 111.2 (s, *C-4*), 105.9 (s, *C-2*).

^{19}F{^{1}H} NMR (376 MHz, $CDCl_3$, 300 K): δ (ppm) = - 62.8 (s, 6F, -C*F*$_3$).

*2,4-bis[(3,5-(bisperfluorohexyl)phenyl]-9-[(3,5-bistrifluoromethyl)phenyl]-naphthalen-1-amine (**3c-C$_6$F$_{13}$**)*

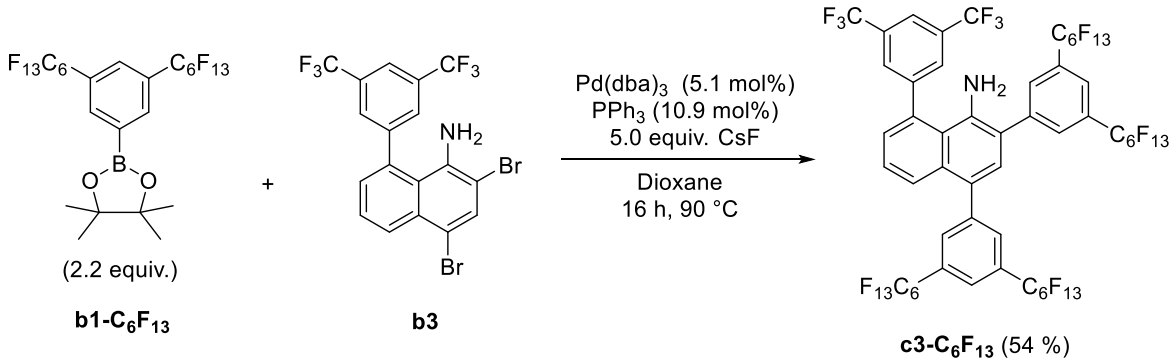

Scheme 4.6. Synthesis of the 2,4,6-tri-substituted-naphthalen-1-amine derivative **c3-C$_6$F$_{13}$** by palladium-catalyzed Suzuki coupling of 2,4-dibromo-8-(3,5-bis(trifluoromethyl)phenyl)naphthalen-1-amine (**b3**) with the respective boronic acid ester **b1-C$_6$F$_{13}$**.

Compound **b1-C$_6$F$_{13}$** (5.4 g, 6.5 mmol, 2.2 equiv.), compound **b3** (1.5 g, 2.9 mmol, 1 equiv.) and cesium fluoride (2.2 g, 14.7 mmol, 5.0 equiv.) were added to dioxane (150 mL). A catalyst solution of $Pd(dba)_2$ (137.0 mg, 0.15 mmol, 0.05 equiv.) and PPh_3 (84.0 mg, 0.32 mmol, 0.11 equiv.) in dioxane (10 mL) was added and the reaction mixture stirred at 90 °C for 16 h. Then, the solvent was removed in vacuum and the resulting residue dissolved in pentane. Insoluble components were filtered off and the organic phase extracted with methanol (3 x 100 mL; in case of no visible phase separation, several droplets of water were added to the polar phase). The resulting pentane phase was dried over Na_2SO_4 and concentrated under reduced pressure,

yielding the crude product as a brown sticky oil. The crude product was purified over column chromatography on silica (pentane, R_F = 0.5) to obtain pure compound **3c-C_6F_{13}** as dark oil. Yield: 54 %, 1.6 mmol, 2.8 g.

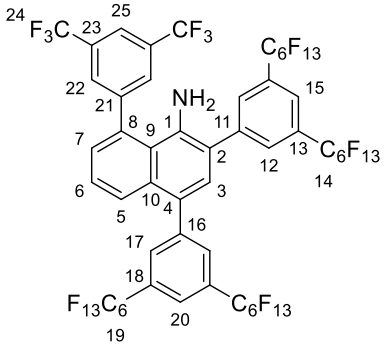

M = 1779.6 g/mol

c3-C_6F_{13}, yield: 54 %

^{1}H NMR (400 MHz, $CDCl_3$, 300 K): δ (ppm) = 8.04 (d, $^4J_{HH}$ = 1.58 Hz, 2H, *H-12*), 7.99 (m, 6H, *H-15*, *H-17*, *H-20*, *H-22*), 7.90 (s, 1H, *H-25*), 7.79 (d, $^3J_{HH}$ = 8.72 Hz, 1H, *H-5*), 7.56 (t, $^3J_{HH}$ = 7.58 Hz, 1H, *H-6*), 7.41 (d, $^2J_{HH}$ = 6.94 Hz, 1H, *H-7*), 7.26 (s, 1H, *H-3*), 3.74 (s, 2H, NH_2).

^{19}F{^{1}H} NMR (376 MHz, $CDCl_3$, 300 K): δ (ppm) = -63.2 (s, 6F, CF_3), -81.05 (m, 12F, CF_2CF_3), -111.1 (m, 8F, $C_{arom}CF_2$), -121.8 (m, 16F, CF_2), -122.9 (m, 8F, CF_2), -126.3 (m, 8F, CF_2).

^{13}C{^{1}H} NMR (101 MHz, $CDCl_3$, 300 K): δ (ppm) = 144.2 (s, *C-21*), 142.3 (s, *C-11* or *C-16*), 140.7 (s, *C-11* or *C-16*), 135.8 (s, *C-8*), 133.4 (s, *C-10*), 132.4 (m, *C-12*), 132.3 (s, *C-23*), 132.1 (m, *C-17* or *C-20*), 131.7 (m, *C-17* or *C-20*), 131.3 (t, $^2J_{CF}$ = 25.0 Hz, *C-13* or *C-18*), 130.5 (s, *C-7*), 130.2 (t, $^2J_{CF}$ = 25.0 Hz, *C-13* or *C-18*) 129.7 (s, *C-22*), 129.5 (m, *C-15*), 129.2 (s, *C-12*), 128.2 (s, *C-4*), 126.5 (m, *C-5*, *C-6*), 124.3 (s, *C-25*), 122.8 (m, *C-23*), 121.5 (s, *C-2*), 120.3 (s, *C-1*), 119.8 (s, *C-9*), 119 – 106 (-C_6F_{13}, *broad due to multiple* $^XJ_{CF}$ *couplings*, *C-14*, *C-19*, *C-24*).

3-(9-anthryl)-N-{2,4-bis[(3,5-(bis)perfluorohexyl)phenyl]-9-[(3,5-bistrifluoro-methyl)-phenyl]-naphthalen-1-amine}-salicylaldimine (**3^{Ant}-C_6F_{13}**)

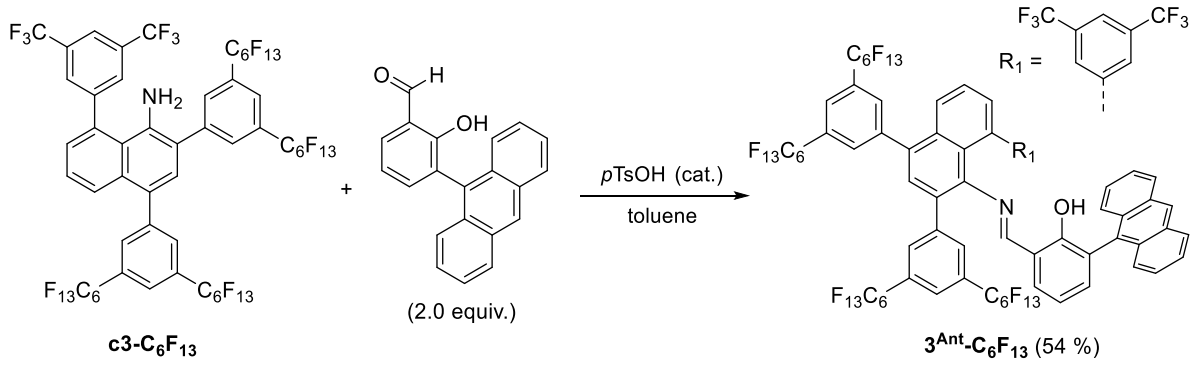

c3-C_6F_{13} **3^{Ant}-C_6F_{13}** (54 %)

Scheme 4.7. 3-(9-anthryl)-*N*-{2,4-bis[(3,5-(bis)perfluorohexyl)phenyl]-9-[(3,5-bistrifluoro-methyl)-phenyl]-naphthalen-1-amine}-salicylaldimine (**3^{Ant}-C_6F_{13}**) was obtained from acid catalyzed condensation of the respective 2,4,6-tri-substituted-naphthalen-1-amine derivative **c3-C_6F_{13}** with 3-(9-anthryl)salicylaldehyde.

Compound **c3-C_6F_{13}** (1.2 g, 0.7 mmol, 1.0 equiv.), 3-(9-anthryl)salicylaldehyde (0.4 g, 1.4 mmol, 2.0 equiv.) and *p*-toluenesulfonic acid (50 mg) were added to toluene (250 mL). The solution was stirred over molecular sieve (3 Å; molecular sieve filled in porous glass inlet) at 100 °C for 48 h. The molecular sieve was removed, the reaction flask was equipped with a Dean-Stark apparatus filled with fresh molecular sieve and toluene, and the reaction mixture heated to intense reflux. After another 12 hours, the solvent was removed through the outlet trap of the Dean-Stark apparatus. The dark residue was dried in vacuum and purified by column chromatography on silica (pentane/diethylether [95:5]; R_F = 0.6) to give compound **3^{Ant}-C_6F_{13}** as brown powder. Yield: 0.76 g, 0.4 mmol, 54 %.

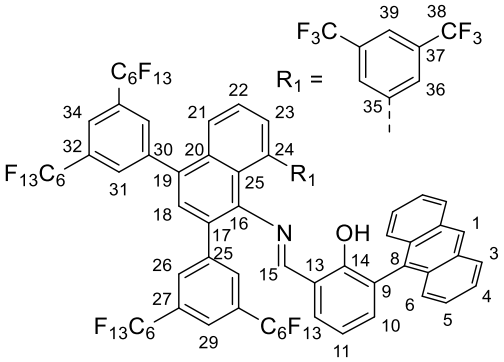

M = 2095.9 g/mol

3^{Ant}-C_6F_{13}, yield: 54 %

^{1}H NMR (400 MHz, $CDCl_3$, 300 K): δ (ppm) = 10.66 (s, 1H, O*H*), 8.52 (s, 1H, *H-1*), 8.07 (d, $^3J_{HH}$ = 8.6 Hz, 2H, *H-3*), 8.03 (s, 2H, *H-31*), 8.01 (s, 1H, *H-15*), 7.96 (s, 1H, *H-34*), 7.81 – 7.77 (m, 3H, *H-26*, *H-21*), 7.71 (s, 1H, *H-29*), 7.60 (dd, $^3J_{HH}$ = 8.52 Hz, $^3J_{HH}$ = 7.1 Hz, *H-22*), 7.5 (m, 3H, *H-18*, *H-36*), 7.49 (m, 4H, *H-4*, *H-23*, *H-39*), 7.41 – 7.35 (m, 6H, *H-10*, *H-5*, *H-6*), 6.97 (m, 2H, *H-11*, *H-12*).

^{19}F{^{1}H} NMR (376 MHz, $CDCl_3$, 300 K): δ (ppm) = -63.3 (s, 6F, CF_3), -80.9 (m, 12F, CF_2CF_3), -111.0 (m, 8F, $C_{arom}CF_2$), -121.6 (m, 16F, CF_2), -122.8 (m, 8F, CF_2), -126.2 (m, 8F, CF_2).

^{13}C{^{1}H} NMR (101 MHz, $CDCl_3$, 300 K): δ (ppm) = 170.7 (s, *C-15*), 159.5 (s, *C-14*), 145.9 (s, *C-16*), 145.2 (s, *C-35*), 141.8 (s, *C-25* or *C-30*), 141.6 (s, *C-25* or *C-30*), 138.1 (s, *C-10*), 137.6 (s, *C-24*), 136.0 (s, *C-19*), 133.4 (s, *C-20*), 132.7 (s, *C-8*, *C-23*), 132.4 (s, *C-31*), 132.3 (br s, *C-26*), 131.6 (s, *C-2*), 130.9 (q, $^3J_{CF}$ = 6 Hz, *C-34*), 130.7 (t, $^2J_{CF}$ = 24 Hz, *C-27*, *C-32*), 130.4 (s, *C-7*), 129.3 (m, *C-18*, *C-36*), 128.7 (s, *C-3*), 127.4 (s, *C-17*), 127.2 (s, *C-22*), 127.1 (s, *C-1*), 126.7 (s, *C-13*), 126.6 (s, *C-21*), 126.5 (s, *C-6*), 125.5 (s, *C-12*), 125.4 (s, *C-5*), 125.1 (m, *C-4*, *C-37*), 124.3 (m, *C-29*), 123.0 (t, $^1J_{CF}$ = 275 Hz, *C-38*), 121.6 (m, *C-39*), 120 – 107 (-C_6F_{13}, *broad due to multiple* $^XJ_{CF}$ *couplings*, *C-33, C-28*), 119.3 (s, *C-11*), 118.1 (s, *C-9*).

4.4.4 Synthesis of complexes

Synthesis of κ²-(N,O)-salicylaldiminato nickelI(II) methyl pyridine complexes (1^{Ant}-R^F/Pyr, 2^{Ant}-R^F/Pyr and 3^{Ant}-R^F/Pyr)

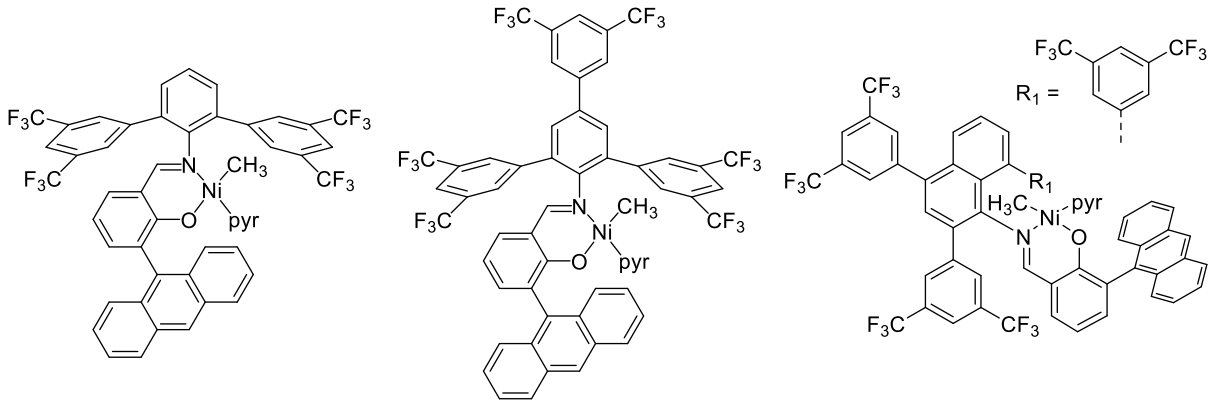

The reference catalysts **1^{Ant}-CF_3/Pyr**[108], **2^{Ant}-CF_3/Pyr**[178,381] and **3^{Ant}-CF_3/Pyr**[125] were synthesized and characterized according to reported procedures.

{3-(9-anthryl)-N-[2,6-bis(3,5-diperfluorohexylphenyl)phenyl]salicylaldiminato- κ² N,O}methyl-pyridinenickel(II) **(1^{Ant}-C_6F_{13}/Pyr)**

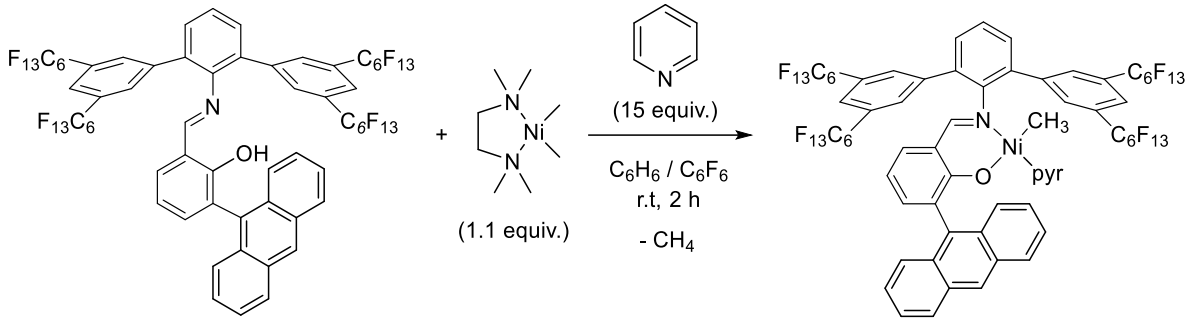

Scheme 4.8. Synthesis of lipophilic κ²-(*N,O*)-salicylaldiminato nickel(II) methyl pyridine complex **1^{Ant}-C_6F_{13}/Pyr** by addition of an excess of pyridine to a mixture of nickel precursor and the respective salicylaldimine.

To 23 mg [(tmeda)$NiMe_2$] (110 µmol, 1.1 equiv.) and 180 mg salicylaldimine **1^{Ant}-C_6F_{13}** (100 µmol, 1 equiv.), a solution of 119 mg pyridine (1.5 µmol, 15 equiv.) in benzene/ hexafluorobenzene [4 mL/0.5 mL] was added. Gas evolution (methane) was observed and the reaction mixture turned orange to red. The reactants were stirred for 2 hours at room

temperature. The formed nickel black was removed via centrifugation and the red supernatant was frozen in liquid nitrogen und the solvent removed by freeze drying to give the desired product **1^{Ant}-C$_6$F$_{13}$/Pyr** as a red powder. Yield: 95%, 95 µmol, 185 mg.

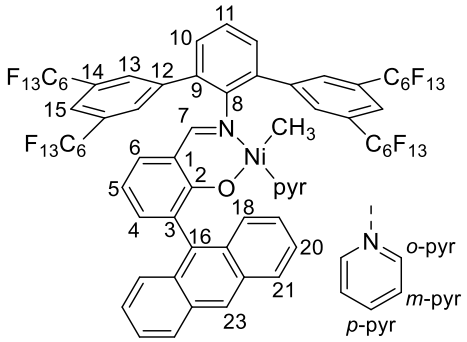

M = 1870.5 g/mol

1^{Ant}-C$_6$F$_{13}$ / Pyr, yield: 95 %

^{1}H NMR (400 MHz, C_6D_6, 300 K): δ (ppm) = 8.36 (s, 4H, *H-13*), 8.08 (s, 1H, *H-23*), 7.98 (s, 2H, *H-15*), 7.81 (d, 2H, $^3J_{HH}$ = 8.8 Hz, *H-21*), 7.73 (d, 2H, $^3J_{HH}$ = 8.5 Hz, *H-18*), 7.41 (m, 2H, *o-Pyr*), 7.31 (m, 2H, *H-20*), 7.21 (m, 2H, *H-19*), 7.12 (dd, 1H, $^2J_{HH}$ = 1.9 Hz, $^3J_{HH}$ = 7.0 Hz, *H-4*), 7.06 (s, 1H, *H-7*), 7.00 (m, 2H, *H-10*), 6.94 (m, 1H, *H-11*), 6.70 (dd, 1H, $^2J_{HH}$ = 1.9 Hz, $^3J_{HH}$ = 8.1 Hz, *H-6*), 6.40 (dd, 1H, $^3J_{HH}$ = 7.0 Hz, $^3J_{HH}$ = 8.1 Hz, *H-5*), 6.23 (m, 1H, *p-Pyr*), 5.65 (m, 2H, *m-Pyr*), -1.02 (s, 3H, Ni-CH_3).

^{19}F{^{1}H} (376 MHz, C_6D_6, 300 K): δ (ppm) = -81.1 (t, J_{FF} = 10 Hz, 12F, *C*F_3), -110.4 (t, $^3J_{FF}$ = 15 Hz, 4F, C_{arom}*C*F_2), -110.6 (t, $^3J_{FF}$ = 15 Hz , 4F, C_{arom}*C*F_2), -121.2 (m, 8F, *C*F_2), -121.5 (m, 8F, *C*F_2), -122.7 (m, 8F, *C*F_2), -126.2 (m, 8F, *C*F_2).

^{13}C{^{1}H} NMR (101 MHz, C_6D_6, 300 K): δ (ppm) = 168.0 (s, C-7), 166.3 (s, *C-2*), 151.1 (s, *C-8*), 150.3 (br. s, *o-Pyr*), 141.9 (s, *C-12*), 138.1 (s, *C-4*), 136.2 (s, *C-16*), 135.4 (br. s, *p-Pyr*), 133.6 (s, *C-9*), 133.3 (s, *C-6*), 132.8 (t, $^3J_{CF}$ = 5 Hz, *C-13*), 131.9 (*C-17*), 131.1 (m, C-3, C-10, *C-22*), 130.4 (t, $^2J_{CF}$ = 25 Hz, *C-14*), 128.2 (s, *C-18*), 128.0 (s, *C-21*), 126.8 (s, *C-11*), 125.6 (s, *C-23*), 125.1 (s, *C-19*), 124.6 (s, *C-20*), 124.5 (m, *C-15*), 122.1 (br. s, *m-Pyr*), 119.4 (s, *C-1*), 119-105 (-*C$_6$F$_{13}$, broad due to multiple $^XJ_{CF}$ couplings*), 114.0 (s, *C-5*).

Elemental analysis (%) for $C_{69}H_{30}F_{52}N_2NiO$: Found (Calculated):
C 42.39 (42.51); H 1.32 (1.55); N 1.69 (1.44)

{3-(9-anthryl)-N-[2,4,6-tris(3,5-diperfluorohexylphenyl)phenyl]salicyl-aldiminato-κ²-N,O}methylpyridinenickel(II) (**2^{Ant}-C$_6$F$_{13}$/Pyr**)

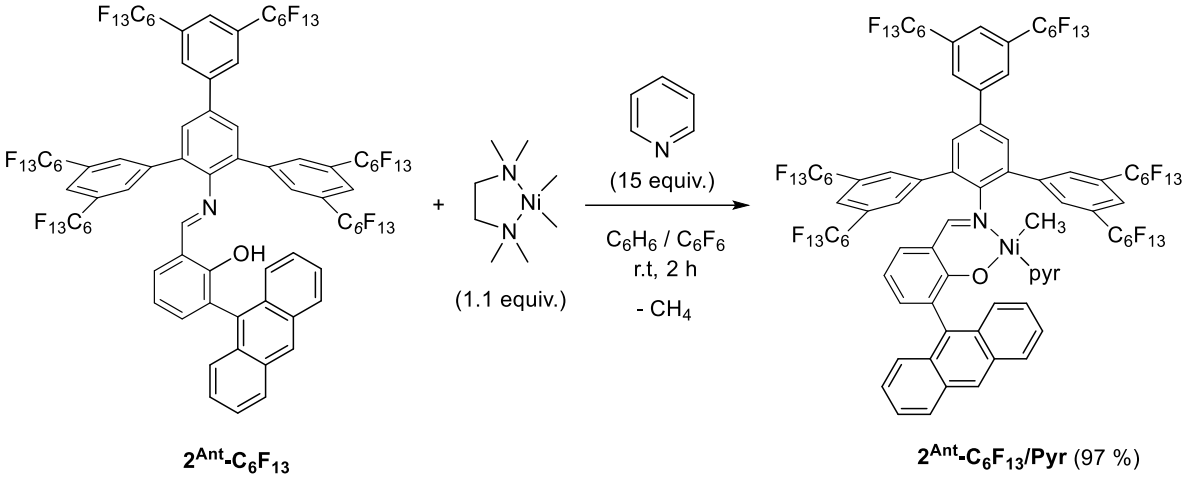

Scheme 4.9. Synthesis of lipophilic κ^2-(*N,O*)-salicylaldiminato nickel(II) methyl pyridine complex **2^{Ant}-C$_6$F$_{13}$/Pyr** by addition of an excess of pyridine to a mixture of nickel precursor and the respective salicylaldimine.

To 23 mg [(tmeda)NiMe$_2$] (110 µmol, 1.1 equiv.) and 251 mg salicylaldimine **2^{Ant}-C$_6$F$_{13}$** (100 µmol, 1 equiv.), a solution of 119 mg pyridine (1.5 µmol, 15 equiv.) in benzene/hexafluorobenzene [4 mL/1 mL] was added. Gas evolution (methane) was observed and the reaction mixture turned orange to red. The reactants were stirred for 2 hours at room temperature. The formed nickel black was removed via centrifugation and the red supernatant was frozen in liquid nitrogen und the solvent removed by freeze drying to give the desired product **2^{Ant}-C$_6$F$_{13}$/Pyr** as a red powder. Yield: 97 %, 97 µmol, 260 mg.

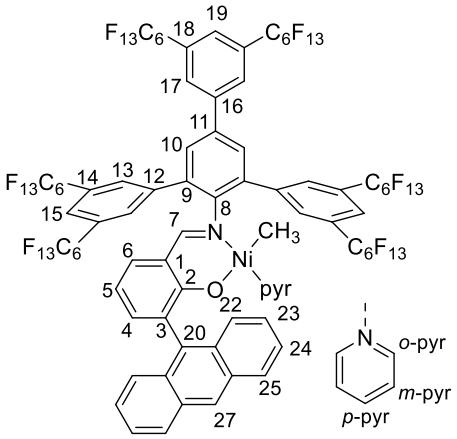

M = 2661.8 g/mol

2^{Ant}-C$_6$F$_{13}$ / Pyr, yield: 97 %

^{1}H NMR (400 MHz, C_6D_6/C_6F_6, 300 K): δ (ppm) = 8.52 (s, 4H, *H-13*), 8.11 (s, 2H, *H-17*), 8.04 (m, 4H, *H-19, H-15, H-27*), 7.73 (vt, 4H, *H-22, H-25*), 7.57 (s, 2H, *H-10*), 7.41 (d, $^3J_{HH}$ = 5.6 Hz, 2H, *o-Pyr*), 7.33-7.19 (m, 6H, *H-4, H-7, H-23, H-24*), 6.83 (dd, 1H, ^3J = 8.1 Hz, ^4J = 1.8 Hz, *H-6*), 6.45 (dd, 1H, $^3J_{HH}$ = 7.0 Hz, $^3J_{HH}$ = 8.0 Hz, *H-5*), 6.36 (t, 1H, $^3J_{HH}$ = 7.5 Hz, *p-Pyr*), 5.72 (t, 2H, $^3J_{HH}$ = 6.6 Hz, *m-Pyr*), -1.00 (s, 3H, *Ni-CH$_3$*).

^{19}F{^{1}H} NMR (376 MHz, C_6D_6/C_6F_6, 300 K): δ (ppm) = -81.6 (t, J_{FF} = 10 Hz, 12F, *CF_3*), -81.7 (t, J_{FF} = 10 Hz, 6F, *CF_3*), -110.5 (m, 8F, C_{arom}*CF_2)*, -111.5 (t, J_{FF} = 15 Hz, 4F, C_{arom}*CF_2*), -121.3 to -122.4 (m, 24F, *CF_2*), -123.2 (m, 12F, *CF_2*), -126.7 (m, 12F, *CF_2*).

^{13}C{^{1}H} NMR (101 MHz, C_6D_6/C_6F_6, 300 K): δ (ppm) = 167.9 (s, *C-7*), 166.8 (s, *C-2*), 152.1 (s, *C-8*), 150.5 (br. s, *o-Pyr*), 142.2 (s, *C-16*), 141.4 (s, *C-12*), 137.0 (s, *C-11*), 136.0 (s, *C-20*), 135.7 (br s., *p-Pyr*), 135.6 (s, *C-5*), 135.3 (s, *C-9*), 133.4 (s, *C-6*), 133.0 (t, $^{4}J_{CF}$ = 5 Hz, *C-13*), 132.0 (s, *C-26*), 131.8 (t, $^{2}J_{CF}$ = 25 Hz, *C-18*), 131.5 (s, *C-3*), 131.1 (m, *C-14, C-21*), 129.4 (m, *C-10, C-17*), 128.2 (s, *C-23 or C-24*), 127.9 (s, *C-23 or C-24*), 125.7 (m, *C-19*), 125.2 (m, *C-4, C-15, C-27*), 125.1 (s, *C-25*), 124.8 (s, *C-22*), 122.4 (br. s, *m-Pyr*), 119.6 (s, *C-1*), 119-105 (*-C_6F_{13}, broad due to multiple $^{X}J_{CF}$ couplings*), -9.0 (s, *Ni-CH_3*).

Elemental analysis (%) for $C_{87}H_{32}F_{78}N_2NiO$: Found (Calculated):
C 39.60 (39.26); H 2.16 (1.21); N 1.37 (1.05)

{3-(9-anthryl)-N-{2,4-bis[(3,5-(bis)perfluorohexyl)phenyl]-9-[(3,5-bistrifluoro-methyl)phenyl]-naphthalen}salicylaldiminato- κ²-N,O}methylpyridinenickel(II) (**3^{Ant}-C_6F_{13}/Pyr**)

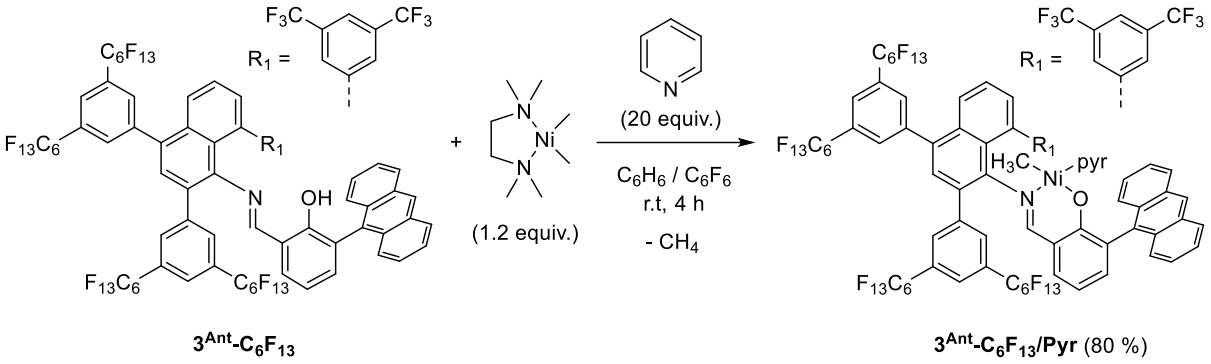

3^{Ant}-C_6F_{13} **3^{Ant}-C_6F_{13}/Pyr** (80 %)

Scheme 4.10. Synthesis of lipophilic κ²-(*N,O*)-salicylaldiminato nickel(II) methyl pyridine complex **3^{Ant}-C_6F_{13}/Pyr** by addition of an excess of pyridine to a mixture of nickel precursor and the respective salicylaldimine.

12.5 mg [(tmeda)$NiMe_2$] (60 µmol, 1.2 equiv.) and 103 mg salicylaldimine **3^{Ant}-C_6F_{13}** (50 µmol, 1 equiv.) were dissolved in benzene/hexafluorobenzene [5 mL/1 mL]. To this solution 79 mg pyridine (1 mmol, 20 equiv.) dissolved in 1 mL benzene were added. Gas evolution (methane) was observed and the reaction mixture turned orange to red. The reactants were stirred for 4 hours at room temperature. The formed nickel black was removed via centrifugation and the red supernatant was frozen in liquid nitrogen und the solvent removed by freeze drying to give the desired product **3^{Ant}-C_6F_{13}/Pyr** as a red powder. Yield: 80 %, 40 µmol, 89 mg.

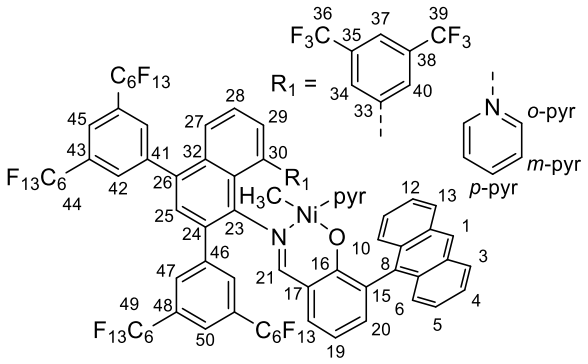

M = 2212.8 g/mol

3-C_6F_{13}/Pyr, yield: 80 %

^{1}H NMR (400 MHz, C_6D_6/C_6F_6, 300 K): δ (ppm) = 8.97 (s, 1H, *H-40* or *H-34*), 8.70 (s, 2H, *H-42* or *H-47*), 8.09 (s, 1H, *H-1*), 8.07 (s, 1H, *H-45* or *H-50*), 8.04 (s, 2H, *H-42* or *H-47*), 8.00 (s, 1H, *H-45* or *H-50*), 7.94 (s, 1H, *H-37*), 7.88 (d, $^3J_{HH}$ = 8.3 Hz, 1H, *H-6*), 7.83 (d, $^3J_{HH}$ = 8.3 Hz, 1H, *H-3*), 7.76 (d, $^3J_{HH}$ = 8.8Hz, 1H, *H-27*), 7.72 (d, $^3J_{HH}$ = 8.5 Hz, 1H, *H-13*), 7.63 (d, $^3J_{HH}$ = 8.5 Hz, 1H, *H-10*), 7.45 (t, $^3J_{HH}$ = 7.0 Hz, 1H, *H-5*), 7.40 – 7.33 (m, 5H, *H-4*, *H-11*, *H-34* or *H-40*, *o*-Pyr), 7.24 – 7.19 (m, 2H, *H-28*, *H-12*), 7.17 (s, 1H, *H-21*), 7.16 (s, 1H, *H-25*), 7.15 (m, 1H, *H-20*), 6.96 (d, $^3J_{HH}$ = 6.1, 1H, *H-29*), 6.74 (dd, $^3J_{HH}$ = 8.2 Hz, $^4J_{HH}$ = 1.9 Hz, 1H, *H-18*), 6.46 (t, $^3J_{HH}$ = 7.6 Hz, 1H, *H-19*), 6.39 (tt, $^3J_{HH}$ = 7.7 Hz, $^4J_{HH}$ = 1.6 Hz, 1H, *p*-Pyr), 5.76 (t, $^3J_{HH}$ = 6.9 Hz, 2H, *m*-Pyr), -1.20 (s, 3H, Ni-CH_3).

^{19}F{^{1}H} NMR (376 MHz, C_6D_6/C_6F_6, 300 K): δ (ppm) = -62.4 (s, 3F, CF_3), -62.9 (s, 3F, CF_3), -81.5 (m, 12F, CF_3), - 110.8 (m, 8F, $C_{arom}CF_2$), -121.6 (m, 16F, CF_2), -123.0 (m, 8F, CF_2), -126.5 (m, 8F, CF_2).
^{13}C{^{1}H} NMR (101 MHz, C_6D_6/C_6F_6, 300 K): δ (ppm) = 168.5 (s, *C-21*), 166.7 (s, *C-16*), 151.2 (s, *C-23*), 150.9 (s, *o*-Pyr), 146.5 (s, *C-33*), 142.7 (s, *C-46* or *C-41*), 142.6 (s, *C-41* or *C-46*), 138.4 (s, *C-20*), 138.2 (s, *C-30*), 136.6 (s, *C-25*), 136.4 (s, *C-8*), 136.3 (s, *C-26*), 136.1 (s, *p*-Pyr), 133.5 (s, *C-18*), 133.4 (s, *C-29*), 133.2 – 129.8 (m, *C-2, C-14, C-7, C-9, C-17, C-24, C-34, C-35, C-38, C-40, C-42, C-43, C-47, C-48*), 128.5 (s, *C-3*), 128.0 (s, *C-32*), 127.3 (s, C-31), 127.1 (s, *C-28*), 126.7 (s, *C-27*), 125.7 (s, *C-11*), 125.6 (s, *C-4* or *C-12*), 125.5 (*C-4* or *C-12*), 125.3 (s, *C-5*), 125.1 (s, *C-45* or *C-50*), 125.0 (s, *C-45* or *C-50*), 124.6 (s, *C-1*), 123.9 (q, $^1J_{CF}$ = 273 Hz, *C-36*, *C-39*) 122.3 (s, *m*-Pyr), 121.7 (m, *C-37*), 119.6 (s, *C-15*), 114.3 (s, *C-19*), 120-109 (-C_6F_{13}, *broad due to multiple* $^XJ_{CF}$ *couplings*), -8.8 (s, Ni-CH_3). Resonances for *C-13*, *C-6* and *C-10* are obscured by benzene-d_6 resonance (128.4, 128.0 and 128.4; assigned by ^{1}H,^{13}C-HSQC).

Elemental Analysis (%) for $C_{81}H_{34}F_{58}N_2NiO$: Found (Calc.)
C 44.78 (43.99); H 2.88 (1.55); N 1.98 (1.27)

Synthesis of κ²-(N,O)-salicylaldiminato nickelI(II) methyl [α-methoxy-ω-amino poly(ethylene glycol)] complexes (1^{Ant}-R^F/PEG, 2^{Ant}-R^F/PEG and 3^{Ant}-R^F/PEG)

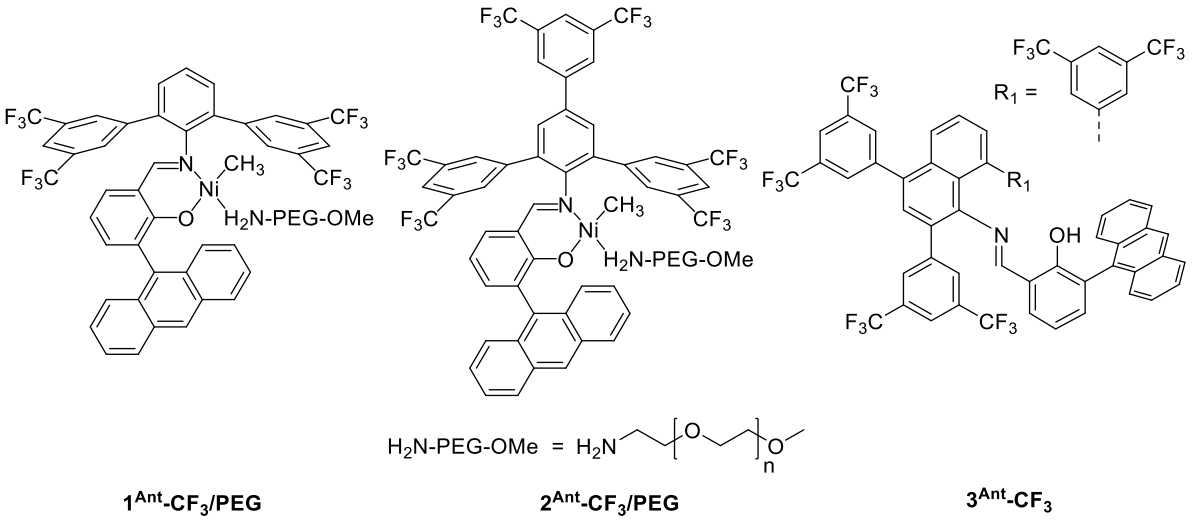

The reference catalysts **1^{Ant}-CF_3/PEG**[177] and **2^{Ant}-CF_3/PEG**[178,381] and salicylaldimine **3^{Ant}-CF_3**[125] were synthesized and characterized according to reported procedures.

{3-(9-anthryl)-N-[2,6-bis(3,5-diperfluorohexylphenyl)phenyl]salicylaldiminato- κ²-N,O}methyl[α-methoxy-ω-amino poly(ethylene glycol)]nickel(II) (**1^{Ant}-C_6F_{13}/PEG**)

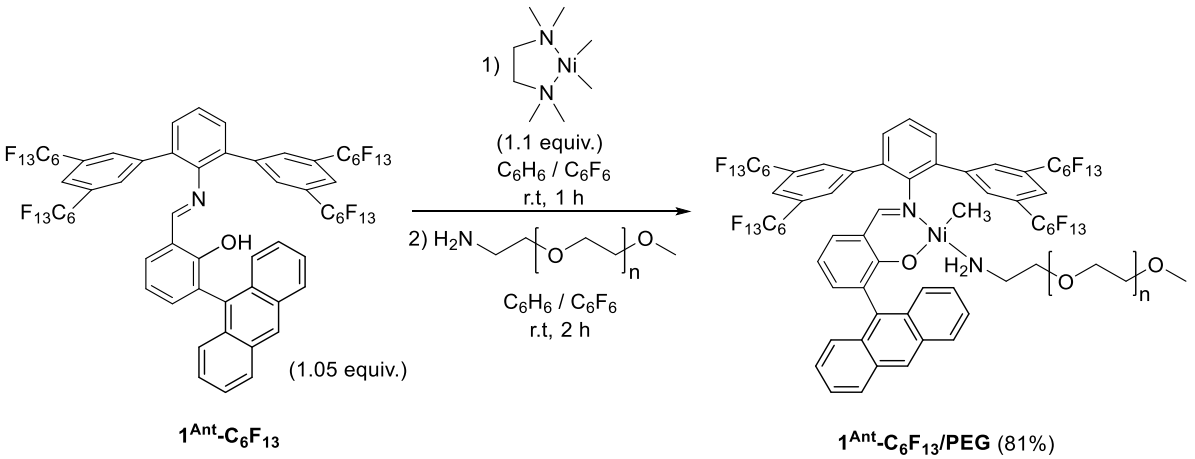

Scheme 4.11. Synthesis of hydrophilic κ²-(*N,O*)-salicylaldiminato nickel(II) methyl complex **1^{Ant}-C_6F_{13}/PEG**. The labile ligand (α-methoxy-ω-amino poly[ethylene glycol]) was added to a reacted mixture of nickel precursor and salicylaldimine and stirred at room temperature.

To 17 mg [(tmeda)$NiMe_2$] (83 µmol, 1.1 equiv.) was added a solution of 142 mg salicylaldimine **1^{Ant}-C_6F_{13}** (79 µmol, 1.05 equiv.) in a mixture of benzene/hexafluorobenzene (4.5 mL/1.5 mL) and stirred for 1 hour at room temperature. During the addition, methane evolution was observed

and an orange to red solution (slightly turbid) was obtained. 147 mg [α-Methoxy-ω-amino poly(ethylene glycol)] (75 µmol, 1 equiv., M = 1981 g mol^{-1}) in 1 mL benzene was then added and the reaction was stirred for further 2 hours at room temperature (the solution cleared up). After filtration through a syringe filter to remove nickel black, the solvent was removed under vacuum. The orange residue was washed with pentane (3-5 times, 7.5 mL each) until the filtrate remained almost colorless (slightly orange). After drying under vacuum, the desired product was obtained as an orange powder. Yield: 88 %, 66 µmol, 254 mg.

An analogous complex with M(H_2N-PEG-OMe) = 5516 g mol^{-1} was prepared by an identical procedure.

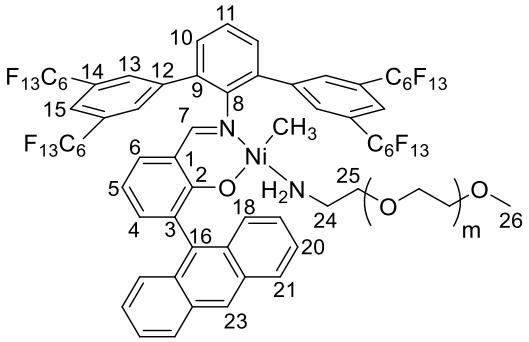

M = 3852 g/mol

1^{Ant}-C_6F_{13} / PEG, yield: 88 %

^{1}H NMR (400 MHz, C_6D_6, 300 K): δ (ppm) = 8.28 (s, 4H, *H-13*), 8.24 (s, 1H, *H-23*), 7.95 (s, 2H, *H-15*), 7.88 (m, 2H, *H-21, H-18*), 7.40 (m, 2H, *H-19*), 7.31 (m, 2H, *H-20*), 7.05 (s, 1H, H-7), 7.02-6.88 (m, 3H, *H-10, H-11*), 6.92 (m, 1H, H-11), 6.69 (dd, 1H, $^3J_{HH}$ = 8.1 Hz, $^4J_{HH}$ = 1.9 Hz, *H-6*), 6.41 (dd, 1H, ^3J = 7.0 Hz, ^3J = 8.1 Hz, *H-5*), 3.80 - 3.08 (m, 225H, *H*-PEG, *H-26*), 2.10 (t, $^3J_{HH}$ = 4.9 Hz, 2H, *H-25*), 1.58 (m, *H-24*), 0.03 (t, 2H, ^3J = 6.9 Hz, *-NH_2*), -1.41 (s, 3H, *Ni-CH_3*). Resonance for *H-4* obscured by benzene-d_6 resonance (7.14 ppm; assigned by ^{1}H,^{1}H-COSY).

^{19}F{^{1}H} (376 MHz, C_6D_6, 300 K): δ (ppm) = -81.0 (t, J_{FF} = 10 Hz, 12F, *CF_3*), -110.4 (t, $^3J_{FF}$ = 14 Hz , 4F, C_{arom}*CF_2*), -110.6 (t, $^3J_{FF}$ = 14 Hz , 4F, C_{arom}*CF_2*), -121.2 (m, 8F, *CF_2*), -121.6 (m, 8F, *CF_2*), -122.7 (m, 8F, *CF_2*), -126.1 (m, 8F, *CF_2*).

^{13}C{^{1}H} NMR (101 MHz, C_6D_6, 300 K): δ (ppm) = 167.7 (s, *C-7*), 165.4 (s, *C-2*), 150.8 (s, *C-8*), 141.9 (s, *C-12*), 137.8 (s, C-4), 136.2 (s, *C-16*), 133.4 (s, *C-9*), 133.3 (s, *C-6*), 132.7 (t, $^3J_{CF}$ = 5 Hz, *C-13*), 132.0 (s, *C-22*), 131.3-130.9 (m, *C-10*, *C-17*), 130.8 (s, *C-3*), 130.3 (t, $^3J_{CF}$ = 24 Hz, *C-14*), 128.6 (s, *C-21*), 127.9 (s, *C-18*), 126.8 (s, *C-11*), 126.1 (s, *C-23*), 125.3 (s, *C-20*), 124.9 (s, *C-19*), 124.5 (m, *C-15*), 119.8 (s, *C-1*), 114.1 (s, *C-5*), 121-105 (*-C_6F_{13}, broad due to multiple $^XJ_{CF}$ couplings*), 72.7-69.2 (m, *C*-PEG), 69.9 (s, *C-25*), 58.7 (s, *C-26*), 42.1 (s, *C-24*), -14.4 (s, *Ni-CH_3*).

Elemental analysis (%) for $C_{153}H_{206}F_{52}N_2NiO_{45}$: Found (Calculated):
C 47.58 (47.86); H 5.82 (5.41); N 0.84 (0.73)

{3-(9-anthryl)-N-[2,4,6-tris(3,5-diperfluorohexylphenyl)phenyl]salicylaldiminato-κ²-N,O}methyl-[α-methoxy-ω-amino poly(ethylene glycol)]nickel(II) (**2^{Ant}-C$_6$F$_{13}$/PEG**)

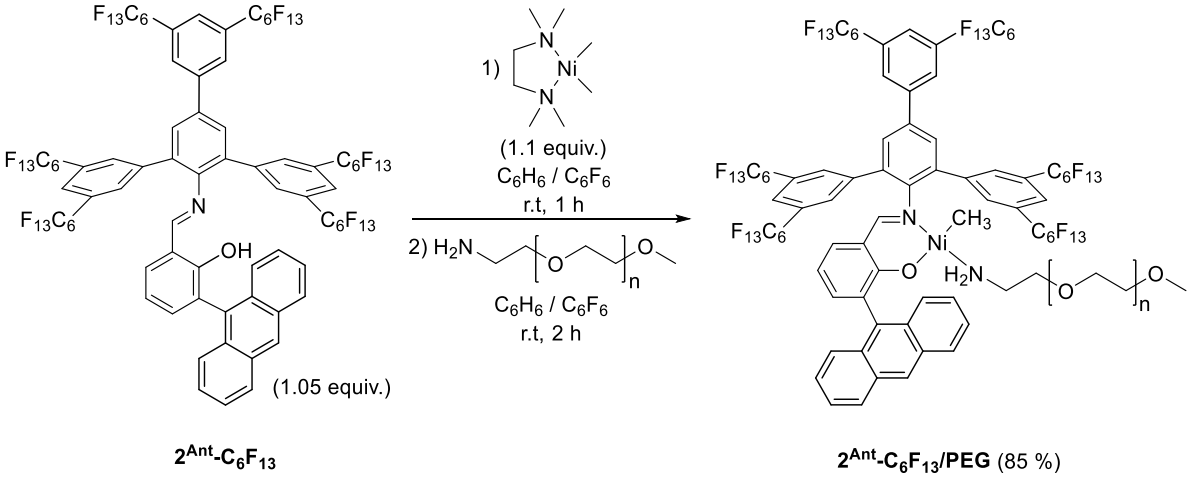

2^{Ant}-C$_6$F$_{13}$ **2^{Ant}-C$_6$F$_{13}$/PEG** (85 %)

Scheme 4.12. Synthesis of the hydrophilic κ²-(*N,O*)-salicylaldiminato nickel(II) methyl complex **2^{Amt}-C$_6$F$_{13}$/PEG**. The labile ligand (α-methoxy-ω-amino poly[ethylene glycol]) was added to a reacted mixture of nickel precursor and salicylaldimine and stirred at room temperature.

To 23 mg [(tmeda)NiMe$_2$] (110 µmol, 1.1 equiv.) was added a solution of 264 mg salicylaldimine **2^{Ant}-C$_6$F$_{13}$** (105 µmol, 1.05 equiv.) in a mixture of benzene/hexafluorobenzene (7 mL/3 mL) and stirred for 1 hour at room temperature. During the addition, methane evolution was observed and an orange to red solution (slightly turbid) was obtained. 198 mg [α-Methoxy-ω-amino poly(ethylene glycol)] (100 µmol, 1 equiv., M = 1981 g mol^{-1}) in 1 mL benzene was then added and the reaction stirred for further 2 hours at room temperature (the solution cleared up). After filtration through a syringe filter to remove nickel black, the solvent was removed under vacuum. The orange residue was washed with pentane (3-5 times, 7.5 mL each) until the filtrate remained almost colorless (slightly orange). After drying under vacuum, the desired product was obtained as orange powder. Yield: 85 %, 85 µmol, 388 mg.

An analogous complex with M(H$_2$N-PEG-OMe) = 5516 g mol^{-1} was prepared by an identical procedure.

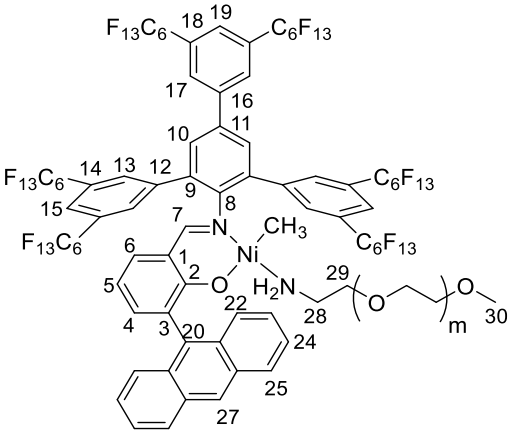

M = 4564 g/mol

2^{Ant}-C_6F_{13} / PEG, yield: 85 %

^{1}H NMR (400 MHz, C_6D_6, 300 K) δ (ppm) = 8.44 (s, 4H, *H-13*), 8.26 (s, 1H, *H-27*), 7.99 (s, 4H, *H-15, H-17*), 7.96-7.87 (m, 5H, *H-19*, *H-22*, *H-25*), 7.48 (s, 2H, *H-10*), 7.43 (m, 2H, *H-23 or H-24*), 7.33 (m, 3H, *H-7*, *H-23 or H-24*), 7.18 (m, 1H, *H-4*), 6.80 (dd, 1H, $^3J_{HH}$ = 1.5 Hz, $^4J_{HH}$ = 8.2 Hz, *H-6*), 6.42 (t, 1H, $^3J_{HH}$ = 7.5 Hz, *H-5*), 3.80-3.25, 3.15-3.09. 2.92 (m, 206H, *H-PEG*, *H-30*), 2.12 (m, 2H, $^3J_{HH}$ = 4.9 Hz, *H-29*), 1.61 (m, 2H, *H-28*), 0.09 (t, 2H,$^3J_{HH}$ = 7.1 Hz, *-NH₂*), -1.30 (s, 3H, *Ni-CH₃*).

^{19}F{^{1}H} NMR (376 MHz, C_6D_6, 300 K): δ (ppm) = -81.2 (t, J_{FF} = 10 Hz, 12F, *CF₃*), -81.4 (t, J_{FF} = 10 Hz, 6F, *CF₃*), -110.6 (m, 8F, C_{arom}*CF₂*), -111.2 (t, J_{FF} = 15 Hz, 4F, C_{arom}*CF₂*), -121.1 to -122.2 (m, 24F, *CF₂*), -123.0 (m, 12F, *CF₂*), -126.4 (m, 12F, *CF₂*).

^{13}C{^{1}H} NMR (101 MHz, C_6D_6, 300 K): δ (ppm) = 167.6 (s, *C-7*), 165.8 (s, *C-2*), 151.6 (s, *C-8*), 141.8 (s, *C-16*), 141.2 (s, *C-12*), 138.3 (s, *C-4*), 136.7 (s, *C-11*), 135.8 (s, *C-20*), 134.8 (s, *C-9*), 133.3 (s, *C-6*), 132.7 (m, *C-13*), 132.0 and 131.1 (s each, *C-21, C-26*), 131.5 (t, $^3J_{CF}$ = 25.0 Hz, *C-18*), 131.1 (s, *C-3*), 130.8 (t, $^3J_{CF}$ = 25.0 Hz, *C-14*), 129.9 (s, *C-10*), 129.2 (m, *C-15*), 128.7 and 127.9 (s each, *C-22, C-25*), 126.2 (s, *C-27*), 125.4 (s, *C-7*), 125.0 (m, *C-17, C-19, C-23, C-24*), 119.8 (s, *C-1*), 122-107 (*-C_6F_{13}, broad due to multiple $^XJ_{CF}$ couplings*), 72.4, 71.4-70.6, 70.4, 69.9 (*C-PEG*), 70.4 (s, *H-29*), 58.7 (s, *H-30*), 42.2 (s, *H-28*), -14.3 (s, *Ni-CH₃*).

Elemental analysis (%) for $C_{171}H_{208}F_{78}N_2NiO_{45}$: Found (Calculated):
C 45.38 (45.12); H 4.92 (4.61); N 0.68 (0.62)

{3-(9-anthryl)-N-{2,4,9-tris[(3,5 bistrifluoro-methyl)phenyl]-naphthalen}salicylaldiminato-κ²-N,O}methyl[α-methoxy-ω-amino poly(ethylene glycol)]-nickel(II) (**3^{Ant}-CF$_3$/PEG**)

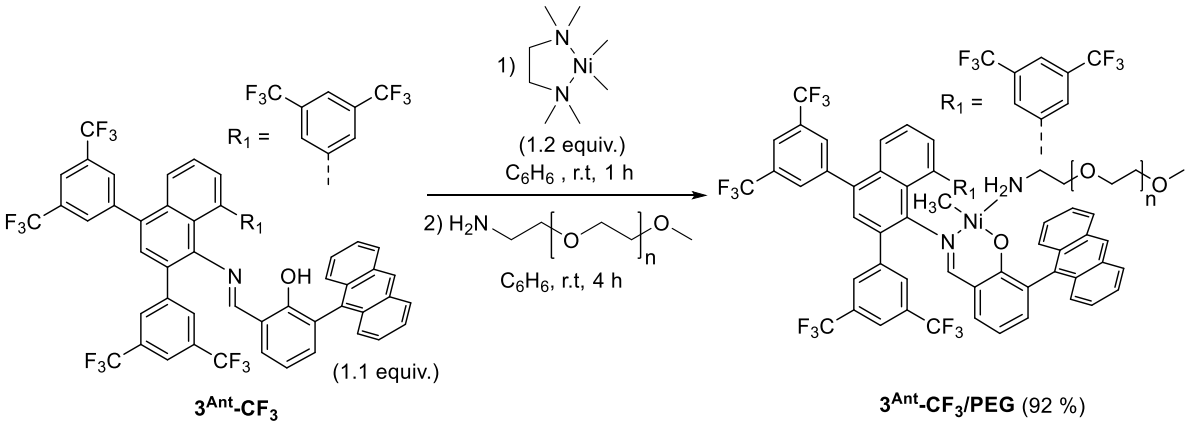

Scheme 4.13. Synthesis of the hydrophilic κ²-(*N,O*)-salicylaldiminato nickel(II) methyl complex **3^{Ant}-CF$_3$/PEG**. The labile ligand (α-methoxy-ω-amino poly[ethylene glycol]) was added to a reacted mixture of nickel precursor and salicylaldimine and stirred at room temperature.

To 19 mg [(tmeda)NiMe$_2$] (90 µmol, 1.2 equiv.) was added a solution of 91 mg salicylaldimine **3^{Ant}-CF$_3$** (82.5 µmol, 1.1 equiv.) in 7 mL of benzene for 1 hour at room temperature. During the addition, methane evolution was observed and an orange to red solution (slightly turbid) was obtained. 414 mg [α-Methoxy-ω-amino poly(ethylene glycol)] (75 µmol, 1 equiv., M = 5516 g/mol) in 1 mL benzene was then added and the reaction stirred for further 4 hours at room temperature (the solution cleared up). After filtration through a syringe filter to remove nickel black, the solvent was removed under vacuum. The orange residue was washed with pentane (3-5 times, 7.5 mL each) until the filtrate remained almost colorless (slightly orange). After drying under vacuum, the desired product was obtained as orange powder. Yield: 92 %, 69 µmol, 461 mg.

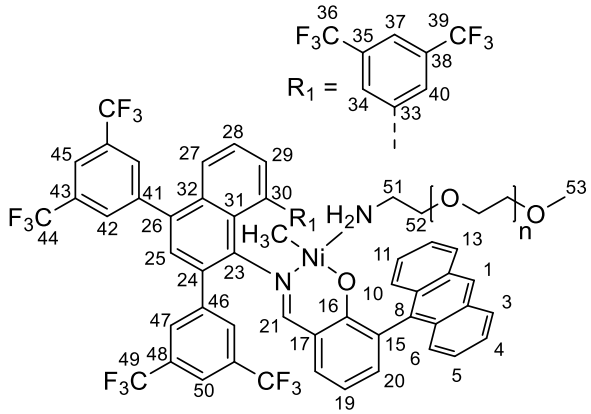

M = 6650 g/mol

3^{Ant}-CF$_3$ / PEG, yield: 92 %

^{1}H NMR (400 MHz, C_6D_6, 300 K): δ (ppm) = 8.91 (s, 1H, *H-34* or *H-40*), 8.39 (s, 2H, *H-42* or *H-47*), 8.25 (s, 1H, *H-1*), 7.93 (d, $^3J_{HH}$ = 8.7 Hz, 1H, *H-13*), 7.91 (s, *H-45* or *H-50*), 7.85 (m, 5H, *H-6*, *H-10*, H-37, *H-42 or H-47*), 7.80 (s, *H-45* or *H-50*), 7.73 (d, $^3J_{HH}$ = 8.8 Hz, 1H, *H-3*), 7.54 (dd, $^3J_{HH}$ = 8.5 Hz, $^4J_{HH}$ = 1.3 Hz, 1H, *H-27*), 7.46 (dd, $^3J_{HH}$ = 9.0 Hz, $^3J_{HH}$ = 6.3 Hz, 1H, *H-12*), 7.39 (m, 2H, *H-4*, *H-*

11), 7.25 (m, 2H, *H-5*, *H-34* or *H-40*), 7.18 (s, 1H, *H-25*), 7.13 (dd, $^{3}J_{HH}$ = 7.0 Hz, $^{4}J_{HH}$ = 1.8 Hz, 1H, *H-20*), 7.09 (t, $^{3}J_{HH}$ = 7.8 Hz, 1H, *H-28*), 6.99 (s, 1H, *H-21*), 6.91 (dd, $^{3}J_{HH}$ = 7.2 Hz, $^{4}J_{HH}$ = 1.3 Hz, 1H, *H-29*), 6.64 (dd, $^{3}J_{HH}$ = 8.1 Hz, $^{4}J_{HH}$ = 1.9 Hz, 1H, *H-18*), 6.41 (t, $^{3}J_{HH}$ = 7.5 Hz, 1H, *H-19*), 3.95-2.84 (m, 563H, *H*-PEG), 3.12 (s, 3H, *H-53*), 2.43 (dt, $^{2}J_{HH}$ = 9.5 Hz, $^{3}J_{HH}$ = 3.7 Hz, 1H, *H-52a*), 1.81 (td, $^{2}J_{HH}$ = 10.1 Hz, $^{3}J_{HH}$ = 2.9 Hz, 1H, *H-52b*), 1.72 (m, 1H, *H-51a*), 1.53 (m, 1H, *H-51b*), 0.70 (td, $^{3}J_{HH}$ = 10.8 Hz, $^{2}J_{HH}$ = 4.0 Hz, 1H, -N*H*$_2$a), -0.13 (td, $^{3}J_{HH}$ = 10.1 Hz, $^{2}J_{HH}$ = 2.6 Hz, 1H, -N*H*$_2$b), -1.56 (s, 3H, Ni-C*H*$_3$).

^{19}F{^{1}H} NMR (376 MHz, C_6D_6, 300 K): δ (ppm) = 62.0 (s, 3F, -*CF*$_3$), 62.2 (s, 6F, 2 x -*CF*$_3$), 62.4 (br. s, 6F, 2 x -*CF*$_3$), 62.6 (s, 3F, -*CF*$_3$).

^{13}C{^{1}H} NMR (101 MHz, C_6D_6, 300 K): δ (ppm) = 167.9 (s, *C-21*), 165.3 (s, *C-16*), 150.3 (s, *C-23*), 146.3 (s, *C-33*), 142.7 (s, *C-41* or *C-46*), 142.3 (s, *C-41* or *C-46*), 137.7 (s, *C-30*), 137.6 (s, *C-20*), 136.0 (s, *C-24*), 135.9 (s, *C-26*), 133.3 (s, *C-18*), 132.8 (m, *C-29*, *C-32*), 131.6 (s, *C-7*), 131.3-130.5 (m, *C-2, C-9, C-14, C-34* or *C-40, C-42, C-47*), 130.4 (s, *C-15*), 129.3 (s, *C-25*), 127.9 (*C-3*), 127.0 (s, *C-28*), 126.8 (s, *C-27*), 126.4 (s, *C-31*), 126.0 (s, *C-1*), 125.6-124.7 (m, *C-4, C-5, C-8, C-12, C-34* or *C-40*, *C-35, C-38, C-43* or *C-48*), 124.2 (q, $^{1}J_{CF}$ = 274 Hz, -*C*F$_3$), 124.1 (q, J = 273 Hz, -*C*F$_3$), 123.8 (q, J = 273 Hz, -*C*F$_3$), 122.7 (s, *C-43* or *C-48*), 122.2-120.9 (m, *C-37*, *C-45*, *C-50*), 119.8 (s, *C-17*), 114.3 (s, *C-19*), 72.6-69.7 (m, *C*-PEG), 70.4 (s, *C-51*), 58.7 (s, C-53), 42.2 (s, C-52), -14.1 (s, Ni-*C*H$_3$). Resonances for *C-3*, *C-6*, *C-10*, *C-11* and *C-13* are obscured by benzene-d$_6$ resonance (128.6, 128.4, 128.2 and 128.1 respectively; assigned by ^{1}H,^{13}C-HSQC).

Elemental analysis (%) for $C_{307}H_{534}F_{18}N_2NiO_{126}$: Found (Calculated):
C 55.19 (55.28); H 8.19 (8.07); N 0.49 (0.42)

{3-(9-anthryl)-N-{2,4-bis[(3,5-(bis)perfluorohexyl)phenyl]-9-[(3,5 bistrifluoro-methyl)phenyl]-naphthalen}salicylaldiminato- κ^2-N,O}methyl[α-methoxy-ω-amino poly(ethylene glycol)]-nickel(II) (**3^{Ant}-C$_6$F$_{13}$/PEG**)

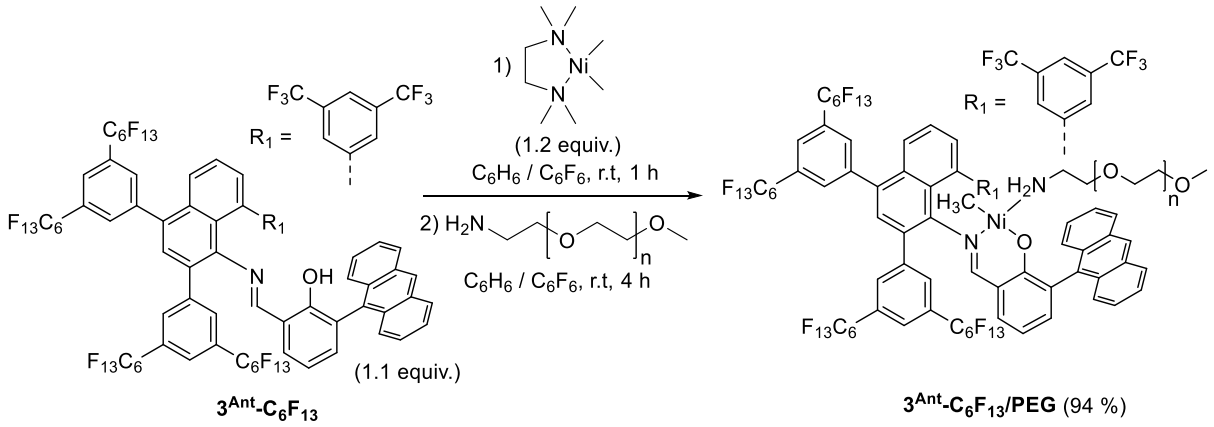

Scheme 4.14. Synthesis of the hydrophilic κ^2-(*N,O*)-salicylaldiminato nickel(II) methyl complex **3^{Ant}-C$_6$F$_{13}$/PEG**. The labile ligand (α-methoxy-ω-amino poly[ethylene glycol]) was added to a reacted mixture of nickel precursor and salicylaldimine and stirred at room temperature.

To 19 mg [(tmeda)NiMe$_2$] (90 μmol, 1.2 equiv.) was added a solution of 170 mg salicylaldimine **3^{Ant}-C$_6$F$_{13}$** (82.5 μmol, 1.1 equiv.) in a mixture of benzene/hexafluorobenzene [6

mL/1 mL] for 1 hour at room temperature. During the addition, methane evolution was observed and an orange to red solution (slightly turbid) was obtained. 414 mg [α-Methoxy-ω-amino poly(ethylene glycol)] (75 µmol, 1 equiv., M = 5516 g/mol) in 1 mL benzene was then added and the reaction stirred for further 4 hours at room temperature (the solution cleared up). After filtration through a syringe filter to remove nickel black, the solvent was removed under vacuum. The orange residue was washed with pentane (3-5 times, 7.5 mL each) until the filtrate remained almost colorless (slightly orange). After drying under vacuum, the desired product was obtained as orange powder. Yield: 94 %, 71 µmol, 540 mg.

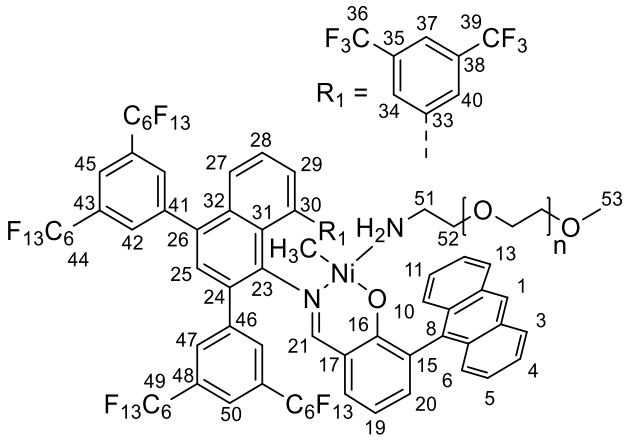

M = 7649 g/mol

3^{Ant}-C_6F_{13} / PEG, yield: 94 %

^{1}H NMR (400 MHz, C_6D_6, 300 K): δ (ppm) = 8.96 (s, 1H, *H-34* or *H-40*), 8.50 (s, 2H, *H-42* or *H-47*), 8.25 (s, 1H, *H-1*), 7.97 (s, 1H, *H-45* or *H-50*), 7.95 (m, 4H, *H-6, H-13, H-42 or H-47*), 7.91 (s, 1H, *H-45 or H-50*), 7.84 (s, 1H, *H-37*), 7.83 (d, $^3J_{HH}$ = 9.1 Hz, 1H, *H-10*), 7.72 (d, $^3J_{HH}$ = 8.9 Hz, 1H, *H-3*), 7.69 (dd, $^3J_{HH}$ = 8.5 Hz, $^4J_{HH}$ = 1.3 Hz, 1H, *H-27*), 7.46 (m, 1H, *H-5*), 7.39 (m, 2H, *H-4, H-12*), 7.30 (s, 1H, *H-25*), 7.25 (m, 2H, *H-11, H-34 or H-40*), 7.14 (m, 1H, *H-15*), 7.13 (dd, $^3J_{HH}$ = 7.0 Hz, $^4J_{HH}$ = 1.8 Hz, 1H, *H-20*), 7.06 (s, 1H, *H-21*), 6.93 (dd, $^3J_{HH}$ = 7.2 Hz, $^4J_{HH}$ = 1.3 Hz, 1H, *H-29*), 6.65 (dd, $^3J_{HH}$ = 8.2 Hz, $^4J_{HH}$ = 1.8 Hz, 1H, *H-18*), 6.40 (dd, $^3J_{HH}$ = 8.0 Hz, $^3J_{HH}$ = 6.9 Hz, 1H, H-19), 3.80-2.83 (m, 675H, *H*-PEG), 3.13 (s, 3H, H-53), 2.41 (dt, $^2J_{HH}$ = 10.0 Hz, $^3J_{HH}$ = 3.8 Hz, 1H, *H-52a*), 1.81 (td, $^2J_{HH}$ = 10.0 Hz, $^3J_{HH}$ = 2.8 Hz, 1H, *H-52b*), 1.72 (m, 1H, *H-51a*), 1.54 (m, 1H, *H-51b*), 0.75 (td, $^3J_{HH}$ = 11.1 Hz, $^2J_{HH}$ = 3.4 Hz, 1H, -NH_2a), -0.10 (td, $^3J_{HH}$ = 10.3 Hz, $^2J_{HH}$ = 2.1 Hz, 1H, -NH_2b), -1.52 (s, 3H, Ni-CH_3). Resonance for *H-28* obscured by benzene-d_6 resonance.

^{19}F{^{1}H} NMR (376 MHz, C_6D_6, 300 K): δ (ppm) = -62.1 (s, 3F, CF_3), -62.6 (s, 3F, CF_3), -81.2 (m, 12F, CF_3), -110.6 (m, 8F, $C_{arom}CF_2$), -121.6 (m, 16F, CF_2), -123.0 (m, 8F, CF_2), -126.5 (m, 8F, CF_2).

^{13}C{^{1}H} NMR (101 MHz, C_6D_6, 300 K): δ (ppm) = 167.4 (s, *C-21*), 165.1 (s, *C-16*), 150.3 (s, *C-23*), 145.8 (s, *C-33*), 142.1 and 142.0 (s, *C-41* and *C-46*), 137.7 (s, *C-30*), 137.4 (s, *C-20*), 135.7 (s, *C-26*), 135.4 (s, *C-24*), 134.0 (s, *C-18*), 132.9 (s, *C-29*), 132.5 (s, *C-43* or *C-48*), 132.4 (s, *C-32*, *C-42* or *C-47*), 132.1 (s, *C-42* or *C-47*), 131.9 (s, *C-14*), 131.0-129.0 (m, *C-2*, *C-7*, *C-17*, *C-25*, *C-35*, *C-34*, *C-38*, *C-40*), 126.9 (s, *C-28*), 126.3 (s, *C-27*, *C-31*), 126.1 (s, *C-1*), 125.8 (q, $^1J_{CF}$ = 284 Hz, *C-36* or *C-39*), 125.2-123.8 (m, *C-4, C-5, C-9, C-8, C-11, C-12, C-43* or *C-48*, *C-45* or *C-50*), 124.0 (s, *C-45* or *C-50*), 123.7 (q, $^1J_{CF}$ = 275 Hz, *C-36* or *C-39*), 121.1 (s, *C-37*), 120-105 (-C_6F_{13}, *broad due to multiple* $^XJ_{CF}$ *couplings*), 119.4 (s, *C-15*),

113.9 (s, *C-19*), 58.3 (s, *C-53*), 73.2-68.1 (m, *C-PEG*), 70.7 (s, *C-52*), 41.8 (s, *C-51*), -14.8 (s, *C-22*). Resonances for *C-3*, *C-6*, *C-10* and *C-13* are obscured by benzene-d_6 resonance (127.6, 127.7, 127.8 and 127.6 respectively; assigned by $^{1}H,^{13}C$-HSQC).

Elemental Analysis (%) for $C_{327}H_{534}F_{58}N_2NiO_{126}$: Found (Calc.)
C 51.45 (51.20); H 7.02 (7.49); N 1.04 (0.37)

4.4.5 Cyclic voltammetry of complexes (1^{Ant}-R^F/Pyr, 2^{Ant}-R^F/Pyr and 3^{Ant}-R^F/Pyr)

All electrochemical measurements were carried out with a computer-controlled BAS potentiostat, connected to a custom-built cyclindrical one-compartment cell (Prof. Winter research group). The experiments were performed under inert argon atmosphere. A spiral-shaped Pt wire and an Ag wire, sealed into glass capillaries, were used as counter and reference electrodes and introduced at opposite sides of the cell. A platinum electrode was used as working electrode and introduced through the top port of the cell. Prior to all experiments, the working electrode was polished with 1 µm and 0.25 µm diamond paste (purchased from *Buehler-Wirtz*). The complex was dissolved in approximately 6 mL of dichloromethane mixed with NBu_4^+ PF_6^- (0.1 M) as supporting electrolyte. Referencing was performed by addition of decamethylferrocene (Cp^*_2Fe) as an internal standard to the analyte solution, after all data of interest had been acquired, and another set of scans was recorded. Final referencing was performed against the ferrocene/ferrocenium couple with $E_{1/2}(Cp^*_2Fe)$ = -550 mV vs. $Cp_2Fe^{o/+}$. Electrochemical data were acquired with a standard sweep rate of 400 mV s^{-1}.

All cyclic voltammetry measurements of complexes showed oxidation and reduction transitions for the Ni(II)/Ni(III) pair. Only partial reversibility was observed, in line with an expected rapid decomposition of the formed Ni(III) species. Additional measurements of the free salicylaldehydes performed under otherwise identical conditions did not show redox transitions in the region of the corresponding pyridine precatalysts, suggesting metal centered oxidation and reduction processes.

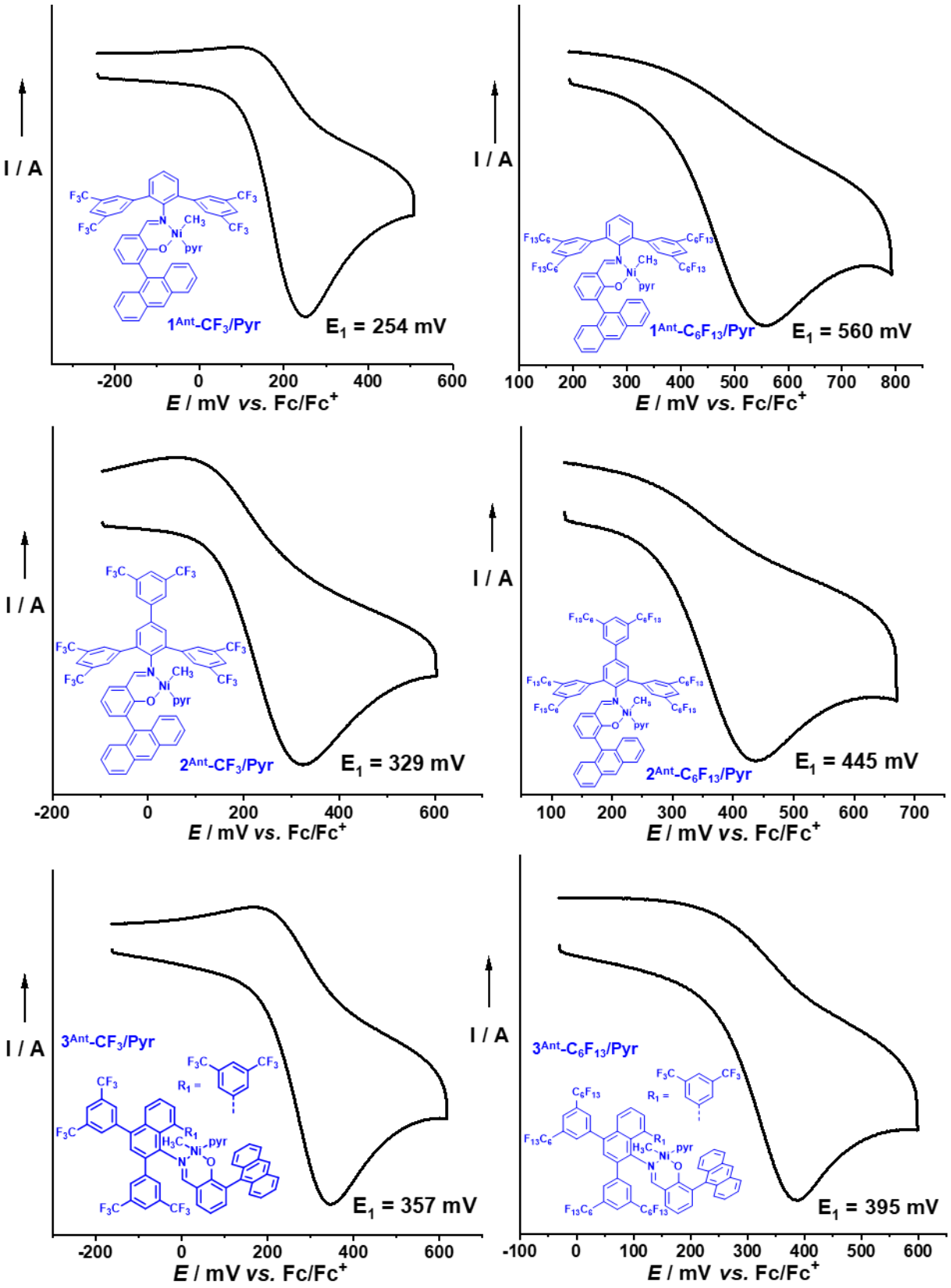

Figure 4.6. Cyclic voltammograms of complexes **1^{Ant}-R^{F}/Pyr** (*top*), **2^{Ant}-R^{F}/Pyr** (*center*) and **3^{Ant}-R^{F}/Pyr** (*bottom*).

4.4.6 Additional polymerization experiments in water

Table 4.3. Ethylene polymerization results of catalyst **1^{Ant}-C_6F_{13}/PEG** in aqueous surfactant solution after different reaction times.

entry	time [min]	yield PE [g][a]	TON[b]	M_n[c] x 10^3 [g mol^{-1}]	M_w/ M_n[c]	chains/ [Ni]	T_m[d] [°C] (crystallinity [%])	branches/ 1000 C[e]	d_h (Vol.) [nm][f]
1	30	2.34	11.1	354	1.12	0.9	140 (73) / 135 (55) 132	-	19 (0.15)
2	60	5.78	27.5	828	1.18	0.9	141 (72) / 134 (49) 134	-	27 (0.08)
3	90	7.64	36.3	1081	1.25	0.9	140 (70) / 134 (42) 134	-	28 (0.07)
4	120	8.96	42.6	1335	1.24	0.9	142 (72) / 135 (49) 134	< 1.0	30 (0.08)

Polymerization conditions: 7.5 µmol catalyst loading, 10 °C reaction temperature, 12.0 g sodium dodecyl sulfate, 3 g cesium hydroxide, 1.5 mL mesitylene, in 300 mL degassed water, 1000 rpm stirring rate, ultrasound applied prior to ethylene pressurization. [a] Determined by precipitation in methanol. [b] Given in mol [C_2H_4] x mol^{-1} [Ni]. [c] Determined via GPC at 160 °C. [d] Determined via DSC, reported as [1st heating cycle (crystallinity) \ 2nd heating cycle (crystallinity)] with 10 K/min heating rate, second line: 1st heating cycle with 1 K/min heating rate. [e] Determined via selective detection of methyl and methylene IR-bands in 1,2-dichlorobenzene during GPC measurements (calibrated versus samples with known degree of branching). [f] Determined via DLS, volume mean and PDI reported.

Table 4.4. Ethylene polymerization results of catalyst **2^{Ant}-C_6F_{13}/PEG** in aqueous surfactant solution after different reaction times.

entry	time [min]	yield PE [g][a]	TON[b]	M_n[c] x 10^3 [g mol^{-1}]	M_w/ M_n[c]	chains/ [Ni]	T_m[d] [°C] (Crystallinity [%])	branches/ 1000 C[e]	d_h (Vol.) [nm][f]
1	30	3.55	16.9	552	1.24	0.9	135 (70) / 131 (47) 131	-	21 (0.20)
2	60	7.65	36.4	1020	1.26	1.0	138 (68) / 132 (46) 134	-	27 (0.15)
3	90	11.57[g]	55.0	1461	1.28	1.1	141 (69) / 134 (41) 135	-	38 (0.18)
4	120	14.36[h]	68.2	2034	1.23	0.9	143 (70) / 135 (42) 135	< 1.0	40 (0.17)

Polymerization conditions: 7.5 µmol catalyst loading, 10 °C reaction temperature, 12.0 g sodium dodecyl sulfate, 3 g cesium hydroxide, 1.5 mL mesitylene, in 300 mL degassed water, 1000 rpm stirring rate, ultrasound applied prior to ethylene pressurization. [a] Determined by precipitation in methanol. [b] Given in mol [C_2H_4] x mol^{-1} [Ni]. [c] Determined via GPC at 160 °C. [d] Determined via DSC, reported as [1st heating cycle (crystallinity) \ 2nd heating cycle (crystallinity)] with 10 K/min heating rate, second line 1st heating cycle with 1 K/min heating rate. [e] Determined via selective detection of methyl and methylene IR-bands in 1,2-dichlorobenzene during GPC measurements (calibrated versus samples with known degree of branching). [f] Determined via DLS, volume mean and PDI reported. [g] Including 1.1 g agglomerates. [h] Including 1.8 g agglomerates.

Table 4.5. Ethylene polymerization results of catalyst **3^{Ant}-C_6F_{13}/PEG** in aqueous surfactant solution after different reaction times.

entry	time [h]	yield PE [g][a]	TON[b]	M_n[c] x 10^3 [g mol^{-1}]	M_w/ M_n[c]	chains/ [Ni]	T_m[d] [°C] (crystallinity [%])	branches/ 1000 C[e]	d_h (Vol.) [nm][f]
1	0.5	1.59	7.6	471	1.10	0.5	143 (68) / 137 (46) 135	-	17 (0.21)
2	1	3.38	16.1	818	1.16	0.6	142 (60) / 134 (41) 136	-	21 (0.27)
3	2	5.98	28.4	1094	1.19	0.7	143 (68) / 136 (46) 138	-	21 (0.10)
4	4	9.39	44.6	1609	1.21	0.8	142 (65) / 136 (41) 137	< 1.0	21 (0.17)

Polymerization conditions: 7.5 µmol catalyst loading, 15 °C reaction temperature, 6 g sodium dodecyl sulfate, 1.5 g cesium hydroxide, 0.75 mL mesitylene, in 150 mL degassed water, 1000 rpm stirring rate, ultrasound applied prior to ethylene pressurization. [a] Determined by precipitation in methanol. [b] Given in mol [C_2H_4] x mol^{-1} [Ni]. [c] Determined via GPC at 160 °C. [d] Determined via DSC, reported as [1st heating cycle (crystallinity) \ 2nd heating cycle (crystallinity)] with 10 K/min heating rate, second line 1st heating cycle with 1 K/min heating rate. [e] Determined via selective detection of methyl and methylene IR-bands during GPC measurements (calibrated versus samples with known degree of branching). [f] Determined via DLS, volume mean and PDI reported.

4.4.7 Polymerization experiments in toluene

Table 4.6. Ethylene polymerization results in toluene.

entry	precatalyst	E_1[a] [mV]	T [°C]	yield PE [g]	TOF[b]	M_n[c] x 10^3 [g mol^{-1}]	M_w/M_n[c]	chains/ [Ni]	T_m[d] [°C] (cryst. [%])	branches/ 1000 C[e]
1	1^{Ant}-CF_3/Pyr	254	30	2.83	60.6	240	2.5	2.3	132 (46)	1.7
2	1^{Ant}-C_6F_{13}/Pyr	560	30	3.40	72.7	623	1.8	1.1	131 (55)	1.1
3	1^{Ant}-CF_3/Pyr	254	50	6.08	130.1	52	2.2	23.6	120 (47)	9.3
4	1^{Ant}-C_6F_{13}/Pyr	560	50	8.90	190.4	44	1.6	43.8	118 (52)	7.9
5[f]	1^{Ant}-C_6F_{13}/Pyr	560	70	17.50	249.6	7	2.5	444.4	111 (52)	17.2[i]
6[g]	2^{Ant}-CF_3/Pyr	329	30	4.06	43.5	446	1.6	1.8	132 (55)	1.7[i]
7	2^{Ant}-C_6F_{13}/Pyr	445	30	3.08	65.9	309	2.3	2.0	133 (53)	< 1.0
8[g]	2^{Ant}-CF_3/Pyr	329	50	6.91	74.0	32	2.5	43.9	118 (55)	10.6[i]
9	2^{Ant}-C_6F_{13}/Pyr	445	50	6.84	146.3	32	1.7	43.3	114 (47)	10.4
10[f]	2^{Ant}-C_6F_{13}/Pyr	445	70	16.03	228.6	5	2.5	658.5	109 (53)	20.2[i]
11[h]	3^{Ant}-CF_3/Pyr	357	40	2.02	72.0	926	1.1	0.7	136 (41)	< 1.0
12[h]	3^{Ant}-C_6F_{13}/Pyr	395	40	1.55	55.1	843	1.1	0.6	135 (44)	1.9[i]
13[h]	3^{Ant}-CF_3/Pyr	357	50	4.26	152.0	1166	1.1	1.2	134 (62)	1.5[i]
14[h]	3^{Ant}-C_6F_{13}/Pyr	395	50	3.97	141.7	995	1.1	1.3	133 (41)	2.2[i]
15[h]	3^{Ant}-CF_3/Pyr	357	60	7.55	269.1	1297	1.3	1.9	133 (41)	1.5[i]
16[h]	3^{Ant}-C_6F_{13}/Pyr	395	60	6.47	230.5	1170	1.2	1.8	132 (40)	1.7[i]

Polymerization conditions: 5 µmol catalyst loading, 20 minutes reaction time, 40 bar ethylene pressure, in 100 mL toluene. [a] Determined via cyclic voltammetry. [b] Given in mol [C_2H_4] x mol^{-1} [Ni] x h^{-1}. [c] Determined via GPC at 160 °C. [d] Determined via DSC (10 K min^{-1}), 2nd heating cycle reported. [e] Determined via selective detection of methyl and methylene IR-bands in 1,2-dichlorobenzene during GPC measurements (calibrated versus samples with known branching content). [f] 30 minutes reaction time. [g] Data from literature[111], 40 minutes reaction time, otherwise identical conditions. [h] 3 µmol catalyst loading. [i] Determined via ^{13}C-NMR spectroscopy.

4.4.8 Analysis of branch contents by IR measurements (GPC-IR)

GPC requires a detector, that can determine the concentration of polymer in solution after the analyte has passed the separation columns. The obtained curve can then be used in combination with a proper calibration to determine the molecular weight distribution. While refractive index detectors are very common for that propose, infrared detectors are highly suited as well and less sensitive to errors.[382,383] The Polymer Char GPC-IR device employs an IR5 device, incorporating a high-temperature flow-through cell, interference filters at different wavelengths and a high sensitivity thermoelectrically cooled mercury-cadmium-telluride (MCT) IR detector. This ensures a high sensitivity towards the analyte and an excellent baseline stability. With the appropriate filters installed, the occurrence (and concentration) of methylene and methyl groups can be separately determined, directly during a GPC experiment.[383-385] By calibration of the signal ratio between those two groups with samples of known branch content (determined by ^{13}C NMR spectroscopy), the branching degree of the sample can be determined.

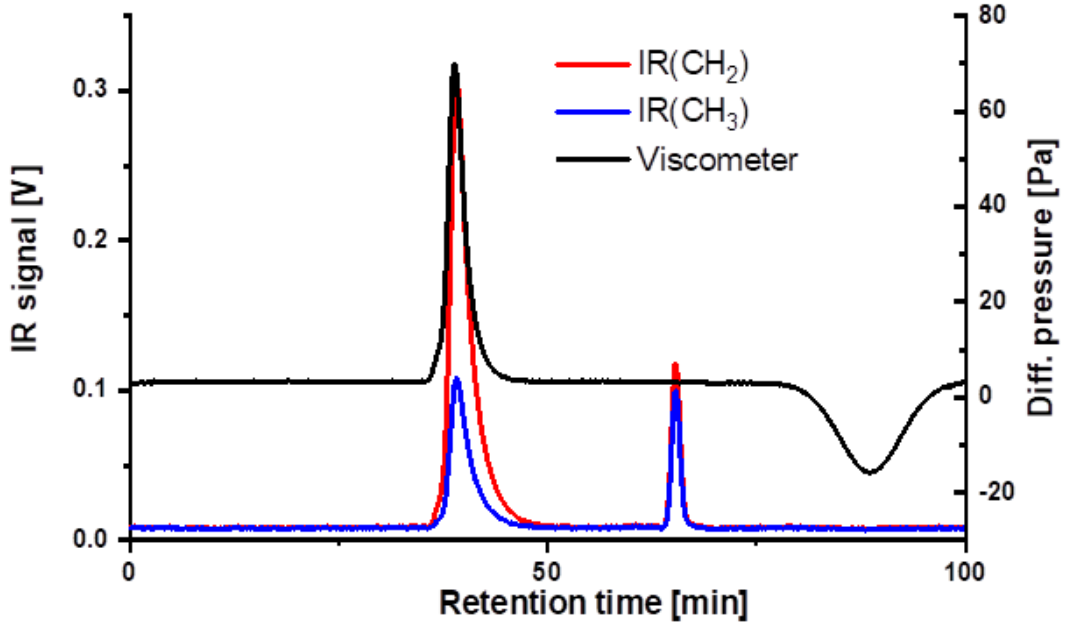

Figure 4.7. GPC elugram of high molecular weight polyethylene with different detector signals shown (*red*: infra red, methylene; *blue*: infra red, methyl; *black*: viscosity). Heptane was added as flow marker.

In detail, the methyl band signal intensity [CH_3] is put into relation with the overall intensity of all groups ([CH_3] + [CH_2]), according to equation 1.

$$\frac{[CH_3]}{[CH_2]+[CH_3]} \quad (1)$$

In principle, the branching degree could then be separately calculated for every molecular weight distribution curve slice and low molecular weight and high molecular weight fractions compared. To ensure comparability with branching degrees determined via ^{13}C-NMR spectroscopy, that always considers the whole sample and, hence, provides mean values over all molecular weight fractions, the whole signal intensity was used in GPC-IR measurements in the form of peak integrals (Figure 4.8).

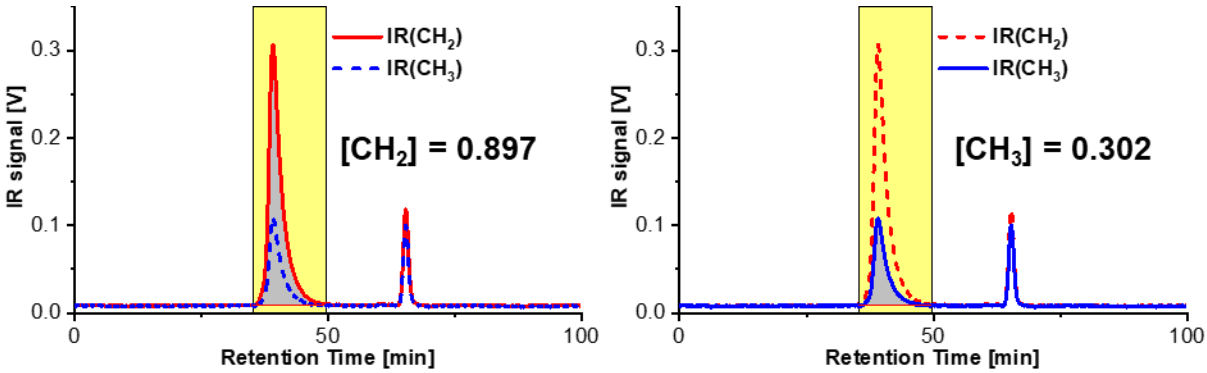

Figure 4.8. Exemplary GPC-IR measurement raw dataset with peak integrals shown to determine methyl ([CH_2]) and methylene ([CH_3]) signal intensities.

The calculated signal ratio from equation 1 could then directly be compared with the calibration curve, created from measurements of samples with known branch content (Figure 4.9).

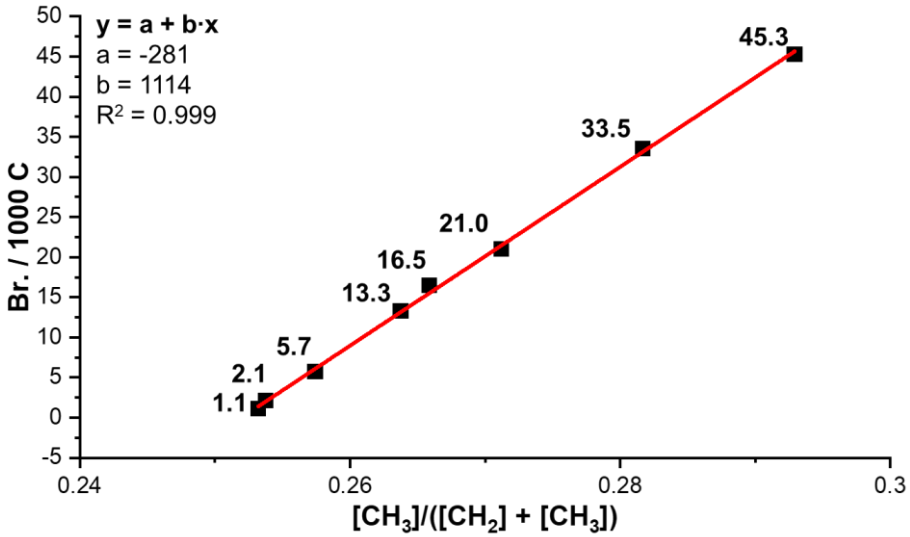

Figure 4.9. Calibration curve used to determine the branch content of polyethylene samples from GPC-IR measurements.

Please note, that due to slight overlapping of methyl and methylene IR bands, a signal at the methyl group detector is always present. This leads to a slightly shifted calibration curve

with the signal intensity ratio being not zero for zero branches per 1000 carbon atoms. Hence, a limited sensitivity for values below 1 branch per 1000 carbon atoms is assumed. Additionally, the measurements do not give any information about the branch length. For polyethylene samples discussed in this thesis, ^{13}C NMR spectroscopy experiments revealed presence of exclusively methyl branches for branch contents below ~10 branches per 1000 carbon atoms.

4.5 Appendix

4.5.1 NMR spectra of complexes

NMR spectra of κ²-(N,O)-salicylaldiminato nickel(II) methyl complexes (1^{Ant}-R^F/Pyr, 2^{Ant}-R^F/Pyr and 3^{Ant}-R^F/Pyr)

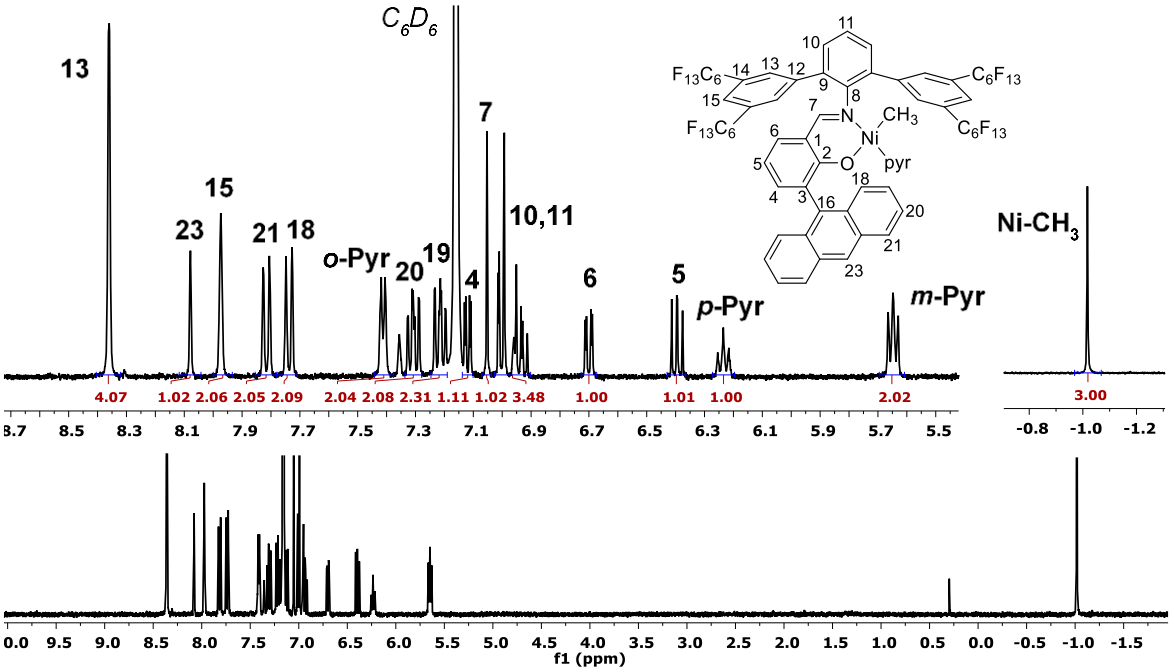

Figure 4.10. ^{1}H NMR spectrum (400 MHz, C_6D_6, 300 K) of complex **1^{Ant}-C_6F_{13}/Pyr.**

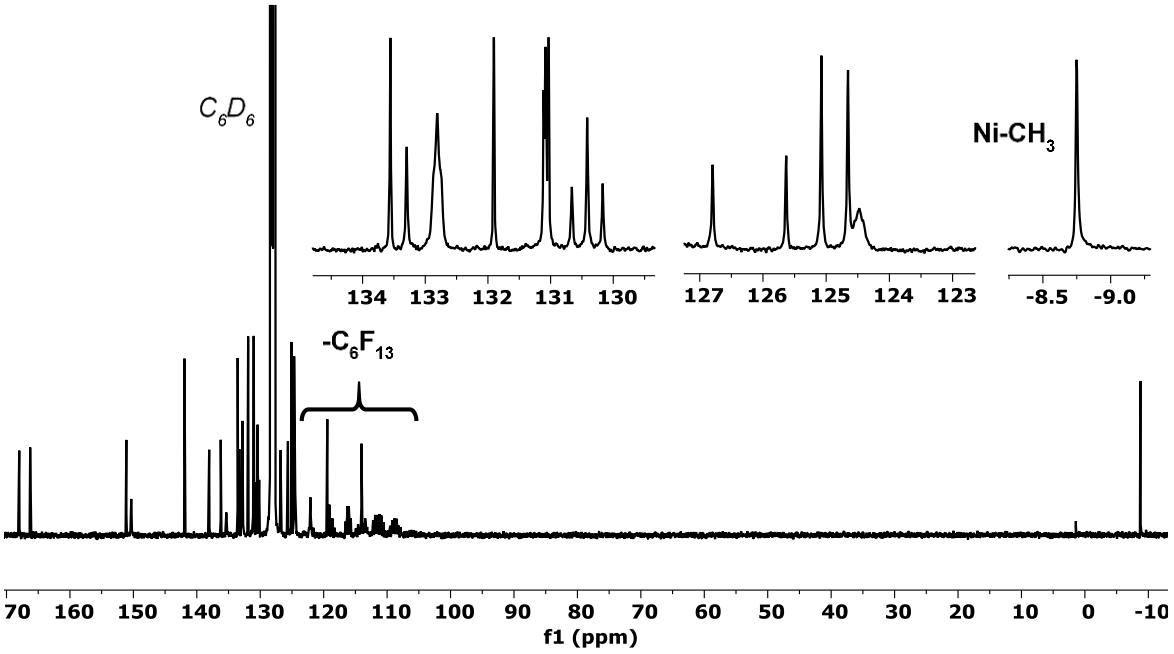

Figure 4.11. $^{13}C\{^1H\}$ NMR spectrum (101 MHz, C_6D_6, 300 K) of complex **1^{Ant}-C_6F_{13}/Pyr.**

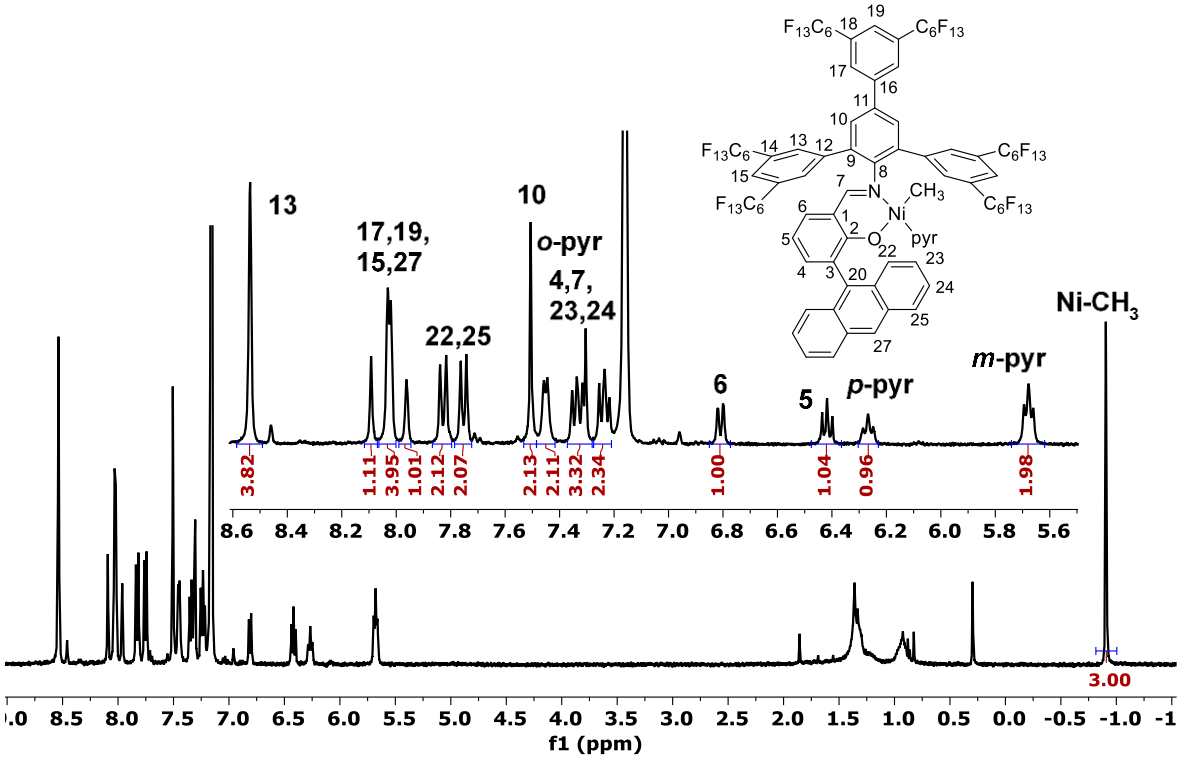

Figure 4.12. ^{1}H NMR spectrum (400 MHz, C_6D_6, 300 K) of complex $\mathbf{2^{Ant}\text{-}C_6F_{13}/Pyr.}$

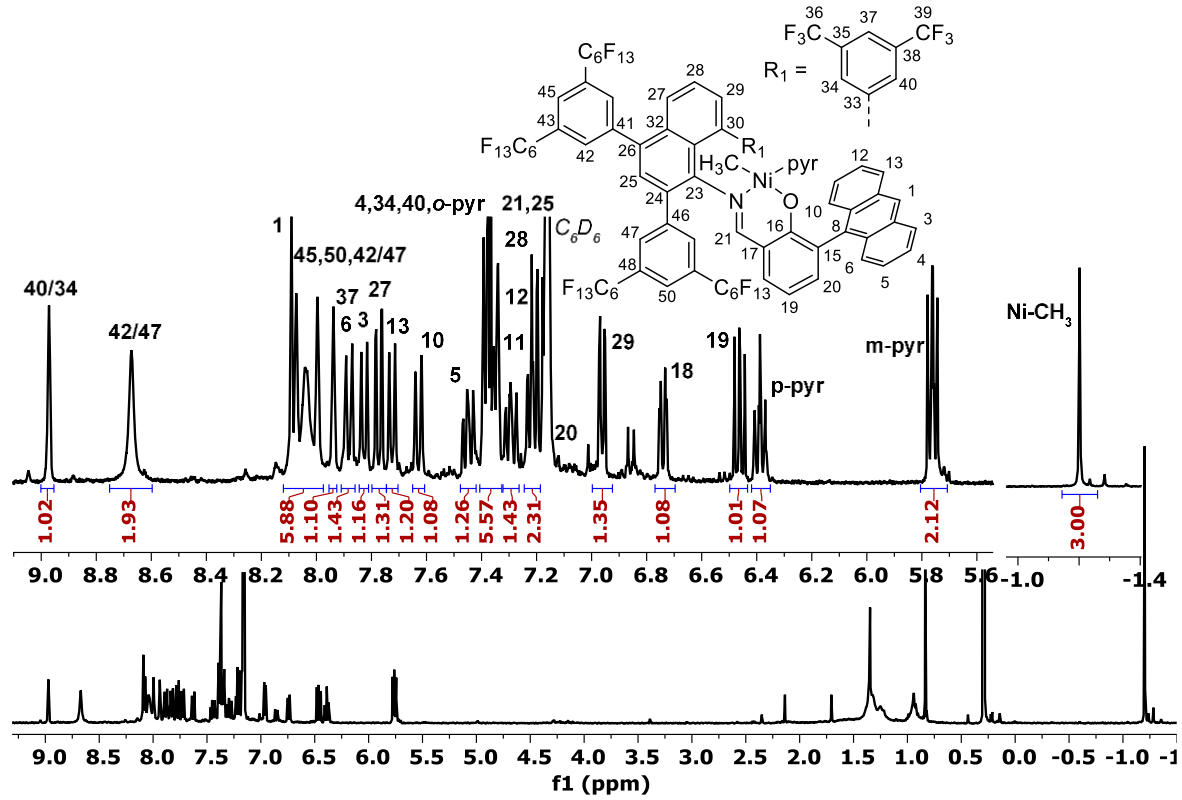

Figure 4.13. ^{1}H NMR spectrum (400 MHz, C_6D_6 / C_6F_6, 300 K) of complex $\mathbf{3^{Ant}\text{-}C_6F_{13}/Pyr.}$

NMR spectra of κ^2-(N,O)-salicylaldiminato nickel(II) methyl [α-methoxy-ω-amino poly(ethylene glycol] complexes (1^{Ant}-R^F/PEG, 2^{Ant}-R^F/PEG and 3^{Ant}-R^F/PEG)

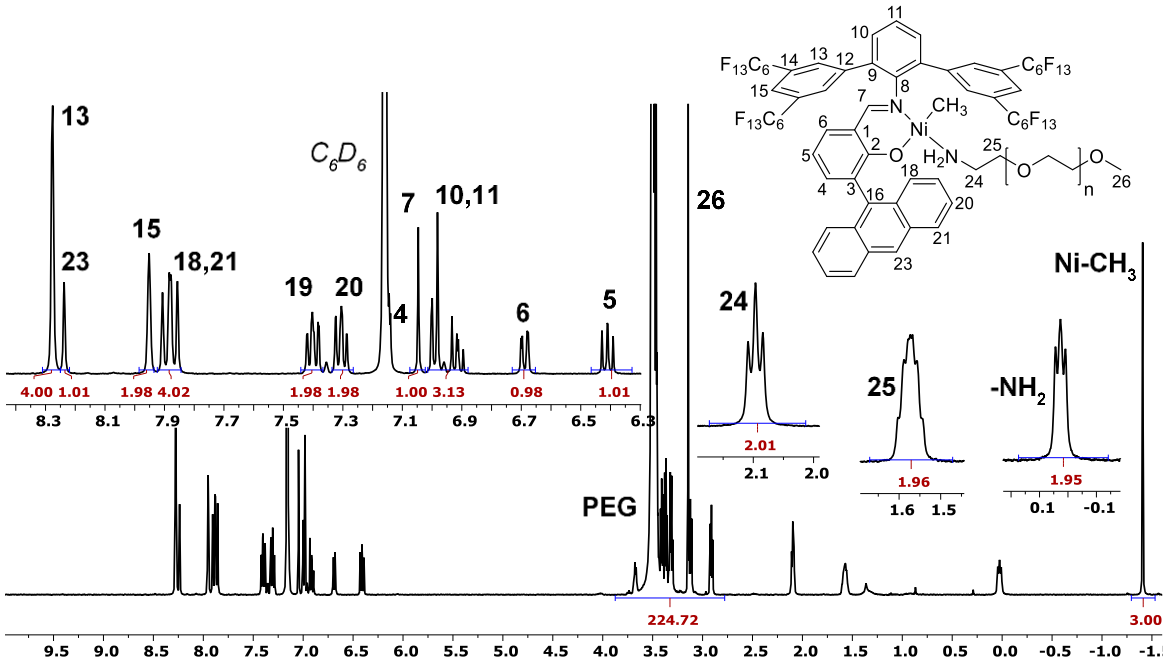

Figure 4.14. ^{1}H NMR spectrum (400 MHz, C_6D_6, 300 K) of complex **1^{Ant}-C_6F_{13}/PEG**.

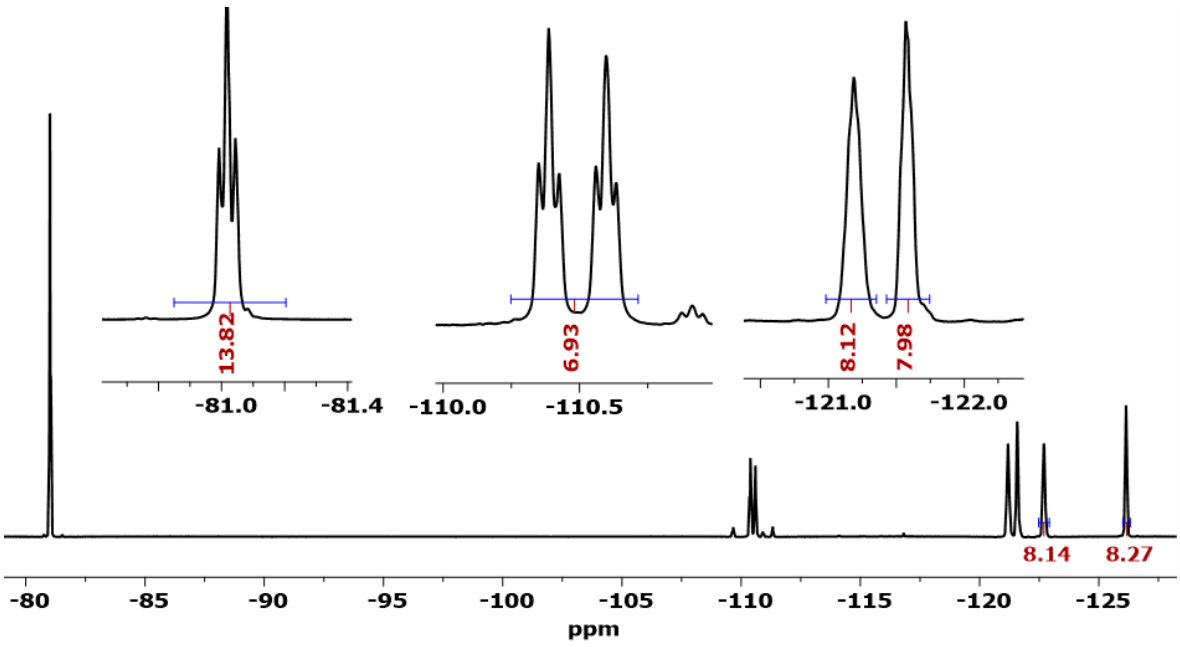

Figure 4.15. ^{19}F{^{1}H} spectrum (376 MHz, C_6D_6, 300 K) of complex **1^{Ant}-C_6F_{13}/PEG**.

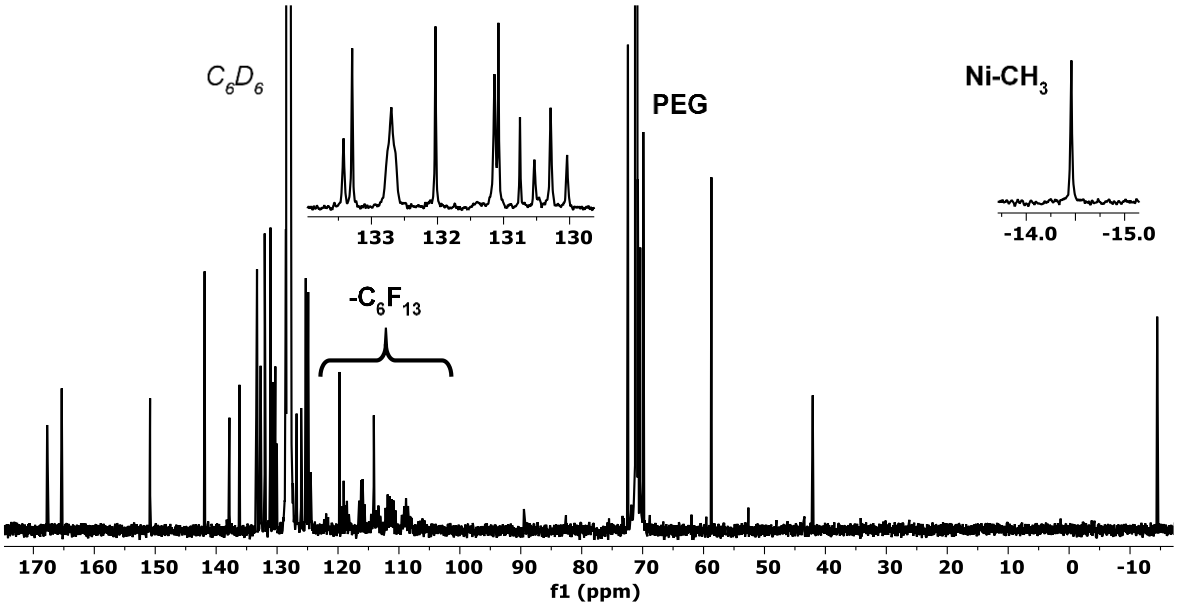

Figure 4.16. $^{13}C\{^{1}H\}$ NMR spectrum (101 MHz, C_6D_6, 300 K) of complex **1^{Ant}-C$_6$F$_{13}$/PEG.**

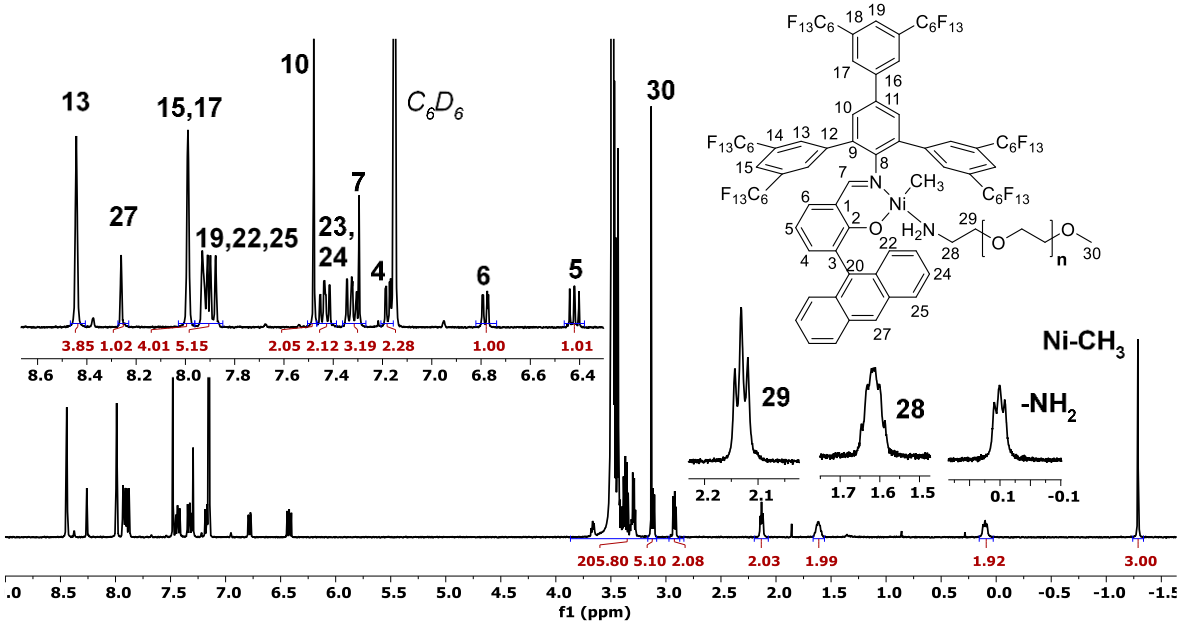

Figure 4.17. ^{1}H NMR spectrum (400 MHz, C_6D_6, 300 K) of complex **2^{Ant}-C$_6$F$_{13}$/PEG**.

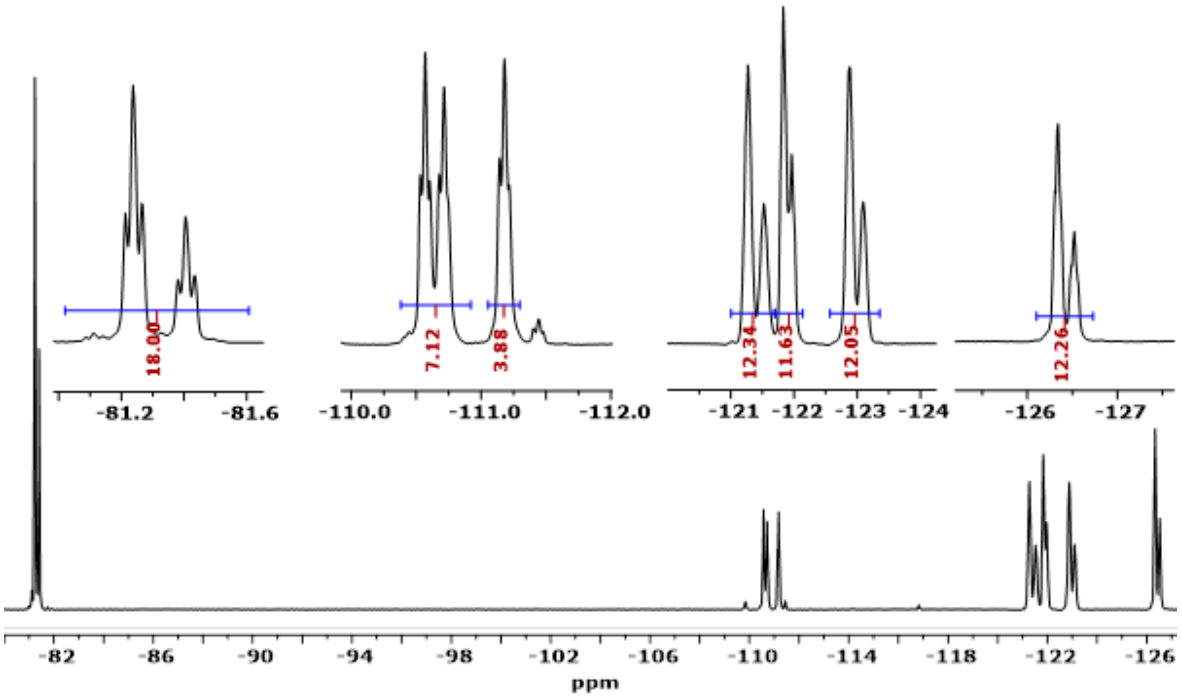

Figure 4.18. $^{19}F\{^{1}H\}$ spectrum (376 MHz, C_6D_6, 300 K) of complex $\mathbf{2^{Ant}\text{-}C_6F_{13}/PEG}$.

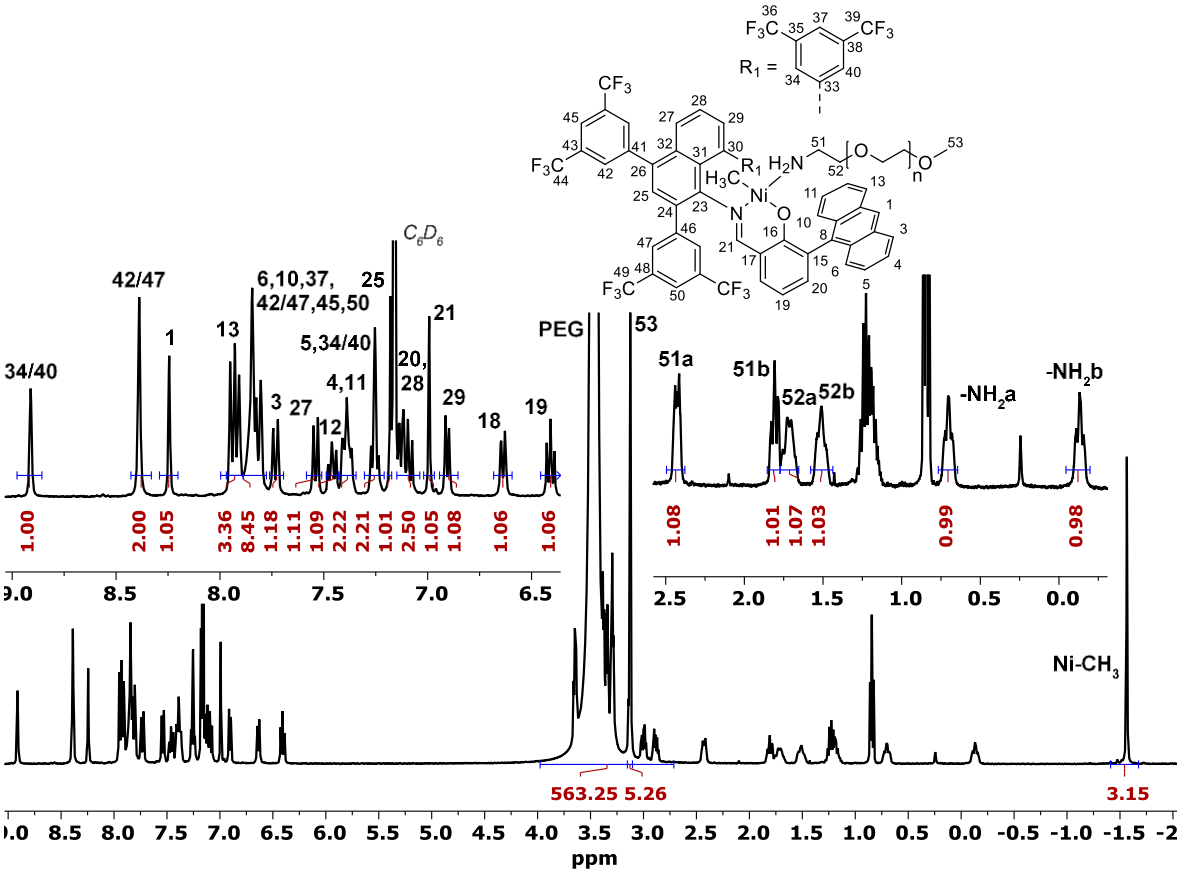

Figure 4.19. ^{1}H NMR spectrum (400 MHz, C_6D_6, 300 K) of complex $\mathbf{3^{Ant}\text{-}CF_3/PEG}$.

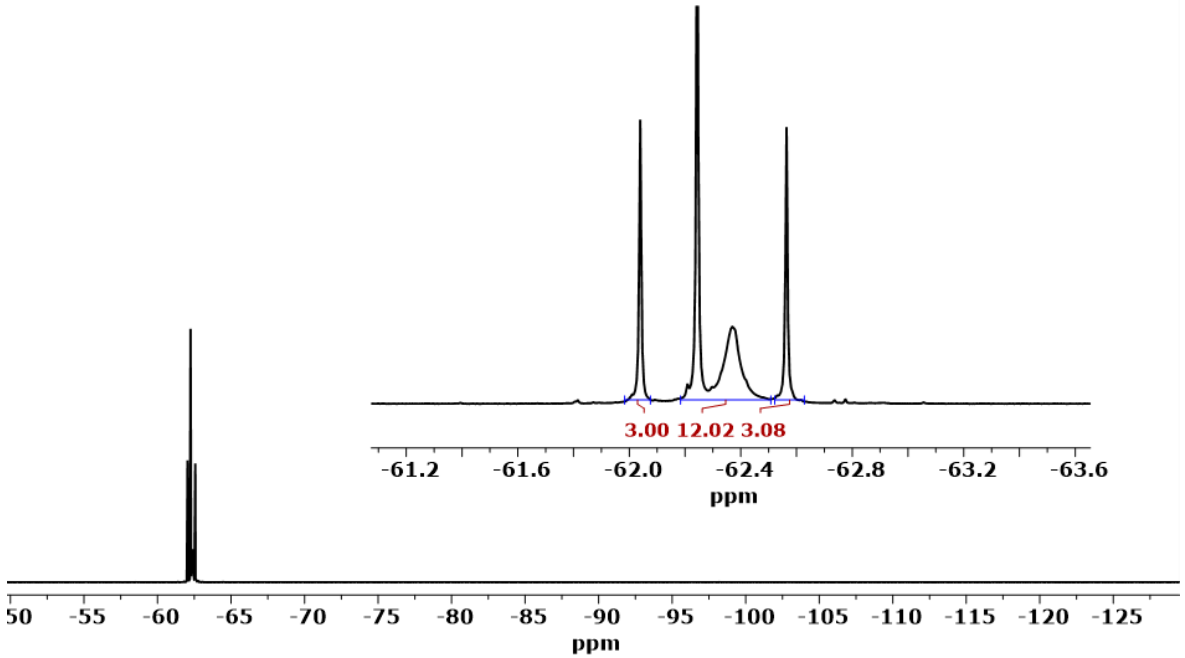

Figure 4.20. $^{19}F\{^{1}H\}$ spectrum (376 MHz, C_6D_6, 300 K) of complex $\mathbf{3^{Ant}\text{-}CF_3/PEG}$

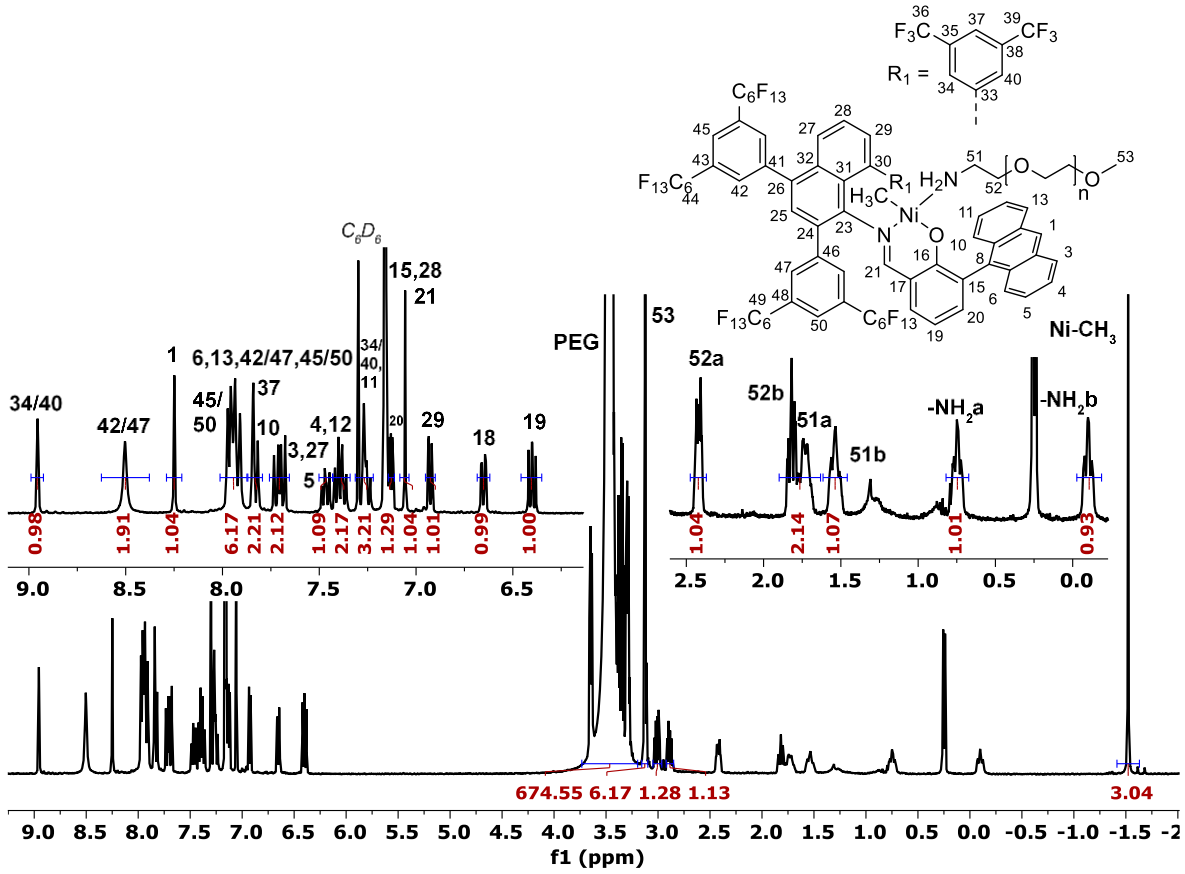

Figure 4.21. ^{1}H NMR spectrum (400 MHz, C_6D_6, 300 K) of complex $\mathbf{3^{Ant}\text{-}C_6F_{13}/PEG}$.

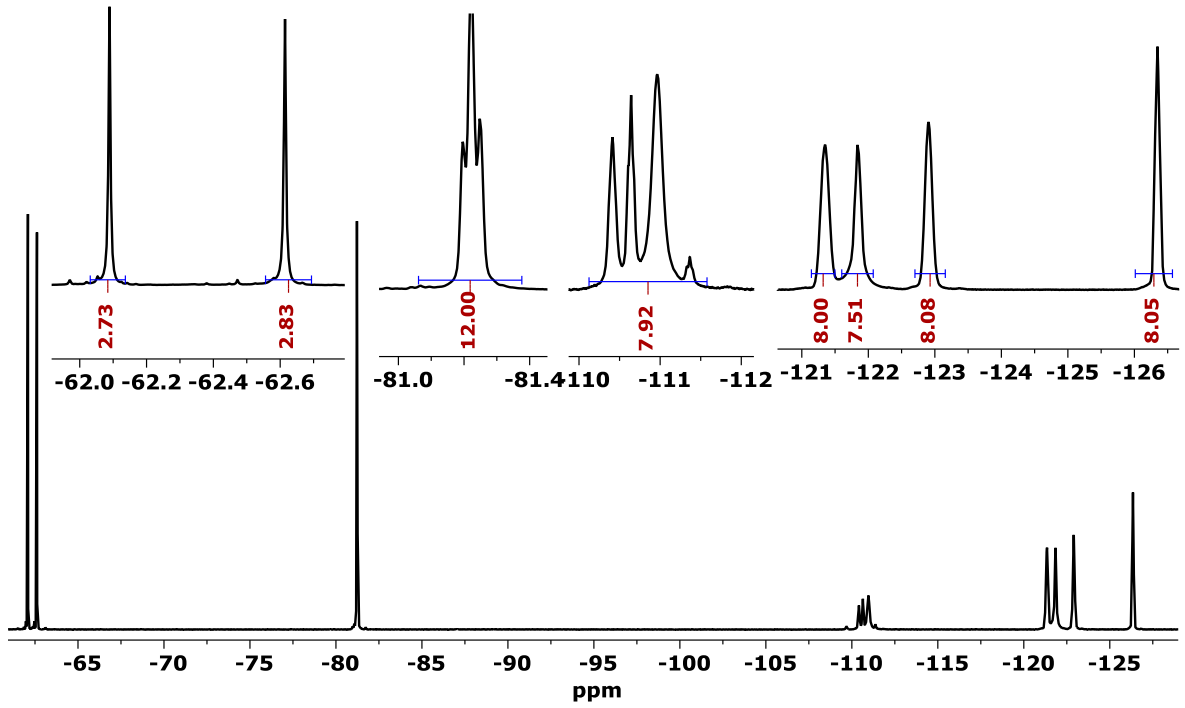

Figure 4.22. $^{19}F\{^{1}H\}$ spectrum (376 MHz, C_6D_6, 300 K) of complex $\mathbf{3^{Ant}\text{-}C_6F_{13}/PEG}$.

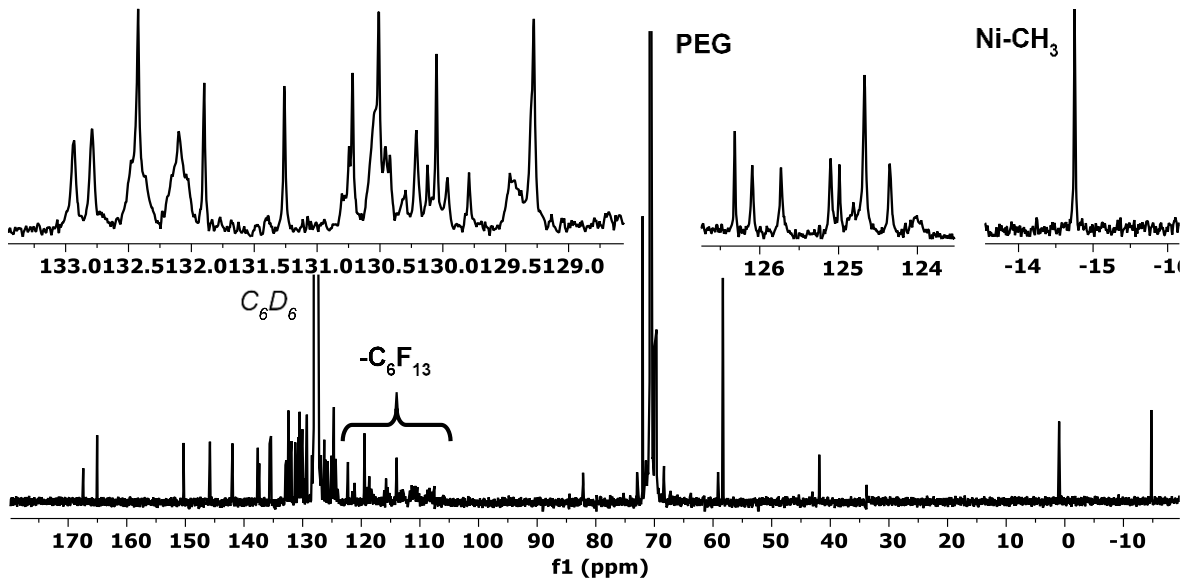

Figure 4.23. $^{13}C\{^{1}H\}$ NMR spectrum (101 MHz, C_6D_6, 300 K) of complex $\mathbf{3^{Ant}\text{-}C_6F_{13}/PEG}$.

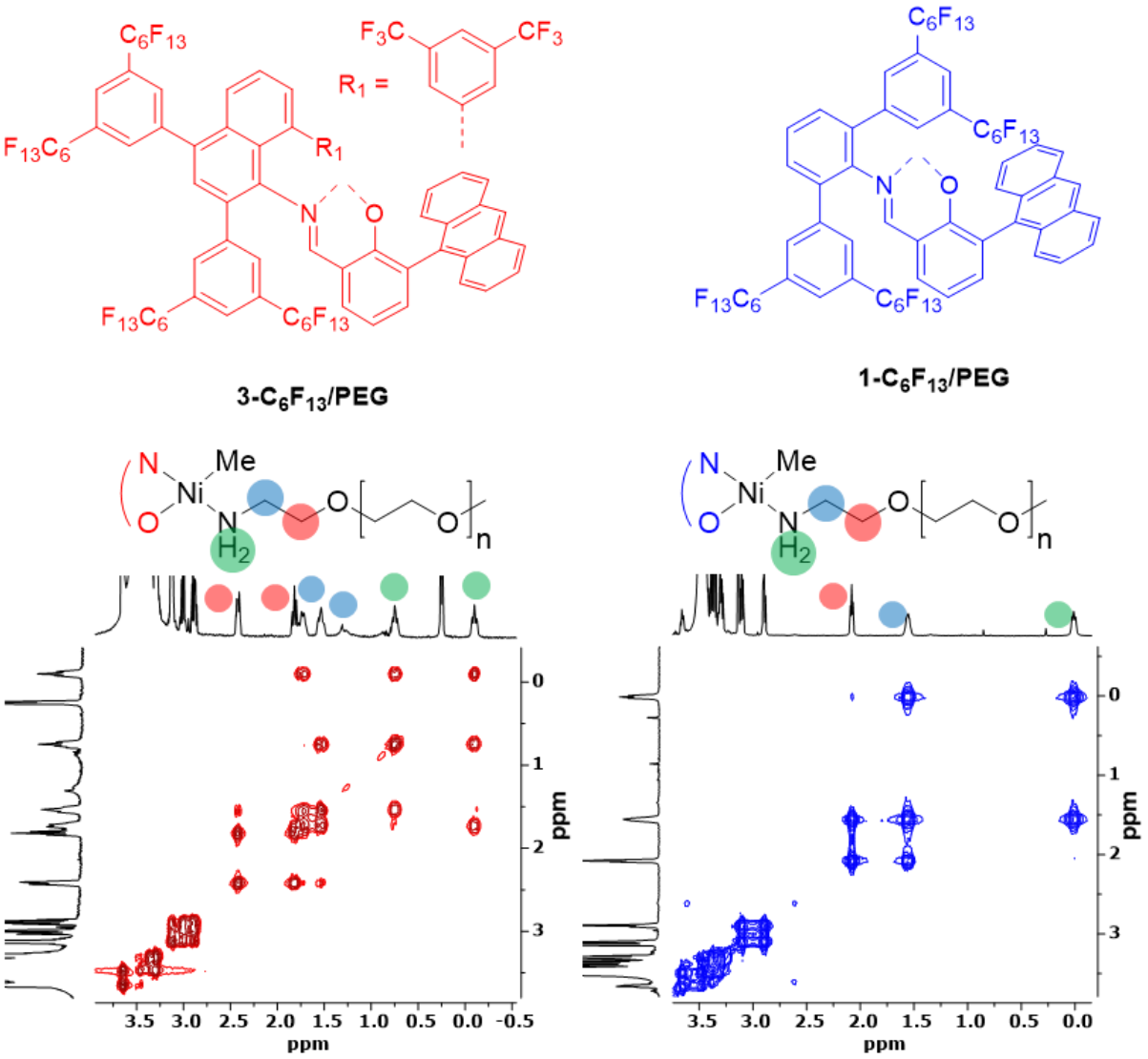

Figure 4.24. Comparison of ^{1}H-^{1}H-COSY spectra in the regime of resonances of the labile amine ligand of precatalysts **3^{Ant}-C$_6$F$_{13}$/PEG** and **1^{Ant}-C$_6$F$_{13}$/PEG.**

4.5.2 DLS data of nanocrystal dispersions

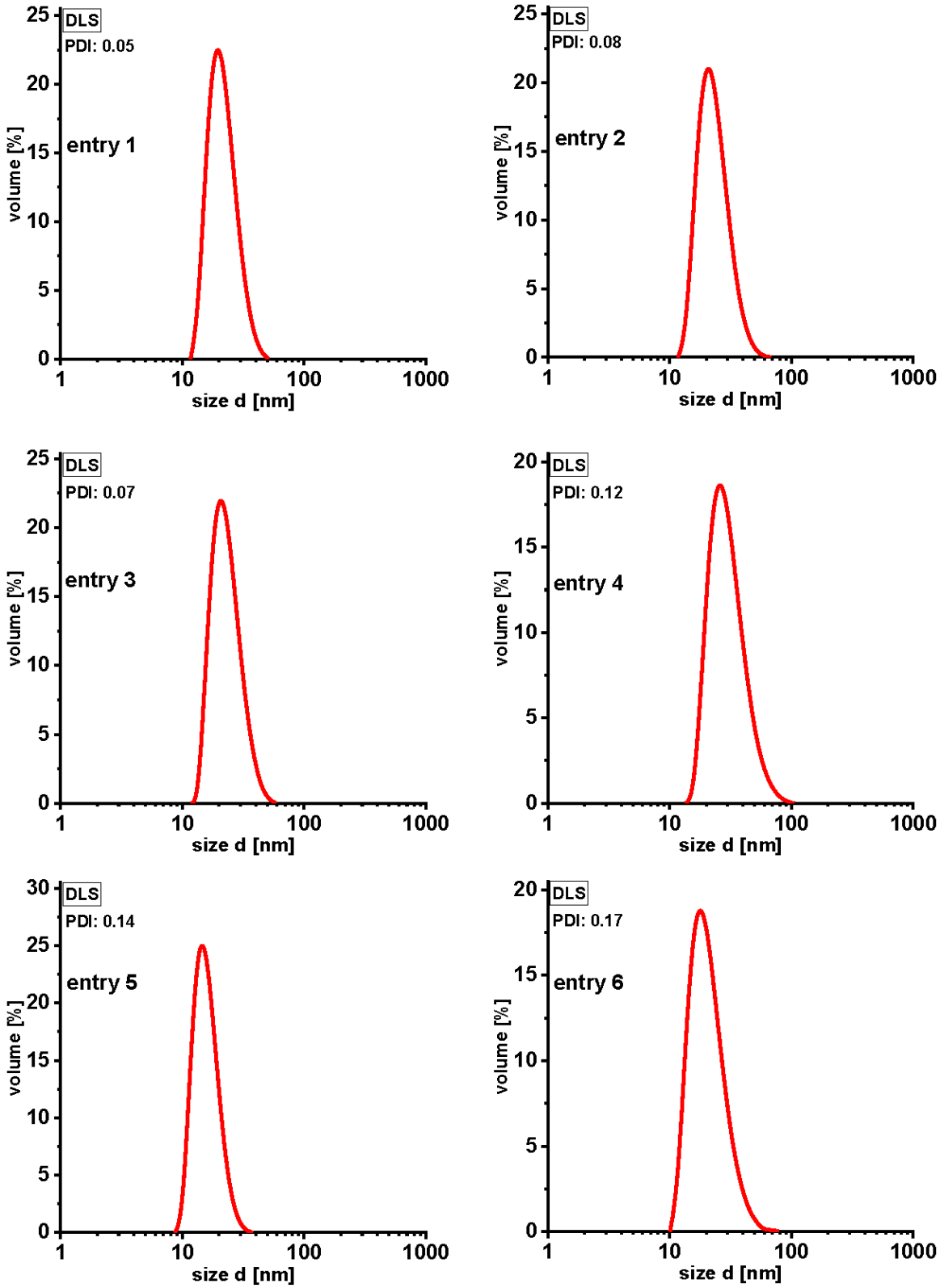

Figure 4.25. DLS traces of polyethylene dispersions (Table 4.2). Volume-based distributions shown. PDI according to *Malvern Zetasizer* software.

4.5.3 DSC traces of polyethylenes obtained in aqueous polymerization

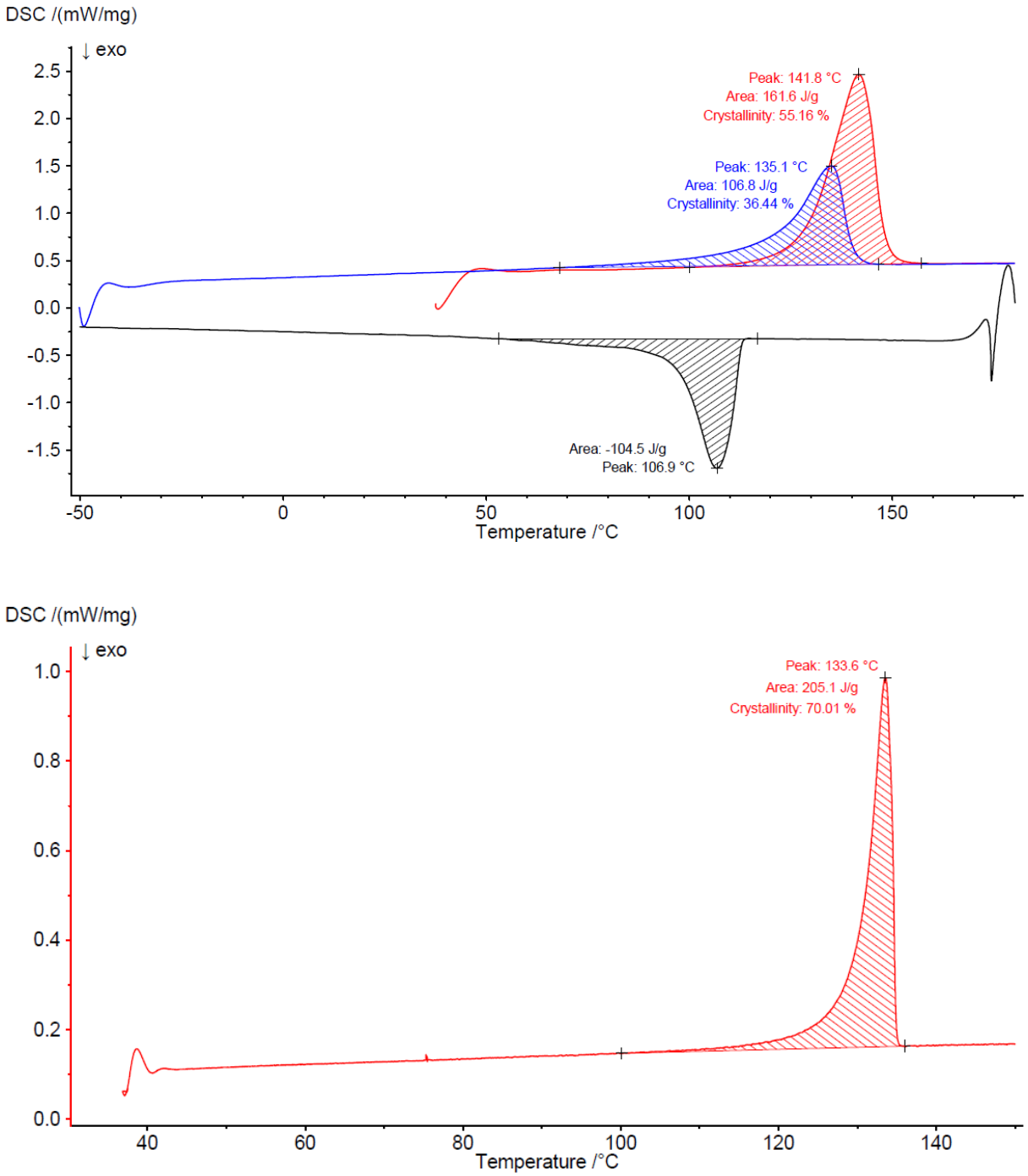

Figure 4.26. DSC traces of polyethylene obtained by aqueous polymerization (Table 4.2, entry 1). *Top*: measured with 10 K min^{-1} heating rate (red curve: 1st heating, black curve: 1st cooling, blue curve: 2nd heating). *Bottom*: measured with 1 K min^{-1} (only first heating shown).

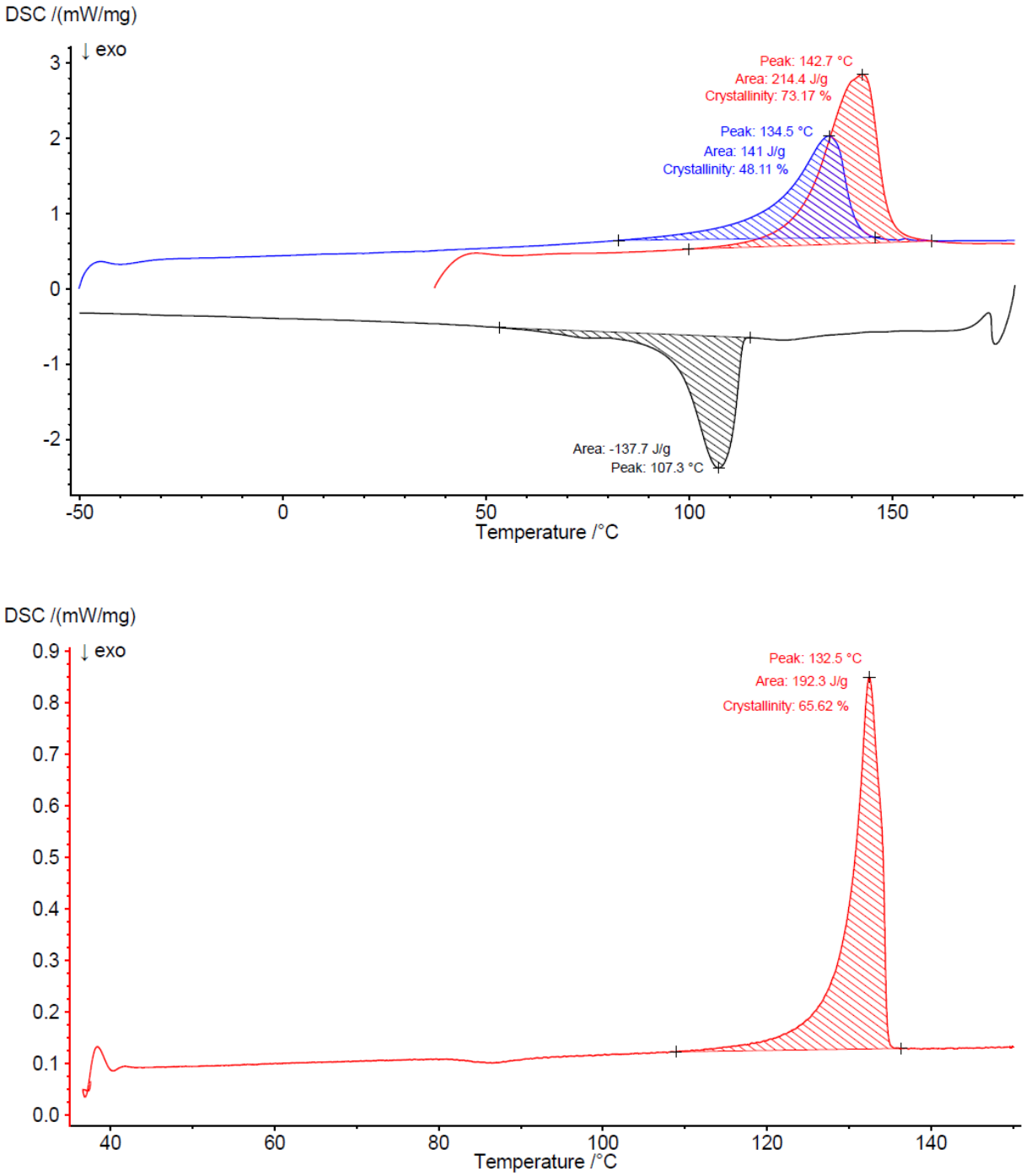

Figure 4.27. DSC traces of polyethylene obtained by aqueous polymerization (Table 4.2, entry 2). *Top*: measured with 10 K min^{-1} heating rate (red curve: 1st heating, black curve: 1st cooling, blue curve: 2nd heating). *Bottom*: measured with 1 K min^{-1} (only first heating shown).

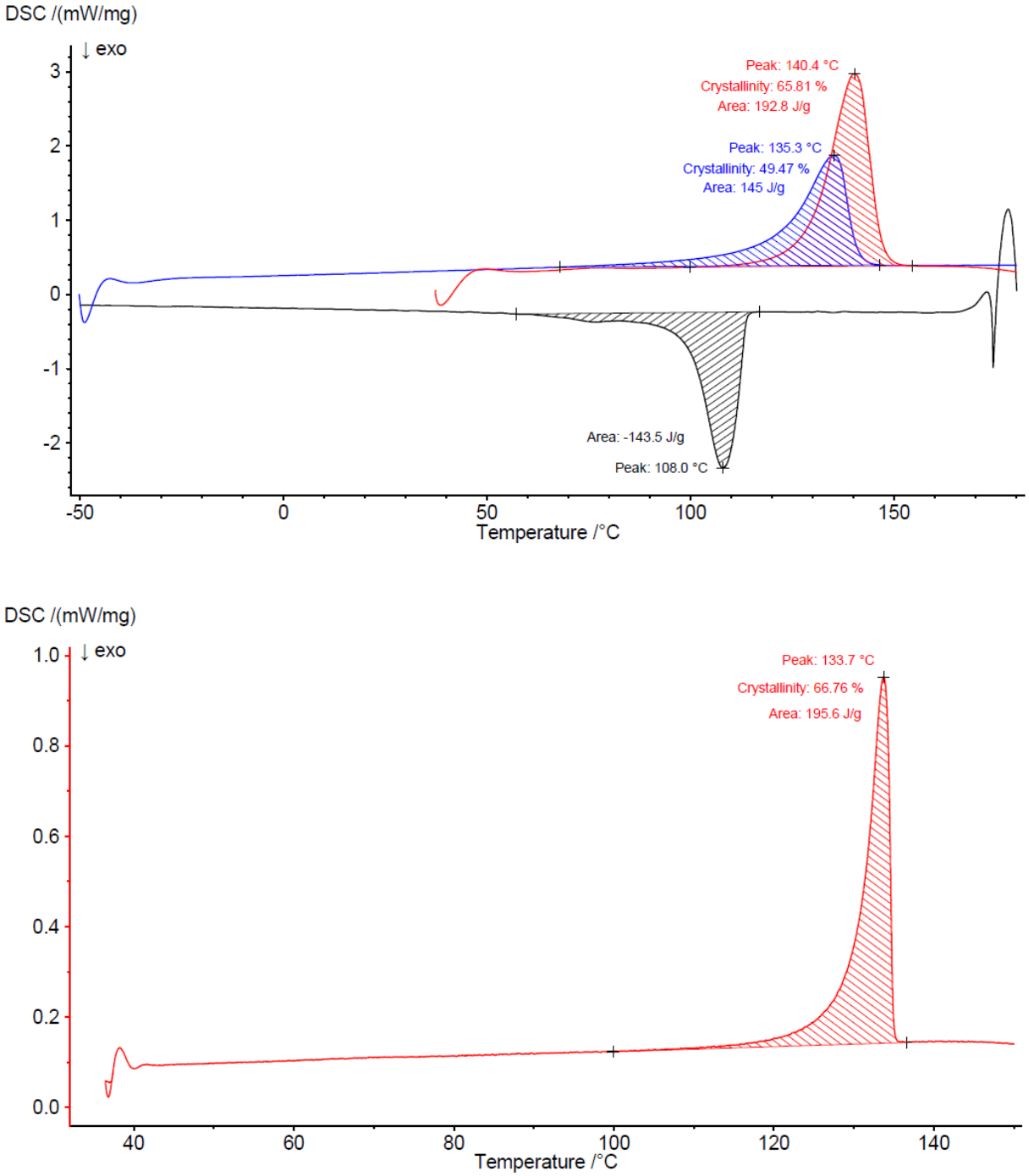

Figure 4.28. DSC traces of polyethylene obtained by aqueous polymerization (Table 4.2, entry 3). *Top*: measured with 10 K min^{-1} heating rate (red curve: 1st heating, black curve: 1st cooling, blue curve: 2nd heating). *Bottom*: measured with 1 K min^{-1} (only first heating shown).

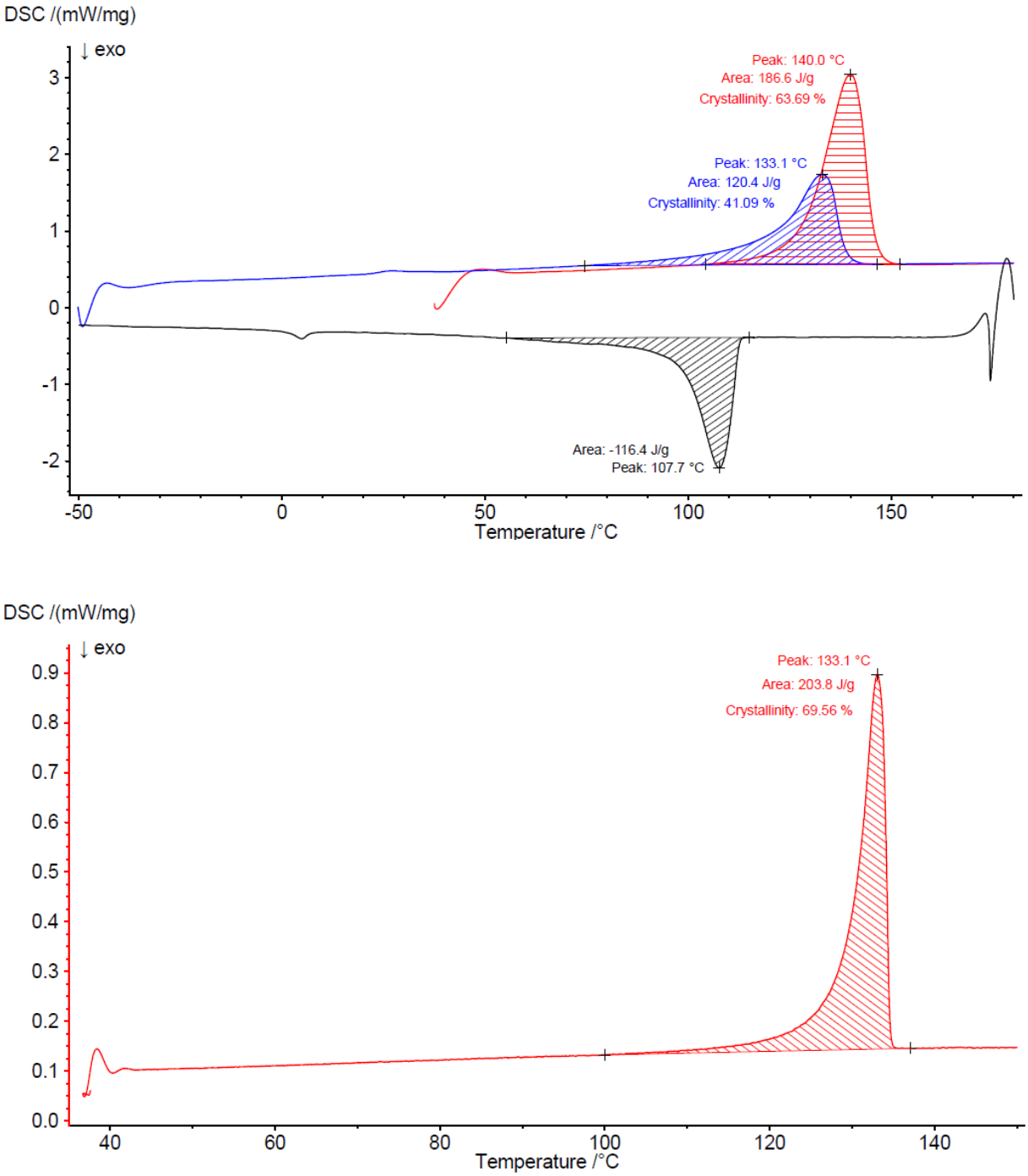

Figure 4.29. DSC traces of polyethylene obtained by aqueous polymerization (Table 2, entry 4). *Top*: measured with 10 K min^{-1} heating rate (red curve: 1st heating, black curve: 1st cooling, blue curve: 2nd heating). *Bottom*: measured with 1 K min^{-1} (only first heating shown).

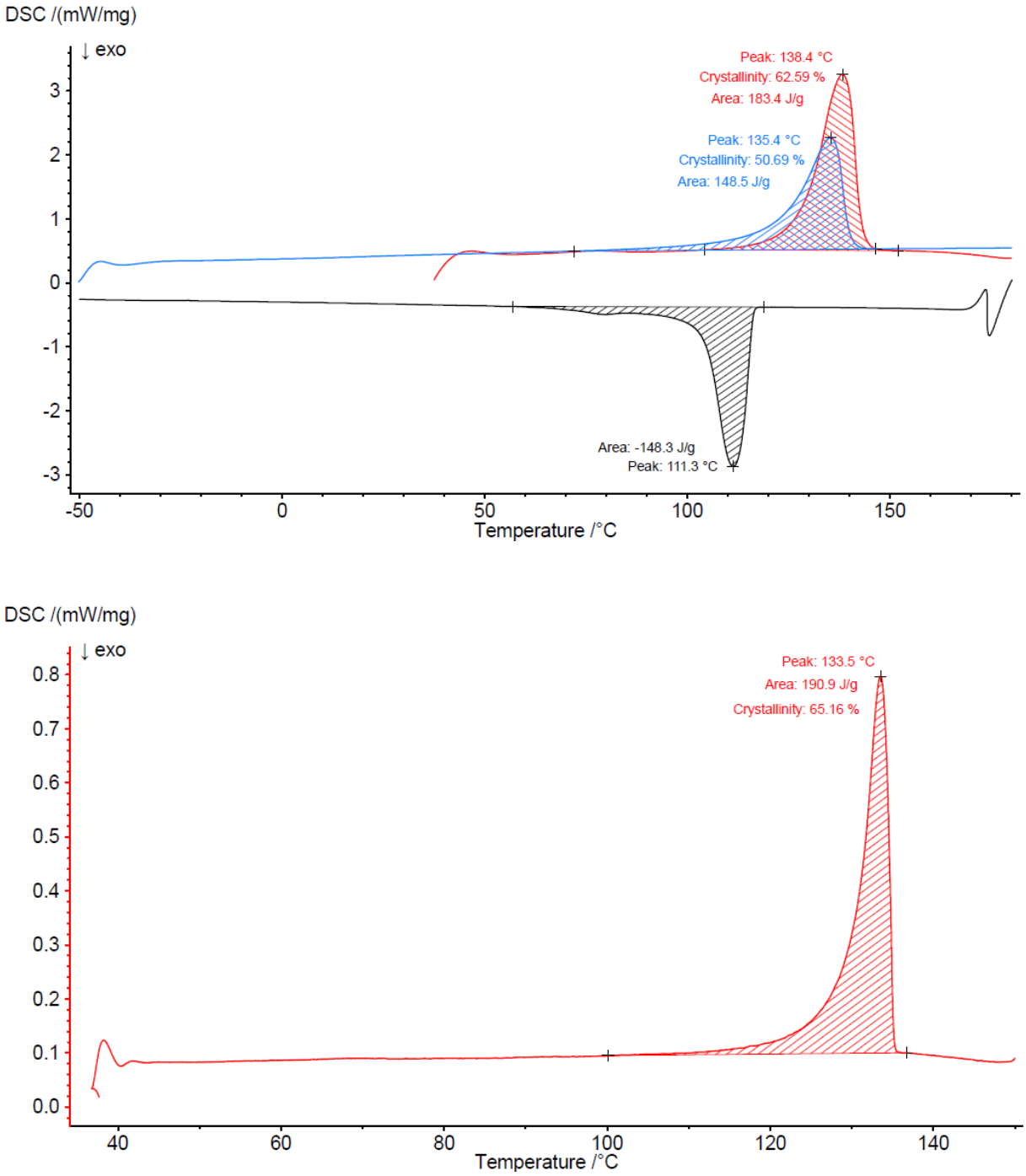

Figure 4.30. DSC traces of polyethylene obtained by aqueous polymerization (Table 4.2, entry 5). *Top*: measured with 10 K min^{-1} heating rate (red curve: 1st heating, black curve: 1st cooling, blue curve: 2nd heating). *Bottom*: measured with 1 K min^{-1} (only first heating shown).

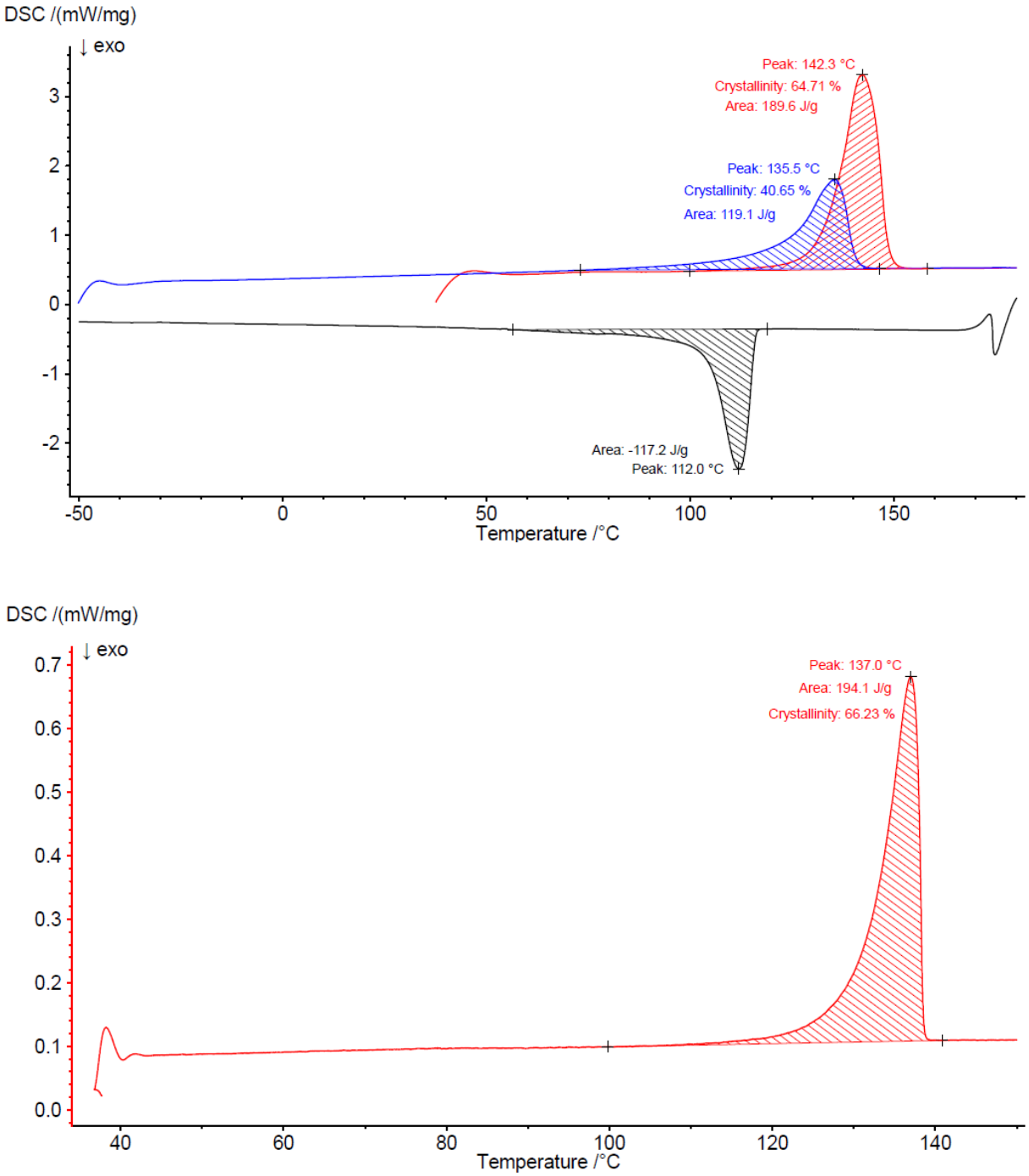

Figure 4.31. DSC traces of polyethylene obtained by aqueous polymerization (Table 4.2, entry 6 and Table 4.5, entry 4). *Top*: measured with 10 K min^{-1} heating rate (red curve: 1st heating, black curve: 1st cooling, blue curve: 2nd heating). *Bottom*: measured with 1 K min^{-1} (only first heating shown).

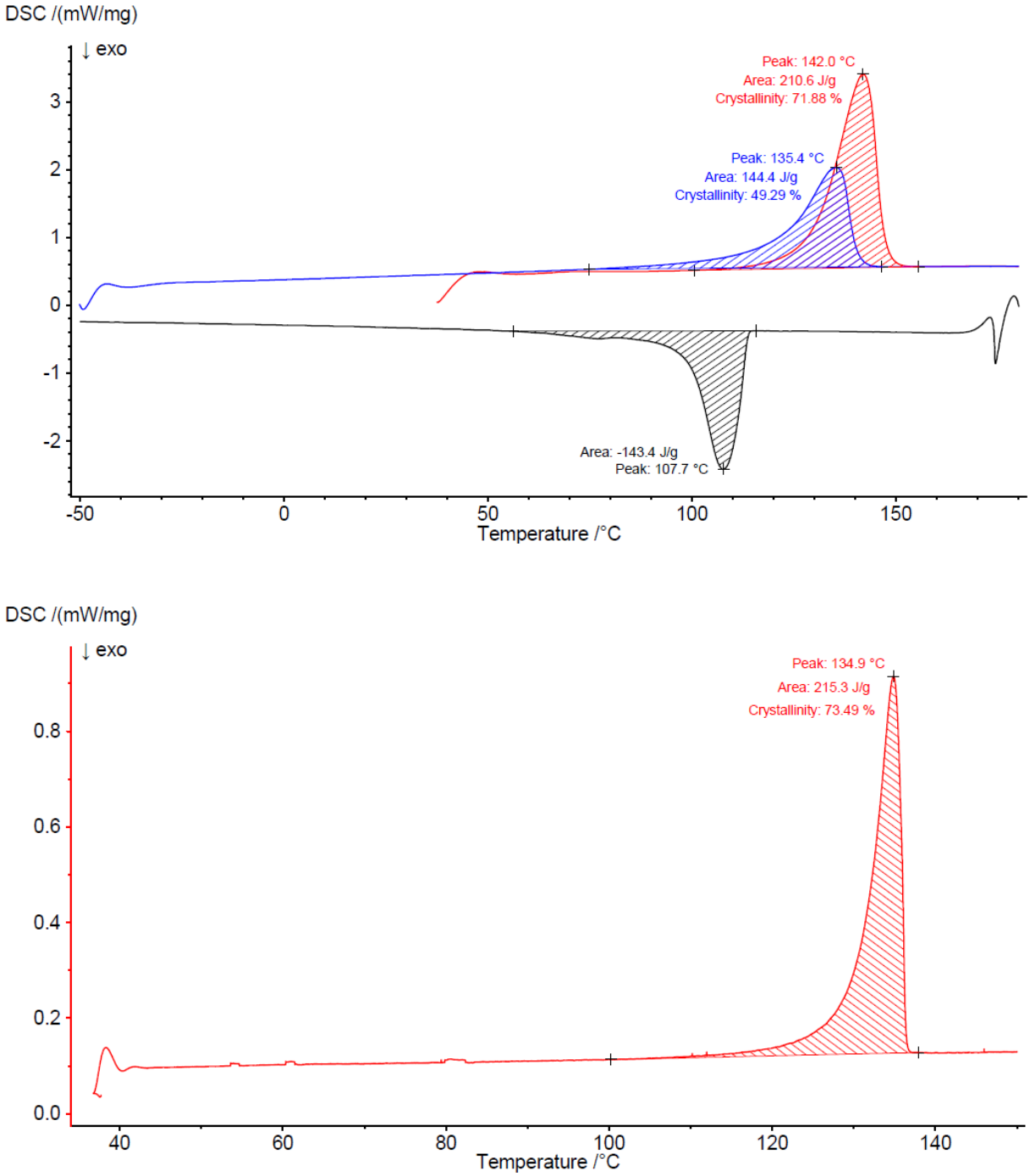

Figure 4.32. DSC traces of polyethylene obtained by aqueous polymerization (Table 4.3, entry 4). *Top*: measured with 10 K min^{-1} heating rate (red curve: 1st heating, black curve: 1st cooling, blue curve: 2nd heating). *Bottom*: measured with 1 K min^{-1} (only first heating shown).

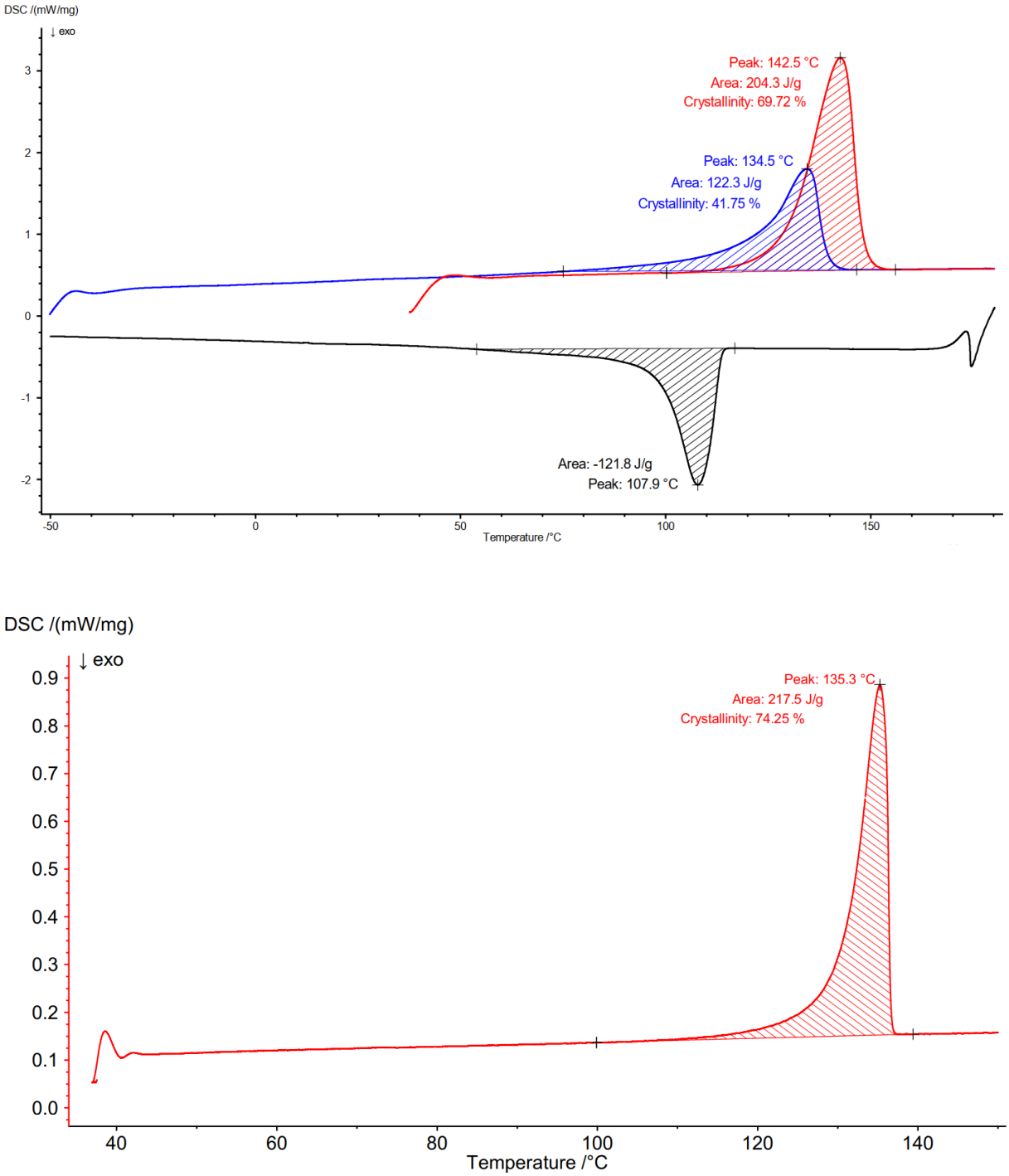

Figure 4.33. DSC traces of polyethylene obtained by aqueous polymerization (Table 4.4, entry 4). *Top*: measured with 10 K min^{-1} heating rate (red curve: 1st heating, black curve: 1st cooling, blue curve: 2nd heating). *Bottom*: measured with 1 K min^{-1} (only first heating shown).

4.5.4 Selected GPC traces of synthesized polyethylenes

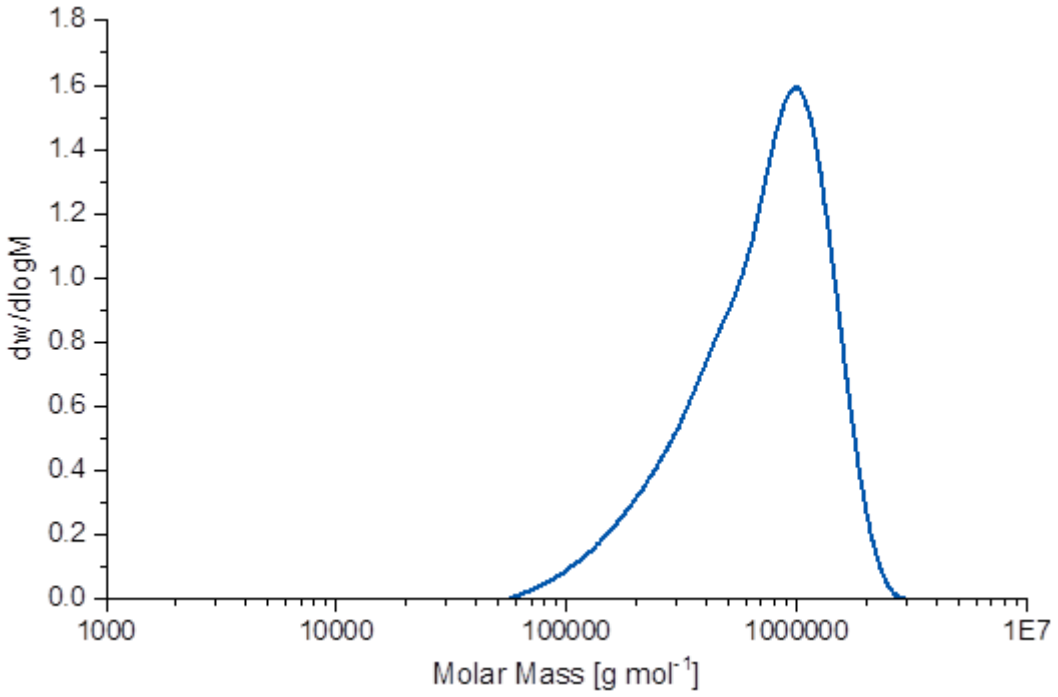

Figure 4.34. GPC trace of polyethylene obtained from polymerization in heptane (Table 4.1, entry 2). M_n = 504000 g/mol M_w = 813000 g/mol M_p = 939000 g/mol M_z = 1080000 g/mol M_v = 772000 g/mol PDI = 1.62

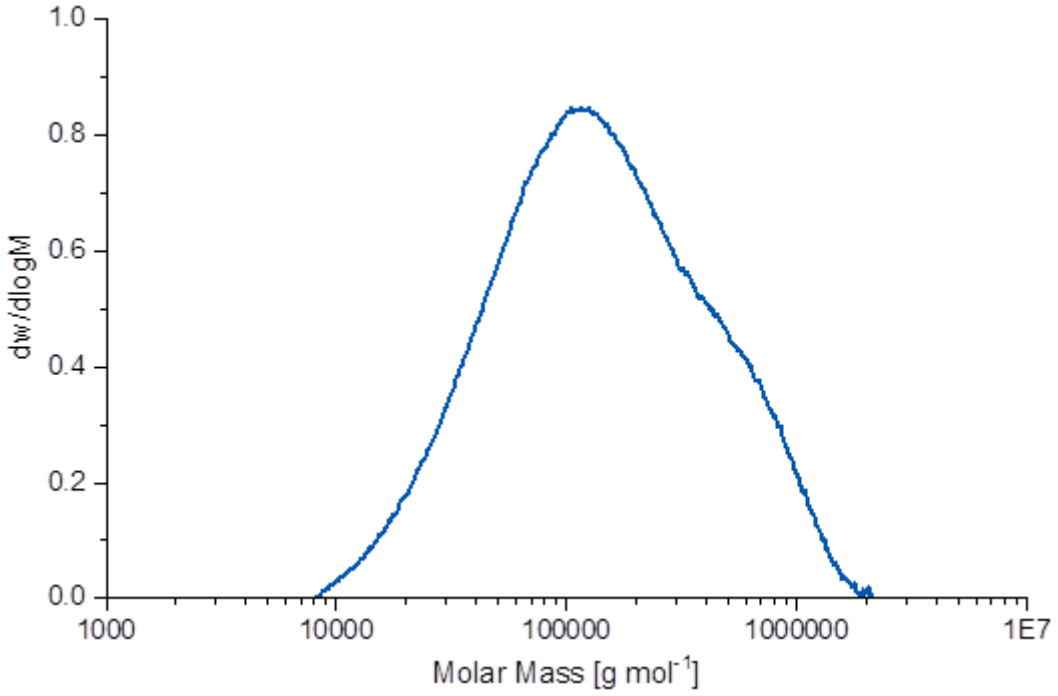

Figure 4.35. GPC trace of polyethylene obtained from polymerization in heptane (Table 4.1, entry 4). M_n =8 2200 g/mol M_w = 235000 g/mol M_p = 106000 g/mol M_z = 532000 g/mol M_v = 207000 g/mol PDI = 2.86

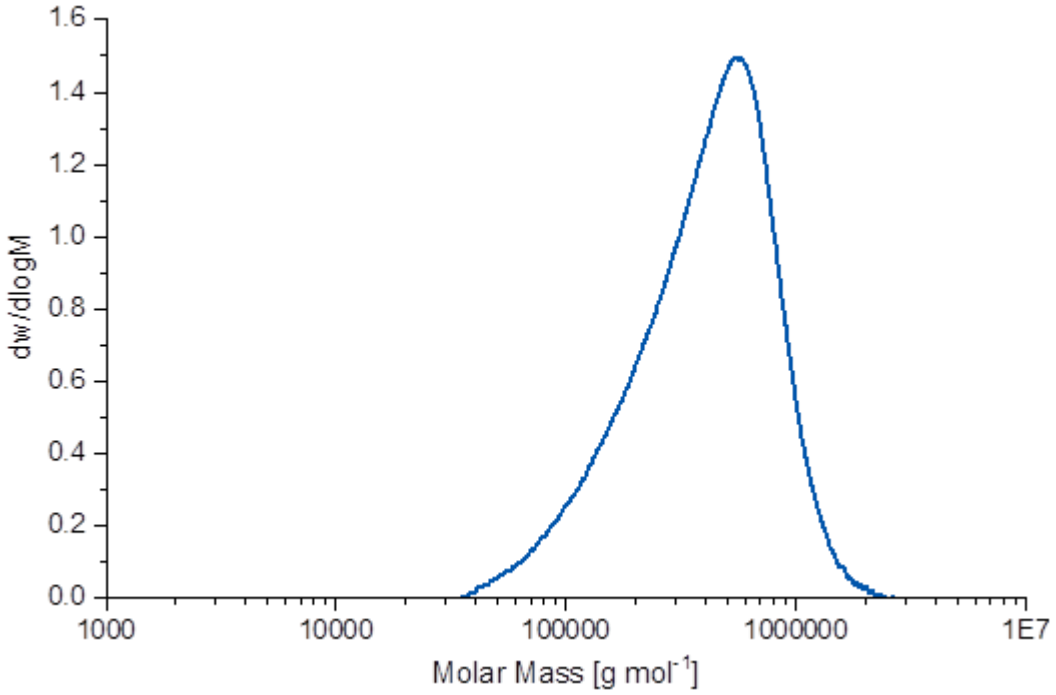

Figure 4.36. GPC trace of polyethylene obtained from polymerization in heptane (Table 4.1, entry 6). M_n = 294000 g/mol M_w = 480000 g/mol M_p = 541000 g/mol M_z = 670000 g/mol M_v = 453000 g/mol PDI = 1.63

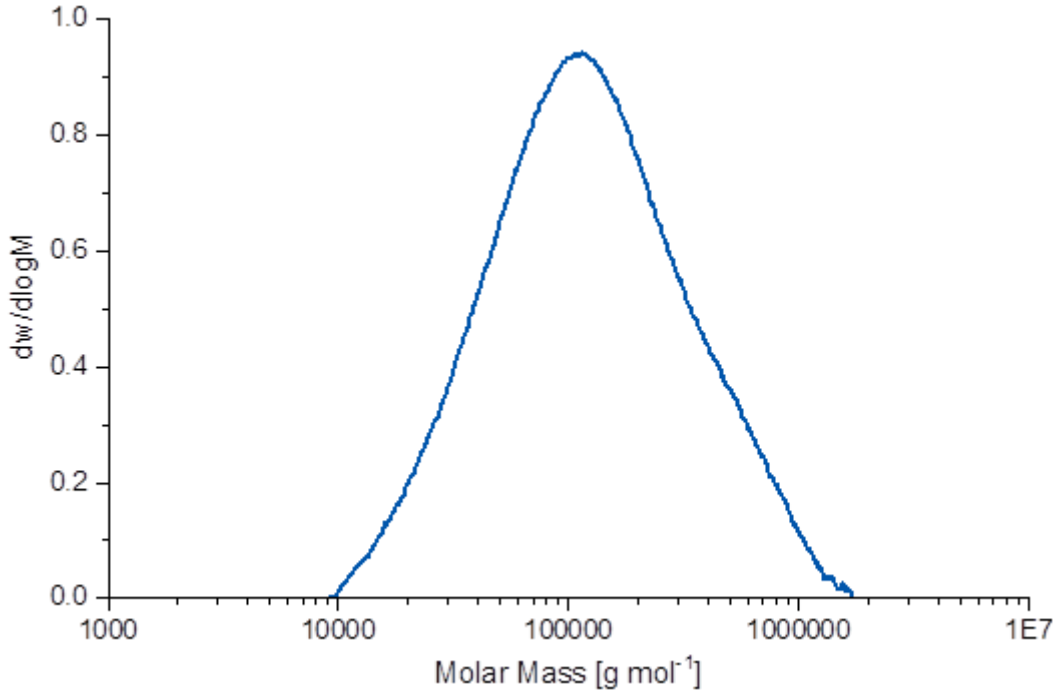

Figure 4.37. GPC trace of polyethylene obtained from polymerization in heptane (Table 4.1, entry 8). M_n = 76900 g/mol M_w = 191000 g/mol M_p = 99100 g/mol M_z = 419000 g/mol M_v = 453000 g/mol PDI = 2.48

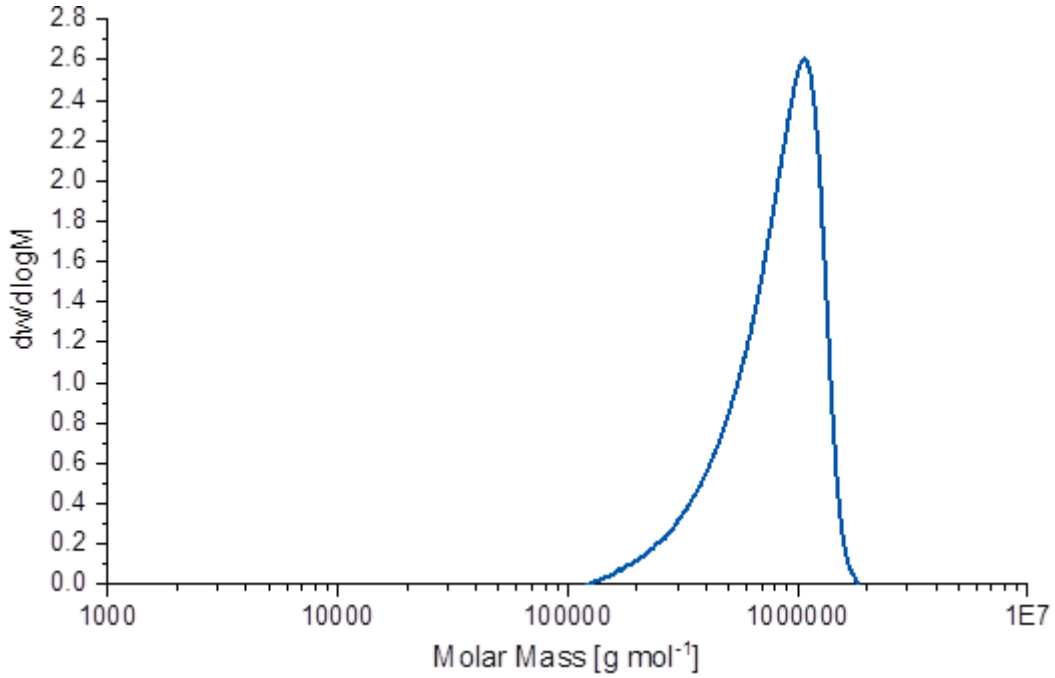

Figure 4.38. GPC trace of polyethylene obtained from polymerization in heptane (Table 4.1, entry 10). M_n = 683500 g/mol M_w = 847500 g/mol M_p = 1040000 g/mol M_z = 970100 g/mol M_v = 842700 g/mol PDI = 1.24

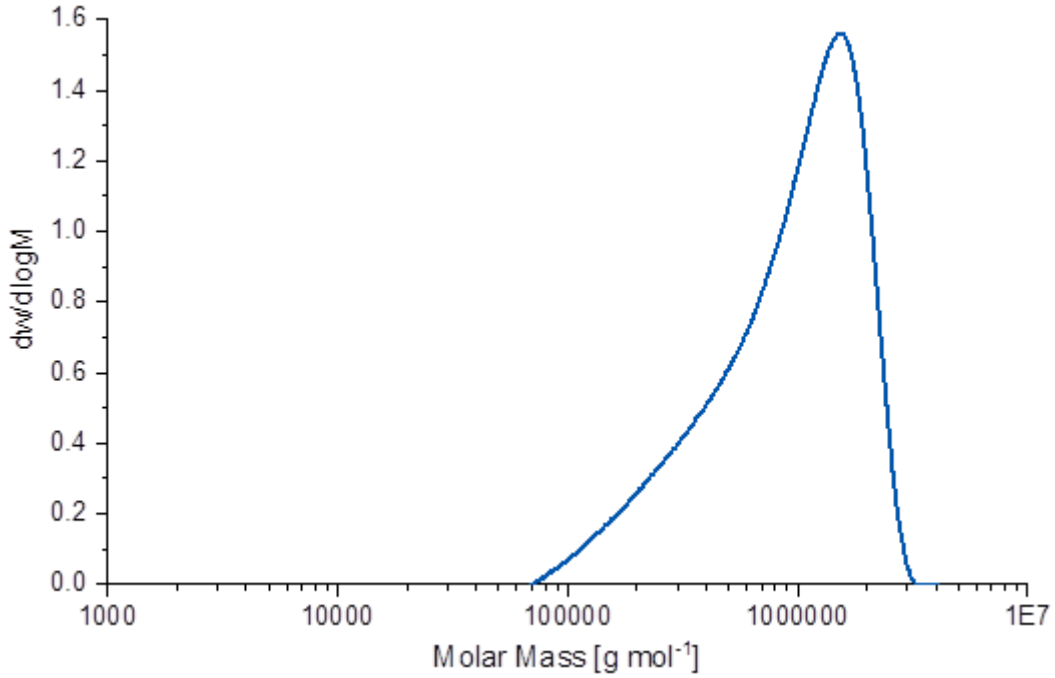

Figure 4.39. GPC trace of polyethylene obtained from polymerization in toluene (Table 4.6, entry 2). M_n = 623000 g/mol M_w = 1100000 g/mol M_p = 1480000 g/mol M_z = 1470000 g/mol M_v = 1020000 g/mol PDI = 1.76

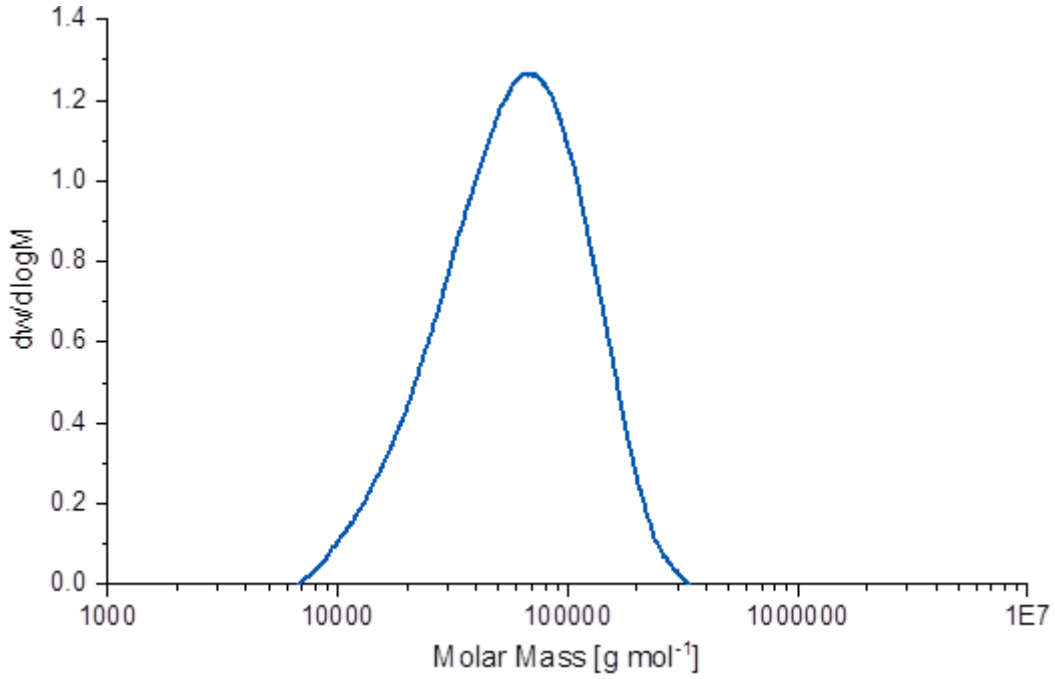

Figure 4.40. GPC trace of polyethylene obtained from polymerization in toluene (Table 4.6, entry 4). M_n = 43900 g/mol M_w = 71500 g/mol M_p = 64300 g/mol M_z = 104000 g/mol M_v = 68400 g/mol PDI = 1.63

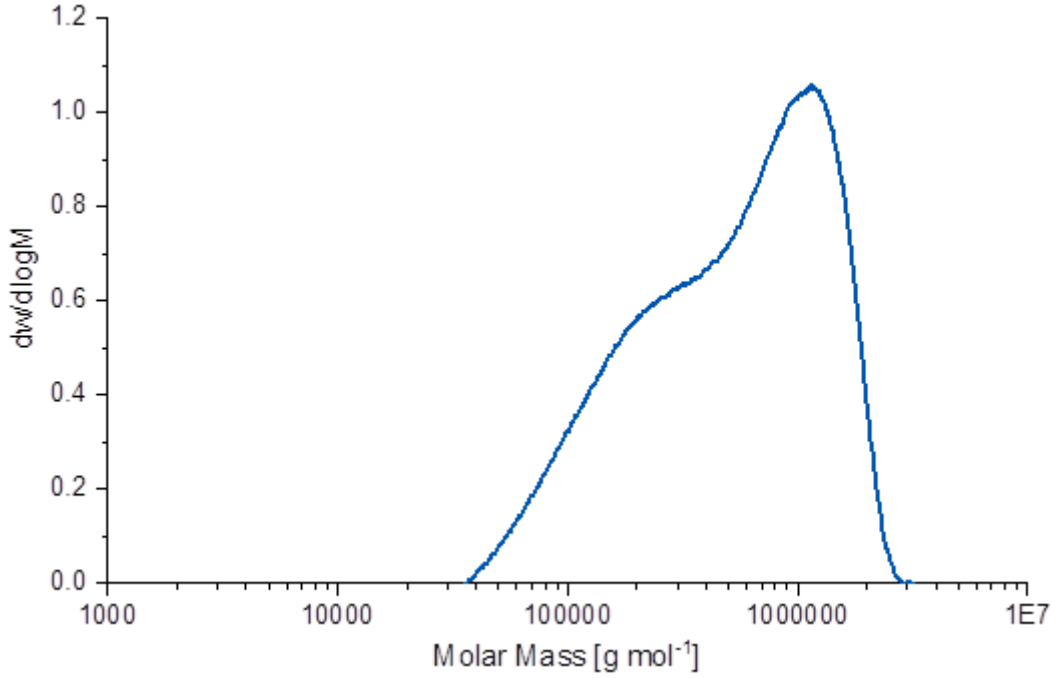

Figure 4.41. GPC trace of polyethylene obtained from polymerization in toluene (Table 4.6, entry 6). M_n = 309000 g/mol M_w = 712000 g/mol M_p = 919000 g/mol M_z = 1130000 g/mol M_v = 642000 g/mol PDI = 2.31

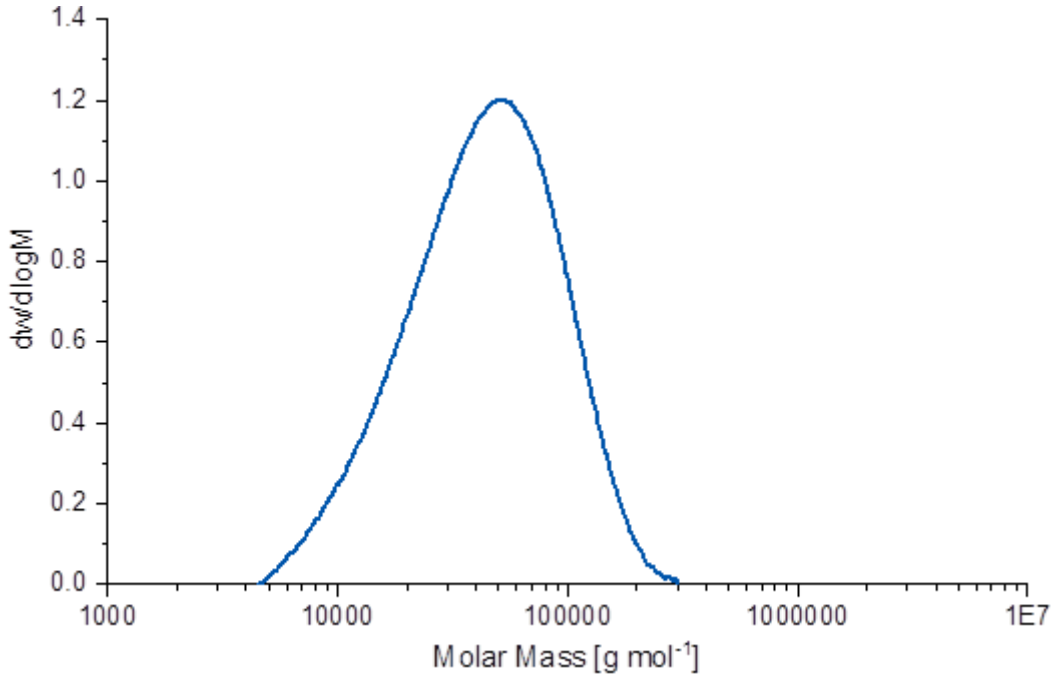

Figure 4.42. GPC trace of polyethylene obtained from polymerization in toluene (Table 4.6, entry 8). M_n=31600 g/mol M_w=54600 g/mol M_p=50300 g/mol M_z=83100 g/mol M_v=50600 g/mol PDI=1.73

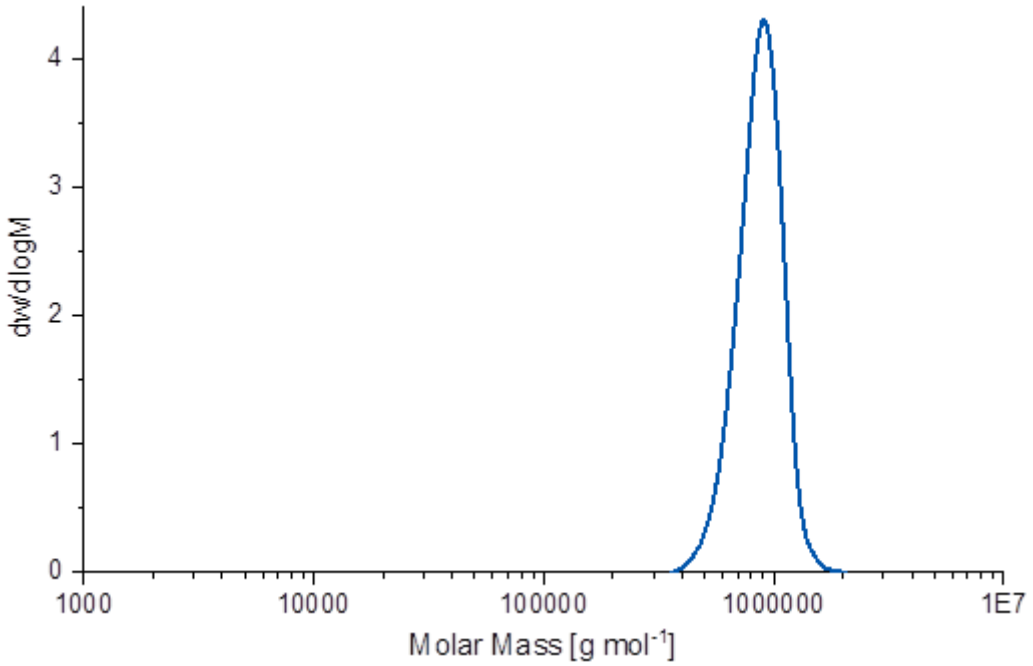

Figure 4.43. GPC trace of polyethylene obtained from polymerization in toluene (Table 4.6, entry 10). M_n = 842810 g/mol M_w = 886516 g/mol M_p = 899603 g/mol M_z = 9294590 g/mol M_v = 880259 g/mol PDI = 1.05

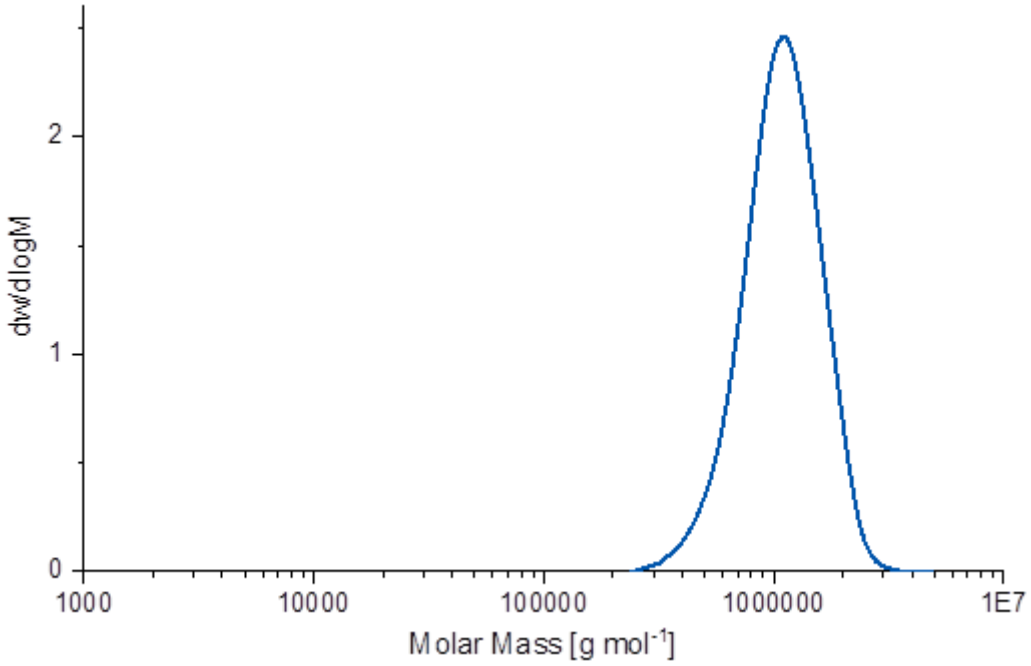

Figure 4.44. GPC trace of polyethylene obtained from polymerization in toluene (Table 4.6, entry 12). M_n = 994839 g/mol M_w = 1150000 g/mol M_p = 1120000 g/mol M_z = 1310000 g/mol M_v = 1130000 g/mol PDI = 1.16

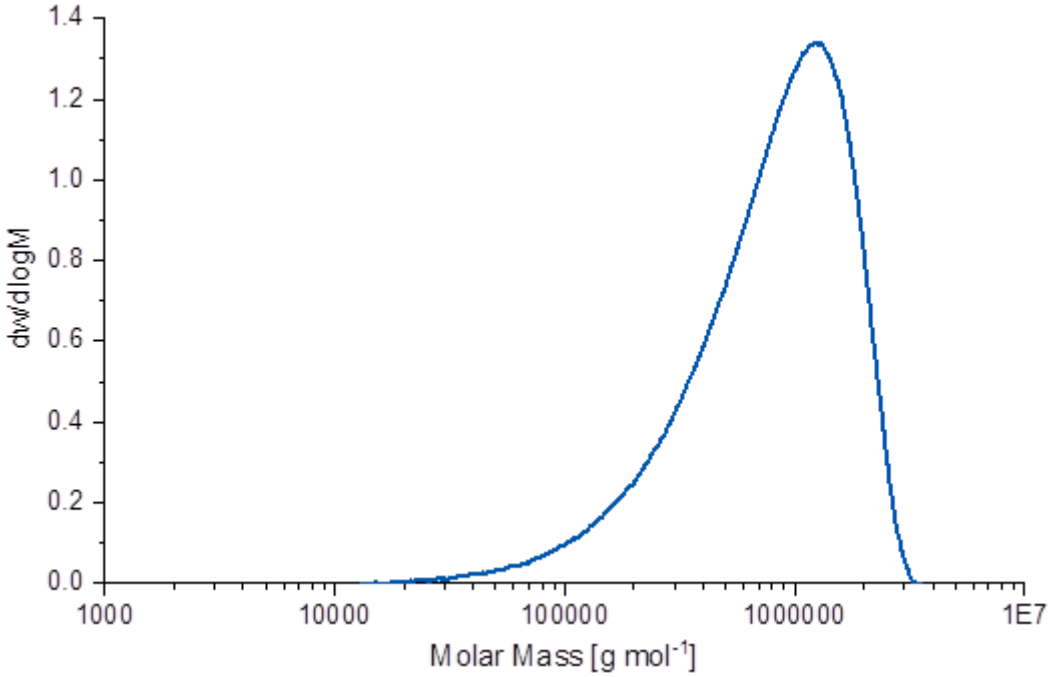

Figure 4.45. GPC trace of polyethylene obtained from polymerization in aqueous surfactant solution (Table 4.2, entry 1). M_n = 484000 g/mol M_w = 981000 g/mol M_p = 1080000 g/mol M_z = 1370000 g/mol M_v = 913000 g/mol PDI = 2.03

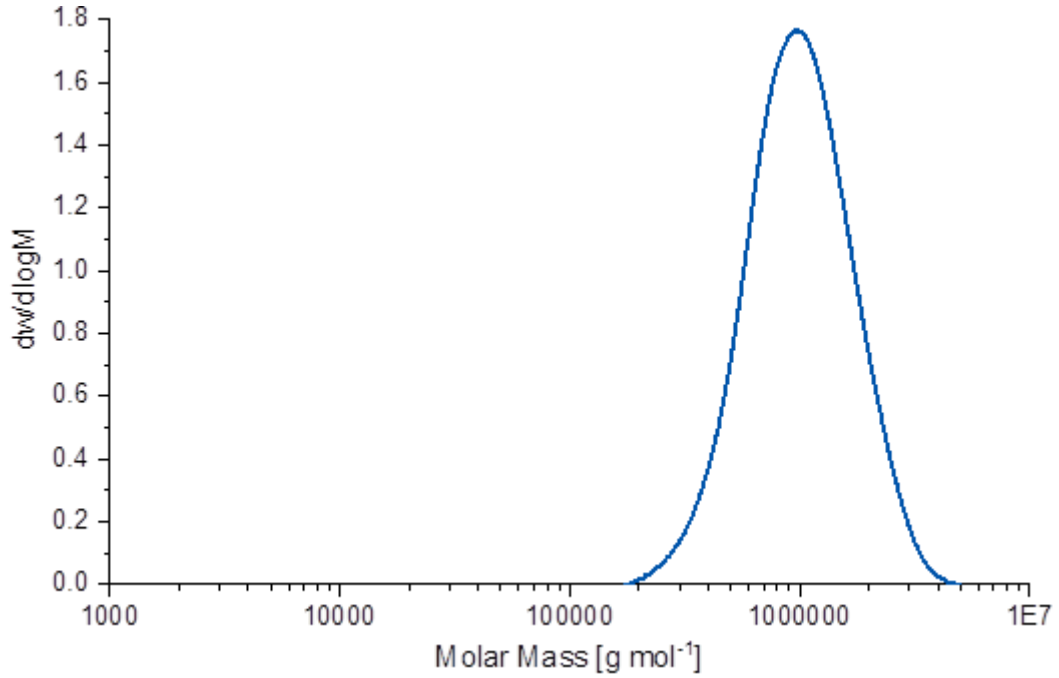

Figure 4.46. GPC trace of polyethylene obtained from polymerization in aqueous surfactant solution (Table 4.2, entry 2). M_n = 865981 g/mol M_w = 1130000 g/mol M_p = 990404 g/mol M_z = 1440000 g/mol M_v = 1080000 g/mol PDI = 1.30

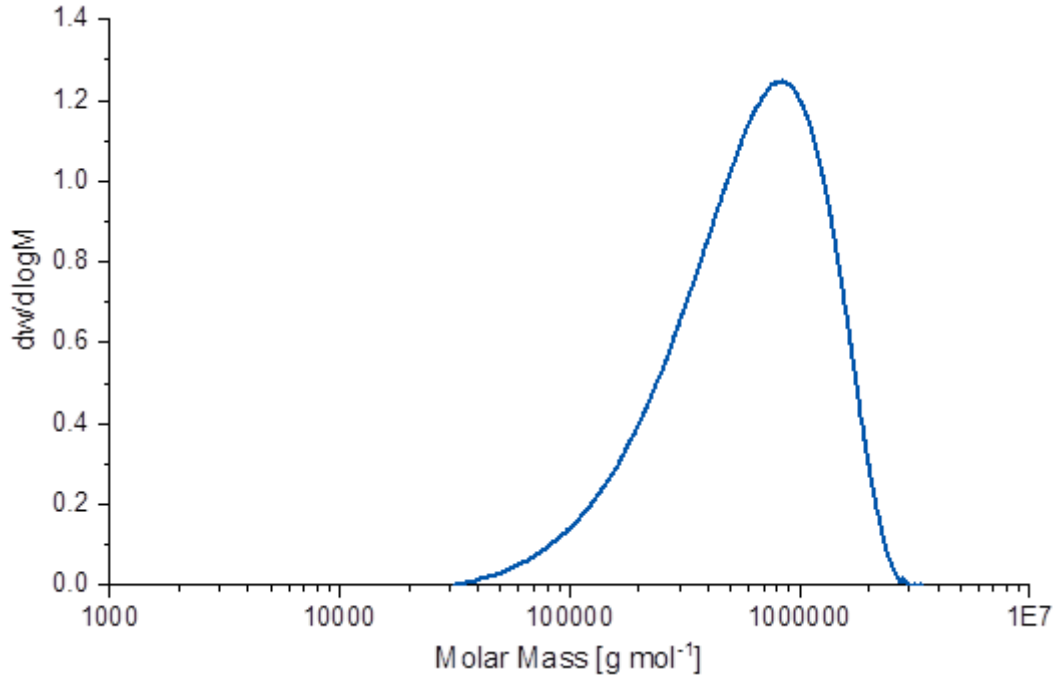

Figure 4.47. GPC trace of polyethylene obtained from polymerization in aqueous surfactant solution (Table 4.2, entry 3). M_n = 408000 g/mol M_w = 740000 g/mol M_p = 759000 g/mol M_z = 1060000 g/mol M_v = 691000 g/mol PDI = 1.82

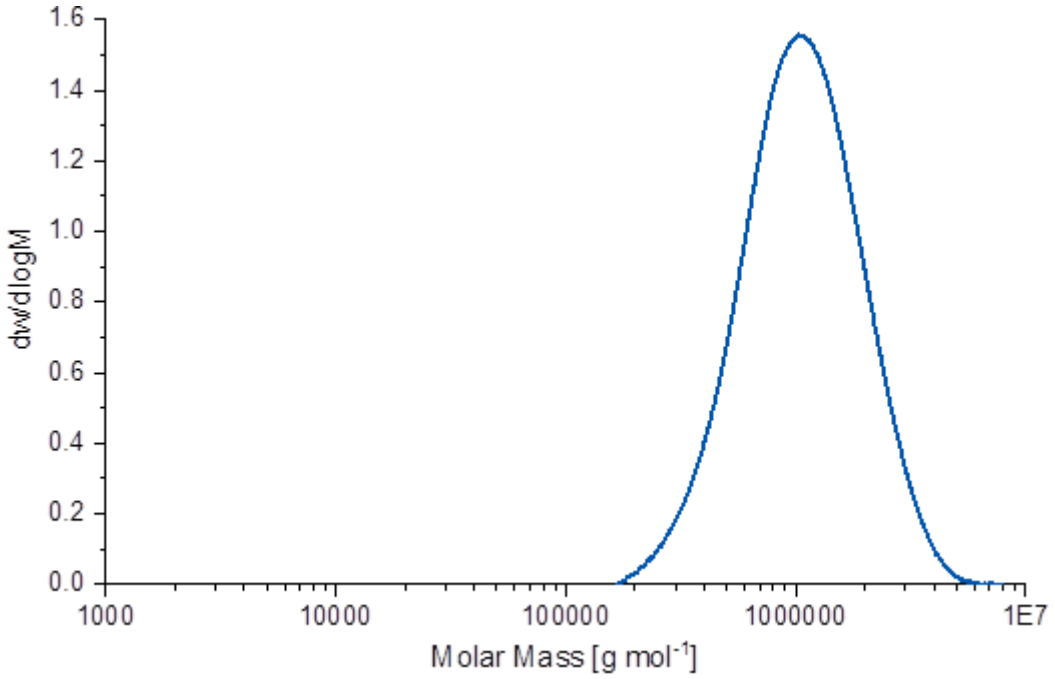

Figure 4.48. GPC trace of polyethylene obtained from polymerization in aqueous surfactant solution (Table 4.2, entry 4). M_n = 860000 g/mol M_w = 1400000 g/mol M_p = 1480000 g/mol M_z = 1910000 g/mol M_v = 1320000 g/mol PDI = 1.63

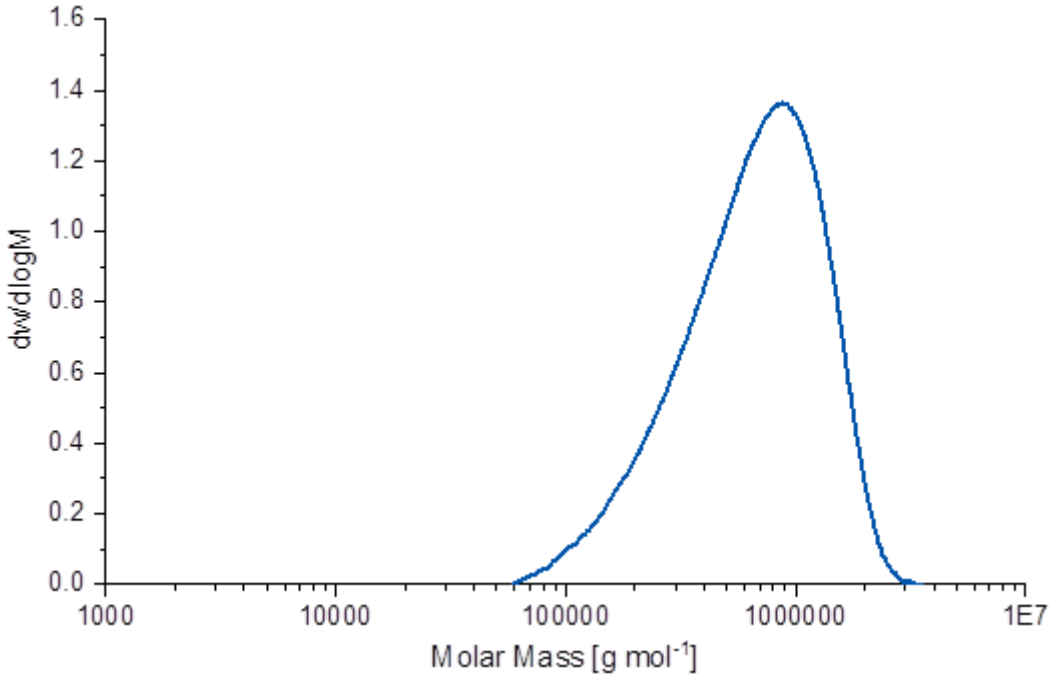

Figure 4.49. GPC trace of polyethylene obtained from polymerization in aqueous surfactant solution (Table 4.2, entry 5). M_n = 480000 g/mol M_w = 777000 g/mol M_p = 813000 g/mol M_z = 1070000 g/mol M_v = 733000 g/mol PDI = 1.62

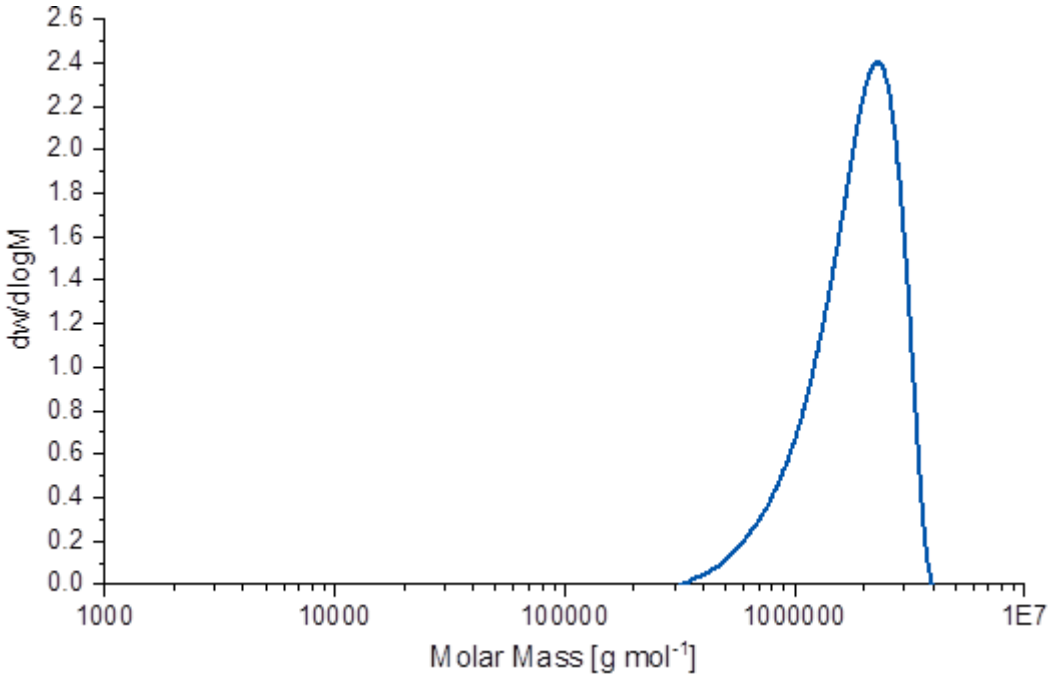

Figure 4.50. GPC trace of polyethylene obtained from polymerization in aqueous surfactant solution (Table 4.2, entry 6). M_n = 1609000 g/mol M_w = 1948000 g/mol M_p = 2116000 g/mol M_z = 2220000 g/mol M_v = 1917000 g/mol PDI = 1.21

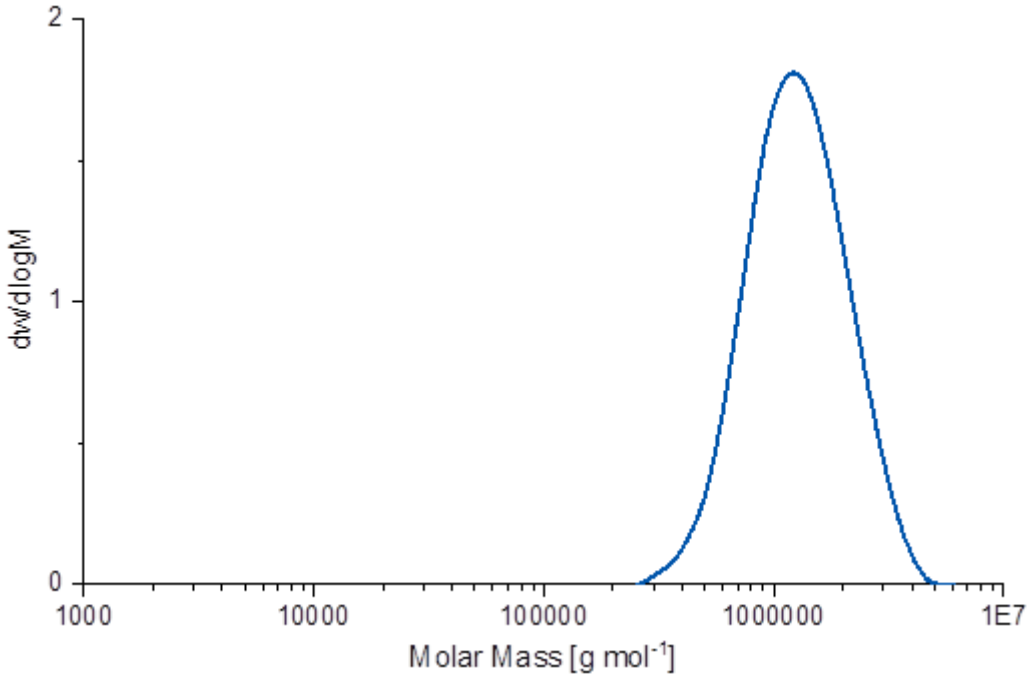

Figure 4.51. GPC trace of polyethylene obtained from polymerization in aqueous surfactant solution (Table 4.3, entry 3).
M_n = 1080861 g/mol M_w = 1354626 g/mol M_p = 1180372 g/mol M_z = 1676303 g/mol M_v = 131962 g/mol PDI = 1.25

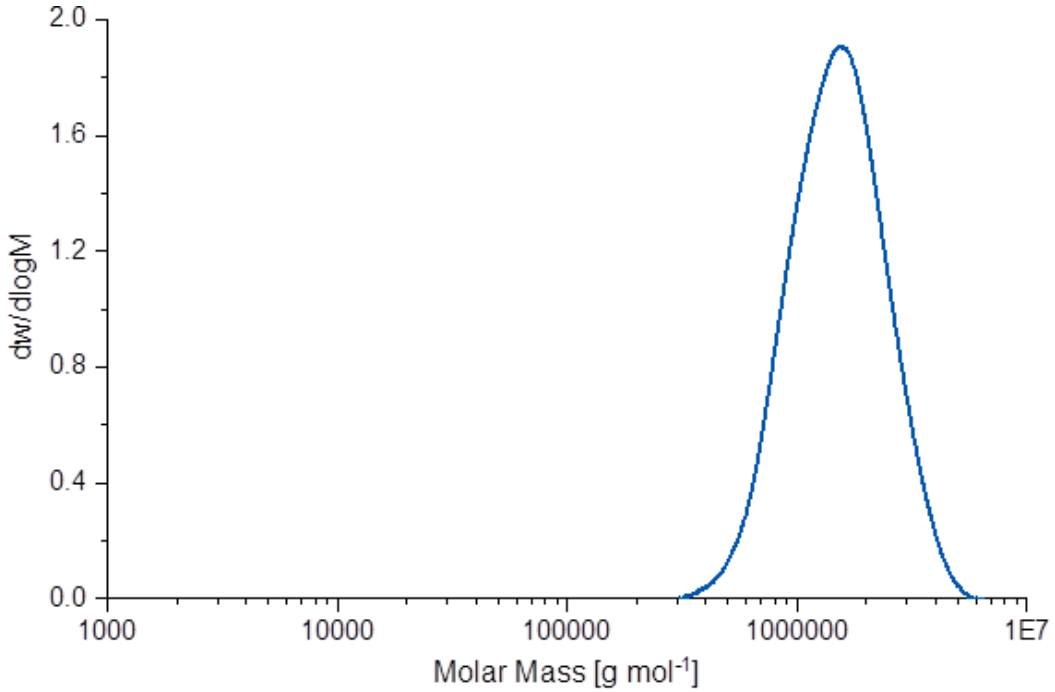

Figure 4.52. GPC trace of polyethylene obtained from polymerization in aqueous surfactant solution (Table 4.3, entry 4). M_n = 1335429 g/mol M_w = 1658147 g/mol M_p = 1542982 g/mol M_z = 2032526 g/mol M_v = 1609496 g/mol PDI = 1.24

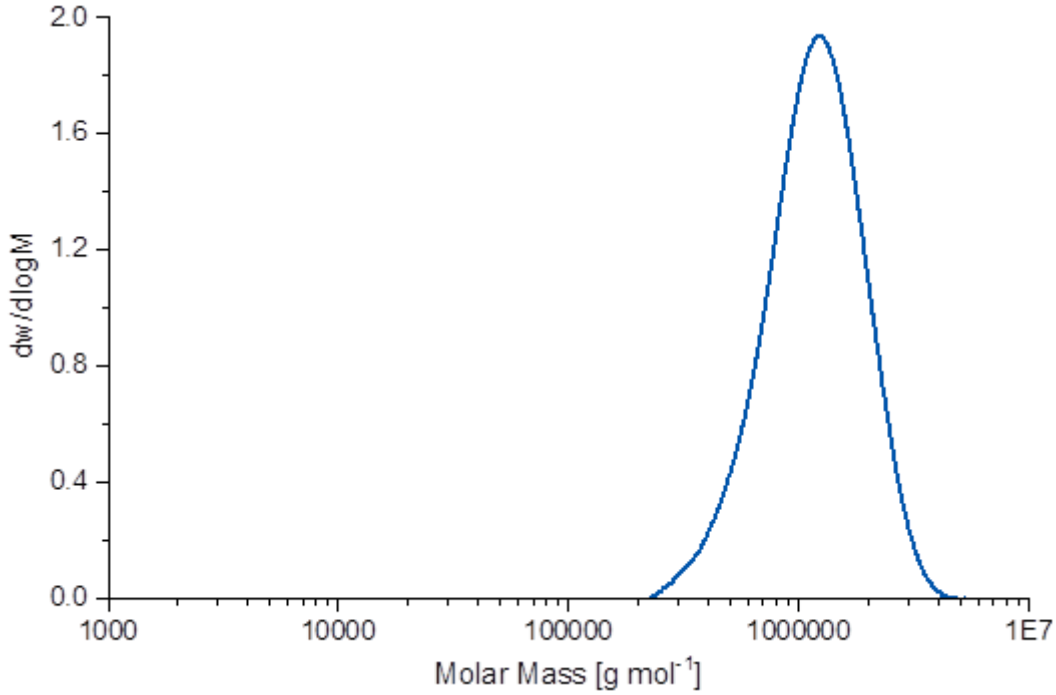

Figure 4.53. GPC trace of polyethylene obtained from polymerization in aqueous surfactant solution (Table 4.4, entry 2). M_n = 1019801 g/mol M_w = 1288066 g/mol M_p = 1205537 g/mol M_z = 1575719 g/mol M_v = 1242648 g/mol PDI = 1.26

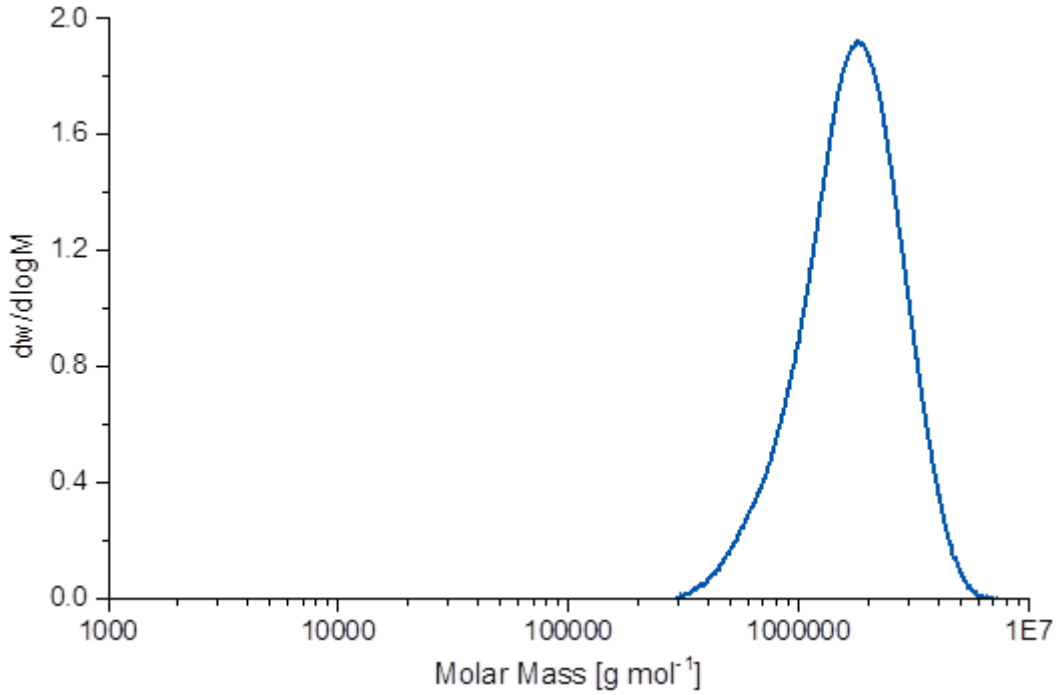

Figure 4.54. GPC trace of polyethylene obtained from polymerization in aqueous surfactant solution (Table 4.4, entry 3). M_n = 1460726 g/mol M_w = 1868576 g/mol M_p = 1798679 g/mol M_z = 2292611 g/mol M_v = 1793866 g/mol PDI = 1.28

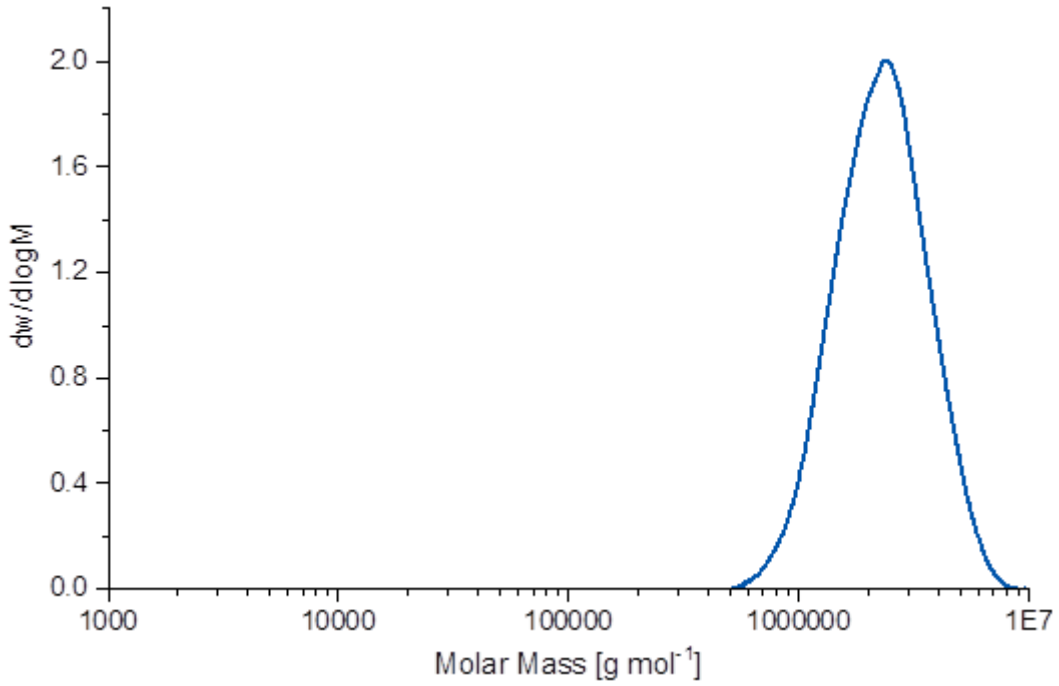

Figure 4.55. GPC trace of polyethylene obtained from polymerization in aqueous surfactant solution (Table 4.4, entry 4). M_n = 2034079 g/mol M_w = 2491043 g/mol M_p = 2326941g/mol M_z = 3011072 g/mol M_v = 2412275 g/mol PDI = 1.23

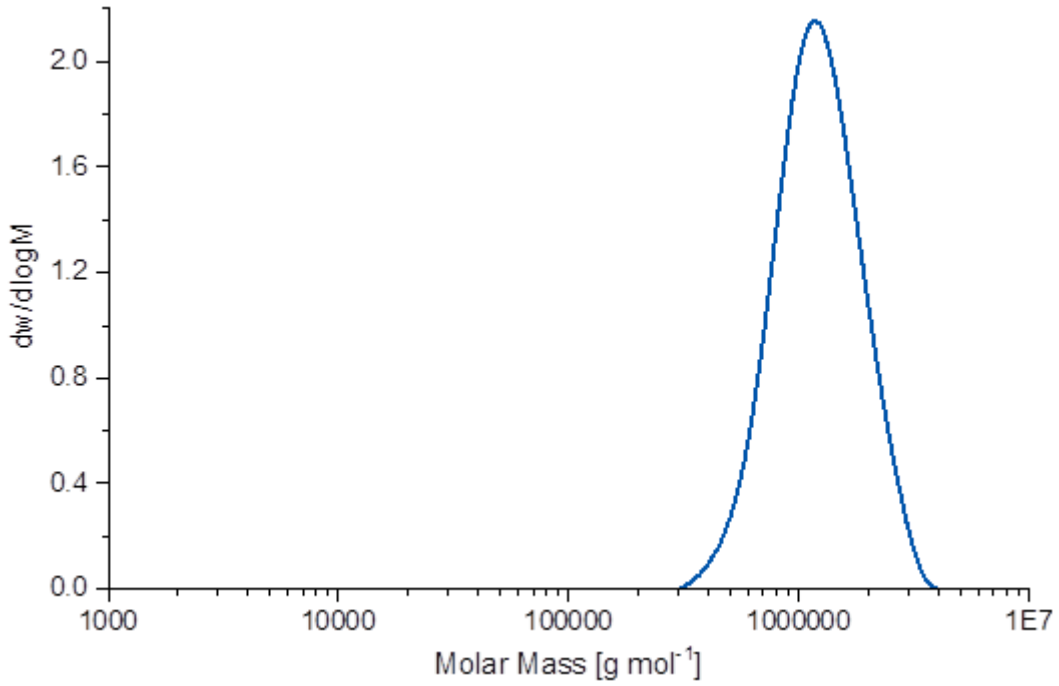

Figure 4.56. GPC trace of polyethylene obtained from polymerization in aqueous surfactant solution (Table 4.5, entry 3). M_n = 1093733 g/mol M_w = 1303642 g/mol M_p = 1172070 g/mol M_z = 1539043 g/mol M_v = 1271337 g/mol PDI = 1.19

5 Pentafluorophenyl Groups as Remote Substituents in Ni(II) Polymerization Catalysis

5.1 Introduction

The importance of perfluoroaromatic molecules has grown over decades and became subject of considerable interest in different chemical fields.[386-389] As prominent representative, the pentafluorophenyl group is well-known for its highly electron-withdrawing character due to inductive effects of the fluorine atoms.[390,391] In contrast to saturated electron-withdrawing groups, the aromatic character enables a broad variety of tunable π interactions that differ from non-fluorine counterparts.[392-396] These unique properties allow for various applications as crucial substituent, e.g. in active esters for synthesis of functional macromolecules.[397-399] The discovery of tris(pentafluorophenyl)borane[400-402] as a milestone of boron chemistry unlocked a broad variety of bond activation reactions[403,404] and was key in the development of the 'frustrated Lewis pair' chemistry[405-408] or of weakly coordinating anions in catalysis.[409-412]

Pentafluorophenyl groups have been used in polymerization catalysts, in the form of the aforementioned weakly coordinating counterions or to provide stabilizing non-covalent metal-fluorine interactions.[112,115,413-417] They have been less studied as primarily electron-withdrawing groups. As practically useful example, late transition metal catalyst show a versatile behavior in ethylene polymerization depending on the electronic influence in selected positions of the

Parts of *chapter 5* are published in *Organometallics* **2020**, *39*, 13-17.

ligand structure.[49,377] In case of mechanistically instructive neutral Ni(II) *N*-terphenyl salicylaldiminato catalysts, electron-withdrawing substituents in remote positions are crucial to generate linear high molecular weight polyethylene.[107,108] This strong influence can be traced to a weak interaction between the distal aryl rings and the metal atom that favors β-hydride elimination (BHE) and chain transfer (see Figure 5.1).[53]

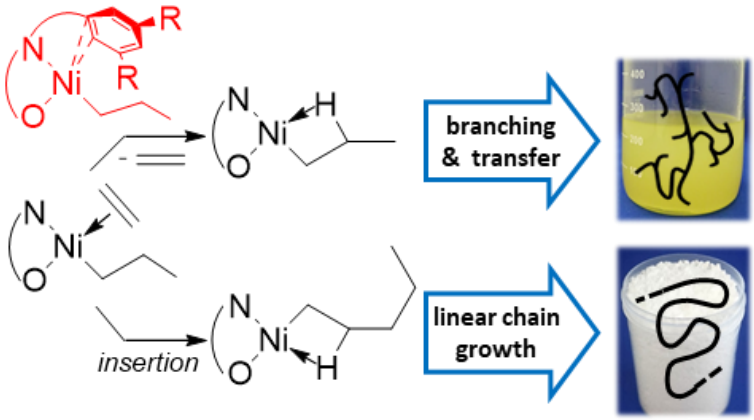

Figure 5.1. Mechanistic rationale of the effect of remote substituents in *N*-terphenyl salicylaldiminato Ni(II) catalysts. A release of ethylene from the alkyl-olefin intermediate is favored by an Ni-aryl interaction (shown in red). The latter is only operative for electron rich substituents R, e.g. R = Me. It renders β-hydride elimination and consequently chain transfer and branch formation competitive with chain growth.[53]

To this end, several saturated electron withdrawing groups (e.g. $-CF_3$, $-SF_5$ or $-NO_2$) have been studied to suppress chain transfer reactions up to an extent, that truly living polymerization conditions under aqueous polymerization conditions are achieved (see *chapters 3 and 4*).[110,111] This chapter will report on the use of pentafluorophenyl groups as first example of aromatic electron-withdrawing substituents in remote positions to generate high molecular weight polyethylene in different solvents.

5.2 Results and discussion

To synthesize the desired pentafluorophenyl-substituted salicylaldimine, a palladium-catalyzed arylation reaction provided access to 1,3-di(pentafluorophenyl)benzene (see *Experimental Section* for details on synthesis and characterization of all catalyst precursors).[418] Subsequent iridium-catalyzed borylation and Suzuki coupling with 2,6-dibromo-4-fluoroaniline produced the respective terphenylamine, that was converted to the salicylaldimine by condensation reaction with 3,5-diiodosalicylaldehyde. Precatalysts $\mathbf{4^I\text{-}C_6F_5/L}$ were obtained by reaction with [(tmeda)$NiMe_2$] in presence of the desired labile ligand

(Figure 5.2). Pyridine (L = Pyr) was added here to obtain the lipophilic precatalyst suitable for polymerization in toluene, respectively, α-methoxy-ω-amino poly(ethylene glycol) (L = H_2N-PEG-OMe) to obtain the hydrophilic counterpart for polymerization in aqueous surfactant solution.

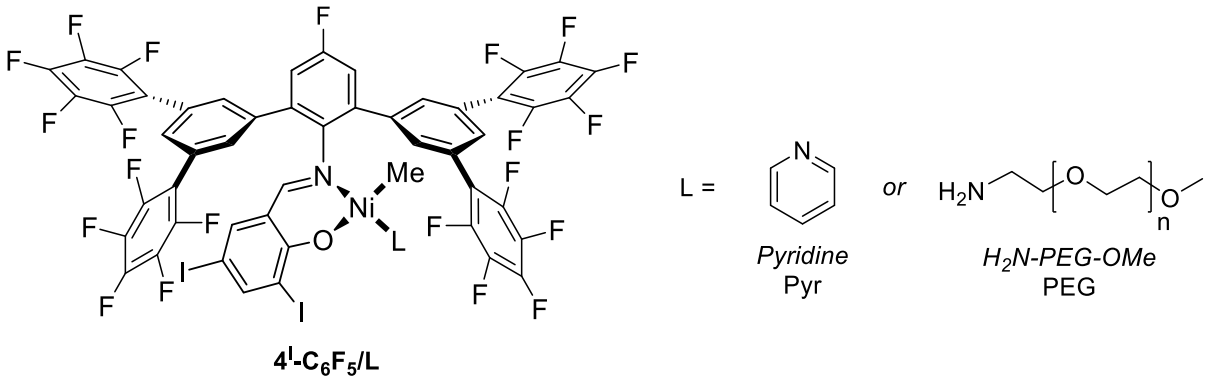

Figure 5.2. Catalyst precursors **4^{I}-C_6F_5/L** with pentafluorophenyl substituents in remote positions studied in this work. The coordinated labile ligand differs for the lipophilic precursor (L = Pyr) and hydrophilic precursor (L = PEG) for aqueous polymerizations.

Table 5.1. Polymerization experiments with catalysts **4^{I}-C_6F_5/L** in different solvents.

entry (cond.)	solvent	T [°C]	time [min]	yield PE [g]	TON[a]	M_n[c] x 10^3 [g mol^{-1}]	M_w/ M_n[b]	T_m[c] [°C] (cryst. [%])	br./ 1000 C[d]	d_h (Vol.)[e] [nm]
1^{A}	toluene	30	0.5	2.63	18.7	111	1.9	129 (60) / 127 (53) -	9	-
2^{A}	toluene	50	0.5	4.83	34.4	23	1.8	117 (51) / 117 (51) -	11	-
3^{A}	toluene	70	0.5	11.79	84.1	10	1.8	113 (55) / 114 (49) -	18	-
4^{B}	water	15	60	2.98	14.2	268	1.7	135 (65) / 131 (46) 128 (64)	5	36 (0.08)
5^{B}	water	15	120	5.14	24.4	304	1.7	135 (61) / 131 (48) 129 (62)	6	43 (0.11)
6^{B}	water	15	240	13.97	66.4	338	1.7	136 (64) / 132 (48) 130 (66)	5	46 (0.06)

Polymerization conditions: (A) 5 µmol **4^{I}-C_6F_5/Pyr**, 40 bar ethylene pressure, in 100 mL toluene; (B) 7.5 µmol **4^{I}-C_6F_5/PEG**, 40 bar ethylene pressure, 12 g sodium dodecyl sulfate, 3 g cesium hydroxide, 1.5 mL toluene, in 300 mL water, polymer obtained by precipitation in methanol. [a] Given in mol [C_2H_4] x mol^{-1} [Ni]. [b] Determined via GPC at 160 °C in 1,2-dichlorobenzene. [c] Determined via DSC with 10 K/min heating rate, reported as [1st heating cycle (crystallinity) / 2nd heating cycle (crystallinity)], second line: 1st heating cycle (crystallinity) with 1 K/min heating rate. [d] Determined via selective detection of methyl and methylene IR-bands during GPC measurements (calibrated versus samples with known degree of branching). [e] Determined via DLS (volume mean and PDI reported).

Ethylene polymerizations in toluene were conducted at different temperatures (Table 5.1, entries 1-3) to study the effects of the pentafluorophenyl substitution. Remarkably, catalyst **4^{I}-C$_6$F$_5$/Pyr** is capable of producing low branched high molecular weight polyethylene of $M_n > 10^5$ g/mol (entry 1) at 30 °C reaction temperature and compares favorably under otherwise identical conditions to the intensively studied reference catalyst bearing CF_3 groups in remote positions (1.1 x 10^5 g/mol [-C_6F_5] vs. 2.8 x 10^5 g/mol [-CF_3] and 6 branches/1000 carbon atoms [-C_6F_5] vs. 3 branches/1000 carbon atoms [-CF_3], see Table 3.1 and Table 5.1). By contrast, catalyst derivatives with electron-donating alkyl groups in remote positions produce hyperbranched oligomers of significantly lower molecular weights.[109] When **4^{I}-C$_6$F$_5$/Pyr** is used at higher polymerization temperatures, molecular weights generally decrease (and branching increases) as expected for this catalyst type due to an increase in BHE.

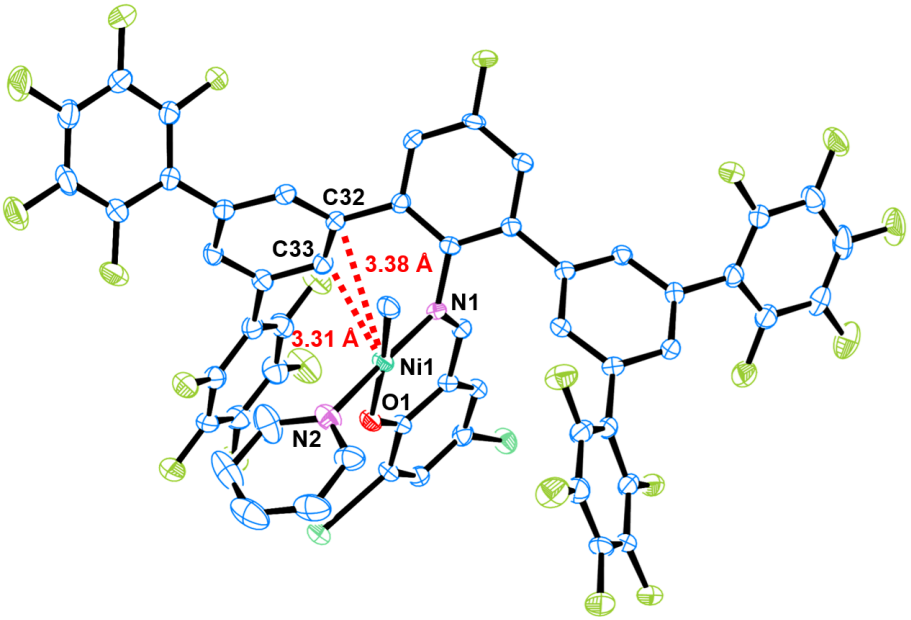

Figure 5.3. ORTEP plot (50 % probability ellipsoids, hydrogens are omitted for clarity) of **4^{I}-C$_6$F$_5$/Pyr** determined by X-ray diffraction. Selected nickel-aryl distances are given.

As BHE and chain transfer are enhanced by interactions between the nickel center and the distal aryl rings of the ligand backbone[53], we studied the nickel-aryl distance in the complex **4^{I}-C$_6$F$_5$/Pyr** in the solid state by X-ray diffraction analysis (Figure 5.3). We found a distance of 3.38 Å and 3.31 Å between the carbon atoms (C32 and C33) of the nearer distal aryl ring and the nickel center. This is a slightly closer proximity compared to the CF_3 reference (3.58 Å and 3.35 Å)[53], but clearly more distant than in the electron-rich substituted methyl derivative (3.16 Å and 3.05 Å)[53]. This fits well to the molecular weights obtained with **4^{I}-C$_6$F$_5$/Pyr**, that are slightly lower compared to the CF_3 reference but still two orders of magnitude higher than found for the

respective catalysts with alkyl groups in remote positions.[109] Accordingly, **4^{I}-C_6F_5/Pyr** produces polyethylene with significantly lower degree of branching, that is also reflected in well-defined melting properties (see *Experimental Section* for DSC traces).

The aforementioned remote substituent's effect, which can influence the polymer microstructure during catalysis, also reflects in the electron density at the metal in the catalyst precursor.[53] To this end, cyclic voltammetry experiments were performed on precatalyst **4^{I}-C_6F_5/Pyr**. The found oxidation and reduction processes for the Ni(II)/Ni(III) pair revealed a forward peak potential of 323 mV vs. 331 mV for the CF_3 analogue and -33 mV[53] for the methyl analogue (see *Experimental Section* for CV data of **4^{I}-C_6F_5/Pyr**, and *chapters 3 and 4* for CV data of other complexes). This correlates qualitatively with the found experimental polymer properties, as both precatalysts with similar high forward peak potentials produce high molecular weight polyethylenes.

A key feature of low branched high molecular weight polyethylene is its ability to form crystalline structures. The pentafluorophenyl-substituted catalyst was studied under conditions, where the crystallization of the formed polymer is essential. Late transition metal catalysts are extremely tolerant towards polar compounds and can be used even in polar protic solvents.[74,185,378,419] Under aqueous conditions, Ni(II) salicylaldiminato catalysts can produce polyethylenes in the unusual morphology of nanoscale single-crystals.[177] During this process, the formed chain directly crystallizes on the crystal growth front without any disorder.[178] By this crystallization-driven structure forming principle, uniform size and shape anisotropic particles can be generated, that enable generation of unique materials and composites.[186-188,294,420]

Polymerizations in aqueous surfactant solution were carried out at 15 °C reaction temperature and different reaction times (Table 5.1, entries 4-6). The hydrophilic catalyst **4^{I}-C_6F_5/PEG** was active for > 4 hours and produced polyethylene of M_n = 3.4 x 10^5 g/mol and a low branching degree (5 branches/1000 carbon atoms, entry 6). With increasing reaction time yield, molecular weights and particle sizes of the formed nanocrystals (column d_h) were found to increase. However, living chain and particle growth was not observed. This can be related to the fact, that pentafluorophenyl groups are less electron-withdrawing than highly electron poor perfluoroalkyl systems, that are essential to achieve full suppression of chain transfer and living polymerization conditions with these catalyst types (see *chapters 3 and 4*, Hammett substitution constants: $\sigma_m(C_4F_9)$ = 0.47[379] and $\sigma_m(C_6F_5)$ = 0.26[379]).

DLS experiments revealed a non-aggregated nature of the dispersions formed with one well-defined particle population (see *Appendix* for DLS traces). This was further confirmed by TEM

analysis, where defined and isolated truncated-lozenge to lozenge shaped particles with lateral sizes of usually between 70 and 90 nm were present (Figure 5.4). The particles are composed of disentangled polyethylene chains, as evidenced by high first melting points that are not observed or slow heating rates.[255] Crystallinities are adequate and compare well to previously reported systems.

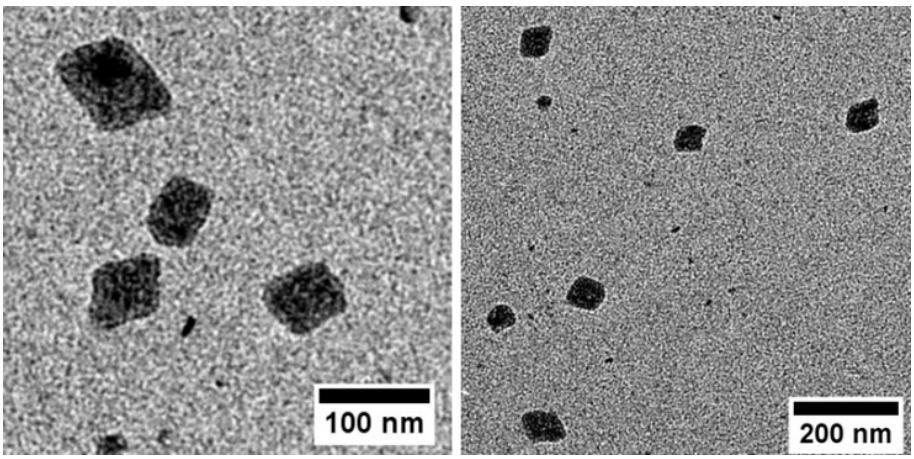

Figure 5.4. TEM images of polyethylene nanocrystals obtained from aqueous polymerization after 4 hours reaction time (Table 5.1, entry 6).

5.3 Conclusion

In summary, the synthesis and application of pentafluorophenyl-substituted *N*-terphenyl salicylaldiminato Ni(II) catalysts in ethylene polymerizations to generate high molecular weight low branched polyethylene of $M_n > 10^5$ g/mol has been demonstrated. Under aqueous conditions, dispersions of well-defined nanocrystals are generated. These findings show the effective suppression of chain transfer and branch formation, even when the electron-withdrawing remote substituents are part of the ligand's conjugated system. The electron-withdrawing impact is not generated by saturated inert groups (e.g. perfluorinated atoms), but through a highly electron-poor π system directly connected to the ligand's backbone. The resulting suppression of undesired interactions in the catalyst was further confirmed by X-ray crystal analysis and cyclic voltammetry experiments on the catalyst precursor, that showed large nickel-aryl distances, respectively, low electron densities at the nickel center. These findings underline the potential use of pentafluorophenyl substituents in ligand structures to precisely tune the metal center, as alternative to widely used saturated groups (e.g. $-CF_3$).

5.4 Experimental Section

5.4.1 Materials and general considerations

All manipulations involving air- and/or moisture-sensitive substances were carried out under inert atmosphere using standard Schlenk and glovebox techniques. Solvents were dried and degassed using standard laboratory techniques. Pentane, diethyl ether and toluene were dried and freed from oxygen by passing over columns with *BASF R3-11* catalyst and molecular sieves. Heptane was distilled over calcium hydride. Dioxane and benzene, purchased from *Merck*, were distilled over sodium. Pyridine, purchased from *Merck*, was distilled from potassium hydroxide. Dimethylacetamide, purchased from *Schuchardt*, was dried over molecular sieves. Water was deoxygenated by distillation under a constant nitrogen stream. Ethylene 3.5 was purchased from *Air Liquide* and used as obtained. 1,3-Dibromobenze, 2,6-dibromo-4-fluoroaniline and [Pd(dba)$_2$] were purchased from *TCI chemicals* and used as obtained. P^{t}Bu$_3$Me-HBF$_4$, triphenylphosphine, sodium dodecyl sulfate pellets, 4,4'-di-tert-butyl-2,2'-dipyridyl and *p*-toluene sulfonic acid were purchased from *sigma-aldrich* and used as obtained. Cesium fluoride, hexafluorobenzene, Pd(OAc)$_2$ and 3,5-diiodosalicylaldehyde, purchased from *abcr*, were used as obtained (liquids were dried over molecular sieves). Pentafluorobenzene, purchased from *Apollo Scientific*, was dried over molecular sieves. [(tmeda)NiMe$_2$], purchased from *MCat*, was stored at -30 °C prior to use.[349] Sodium sulfate, sodium carbonate and sodium chloride, purchased from Fisher Scientific, were used as obtained. Bis(pinacolato)diboron, purchased from *Activate Scientific*, was used as obtained. H$_2$N-PEG-OMe, purchased from *Iris Biotech*, was stored at -30 °C prior to use. Molecular sieves (4 Å, 0.4 nm, Type 514) were purchased from *Carl Roth*. Deuterated solvents for NMR spectroscopy, purchased from *Eurisotop*, were purged with nitrogen and dried over molecular sieves. [Ir(COE)$_2$Cl]$_2$ was synthesized according to reported procedures.[350]

NMR spectra were recorded on a *Bruker Avance III 400* instrument with a BBFO plus probe with Z-gradient, *Bruker Avance III HD 400* with a TBO probe with Z-gradient or a *Bruker Avance Neo 800* with TCI-H&F-C/N-D triple resonance cryoprobe. Chemical shifts were referenced to the signal of the solvent (residual proton signal for ^{1}H spectra, carbon signal for ^{13}C spectra). Multiplicities are reported as follows: s (singlet), doublet (d), triplet (t), quartet (q), quintet (quint.), pentet (p), virtual multiplet (v), multiplet (m), broad (br.) and combination thereof. The NMR assignments were confirmed by common 2D NMR experiments (^{1}H,^{1}H-COSY; ^{19}F,^{19}F-

COSY; $^{1}H,^{13}C$-HSQC; $^{1}H,^{13}C$-HMBC; $^{19}F,^{13}C$-HSQC and $^{19}F,^{13}C$-HMBC). *MestReNova* software by *Mestrelab Research S.L.* was used for data evaluation. Elemental analysis were carried out on an *Elementar vario MICRO cube* instrument at the Department of Chemistry at the University of Konstanz. Molecular weights of synthesized polyethylenes were determined by high temperature gel permeation chromatography (GPC) in 1,2-dichlorobenzene at 160 °C on a *Polymer Char GPC-IR instrument*, equipped with *PSS Polefin Linear XL* columns (3 x 30 cm, additional guard column), an infrared detector (*IR5 MCT*, concentration signal) and a viscometer. A standard flow rate of 1 mL/min was used, whereas a reduced flow rate of 0.5 mL/min was used for samples with expected $M_n > 10^5$ g/mol to avoid sample shearing on the columns. Molecular weights were determined via universal calibration versus narrow polystyrene standards from *PSS Polymer Standards* (software: *PSS WinGPC*, version 8.32). The infrared detector was equipped with interference filters of different wavelengths that enabled the selective and simultaneous measurements of methyl and methylene bands and allowed for determination of the methyl branch content from GPC measurements (calibrated versus samples with known degree of branching, determined via high temperature ^{13}C-NMR experiments; for details see *chapter 4.4.8*). Differential scanning calorimetry (DSC) measurements of polymers were carried out on a *Netzsch DSC 204 F1* instrument (software: *Netzsch Proteus Thermal Analysis*, version 6.1.0) with a heating/cooling rate of 10 K min^{-1}. Additional measurements to investigate the polymer chain disentanglement of samples from aqueous polymerizations were performed with a heating/cooling rate of 1 K min^{-1} (only first heating cycle reported). Dynamic light scattering (DLS) was performed on diluted polyethylene dispersions (1 droplet dispersion in 2 mL water) using a *Malvern Zetasizer Nano-ZS ZEN 3600* instrument (633 nm) in backscattering mode (173°) at 25 °C. The data was analyzed to yield particle size distributions and polydispersity indices (PDIs; dimensionless number between 0 and 1; 1 being highly polydisperse; determined from gradient of cumulants analysis) using the *Malvern Zetasizer Software*, version 7.12. Electrochemical measurements were performed on instruments of Prof. Rainer Winter's research group (*vide infra*). Transmission electron microscopy (TEM) images were recorded on a *Zeiss Libra 120 EF-TEM* instrument equipped with a CCD camera system by *TRS Tröndle*. Polyethylene dispersion samples were dialyzed versus demineralized water using *Spectra/Por Dialysis Membranes* 2, MWCO 12 – 14 kD and TEM samples prepared by drop casting (diluted to 0.01 wt-%) directly on the grid. The decrease of surfactant content during dialysis was monitored by tensiometry measurements. TEM images were analyzed using *Sysprog ImageSP* software and *ImageJ/Fiji*[351-353] software.

5.4.2 Polymerization procedures

Polymerization experiments in toluene

All ethylene polymerizations in toluene were conducted in a *Büchi miniclave* reactor with a 280 mL vessel. The reactor was equipped with a mechanical stirrer, a heating and cooling jacket connected to a thermostat, a thermocouple dipping into the polymerization mixture and a nitrogen/vacuum supply. Prior to all polymerization experiments, the reactor was evacuated and heated up (thermostat temperature: 90 °C). When the reactor temperature was > 60 °C, the reactor was flushed with nitrogen and evacuated three times. The reactor was brought 3 °C below the desired reaction temperature and filled with 100 mL of toluene via cannula transfer and the solution stirred with 500 rpm. The catalyst was dissolved in 5 mL of toluene and transferred into the reactor via syringe. Immediately after addition, the stirring rate was increased to 1000 rpm and the reactor was pressurized to the desired pressure (40 bar). During the pressurization procedure the temperature was adjusted to the desired reaction temperature. All experiments were conducted at constant pressure over the entire polymerization experiment with the ethylene feed controlled and monitored by two *Bronkhorst* mass flow meters (up to 15 g h^{-1} and 150 g h^{-1}, respectively). After the desired reaction time, the ethylene flow was stopped and the reactor carefully vented. The reactor content was poured into 300 mL of methanol and stirred for 30 minutes. The precipitated polymer was filtrated, washed with methanol and dried in a vacuum oven (60 °C, 30 mbar) overnight.

Polymerization experiments in aqueous surfactant solution

All ethylene polymerizations in water were conducted in a *Büchi ecoclave* reactor with a 600 mL vessel (see *chapter 6.2.1* for details on the reactor setup). The reactor was equipped with a heating and cooling jacket connected to a thermostat, a mechanical stirrer, a nitrogen/vacuum supply, and an ultrasonotrode (*Hielscher UIP250*) and a thermocouple couple both dipping into the reaction mixture. A *Bronkhorst* MassFlow apparatus consisting of two flow meters (up to 20 g h^{-1} and 200 g h^{-1} ethylene), a pressure meter and a compressed air-driven badger valve was used to work under constant ethylene pressure. All gas valves and devices were connected to a *HiTec Zang LabBox* and operated by *HiTec Zang LabVision®* software (ver. 2.13). The software allowed for a precise process visualization, control and recording of all relevant parameters in one single process flow chart. The integration of *HiText™* programming language enabled the construction of several automation scripts (e.g. for pressurization, temperature control, venting,

etc.). Prior to all polymerization experiments, the reactor was evacuated and heated up (thermostat temperature: 90 °C) using a custom *HiText*™ script. When the reactor temperature was > 60 °C, the reactor was flushed with nitrogen, evacuated three times and automatically cooled down to 2 °C below the desired polymerization temperature. The desired amount of surfactant (e.g. sodium dodecyl sulfate) and base (e.g. cesium hydroxide) and a magnetic stirrer bar were placed in a Schlenk flask, and the flask was transferred into a glovebox. After addition of lipophilic solvent (e.g. mesitylene) and catalyst, the flask was sealed, brought outside the glovebox and water was added under vigorous stirring via cannula transfer. The clear orange solution (after 3-5 minutes of stirring) was then transferred to the reactor and stirred at 500 rpm. The polymerization experiment was started using a custom *HiText*™ program with a graphical interface to adjust ultrasound application power and duration, reaction time and reaction temperature control. The reaction mixture was then automatically treated with ultrasound (usually for 2 minutes with 120 Watt power) and the solution temperature monitored to stay around 15 °C. Immediately afterwards, the stirring rate was increased to 1000 rpm and the reactor pressurized stepwise to 40 bar ethylene pressure within 30 seconds. The ethylene flow was then controlled and recorded by the mass flow meter and a constant pressure kept over the entire polymerization experiment. The reaction temperature was automatically adjusted to 15 °C. After the desired reaction time, the pressure was automatically released stepwise. Below 15 bar residual pressure, the reactor was vented manually into a beaker to collect migrating dispersion due to foaming. The entire dispersion was weighed, filtered over cotton wool and the solids content determined by precipitation of a 50 g aliquot of dispersion in 300 mL of methanol. After stirring for 30 minutes, the precipitated bulk polymer was filtered and washed thoroughly with water and methanol and dried in a vacuum oven (60 °C, 30 mbar) overnight.

5.4.3 Ligand synthesis (4^{I}-C_6F_5)

1,3-Bis(pentafluorophenyl)benzene (**a1-C_6F_5**)

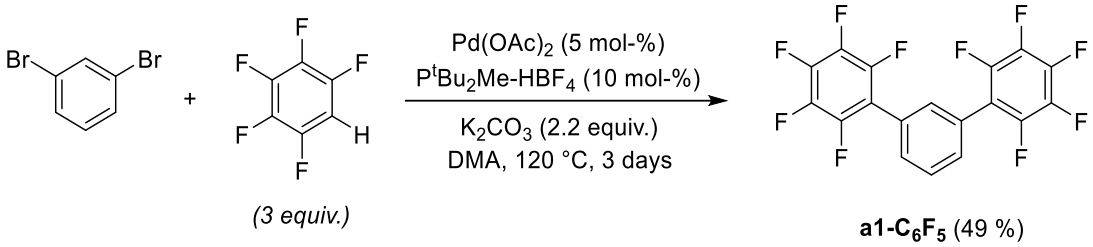

Scheme 5.1. Synthesis of 1,3-bis(pentaflurophenyl)benzene (**a1-C_6F_5**) starting from 1,3-dibromobenzene via palladium-catalyzed arylation reaction with pentafluorobenzene.

Compound **a1-C_6F_5** was synthesized according to a modified literature procedure.[418] 6.08 g K_2CO_3 (44 mmol, 2.2 equiv.), 500 mg P^tBu_2Me-HBF_4 (2 mmol, 0.1 equiv.), 225 mg $Pd(OAc)_2$ (1 mmol, 0.05 equiv.), 4.72 g 1,3-dibromobenzene (20 mmol, 1.0 equiv.) and 10.08 g pentafluorobenzene (60 mmol, 3.0 equiv.) were stirred in 15 mL dimethylacetamide (DMA) at 120 °C for 3 days (red suspension). Upon completion, the reaction mixture was allowed to cool down to room temperature and poured into 100 mL water. The mixture was extracted with 3 x 100 mL diethyl ether and the organic layer was washed with water, brine and dried over sodium sulfate. The solvent was removed under vacuum and the dark residue purified via column chromatography on silica using pentane as eluent to give the desired product as white powder. Yield: 4.02 g, 9.8 mmol, 49 %.

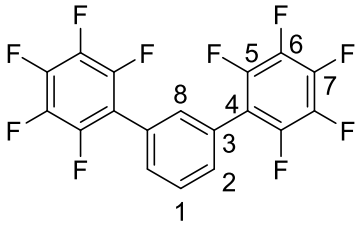

M = 410.2 g/mol

a1-C_6F_5, yield: 49 %

^{1}H NMR (600 MHz, 300 K, $CDCl_3$): δ (ppm) = 7.66 (t, $^3J_{HH}$ = 7.8 Hz, 1H, *H-1*), 7.56 (d, $^3J_{HH}$ = 7.8 Hz, 2H, *H-2*), 7.55 (s, 1H, *H-8*).

^{19}F NMR (753 MHz, 298 K, $CDCl_3$): δ (ppm) = -143.3 (dd, $^3J_{FF}$ = 22.8 Hz, $^5J_{FF}$ = 8.2 Hz, 2F, *F-5*), -154.8 (t, $^3J_{FF}$ = 20.9 Hz, 1F, *F-7*), -162.0 (td, $^3J_{FF}$ = 21.9 Hz, $^5J_{FF}$ = 8.1 Hz, 2F, *F-6*).

^{13}C{^{1}H} NMR (151 MHz, 300 K, $CDCl_3$): δ (ppm) = 144.4 (dm, $^1J_{CF}$ = 248.7 Hz, *C-5*), 140.9 (dm, $^1J_{CF}$ = 254.8 Hz, *C-7*), 138.0 (dm, $^1J_{CF}$ = 251.5 Hz, *C-6*), 132.0 (s, *C-8*), 131.2 (s, *C-2*), 129.3 (s, *C-1*), 127.3 (m, *C-3*), 115.2 (td, $^2J_{CF}$ = 16.9 Hz, $^4J_{CF}$ = 4 Hz, *C-4*).

Elemental analysis (%) for $C_{18}H_4F_{10}$: Found (Calculated):
C 52.83 (52.70); H 1.85 (0.98)

3,5-Bis(pentafluorophenyl)phenyl boronic acid pinacol ester (**b1-C_6F_5**)

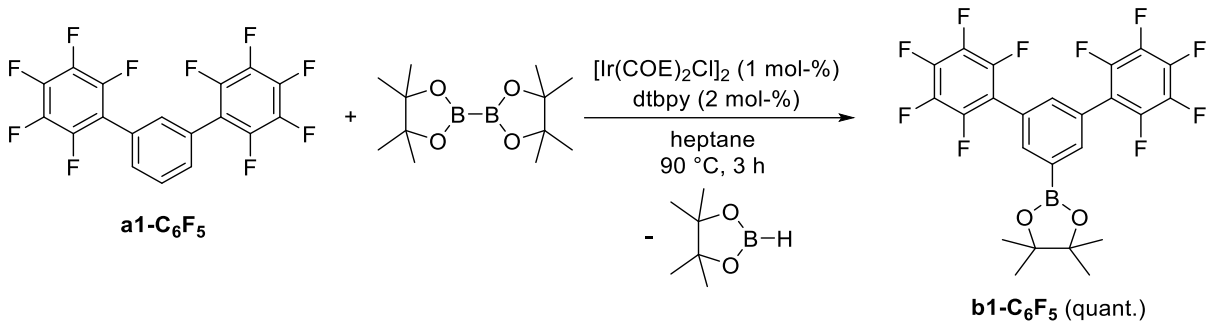

Scheme 5.2. Synthesis of 3,5-bis(pentafluorophenyl)phenylboronic acid pinacol ester (**b1-C_6F_5**) starting from 1,3-bis(pentaflurophenyl)benzene via iridium catalyzed borylation reaction.

Compound **b1-C_6F_5** was synthesized according to a modified literature procedure.[355] 74 mg $[Ir(COE)_2Cl]_2$ (82 µmol, 0.01 equiv.) and 39 mg 4,4'-di-tert-butyl-2,2'-dipyridyl (164 µmol, 0.02 equiv.) were stirred in 10 mL pentane for 5 minutes to give a dark purple catalyst solution. This was transferred to a mixture of 3.37 g 1,3-bis(pentafluorophenyl)benzene (**a1-C_6F_5**, 8.2 mmol, 1.0 equiv.) and 2.09 g bis(pinacolato)diboron (8.2 mmol, 1.0 equiv.) in 150 mL heptane. The reaction mixture was stirred for 3 hours at 90 °C. After cooling to room temperature, the solvent was removed under reduced pressure and the residue kept under vacuum for several hours to remove residues of pinacolborane. The product was obtained as red solid in quantitative yield. Yield: 4.37 g, 8.2 mmol, quant.

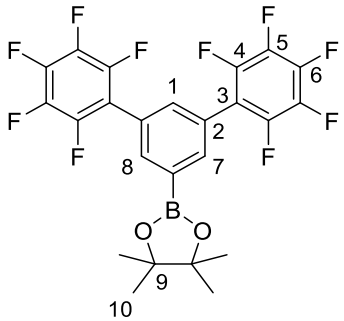

M = 536.2 g/mol

b1-C_6F_5, yield: quant.

^{1}H NMR (400 MHz, 300 K, $CDCl_3$): δ (ppm) = 7.71 (s, 4H, *H-6*), 7.55 (s, 2H, *H-12*), 7.00 (d, $^3J_{HF}$ = 8.7 Hz, 2H, *H-2*), 3.85 (br. s, 2H, -N*H*$_2$).

^{19}F{^{1}H} NMR (376 MHz, 300 K, $CDCl_3$): δ (ppm) = -126.5 (s, 1F, *F-1*), -142.9 (dd, $^3J_{FF}$ = 22.7 Hz, $^5J_{FF}$ = 8.2 Hz, 8F, *F-9*), -153.7 ($^3J_{FF}$ = 20.9 Hz, 4F, *F-11*), -161.2 (m, 8F, *F-10*).

^{13}C{^{1}H} NMR (101 MHz, 300 K, $CDCl_3$): δ (ppm) = 156.2 (d, $^1J_{CF}$ = 238.1 Hz, *C-1),* 144.4 (dm, $^1J_{CF}$ = 249.2 Hz, *C-9*), 141.0 (dm, $^1J_{CF}$ = 255.5 Hz, *C-11*), 139.9 (d, $^4J_{CF}$ = 1.7 Hz, *C-5*), 137.9 (dm, $^1J_{CF}$ = 252.6 Hz, *C-10*), 137.4 (s, *C-4*), 131.9 (s, *C-6*), 131.3 (s, *C-12*), 128.1 (s, *C-7*), 127.3 (d, $^3J_{CF}$ = 7.3 Hz, *C-3*), 117.2 (d, $^1J_{CF}$ = 22.6 Hz, *C-2*), 114.7 (td, $^2J_{CF}$ = 16.8, $^4J_{CF}$ = 4.0 Hz, *C-8*).

Elemental analysis (%) for $C_{24}H_{15}BF_{10}O_2$: Found (Calculated):
C 53.73 (53.76); H 3.74 (2.82)

2,6-Bis(3,5-pentafluorophenyl)-4-fluoroaniline (**c4-C_6F_5**)

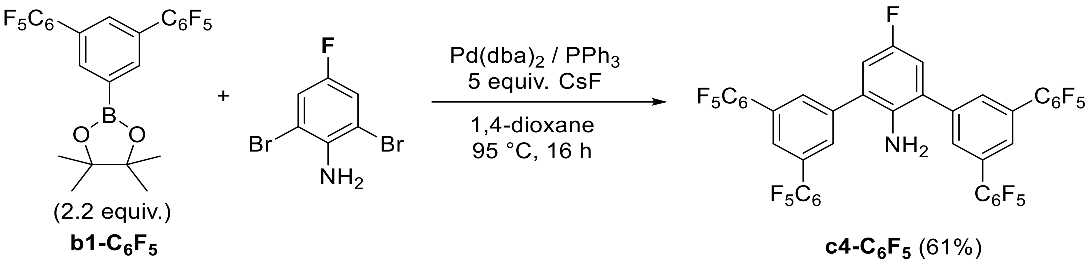

Scheme 5.3. Synthesis of 2,6-bis(3,5-pentafluorophenyl)-4-fluoroaniline (**c4-C_6F_5**) from palladium-catalyzed Suzuki coupling of 3,5-bis(pentafluorophenyl)boronic acid pinacol ester with 2,6-dibromo-4-fluoroaniline.

78 mg Pd(dba)$_2$ (136 µmol, 0.05 equiv.) and 78 mg PPh$_3$ (299 µmol, 0.11 equiv.) were dissolved in 5 mL 1,4-dioxane to give an orange catalyst solution. This was added to a mixture of 1.46 g 3,5-dipentafluorophenylphenyl boronic acid pinacol acid (**b1-C_6F_5**, 2.7 mmol, 2.2 equiv.), 332 mg 2,6-dibromo-4-fluoroaniline (1.2 mmol, 1.0 equiv.) and 2.07 g CsF (13.6 mmol, 5 equiv.) in 150 mL 1,4-dioxane and stirred for 16 hours at 95 °C. After the reaction mixture was allowed to room temperature, the solvent was removed under reduced pressure and the residue suspended in a mixture of 100 mL water and 100 mL diethyl ether. The phases were separated, and the aqueous phase extracted with one more portion of 100 mL diethyl ether. The organic layers were combined and dried over sodium sulfate. After column chromatography on silica (pentane/diethyl ether/triethylamine [95:4:1]), the product was obtained as dark solid. Yield: 687 mg, 756 µmol, 61 %.

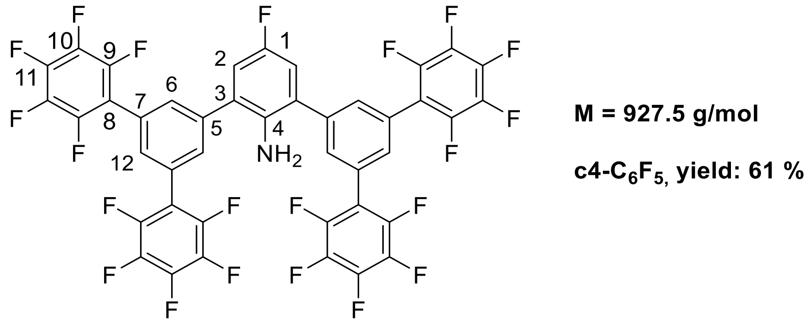

^{1}H NMR (400 MHz, 300 K, CDCl$_3$): δ (ppm) = 7.71 (s, 4H, *H-6*), 7.55 (s, 2H, *H-12*), 7.00 (d, $^3J_{HF}$ = 8.7 Hz, 2H, *H-2*), 3.85 (br. s, 2H, -N*H$_2$*).

^{19}F{^{1}H} NMR (376 MHz, 300 K, CDCl$_3$): δ (ppm) = -126.5 (s, 1F, *F-1*), -142.9 (dd, $^3J_{FF}$ = 22.7 Hz, $^5J_{FF}$ = 8.2 Hz, 8F, *F-9*), -153.7 ($^3J_{FF}$ = 20.9 Hz, 4F, *F-11*), -161.2 (m, 8F, *F-10*).

^{13}C{^{1}H} NMR (101 MHz, 300 K, CDCl$_3$): δ (ppm) = 156.2 (d, $^1J_{CF}$ = 238.1 Hz, *C-1*), 144.4 (dm, $^1J_{CF}$ = 249.2 Hz, *C-9*), 141.0 (dm, $^1J_{CF}$ = 255.5 Hz, *C-11*), 139.9 (d, $^4J_{CF}$ = 1.7 Hz, *C-5*), 137.9 (dm, $^1J_{CF}$ = 252.6

Hz, *C-10*), 137.4 (s, *C-4*), 131.9 (s, *C-6*), 131.3 (s, *C-12*), 128.1 (s, *C-7*), 127.3 (d, $^{3}J_{CF}$ = 7.3 Hz, *C-3*), 117.2 (d, $^{1}J_{CF}$ = 22.6 Hz, *C-2*), 114.7 (td, $^{2}J_{CF}$ = 16.8, $^{4}J_{CF}$ = 4.0 Hz, *C-8*).

Elemental analysis (%) for $C_{42}H_{10}F_{21}N$: Found (Calculated):
C 54.61 (54.39); H 2.13 (1.09); N 1.80 (1.51)

N-[2,6-Bis(3,5-pentafluorophenyl)-4-fluorophenyl]-4,6-diiodosalicylaldimine (**4^{I}-C$_6$F$_5$**)

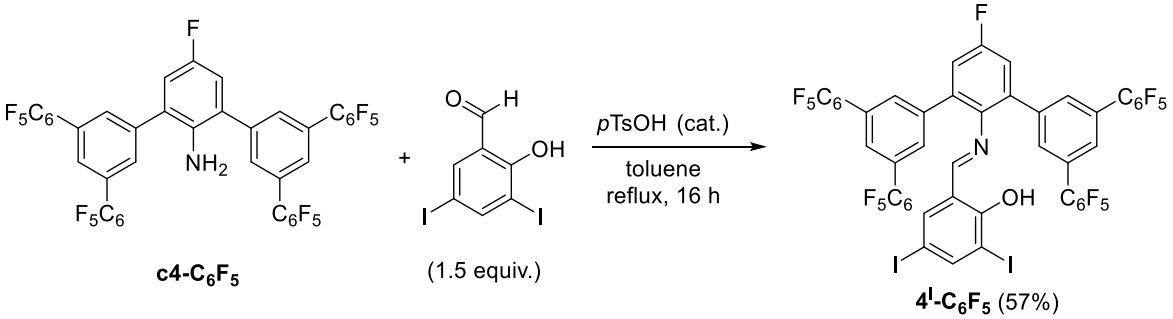

Scheme 5.4. Synthesis of *N*-[2,6-bis(3,5-bis(pentafluorophenyl)4-fluorophenyl)phenyl]-4,6-diiodosalicyl-aldimine (**4^{I}-C$_6$F$_5$**) by acid catalyzed condensation reaction with 3,5-diidosalicyladehyde.

676 mg 2,6-Bis(3,5-pentafluorophenyl)-4-fluoroaniline (**c4-C$_6$F$_5$**, 729 µmol, 1.0 equiv.), 555 mg 3,5-diiodosalicylaldehyde (1.09 mmol, 1.5 equiv.) and *p*-toluenesulfonic acid (25 mg) were dissolved in 200 mL toluene. The reaction flask was equipped with a Dean-Stark apparatus, filled with fresh molecular sieve and toluene, and the reaction mixture heated to intense reflux for 16 hours. The condensing solvent was removed through the outlet trap of the Dean-Stark apparatus and the dark residue purified by column chromatography on silica (pentane/diethyl ether, [95:5]) to give the desired product as yellow powder. Yield: 533 mg, 415 µmol, 57 %.

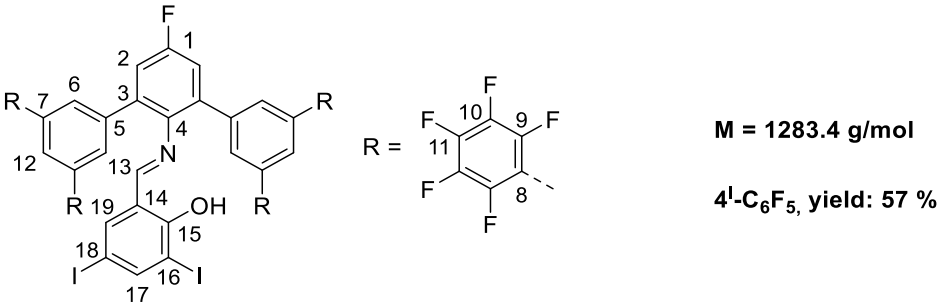

M = 1283.4 g/mol

4^{I}-C$_6$F$_5$, yield: 57 %

^{1}H NMR (800 MHz, 298 K, $CDCl_3$): δ (ppm) = 13.19 (s, 1H, *-OH*), 8.01 (d, $^{4}J_{HH}$ = 2.1 Hz, 1H, H-17), 7.84 (s, 1H, *H-13*), 7.54 (s, 4H, *H-6*), 7.45 (s, 2H, *H-12*), 7.29 (d, $^{3}J_{HF}$ = 8.3 Hz, *H-2*), 7.13 (d, $^{4}J_{HH}$ = 2.2 Hz, 1H, *H-19*).

^{19}F NMR (753 MHz, 298 K, $CDCl_3$): δ (ppm) = -114.8 (t,$^{3}J_{FH}$ = 8.3 Hz, 1F, F-1), -142.7 (dd, $^{3}J_{FF}$ = 23.1 Hz, $^{5}J_{FF}$ = 8.1 Hz, 8F, F-9), -153.6 (t, $^{3}J_{FF}$ = 21.0 Hz, 4F, F-11), -161.1 (td, $^{3}J_{FF}$ = 22.3 Hz, $^{5}J_{FF}$ = 8.1 Hz, 8F, *F-10*).

$^{13}C\{^1H\}$ NMR (201 MHz, 298 K, $CDCl_3$): δ (ppm) = 168.0 (s, *C-13*), 160.7 (d, $^1J_{CF}$ = 248.9 Hz, *C-1*), 159.8 (s, *C-15*), 150.0 (s, *C-17*), 144.2 (dm, $^1J_{CF}$ = 250.6 Hz, *C-9*), 141.1 (dm, $^1J_{CF}$ = 257.2 Hz, *C-11*), 141.0 (s, *C-4*), 140.5 (s, *C-19*), 139.2 (s, *C-5*), 138.1 (dm, $^1J_{CF}$ = 251.4 Hz, *C-10*), 135.2 (d, $^3J_{CF}$ = 7.7 Hz, *C-3*), 132.2 (s, *C-6*), 131.4 (s, *C-12*), 127.9 (s, *C-7*), 119.8 (s, *C-14*), 117.8 (d, $^2J_{CF}$ = 22.6 Hz, *C-2*), 114.4 (td, $^2J_{CF}$ = 16.9, $^4J_{CF}$ = 3.6 Hz, *C-8*), 86.5 (s, *C-16*), 80.1 (s, C-18).

Elemental analysis (%) for $C_{49}H_{12}F_{21}I_2NO$: Found (Calculated)
C 46.78 (45.86); H 1.62 (0.94); N 1.05 (1.09)

5.4.4 Synthesis of complexes (4^I-C_6F_5/L)

*{3,5-Diiodo-N-[2,6-bis(3,5-(dipentafluorophenyl)phenyl)phenyl]salicylaldiminato-κ²-N,O}methyl-pyridine-nickel(II) (**4^I-C_6F_5/Pyr**)*

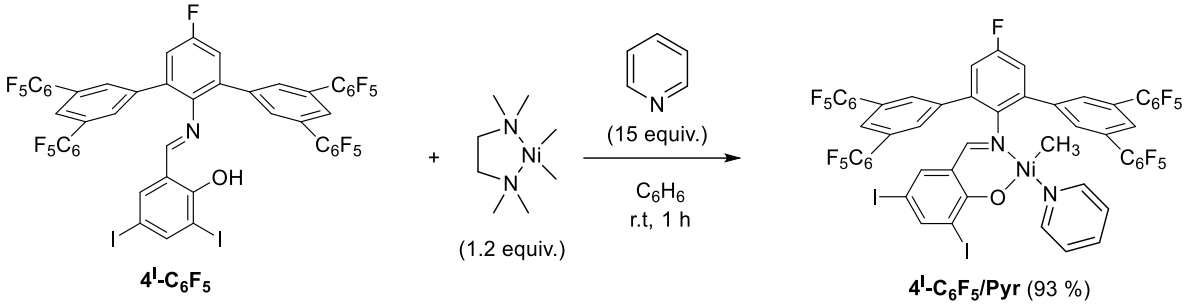

Scheme 5.5. Synthesis of the pentafluorophenyl-substituted κ²-(*N,O*)-salicylaldiminato nickel(II) methyl pyridine complex (**4^I-C_6F_5/Pyr**). The labile ligand (pyridine) was added to a mixture of nickel precursor and salicylaldimine to generate the respective nickel complex.

To 18.4 mg [(tmeda)$NiMe_2$] (90 µmol, 1.2 equiv.) and 96.3 mg salicylaldmine **4^I-C_6F_5** (75 µmol, 1.0 equiv.) was added a solution of 89 mg pyridine (1125 µmol, 15.0 equiv.) in 5 mL benzene. Gas evolution (methane) was observed and the reaction mixture turned red. The reactants were stirred for 1 hour at room temperature. The formed nickel black was removed via centrifugation. The red solution was frozen in liquid nitrogen und the solvent removed by freeze drying to give the desired product as a red powder. Yield: 100 mg, 69.8 µmol, 93 %.

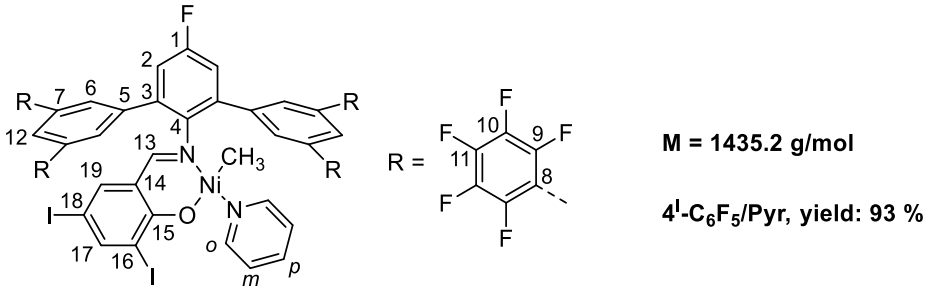

^1H NMR (800 MHz, 298 K, C_6D_6): δ (ppm) = 8.37 (d, $^3J_{HH}$ = 4.8 Hz, 2H, *o-Pyr*), 7.87 (d, $^4J_{HH}$ = 2.2 Hz, 1H, *H-17*), 7.77 (s, 4H, *H-6*), 7.43 (s, 2H, *H-12*), 7.10 (d, $^3J_{HF}$ = 8.4 Hz, 2H, *H-2*), 6.93 (s, 1H, *H-*

13), 6.85 (d, $^{4}J_{HH}$ = 2.3 Hz, 1H, *H-19*), 6.71 (t, $^{3}J_{HH}$ = 7.7 Hz, 1H, *p-Pyr*), 6.56 (t, $^{3}J_{HH}$ = 7.7 Hz, 2H, *m-Pyr*), -0.69 (s, 3H, Ni-CH_3).

^{19}F NMR (753 MHz, 298 K, C_6D_6): δ (ppm) = 114.8 (t, $^{3}J_{HF}$ = 8.5 Hz, 1F, *F-1*), -143.5 (dd, $^{3}J_{FF}$ = 24.2 Hz, $^{5}J_{FF}$ = 7.6 Hz, 8F, F-9), -154.1 (t, $^{3}J_{FF}$ = 21.7 Hz, 4F, F-11), -161.4 (td, $^{3}J_{FF}$ = 23.1 Hz, $^{5}J_{FF}$ = 7.7 Hz, 8F, *F-10*).

^{13}C{^{1}H} NMR (201 MHz, 298 K, C_6D_6): δ (ppm) = 168.9 (s, *C-13*), 163.8 (s, *C-15*), 160.7 (d, $^{1}J_{CF}$ = 247.0 Hz, *C-1*), 151.7 (br. s, *o-Pyr*), 149.8 (s, *C-17*), 146.7 (s, *C-4*), 144.4 (dm, $^{1}J_{CF}$ = 250.2 Hz, *C-9*), 142.0 (s, *C-19*), 141.0 (dm, $^{1}J_{CF}$ = 254.0, *C-11*), 140.0 (s, *C-5*), 138.2 (dm, $^{1}J_{CF}$ = 251.0, *C-10*), 136.7 (br. s., *p-Pyr*), 136.3 (d, $^{3}J_{CF}$ = 7.9 Hz, *C-3*), 133.1 (s, *C-6*), 131.4 (s, *C-12*), 123.3 (br. s, *m-Pyr*), 120.5 (s, *C-14*), 117.4 (d, $^{2}J_{CF}$ = 22.7 Hz, *C-2*), 114.7 (t, $^{2}J_{CF}$ = 16.5 Hz, *C-8*), 96.6 (s, *C-16*), 75.5 (s, *C-18*), -7.7 (s, Ni-CH_3). Resonance for *C-7* is obscured by benzene-d_6 resonance (127.8, assigned by ^{1}H,^{13}C-HMBC and ^{19}F,^{13}C-HMBC).

Elemental analysis (%) for $C_{55}H_{19}F_{21}I_2N_2NiO$: Found (Calculated)
C 46.92 (46.03); H 1.58 (1.33); N 2.19 (1.95)

{3,5-Diiodo-N-[2,6-bis(3,5-bispentafluorophenyl)phenyl]salicylaldiminato-κ²-N,O}methyl[α-methoxy-ω-amino poly(ethylene glycol)]lnickel(II) (**4^{I}-C$_6$F$_5$/PEG**)

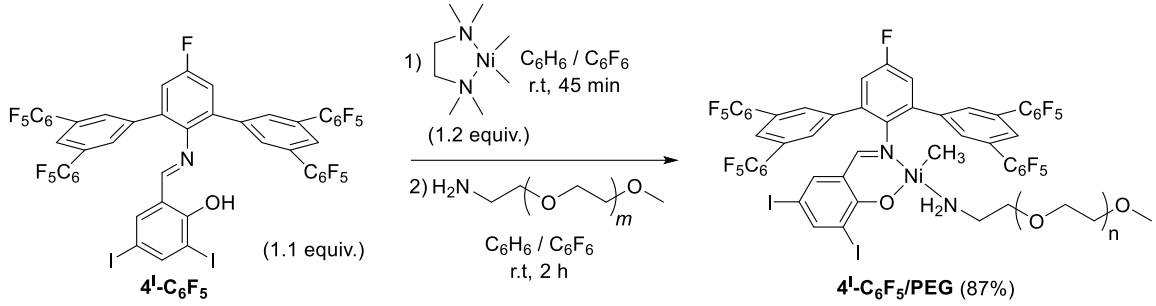

Scheme 5.6. Synthesis of the pentafluorophenyl-substituted κ²-(*N,O*)-salicylaldiminato nickel(II) methyl [α-methoxy-ω-amino poly(ethylene glycol)] complex (**4^{I}-C$_6$F$_5$/PEG**). The labile ligand (α-methoxy-ω-amino poly[ethylene glycol]) was added to a reacted mixture of nickel precursor and salicylaldimine to generate the respective nickel complex.

To 12.3 mg [(tmeda)NiMe$_2$] (60 μmol, 1.2 equiv.) was added a solution of 70.6 mg salicylaldimine **4^{I}-C$_6$F$_5$** (55 μmol, 1.1 equiv.) in a mixture of benzene/hexafluorobenzene (4 mL / 1 mL) and stirred for 45 minutes at room temperature. During the addition, gas evolution (methane) was observed and an orange to red solution (slightly turbid) was obtained. α-Methoxy-ω-amino poly(ethylene glycol) (1.0 equiv.; M = 5516 g mol^{-1} or 1981 g mol^{-1}) in 1 ml of benzene was added and the reaction was stirred for further 2 hours at room temperature (the solution cleared up). After filtration through a syringe filter to remove nickel black, the solvent was removed under vacuum. The orange residue was washed with portions of pentane (3 times, 7.5 mL each) until the filtrate remained almost colorless (slightly yellow). After drying under

vacuum, the desired product was obtained as an orange powder. Yield: 300 mg, 43.5 µmol, 87 % (for M(PEG) = 5516 g mol^{-1}).

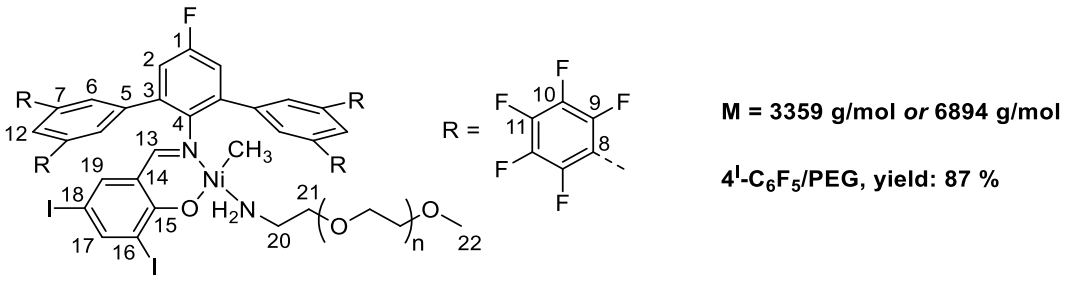

^{1}H NMR (800 MHz, 298 K, C_6D_6): δ (ppm) = 7.89 (d, $^{4}J_{HH}$ = 2.2 Hz, 1H, *H-17*), 7.69 (s, 4H, *H-6*), 7.43 (s, 2H, *H-12*), 7.03 (d, $^{3}J_{HF}$ = 8.4 Hz, 2H, *H-2*), 7.01 (s, 1H, *H-13*), 6.89 (d, $^{3}J_{HH}$ = 2.2 Hz, 1H, *H-19*), 3.8-3.1 (m, 328 H, *H-21*, *H-22*, *H-PEG*), 2.56 (m, 2H, *H-20*), 1.10 (t, $^{3}J_{HH}$ = 7.1 Hz, 2H, -NH_2), -1.03 (s, Ni-CH_3).

^{19}F NMR (753 MHz, 298 K, C_6D_6): δ (ppm) = 115.0 (t, $^{3}J_{HF}$ = 8.4 Hz, 1F, *F-1*), -143.3 (dd, $^{3}J_{FF}$ = 23.7 Hz, $^{5}J_{FF}$ = 7.9 Hz, 8F, F-9), -154.1 (t, $^{3}J_{FF}$ = 21.5 Hz, 4F, F-11), -161.2 (td, $^{3}J_{FF}$ = 23.1 Hz, $^{5}J_{FF}$ = 7.9 Hz, 8F, *F-10*).

^{13}C{^{1}H} NMR (201 MHz, 298 K, C_6D_6): δ (ppm) = 168.1 (s, *C-13*), 162.9 (s, *C-15*), 160.5 (d, $^{1}J_{CF}$ = 247.1 Hz, *C-1*), 149.4 (s, *C-17*), 146. 6 (s, *C-4*), 144.4 (dm, $^{1}J_{CF}$ = 247.9 Hz, *C-9*), 142.0 (s, *C-19*), 141.1 (dm, $^{1}J_{CF}$ = 256.8 Hz, *C-11*), 140.0 (s, *C-5*), 138.2 (dm, $^{1}J_{CF}$ = 252.1 Hz, *C-10*), 136.1 (d, $^{3}J_{CF}$ = 7.9 Hz, *C-3*), 133.0 (s, *C-6*), 131.4 (s, *C-12*), 120.5 (s, *C-14*), 117.4 (d, $^{2}J_{CF}$ = 22.4 Hz, *C-2*), 114.7 (t, $^{2}J_{CF}$ = 16.7 Hz, *C-8*), 96.8 (s, *C-16*), 72.7 (s, *C-18*), 72.5-72.0 (m, *C-PEG*), 70.3 (s, *C-22*), 58.7 (s, *C-21*), 43.2 (s, *C-20*), -13.0 (s, Ni-*C*H_3). Resonance for *C-7* is obscured by benzene-d_6 resonance (127.7, assigned by ^{1}H,^{13}C-HMBC and ^{19}F,^{13}C-HMBC).

Elemental analysis (%) for $C_{300}H_{519}F_{21}I_2N_2NiO_{126}$: Found (Calculated)
C 52.19 (52.44); H 7.21 (7.59); N 0.53 (0.41)

5.4.5 Cyclic voltammetry (4^{I}-C_6F_5/Pyr)

All electrochemical measurements were carried out with a computer-controlled BAS potentiostat, connected to a custom-built cyclindrical one-compartment cell (Prof. Winter research group). The experiments were performed under inert argon atmosphere. A spiral-shaped Pt wire and an Ag wire, sealed into glass capillaries, were used as counter and reference electrodes and introduced at opposite sides of the cell. A platinum electrode was used as working electrode and introduced through the top port of the cell. Prior to all experiments, the working electrode was polished with 1 µm and 0.25 µm diamond paste (purchased from *Buehler-Wirtz*). The complex was dissolved in approximately 6 mL of dichloromethane mixed with NBu_4^+ PF_6^- (0.1 M) as supporting electrolyte. Referencing was performed by addition of decamethylferrocene (Cp^*_2Fe) as an internal standard to the analyte solution, after all data of interest had been acquired, and another set of scans was recorded. Final referencing was performed against the ferrocene/ferrocenium couple with $E_{1/2}(Cp^*_2Fe)$ = -550 mV vs. $Cp_2Fe^{o/+}$. Electrochemical data were acquired with a standard sweep rate of 400 mV s^{-1}.

All cyclic voltammetry measurements of complexes showed oxidation and reduction transitions for the Ni(II)/Ni(III) pair. Only partial reversibility was observed, in line with an expected rapid decomposition of the formed Ni(III) species.

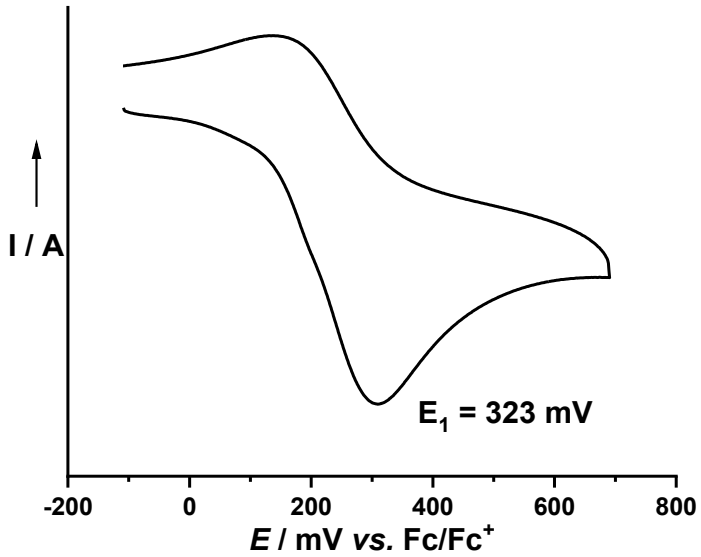

Figure 5.5. Cyclic voltammogram of complex **4^{I}-C_6F_5/Pyr**.

5.4.6 Crystallographic data (4^{I}-C_6F_5/Pyr)

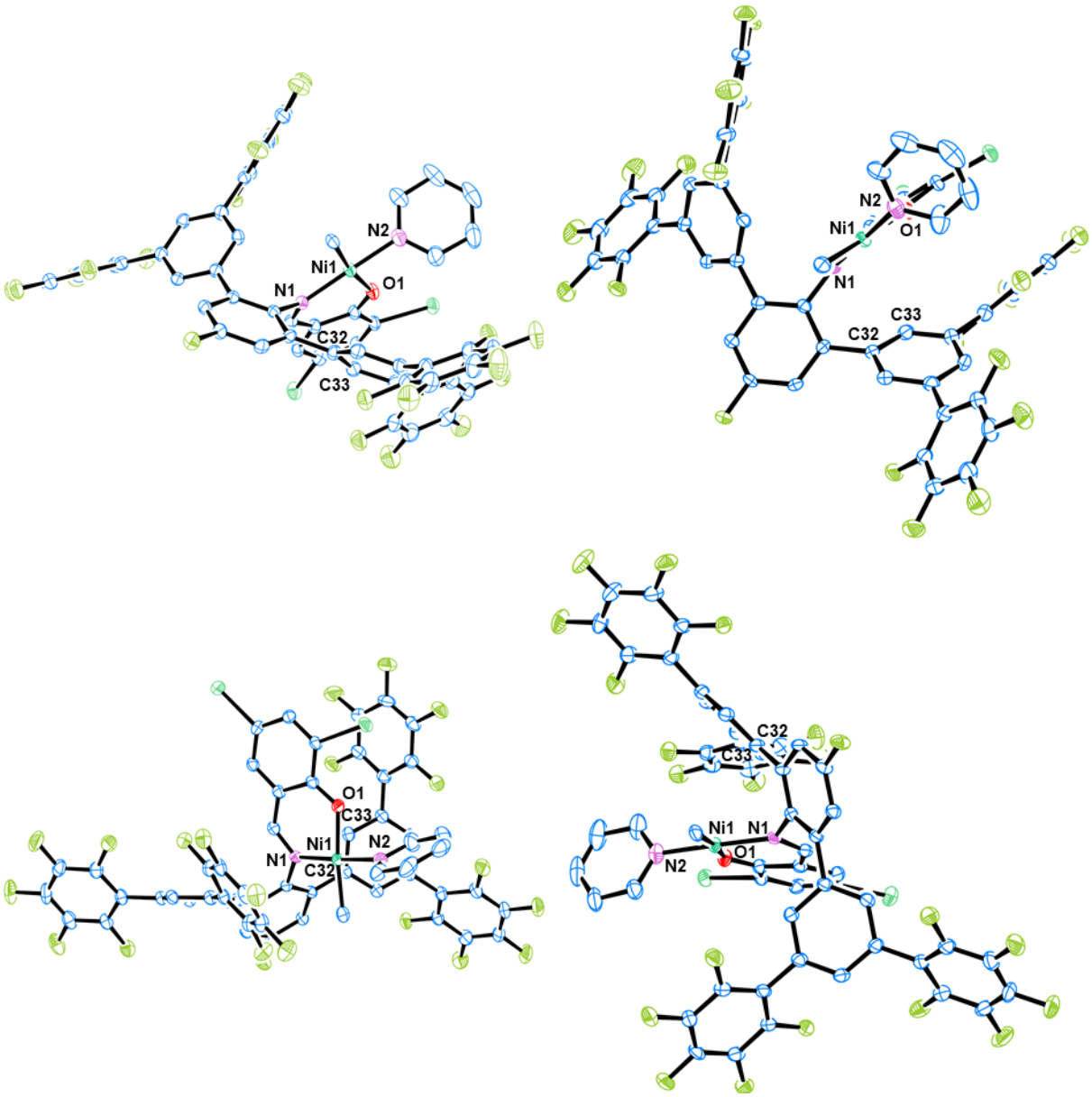

Figure 5.6. ORTEP plots (50 % probability ellipsoids, hydrogens are omitted for clarity) of the structure determined by X-ray diffraction of **4^{I}-C_6F_5/Pyr** from different perspectives.

Crystal data and structure refinement for complex **4^{I}-C_6F_5/Pyr**:

Identification code	CCDC 1966193
Empirical formula	$C_{61}H_{25}F_{21}I_2N_2NiO$
Formula weight	1513.34
Temperature/K	100.15
Crystal system	triclinic
Space group	P-1
a/Å	13.4818(13)
b/Å	14.1718(13)
c/Å	15.2159(71)
α/°	101.333(8)
β/°	97.347(8)
γ/°	97.595(8)
Volume/Å^3	2789.9(5)
Z	2
ρ_{calc} g/cm^3	1.802
μ/mm^{-1}	1.570
F(000)	1472.0
Crystal size/mm^3	0.2 × 0.2 × 0.2
Radiation	Mo K_α (λ = 0.71073)
2Θ range for data collection/°	3.922 to 55.15
Index ranges	-17 ≤ h ≤ 17, -15 ≤ k ≤ 18, -19 ≤ l ≤ 19
Reflections collected	26333
Independent reflections	12751 [R_{int} = 0.0273, R_{sigma} = 0.0401]
Data/restraints/parameters	12751/0/794
Goodness-of-fit on F^2	1.058
Final R indexes [I>=2σ (I)]	R1 = 0.0376, wR2 = 0.0935
Final R indexes [all data]	R1 = 0.0614, wR2 = 0.1033
Largest diff. peak/hole / e Å^{-3}	0.59 / -1.38

Experimental:

Single crystals of $C_{61}H_{25}F_{21}I_2N_2NiO$ (**4^{I}-C_6F_5/Pyr**) were obtained by layering a benzene solution with pentane. A suitable crystal was selected and placed on a STOE IPDS 2T diffractometer. The crystal was kept at 100 K during data collection. The structure was solved with ShelXT[357] (Intrinsic Phasing) structure solution program in Olex2 (v.1.2)[358] and refined with the ShelXL[359] (Least Squares minimization) refinement package. Graphical representations were created in ORTEP-3 (v.2014.1)[361] for Windows.

5.5 Appendix

5.5.1 NMR spectra of complexes (4^{I}-C_6F_5/L)

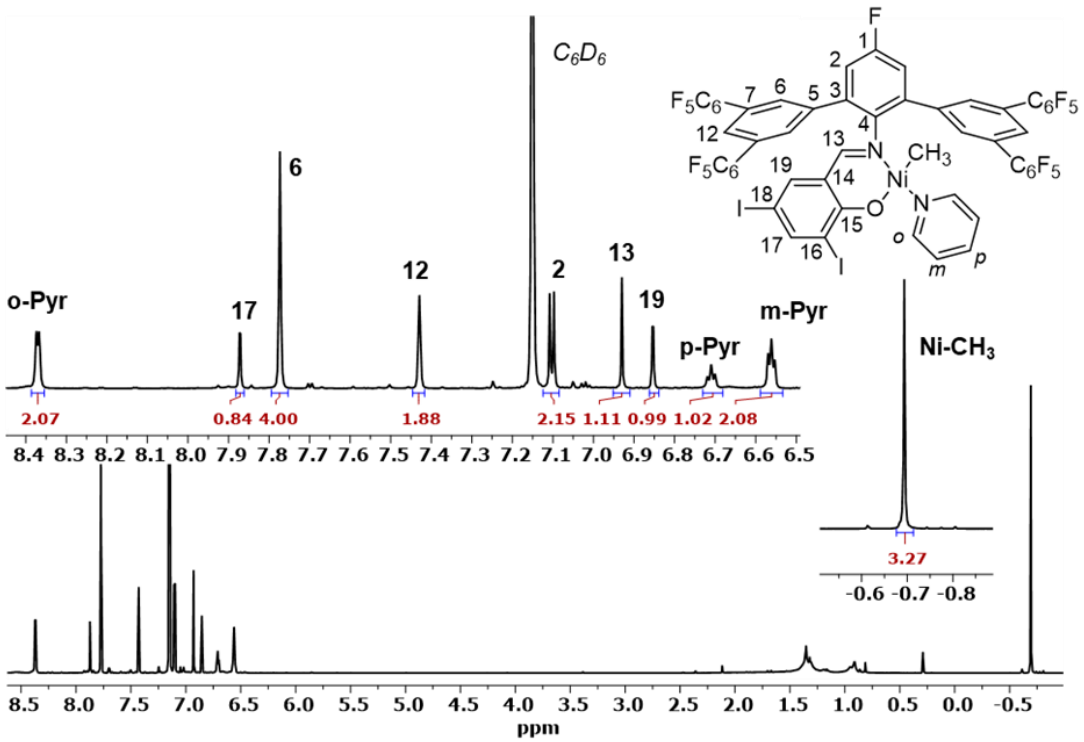

Figure 5.7. ^{1}H NMR spectrum (800 MHz, 298 K, C_6D_6) of complex **4^{I}-C_6F_5/Pyr**.

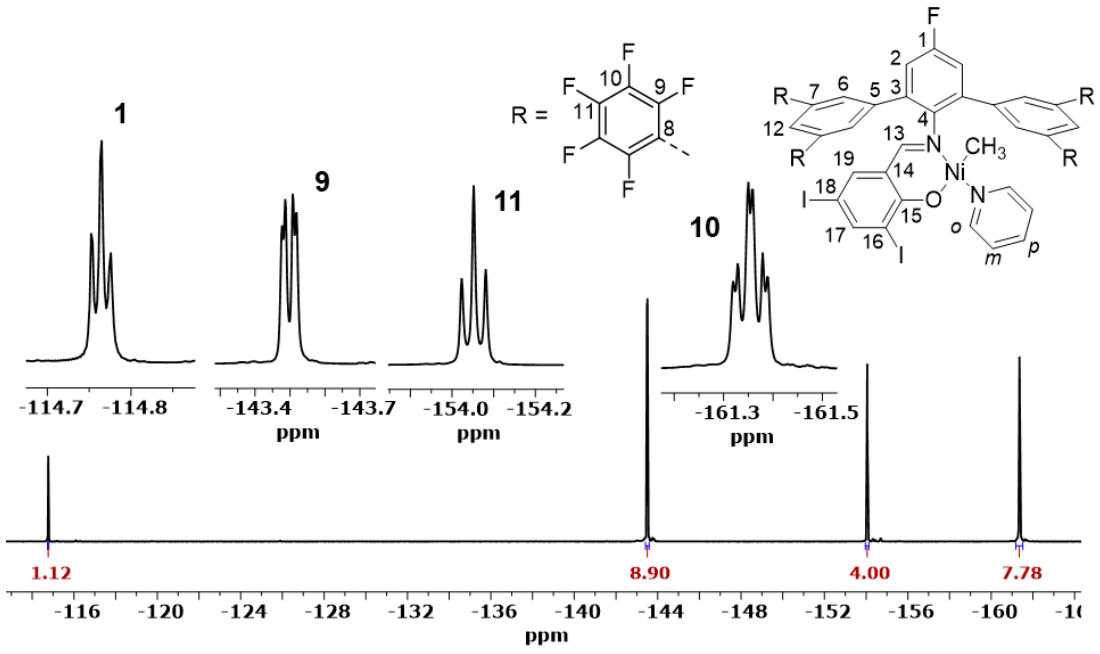

Figure 5.8. ^{19}F NMR spectrum (753 MHz, 298 K, C_6D_6) of complex **4^{I}-C_6F_5/Pyr**.

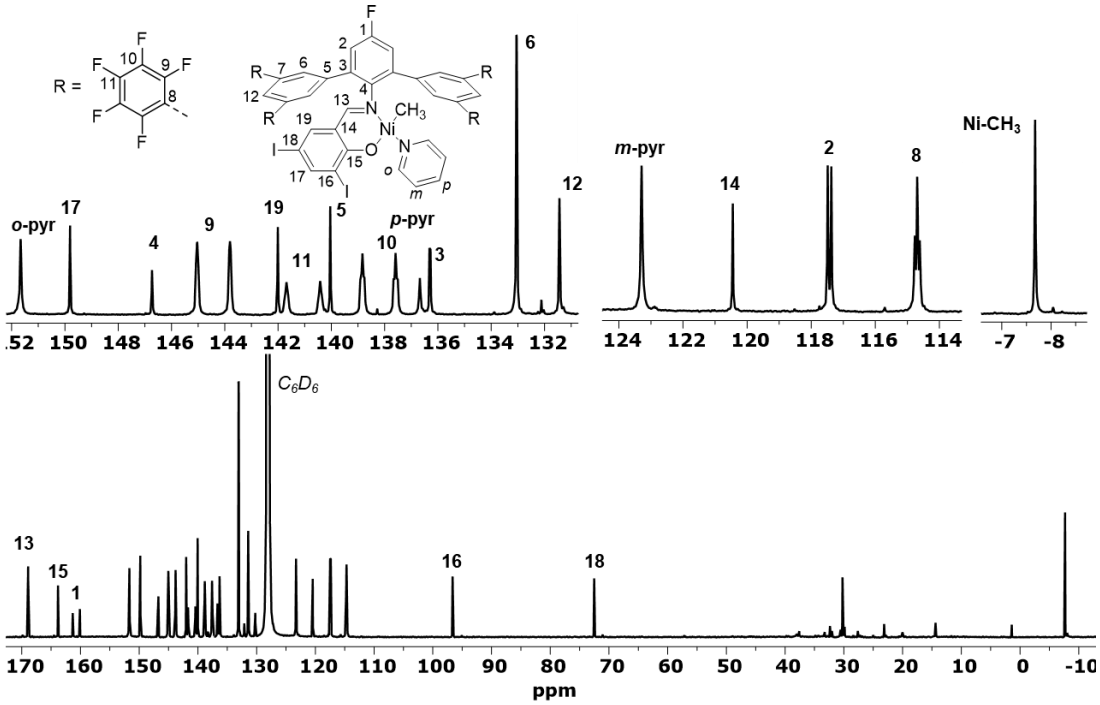

Figure 5.9. $^{13}C\{^{1}H\}$ NMR spectrum (201 MHz, 298 K, C_6D_6) of complex **4^{I}-C$_6$F$_5$/Pyr.**

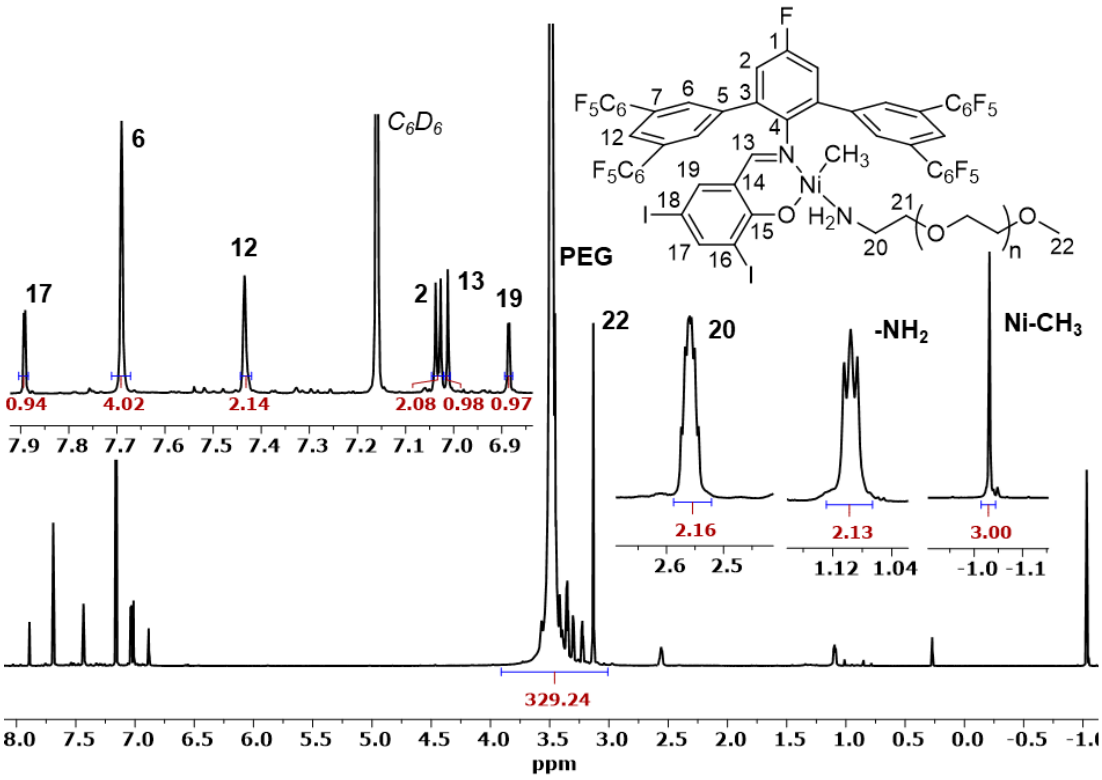

Figure 5.10. ^{1}H NMR spectrum (800 MHz, 298 K, C_6D_6) of complex **4^{I}-C$_6$F$_5$/PEG** (with M(PEG) = 1981 g/mol).

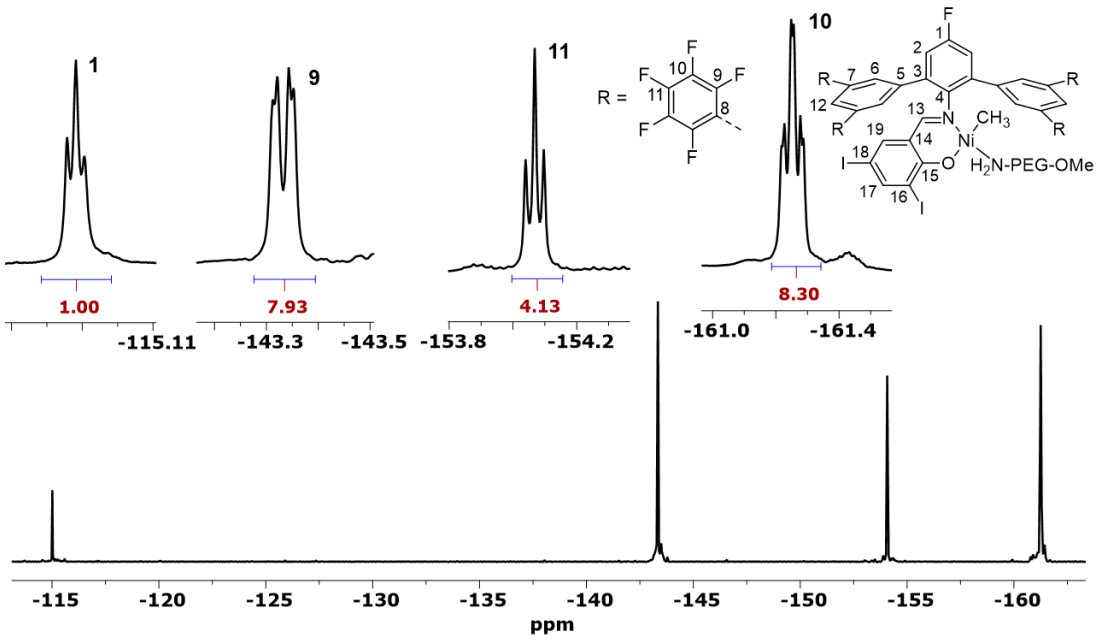

Figure 5.11. ^{19}F NMR spectrum (753 MHz, 298 K, C_6D_6) of complex **4^I-C_6F_5/PEG** (with M(PEG) = 1981 g/mol).

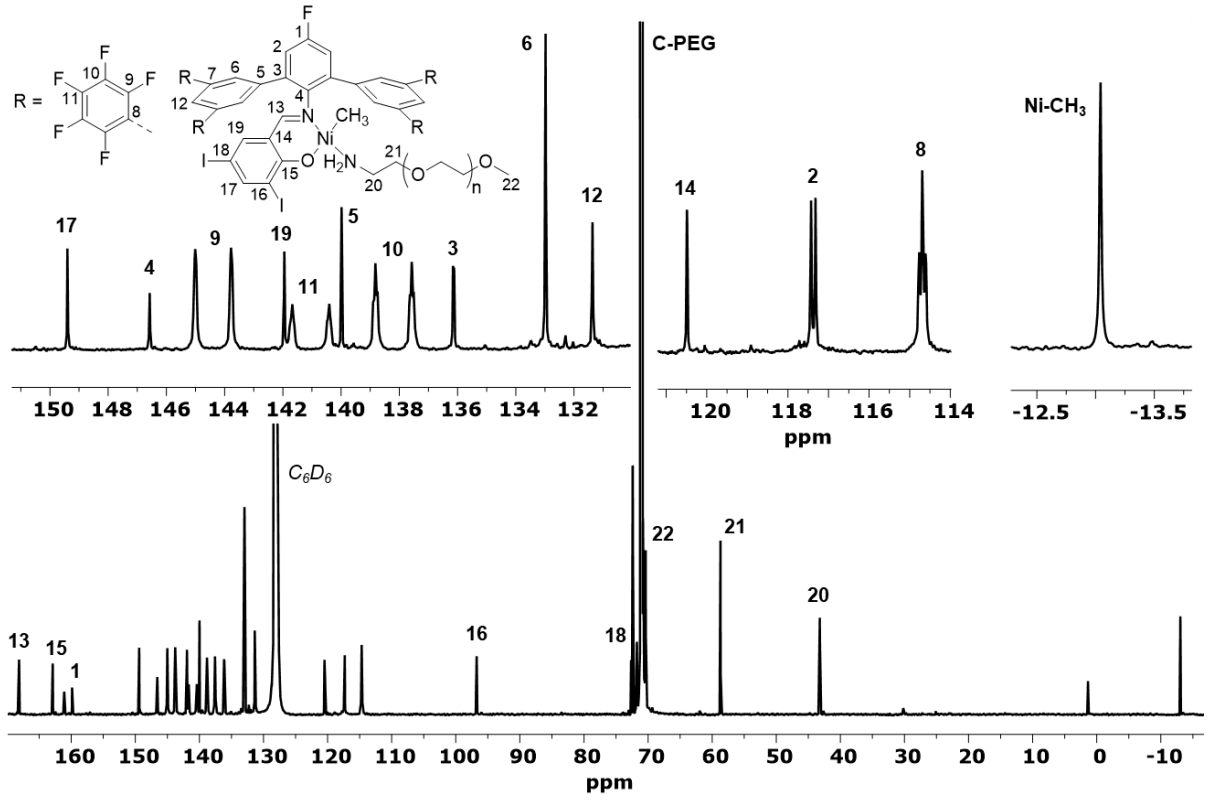

Figure 5.12. $^{13}C\{^1H\}$ NMR spectrum (201 MHz, 298 K, C_6D_6) of complex **4^I-C_6F_5/PEG** (with M(PEG) = 1981 g/mol).

5.5.2 GPC traces of synthesized polyethylenes

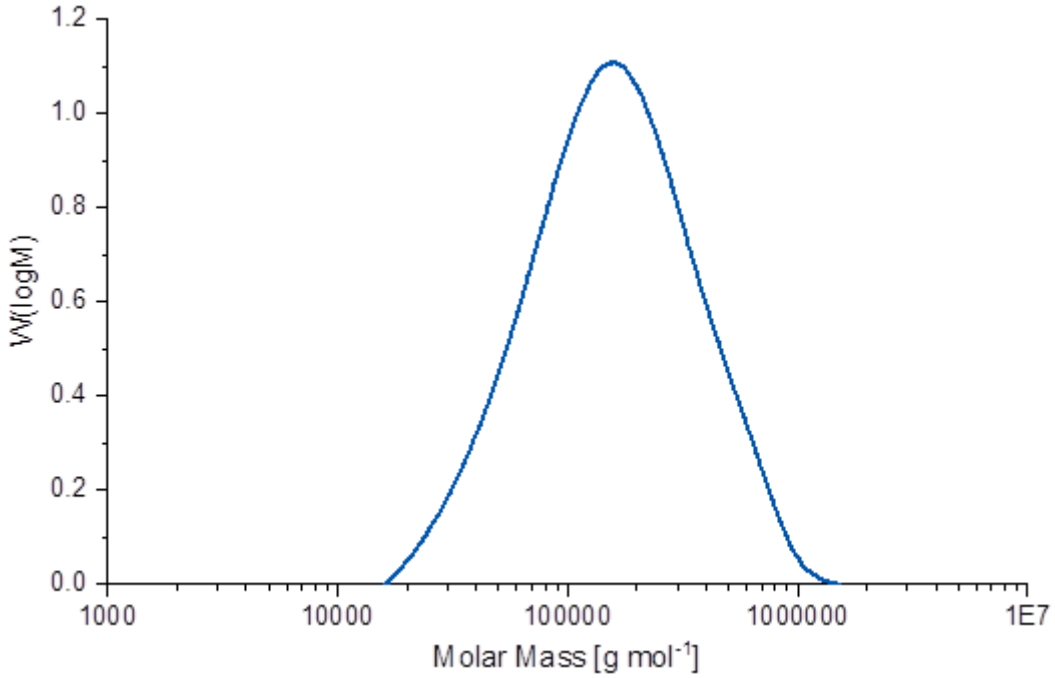

Figure 5.13. GPC trace of polyethylene obtained from polymerization in toluene (Table 5.1, entry 1). M_n = 111400 g/mol M_w = 210300 g/mol M_p = 147200 g/mol M_z = 359100 g/mol M_v = 199400 g/mol PDI = 1.89

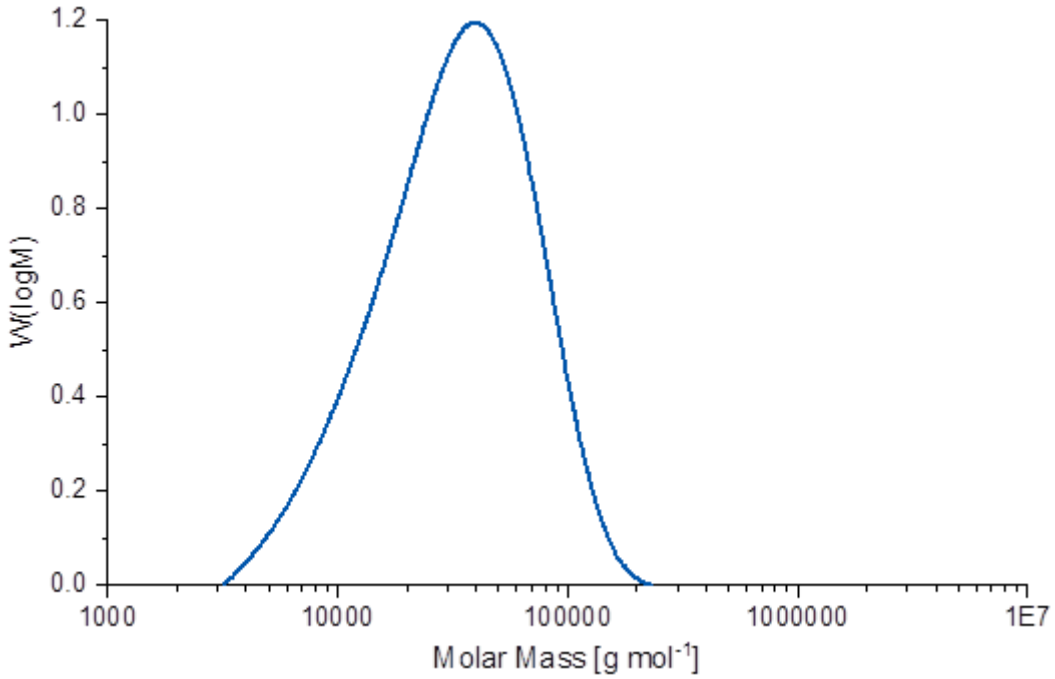

Figure 5.14. GPC trace of polyethylene obtained from polymerization in toluene (Table 5.1, entry 2). M_n = 23350 g/mol M_w = 41240 g/mol M_p = 39200 g/mol M_z = 62780 g/mol M_v = 38790 g/mol PDI = 1.77

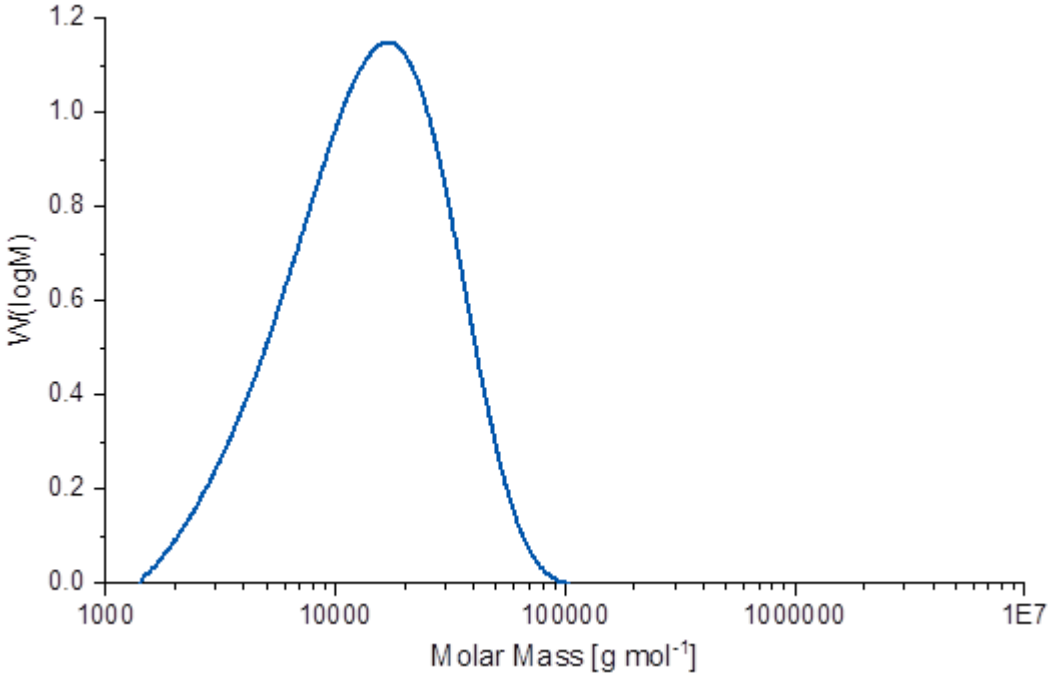

Figure 5.15. GPC trace of polyethylene obtained from polymerization in toluene (Table 5.1, entry 3). M_n = 9840 g/mol M_w = 17620 g/mol M_p = 17710 g/mol M_z = 27220 g/mol M_v = 16620 g/mol PDI = 1.79

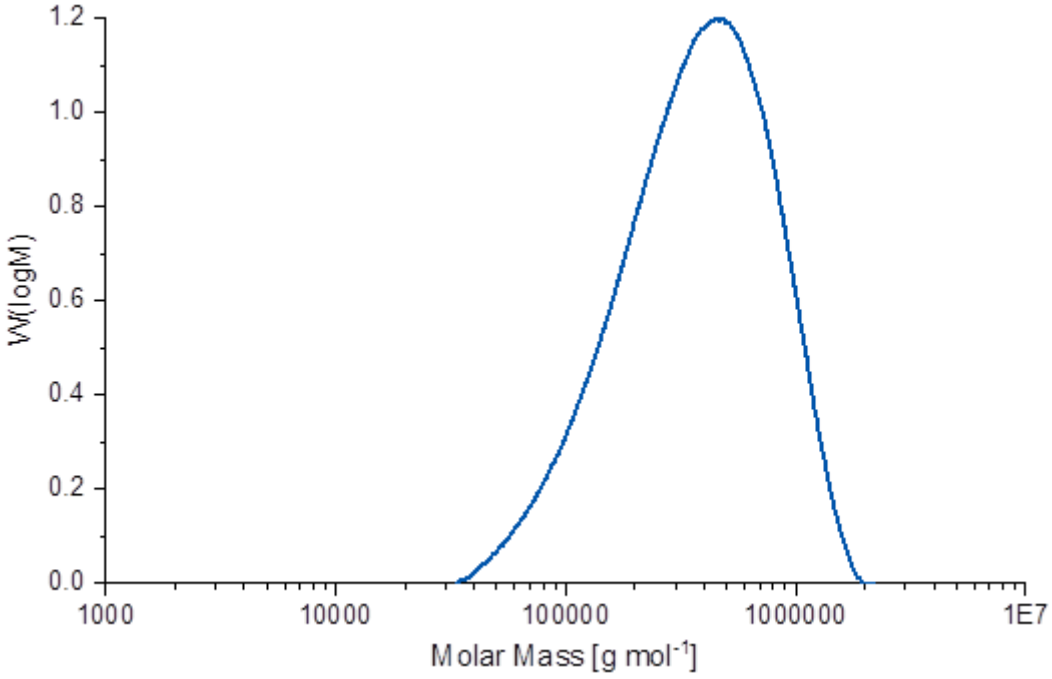

Figure 5.16. GPC trace of polyethylene obtained from polymerization in aqueous surfactant solution (Table 5.1, entry 4). M_n = 268200 g/mol M_w = 461700 g/mol M_p = 384300 g/mol M_z = 676600 g/mol M_v = 434000 g/mol PDI = 1.72

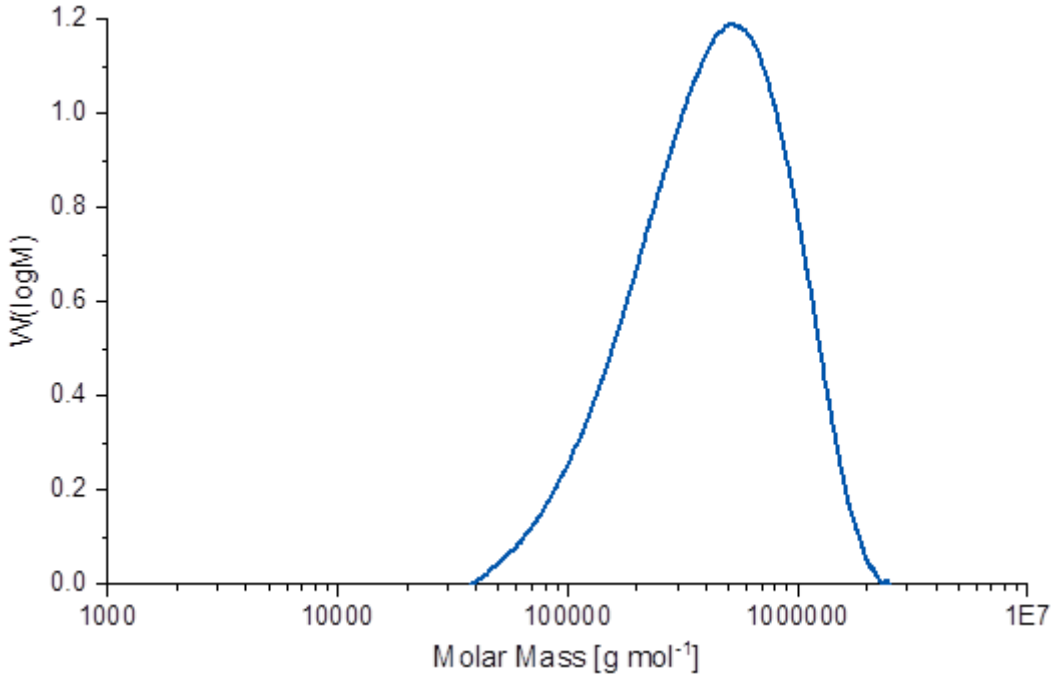

Figure 5.17. GPC trace of polyethylene obtained from polymerization in aqueous surfactant solution (Table 5.1, entry 5).
M_n = 304100 g/mol M_w = 528800 g/mol M_p = 480800 g/mol M_z = 782300 g/mol M_v = 495400 g/mol PDI=1.74

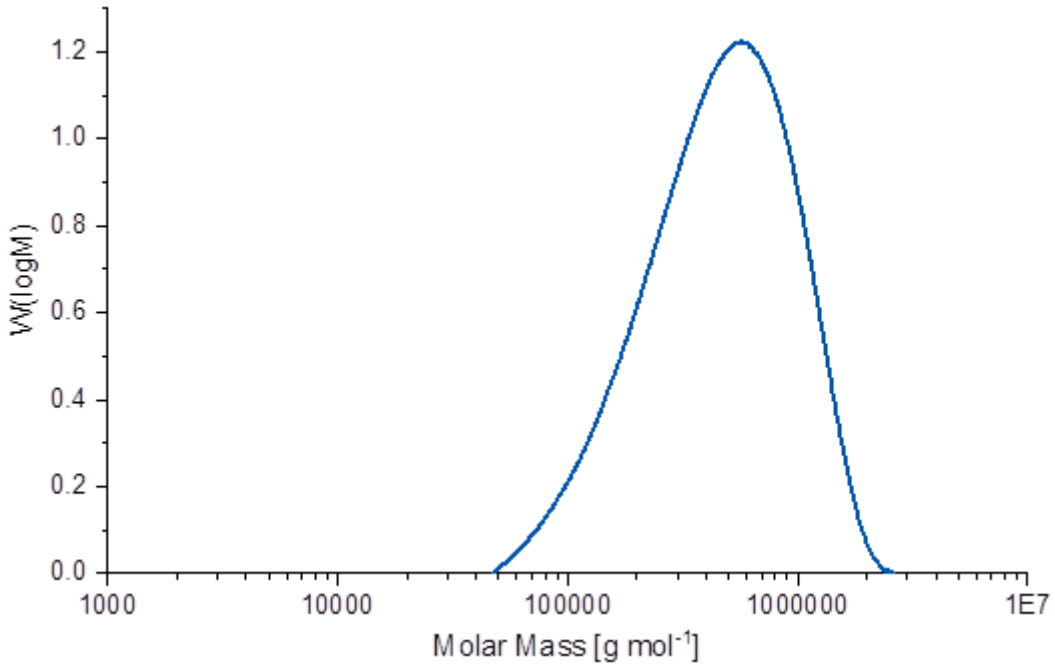

Figure 5.18. GPC trace of polyethylene obtained from polymerization in aqueous surfactant solution (Table 5.1, entry 6). M_n = 337700 g/mol M_w = 567800 g/mol M_p = 512500 g/mol M_z = 823600 g/mol M_v = 532700 g/mol PDI = 1.68

5.5.3 DSC traces of synthesized polyethylenes

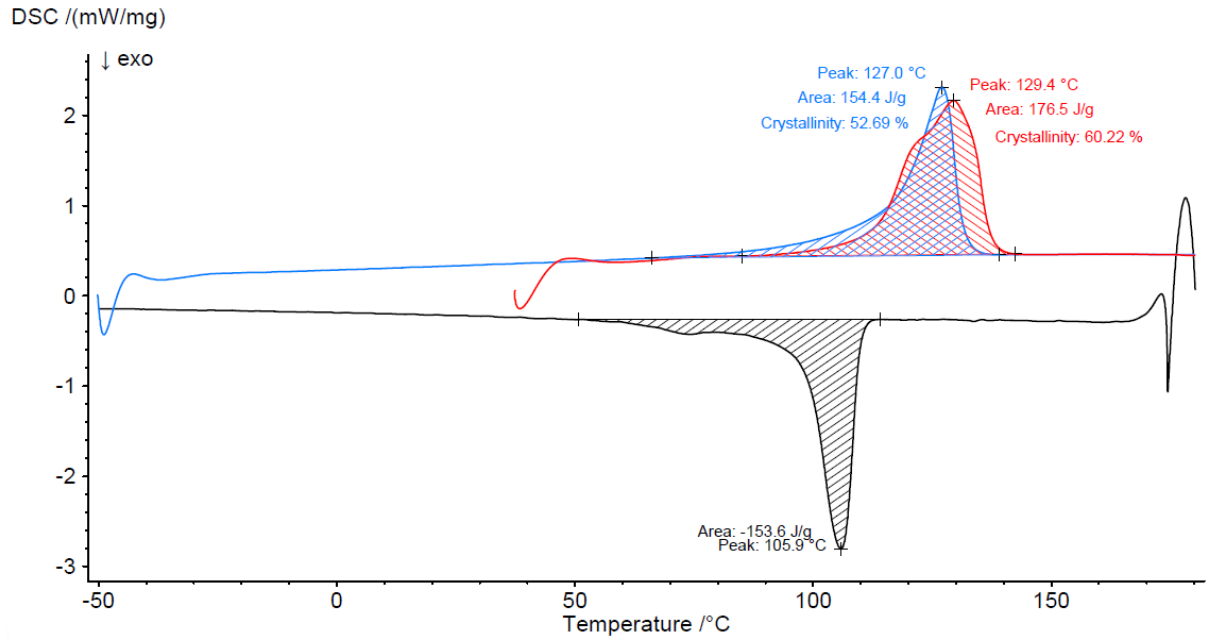

Figure 5.19. DSC traces of polyethylene obtained by polymerization in toluene (Table 5.1, entry 1; measured with 10 K min^{-1} heating rate, red curve: 1st heating, black curve: 1st cooling, blue curve: 2nd heating).

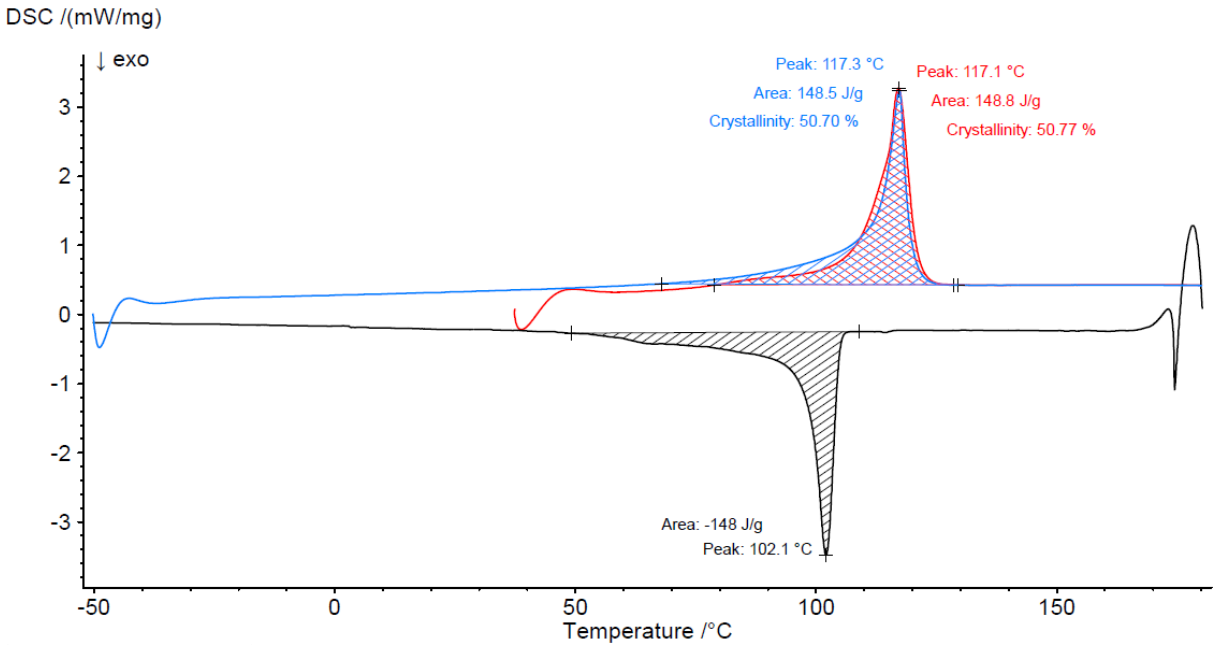

Figure 5.20. DSC traces of polyethylene obtained by polymerization in toluene (Table 5.1, entry 2; measured with 10 K min^{-1} heating rate, red curve: 1st heating, black curve: 1st cooling, blue curve: 2nd heating).

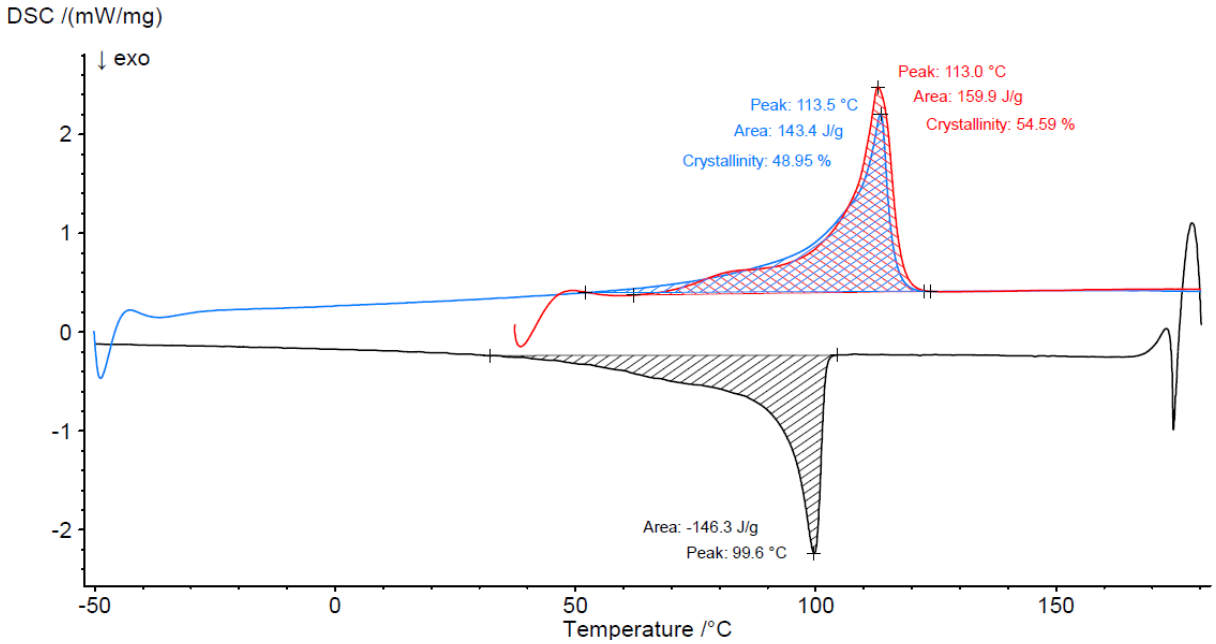

Figure 5.21. DSC traces of polyethylene obtained by polymerization in toluene (Table 5.1, entry 3; measured with 10 K min^{-1} heating rate, red curve: 1st heating, black curve: 1st cooling, blue curve: 2nd heating).

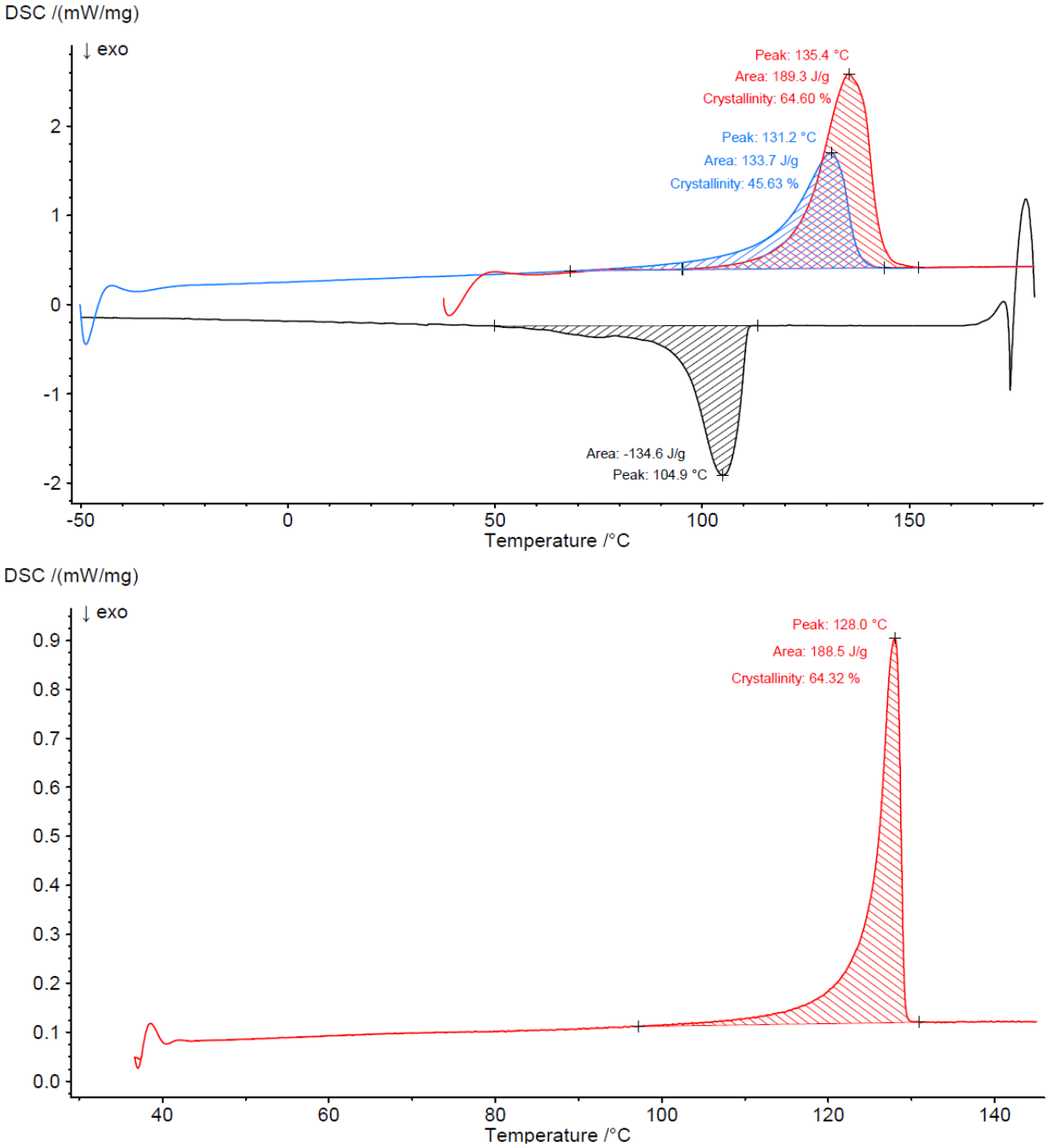

Figure 5.22. DSC traces of polyethylene obtained by aqueous polymerization (Table 5.1, entry 4). *Top*: measured with 10 K min^{-1} heating rate (red curve: 1st heating, black curve: 1st cooling, blue curve: 2nd heating). *Bottom*: measured with 1 K min^{-1} (only first heating shown).

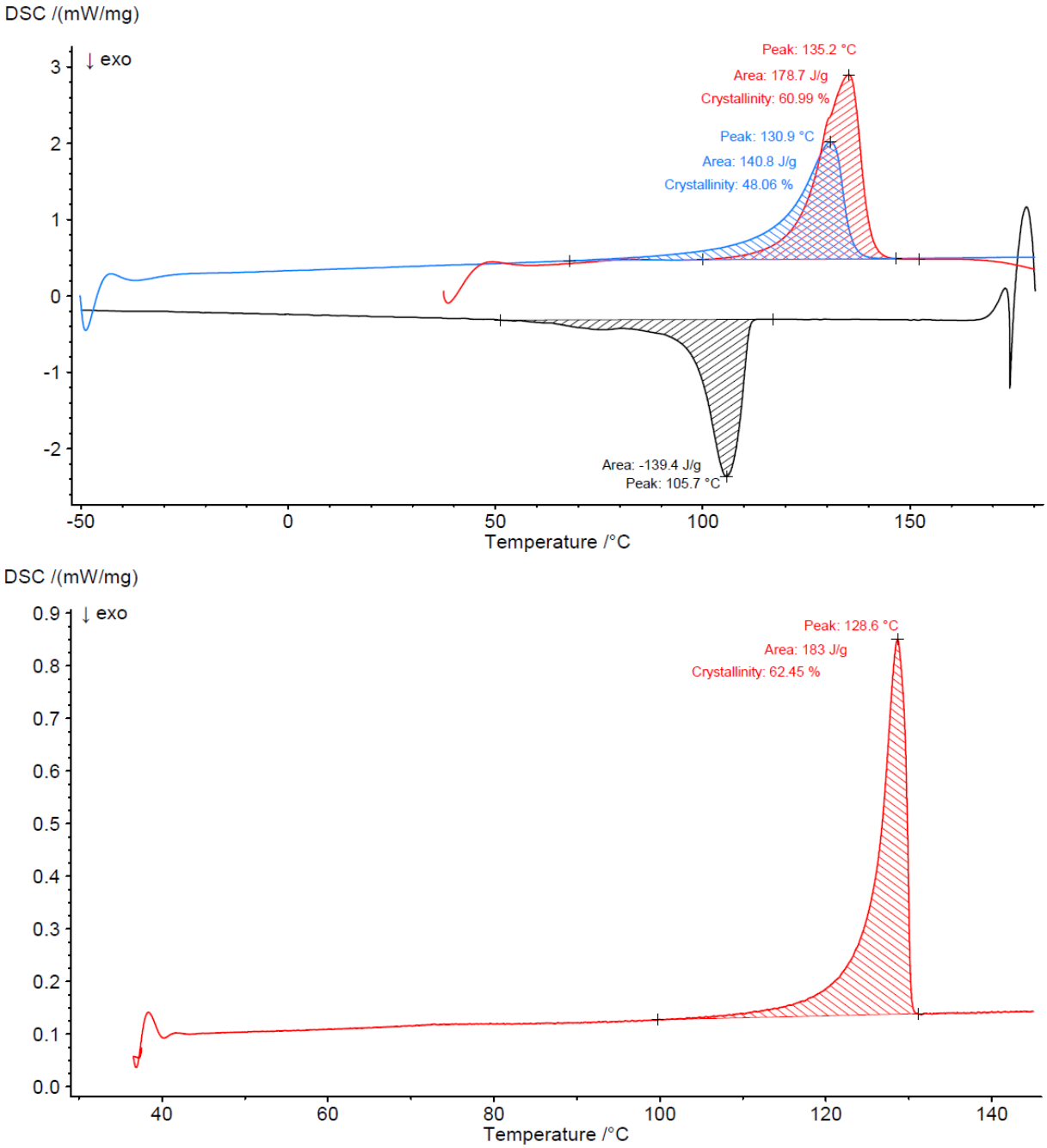

Figure 5.23. DSC traces of polyethylene obtained by aqueous polymerization (Table 5.1, entry 5). *Top*: measured with 10 K min^{-1} heating rate (red curve: 1st heating, black curve: 1st cooling, blue curve: 2nd heating). *Bottom*: measured with 1 K min^{-1} (only first heating shown).

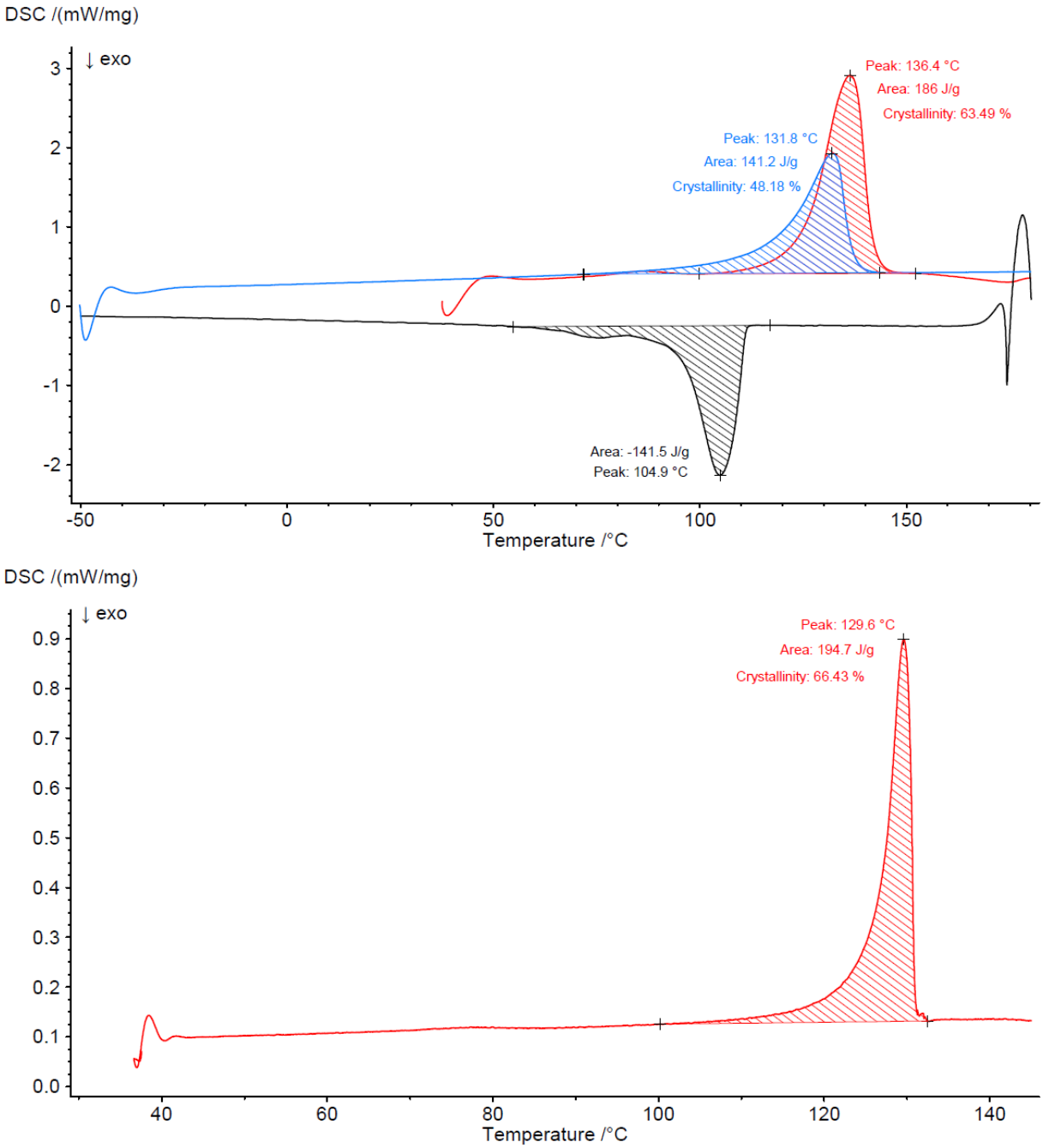

Figure 5.24. DSC traces of polyethylene obtained by aqueous polymerization (Table 5.1, entry 6). *Top*: measured with 10 K min^{-1} heating rate (red curve: 1st heating, black curve: 1st cooling, blue curve: 2nd heating). *Bottom*: measured with 1 K min^{-1} (only first heating shown).

5.5.4 DLS data of nanocrystal dispersions

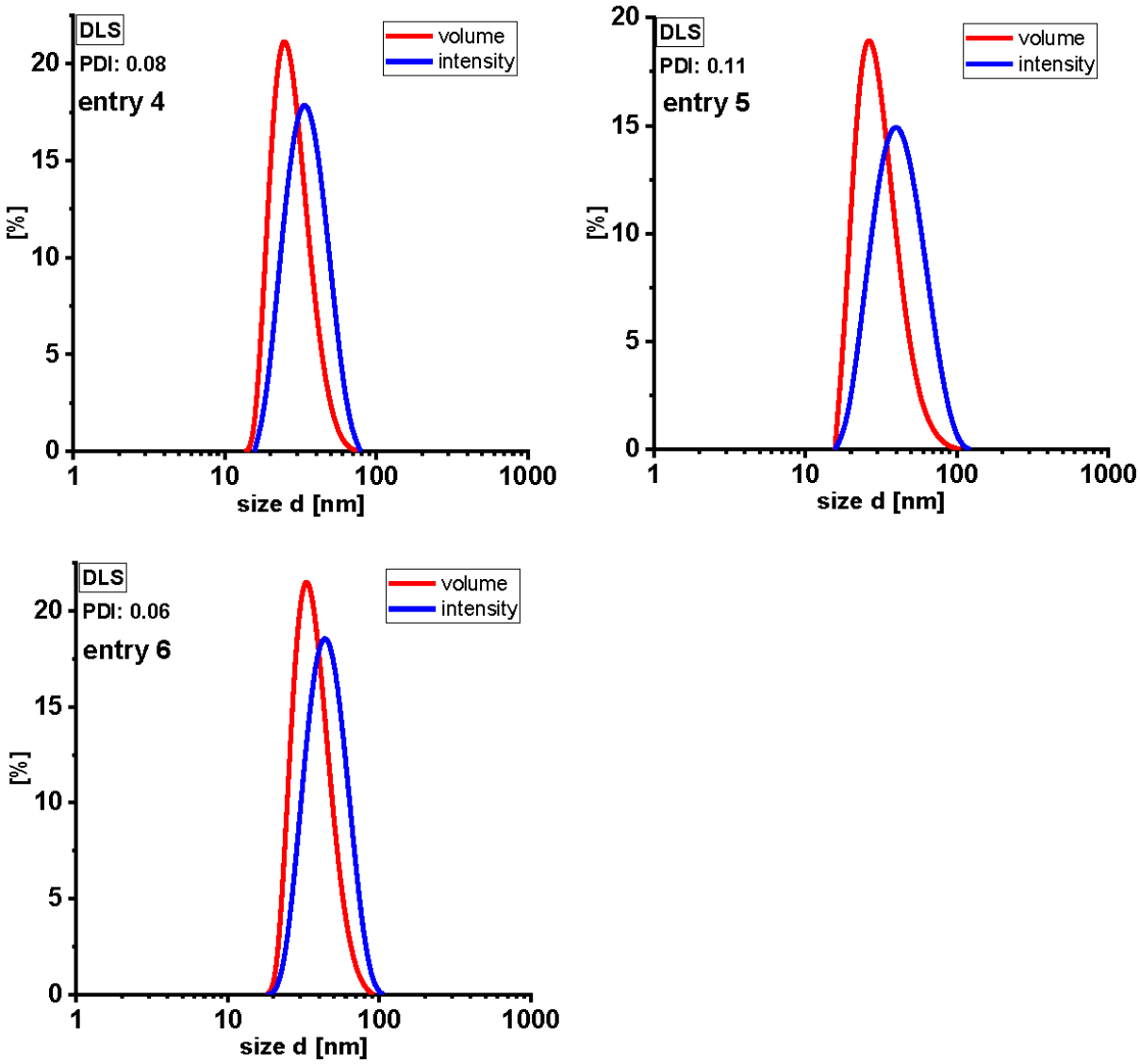

Figure 5.25. DLS traces of polyethylene dispersions (Table 5.1, entries 4-6). Volume- and intensity-based distributions shown. PDI according to *Malvern Zetasizer* software.

6 Process Design for Aqueous Catalytic Polymerization

6.1 Introduction

In a well-designed catalytic process, the reactor technology needs to be tailored to the catalyst and vice versa. For the case of polymerization catalysis, this is nicely illustrated by the evolution from the first laboratory reactors used in Ziegler's pioneering discoveries of the 'Mülheim low pressure process' to a modern industrial gas phase polymerization reactor (Figure 6.1).[13]

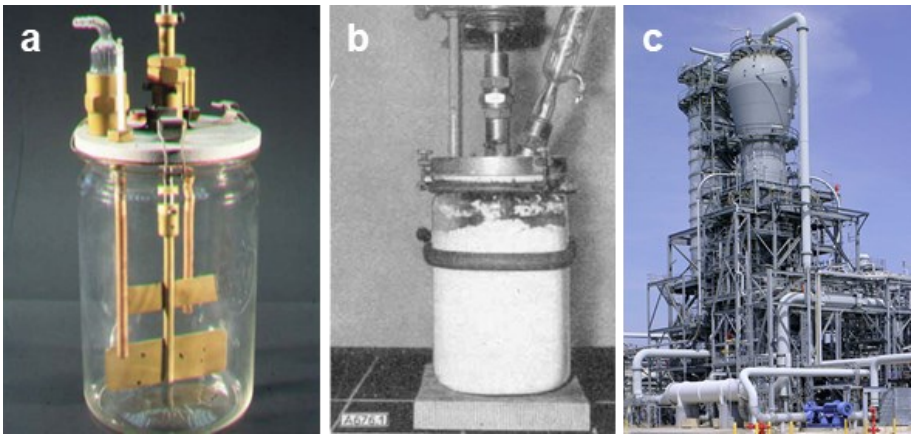

Figure 6.1. Evolution of reactors used for low pressure ethylene polymerizations. a) Karl Ziegler's glass reactor used for his first experiments.[65] b) Same reactor filled with polyethylene after catalyst quenching (from Ziegler's original publication).[13] c) Modern fluidized bed gas reactor for industrial scale catalytic polyethylene production.[421] Adapted with permission from Wiley-VCH (*Macromol. Chem. Phys.* **2003**, *204*, 289–327; Copyright 2003 and *Angew. Chem.* **1955**, *67*, 541–547; Copyright 2006).

For the aim of a well-controlled aqueous dispersion polymerization pursued here, the design of the polymerization procedure has to meet several challenges. The initial polymerization mixture needs to be in a highly disperse state to enable the nucleation and subsequent growth of particles by a single active site, rather than the occurrence of any aggregated species (see also *chapter 1.1.3*). This is achieved by the addition of very small amounts of lipophilic compounds and ultrasonication by means of a powerful ultrasonotrode integrated in the pressure reactor. Presumably, this is supportive to disperse the catalyst molecules, which are primarily hydrophilic (due to the PEG-amine ligands) but also contain lipophilic portions into micelles swollen with this solvent. Further, to ensure a living polymerization the catalyst needs to be fully stable over extended periods of several hours under polymerization conditions. This is achieved via the choice of optimum conditions with regard to pH of the reaction medium[179], combined with the choice of surfactant and organic solvent as well as reaction conditions. To achieve stable particles, that also grow in a living fashion, the surfactant and reaction conditions are also crucial. To achieve a reproducible interplay of all these factors, an automated polymerization procedure was employed.

6.2 Results and discussion

6.2.1 Reactor setup

All aqueous polymerization experiments were conducted in an automatized reactor setup with a *Büchi ecoclave* steel autoclave (600 mL vessel, heating/cooling jacket connected to a thermostat; see Figure 6.2 for reactor setup overview). The reactor was equipped with a mechanical stirrer (*Büchi Cyclone cc075dc*) with integrated rotational speed monitoring and torque measurement, a ultrasonotrode (*Hielscher UIP250*) with intensity control and a liquid dosing pump (*Knauer Azura P 4.1s*) for e.g. catalyst addition under pressure conditions. Several thermocouples were used to measure e.g. the reaction mixture's temperature or the thermostat's internal temperature. Gas supplies for ethylene, carbon monoxide (not used) and vacuum/nitrogen were present for polymerization experiments and experiment prearrangement procedures (e.g. freeing the autoclave atmosphere from oxygen).

In contrast to a manual reactor setup, magnetic valves were installed to monitor gas flows and those connected to a *HiTec Zang LabManager®* box for controlling. All above mentioned devices were connected and implemented as well. The control box interacted with the *LabVision®* software for modular visualization, monitoring and programming (Figure 6.2, top). In detail, the control box generates a certain variable to describe a device parameter from the reactor setup, that can then be manipulated by the software. In the simple case of e.g. a thermocouple, the analog signal from the device is converted to a concrete variable, that is defined as temperature. For valves, a certain electronic current to open the outlet is generated by the control box and expressed in the software as binary variable (0 = closed, 1 = open). But even more complex devices with an own integrated software (e.g. thermostat, mechanical stirrer) could be connected via COM port and their specific communication protocol implemented within the control box environment. This greatly simplified programming and controlling, as all setup parameters of all devices were bundled in a uniform variable environment.

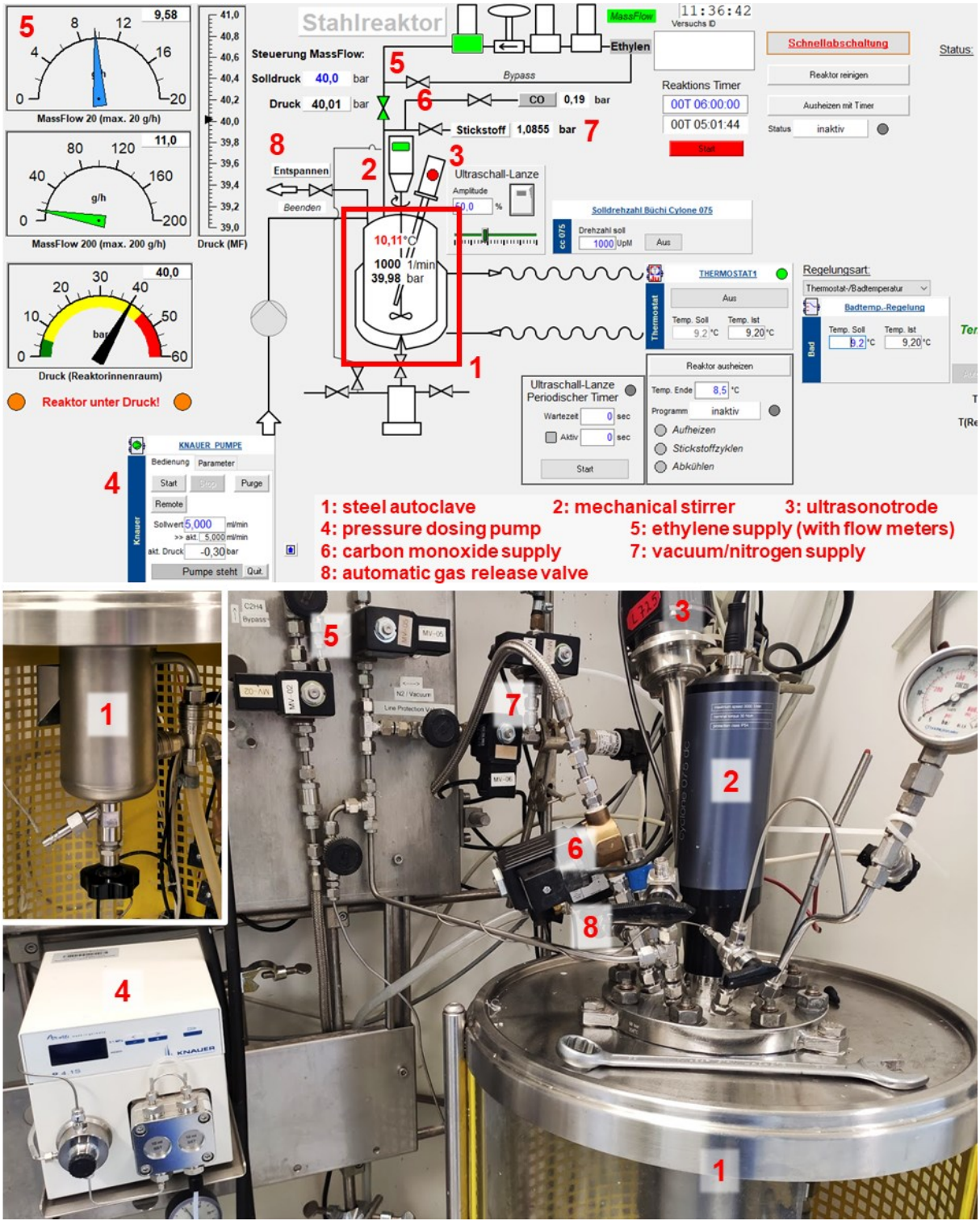

Figure 6.2. Automatized reactor setup used for all aqueous polymerization experiments. The control software (*top*) allows for precise control and monitoring of all reaction parameters, reactor devices and valves (*bottom*).

Sequence programming and execution of manual commands were directly conducted in the *LabVision®* software. Device parameters could be compiled, the control box environment imported, dynamic setup flow diagrams generated, or sequences written. The *HiText®* sequence programming language contained a versatile library of different commands, that are executed line-by-line and used as basic framework for every interactive element of the flow diagram (excellent tutorials and manuals for *HiText®*, also suited for non-programmers, are integrated within the *LabVision®* software). Clicking on e.g. a valve in the flow chart starts a specific *HiText®* script that changes the respective valve position variable from 0 (closed) to 1 (open; the control box generates a current to put the valve in open position). Even more complex sequences were implemented, e.g. a program for an automated pressurization procedure. Starting the sequence invoked a graphical window, where the user could specify the desired reaction parameters (e.g. temperature, ethylene pressure, stirring rate, etc.). Depending on the selection, several different scripts were then initiated to start the stirrer or apply ultrasound, followed by opening the ethylene supply for stepwise gas feeding until the desired pressure was reached. The sequence was finished by handing over the pressure control to the ethylene mass flow meters and starting the automated reaction temperature control. Another program for automated reactor preparation conducted several cycles of evacuation and flushing with nitrogen at elevated temperature to free the reactor atmosphere, from residual solvents or oxygen prior to every polymerization experiment. The procedure took about 1 hour without any manual interaction necessary and could be scheduled for any desired time for automated initiation.

All parameters were monitored and recorded over the course of an entire polymerization experiment. Major divergences from defined reaction parameters (e.g. substantial temperature increase due to ethylene hydrate formation) were reported and could be considered when analyzing the synthesized dispersion. Online visualization of ethylene mass flow data was of major importance to track the catalytic activity during a polymerization experiment (Figure 6.3). In the particular case of long-term experiments over several hours, the duration of an experiment could be adjusted to the activity present.

The software controlling allowed for implementation of several security features and permanently active monitoring scripts. Especially under pressure conditions, all pressure sensitive components (e.g. vacuum/nitrogen supply) were locked and could not be used. During the pressurization procedure, the pressure dropping behavior was analyzed and the ethylene feed closed when the presence of a leakage was assumed. Critical features were directly implemented in the control box environment to ensure them to be active, even when the

computer with the software running crashed (e.g. exceeding the maximum pressure of 55 bar lead to immediate pressure release in all cases). Beside these software-induced security features, physical burst discs, needle valves and back pressure valves, protecting critical components, were present as well.

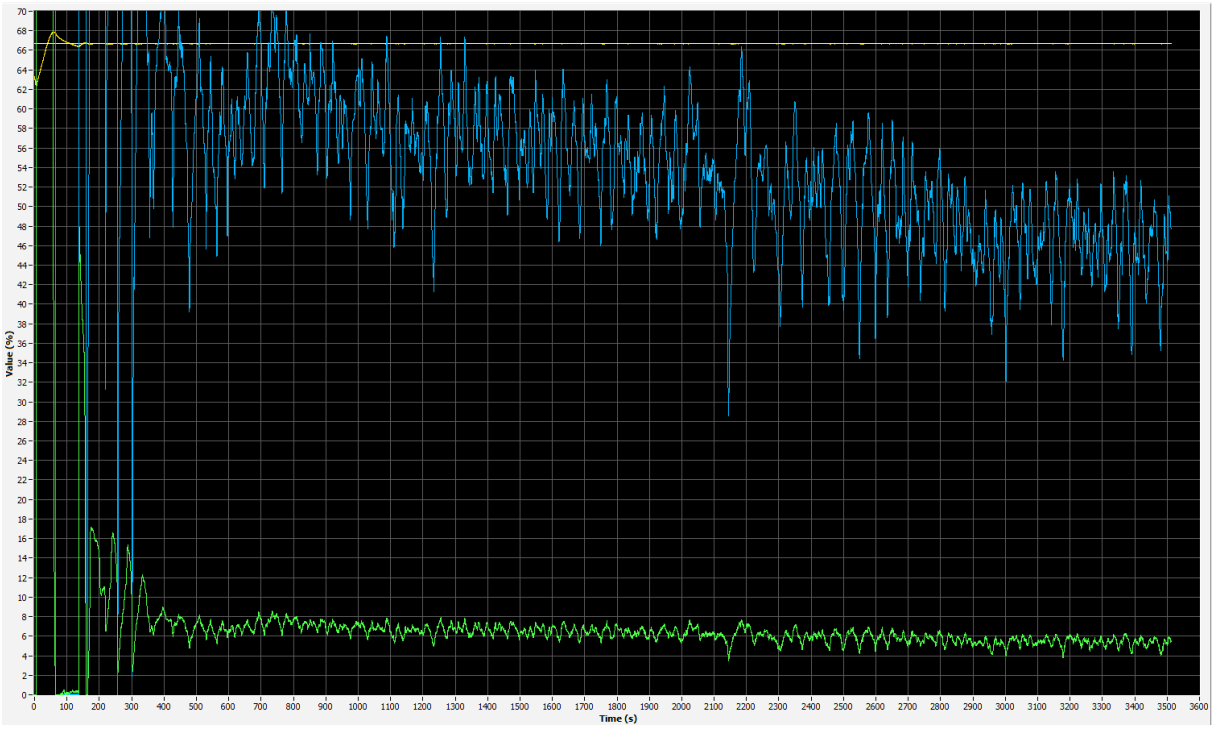

Figure 6.3. Ethylene mass flow meter raw data record. Y-axis: percentage amount of maximum flow (valve opening degree, 0 – 70 % shown) per mass flow meter (blue: 100 % ≙ 20 g h^{-1}, green: 100 % ≙ 200 g h^{-1}). X-axis: time in seconds (1 hour shown). As expected for a living polymerization, the ethylene consumption stays almost constant over time (after initial flow equilibration).

6.2.2 Choice of lipophilic solvents in aqueous systems

To ensure a maximum degree of dispersion of the catalyst in the initial reaction mixture, decisive for an undisturbed particle growth process, the addition of small amounts organic solvents to the aqueous surfactant solution was studied. A range of aliphatic and aromatic, as well as fluorinated and non-fluorinated compounds (Figure 6.4) were investigated to further reveal the nature of this effect. These different organic compounds were studied in aqueous polymerization experiments with catalyst **1^{I}-C_6F_{13}/PEG** under otherwise identical conditions (Table 6.1). All solutions were sonicated with ultrasound prior to ethylene pressurization to ensure a sufficient mixing. In all cases, a crucial influence of the additive was found, when compared to the control experiment without added solvent (entries 26 and 27).

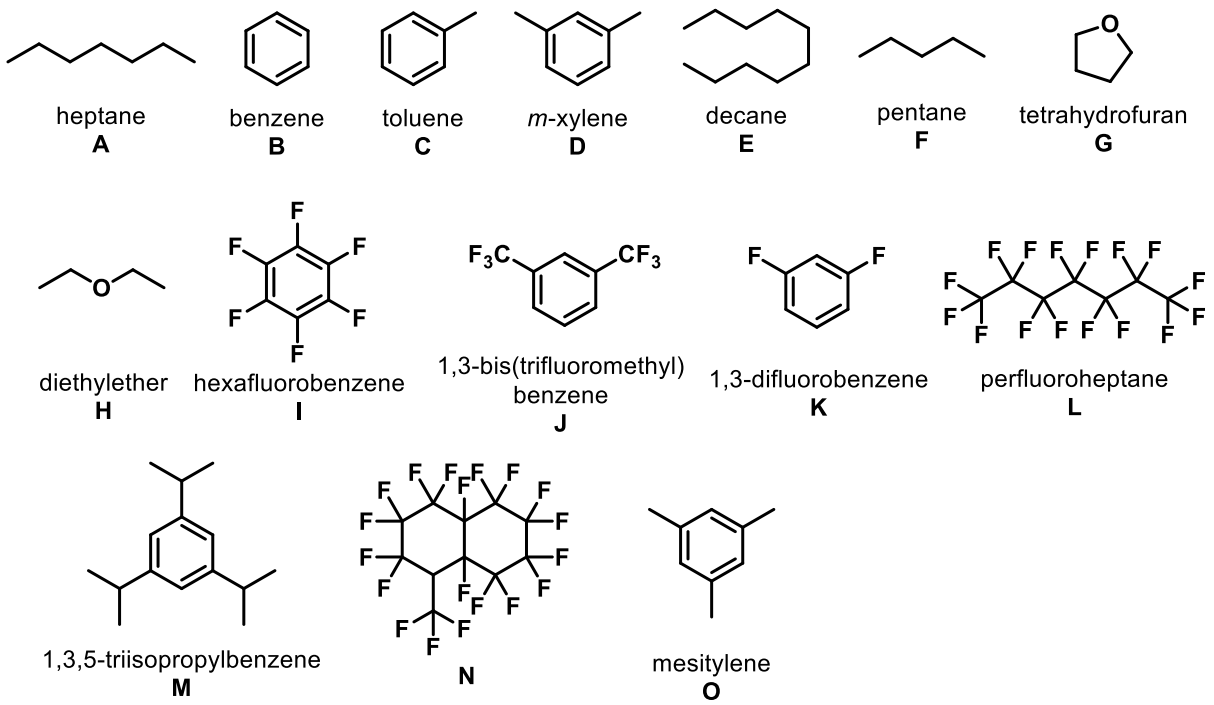

Figure 6.4. Organic compounds studied as lipophilic solvents for polymerizations in aqueous surfactant solution. The labels refer to the "additive" column in Table 6.1.

The catalyst precursor **1^{I}-C_6F_{13}/PEG**, with its hydrophobic fluorinated portions and its hydrophilic PEG segment, shows a versatile solubility behavior in a variety of different organic solvents of different polarities (e.g. toluene, acetone, or methanol). This is in strong contrast to the previously reported TPPTS-coordinated precatalysts (e.g. **1^{I}-CF_3/TPPTS**) that were found to be soluble in very polar solvents, like water or methanol, exclusively.[177] **1^{I}-C_6F_{13}/PEG** showed to be only slightly soluble in pure water, but dissolved completely when surfactant was added.

While NMR studies of **1^{I}-CF_3/TPPTS** in D_2O suggested immediate dissociation of the labile ligand in water[177], we assume the stronger binding H_2N-PEG-OMe molecule to stay coordinated to the metal center until the solution is pressurized with ethylene. Thus, the catalyst precursor molecules **1^{I}-C_6F_{13}/PEG**, with their versatile solubility, can move freely between aqueous phase and the surfactant micelles swollen with hydrophobic compound to generate a homogenous, molecular solution and the desired high dispersion of the catalyst molecules in the initial reaction mixture. This picture is further supported by the fact, that nanocrystal dispersions of identical properties were formed regardless weather the precatalyst was dissolved in the hydrophobic compound and added to aqueous surfactant solution, or whether the precatalyst was dissolved in the aqueous surfactant solution and the hydrophobic compound was added afterwards.

Table 6.1. Results of polymerization experiments in aqueous surfactant solution using different solvents as additives. For designation of additives, see Figure 6.4.

entry	additive	reaction time [min]	yield PE[a] [g]	M_n[b] [10^3 g mol^{-1}]	M_w / M_n[b]	chains/ [Ni]	T_m[c] [°C] (crystallinity [%])	particle size[d] [nm]
1	A	240	9.11	1229	1.3	1.0	145 (74) / 137 (58)	22 (0.22)
2		120	7.21	842	1.4	1.1	143 (68) / 137 (50)	21 (0.15)
3		60	6.25	738	1.1	1.2	142 (65) / 136 (49)	19 (0.11)
4		30	3.84	385	1.1	1.3	141 (65) / 137 (48)	16 (0.11)
5	B	30	3.90	376	1.2	1.4	139 (69) / 136 (49)	16 (0.14)
6	C	30	4.29	623	1.2	0.9	140 (64) / 135 (47)	15 (0.16)
7	D	240	9.22	1242	1.1	1.0	143 (66) / 135 (47)	21 (0.08)
8		60	7.24	778	1.4	1.2	142 (65) / 137 (41)	19 (0.06)
9		30	4.88	779	1.1	0.8	139 (65) / 135 (45)	16 (0.23)
10	E	240	6.73	882	1.3	1.0	143 (67) / 136 (48)	28 (0.37)
11		60	6.29	893	1.2	0.9	142 (66) / 136 (48)	19 (0.13)
12	F	60	4.52	870	1.3	0.7	142 (65) / 136 (48)	19 (0.13)
13	G	30	3.65	466	1.2	1.0	142 (62) / 135 (44)	17 (0.21)
14	H	60	2.60	536	1.1	0.7	141 (68) / 136 (44)	19 (0.12)
15	I	240	8.32	912	1.2	1.2	144 (67) / 136 (47)	21 (0.13)
16		120	6.20	802	1.3	1.0	142 (72) / 136 (52)	22 (0.10)
17[e]		60	4.56	493	1.1	1.2	143 (68) / 136 (49)	16 (0.17)
18		30	4.00	742	1.2	0.7	140 (65) / 136 (44)	16 (0.15)
19	J	240	5.20	669	1.3	1.0	144 (66) / 137 (49)	21 (0.11)
20	K	240	8.53	1113	1.2	1.0	142 (65) / 135 (46)	20 (0.13)
21	L	30	2.95	483	1.3	0.8	141 (65) / 136 (50)	18 (0.26)
22	M	240	3.62	506	1.2	1.0	143 (62) / 137 (46)	20 (0.37)
23	N	30	3.55	386	1.1	1.2	143 (68) / 137 (49)	18 (0.40)
24	O	240	9.91	1348	1.2	1.0	142 (66) / 135 (45)	24 (0.04)
25		60	7.07	1020	1.1	0.9	140 (65) / 134 (46)	19 (0.05)
26	-	240	4.80	701	1.5	0.9	144 (66) / 138 (48)	348 (0.50)
27		30	3.42	370	1.1	1.2	141 (68) / 137 (51)	17 (0.30)

Polymerization conditions: 7.5 µmol precatalyst **1^1-C_6F_{13}/PEG**, 6.0 g SDS, 1.5 g CsOH, 0.3 mL additive, 40 bar ethylene pressure, in 150 mL water, 15 °C reaction temperature, (for experiments with 60, 120, 240 and 360 minutes reaction time); 7.5 µmol precatalyst, 4.5 g SDS, 1.5 g CsOH, 0.2 mL additive, 40 bar ethylene pressure, 15 °C (for experiments with 30 minutes reaction time); catalyst solution was ultrasonicated (4 min, 120 Watt) prior to ethylene pressurization. [a] Determined via precipitation in methanol. [b] Determined via GPC at 160 °C in 1,2,4-trichlorobenzene. [c] Determined by DSC (10 K min^{-1} heating rate), reported as [first heating / second heating]. [d] Volume average size from DLS (particle size polydispersity index). [e] 0.1 mL additive added.

When ethylene displaced the labile ligand, the surfactant stabilized the formed hydrophobic, well-dispersed active species that could grow single particles not interfering each other. By strong contrast the perfluorobutyl-substituted, TPPTS-coordinated model precursor **1^{I}-C_4F_9/TPPTS** was capable of producing UHMWPE (M_n = 1.2 x 10^6 g/mol, M_w/M_n = 1.4), but in the form of multi-disperse, ill-defined nanoparticles (see *Experimental Section* for details on synthesis, characterization and polymerization experiments). We attribute this to the immediate dissociation of the TPPTS ligand in water and subsequent agglomeration of the highly hydrophobic catalyst molecules, that hampers undisturbed growth of single particles.

The addition of small amounts organic lipophilic compounds (0.1 vol-%) significantly increased the polymer yield and the quality of the dispersion obtained after polymerization with **1^{I}-C_6F_{13}/PEG** in terms of stability and particle size distribution, quantified by DLS measurements, in all cases (see Figure 6.5).

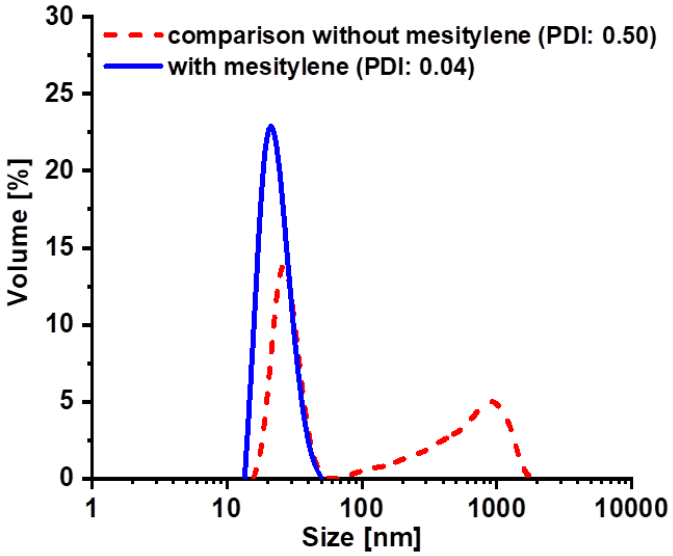

Figure 6.5. DLS traces of PE dispersions obtained from polymerization experiments with **1^{I}-C_6F_{13}/PEG** in water with mesitylene added (*blue curve*; Table 6.1, entry 4) and without (*red curve*) under otherwise identical conditions.

However, the choice of compound does impact the outcome of polymerization (e.g. entry 19 vs. entry 24, Table 6.1). The overall data gives no indication that the lipophilic compound directly interacts with the active center and alters its catalytic properties with regard to chain growth and chain microstructure. This is evident from the fact that in all cases polyethylene with comparable thermal properties was formed in a living polymerization as suggested from chains per nickel ratios close to unity and narrow molecular weight distributions (molecular weights differ in accordance with yield). Rather, the polymerization results appear to depend on the lipophilic solvents' ability to dissolve/distribute the precatalyst/active center in solution,

respectively, and on its ability to form stable and highly dispersed emulsions in the water/SDS system. With this in mind, the organic compound did not influence the polymer formation mechanism itself, but rather the way the catalysts' polymer chains formed ordered single nanocrystals during chain growth and in particular the initial stages of the polymerization experiment. As alkanes and alkylbenzenes are known to form very stable emulsions with SDS[422], their superior role as lipophilic solvents compared to e.g. fluorinated solvents is plausible. The importance of a sufficient emulsion formation is further underlined by direct correlation of particle size distributions and yields. Reduced yields are usually found for dispersions with broad particle size distributions and vice versa. As particle/catalyst agglomeration disturbs chain growth and consequently influences yield, respectively, molecular weight, the found relation is expected.

Table 6.2. Polymerization experiments in aqueous surfactant solution with different amounts of mesitylene as a lipophilic solvent.

entry	mesitylene [mL]	yield PE[a] [g]	M_n[b] [10^3 g mol^{-1}]	M_w / M_n[b]	chains/ [Ni]	T_m[c] [°C] (crystallinity [%])	particle size[d] [nm]
1	0.1	4.65	772	1.3	0.8	145 (67) / 139 (45)	20 (0.09)
2	0.15	5.22	666	1.3	1.0	144 (63) / 136 (41)	20 (0.05)
3	0.3	7.07	1020	1.1	0.9	140 (65) / 134 (46)	19 (0.05)
4	0.6	7.27	1141	1.2	0.9	141 (68) / 135 (45)	20 (0.04)
5	0.75	7.09	846	1.2	1.1	143 (64) / 135 (43)	20 (0.03)
6	0.9	7.57	941	1.3	1.1	139 (64) / 133 (44)	20 (0.03)

Polymerization conditions: 7.5 µmol precatalyst **1^1-C_6F_{13}/PEG**, 6.0 g SDS, 1.5 g CsOH, 40 bar ethylene pressure, 15 °C, 60 minutes reaction time, in 150 mL water; catalyst solution was ultrasonicated (4 min, 120 Watt) prior to ethylene pressurization. [a] Determined via precipitation in methanol. [b] Determined via GPC at 160 °C in 1,2,4-trichlorobenzene. [c] Determined by DSC (10 K min^{-1} heating rate), reported as [first heating / second heating]. [d] Volume average size from DLS (particle size polydispersity index).

We found mesitylene (and simple alklybenzenes in general) to be the solvent of choice that promotes high yields and molecular weights as well as narrow particle size distributions (entries 26 and 27, Table 6.1). For the case of mesitylene even in the absence of ultrasonication similar favorable polymerization results were found, which underlines the suitability of this system to distribute the catalyst in the initial reaction mixture well. Studies with variable amounts of mesitylene showed the minimal concentration required to be 0.2 vol-% (entry 3, Table 6.2). Experiments performed with lower amounts showed reduced yields and broadening in particle size distributions (entries 1 and 2, Table 6.2). Above this concentration no significant impact of mesitylene loadings was found.

6.2.3 Role of surfactant type and concentration

The surfactant is of major importance for a favorable particle formation process. Experiments conducted without surfactant led to immediate polymer precipitation and polymerization activity ceasing within minutes. As the surfactant is absorbed during the reaction on the growing crystals surface, it is one major limiting factor of that reaction type and limits the polymerization progress. We further hypothesize that the employed hydrophobic catalyst systems with their perfluorinated alkyl chains require a certain amount of free surfactant in solution to be stabilized in the initial reaction mixture in order to perform undisturbed chain and particle growth. Usually a polyethylene content of 1.5- to 2.0-times the sodium dodecyl sulfate content (by mass) was found to be formed before the activity suddenly decreased. This is evident from the ethylene mass flow curves recorded during the polymerization experiment that allows for a precise monitoring of the catalytic activity (Figure 6.6).

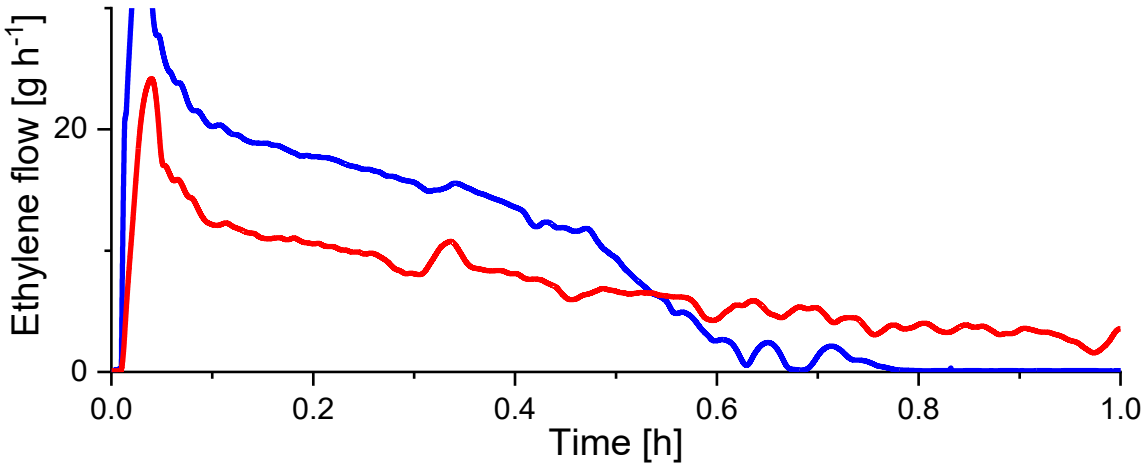

Figure 6.6. Ethylene mass flow traces of aqueous polymerization experiments with different catalyst loadings under otherwise identical conditions. With high catalyst loading (7.5 µmol, *blue*), a sudden decrease in activity within 1 hour reaction time due to insufficient surfactant concentration is visible. With lower catalyst loading (5 µmol, *red*), the initial overall ethylene consumption is lower but lasts for at least 1 hour reaction time as enough free surfactant per active center is available (cond.: 7.5 or 5 µmol precatalyst **1^{I}-C_6F_{13}/PEG**, 4.5 g SDS, 1 g CsOH, 0.5 mL mesitylene, catalyst solution ultrasonicated prior to ethylene pressurization (2 min, 120 Watt), 15 °C reaction temperature, 40 bar ethylene pressure, 1 hour reaction time).

Considering this, a sufficiently high amount of surfactant per nickel center is desirable to provide colloidal stabilization of both the catalyst in the (initial) reaction mixture, as well as the formed nanoparticles. However, the surfactant concentration is limited by its solubility in water at 15 °C, the increasing viscosity of the reaction mixture that hinders sufficient mixing, and the

potential formation of ethylene hydrate.[179,423-425] To increase the amount of free surfactant per active center, the total volume of the reaction mixture was varied while keeping the surfactant (and other additives) concentration constant and reducing the catalyst concentration (identical amounts of catalyst were used in increased reaction mixture volumes). The results are summarized in Table 6.3.

Table 6.3. Polymerization experiments in aqueous surfactant solution with different surfactant per active center ratios, respectively, different precatalyst concentrations. Two sets of identical experiments were performed with precatalysts bearing labile ligands of different PEG-chain lengths.

entry (cond.)	surfactant / active center [10^3 molecules]	yield PE[a] [g]	M_n[b] [10^3 g mol^{-1}]	M_w / M_n[b]	chains/ [Ni]	T_m[c] [°C] (crystallinity [%])	particle size[d] [nm]
1^{A}	4.2	8.27	994	1.2	1.1	142 (68) / 134 (46)	23 (0.06)
2^{B}	5.5	12.98	1686	1.3	1.0	143 (64) / 133 (42)	30 (0.04)
3^{C}	8.3	17.08	1974	1.2	1.2	142 (65) / 135 (38)	34 (0.03)
4^{A}	4.2	10.47	1214	1.3	1.1	142 (68) / 134 (46)	31 (0.07)
5^{B}	5.5	15.64	1810	1.3	1.1	141 (65) / 133 (43)	37 (0.05)
6^{C}	8.3	18.42	2616	1.3	0.9	142 (68) / 134 (46)	43 (0.06)

Polymerization conditions: 40 bar ethylene pressure, 2 hours reaction time, 15 °C reaction temperature, 7.5 µmol catalyst loading (**1^{I}-C_6F_{13}/PEG**, entries 1-3 with M(H_2N-PEG-OMe) = 1981 g mol^{-1}, entries 4-7 with M(H_2N-PEG-OMe) = 5516 g mol^{-1}), 0.137 mol L^{-1} sodium dodecyl sulfate, 0.067 mol L^{-1} cesium hydroxide, 5 mL L^{-1} mesitylene, catalyst solution was ultrasonicated (4 min, 120 Watt) prior to ethylene pressurization; in 150 mL (A), 300 mL (B) or 450 mL (C) water; [a] Determined via precipitation in methanol. [b] Determined via GPC at 160 °C in 1,2,4-trichlorobenzene. [c] Determined by DSC (10 K min-1 heating rate), reported as [first heating / second heating]. [d] Volume average size from DLS (particle size polydispersity index).

The yields were found to increase for experiments, where more free surfactant per nickel center is available. On the other hand, also molecular weights and particle sizes were higher. This shows that the surfactant content directly influences the amount of polymer that is formed by an active center. A high content enabled the synthesis of particles with > 80 nm lateral size and molecular weights of M_n > 3 x 10^6 g mol^{-1} (Table 3.2), while yield, molecular weight and particle size were reduced when half the amount of surfactant is used (entries 4 and 7, Table 3.2). In contrast, the molecular mechanism of chain growth itself was not influenced as in all cases polyethylene with comparable thermal properties was formed in a living polymerization.

Besides the amount added, the employed type of surfactant is of crucial importance to obtain stable polyethylene dispersions by aqueous catalytic polymerization. The various surfactants differ in polarity of their headgroups and structure of their nonpolar tail to allow for a broad variety of different applications.[426] They are generally classified according to their head group's nature being anionic, nonionic, cationic or zwitterionic.

As a simple and well-known anionic surfactant, sodium dodecyl sulfate and its shorter/longer homologues have been studied intensively and are produced in a total volume of 5 million tons per year.[426] It is commonly used as emulsifier in household applications and for scientific proposes in biology (e.g. as main component in gel electrophoreses, SDS-PAGE).[427-429] However, it has often been replaced on industrial scale due to the development of more specific surfactants and the occurrence of hydrolysis reactions (head group) that form the respective alkyl alcohol and corrosive hydrogen sulfates.[430] To test more common (and maybe more suited) methods in aqueous catalytic polymerization, benchmarking of different surfactants was performed (see Figure 6.7 and Table 6.4). In initial experiments, aqueous solutions of ionic and nonionic surfactants were treated with small portions of mesitylene to qualitatively check the presence of regular micelles via DLS (see *Appendix* for DLS traces). Nonionic surfactants were found to form larger micelles with broader size distribution, compared to SDS solutions.

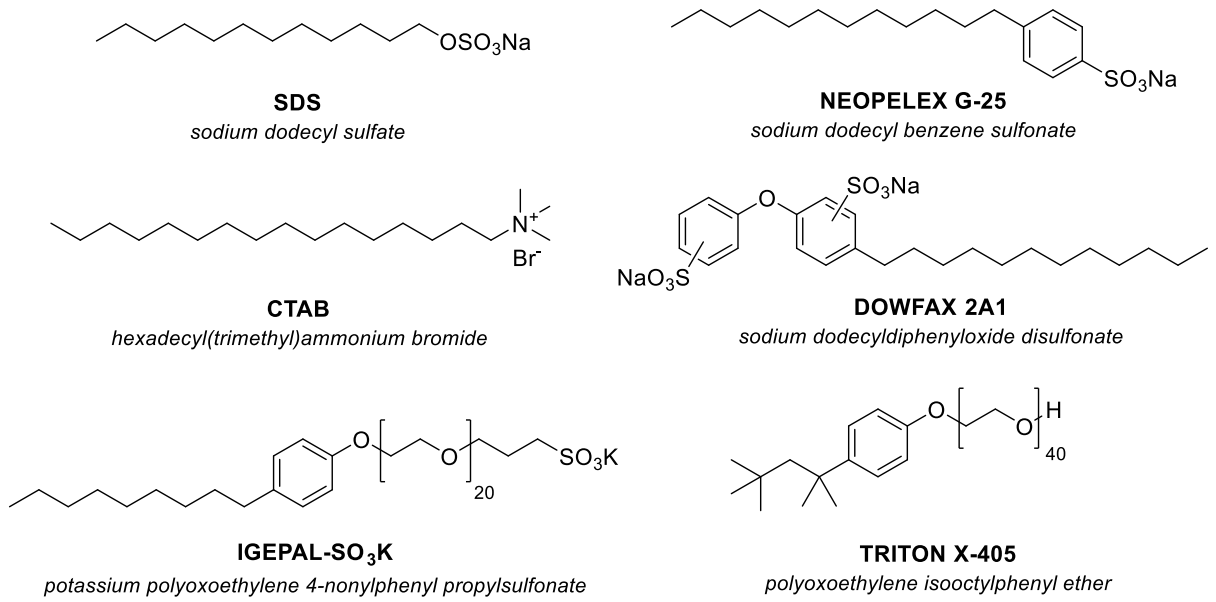

Figure 6.7. Surfactants tested in aqueous catalytic ethylene polymerization (experimental data summarized in Table 6.4).

Cetyltrimethylammonium bromide (CTAB) is a common and simple cationic surfactant and mainly used for microbiological applications and in nanoparticle synthesis.[431] Experiments with CTAB (entry 3) did not yield any polymer as the catalyst's active site has been blocked presumably by coordination of free amines, formed by in-situ head group hydrolysis reactions.[432] After venting the reactor, the catalyst did not decompose for hours (solution stayed red) pointing to an effective exchange of the labile amino-PEG ligand by a strongly binding species.

Table 6.4. Polymerization experiments in aqueous solution using different surfactants (chemical structures of surfactants, see Figure 6.7).

entry	surfactant type	yield PE[a] [g]	M_n[b] [10^3 g mol^{-1}]	M_w / M_n[b]	chains/ [Ni]	T_m[c] [°C] (Crystallinity [%])	particle size[d] [nm]
1[A]	SDS	12.94	1912	1.2	0.9	143 (60) / 134 (37) 136	32 (0.05)
2[B]	Neopelex G-25	11.66	1292	1.3	1.2	140 (54) / 134 (37) 135	30 (0.08)
3[C]	CTAB	*no*	-	-	-	-	-
4[D]	Triton X-405	*no*	-	-	-	-	-
5[E]	IGEPAL-SO_3K	*no*	-	-	-	-	-
6[F]	DowFax 2A1	0.96	216	1.1	0.6	139 (66) /136 (52) 131	19 (0.25)
7[G]	DowFax 2A1	0.30	148	1.1	0.3	135 (73) / 135 (62) *n.d.*	22 (0.35)

Polymerization conditions: 7.5 µmol **1^I-C_6F_{13}/PEG**, 40 bar ethylene pressure, ultrasound applied prior to ethylene pressurization, 15 °C reaction temperature, 60 minutes reaction time. (A) 12 g SDS, 3 g CsOH, 1.5 mL mesitylene, in 300 mL water. (B) 14.5 g Neopelex G-25, 1.5 g CsOH, 1.5 mL mesitylene. (C) 3.8 g CTAB, 0.75 g CsOH, 0.3 mL mesitylene. (D) 29.2 g Triton X-405, 0.75 g CsOH, 0.3 mL mesitylene. (E) 13 g IGEPAL-SO_3K, 0.75 g CsOH, 0.3 mL mesitylene. (F) 13.3 g DowFax 2A1, 0.75 g CsOH, 0.75 mL mesistylene. (G) 15 g DowFax 2A1, 0.9 g CsOH, 0.1 mL C_6F_6. [a] Determined via precipitation in methanol. [b] Determined via GPC at 160 °C. [c] Determined via DSC, reported as [1st heating cycle (crystallinity) \ 2nd heating cycle (crystallinity)] with 10 K/min heating rate, second line: 1st heating cycle with 1 K/min heating rate. [d] Determined via DLS, volume mean and PDI reported.

The ionic surfactant DowFax 2A1, a linear alkyl arylsulfonate, with its various industrial applications (e.g. cleaners, textiles) offers low-foaming properties and high solution stabilities (no significant hydrolysis reactions). Its general properties are comparable to SDS and, thus, PE nanocrystal dispersions were obtained (entries 6-7). However, the catalyst activity was significantly lowered. As this effect was less pronounced when the more electron-rich trifluoromethyl substituted catalyst derivative was used[179], an activity lowering effect by coordination of the surfactant to the active center is suggested. This is also reflected in chains per nickel ratios clearly below 1 (inactive catalyst molecules) and very narrow molecular weight distributions of $M_w/M_n < 1.1$, as the presence of additional coordination species are known to influence productivities and polymer microstructures.[131] Particle size distributions, however, were found to be significantly broadened in comparison to polymerization experiments, where SDS was used. As variations in amount of base and lipophilic solvent did not result in significant improvements, DowFax 2A1 was not further tested as surfactant to obtain uniform shape and size polyethylene nanocrystals.

To identify impacts of surfactant hydrolysis on the chain and particle growth mechanism, a SDS derivative with a linear alkyl chain and an aromatic sulfonate head group (Neopelex G-25) was employed (entry 2). As this showed comparable results to experiments with regular SDS, a

significant impact of surfactant hydrolysis under the established polymerization conditions can be excluded.

In contrast to ionic surfactants, the polarity in Triton X-405 is created with nonionic PEG units. It has been used for various applications in nanoparticle chemistry, e.g. for synthesis of anisotropic conjugated polymers.[433,434] Mixing the precatalyst with an aqueous Triton X-405 solution did result in immediate catalyst decomposition presumably due to the presence of a free hydroxy group at the PEG chain end, that reacts with the highly acid-sensitive precatalyst (entry 4). Hence, a derivative substituted with a potassium sulfonate group at the PEG chain end (IGEPAL-SO_3K) was tested as well (entry 5). In contrast to regular Triton X-405, a decomposition of the precatalyst was not observed. However, polymerization did result in immediate polymer precipitation and deactivation due to insufficient colloidal stabilization.

As a general compatibility of nonionic surfactants with the colloidal system of these anisotropic PE nanocrystals was not studied so far, various nonionic surfactants (Figure 6.8) were added to a dispersion synthesized with SDS (entry 1, Table 6.4). Immediate PE precipitation occurred during addition of Brij L4 bearing the shortest PEG segment, while the colloidal stability was not affected in case of other surfactants tested (Figure 6.8 and Figure 6.9, left).

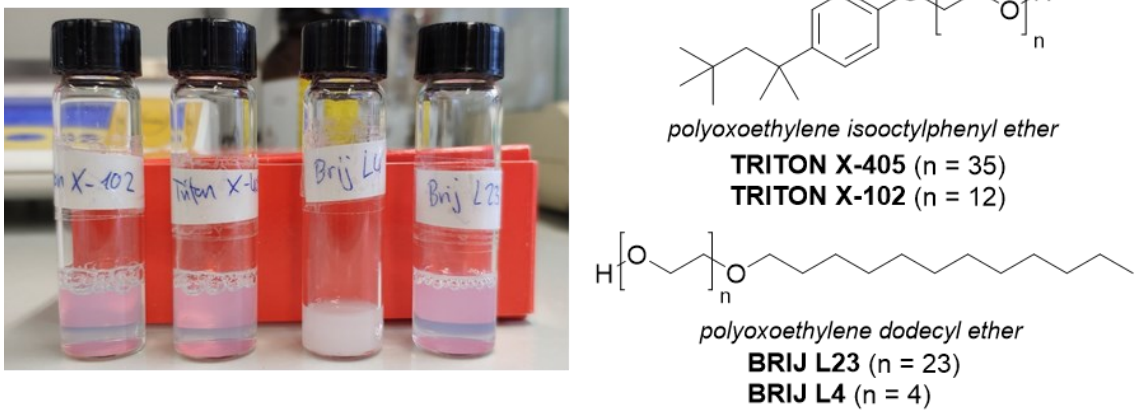

Figure 6.8. Samples of SDS-containing PE nanocrystal dispersions, with different non-ionic surfactants added. Colloidal destabilization was observed only after mixing with Brij L4. Parts of the obtained turbid liquid were further diluted with water to exclude surfactant precipitation due to concentration issues.

In a second step, full replacement of adsorbed surfactant by sequential addition of the second surfactant was tested. Hence, the dispersion initially stabilized with SDS and mixed with Triton X-405, was dialyzed to remove any remaining free surfactant. Then, a second portion of Triton X-405 in excess was added to allow for further exchange between SDS and Triton X-405 at the particle surfaces. The dispersion was dialyzed again, and the zeta potential measured after every dialysis cycle (Figure 6.9, right).

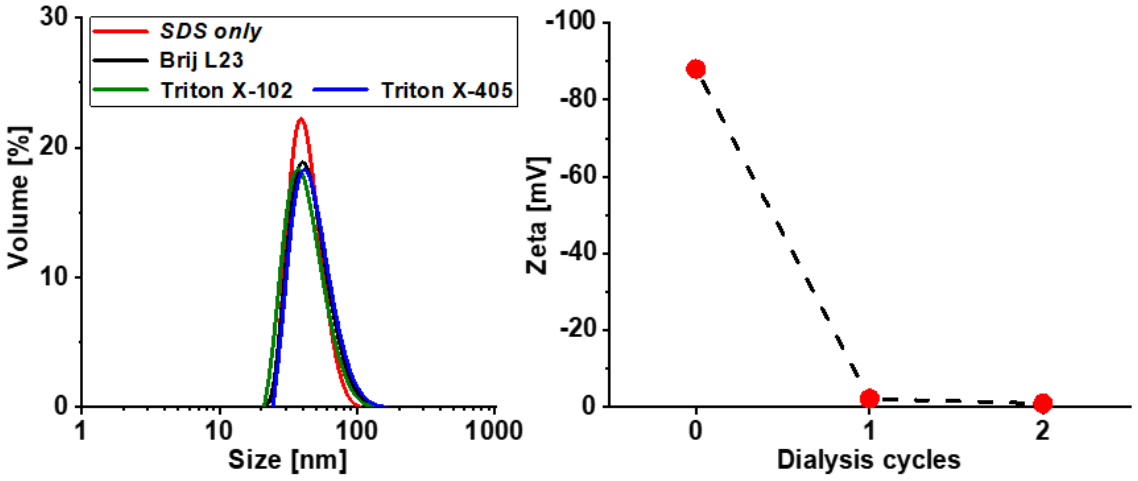

Figure 6.9. DLS traces of PE nanocrystal dispersions obtained after polymerization in SDS solution and after addition of Brij L23, Triton X-102 and Triton X-405 (*left*). After dialysis, a further portion of Triton X-405 was added to allow for surfactant exchange on the particles surface. This is reflected in a decline in Zeta potential after every addition and dialysis step, as the ionic SDS was replaced by the nonionic surfactant (*right*).

After two cycles, the zeta potential previously generated by ionic head groups of SDS adsorbed on the particle surface vanished completely, while the colloidal stability was not altered. This reveals (1) the general ability of surfactant exchange on the PE nanocrystals' surface (a possible co-crystallization of the nonpolar alkyl chain segments with the PE chains does not hinder the release of surfactant) allowing for further surface functionalization, and (2) the suitability of nonionic surfactants in stabilizing the investigated anisotropic PE nanocrystals. However, as polymerization experiments with Triton X-405 did not yield stable dispersions, nonionic surfactants may not be compatible with the polymerization process, respectively, particle formation and growth.

6.2.4 Further suppression of catalyst hydrolysis

Adding base is of crucial importance to suppress hydrolysis, or more precisely, protonolysis reactions, that lead to catalyst decomposition and broadening of molecular weight and particle size distributions.[111,179] The employed base should fulfill several requirements: (1) high base strength, (2) no formation of insoluble salts with SDS, like e.g. potassium hydroxide does, and (3) no interference with chain propagation by e.g. coordination and blocking of active sites (*vide infra*).

As several bases were benchmarked in previous studies, their influence in the particular case of perfluoroalkyl-substituted catalysts on activity and particle uniformity was investigated

(Table 6.5).[179,435] Beside basic strength, the metal cation's influence on the colloidal system was assumed to be highly important as well.[436] Experiments with sodium dodecyl sulfate and sodium hydroxide were interpreted as reference, as no further metal species was present (entries 3-4).

Table 6.5. Polymerization experiments with **1^{I}-C_6F_{13}/PEG** in water with different bases used to suppress hydrolysis.

entry	base	time [h]	yield PE[a] [g]	TOF[b] x 10^3	M_n[c] x 10^3 [g mol^{-1}]	M_w / M_n[c]	chains/ [Ni]	T_m[d] [°C] (crystallinity [%])	particle size[e] [nm]
1	LiOH (55 mmol/L)	0.5 h	0.94	8.9	318.7	1.2	0.4	137 (68) / 136 (54)	14 (0.31)[g]
2	LiOH (110 mmol/L)	0.5 h	1.15	10.9	386.0	1.1	0.4	139 (67) / 137 (54)	17 (0.38)[g]
3	NaOH (67 mmol/L)	1 h	4.06	19.3	583.2	1.1	0.9	140 (65) / 135 (44)	16 (0.07)
4	NaOH (133 mmol/L)	1 h	4.11	19.5	480.0	1.1	1.1	140 (66) / 136 (44)	16 (0.14)
5	CsOH (67 mmol/L)	1 h	7.75	36.8	1015.1	1.2	1.0	142 (62) / 133 (43)	20 (0.07)
6[f]	CsOH (133 mmol/L)	1 h	50.92	121.1	*n.d.*	*n.d.*	*n.d.*	142 (64) / 135 (42)	28 (0.09)

Polymerization conditions: 40 bar ethylene pressure, 7.5 µmol **1^{I}-C_6F_{13}/PEG** catalyst loading, 6 g sodium dodecyl sulfate, 0.3 mL mesitylene added, 15 °C reaction temperature, in 150 mL water, ultrasound applied prior to ethylene pressurization. [a] Determined by precipitation in methanol. [b] Given in mol [C_2H_4] x mol^{-1} [Ni] x h^{-1}. [c] Determined by GPC at 160 °C. [d] Determined via DSC (10 K min^{-4} heating rate). [e] Determined via DLS (volume mean and PDI reported). [f] 15 µmol **1^{I}-C_6F_{13}/PEG** catalyst loading, 24 g sodium dodecyl sulfate, in 300 mL water. [g] Multimodal and several agglomerates formed.

By contrast, experiments performed in the presence of similar concentrated lithium hydroxide showed less activity and multimodal particle size distributions with several agglomerates formed. TEM analysis revealed an undefined particle shape (see *Appendix* for TEM images). This is evident from the fact, that the presence of lithium ions significantly alters the surfactant's micellar structure by coordination of several sulfate groups to one lithium center.[437,438] The resulting very compact structure seems to interfere the particle formation process.

A change in micelle structure can be also observed, when cesium ions are added. Several studies suggested the properties of cesium dodecyl sulfate to be substantially different from the sodium analogue.[439-441] However, a recent study titled "Almost Fooled Again" by Bates and coworkers presents several difficulties in understanding the structure of cesium dodecyl sulfate micelles.[442] They were able to clarify their structure by cryo-TEM analysis, in consistence with scattering data, and proposed a highly flexible structure of thick shell spheres becoming cylindric at higher concentrations. This unique micelle structure seems to have a favorable

impact on the particle growth mechanism, as experiments with cesium hydroxide showed large particle sizes with narrow distributions (high yields and molecular weights, respectively; entries 5-6). The environment around the active nickel center, created by cesium dodecyl molecules, may further support chain growth, leading to enhanced activities. With increased catalyst and surfactant loadings, dispersions of > 13 wt-% polyethylene can be generated within one hour (entry 6). Suppression of hydrolysis by working in deuterium oxide, as previously reported, with and without base, did not reveal any remarkable advances in this case.[179]

Besides the strategy to work under basic conditions to circumvent occurrence of acidic hydrolysis reactions, addition of Lewis basic compounds can massively stabilize the active species by formation of dormant states.[131,179] By blockage of relevant sites, a presumed coordination of water, leading to hydrolysis, is not possible.[161,181] Addition of dimethylformamide (DMF) was found to be highly suited for that propose, enabling extended reaction times of several hours (at the expense of polymerization rates, however).[179] Polymerizations with catalyst **1^{I}-C_6F_{13}/PEG** in presence of different DMF concentrations were performed to investigate the influence on catalytic lifetimes (Table 6.6).

Table 6.6. Polymerization experiments with **1^{I}-C_6F_{13}/PEG** in water and different amounts of dimethyl-formamide (DMF) added.

entry	DMF/[Ni] (vol. DMF)	time [h]	yield PE[a] [g]	TOF[b] x 10^3	M_n[c] x 10^3 [g mol^{-1}]	M_w / M_n[c]	chains/ [Ni]	T_m[d] [°C] (crystallinity [%])	particle size[e] [nm]
1	173 equiv. (0.1 mL)	3	-	-	-	-	-	-	-
2	43 equiv. (0.025 mL)	3	-	-	-	-	-	-	-
3	8.7 equiv. (0.005 mL)	2	3.7	8.9	575	1.2	1.0	140 (62) / 136 (49)	16 (0.12)
4	3.5 equiv. (0.002 mL)	2	6.3	14.9	809	1.3	0.9	141 (66) / 136 (42)	19 (0.05)
5	1.7 equiv (0.001 mL)	2	8.0	18.9	914	1.4	1.2	143 (66) / 135 (42)	21 (0.05)
6	-	2	8.7	20.6	1157	1.2	1.0	142 (66) / 135 (43)	23 (0.04)

Polymerization conditions: 40 bar ethylene pressure, 7.5 µmol **1^{I}-C_6F_{13}/PEG** catalyst loading, 6 g sodium dodecyl sulfate, 1.5 g cesium hydroxide, 0.3 mL mesitylene added, 15 °C reaction temperature, in 150 mL water, ultrasound applied prior to ethylene pressurization. [a] Determined by precipitation in methanol. [b] Given in mol [C_2H_4] x mol^{-1} [Ni] x h^{-1}. [c] Determined by GPC at 160 °C in 1,2,4-trichlorobenzene. [d] Determined via DSC (10 K min^{-4} heating rate). [e] Determined via DLS (volume mean and PDI reported).

Remarkably, catalytic activity completely vanished when more than ~ 9 equiv. of DMF molecules per nickel center were present in solution. The obtained reaction mixture stayed red for days under air, indicating the catalyst structure to remain intact in a totally deactivated,

stabilized state (entry 3). Even, addition of ~ 2 equiv. DMF affected the activity noticeably. This differs substantially from previous experiments with the trifluoromethyl-substituted catalyst, where the presence of > 2,500 equiv. DMF per catalyst molecule sufficiently stabilized chain propagation with a TOF of ~ 2,000 TO h^{-1}. The observed differences can be tracked back to a strong coordination bonding of DMF to the highly electron-poor nickel center, generated by the electron-withdrawing perfluoroalkyl substituents (see *chapters 3 and 4* for comparison of electron densities at the nickel center in perfluoroalkyl-substituted and reference trifluoromethyl catalysts).

In summary, hydrolysis, the most relevant deactivation side reaction in aqueous catalytic polymerization, can be effectively suppressed by addition of cesium hydroxide. The cesium ions seem to have a beneficial influence on the colloidal system and the particle growth process (and chain growth, respectively). By contrast, increasing the catalyst's lifetime by addition of coordinating additives was not possible in case of catalysts bearing long perfluoroalkyl substituents as coordination sites of the highly electron-poor active center seemed to be blocked for chain propagation. Therefore, presence of strongly coordinating species in the reaction mixture should be avoided.

6.2.5 Influence of different polymerization temperatures

The polymerization temperature has a remarkable influence on the catalytic behavior of active sites. While an increased reaction temperature can significantly enhance the catalytic activity, catalyst decomposition and other side reactions may proceed faster as well. In the particular case of late transition metal catalysts, an increased reaction temperature promotes β-hydride elimination, the key step towards branch formation and chain transfer.[69] Hence, for typical *N*-terphenyl Ni(II) salicylaldiminato catalyst systems, branched polyethylene of lower molecular weight is formed under elevated temperatures.[110,111]

Previous studies identified 15 °C as most suited reaction temperature for catalytic aqueous polymerizations, as (1) the low temperature suppresses β-hydride elimination to allow for generation of low branched high molecular weight polyethylene, and (2) undesired ethylene hydrate formation does not occur. The influence of higher temperatures on perfluoroalkyl-substituted catalysts under aqueous conditions was tested for **1^{I}-C_6F_{13}/PEG** and **3^{Ant}-C_6F_{13}/PEG** (Table 6.7).

As expected for *N*-terphenyl type systems, molecular weight and particle size distributions broadened when increasing the reaction temperature from 15 °C to 30°C (**1^{I}-C_6F_{13}/PEG**, entry 1

vs. entry 2). In addition, catalytic activity quickly ceased within 30 minutes, pointing to intensified catalyst decomposition (presumably hydrolysis), as already previously reported.[177,179] The chains per nickel ratios close to unity may indicate random catalyst deactivation to be responsible for broadening of distributions, rather than occurrence of chain transfer.

Table 6.7. Ethylene polymerization experiments in aqueous surfactant solution at different temperatures.

entry	catalyst	reaction temp. [°C]	yield PE[a] [g]	M_n[b] x 10^3 [g mol^{-1}]	M_w / M_n[b]	chains/ [Ni]	T_m[c] [°C] (crystallinity [%])	particle size[d] [nm]
1	1^I-C_6F_{13}/PEG	15	7.09	896	1.2	1.1	143 (64) / 135 (43)	20 (0.03)
2	1^I-C_6F_{13}/PEG	30	3.98	568	1.5	0.9	141 (64) / 135 (45) *n.d.*	17 (0.25)
3	3^{Ant}-C_6F_{13}/PEG	15	1.59	471	1.1	0.5	143 (68) / 137 (46) 135	17 (0.21)
4	3^{Ant}-C_6F_{13}/PEG	20	2.39	715	1.2	0.4	142 (68) / 137 (45) 135	17 (0.14)
5	3^{Ant}-C_6F_{13}/PEG	25	3.09	721	1.3	0.6	145 (67) / 138 (46) 136	17 (0.20)
6	3^{Ant}-C_6F_{13}/PEG	30	2.03	718	1.4	0.4	140 (62) / 136 (44) 134	17 (0.30)

Polymerization conditions: 40 bar ethylene pressure, 6 g sodium dodecyl sulfate, 1.5 g cesium hydroxide, 7.5 µmol catalyst loading, 0.75 mL mesitylene, in 150 mL water, ultrasound applied prior to pressurization, entries 1-2: 60 minutes reaction time, entries 3-6: 30 minutes reaction time. [a] Determined by precipitation in methanol. [b] Determined by GPC at 160 °C in 1,2,4-trichlorobenzene. [c] Determined via DSC, reported as [1st heating cycle (crystallinity) \ 2nd heating cycle (crystallinity)] with 10 K/min heating rate, second line: 1st heating cycle with 1 K/min heating rate. [d] Determined via DLS, volume mean and PDI reported.

By contrast, *N*-naphthyl type systems produce high molecular weight polyethylene even at elevated temperatures, as the axial positions of the active center are sterically shielded and the rate of chain transfer relative to propagation inhibited.[125,126] A slight increase in molecular weight at higher temperatures in accordance with activity was observed (**3^{Ant}-C_6F_{13}/PEG**, entry 3 vs. entries 4-6). However, molecular weight and particle size distributions broadened as well. The increase in polymer outcome can be explained by a relieved catalyst activation at higher temperatures (decoordination of the strongly bound labile ligand, see *chapter 4*). This initial phase of higher activity quickly vanished within several minutes (see *Appendix* for ethylene mass flow traces at different temperatures). At 30 °C reaction temperature catalyst deactivation was clearly higher, leading to a decline in overall polymer yield.

The experiments demonstrated the importance of the reaction temperature as already small variations can have a significant influence on activity and polymer properties. It was shown, that reactions at a reduced polymerization temperature of 10 °C are possible by addition of polyethylene glycol and ethylene glycol to the reaction mixture, which inhibit formation of

ethylene hydrate for a certain time.[443,444] These conditions allowed for generation of polyethylene nanocrystals with unprecedented high crystallinities (see also *chapter 1.3.1*).[178]

Mixing ethylene glycol with catalyst **1^{I}-C$_6$F$_{13}$/PEG** led to immediate catalyst deactivation. However, the question arose if these additional compounds are even necessary as (1) the relatively high SDS loadings, used here, slightly hamper ethylene hydrate formation,[424] and (2) catalyst **1^{I}-C$_6$F$_{13}$/PEG** bears a long polyethylene glycol unit as labile ligand (H_2N-PEG-OMe), that could act as inhibitor. Initial experiments were performed under previously identified reaction conditions, but at 10 °C reaction temperature and without any additional inhibitors (Table 6.8).

Table 6.8. Ethylene polymerization experiments with **1^{I}-C$_6$F$_{13}$/PEG** in aqueous surfactant solution at 10 °C reaction time after different reaction times.

entry	reaction time [h]	yield PE[b] [g]	TON[c] x 10^3	M_n[d] [10^3 g mol^{-1}]	M_w / M_n[d]	chains/ [Ni]	T_m[e] [°C] (crystallinity [%])	particle size[f] [nm]
1	1	8.76	32.0	1225	1.2	1.0	143 (74) / 138 (56) 136	28 (0.08)
2	2	16.73	79.5	2420	1.2	0.9	141 (72) / 134 (48) 137	34 (0.03)
3	4	23.37	111.1	3197	1.3	1.0	146 (77) / 138 (46) 137	44 (0.05)
4[a]	6	24.66	175.8	4529	1.3	1.1	146 (82) / 136 (46) 137	49 (0.06)

Polymerization conditions: 40 bar ethylene pressure, 7.5 µmol **1^{I}-C$_6$F$_{13}$/PEG** catalyst loading, 12 g sodium dodecyl sulfate, 3 g cesium hydroxide, 1.5 mL mesitylene added, 10 °C reaction temperature, in 300 mL water, ultrasound applied prior to ethylene pressurization. [a] 5 µmol catalyst loading. [b] Determined via precipitation in methanol. [c] Given in mol [C_2H_4] x mol^{-1} [Ni]. [d] Determined via GPC at 160 °C. [e] Determined via DSC, reported as [1st heating cycle (crystallinity) \ 2nd heating cycle (crystallinity)] with 10 K/min heating rate, second line: 1st heating cycle with 1 K/min heating rate. [f] Determined via DLS, volume mean and PDI reported.

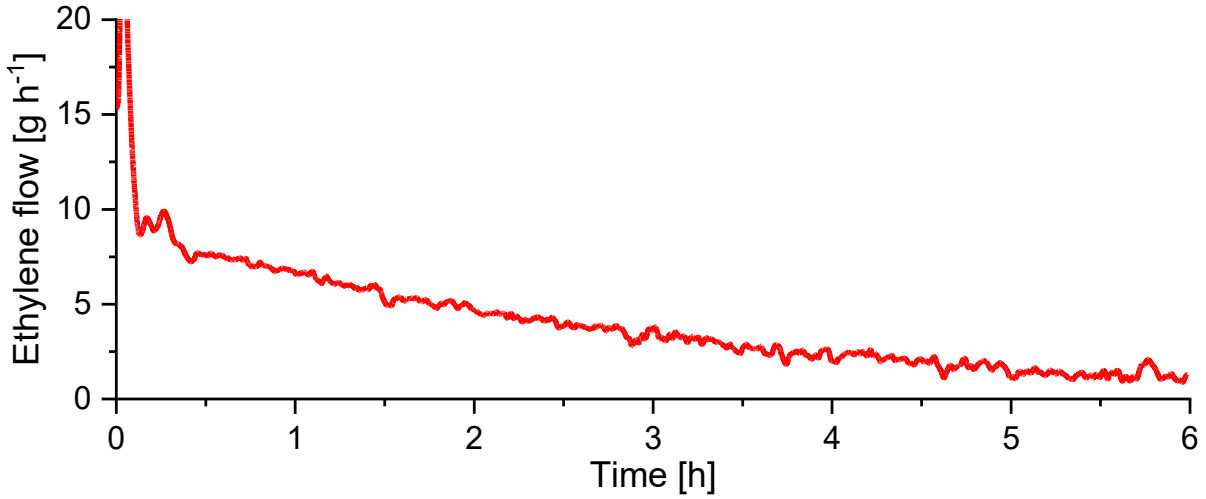

Figure 6.10. Ethylene mass flow trace of a polymerization experiment performed at 10 °C for 6 hours with 5 µmol precatalyst **1^{I}-C$_6$F$_{13}$/PEG** (Table 6.8, entry 4).

Remarkably, catalytic activity was retained for more than 6 hours and molecular weights in excess of $M_n > 4.5 \times 10^6$ g/mol (vs. 3.1×10^6 g/mol [15 °C]; Table 3.2, entry 7) were accessible (Table 6.8, entry 4 and Figure 6.10). Accordingly, a higher volume mean particle size (DLS) of 49 nm (vs. 42 nm [15 °C]; Table 3.2, entry 7) and an enhanced crystallinity of 82 % (vs. 64 % [15 °C]; Table 3.2, entry 7) was found. Note, that the DSC melting behavior still fitted to fully disentangled polyethylene with high first melting points that are not observed for slow heating rates (see *Appendix* for DSC and GPC traces).[255] Branching analysis via IR detection during GPC measurements revealed the presence of < 1 branches per 1000 carbon atoms.

These experiments demonstrated the beneficial influence of reduced temperatures for aqueous catalytic polymerizations. However, further decreasing the reaction temperature is highly critical as this would further promote ethylene hydrate formation and impair the solubility of SDS. No ethylene hydrate formation at 10 °C over the course of 6 hours reaction time were observed, when catalyst **1^I-C_6F_{13}/PEG** with a PEG unit mass of 5516 g/mol was used. By strong contrast, ethylene hydrate formation started after several minutes when using the shorter PEG segment (1981 g/mol) analogue. These findings strongly indicate the (very low concentrated) labile PEG ligand to effectively suppress ethylene hydrate formation.

6.3 Conclusion

Every achievement made in finding an 'ideal catalyst' for a certain reaction goes hand in hand with extensive process design to gain full potential. In the special case of the living aqueous catalytic polymerization towards uniform particles and chain lengths, the suppression of any side reactions during the polymerization process is highly desired. Hence, the efforts to tune the active species by catalyst design must be supported by an optimized overall reaction procedure.

All aqueous polymerization experiments were performed in an automatized pressure reactor to allow for precise monitoring and adjustment of all relevant reaction parameters. Programming of sequences ensured a high reaction reproducibility, identification of deviations and implementation of security features.

A maximum degree of catalyst dispersion in the initial reaction mixture is of crucial importance to ensure an undisturbed particle growth process, without any hydrophobic catalyst molecules aggregated together or adjacent growing particles interfering with each other. It was found that adding a small amount of organic lipophilic compound to the aqueous solution (and

optional treatment with ultrasound) is advantageous and significantly enhances polymer yield and quality of the dispersion obtained.

The surfactant plays a major role in the overall polymerization and particle growth process, as it colloidally stabilizes the active species and nanocrystals formed. Therefore, a sufficiently high amount of surfactant per nickel center is desirable as the free surfactant adsorbs on the growing crystal's surface during particle growth. So far, only ionic surfactants bearing a sulfate/sulfonate head group and a nonpolar alkyl chain tail allowed for nanocrystal synthesis. By contrast, post-polymerization exchange with non-ionic surfactants was found to not affect the colloidal stability. Besides the surfactant, addition of base is crucial to suppress hydrolysis, the main deactivation pathway during chain and particle growth. Cesium hydroxide is the base of choice here, as the presence of cesium ions seems to have an additional beneficial impact on the colloidal system.

Addressing catalyst decomposition and chain transfer reactions, reducing the reaction temperature to 10 °C remarkably enhances catalyst lifetime (> 6 hours) and enables formation of highly crystalline (> 80 % crystallinity by DSC) polyethylene with molecular weights in excess of $M_n > 4.5 \times 10^6$ g/mol ($M_w/M_n = 1.3$). Key here is the presence of the labile amino-PEG ligand (H_2N-PEG-OMe) in the reaction mixture, that seems to inhibit undesired ethylene hydrate formation.

This process design study for the particular case of aqueous catalytic ethylene polymerization demonstrates the remarkable influence of several selected parameters on the overall process. As all major influences seem to have been identified, substantial enhancements in e.g. polymer outcome or molecular weights by further optimization testing is questionable. Promoting chain growth, by e.g. enhancing the ethylene pressure or further decreasing the polymerization temperature, may result in negative side effects like surfactant precipitation or ethylene hydrate formation. However, identifying an industrially more relevant surfactant being compatible with the dispersion generation process would be highly desirable.

6.4 Experimental Section

6.4.1 Materials and general considerations

Solvents were dried and degassed using standard laboratory techniques. Pentane, diethyl ether, toluene and dichloromethane were dried and freed from oxygen by passing over columns with *BASF R3-11* catalyst and molecular sieves. Heptane was distilled over calcium hydride. *m*-Xylene and benzene, purchased from *Merck*, were distilled over sodium. Dimethylformamide (DMF), was purchased from *Merck* and degassed. Mesitylene, purchased from *sigma-aldrich*, was distilled under nitrogen (first fraction of 10 % discarded). Water was deoxygenated by distillation under a constant nitrogen stream. Ethylene 3.5 was purchased from *Air Liquid*e and used as obtained. 1,3-Bis(trifluoro)methylbenzene, 1,3-difluorobenzene, and 1,3,5-triisopropylbenzene, purchased from *sigma-aldrich*, were degassed and dried over molecular sieves. Perfluoroheptane, purchased from *fluorochem*, were degassed and dried over molecular sieves. Hexafluorobenzene, purchased from *abcr*, was dried over molecular sieves. Sodium dodecyl sulfate pellets, hexadecyl(trimethyl)ammonium bromide, polyoxoethylene isooctylphenyl ether (Triton X-405 & Triton X-102), polyoxoethylene dodecyl ether (Brij L23 & Brij L4), potassium polyoxoethylene 4-nonylphenyl propylsulfonate (IGEPAL-SO_3K), lithium hydroxide and sodium hydroxide were purchased from *sigma-aldrich* and used as obtained. A sample of DowFax 2A1 was kindly provided from *Reininghaus-Chemie*. Sodium dodecyl benzene sulfonate was purchased from *TCI chemicals* and used as obtained. Cesium hydroxide was purchased from *abcr* and used as obtained. Trisodium 3,3',3-phosphinetriyltribenzenesulfonate (TPPTS, > 95 %) was purchased from *sigma-aldrich* and dried at 100 °C under vacuum prior to use. Molecular sieves (4 Å, 0.4 nm, Type 514) were purchased from *Carl Roth*. [(tmeda)$NiMe_2$], purchased from *MCat*, was stored at -30 °C prior to use.[349] The catalysts were prepared as described in *chapters 3 and 4* (for synthesis of **1^I-C_4F_9/TPPTS**, *vide infra*).

Molecular weights of synthesized polyethylenes were determined by high temperature gel permeation chromatography (GPC) in 1,2,4-trichlorobenzene or 1,2-dichlorobenzene at 160 °C. A standard flow rate of 1 mL/min was used, whereas a reduced flow rate of 0.5 mL/min was used for samples with expected $M_n > 5 \times 10^5$ g/mol to avoid sample shearing on the columns. Measurements in 1,2,4-trichlorobenzene were carried out on a *Polymer Laboratories 220* instrument equipped with *PLgel Olexis* columns (3 x 30 cm), a refractive index detector (concentration signal), a viscometer (*Viskotek 210 Differential Viscometer*) and light scattering

detector (*Agilent PD2040*). Molecular weights were determined via a triple detection method versus narrow polystyrene standards (software: *Cirrus Multi Offline GPC/SEC* software, version 3.3). Measurements in 1,2-dichlorobenzene were performed on a *Polymer Char GPC-IR* instrument equipped with *PSS Polefin Linear XL* columns (3 x 30 cm, additional guard column), an infrared detector (*IR5 MCT*, concentration signal) and a viscometer. Molecular weights were determined via universal calibration versus narrow polystyrene standards (software: *PSS WinGPC*, version 8.32). Selected samples were measured on both instruments to ensure identical results for molecular weight determination. Chains per nickel numbers were calculated using M_n (determined via GPC) and TON (turnover number). Differential scanning calorimetry (DSC) measurements of polymers were carried out on a *Netzsch DSC 204 F1* instrument (software: *Netzsch Proteus Thermal Analysis*, version 6.1.0) with a heating/cooling rate of 10 K min^{-1}. Additional measurements to investigate the polymer chain disentanglement were done with a heating/cooling rate of 1 K min^{-1} (only first heating cycle reported). Dynamic light scattering (DLS) was performed on diluted polyethylene dispersions using a *Malvern Zetasizer Nano-ZS ZEN 3600* instrument (633 nm) in backscattering mode (173°) at 25 °C. The data was analyzed to yield particle size distributions and polydispersity indices (PDIs; dimensionless number between 0 and 1; 1 being highly polydisperse; determined from gradient of cumulants analysis) using the *Malvern Zetasizer Software*, version 7.12. Transmission electron microscopy (TEM) images were recorded on a *Zeiss Libra 120 EF-TEM* instrument using dialyzed dispersions and analyzed using the *iTEM* software.

6.4.2 Polymerization procedure in aqueous surfactant solution

All ethylene polymerizations in water were conducted in a *Büchi ecoclave* reactor with a 600 mL vessel. The reactor was equipped with a heating and cooling jacket connected to a thermostat, a mechanical stirrer, a nitrogen/vacuum supply, an ultrasonotrode (*Hielscher UIP250*) and a thermocouple both dipping into the reaction mixture (for more details, see *chapter 6.2.1*). A *Bronkhorst* MassFlow apparatus consisting of two flow meters (up to 20 g L^{-1} and 200 g L^{-1} ethylene), a pressure meter and a compressed air-driven badger valve was used to work under constant ethylene pressure. All gas valves and devices were connected to a *HiTec Zang LabBox* and operated by *HiTec Zang LabVision®* software (ver. 2.13). The software allowed for a precise process visualization, control and recording of all relevant parameters in one single process flow chart. The integration of *HiText™* programming language enabled the construction of several automation scripts (e.g. for pressurization, temperature control, venting, etc.). Prior

to all polymerization experiments, the reactor was evacuated and heated up (thermostat temperature: 90 °C) using a custom *HiText*™ program. When the reactor temperature was > 60 °C, the reactor was flushed with nitrogen, evacuated three times and automatically cooled down to 13 °C or 9 °C. The desired amount of surfactant (e.g. sodium dodecyl sulfate), base (e.g. cesium hydroxide) and a magnetic stirrer bar were put into a Schlenk flask, which was transferred into a glovebox. Liquid surfactants were carefully degassed (due to foaming) using standard Schlenk techniques prior to transfer into the glove box. After addition of lipophilic solvent (e.g. mesitylene), catalyst and further compounds (e.g. DMF), the flask was sealed, brought outside the glovebox and water was added under vigorous stirring via cannula transfer. The clear orange solution (after 3-5 minutes of stirring) was then transferred to the reactor and stirred at 500 rpm. The polymerization experiment was started using a custom *HiText*™ program with a graphical interface to adjust ultrasound application power and duration, reaction time and reaction temperature control. The reaction mixture was then automatically treated with ultrasound (usually for 4 minutes with 120 Watt power) and the solution temperature monitored to stay around 15 °C or 10 °C. Immediately afterwards, the stirring rate was increased to 1000 rpm and the reactor pressurized stepwise to 40 bar ethylene pressure within 30 seconds. The ethylene flow was then controlled and recorded by the mass flow meter to ensure a constant pressure over the entire polymerization experiment. The reaction temperature was automatically adjusted to 15 °C or 10 °C. After the desired reaction time, the pressure was automatically released stepwise. Below 15 bar residual pressure, the reactor was vented manually into a beaker to collect migrating dispersion due to foaming. The entire dispersion was weighed, filtered over cotton wool and the solids content determined by precipitation of a 50 g aliquot of dispersion in 300 mL of methanol. After stirring for 30 minutes, the precipitated bulk polymer was filtered, washed thoroughly with water and methanol, and dried in a vacuum oven (60 °C, 30 mbar) overnight.

6.4.3 TPPTS-coordinated perfluorobutyl-substituted precatalyst (1^{I}-C_4F_9/TPPTS)

Preliminary studies on aqueous catalytic polymerization with Ni(II) sailcylaldiminato catalysts showed TPPTS to be a highly suited hydrophilic labile ligand, that renders the catalyst precursor water-soluble. To investigate the role of the labile ligand in case of the herein presented perfluoroalkyl-substituted catalysts, a route to the TPPTS-coordinated representatives was sought. However, the synthesis of such complexes requires a medium that

dissolves the salicylaldimine, the nickel precursor and the trisodium sulfonic acid (TPPTS). While DMF was identified as solvent of choice in preliminary studies, the highly hydrophobic salicylaldimines with their long perfluoroalkyl groups were not soluble in DMF. Further, solvent mixtures turned out to be not well suited as their ratio could not be kept constant upon solvent evaporation, leading to precipitation of the DMF-coordinated complex while the TPPTS molecules stayed in solution. However, in case of the shortest fluorocarbon chain length salicylaldimine $\mathbf{1^{I}\text{-}C_4F_9}$, the solubility in DMF could be significantly enhanced by addition of small portions C_6F_6 and allowed for generation of the corresponding TPPTS-coordinated precatalyst ($\mathbf{1^{I}\text{-}C_4F_9/TPPTS}$).

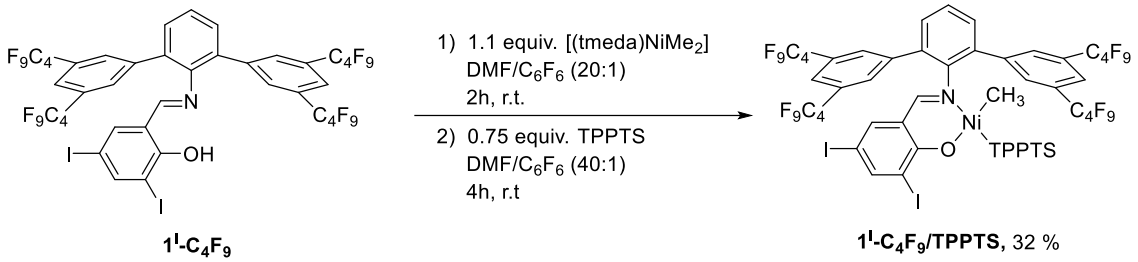

$\mathbf{1^{I}\text{-}C_4F_9}$ $\mathbf{1^{I}\text{-}C_4F_9/TPPTS}$, 32 %

Scheme 6.1. Synthesis of the hydrophilic perfluorobutyl-substituted κ^2-(*N,O*)-salicylaldiminato nickel(II) methyl complex with TPPTS coordinated as labile ligand.

Experimental: To 30 mg of solid [(tmeda)$NiMe_2$] (146 µmol, 1.1 equiv.) and 204 mg salicylaldimine $\mathbf{1^{I}\text{-}C_4F_9}$ (138 µmol, 1 equiv.), 3 mL DMF/C_6F_6 (20:1) were added (methane evolution) and stirred vigorously for 2 hours at room temperature to give a clear, deep red solution. 64 mg TPPTS (100 µmol, 0.75 equiv.) were dissolved in 3 mL DMF, added to the reaction mixture and this stirred for 4 hours at room temperature (red solution). The solvent was removed carefully under reduced pressure and the red residue washed with portions of diethyl ether (3 times, 7.5 mL each). The desired product was obtained as orange powder and dried under vacuum overnight. The amount of residual non-coordinated/unreacted TPPTS (2.1 equiv.) and DMF (1.7 equiv. DMF), relative to complex formed, was determined from NMR spectra in MeOD-d_4 (*vide infra*) and the molecular weight per Nickel species (3398 g mol^{-1} $[Ni]^{-1}$) corrected, correspondingly.[111] Due to the small portion of desired product in the compound mixture and their extensive overlap of resonances in NMR spectra a detailed characterization could not be performed. However, presence of two species in ^{31}P-NMR spectra (coordinated and non-coordinated TPPTS) and a doublet for the Ni-Me species in ^{1}H-NMR spectra confirmed coordination of the phosphine to the nickel atom (*vide infra*). Yield: 32 %, 107 mg, 32 µmol.

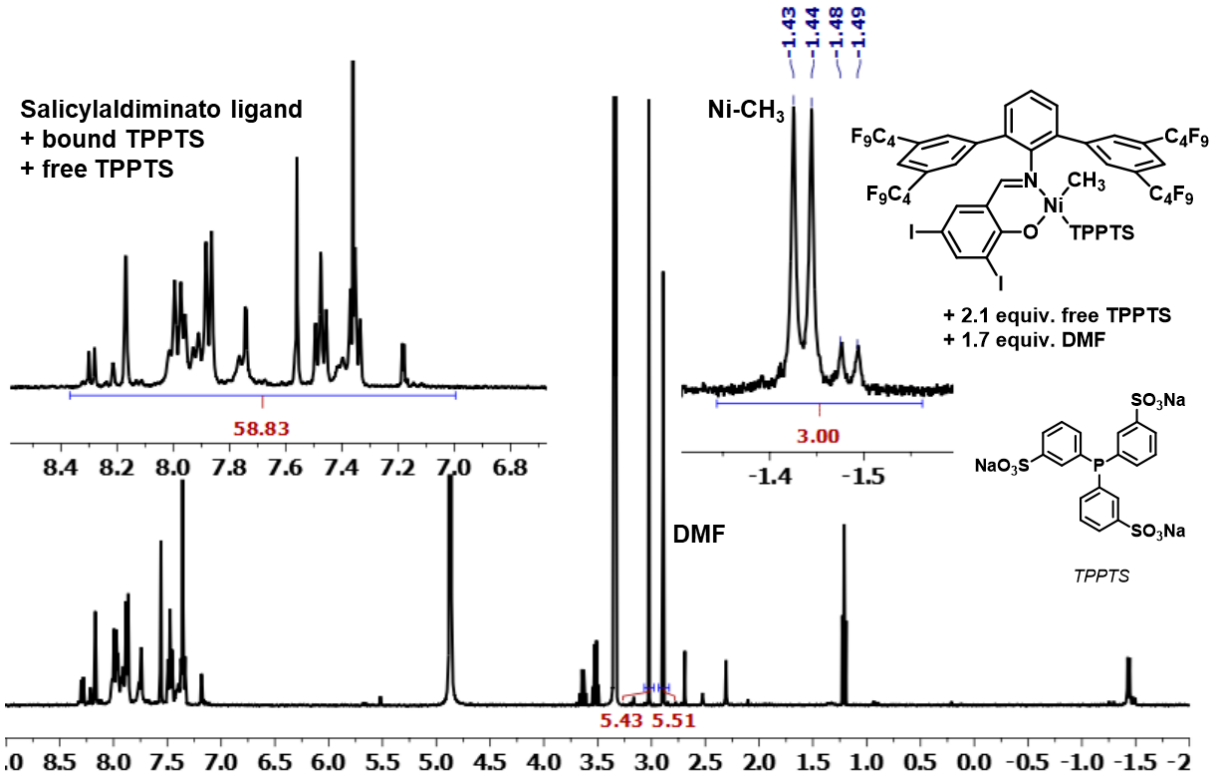

Figure 6.11. ^{1}H NMR spectrum (400 MHz, 300 K, MeOD-d_4) of **1^{I}-C$_4$F$_9$/TPPTS**.

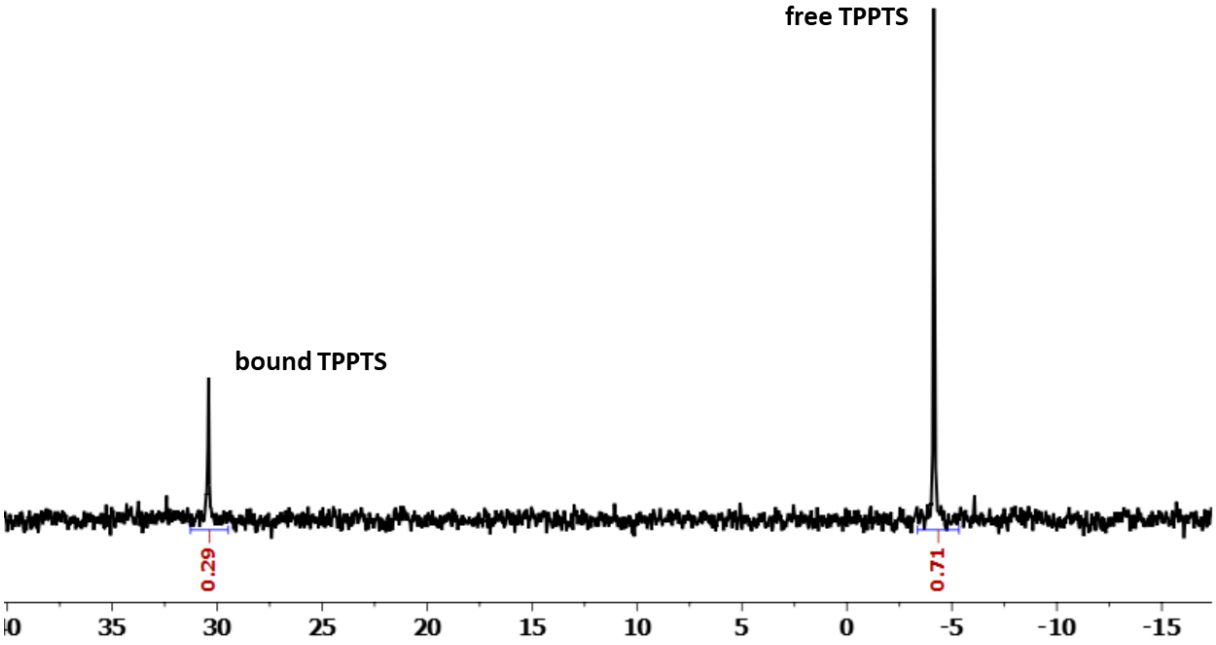

Figure 6.12. ^{31}P{^{1}H} NMR spectrum (162 MHz, 300 K, MeOD-d_4) of **1^{I}-C$_4$F$_9$/TPPTS**.

Polymerization experiments: **1^{I}-C_4F_9/TPPTS** was tested in aqueous polymerization, in direct comparison with the respective H_2N-PEG-OMe coordinated catalyst (Table 6.9). While both catalysts produced polyethylenes of comparable properties and in comparable yields (considering the formation of agglomerates in case of **1^{I}-C_4F_9/TPPTS**), particles sizes and the distributions thereof were substantially different. **1^{I}-C_4F_9/TPPTS** produced turbid dispersions with a limited colloidal stability as indicated by formation of agglomerates during polymerization and afterwards. This was also reflected in DLS measurements that showed huge particle sizes and extraordinary broad particle size distributions in case of the TPPTS catalyst. We attribute this to an insufficient dispersion of the precatalyst in the initial reaction mixture (see also *Results and Discussion*).

Table 6.9. Polymerization experiments with perfluorobutyl-substituted catalysts bearing different hydrophilic labile ligands in aqueous surfactant solution.

entry	catalyst	yield PE[a] [g]	TOF[b] x 10^3	M_n[c] x 10^3 [g mol^{-1}]	M_w / M_n[c]	chains/ [Ni]	T_m[d] [°C] (crystallinity [%])	particle size[e] [nm]
1	1^{I}-C_4F_9/TPPTS	6.02[f]	7.2	1202	1.4	0.7	142 (65) / 136 (42) 136	394 (0.32)
2	1^{I}-C_4F_9/PEG	8.50	10.1	1140	1.3	1.0	142 (67) / 135 (45) 137	24 (0.05)

Polymerization conditions: 40 bar ethylene pressure, 7.5 µmol catalyst loading, 6 g sodium dodecyl sulfate, 1.5 g cesium hydroxide, 0.3 mL mesitylene added, 14 °C reaction temperature, in 150 mL water, 4 hours reaction time, ultrasound applied prior to ethylene pressurization. [a] Determined via precipitation in methanol. [b] Given in mol [C_2H_4] x mol^{-1} [Ni]. [d] Determined via GPC at 160 °C. [d] Determined via DSC, reported as [1st heating cycle (crystallinity) \ 2nd heating cycle (crystallinity)] with 10 K/min heating rate, second line: 1st heating cycle with 1 K/min heating rate. [e] Determined via DLS, volume mean and PDI reported. [f] Formation of several agglomerates was observed.

6.5 Appendix

6.5.1 Selected GPC data

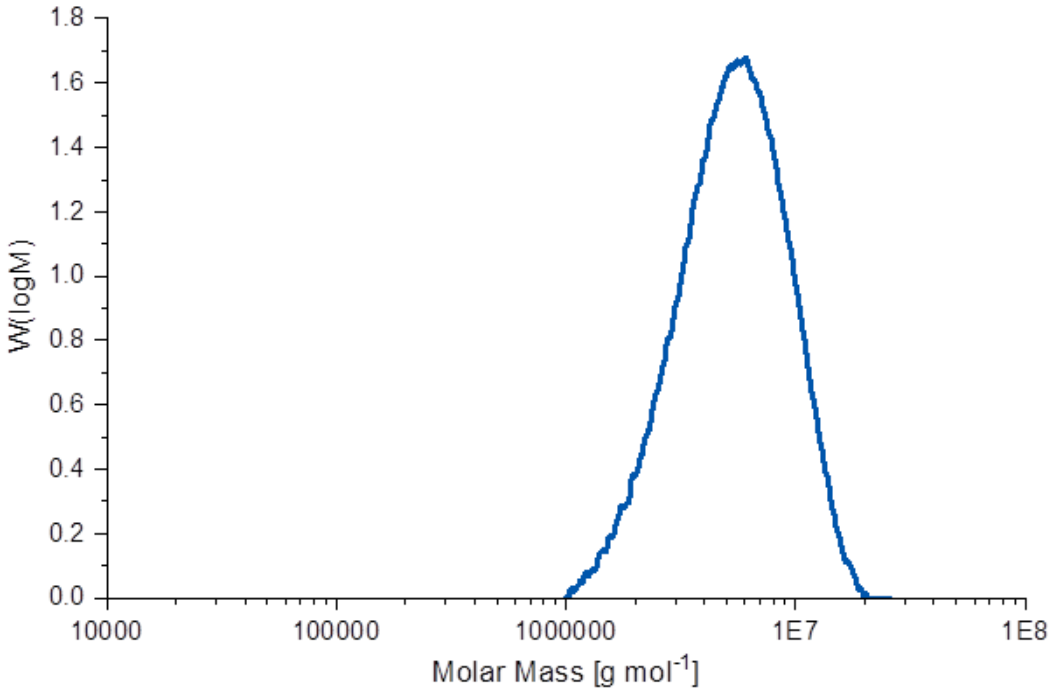

Figure 6.13. GPC trace of polyethylene obtained from polymerization in aqueous surfactant solution at 10 °C reaction temperature (Table 6.8, entry 4).
M_n = 4529000 g/mol M_w = 6012500 g/mol M_p = 6055700 g/mol M_z = 7629300 g/mol M_v = 6132100 g/mol
PDI = 1.33

6.5.2 Selected DSC data

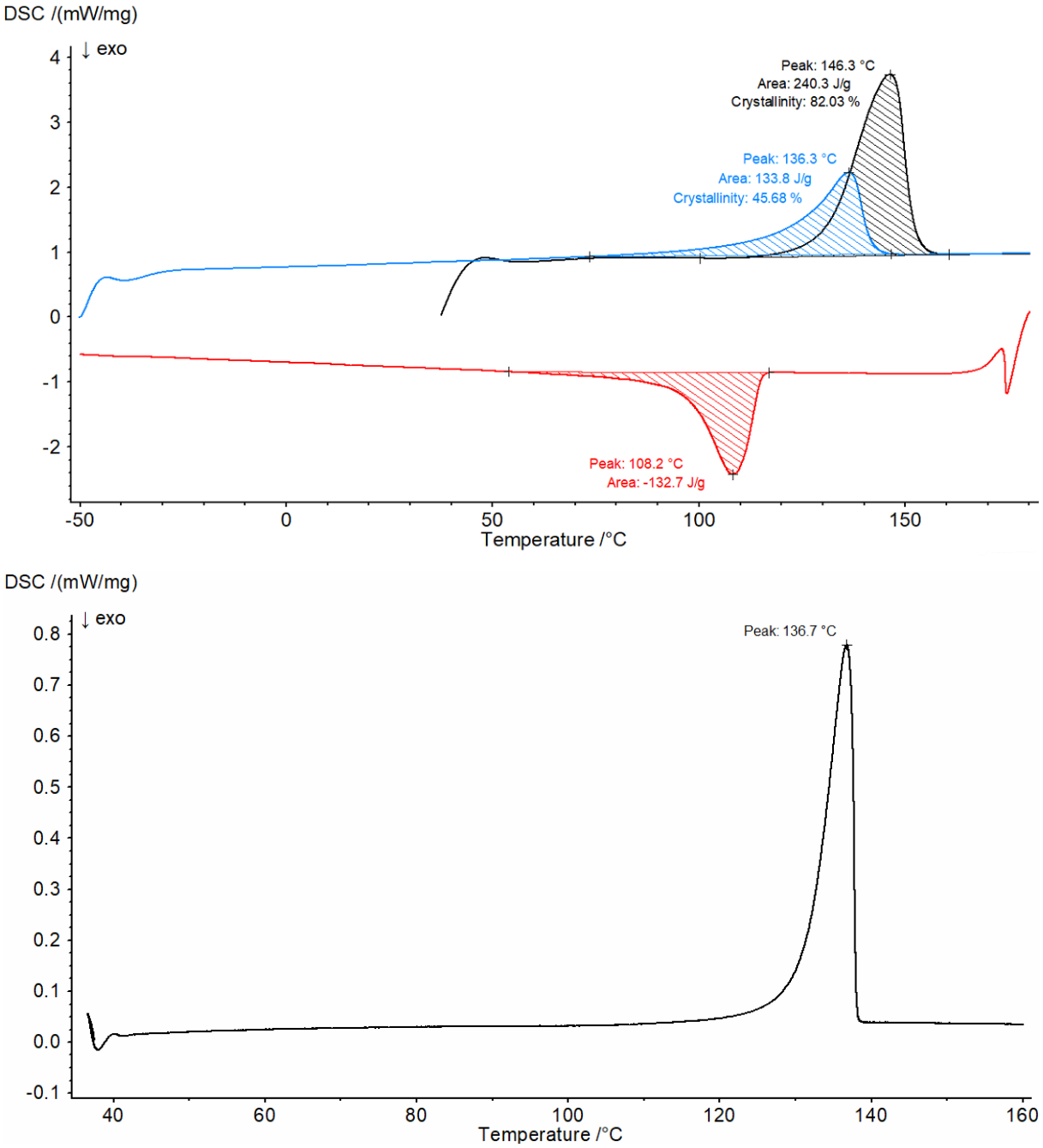

Figure 6.14. DSC traces of polyethylene obtained in aqueous polymerization at 10 °C reaction temperature (Table 6.8, entry 4). *Top*: measured with 10 K min^{-1} heating rate (black curve: 1st heating, red curve: 1st cooling, blue curve: 2nd heating). *Bottom*: measured with 1 K min^{-1} (only first heating shown).

6.5.3 DLS traces

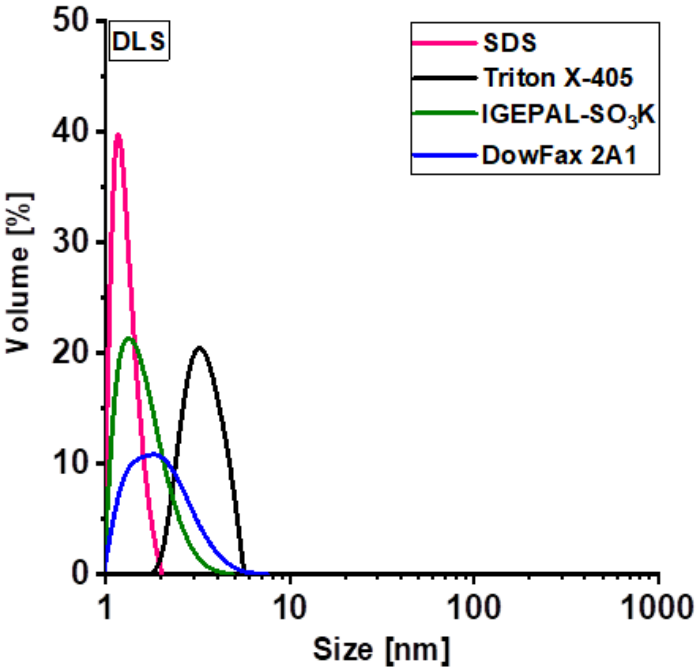

Figure 6.15. DLS traces of aqueous solutions containing different surfactants and a small portion of mesitylene (1 mmol surfactant, 15 µL mesitylene, in 10 mL water; stirred for 15 minutes). Emulsions were at least stable for 12 hours. No stable emulsion was formed with Brij L4.

6.5.4 Mass flow traces

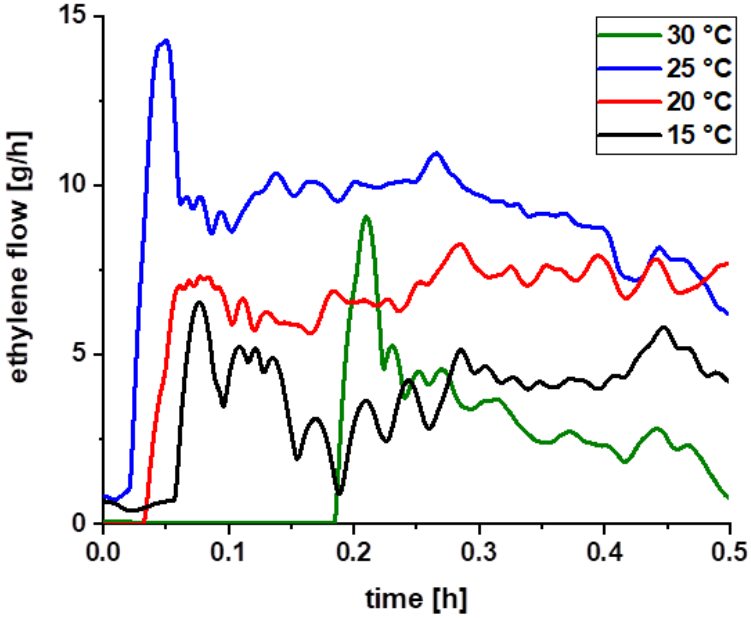

Figure 6.16. Ethylene mass flow traces of polymerization experiments with catalyst $\mathbf{3^{Ant}\text{-}C_6F_{13}/PEG}$ in aqueous surfactant solution at different temperatures (Table 6.7).

6.5.5 TEM images

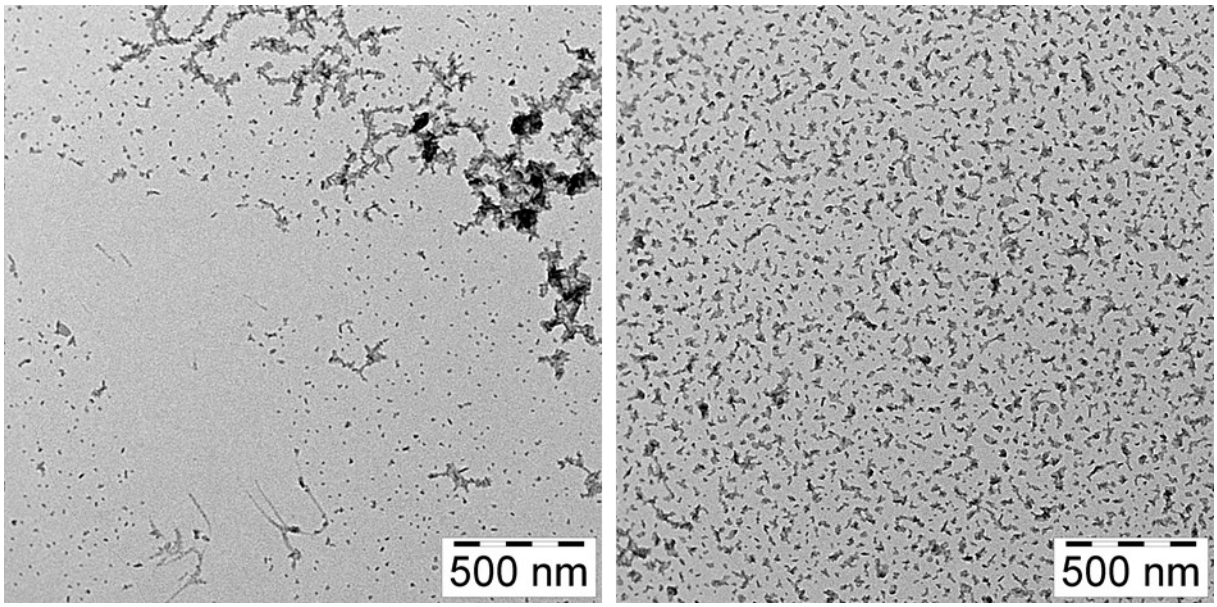

Figure 6.17. TEM images of nanocrystals synthesized in the presence of lithium hydroxide as base (Table 6.5).

7 Materials from UHMWPE Dispersions

7.1 Introduction

The intensive studies on nanostructures made of organic and inorganic materials, their synthesis and their characterization has created a large library of available building blocks with properties not exclusively related to the pure chemical composition.[445-448] Having these nanostructures with their unique characteristics in hand, the challenging question of generating new materials by their (self-)assembly arises.[328,449-452] In particular, assemblies of particles with anisotropic shapes unlock new perspectives in generation of 'particle-based materials', with properties arising from anisotropic direction-dependent interactions and variable symmetries (Figure 7.1).[20,21,267,453]

While the basic concept of arranging single particles into larger structures, where every particle contributes to the overall properties, remains apparently obvious, this has rarely been achieved on a truly macroscopic level of several micro- or milimeters.[298,305,327,454-459] On the other hand, macroscopic material processing methods are often not compatible with the fundamental concept of precise initial soft assembly formation and further solidification.

This chapter will demonstrate the application of uniform anisotropic UHMWPE nanocrystals (see *chapter 3*) for generating macroscopic particle-based materials by common methods for polymer processing like e.g. fiber spinning or 3D printing techniques.

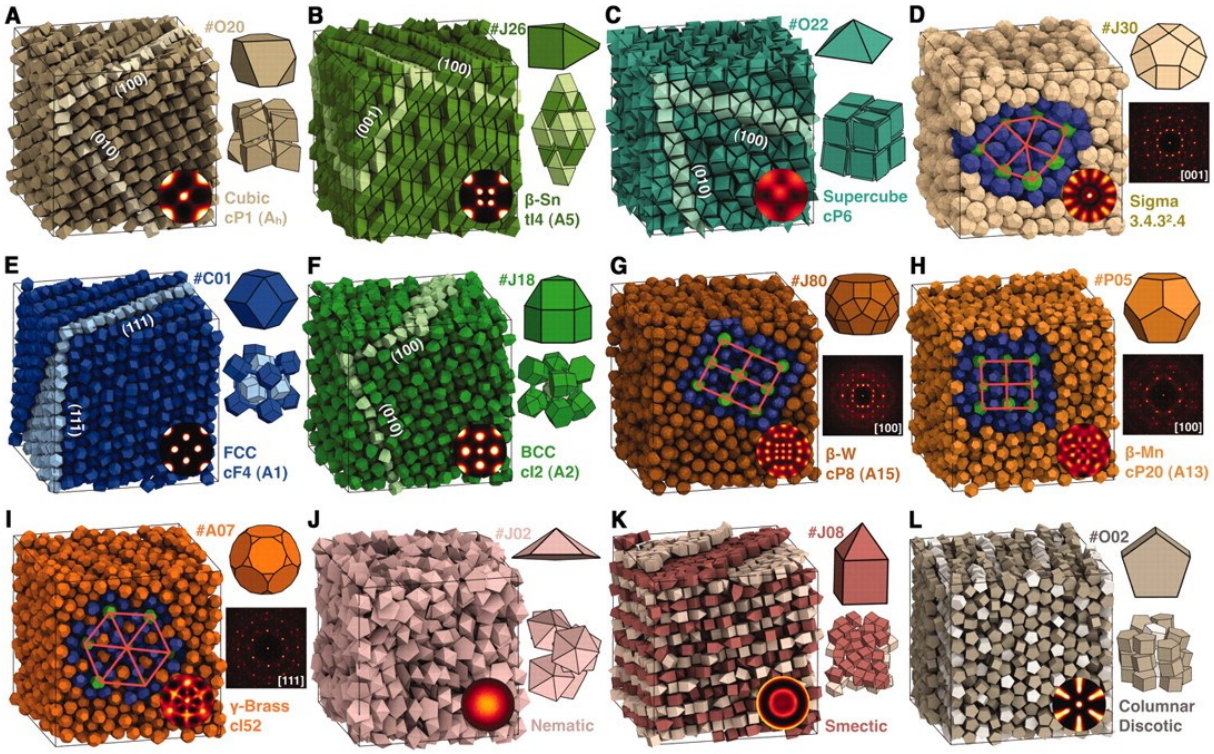

Figure 7.1. Systems of 2048 anisotropic polyhedra assembled starting from the disordered fluid. In each subfigure, a snapshot of the simulation box (left), the bond-order diagram for nearest neighbors (inset), the polyhedron shape and ID (top right), a small group of particles or the diffraction pattern (middle right), and the crystallographic characterization (bottom right) is shown.[267] Reprinted with permission from the AAAS (*Science* **2012**, *337*, 453–457; Copyright 2012).

The employed dispersions serve several benefits: (1) they are on aqueous base and all additional compounds (e.g. remaining free surfactant) can be easily removed by dialysis; (2) in their highly dispersed state they can be homogenously mixed with other materials to generate hybrid materials; and (3) they can be generated in high yields of > 25 g per batch, desirable to form macroscopic materials, with molecular weights of $M_n > 3 \times 10^6$ g/mol and nanocrystal lateral sizes of > 100 nm. As every particle consists of one single, crystallized and oriented polymer chain of ultra high molecular weight, the mechanical aspects of the generated components will be analyzed. The disentangled character can enable entirely new ways of processing, which is generally limited for traditional commercial UHMWPE due to its entanglements (see *chapter 1.2*). However, the fate of one nanocrystal upon material formation might be difficult to analyze as polymeric materials tend to coalescence in dense packings with discrete particle boundaries disappearing (see monolayer assemblies in *chapter 3*).[460]

Please note that the final research progress presented in this chapter was strongly affected by the COVID-19 pandemia (caused by SARS-CoV-2) in 2020. In case of missing conclusive experiments or analytical data, detailed perspectives and outlooks will be presented.

7.2 Results and discussion

UHMWPE single-chain nanocrystal dispersions of M_n > 3 x 10^6 g/mol were synthesized as demonstrated in the previous chapters at 10 °C reaction temperature with polymerization times of > 4 hours. After the reactor was vented, the ready-to-use dispersion was collected. However, free remaining surfactant and inorganic base, dissolved in solution, can have a disruptive impact on the material properties after water removal/evaporation as these additives can e.g. hinder beneficial interactions between the polymer chains, respectively, particle surfaces or form separate packings and phases. This issue can be addressed by either polymer precipitation in a medium that dissolves the surfactant while the polymer solidifies, or by dialysis.

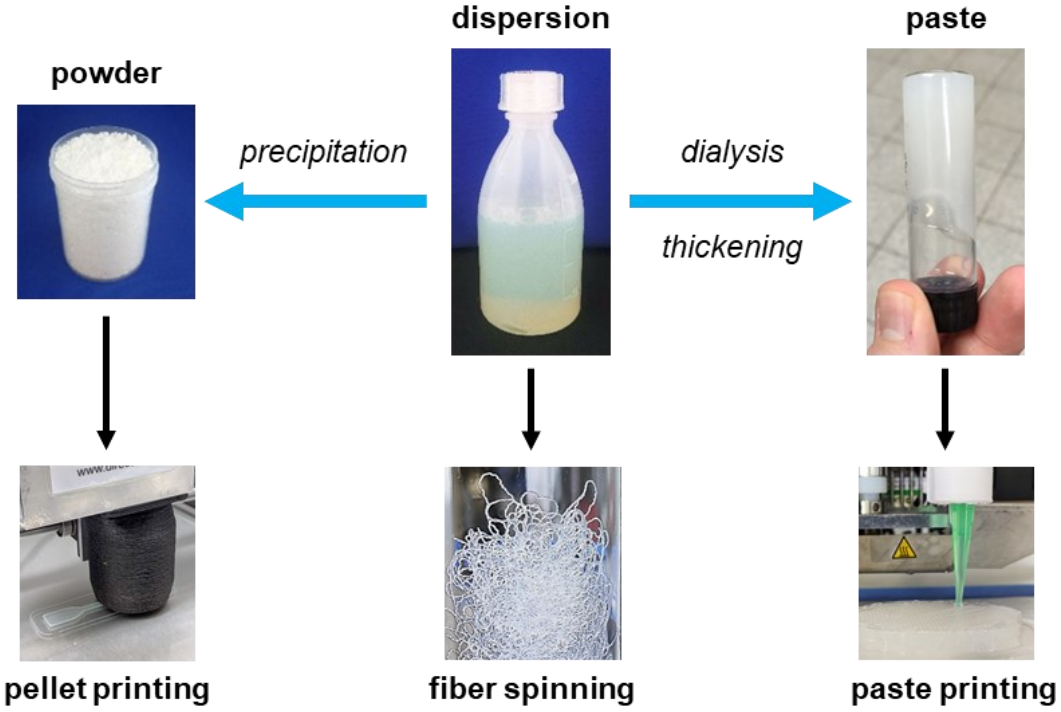

Figure 7.2. Overview of fabrication processes studied. The pure polymer powder could be obtained by precipitation in methanol and was fed into a pellet 3D printer (*left*). The dispersion, as directly obtained from polymerization, could be spun by addition through a needle into a coagulation agent to form well-defined fibers (*center*). Thickening of obtained dispersions increased their viscosity drastically to make them suited for 3D paste printing (*right*).

Pouring the dispersion into stirred methanol led to immediate polymer precipitation (colloidal electrostatic stabilization vanishes), with the adsorbed surfactant leaving the particles' surface and the solid forming larger agglomerates (see *Experimental Section* for analysis of residual surfactant in precipitated polymer powders and dialyzed dispersions). After washing and drying, a UHMWPE granulate with grain sizes of 0.5 – 2 mm, suited for direct use in a 3D pellet printer, was obtained (see *chapter 7.2.1*; Figure 7.2, left). By contrast, slow continuous

addition of dispersion by means of a pump into ethanol (coagulation agent) led to a slow and controlled precipitation process forming well-defined soft fibers (see *chapter 7.2.2*; Figure 7.2, center). During all solidification processes the nanocrystals stayed intact as single disentangled crystallized chains as evidenced by DSC studies. Fabrication of the highly dispersed nanocrystals was facilitated by dialysis and subsequent concentration to significantly increase the dispersion's viscosity, enabling 3D printing techniques for paste-like materials (see *chapter 7.2.3*; Figure 7.2, right).

7.2.1 Direct 3D printing of powders

3D printing (also known as 'additive manufacturing') of polymers has become a fundamental industrial material processing technique and allows for rapid manufacturing with, simultaneously, high flexibility and precision.[461,462] The basic principle of generating computer-designed, complex 3D objects has encouraged development of several printing platforms to manufacture soft materials (resins, polymer powders or thermoplastic monofilaments).[463,464] But also examples for printing of metals[465], alloys[466] or glass[467] have been recently presented. Most common techniques vary from laser-assisted solidification techniques (laser sintering) to extrusion of filaments (fused deposition modeling, FDM; Figure 7.3, left).

Extrusion-based techniques are in widespread use to build up 3D objects via layer-by-layer deposition of molten material through a heated nozzle.[468] Precise design of 3D models and printing routines are important to generate accurate objects (Figure 7.3, right). The printer machines are usually not capable of processing 3D models directly into printing routines but can only interpret simple commands (e.g. extrusion at a certain rate while moving in certain direction; so-called 'g-codes'). Creating these commands is done by 'slicing' with suited computer software, that can strongly influence the quality of 3D printed parts.[469,470] During slicing, a 3D object file is loaded, processed into layered data and concrete printing paths depending on multiple parameters (e.g. nozzle diameter, filament diameter, infill pattern and filling degree, layer height, etc.). The created g-code file can then be interpreted by the printer machine.

FDM techniques require a thermoplastic filament feed, and consideration of a balance of polymer melt rheology, processing temperature (typically slightly above melting temperature), shape parameters, etc. This results in a rather narrow processing window.[464] Printing of HDPE, an important plastic material, is challenging as its crystallization accounts for massive thermal shrinkage and warpage upon cooling down the extruded melt.[471,472] This negatively impacts

adhesion of printed objects on the build plate and hampers polymer chain diffusion between adjacent strands. Concerning the massively higher melt viscosity of UHMWPE caused by its entanglements[200], extrusion-based 3D printing of this material is even more difficult. To this end, only approaches fabricating composites of UHMWPE and HDPE (wax)[473,474], PEG[474,475], polycarbonate-urethane (PCU)[476] or ABS[477], or by 3D printing based on laser-sintering[478], have been reported.

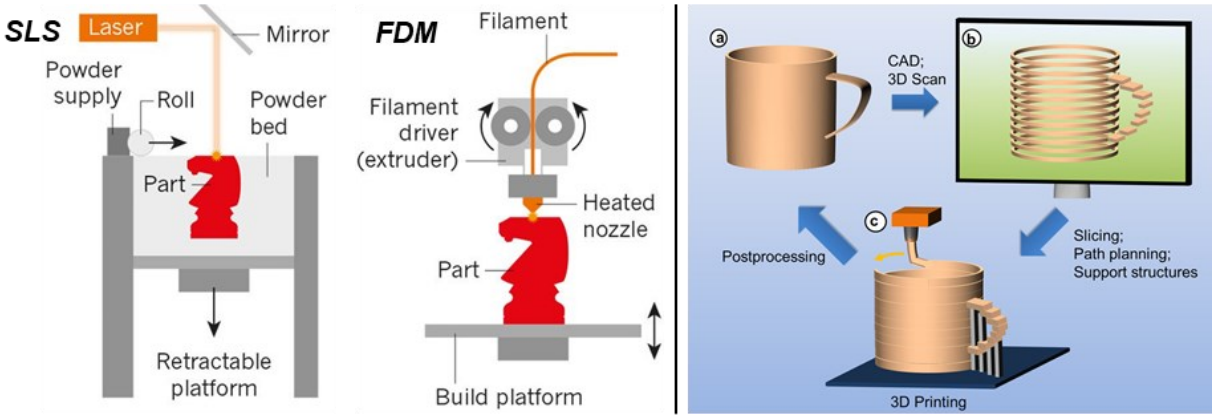

Figure 7.3. *Left:* Schematic illustration of selective laser sintering (SLS) and fused deposition modeling (FDM) as common 3D printing techniques.[463] *Right:* Basic principles of 3D printing: development of a product idea (3D model; a), preprocessing (slicing; b) of virtual model into layered data and adjustment of path planning and extrusion, and 3D printing process (postprocessing to remove artifacts like support structures; c).[464] Adapted with permission from Springer Nature (*Nature* **2016**, *540*, 371–378; Copyright 2016) and the American Chemical Society (*Chem. Rev.* **2017**, *117*, 10212–10290; Copyright 2018, CC BY license).

The herein reported UHMWPE nanocrystals exhibit the exceptional feature of a fully disentangled nature. This state significantly reduces the melt viscosity upon initial melting.[200,252] However, in melt the polymer chains can entangle quickly and the processability is lost after the polymer solidifies by cooling (e.g. after filament formation).[479] Hence, converting the UHMWPE powder to a filament for 3D printing by hot extrusion is difficult. Consequently, a printer setup where the polymer powder can be directly fed into the extruder without preprocessing has to be employed. 3D powder printing fully bypasses filament-processing to simplify manufacturing of new materials.[480] However, maintaining a consistent material flow and simultaneous high printing resolution is challenging due to the irregular nature of powders compared to filaments. Here, direct printing of polyethylene powders and pellets is demonstrated. In case of powders obtained by aqueous polymerization, their highly disentangled nature will be examined in being supportive for hot extrusion of UHMWPE in 3D pellet printing.

Figure 7.4. *Left:* Direct3D Pellet Extruder printer head including a funnel filled with material (middle), hot end with nozzle printing on build glass plate (bottom) and gear connected to motor and auger (top). *Right:* Schematic design of a standard pellet printer setup (RRUPE design).[480] Adapted with permission from Elsevier (*Addit. Manuf.* **2019**, *29*, 100811; Copyright 2019).

All printing experiments were performed on a commercially available Direct3D Pellet Extruder printer, where the print feed could be directly filled into a funnel suited to the printer head (Figure 7.4, left). An auger placed inside the funnel acts as key component, that directs the material to the hot end (i.e. the nozzle), and controls the extrusion process (Figure 7.4, right). The auger is connected to large gear, spun by smaller gear, attached to a stepper motor.

The design of appropriate slicing routines was of major importance, as automated calculations for extrusion rates based on filament diameters do not apply. Please note that a precise calibration of extrusion rates depending on granulate sizes and bulk densities, extrusion temperatures, etc. was necessary prior to every print set. Slicing profiles were constructed and optimized by printing of commercial grade HDPE pellets, using basic parameters from a previous study for HDPE filament printing by Mülhaupt and coworkers[471] (see *Experimental Section* for details). A large nozzle diameter of 0.8 mm was chosen to allow even highly viscous melts to be extruded appropriately (at the expense of printing resolution). The material was extruded at a rather high hot end temperature of 240 °C to ensure entire melting of the granulate even at high printing/extrusion speeds and to reduce the melt viscosity. A substantially higher bed temperature of 120 °C was chosen, in contrast to the reported 60 °C, to keep the first layer of the printed object in a molten state. This ensured both, sufficient form stability to support subsequent layers, and adhesion to the glass plate. In contrast to previous reports, no special adhesion compounds or support materials between glass plate and substrate were necessary.

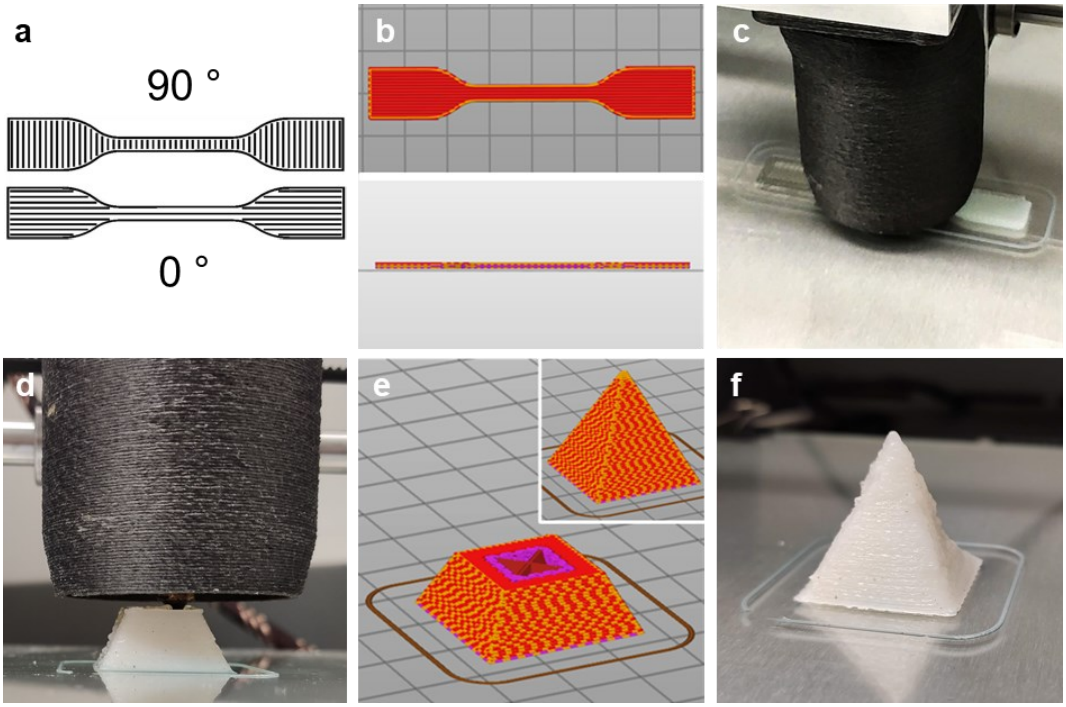

Figure 7.5. 3D powder printing of HDPE granulates. a) Illustration of different infill pattern angles having direct impact on material properties. b) Sliced 3D object models for dogbone specimens (ISO 527-2; height: 2 mm), shown in top and side view. c) Printing of a dogbone specimen, showing the first layer being molten and transparent (left side) while the subsequent layer solidifies (right side). d) Side view of the pyramid's printing process showing well defined evolution of the object's height and outer walls. e) Pyramid 3D slice model cross section showing the complex infill patterns (purple: grid pattern for inner core, red: outer wall thickness), size: 25 x 25 x 25 mm. f) 3D printed pyramid showing a well-defined change in lateral extension from bottom to top with slight irregularities on the surface.

Printing of dogbone tensile test specimens was performed with the designed slicing routines. It was shown, that the infill pattern (lines) direction (Figure 7.5, a) has a direct influence on the mechanical properties.[471] Specimens with infill direction parallel (0° infill angle) to the direction of strain showed a substantially higher elongation at break, compared to specimens with infill directions being perpendicular (90° infill angle). Printing experiments described here were performed with an alternating infill pattern (lines) with 4 layers in total (0°, 90°, 0°, 90°) of identical height (Figure 7.5, b). After the print was finished, the heaters were deactivated, and the object left on the glass plate until the bed temperature was below 50 °C.

Although the first layer remained in a transparent molten state during printing (Figure 7.5, c), no significant formation of flow artifacts (so-called 'elephant's foot') was observed. The measured mechanical properties compared well to previously reported data for filament printed HDPE specimens with a Young's modulus of 955 MPa [0°, 90°] (vs. 1020 MPa [0°] and 990 MPa [90°])[471] and an elongation at break of 52 % [0°, 90°] (vs. 90 % [0°] and 15 % [90°])[471]. These results

clearly demonstrated that the pellet-based approach was able to generate printings of comparable quality to common FDM filament printing techniques.

With the difficulties of HDPE 3D printing in mind, a more demanding test object was sought to further benchmark the elaborated parameters. A pyramid (common calibration test specimen) was chosen since its printing requires a high precision with increasing object height as the lateral extension varies. Irregularities in extrusion rate/volume or layer height (Z movement) would immediately result in an object tilt, etc. Additionally, a partial infill degree (20 %, grid pattern) with an enhanced outer walls thickness (45° infill angle) was chosen (Figure 7.5, e). During printing, a well-defined evolution in height was observed, with slight irregularities occurring upon solidification of the extruded material due to the aforementioned warpage and shrinking effects (Figure 7.5, d). After 2 hours, the print was finished and carefully detached from the glass bed showing clearly the shape of a pyramid with an upright tip (Figure 7.5, f).

UHMWPE powders of $M_n > 3 \times 10^6$ g/mol, obtained by precipitation of aqueous dispersions, were directly filled into the material funnel. Residues of HDPE were slowly extruded until a substantial increase in melt viscosity (extrusion volume decreased) was observed. Please note, that the hot end was kept above 160 °C at any time when UHMWPE printing experiments were performed to avoid clogging by solidified polymer. Before the machine was allowed to cool down to room temperature, the extruder was 'rinsed' with HDPE to remove any residues of UHMWPE. Initial printing experiments showed that the UHMWPE melt could be in principle extruded but requires a high rotation speed of the extrusion auger. Over time the melt viscosity further increased and hindered a consistent extrusion behavior during the printing process. While the rather high extrusion temperature was chosen to keep the melt viscosity low, it can, however, facilitate quick re-entangling by polymer chain diffusion generating a substantial viscosity increase.[479] It was reported, that upon melting of disentangled isolated UHMWPE single crystals the properties of the corresponding entangled bulk material are much faster recovered as theoretically predicted (so-called 'chain explosion', see also *chapter 1.2.2*).[254,481,482] The relatively long time the polymer stays molten in the large pellet extruder upon extrusion is problematic here, compared to the rather short hot end length of filament printers. Additionally, conveying of the fluffy UHMWPE powder seemed to be more difficult than for the much more compact HDPE pellets. This directly results in a reduced pressure acting on the melt, being important for effective extrusion. Therefore, further modifications in the polymer powders morphology might be necessary to achieve extrusion rates suitable for proper printing.

In summary, an alternative approach of 3D printing of polyethylene directly without preprocessing to a filament was presented. The pellet-based approach serves several challenges and requires a careful adjustment of printing parameters and slicing routines. Peculiarities of polyethylene (warpage and shrinking effects) further impede its processing. By employing a rather high hot end (240 °C) and glass bed (120 °C) temperature, difficulties arising from melt viscosity and adhesion to the glass surface could be addressed. In contrast to previous approaches, no special coatings or bed materials to prevent self-detaching from the build plate during printing were necessary. The mechanical properties of printed test specimens compare well to previous filament-based reports and the elaborated routines allow for printing of even more complex objects. Working with smaller nozzle diameters will further increase the printing resolution and enhance mechanical properties of printed objects.

Employing the presented routines as basis for powder printing of disentangled UHMWPE showed, that the melt viscosity drastically increases over time due to re-entangling by polymer chain diffusion. Future experiments will test reduced extrusion temperatures and UHMWPE of the lower molecular weight regime (M_n ~ 1-2 x 10^6 g/mol), as the polymer chain length directly influences the effects of re-entanglement formation.[479] Key here could be also a rather slow heating rate that would lead to formation of a heterogenous melt with a slow re-entangling rate (see also *chapter 1.2.2*).[252] Finding conditions where the UHMWPE stays extrudable and does not change its melt viscosity significantly during printing will be crucial for direct UHMWPE powder additive manufacturing. As possible alternative approach, first experiments of mixing the disentangled UHMWPE powder with low amounts of a polycarbonate in a micro compounder showed promising results.[483] The extruded filament could be used in a common filament FDM 3D printer setup with UHMWPE contents of > 80 wt-%, showing promising mechanical properties. These experiments further demonstrated that the disentangled UHMWPE can be fed to a compounder and processed, extending the range of applicable techniques like e.g. generation of thin foils with a micro cast film line.

7.2.2 UHMWPE fibers by 'dispersion fiber spinning'

Organic fibers made from natural resources (e.g. for yarn and textiles) are used by humanity since thousands of years.[484] Their importance and applications have dramatically grown after understanding the structure of fiber-forming polymers, clarified by Staudinger in 1927, and the development of first synthetic fibers (*Nylon 6,6*) by Carothers in 1935.[485-487] Design of 'tailor-made' fibers and need for mass production encouraged development of several extrusion

manufacturing processes like wet, dry or melt spinning. While many prominent examples for fibers based on polycondensates are known, polyolefin fibers (PP and PE), usually made by melt spinning, have grown in importance as well (e.g. for making tarpaulins, ropes, twines or bristles).[488]

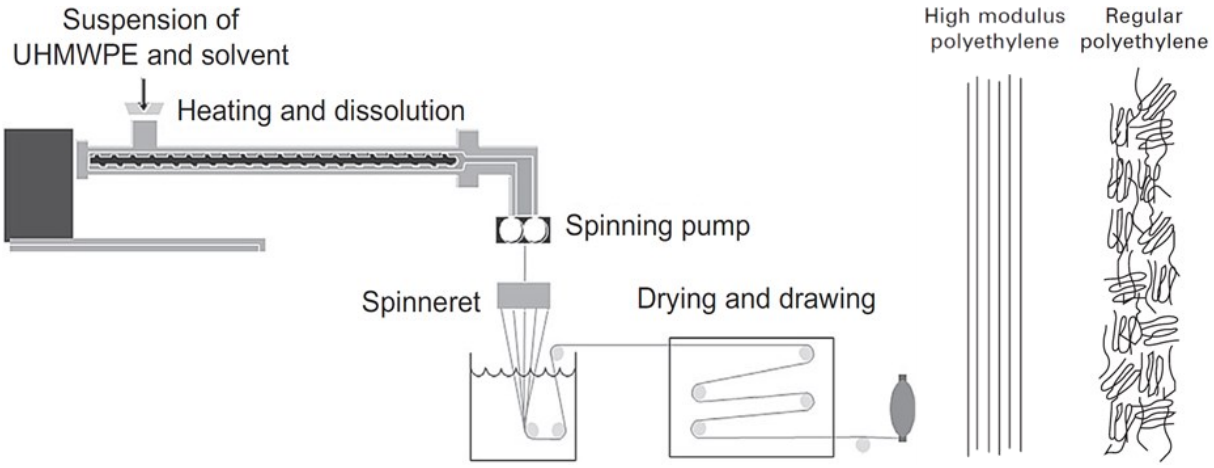

Figure 7.6. Schematic representation of the gel-spinning process,[489] and macromolecular orientation of high-modulus PE in fibers and regular PE.[223] Adapted with permission from Elsevier (van der Werff *et al.* in *Advanced fibrous composite materials for ballistic protection* **2016**, Copyright 2016; Vlasblom *et al.* in *Handbook of Tensile Properties of Textile and Technical Fibers* **2009**, Copyright 2009).

UHMWPE fibers are outstanding in their properties as they combine both, high strength and low weight (see also *chapter 1.2*).[489,490] The chemical nature of polyethylene attributes for beneficial abrasion and fatigue properties, but the melting point limits several application areas.[223] The so-called 'gel-spinning' process (Figure 7.6) was invented by DSM and Pennings and allowed for commercial production of high-strength and high-modulus UHMWPE fibers (commercialized by DSM as Dyneema®; see also *chapter 1.2*).[491,492] In this process, a UHMWPE/solvent suspension is fed to a heated extruder, where the UHMWPE dissolves. This spinning solution is extruded through the spinning holes of a spinneret and the fiber formation is induced by UHWMPE crystallization upon cooling. The obtained fiber is then transferred to solvent removal (e.g. by extraction in a bath) and extensive hot drawing. The high dilution of polymer chains in the initial solution mostly prevents formation of entanglements. Thus, very high draw ratios can be achieved, leading to a high molecular orientation and high fiber strength and modulus (Figure 7.6, right).[493] Beside mechanical properties, thermal conductivities of the highly oriented chains are significantly enhanced as well.[494-496] Recent developments demonstrated several processing improvements, like electrospinning of UHMWPE solutions or improved gel-spinning using vegetable oils as environmental friendly solvent, allowing higher polymer concentrations.[241,497]

The aqueous UHMWPE dispersion provides the material in the very unusual morphology of highly diluted, isolated, fully disentangled polymer chains of uniform length. The individual chains are highly ordered and highly crystalline, a prerequisite for formation of structurally well-defined materials. To employ these dispersions, a totally different fiber formation mechanism is envisaged: while during gel-spinning the mutual crystallization of individual polymer chains from homogenous solution facilitates structural evolution, colloidal destabilization of the nanocrystal building blocks and subsequent macroscopic solidification is used in case of the aqueous UHMWPE dispersions. By utilizing this mechanism, the setup simplifies as no heating or critical organic solvents are needed.

The employed setup was comparable to a simple apparatus for fiber wet spinning[484] (see *Experimental Section* for detailed procedures and additional images of setups and spun fibers). A standard syringe was filled with aqueous UHMWPE dispersion (not dialyzed) and mounted into a syringe pump. A needle was connected to the syringe and kinked rectangular. The end of the needle was then dipped into a cylinder filled with ethanol, acting as coagulation bath (with spinning in direction of gravity). The spinning procedure was then started by operating the syringe pump with a moderate flow of 1 mL/h. Directly after the dispersion stream left the needle, a clearly visible solidification process occurred. Streaks next to the forming fiber indicated a constant mixing between the injected aqueous stream and the surrounding ethanol. After several centimeters, the fiber seemed to be stable in its form as breakages and kinks were only rarely observed. When reaching the bottom of the cylinder, the fiber started to deposit at the glass surface, and stayed fully intact with single fiber strands being clearly distinguishable. After the spinning had finished, the coagulation bath was slowly emptied with the fibers remaining at the outer glass wall (Figure 7.7, a). Collecting and drying led to formation of brittle fiber nests with individual threads clearly distinguishable (Figure 7.7, b). DSC studies revealed that fiber consists of fully disentangled polymer chains and that the presence of intact nanocrystal domains inside the fiber structure can be assumed (see *Appendix* for DSC traces).

To better observe the fiber evolution process and test application of binary material blends, the UHMWPE dispersion was mixed with an aqueous dispersion of anisotropic nanoparticles of conjugated polymer.[434] Exposure with UV light clearly indicated a homogenous mixing of both dispersions without any agglomerates forming, as observable from the uniform fluorescence emission. The mixture was spun as described above and UHMWPE fibers with fluorescent properties were obtained (see Figure 7.7, c and *Appendix*, Figure 7.13). A well-defined fiber was

already visible several millimeters below the needle outlet, moving down the column and being only rarely interrupted.

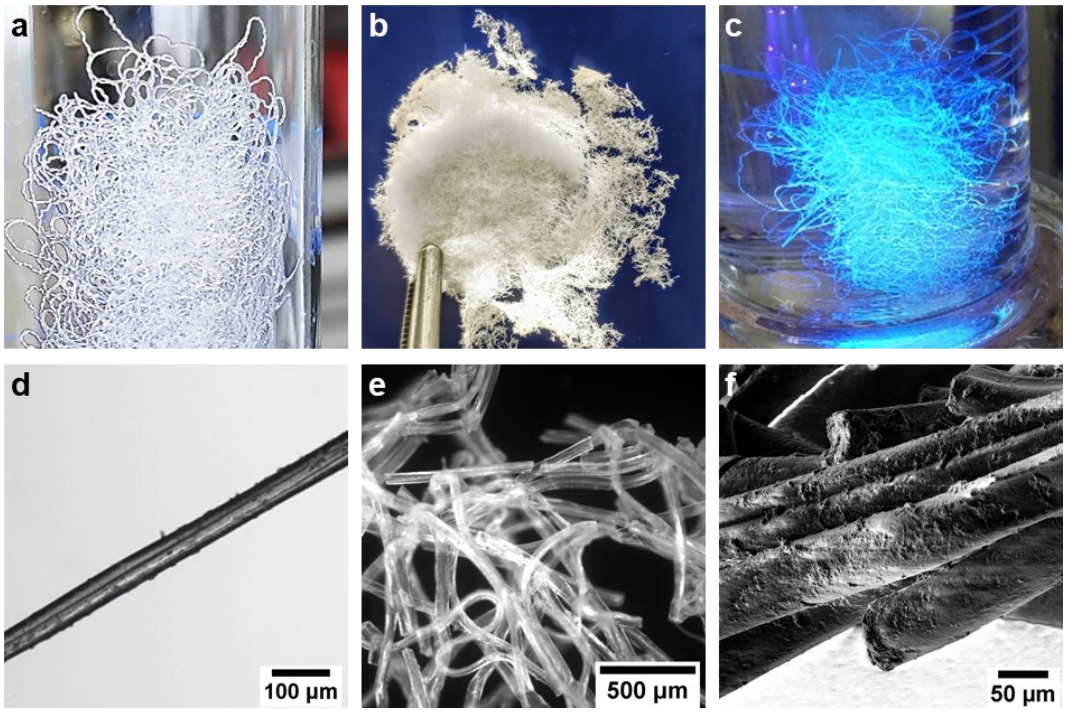

Figure 7.7. UHMWPE fibers obtained by dispersion spinning in ethanol acting as coagulation bath. a) Wet, isolated fibers after ethanol removal situated at the cylinders glass wall. b) Fiber nest obtained after drying. c) Spinning of UHMWPE dispersion mixed with polyfluorene nanoparticles generating fibers with fluorescent properties (under UV light exposure). d) Isolated UHMWPE fiber showing a well-defined fiber thickness of ~50 µm (light microscopy, bright field mode). e) Ensemble of several fibers being fully transparent (light microscopy, dark field mode). f) SEM image of an UHMWPE fiber bundle.

Light microscopy performed on dried fibers (composed of UHMWPE only) revealed a highly regular morphology regarding diameter and surface structure (Figure 7.7, d-f; see *Appendix* for additional light microscopy images of fiber nests and single fibers). With a diameter of ~ 50 µm, they were found to be of comparable size to commercial-grade, melt-spun UHMWPE fibers.[223] The fibers were transparent and several breakages were observed (presumably drying artifacts). A slight illumination was visible, when two polarization filters (with the specimen in between) in perpendicular orientation (0° & 90°) were present in the optical path, that may point to an ordered, crystalline character (see *Appendix*, Figure 7.21). Images of breakage areas revealed that the fibers seemed to be composed of much smaller bundled nano-sized filaments (see *Appendix* for breakage area analysis, Figure 7.22). However, the crystals' near-order and origin of these 'nanofilaments' remained unclear at that point.

In their wet state the fibers were found to be rather sensitive and brittle. Gentle shaking of the fibers swimming in the coagulation bath resulted in rupturing into small fiber fragments.

This behavior is evident from the fact, that the cohesion in highly stable, melt-spun and drawn fibers is generated by beneficial interactions between individual, highly oriented, extended polymer chains (Figure 7.6, left).[498] By strong contrast, the fibers obtained here are composed of single chain nanocrystals with the polymer chains arranged into lamellae. Interactions between individual polymer chains occur via the crystal's surfaces exclusively, as no tie molecules are present. Residues of solvents or surfactant in wet state may additionally hamper these interactions. To prevent fiber ruptures during isolation, a column with an outlet tap connected to the bottom end was employed as coagulation bath (see *Experimental Section*, Figure 7.14). The ethanol could then be slowly released through the tap with the fibers remaining in the lower column part for further drying at room temperature. Light microscopy analysis revealed that these fibers exhibit significantly less breakages than found in prior experiments (see *Appendix* for light microscopy images, Figure 7.23).

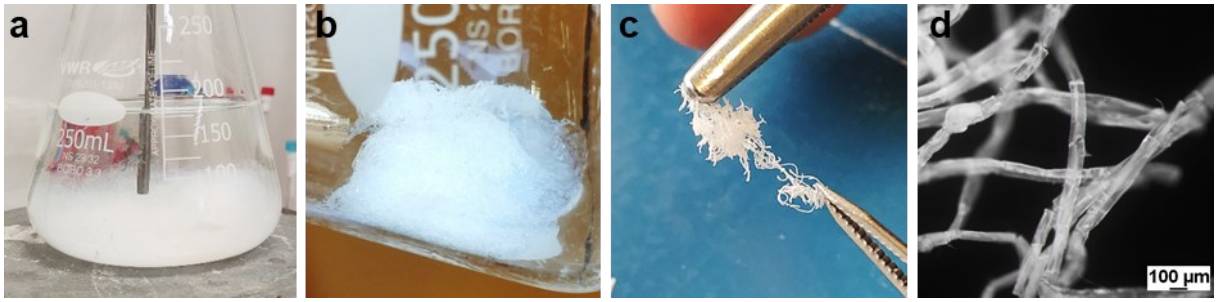

Figure 7.8. Post-processing of UHMWPE fibers made by dispersion spinning in *n*-propanol at room temperature. a) The fibers were collected in a flask during spinning and placed on a hot plate (90 °C, 6 hours) to force polymer chain diffusion between adjacent nanocrystal domains. b) Isolated wet fiber coil. c) Stretching of post-processing fibers (wet state) indicating an enhanced mechanical strength. d) Light microscopy of fibers formed, after post-processing (dark field mode).

To address the mechanical strength, post-processing of fibers by thermal treatment was studied. Annealing of generated fibers in solution should force polymer chain diffusion and formation of strengthening tie molecules between individual crystals.[212,499] As the boiling point of ethanol did not allow for annealing at elevated temperatures, a series of several high-boiling alcohols was benchmarked. Meeting the prerequisites of being miscible with water and dissolving surfactant and base, dispersion spinning experiments in *n*-propanol were conducted. The fibers were collected in a flask (see *Experimental Section*, Figure 7.14) and heated to 90 °C for 6 hours, floating in solution (Figure 7.8, a). Their morphology significantly altered toward a 3D-networked, stable, easy to handle fiber coil, that indicated formation of connections between previously adjacent fiber threads (Figure 7.8, b). Simple stretching experiments of small wet-state fiber clusters revealed a remarkable increase in mechanical strength compared to

unprocessed fibers (Figure 7.8, c). Therefore, annealing of fibers made by aqueous dispersion spinning seems to be suited to significantly increase fiber cohesion and stability. Tie molecule formation by polymer chain diffusion between adjacent nanocrystal domains can be assumed in some cases, as DSC studies on post-processed fibers did not indicate significant changes in melting behavior, respectively, nanocrystal morphology.

A major drawback in so far conducted experiments emerged from the top-to-bottom fiber formation direction: collecting fibers at the bottom of a coagulation bath during spinning by simultaneous e.g. winding (on a spool, reel, etc.) was not possible. However, this could be achieved by reverting the flow direction of the spun dispersion as the formed fibers would then accumulate at the coagulation bath's top surface. As a coagulation agent with a higher density of water is required then, several protic solvents were benchmarked and initial experiments in ethylene glycol were performed. A column was filled with the coagulation agent, the bottom outlet sealed with a septum and punctured with the needle of the syringe containing dispersion (see *Experimental Section* for details on experiments in ethylene glycol). After the spinning process was initiated, the forming fiber was moving upward in a regular fashion. However, the higher viscosity of ethylene glycol significantly hampered diffusion between the ascending water phase and the surrounding coagulation bath. As a direct consequence, the solidification process was slowed and the formed fibers ill-defined. To enhance diffusion and simultaneously increase the fibers' stability already during their formation process, a heated column was employed and spinning experiments at 80 °C coagulation bath temperature were performed. An increased spinning rate was necessary to prevent clogging of the needle outlet at elevated temperatures resulting in less defined fibers of larger diameters. The ejected dispersion solidified immediately and moved upward enabling collection of the fibers formed at the liquid's upper surface. However, the mechanical stability turned out to be still limited and requires further process optimizations as e.g. a gentle drying procedures to remove the high-boiling solvent, a suited fiber collection setup and general apparatus optimizations (needle outlet diameter, column length, etc.) to substantially improve the fiber's regularity.

In summary, a new process to generate UHMWPE fibers from aqueous dispersion by a very simple procedure was presented. The dispersion is spun through a needle into a coagulation bath (e.g. ethanol) and the fiber directly formed as the colloidal stability vanishes. Microscopy analysis revealed a high regularity, regarding surface structure and diameter, being comparable to melt-spun UHMWPE fibers. The properties of fibers formed can be influenced by several parameters (e.g. needle outlet diameter, pump flow, coagulation agent, etc.). Previous mixing of

the UHMWPE dispersion with other colloidal materials enables e.g. generation of UHMWPE fibers with fluorescent properties.

However, freshly made fibers in their wet state are highly sensitive and brittle as they consist of many coagulated nanocrystal domains without any tie polymer chains. This can be overcome by heat post-processing directly after spinning that forces chain diffusion, substantially increasing the mechanical strength. Furthermore, a possible approach to collect fibers directly during the spinning process by using high density coagulation agents was elaborated.

Future experiments will focus on formation of thinner fibers by employing spinnerets or cone-shaped 3D printing nozzles for spinning. Analysis of these fibers can elucidate the structural composition and the fate of one nanocrystal upon spinning (e.g. by scattering experiments). Using sufficiently small spinning/extrusion apertures may further enable orientation of particles directly during fiber formation. As heat post-processing seems to be key to mechanical resistance, the procedure will be optimized to generate fibers suitable for drawing experiments as known for melt-spun fibers. The fiber isolation procedure will play an important role here and coiling of formed fibers by heated rollers will be investigated. As the colloidal nature of UHMWPE dispersion allows for highly effective mixing, spinning of binary mixtures with other materials and the resulting fiber properties will be analyzed. While addition of e.g. graphene can append new features, addition of shorter chain polyethylene (HDPE/wax) may substantially enhance mechanical properties after heat post-processing.[473]

7.2.3 UHMWPE paste printing

Most 3D printing technologies and applications rely on feeds of solid-state materials in the form of dense powders or filaments (see *chapter 7.2.1*). However, this strongly limits the variety of applicable materials to mostly thermoplastic components, particularly in case of FDM or SLS techniques (Figure 7.3, left).[464] 3D printing allows for many biomedical applications, e.g. designing of medical devices, but also approaches to directly print biomatter are sought.[500] Development of paste-like material 3D printing enabled a totally new scientific field of printing biomimetics like tissues and organoids.[501] This techniques were further developed to employ them in 'food printing'[502] or in materials science for fabrication of e.g. metal-organic hybrid frameworks (Figure 7.9)[503], mechanically robust foams[504], hydrogels[505], conductive functional devices[506,507] or robotics[508,509]. As these examples demonstrate the highly versatile character of paste printing techniques, their suitability to fabricate UHMWPE pastes was tested.

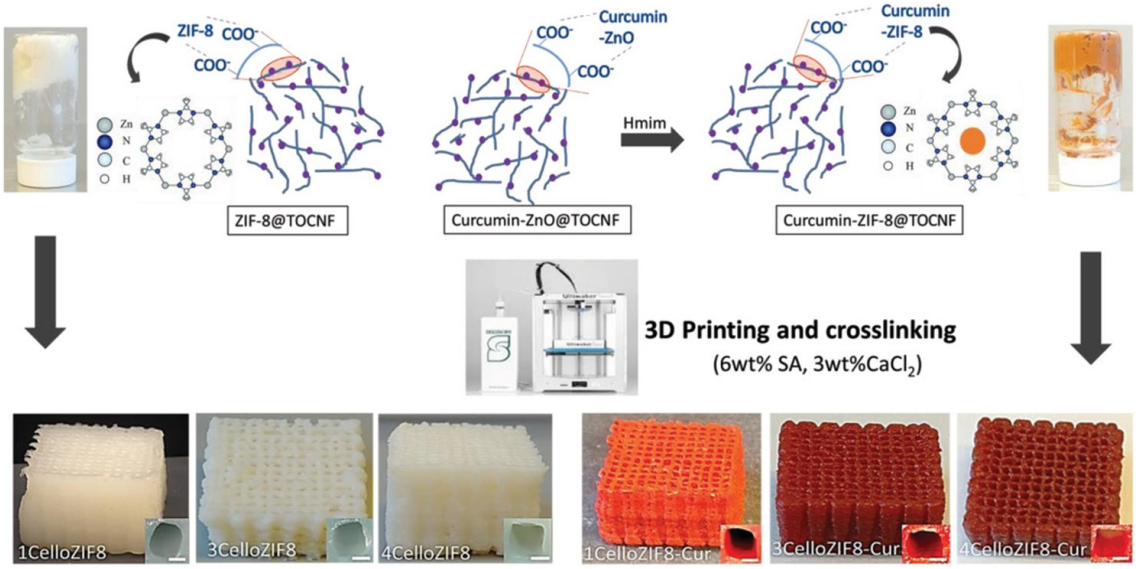

Figure 7.9. Representation of synthesis and 3D paste printing of metal-organic framework ('CelloMOF') hybrid inks (printed with Ultimaker/Discov3ry Complete system). Insets are enlarged images representing the pores of the printed scaffolds.[503] Reprinted with permission from Wiley-VCH (*Adv. Funct. Mater.* **2019**, *29*, 1805372; Copyright 2018).

All paste printing experiments were performed on a commercially available Ultimaker/Discov3ry Complete instrument (see *Experimental section* for experimental details and sliced 3D models of printed objects). Initial experiments were performed with transparent silicone as prominent example for a paste-like filler material.[510,511] Elastomeric silicone, used for joint sealings, exhibits a high viscosity ideal for paste printing and is comparable with high polymer content solutions. It cures under air without significant change in volume. The silicone was directly filled into the syringe and printed on a fixed sheet of wax paper with a 0.84 mm printing tip (Figure 7.10, a). First experiments tested the precision of the technique by printing of complex monolayered structures (Figure 7.10, b) and critical parameters could be identified: (1) an equal flow of the extruded material is of crucial importance and should be ensured before every print (delay between extrusion pump movement and material flow); and (2) major tip movements in X/Y-direction (print bed dimensions) during printing can cause material carryovers, avoidable by a short intermediate movement in Z-direction (so-called 'Z hop'). Surprisingly, the instrument's precision in paste printing detailed structures was on a comparable level to standard filament printing with Ultimaker devices.

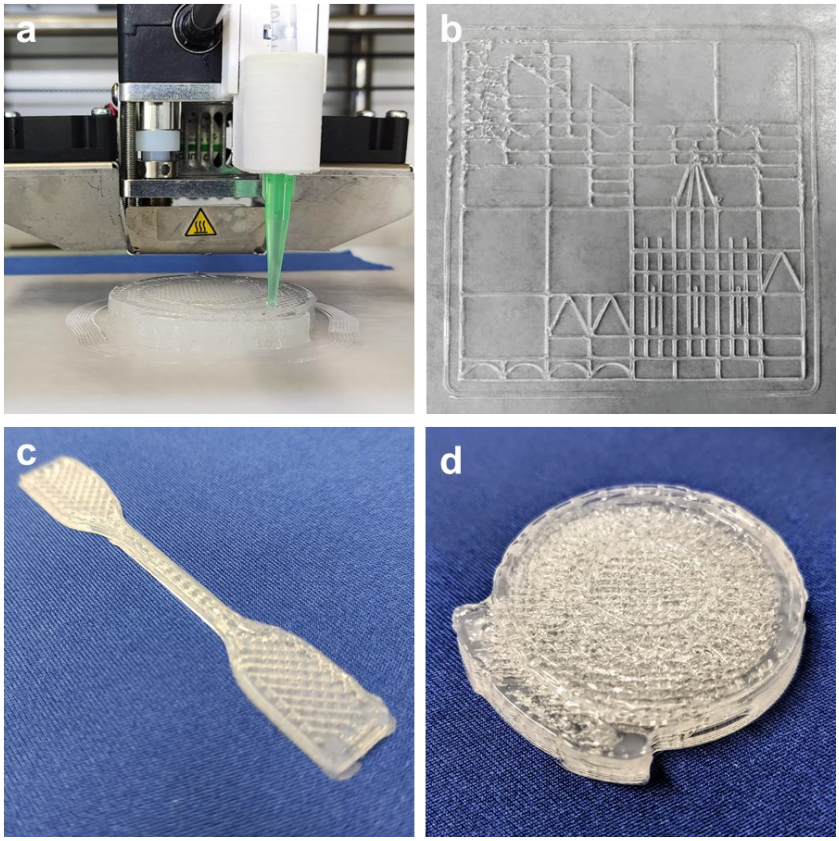

Figure 7.10. Silicone 3D paste printing. a) 3D printing process of d) on wax paper. b) Monolayer print of the University of Konstanz Signet[512] on wax paper (size: 10 x 10 cm). c) 3D print of a multilayer dogbone tensile test specimen (ISO 527-2, height: 2 mm), after curing. d) Model of a "StarWars© HoloCom"[513] as an exemplary more complex structure (size: 4.5 cm x 5 cm x 0.9 cm), after curing.

For multi-layered structures, an ideal height of 0.5-0.6 mm for the first layer was identified to ensure both, a sufficient cohesion between printed parts and stability to support the following layers without undergoing deformation. The implemented air fan was further used to accelerate curing of printed parts and increase their stability. First, tensile test specimens in dogbone shape of 2 mm height were printed (Figure 7.10, c). Tensile test experiments after curing overnight revealed a good cohesion of individual printed strands under the employed parameters (see *Appendix* for tensile test curves). The technique also allowed to print objects of ~ 1 cm height with convexities and overhangs in walls, detailed surfaces and different body shapes, without any visible deformations of lower parts during the printing process (Figure 7.10, d; see *Experimental section* for comparison with sliced 3D models).

UHMWPE nanocrystal pastes were produced by slow water removal (rotary evaporator) from dialyzed dispersions. A remarkable increase in viscosity beginning with solids content of > 18 wt-% without any further modifications was observed. A general viscosity increase for higher solids content is known for polymer dispersions[514,515], but was rather surprising for the

UHMWPE nanocrystals employed here, concerning their relatively low particle concentrations. Above 23 wt-% PE content, a plastic and paste-like material was obtained (Figure 7.2, right), that became less viscous again above a temperature of 60 °C and then allowed for simple transferring into other vessels. Adding water recovered the original dispersion, that could be fully reversible converted back to a paste by removal of water (rotary evaporator) without any visible changes in quality.

Initial printing experiments with UHMWPE pastes were performed with a 20 wt-% PE content paste of lower viscosity to investigate potential critical points, like cohesion between printed parts, flow behavior on different substrates and shrinking upon water evaporation after printing. Monolayer printing on wax paper revealed a rather unfavorable wetting behavior on hydrophobized surfaces (droplet formation). Nevertheless, the wax paper with the printed object was placed in a dry cabinet at 75 °C for several hours to remove water and a dogbone-shaped object could be obtained. Clear shrinking effects of the printed material due to water removal were visible, but were restricted to the object's thickness, while the lateral extensions (X/Y-dimension) remained almost unaffected.

Printing directly on the printer's glass bed showed satisfying form stability and wetting. Due to the relatively low viscosity, printed strands immediately fused together to a closed surface favorable for a print with 100 % infill, but less suited for a multi-layer print that requires high stability of the initial layers. Furthermore, shrinking effects during water removal may be even more critical for an object composed of several layers. Therefore, a layer-by-layer approach was developed. After the first layer was printed on the glass surface, the bed temperature was increased to 90 °C for several minutes to remove water, and a closed dogbone-shaped UHWMPE layer was obtained (Figure 7.11, left). The next layer was then directly printed on the existing one (without skirt) and the water again removed by heating. This deposition process was repeated several times to build up the dogbone's thickness (Figure 7.11, center). The whole glass plate with the printed objected was then put into a dry cabinet for several hours (at 115 °C) to remove traces of remaining water and force diffusion of polymer chains between different nanocrystals to increase the mechanical stability and repair small cracks emerged during the printing/drying process. The specimen could easily be removed from the glass plate and showed hard and brittle mechanical character and a closed packing with, however, a slightly unequal thickness/surface. The experiment demonstrated the possibility of a layer-by-layer deposition approach with intermediate drying steps, but an enhanced printing precision is expected when dispersions of higher viscosity are employed.

Figure 7.11. 3D UHMWPE nanocrystal paste printing following a layer-by-layer approach. The first layer was printed directly on the printer's glass bed and subsequently heated to 90 °C to evaporate water (*left*). Several layers were added (without skirt) and the water removed after every layer (center, 5 layers). The glass bed including the specimen was heated in a dry cabinet to 115 °C for several hours to remove traces of water, repair structure breakages and detach the specimen (*right*).

The viscosity and flow behavior regarding the form stability of printed strands could easily be enhanced by further increasing the dispersion's PE content. However, this does not address the effect of excessive and irregular shrinking upon water removal. By contrast, adding special thickening agents might ensure both, a satisfying paste printing behavior and form stability upon water removal. Fumed (pyrogenic) silicas are known thickeners, that provide several advantages: the rheological properties of liquids can be precisely modified, and the viscosity drastically increased with only low quantities added.[516] This can be attributed to the reversible formation of a three-dimensional network of silica agglomerates, that fixes the surrounding liquid in its pores. Fumed silicas are used as thickeners, reinforcing fillers, dispersants and in many 3D printing applications (commercialized as Aerosil® by Evonik).[517,518] By modification of the surface silanol groups, they can be used in hydrophobic or hydrophilic environments.

UHMWPE dispersions were mixed with hydrophilic fumed silica (Aerosil® 200). This choice is based on the fact that although the hydrophilic silica surface is incompatible with the hydrophobic UHMWPE nanocrystals, the silica material has to be equally distributed in the aqueous system to ensure regular formation of the desired 3D silica network. Initial experiments, where fumed silica powder was added to a non-dialyzed UHMWPE dispersion under stirring showed promising results: the powder dissolved completely with a tremendous increase in viscosity, while the colloidal stability of the nanocrystals was not affected. A dialyzed UHMWPE dispersion (15 wt-% PE) was mixed with fumed silica (vortex mixer) up to a total silica content of 7.5 wt-%, where the dispersion was fully converted into a pasty state. The paste could be filled into a syringe and 3D printed under previously identified conditions. However, quickly afterwards the paste started to destabilize indicated by formation of a clear aqueous phase in

the upper syringe part (and release of water from the printed parts). To enhance the paste's stability, a new batch of paste was heated in a sealed vessel to 140 °C for 10 minutes to enable polymer chain diffusion through the silica 3D network and increase homogeneity on the nanoscale. Initial extrusion experiments through a common syringe did not show any phase separation process. Heating the paste to 140 °C for 15 minutes showed a satisfying form stability upon water removal, desired for multi-layer printing approaches.

In summary, UHMWPE dispersions could be fully converted to pasty materials and their 3D paste printing was demonstrated. Experiments with silicone revealed the versatile and precise character of this technique. UHMWPE pastes were obtained by simple removal of water from dialyzed dispersions and could subsequently be paste printed directly on glass surfaces in a layer-by-layer deposition method. In a second approach, fumed silica thickeners were added to UHMWPE dispersions to significantly increase their viscosity and, simultaneously, enhance the form stability upon water removal by heat.

Future studies will focus on printing these new pastes employing the identified optimized parameters from experiments conducted to date. Likewise, further printing of pastes composed of polyethylene and water exclusively and with enhanced solids content will be tested (and their shrinking behavior evaluated). The generated printings will then be analyzed in terms of their internal structure and mechanical properties. In particular, questions regarding the fate of nanocrystals during processing will be addressed. While paste printing at room temperature should not influence their integrity, effects of water evaporation or heating may alter their structure, respectively, abolish their isolated character towards soft particle assemblies and ensembles inside the generated solid. By reducing the print tip diameter significantly, particles might be oriented directly during the extrusion process and deposited in an ordered way. Modification of infill properties (infill line directions, infill degree, etc.) and layer thicknesses may additionally influence the emerging mechanical properties in a positive way.

7.3 Conclusion

Particle-based materials, constructed by arranging anisotropic shape nanoparticles, hold potential to exhibit yet unmet properties. Uniform shape and size UHMWPE particle dispersions provide the material in the unusual morphology of disentangled polymer single chain nanocrystals. The dispersions can be further converted to pastes and powders, enabling a broad range of applicable processing techniques, like 3D (paste) printing or fiber spinning.

Direct printing of polyethylene powders in 3D pellet printing techniques can circumvent prior processing to filaments and increase versatility in manufacturing of new types of objects. This needs not proceed at an expense of quality, as the printed objects compare well to known reports of polyethylene filament printing. The disentangled UHMWPE could be extruded and shows a promising melt behavior, but further modifications addressing its printability are necessary. In an alternative approach, where the dispersion can be directly used with the anisotropic nanocrystals remaining intact, well-defined UHMWPE fibers are generated by 'dispersion fiber spinning'. Here, the dispersion is spun in a coagulation bath and the polymer solidified to a fiber with the other compounds remaining dissolved. The fibers' mechanical strength can be significantly enhanced by heat post-processing, or binary material mixtures spun to e.g. fluorescent UHMWPE fibers. To combine the advantages of having the material in a highly dispersed anisotropic morphology with the strengths of 3D printing, UHWMPE dispersions were thickened and tested in paste printing. Printable pastes were obtained by simple removal of water from dialyzed dispersions or by addition of fumed silica fillers. Initial printings with silicone showed the precise and versatile character of paste printing techniques. The acquired routines could be directly used for UHMWPE pastes in an enhanced layer-by-layer deposition approach.

This study suggests the direct application of synthesized UHMWPE dispersions in a variety of possibilities, that hold potential to facilitate totally different UHWMPE processing methods. While solid-based techniques focus primarily on the disentangled nature of uniform length polymer chains, dispersion- and paste-based approaches focus on fabrication of uniform size and shape nanocrystals. However, further modifications and advancements are necessary to achieve full transfer of the nanocrystals' unique properties into materials and artifacts.

7.4 Experimental section

7.4.1 Materials and general considerations

Uniform shape UHMWPE single-chain nanocrystals were obtained by aqueous catalytic polymerization at 10 °C reaction temperature and > 4 hours reaction time with catalyst **1^{I}-C_6F_{13}/PEG** as outlined in *chapters 3 and 6*. Commercially available silicone rubber sealant from *DAP* (Product Code: 00683) was used for all silicone paste printing experiments. A sample of *Aerosil® 200* (*Evonik*)[519] for dispersion thickening experiments was kindly provided from *CSC JÄKLECHEMIE GmbH & Co. KG*. Polyethylene (HDPE) pellets with a melt index of 2.2 g/10 min (190 °C, 2.16 kg) and a softening point of 123 °C (Vicat, ASTM D 1525) were purchased from *sigma-aldrich*.

Dialysis was performed versus demineralized water using *Spectra/Por* dialysis membranes (type 2, MWCO 12 – 14 kD) with a large tubing width of 45 mm, until the dialysate remained surfactant free. A single batch of ~300 mL dispersion was filled into ~600 mL of tubing, sealed and slowly stirred in ~20 L water. The dialysate was renewed three times per day (for ~ 4-5 days), while a constant increase in dispersion volume due to diffusion of water into the tube was observed. GPC was measured on a *Polymer Char GPC-IR* instrument in 1,2-dichlorobenzene at 160 °C (0.5 mL/min flow rate, 3 x 30 cm *PLgel Olexis* columns), equipped with IR detectors and viscometer. Universal Calibration versus narrow polystyrene standards (*PSS*) was used for molecular weight determination. Tensile properties were analyzed on a *Zwick-Roell Zwick 1446 Retroline tC II* instrument after preconditioning of samples overnight. A crosshead speed of 0.5 mm/s was used for determination of Young's modulus and 5 mm/min for determination of all other parameters. Data evaluation was performed using the *textXpert* software (by *Zwick-Roell*). DSC experiments were performed on a *Netzsch DSC 204 F1* instrument (software: *Netzsch Proteus Thermal Analysis*, version 6.1.0) with a heating/cooling rate of 10 K/min or 1 K/min for entanglement experiments. Light microscopy was carried out on a *LEICA DM 4000 M* microscope. Transmission electron microscopy (TEM) images were recorded on a *Zeiss Libra 120 EF-TEM* instrument equipped with a CCD camera system by *TRS Tröndle*. Scanning electron microscopy (SEM) was performed on a *Zeiss Auriga FIB-FESEM* instrument.

7.4.2 3D pellet printing

3D pellet printing experiments were performed on a commercially available 3D printer machine running a customized *Marlin*[520] firmware equipped with a *Direct3D Pellet Extruder* (by *Direct3D di Elisa Legnani*, Figure 7.12). Nozzle sizes between 0.4 and 2.5 mm were available allowing an overall throughput of 30 – 250 g/h. The machine was connected via USB/Bluetooth to an *OctoPrint*[521] instance (*OctoPi*[522]), that allowed full network-based remote control (including g-code upload) over the printer's actions and monitored all relevant parameters. Machine firmware parameters (e.g. PID tuning) were edited using the *EEPROM Marlin Editor* plugin[523] for *OctoPrint*. Slicing (conversion of 3D body objects into printed layers and concrete print sequences interpretable by the printer machine) was performed using *PrusaSlicer/Slic3r*[524-526] or *Simplify3D*. 3D object files of calibration test parts (pyramid) were taken from *Thingiverse.com* (CC BY license).[527] Parameters elaborated for slicing routines for HDPE pellet printing of different objects are summarized in Table 7.1.

Before the print job was started, the respective material was carefully filled into the funnel and re-filled if the filling level was less than one third of the total funnel height. Please note, that a sufficient filling level is essential to guarantee a uniform extrusion process. The print process was initiated by loading the g-code file, the heaters automatically activated, and the extrusion started after the measured temperatures remained stable. After the printing had finished, the heaters automatically turned off (not if UHMWPE was used!) and the object was left on the build plate until it had cooled down to below 50 °C.

During printing experiments with precipitated, disentangled UHMWPE (M_n = 3400 x 10^6 g/mol; M_w/M_n = 1.3), the hot end was left on a standby temperature of > 160 °C after a print job had finished. Before switching off the machine, the UHMWPE was fully removed from the funnel, HDPE granulates were added and the extruder was freed from remaining UHMWPE by extrusion for at least 15 minutes.

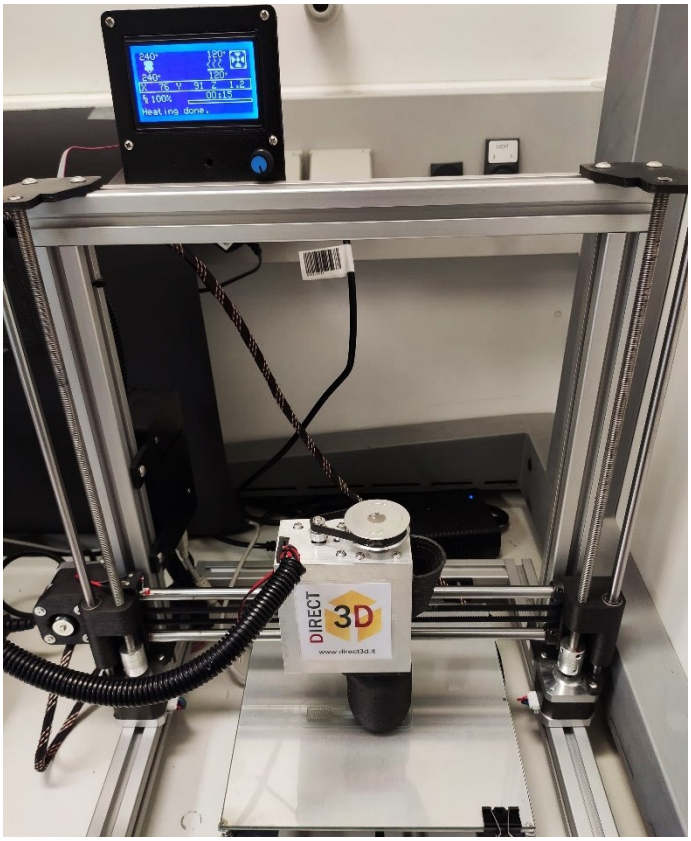

Figure 7.12. Image of the entire Direct3D Pellet Extruder printing machine showing the display with control head (top), printer head and glass build plate with inbuilt heaters.

Table 7.1. Parameters used for 3D pellet printing of HDPE.

Object	**Dogbone**	**Pyramid**
Nozzle	0.8 mm	
Nozzle temperature	240 °C	
Build plate temperature	120 °C	
Layer thickness	0.5 mm	0.4 mm
Extrusion width	0.9 mm	
Filling degree	100 %	20 %
Filling pattern	rectilinear (0° / 90°)	grid & rectilinear (45°)
Solid layers	top: 3, bottom: 3	
Material flow*	filament diameter: 1.75 mm extrusion factor: 30	
Printing speed*	15 mm/s (external perimeters: 50 %)	
Retraction	2 mm Z-lift: 0.4 mm speed: 20 mm/s	
Skirt	1 loop, 6 mm distance, 1 layer	

*Please note, that these parameters are designed for filament printers and cannot be interpreted as absolute values.

7.4.3 Dispersion fiber spinning

Dispersion fiber spinning experiments were performed with a non-dialyzed UHMWPE dispersion, obtained by aqueous catalytic polymerization (PE content: 7 wt-%; M_n = 3204 x 10^6 g/mol; M_w/M_n = 1.19). The dispersion was filled into a 5 mL syringe (*Braun Omnifix®* with *Luer-Lok®* system; *Braun Sterican®* green canula, 0.8 mm x 120 mm) and mounted into a syringe pump (*Harvard PHD 2000* or *Thermo Orion M362*). The coagulation bath (measuring cylinder or column) was filled with agent (e.g. ethanol) and the kinked syringe needle dipped ~ 1 cm into the solution (Figure 7.13, left). The spinning process was initiated by operating the syringe pump with a flow of 1 mL/min (10 mL/min until remaining air was removed from the system). Over time, the coagulation bath slowly filled with fibers formed, with single fiber strands staying intact and clearly distinguishable (Figure 7.13, center). Note, that at least 15 cm distance between needle outlet and already deposited fibers is recommended, to ensure complete solidification. After the spinning process had finished, the needle was removed from the coagulation bath and the agent slowly drained with the formed fibers remaining at the glass wall surface. Alternatively, a column with an outlet tap was used as coagulation bath to allow for gentle agent removal (Figure 7.14, right). Drying was performed at room temperature for at least 24 hours or in a dry cabinet, depending on the coagulation agent's boiling point.

Fluorescent fibers were obtained by mixing 5 mL UHMWPE dispersion with 0.5 mL fluorescent polymer particle dispersion (kindly provided by Annika Sickinger).[434] The obtained blend was then spun at room temperature in ethanol, as described above (Figure 7.13, right).

Spinning experiments for fiber post-processing with heat were performed in a column with a flask connected to the bottom outlet and the entire apparatus filled with *n*-propanol (Figure 7.14, left). After the process had finished, the apparatus was slowly emptied to a liquid level that allowed dismantling the column part, but still high enough to fully cover the spun fibers (Figure 7.8, a). The flask was then placed on a hotplate and the content heated to 90 °C for 6 hours. Over time a change in morphology was observed (previously adjacent situated loose fiber strands started to form 3D-networked structures). The flask content was then allowed to cool down to room temperature and the *n*-propanol slowly emptied with the fibers remaining as linked, plastic coil (Figure 7.8, b). A small part was cut off and the mechanical resistance tested by stretching using two tweezers (Figure 7.8, c). Further drying was performed at 60 °C and a doughy fiber nest obtained.

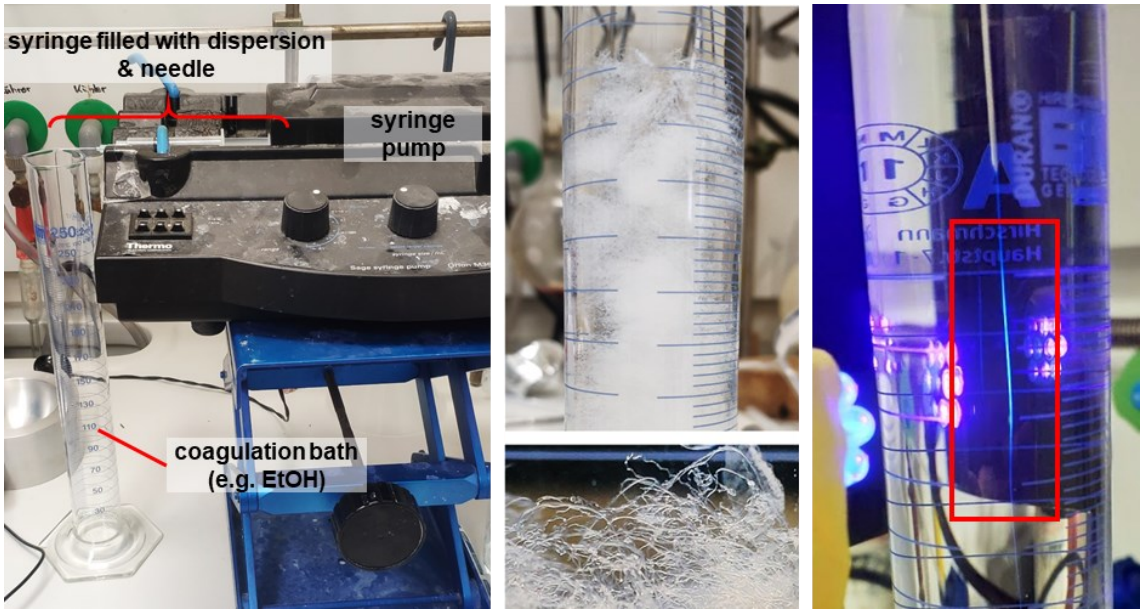

Figure 7.13. *Left:* Setup used to add UHMWPE dispersions through a needle into a coagulation bath leading to fiber formation. *Center:* Coagulation bath filled with fibers (distinct fibers visible). *Right:* Fluorescent fiber directly formed after spinning (UHMWPE dispersion mixed with fluorescent polyfluorene nanoparticles, UV light exposure).

Figure 7.14. Setup modifications to gently collect the spun fibers. *Left:* Flask connected to a column and filled with coagulation agent to allow for post-processing of fibers in solution. *Right:* Column with tap connected to the bottom outlet. The coagulation agent could be gently released to prevent breakages of fibers in their sensitive wet state.

Experiments with inverted spinning direction were performed in ethylene glycol with a syringe pump flow rate of 1 mL/min. The bottom tap outlet of a glass column was sealed with a septum and punctured with the syringe needle, that the needle outlet was situated beyond the stopcock (Figure 7.15). After the spinning had finished, the upward moved fibers were collected at the liquids surface and dried in an evacuated dry cabinet for several hours.

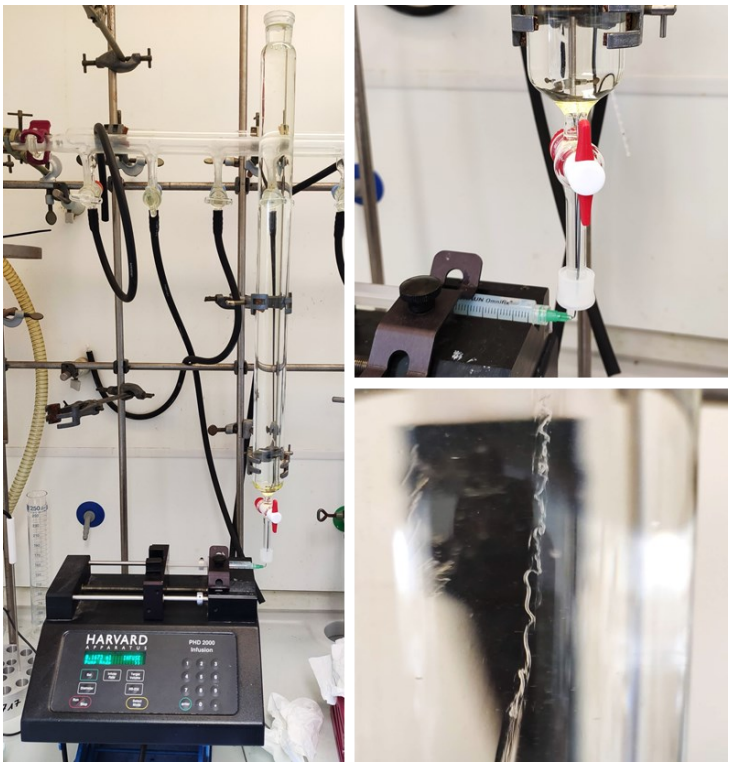

Figure 7.15. Setup to extrude dispersion and form fibers in upward direction (in ethylene glycol at room temperature).

Experiments conducted in a heated coagulation bath were performed using a glass column equipped with a heating and cooling jacket, connected to a thermostat (Figure 7.16). The spinning was performed in ethylene glycol as described above. The temperature probe of the thermostat was dipped into the coagulation bath and the liquid heated to 80 °C before the syringe pump was operated. Due to back-diffusion of coagulation agent into the needle, an increased flow rate of 3 mL/min was necessary to prevent clogging. After the spinning had finished, the formed coagulated fibers were collected at the liquids surface using a spatula.

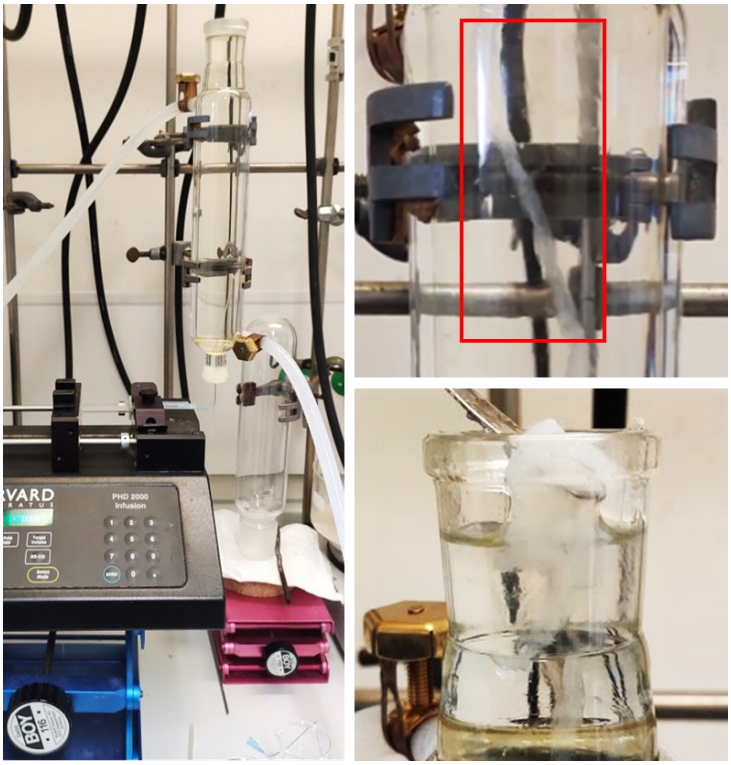

Figure 7.16. Setup for dispersion fiber spinning in ethylene glycol at 80 °C. A column equipped with a heating and cooling jacket was used to heat the coagulation bath. The created fibers could be directly harvested at the liquids surface.

7.4.4 3D paste printing

3D paste printing was performed with an *Ultimaker 2+* (*Ultimaker BV*) 3D printer, equipped with an additional extrusion head connected to a *Discov3ry* syringe extrusion pump (*Structur3D Printing*; Figure 7.17). The printer was connected via USB to an *OctoPrint*[521] instance, that allowed full network-based remote control (including g-code upload) over the printer's actions and monitored all relevant parameters. Initial g-codes to force absolute positioning (G90, M82), and to allow cold extrusion (M302) were automatically added to the start section of every g-code file. Slicing (conversion of 3D body objects into printed layers and concrete print sequences interpretable by the printer machine) was performed using *Cura 4.5* (*Ultimaker*) software with the pre-installed parameters for the employed paste printer device (Figure 7.18). The material profile for silicone and the connected 0.84 mm printing tip were used for all printing experiments. Printings were done in coarse grade (0.4 mm layer height) on a fixed sheet of wax paper (unless otherwise noted) at room temperature (unless otherwise noted). 3D object files were taken from Thingiverse.com (CC BY license).[513] The *University of Konstanz* signet was taken

from the university's website[512] and converted to a 3D object (addition of Z dimension) using *Tinkercad*.[528]

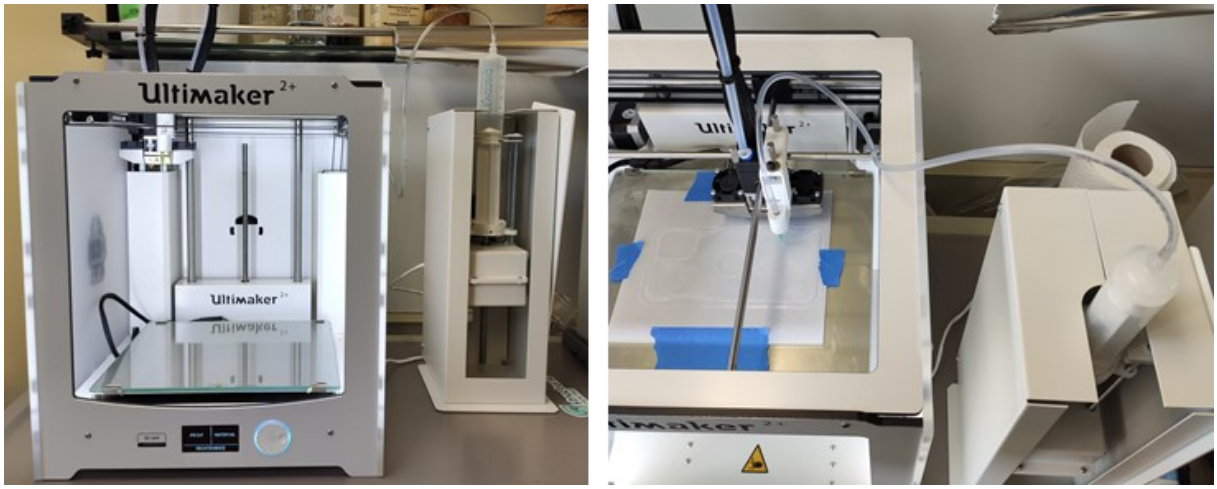

Figure 7.17. *Left:* 3D paste printer Ultimaker 2+ (Ultimaker BV) connected to a Discov3ry syringe extrusion pump (Structur3D Printing). *Right:* Top view during paste printing.

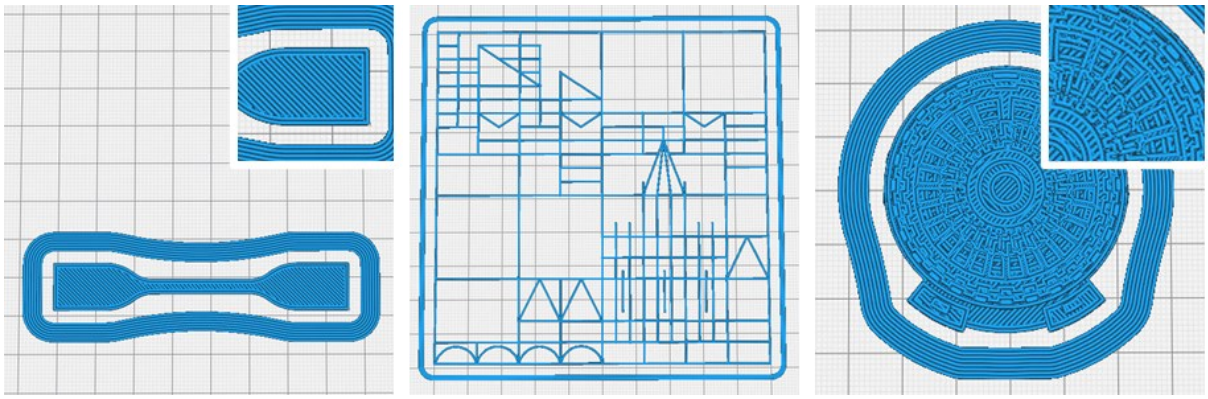

Figure 7.18. Sliced 3D printing models (including skirt) generated by processing of 3D objects with pre-installed profiles for paste printing (software: Cura 4.5 by Ultimaker).

Silicone printing

For silicone paste printing, the material was directly filled into the syringe and mounted into the extrusion pump. The tip was connected to the printer head and a standard PVC tubing was used for connection to the syringe (*Luer-Lok*® connectors). Before printing, the extrusion pump was manually activated stepwise to fill the tubing and tip with material until everything remained bubble-free. A sheet of wax paper was fixed on the glass bed with duct tape. Note, that the object position needs to be adjusted in *Cura* software to ensure entire printing (including skirt) on the wax paper's surface. The distance between wax paper and the tip in zero position was set to a thickness of a standard sheet of paper. A skirt print of minimum 1500 mm length (4-5 loops) was added to the start section of every printing job to ensure a constant material

extrusion during object printing. The job was initiated by loading the respective g-code file in the *OctoPrint* interface. After the machine had finished, the wax paper including the printed object was carefully removed from the glass bed and left at room temperature for curing overnight.

UHMWPE paste printing

A standard aqueous UHMWPE dispersion (PE content: 7.4 wt-%; M_n = 3044 x 10^6 g/mol; M_w/M_n = 1.2; ~ 300 mL volume) was dialyzed versus demineralized water (*vide supra*). The dispersion was then poured into a 1L-flask and water was carefully removed using a rotary evaporator (40 – 70 mbar, 50 °C bath temperature) until the desired PE content was reached (e.g. 20 wt-%, monitored by the amount of water removed and determined using a *Sartorius Moisture Analyzer*). The dispersion was then heated to 60 – 70°C and filtered warm over glass wool directly into the syringe (needle outlet sealed). After allowing to cool down to room temperature, the syringe was installed into the extrusion pump and the printing was performed as outlined for silicone printing (*vide supra*). Monolayer printings on wax paper were dried at 75 °C for three hours in a dry cabinet.

For layer-by-layer deposition printing, the object height was adjusted to the first layer height to print just a monolayer. The printer's glass bed was then manually heated to 90 °C for 10-15 minutes. For printing of the following layers, the skirt was removed from the job routine, and an appropriate Z offset added to print on (but not into) existing layers. After every layer, the heating routine was repeated. After reaching the desired thickness, the glass plate including the printed objects was transferred into a dry cabinet and heated to 115 °C for 3 hours. After allowing to cool down to room temperature, the print could be easily detached from the glass plate.

UHMWPE/silica paste preparation

Fumed silica powder (*Aerosil® 200*) was added in portions to a non-dialyzed (7 wt-% PE) and dialyzed (15 wt-% PE) dispersion. Mixing of low amounts were performed in a vial using a vortex mixer, while larger amounts were mixed by hand with a spatula in a beaker of appropriate size. Please note, that the viscosity further increased (~ 10 minutes) after the addition was finished.

Homogenization experiments were performed with ~2 mL of freshly prepared UHMWPE/silica paste in an 8 mL vial. The vial was sealed properly and placed in shaker at 140 °C for 10 minutes. Afterwards, the vial was allowed to cool down to room temperature, the paste was collected and transferred into a 3 mL syringe to test its extrusion behavior.

7.4.5 Surfactant residue analysis

The amount of surfactant (and base) remaining in the solidified polyethylene (e.g. after precipitation) plays an important role concerning material properties. Hence, an analysis of surfactant residues after different steps of dispersion processing was performed, using GPC measurements with IR-detection (see also *chapter 4.4.8*). With this method, methylene units in structures of polyethylene and SDS could be precisely detected at clearly different retention times (as their molecular weights significantly differ). First, a standard UHMWPE dispersion was fully evaporated and the formed residue, containing all compounds, directly measured (Figure 7.19, a; sample was automatically filtered prior to injection to avoid column clogging by undissolved solids). The polyethylene could be clearly identified by its low elution volume and the corresponding viscosity signal (that was absent for the small molecule SDS). Please note, that not the whole amount of SDS might be soluble in the small 1,2-dichlorobenzene volume and that a quantitative information was not obtained. Measurements of SDS exclusively (b), clearly identified the peak of higher elution volume (~ 26 mL) as the surfactant's elution signal. The aforementioned dispersion was now poured into methanol, the precipitated polyethylene powder collected, not further washed with water, dried and measured (c). Surprisingly, only very small traces of surfactant could be detected indicating that the surfactant leaves the particle's surface during precipitation and that co-precipitation only plays a minor role. By contrast, analysis of evaporated and dialyzed UHMWPE dispersions (d) revealed a small amount of surfactant remaining at the particle's surface to ensure their colloidal stability. Precipitation in methanol from dialyzed dispersion again showed the surfactant to be vanished completely (e). Parallel NMR measurements of corresponding filtrates showed the surfactant to be present in the precipitation supernatant (f).

This experiments clearly showed, that the entire surfactant leaves the polymer structure upon solidification in alcohols, important for formation of well-defined materials. Subsequent washing with water can also remove traces sticking to the powders surface. Dialysis is not capable of full surfactant removal, as small amounts have to stay adsorbed at the particle's surface to ensure their colloidal stability.

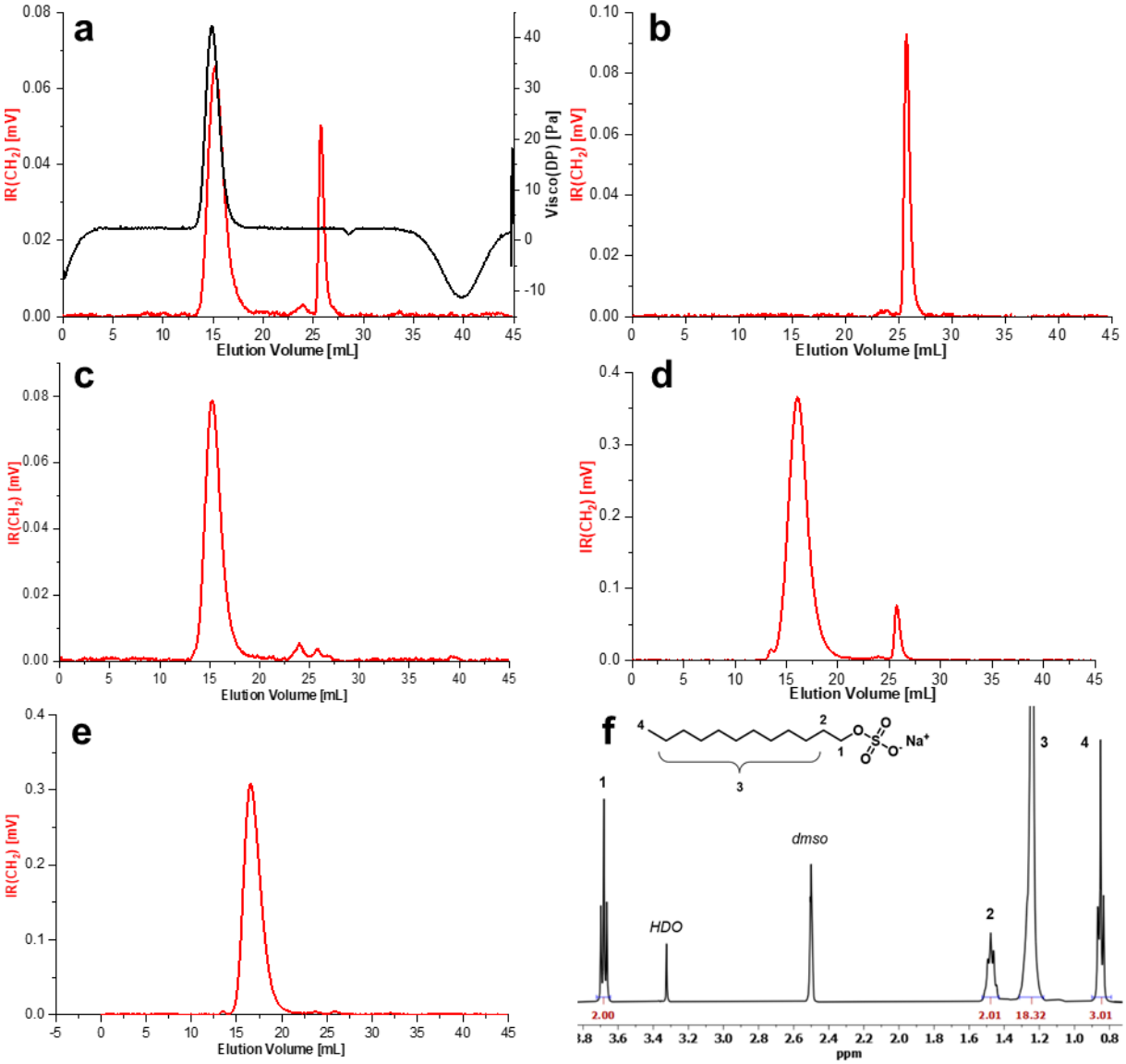

Figure 7.19. Solvent content analysis in dispersions and precipitated powders by IR-detection during GPC measurements (a-e) and NMR (f). a) PE dispersion as obtained from polymerization, red curve: IR (CH_2) signal, black curve: viscosity. b) SDS only. c) Precipitated PE from a. d) PE dispersion after dialysis. e) Precipitated PE obtained from d. f) ^{1}H-NMR (400 MHz, 300 K, dmso-d_6) of supernatant after PE precipitation showing presence of SDS.

7.5 Appendix

7.5.1 Additional images of UHMWPE fibers

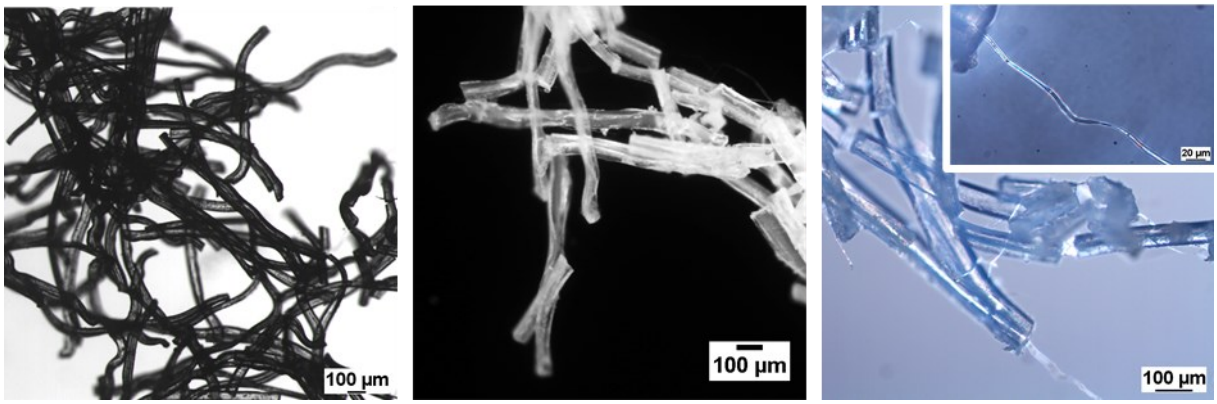

Figure 7.20. Light microscopy images of dried, coagulated UHMWPE fibers obtained by dispersion spinning in ethanol at room temperature. *Left:* Bright field mode. *Center:* Dark field mode. *Right:* Bright field mode, colored, polarized light (0 + 90°).

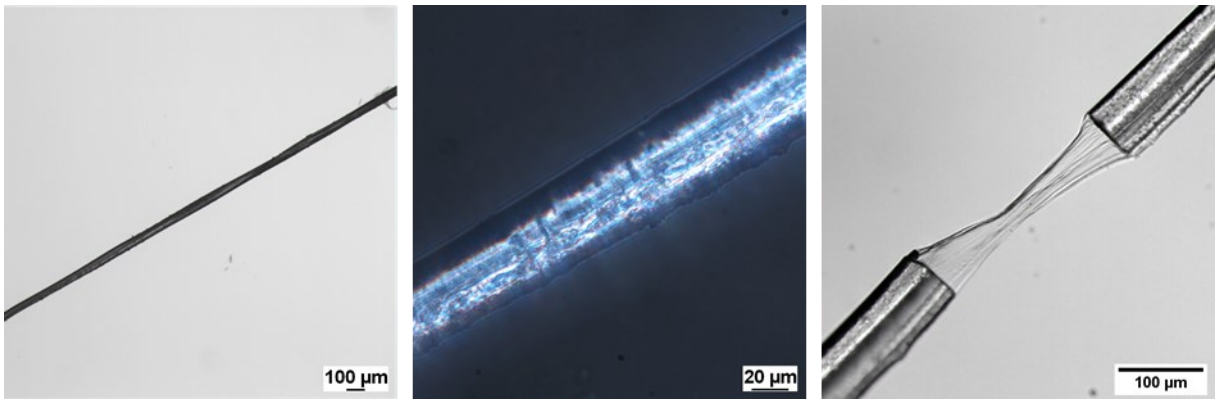

Figure 7.21. Light microscopy images of dried, isolated UHMWPE fibers obtained by dispersion spinning in ethanol at room temperature. *Left:* Illumination mode. *Center:* bright field mode, colorized, polarized light (0 + 90°). *Right:* Bright field mode, artificially created break point.

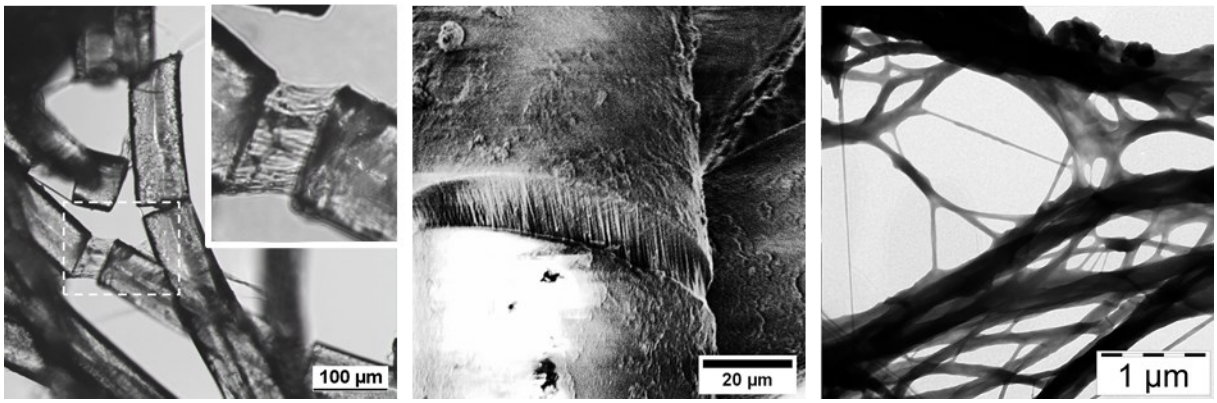

Figure 7.22. Analysis of breakage points in UHMWPE fibers formed, indicating a fibrillar substructure. *Left:* Light microscope image, bright field mode. *Center:* SEM image. *Right:* TEM image of breakage area.

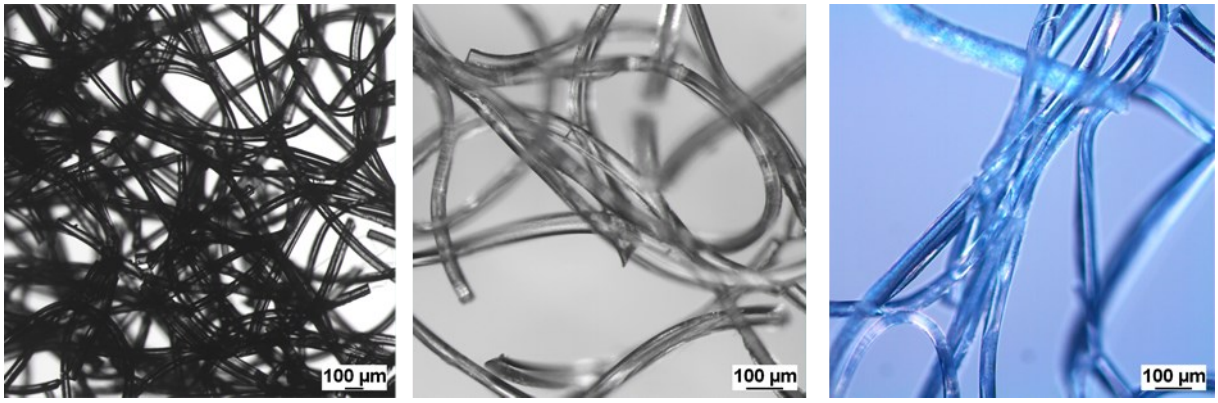

Figure 7.23. Light microscopy images of UHMWPE fibers obtained by dispersion spinning in ethanol at room temperature (after drying). The ethanol was gently released through an outlet at the column's end, leading to less fiber breakages. *Left and center:* bright field mode. *Right:* bright field mode, colorized, polarized light (0 + 90°).

7.5.2 DSC traces

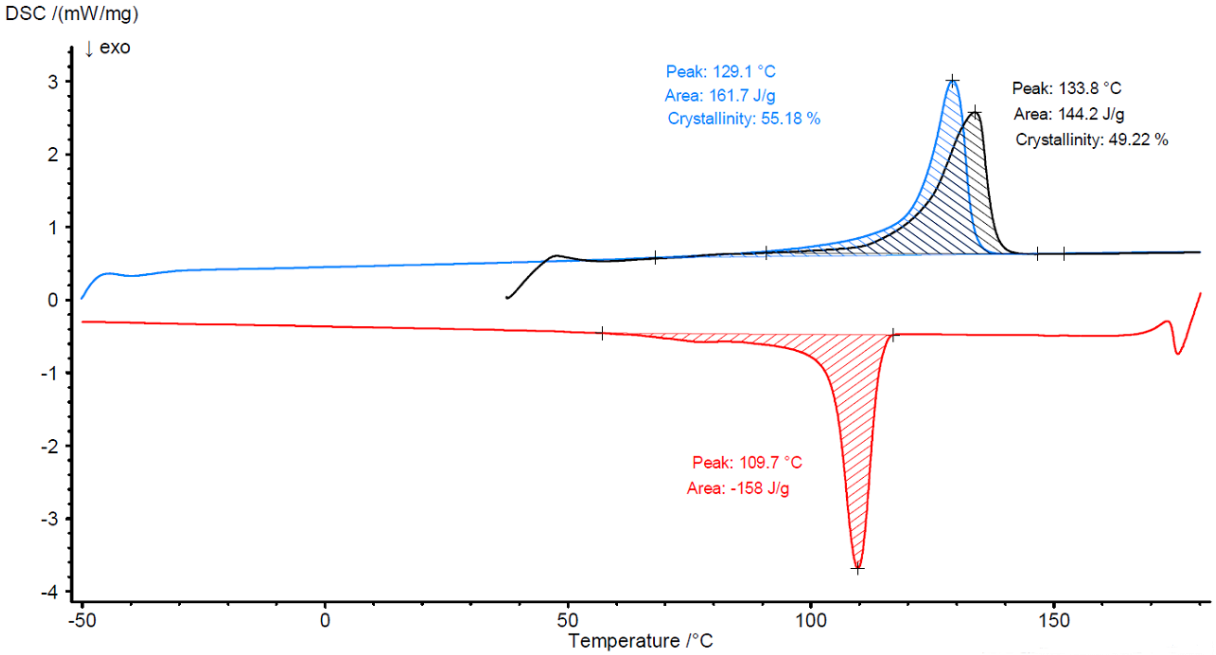

Figure 7.24. DSC traces of HDPE used for pellet printing experiments (measured with 10 K min^{-1} heating rate, black curve: 1st heating, red curve: 1st cooling, blue curve: 2nd heating).

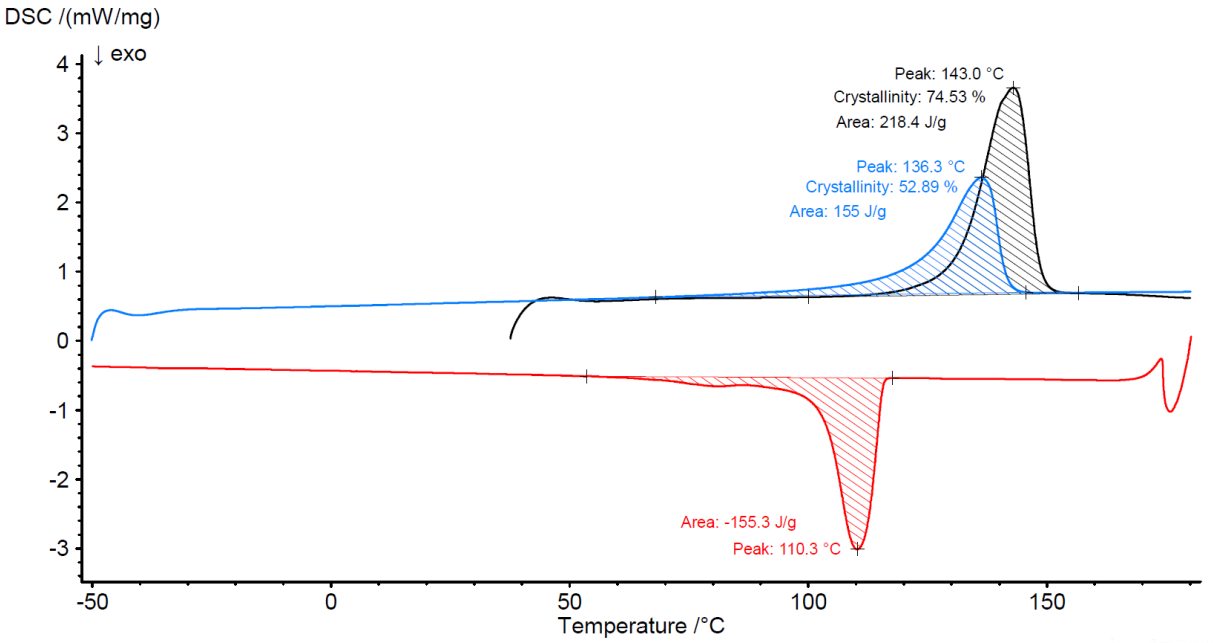

Figure 7.25. DSC traces of UHMWPE used for pellet printing experiments (measured with 10 K min^{-1} heating rate, black curve: 1st heating, red curve: 1st cooling, blue curve: 2nd heating).

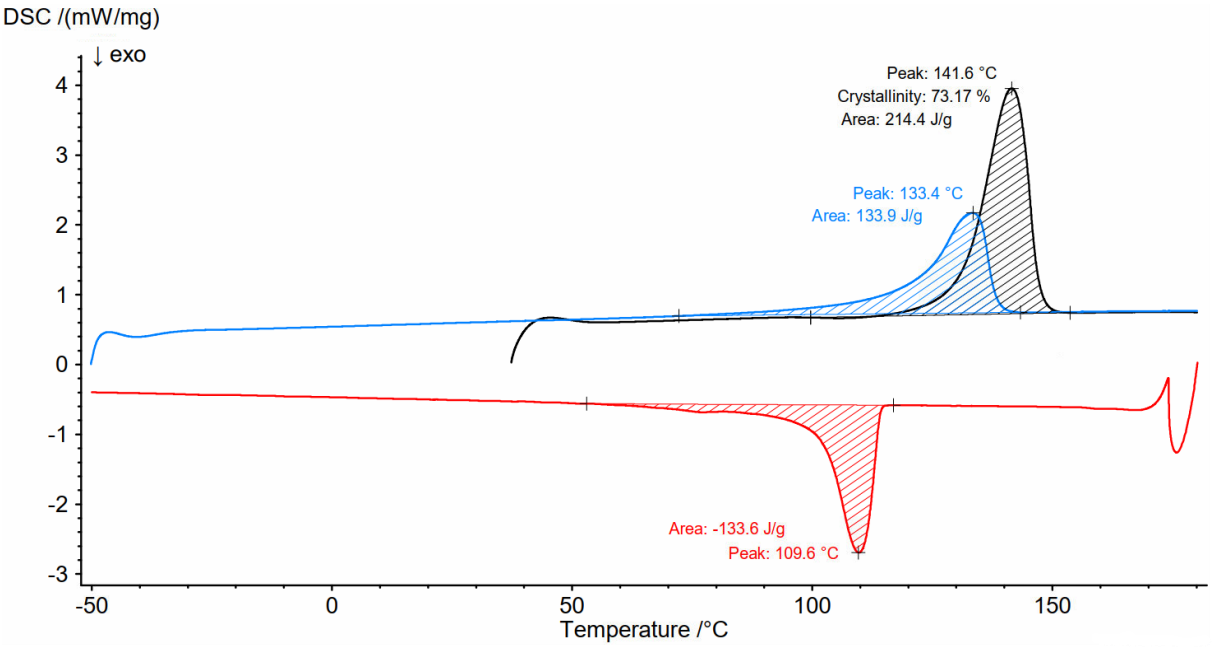

Figure 7.26. DSC traces of UHMWPE fibers made by dispersion spinning in ethanol at room temperature (measured with 10 K min^{-1} heating rate, black curve: 1st heating, red curve: 1st cooling, blue curve: 2nd heating).

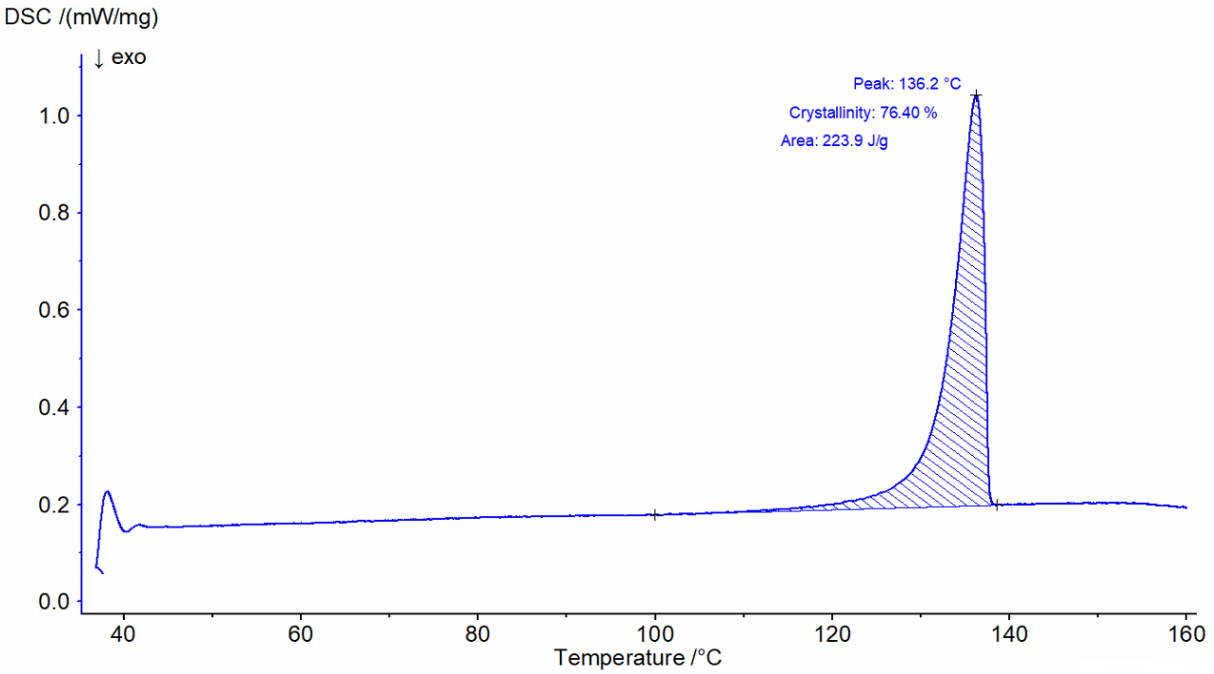

Figure 7.27. DSC traces of UHMWPE fibers made by dispersion spinning in ethanol at room temperature (measured with 1 K min^{-1} heating rate, blue curve: 1st heating).

7.5.3 GPC traces

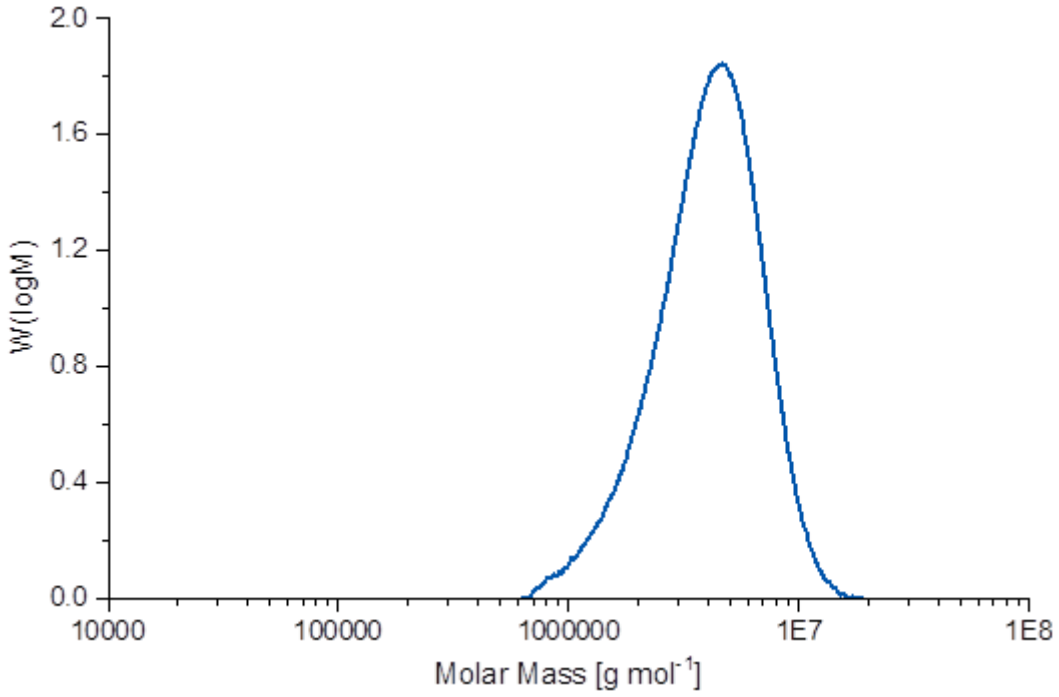

Figure 7.28. GPC trace of UHMWPE used for pellet printing experiments.
M_n = 3400000 g/mol M_w = 4510000 g/mol M_p = 4640000 g/mol M_z = 5630000 g/mol M_v = 4520000 g/mol
PDI = 1.33

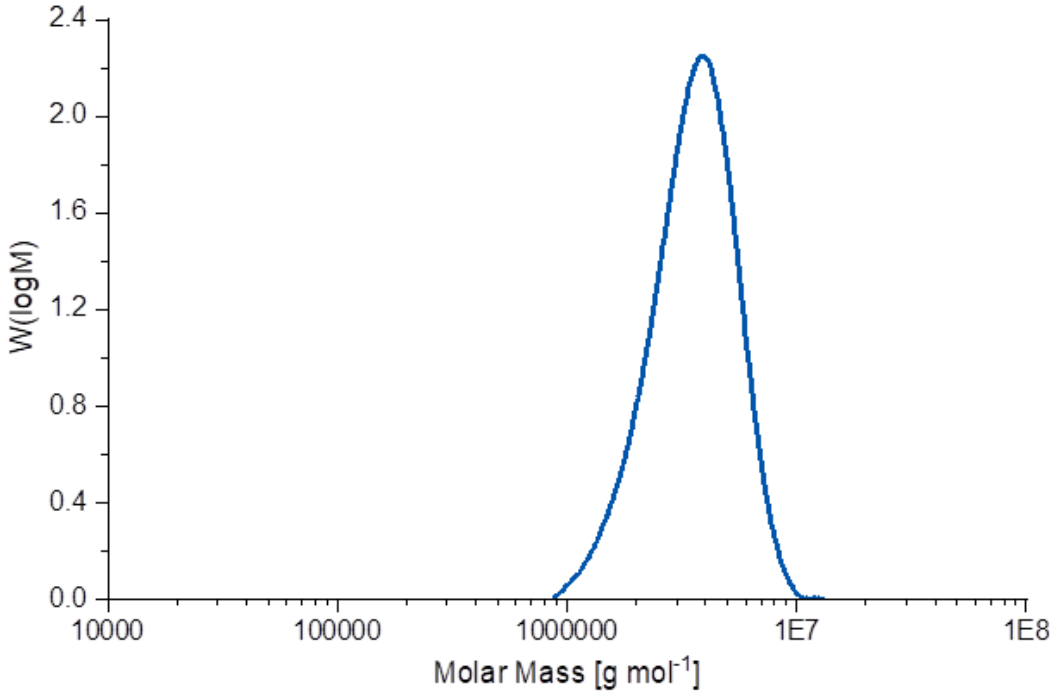

Figure 7.29. GPC trace of UHMWPE used for dispersion fiber spinning experiments.
M_n = 3200000 g/mol M_w = 3820000 g/mol M_p = 3920000 g/mol M_z = 4430000 g/mol M_v = 3920000 g/mol
PDI = 1.19

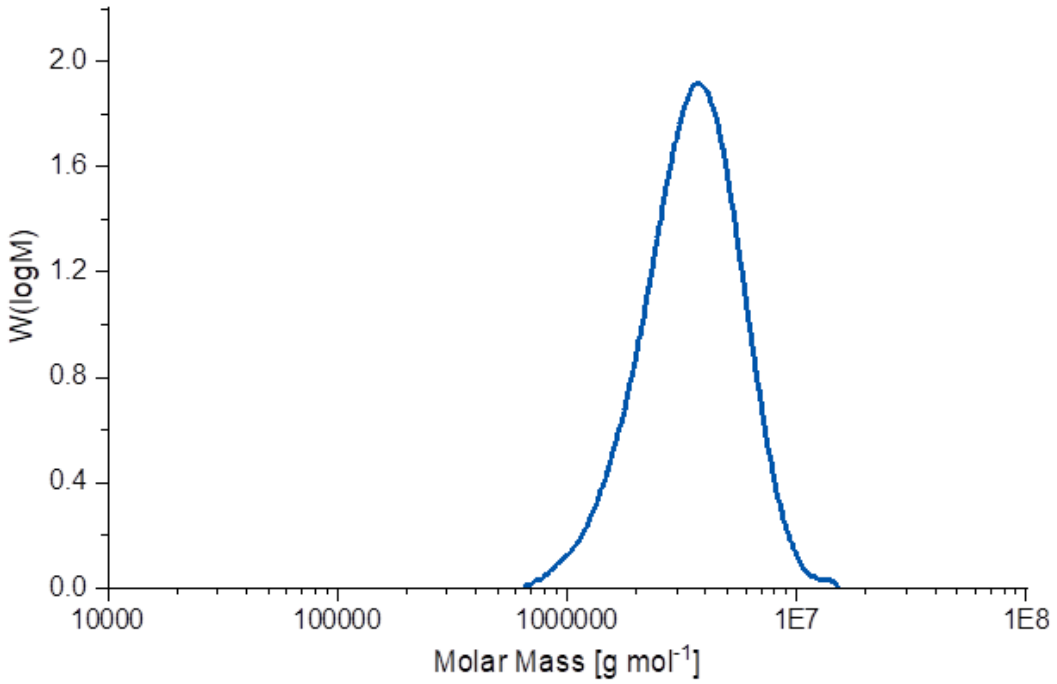

Figure 7.30. GPC trace of UHMWPE used for paste printing experiments.
M_n = 3040000 g/mol M_w = 3870000 g/mol M_p = 3720000 g/mol M_z = 4780000 g/mol M_v = 390000 g/mol
PDI = 1.27

7.5.4 Tensile tests of printed materials

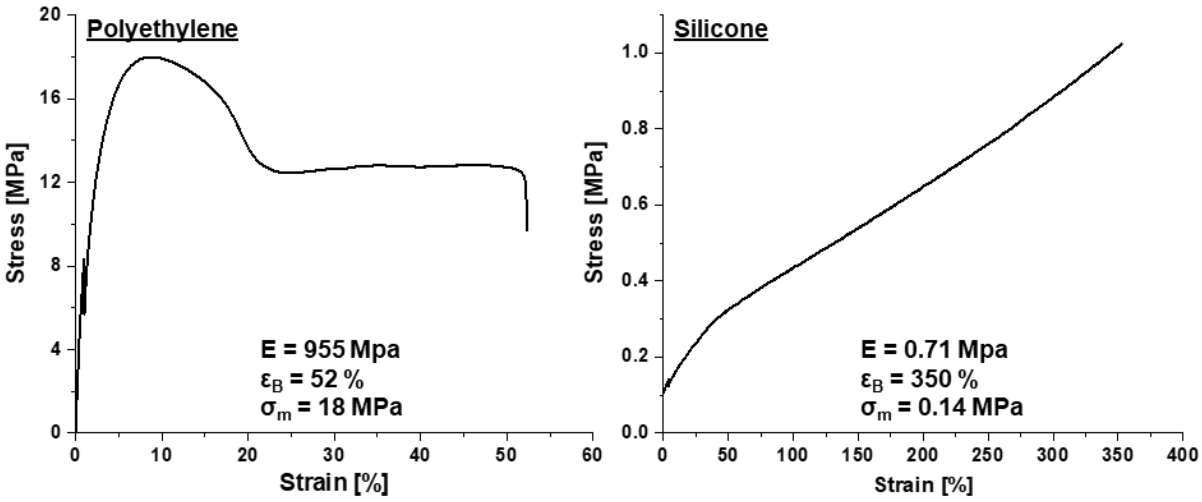

Figure 7.31. Stress-strain curves of 3D pellet printed polyethylene (*left*) and paste printed silicone (*right*) dogbone test specimens with Young's moduli (E), elongations at break (ε_B) and tensile strengths (σ_m) given.

8 General Summary and Conclusion

Catalytic olefin insertion polymerization enables precise control over the polymer chain architecture and provides access to a broad variety of different materials. Polyethylene accounts for approximately one third of the worldwide plastic demand which reflects its versatile use in many different thermoplastic components. In catalytic ethylene polymerization the chain growth process can be favored over chain transfer to an extent that very linear, ultra high molecular weight polyethylene (UHMWPE) in the regime of $M_n > 10^6$ g/mol is formed. Its properties differ substantially from otherwise identical, lower molecular weight polymer and allow for fabrication of e.g. ultrastrong fibers or artificial joint replacements. However, entanglements of the very long polymer chains complicate processing.

The field of applications of polymers is greatly enhanced by aqueous polymer latices, which are widely used in paints or adhesives and provide the material in a totally different morphology that simplifies its handling and allows for particle assembly towards materials. Hence, it would be highly desirable to generate UHMWPE dispersions directly under aqueous conditions in uniform sizes and shapes, decisive to form superstructures of well-defined properties. This would require a living chain growth and, simultaneously, a living particle growth. However, common early transition metal catalysts are highly sensitive to traces of water. This can be overcome by employing less oxophilic late transition metal catalysts.

N-terphenyl salicylaldiminato Ni(II) catalysts exhibit efficient polymer microstructure control by varying the electronic character of substituents in selected remote positions (see Figure 8.1, left). This behavior can be related to a weak interaction between the distal aryl rings

and the metal atom, that promotes decoordination of ethylene and favors β-hydride elimination (BHE). BHE is the key step in chain transfer and branch formation. Electron-donating groups promote these interactions and hyperbranched oligomers are formed. By strong contrast, linear high molecular weight polyethylene is formed when electron-withdrawing groups are present.

Water-soluble types of such catalysts can be used in aqueous surfactant solution to afford dispersions of polyethylene nanocrystals. These crystals are characterized by an extraordinary high degree of order that originates from an ordered deposition of the growing chain on the crystal growth front, directly during the polymerization process (see Figure 8.1, right). As every chain grows in its own confined space, formation of entanglements is excluded.

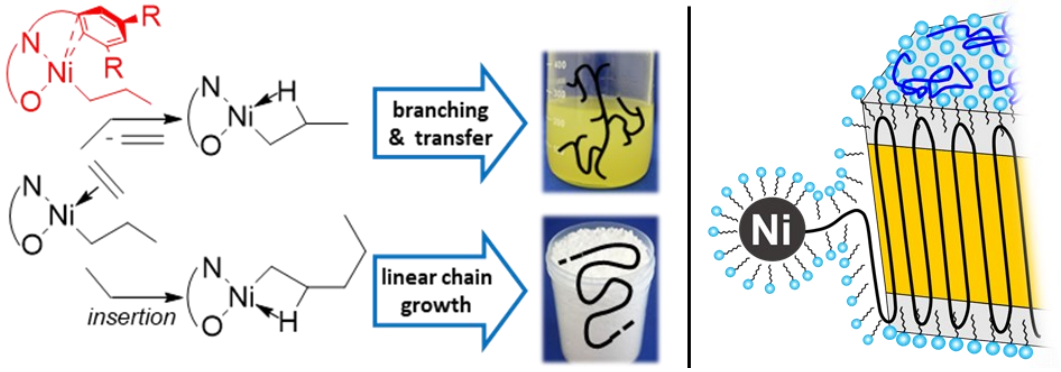

Figure 8.1. *Left:* Mechanistic rationale of the remote substituent effect in *N*-terphenyl salicylaldiminato Ni(II) catalysts. Ethylene decoordination from the active species is favored by a nickel-aryl interaction (red structure), leading to β-hydride elimination and subsequent chain transfer and branch formation. This interaction is only operative for electron-rich substituents R, e.g. R = -CH_3. *Right:* Particle growth mechanism in aqueous catalytic polymerization. The growing chain is directly folded on the crystal growth front in a highly ordered fashion, leaving no opportunity to form any disorder.

Based on insights, how the ligand environment of the active site controls chain growth and chain transfer, and how active sites are terminated by water, perfluoroalkyl-substituents of different lengths in remote positions were targeted (see Figure 8.2, left). This choice is based on the argument that perfluoro groups are highly electron-withdrawing and due to their hydrophobicity possibly hinder an access of water to the active sites. Pressure reactor studies revealed those catalysts to be highly active in formation of linear, high molecular weight polyethylene. Compared with the benchmark precursor (R = -CF_3), catalytic activities and molecular weights were substantially enhanced, while less branches were formed. This indicated a very effective suppression of BHE. Cyclic voltammetry studies revealed that indeed the electron density at the metal is lowered significantly in the perfluoroalkyl complexes, and this correlates qualitatively with the observed catalytic properties and the perfluoroalkyl-chain length (see Figure 8.2, right).

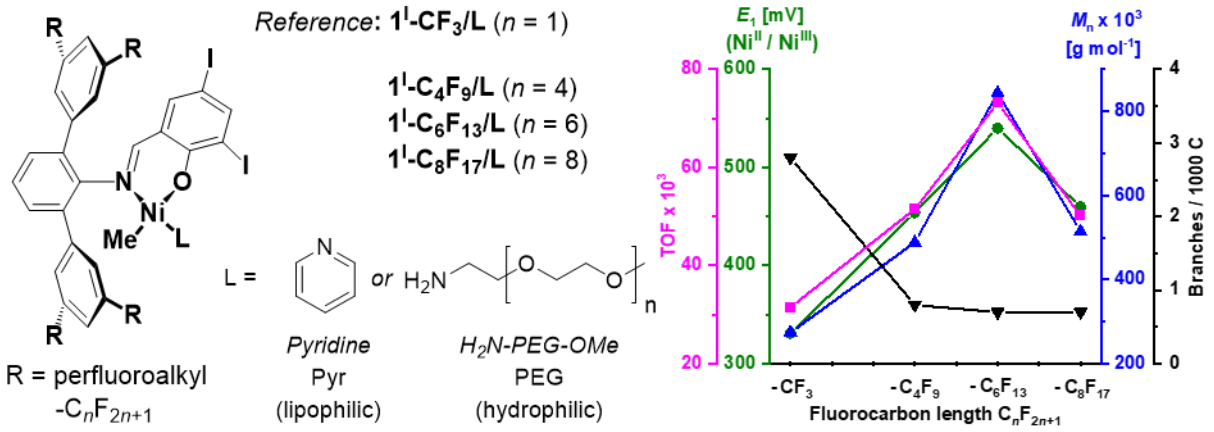

Figure 8.2. Structure of *N*-terphenyl salicylaldiminato Ni(II) catalysts with perfluoroalkyl-groups placed in remote positions -R (*left*). The length of the perfluoroalkyl-substituent significantly alters the electron density at the nickel center, that correlates qualitatively with the observed catalytic properties (*right*; results from polymerization experiments in toluene shown, data from Table 3.1).

Due to the superior performance of perfluorohexyl substituents (-C_6F_{13}), the hydrophilic catalyst **1^I-C_6F_{13}/PEG** was intensively tested for polymerization in aqueous surfactant solution. A space of various experimental parameters was optimized with regard to a uniform nature of the formed particles, molecular weight and catalyst performance (*vide infra*). Under the identified reaction conditions, catalytic activity was retained for > 4 h. Remarkably, this aqueous catalytic polymerization is truly living in nature (see Figure 8.3, left). As a given nickel center grows a single chain over the entire reaction time, linear narrow distributed UHMWPE of $M_n > 10^6$ g mol^{-1} can be produced. DSC studies of isolated polymers indicated a non-entangled nature of the formed UHMWPE. TEM revealed that the particle shape evolves from hexagonal platelets through truncated lozenges to lozenges, and showed a uniform shape and size-distribution and a non-aggregated nature in all cases (see Figure 8.3, right). A comparison of the average mass of a particle with the molecular weight of the formed polymer showed the particles to be composed of a single chain. As one particle is grown by one active site, the final particle size and morphology are determined by the time available for growth, given by the duration of the polymerization experiment. The narrow molecular weight distribution, obtained in living polymerization, is directly reflected in the narrow particle size dispersity. Concerning the potential of these particles for assembly, samples were dried without any additional manipulations and the formation of monolayers with a preferred orientation of adjacent particles was observed (Figure 8.5, a).

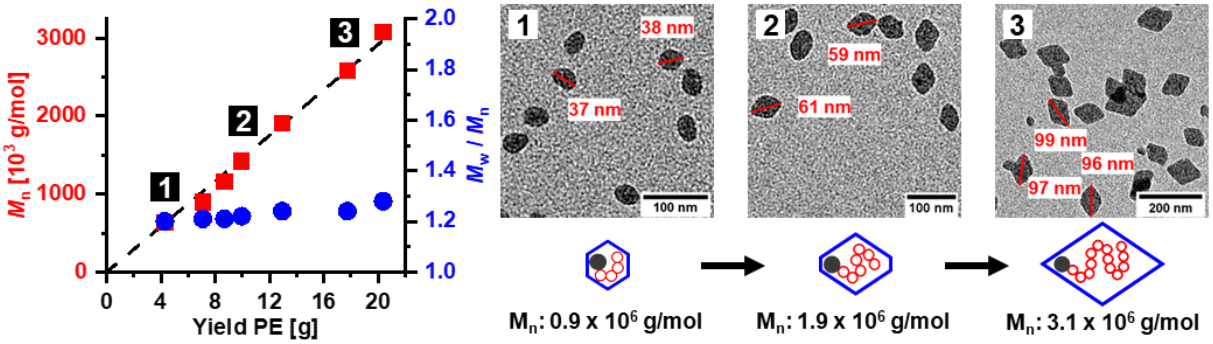

Figure 8.3. Molecular weights and polydispersity indices of the polyethylenes formed in aqueous surfactant solution versus yields (*left*, data from Table 3.2), indicating a living polymerization, and corresponding TEM images of particles (*right*). The particles' shapes and sizes evolve with molecular weight from hexagonal platelets over truncated lozenges to lozenges.

To profoundly understand their role in catalysis, the influence of long perfluoroalkyl substituents in different established salicylaldiminato Ni(II) motifs was investigated (see Figure 8.4, top). C_6F_{13}-groups in positions decisive for relevant nickel-aryl interactions remarkably altered the electron density at the metal center as evident from cyclic voltammetry experiments. Accordingly, BHE was effectively suppressed and less branched, higher molecular weight polyethylene in enhanced activities was produced (compared to the corresponding trifluoromethyl reference systems). In case of *N*-naphthyl catalyst types (**3^{Ant}-R^F/L**), the groups were placed in less relevant ligand backbone positions. Therefore, their effect was less pronounced and only a minor decrease in electron density at the nickel center could be observed. Nevertheless, the water-soluble representative (**3^{Ant}-C_6F_{13}/PEG**) stands out as first reported *N*-naphthyl salicylaldiminato Ni(II) with adequate activities under aqueous conditions (the CF_3-counterpart was inactive). All studied catalysts performed a living polymerization in water when long perfluoroalkyl-substituents were present in their ligand structure and stable UHMWPE dispersions were generated. These findings established a rather general mechanistic picture of a beneficial influence of long perfluororoalkyl substituents in remote positions on the active center toward a more controlled polymerization process.

Having this conclusive picture regarding the influence of perfluoroalkyls and other saturated groups on catalytic behavior in hand, the question arose about the suitability of aromatic remote substituents. Pentafluorophenyl groups are intensively studied in the field of organometallic chemistry and exhibit electron-withdrawing properties, similar to trifluoromethyl groups (according to Hammett substitution parameters). Catalysts bearing pentafluorophenyl-substitutions in remote positions (Figure 8.4, bottom) were prepared and tested in ethylene polymerization. Low-branched high molecular weight polyethylene of

$M_n > 10^5$ g/mol was generated. Under aqueous conditions, dispersions of well-defined nanocrystals were obtained (Figure 8.4, bottom). This indicates effective suppression of BHE (and chain transfer or branch formation), even when the electron-withdrawing substituent is part of the ligand's conjugation and acts as highly electron-poor π system. These findings were supported by X-ray crystal analysis (Figure 8.4, bottom) and cyclic voltammetry experiments on the catalyst precursor, which showed large nickel-aryl distances and low electron densities at the metal center, respectively.

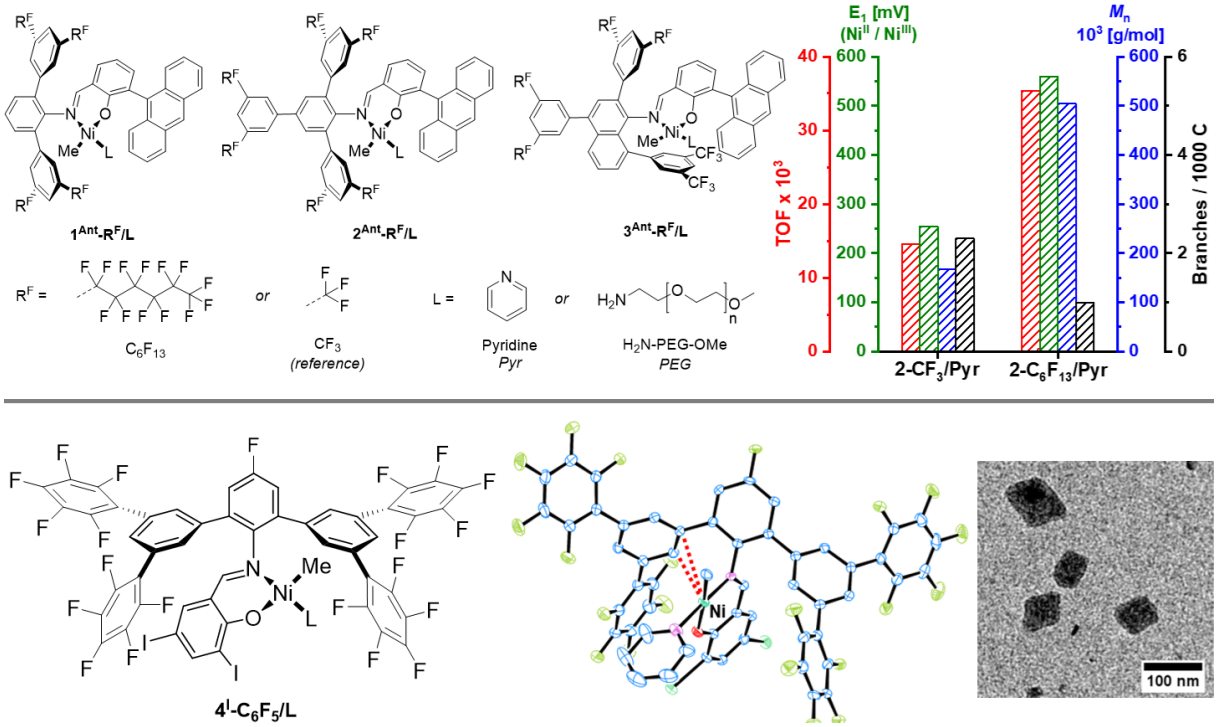

Figure 8.4. *Top:* Set of Ni(II) catalysts (left) used to study the impact of long perfluoroalkyl-substituents in selected ligand positions on the catalytically active center. A rather general beneficial influence of such groups on activity (red), molecular weight (blue) and branching (black) that directly correlates with the electron density at the metal center (green) could be identified (data from polymerization experiments in heptane, Table 4.1). *Bottom:* Chemical structure (left) and ORTEP plot (center; from X-ray diffraction analysis, L = Pyr, nickel-aryl interaction highlighted) of catalysts bearing pentafluorophenyl groups in remote positions. The water-soluble type produced well-defined nanocrystals in aqueous surfactant solution as evident from TEM images (right).

A living aqueous polymerization toward uniform shape UHMWPE nanocrystals requires, on one hand, suited catalysts but also development of a robust procedure by careful process design, on the other hand. Hence, all aqueous polymerizations were conducted in an automatized reactor setup that allowed for precise monitoring of all relevant reaction parameters. A space of different experimental parameters was varied, including surfactant type and concentration, pH, reaction temperature and sonication. A maximum degree of catalyst dispersion in the initial reaction mixture, achieved by addition of a small amount hydrophobic

organic solvent, was found to be very crucial to obtain undisturbed chain and particle growth. In this process the surfactant is adsorbed at the growing crystal's surface. Hence, a high amount of surfactant available per nickel center is important to yield particle shapes and sizes in the lozenge regime. Catalyst deactivation was suppressed by working in basic media und could be further reduced by decreasing the reaction temperature to 10 °C. The free labile PEG ligand, added with the catalyst precursor, effectively suppressed unwanted ethylene hydrate formation and UHMWPE dispersions of $M_n > 4.5 \times 10^6$ g/mol ($M_w/M_n = 1.3$) were accessible.

Such uniform UHMWPE nanocrystal dispersions were tested as precursors to generate macroscopic particle-based materials. Their morphology allowed to convert them further to aqueous pastes or to precipitate the material as powder. Commercial polyethylene granulates were tested in 3D pellet printing, a technique that circumvents pre-processing to filaments (Figure 8.5, b). This must not proceed at an expense of quality, as the printed objects compared well to polyethylene filament printed objects. Initial experiments with UHMWPE powders showed a promising extrusion behavior of the disentangled material. 'Dispersion fiber spinning' of UHMWPE dispersions afforded very regular fibers (Figure 8.5, c), when the dispersion is spun inside a coagulation bath in a very simple setup. The fibers' mechanical strength could be significantly enhanced by thermal post-processing, or binary fiber materials could be created by adding a second component to the initial dispersion. To enable 3D printing in a state where the nanocrystals keep their dispersed anisotropic morphology, UHWMPE dispersions were thickened and tested in paste printing (Figure 8.5, d). Initial experiments demonstrated the versatile character of this technique, that could be directly applied to UHMWPE pastes.

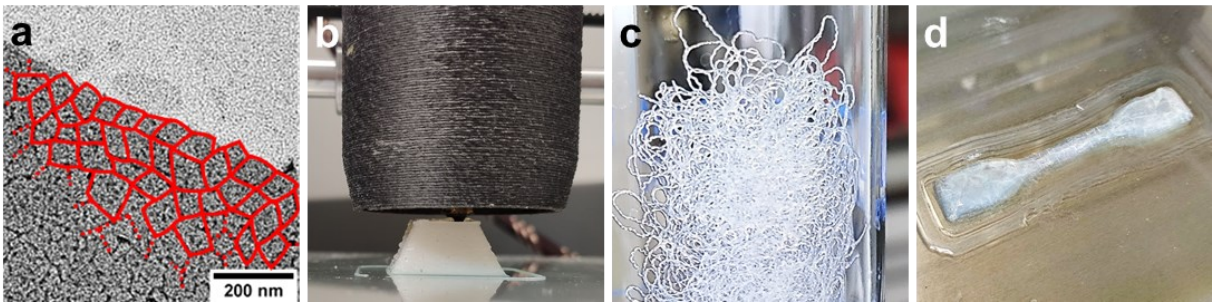

Figure 8.5. Different material processing methods tested in this work. a) Layered structures with short-range order formed by drying of uniform particle dispersions (boundaries marked in red). b) 3D pellet printing of polyethylene granulates. c) Fibers obtained by 'dispersion fiber spinning' of UHMWPE nanocrystal dispersions. d) 3D printing of UHMWPE pastes.

This work introduced the concept of a living catalytic ethylene polymerization under aqueous conditions. Under identified reaction conditions, an equally living particle growth process was achieved that generates uniform, anisotropic shape, monodisperse single-chain

UHMWPE nanocrystals. Key are perfluoroalkyl-substituents placed in selected positions of salicylaldiminato Ni(II) catalysts, that influence the active center to strongly promote chain growth over transfer or deactivation. Simultaneous process design identified important reaction parameters, optimized by using an automatized reactor setup. Towards the aim of particle-based materials, the UHMWPE nanocrystal dispersions were tested as precursors in different processing techniques. 'Dispersion fiber spinning' generated regular UHMWPE fibers in a simple setup. 3D paste printing enabled printing of more complex objects with the individual crystals staying intact in their dispersed state. These findings suggest the direct application of uniform shape UHMWPE nanocrystal dispersions, that hold potential to facilitate totally different UHMWPE processing methods to materials with yet unmet properties.

9 References

[1] Ashby, M. Materials–a brief history. *Philos. Mag. Lett.* **2008**, *88*, 749–755.

[2] Scott, G. Polymers in modern life. *Polymers and the environment*; Royal Society of Chemistry: Cambridge, 2010.

[3] Fratzl, P.; Weinkamer, R. Nature's hierarchical materials. *Progr. Mater. Sci.* **2007**, *52*, 1263–1334.

[4] Jambeck, J. R.; Geyer, R.; Wilcox, C.; Siegler, T. R.; Perryman, M.; Andrady, A.; Narayan, R.; Law, K. L. Plastic waste inputs from land into the ocean. *Science* **2015**, *347*, 768–771.

[5] Hoornweg, D.; Bhada-Tata, P.; Kennedy, C. Environment: Waste production must peak this century. *Nature* **2013**, *502*, 615–617.

[6] Geyer, R.; Jambeck, J. R.; Law, K. L. Production, use, and fate of all plastics ever made. *Sci. Adv.* **2017**, *3*, e1700782.

[7] Gahleitner, M.; Severn, J. R. Designing Polymer Properties. *Tailor-Made Polymers: Via Immobilization of Alpha-Olefin Polymerization Catalysts*; Wiley-VCH: Weinheim, 2008.

[8] Baier, M. C.; Zuideveld, M. A.; Mecking, S. Post-Metallocenes in the Industrial Production of Polyolefins. *Angew. Chem. Int. Ed.* **2014**, *53*, 9722–9744.

[9] Jeremic, D. Polyethylene. *Ullmann's Encyclopedia of Industrial Chemistry*; Wiley-VCH: Weinheim, 2014.

[10] Cantow, H. J.; Dall'Asta, G.; Ferry, J. D.; Fujita, H.; Kern, W.; Natta, G.; Okamura, S.; Overberger, C. G.; Prins, W.; Schulz, G. V.; Slichter, W. P.; Staverman, A. J.; Stille, J. K.; Stuart, H. A.; Ehrlich, P.; Mortimer, G. A. Fundamentals of the free-radical polymerization of ethylene. *Adv. Polym. Sci.* **1970**, 386–448.

[11] Odian, G. Stereochemistry of Polymerization. *Principiles of polymerization*, 4th ed.; Wiley: Hoboken, N.J, 2004.

[12] Kaminsky, W. Olefin polymerization catalyzed by metallocenes. *Adv. Catal.* **2001**, *46*, 89–159.

[13] Ziegler, K.; Holzkamp, E.; Breil, H.; Martin, H. Das Mülheimer Normaldruck-Polyäthylen-Verfahren. *Angew. Chem.* **1955**, *67*, 541–547.

[14] Natta, G.; Pino, P.; Corradini, P.; Danusso, F.; Mantica, E.; Mazzanti, G.; Moraglio, G. Crsytalline High Polymers of α-Olefins. *J. Am. Chem. Soc.* **1955**, *77*, 1708–1710.

[15] Urban, D.; Takamura, K. *Polymer dispersions and their industrial applications*; Wiley-VCH: Weinheim, 2005.

[16] Fitch, R. M. *Polymer colloids: A comprehensive introduction*; Colloid science; Elsevier (Academic Press): Amsterdam, 1997.

[17] Antonietti, M.; Tauer, K. 90 Years of Polymer Latexes and Heterophase Polymerization: More vital than ever. *Macromol. Chem. Phys.* **2003**, *204*, 207–219.

[18] Russell, T. P.; Kumacheva, E. Nanostructured Polymer Materials and Thin Films (Vol. 7). *Polymer science: A comprehensive reference*, (Eds.: Matyjaszewski, K.; Möller, M.); Elsevier Science: Amsterdam, London, 2012.

[19] Lagaly, G. Colloids. *Ullmann's encyclopedia of industrial chemistry*, 7th ed.; Wiley-VCH: Weinheim, 2010.

[20] Glotzer, S. C.; Solomon, M. J. Anisotropy of building blocks and their assembly into complex structures. *Nat. Mater.* **2007**, *6*, 557–562.

[21] Cademartiri, L.; Bishop, K. J. M.; Snyder, P. W.; Ozin, G. A. Using shape for self-assembly. *Phil. Trans. R. Soc. A* **2012**, *370*, 2824–2847.

[22] Mecking, S. Polymer dispersions from catalytic polymerization in aqueous systems. *Colloid. Polym. Sci.* **2007**, *285*, 605–619.

[23] Qiu, J.; Charleux, B.; Matyjaszewski, K. Controlled/living radical polymerization in aqueous media: homogeneous and heterogeneous systems. *Prog. Polym. Sci.* **2001**, *26*, 2083–2134.

[24] Donner, A.; Trepka, B.; Theiss, S.; Immler, F.; Traber, J.; Polarz, S. NHC-Metallosurfactants as Active Polymerization Catalysts. *Langmuir* **2019**, *35*, 16514–16520.

[25] Cunningham, M. F. Living/controlled radical polymerizations in dispersed phase systems. *Prog. Polym. Sci.* **2002**, *27*, 1039–1067.

[26] Billuart, G.; Bourgeat-Lami, E.; Lansalot, M.; Monteil, V. Free Radical Emulsion Polymerization of Ethylene. *Macromolecules* **2014**, *47*, 6591–6600.

[27] Grau, E.; Dugas, P.-Y.; Broyer, J.-P.; Boisson, C.; Spitz, R.; Monteil, V. Aqueous dispersions of nonspherical polyethylene nanoparticles from free-radical polymerization under mild conditions. *Angew. Chem. Int. Ed.* **2010**, *49*, 6810–6812.

[28] Brunel, F.; Billuart, G.; Dugas, P.-Y.; Lansalot, M.; Bourgeat-Lami, E.; Monteil, V. Crystallization of Nanodomains in Polyethylene Latexes. *Macromolecules* **2017**, *50*, 9742–9749.

[29] Teixeira, R. F. A.; Bon, S. A. F. Hybrid Latex Particles. *Physical Methods for the Preparation of Hybrid Nanocomposite Polymer Latex Particles (ed. Herk, Alex M.; Bon, S. A. F.)*; Springer-Verlag: Berlin, Heidelberg, 2011.

[30] Morgen, T. O.; Krumova, M.; Luttikhedde, H.; Mecking, S. Free-Radical Dispersion Polymerization of Ethylene with Laponite to Polyethylene–Clay Nanocomposite Particles. *Macromolecules* **2018**, *51*, 4118–4128.

[31] Morgen, T. O.; Luttikhedde, H.; Mecking, S. Aqueous Dispersions of Ethylene Copolymers and Their Laponite Clay Nanocomposites from Free-Radical Dispersion Polymerization. *Macromolecules* **2019**, *52*, 4270–4277.

[32] Hamer, D. A.; Frederick J. K. Spheroidal polymerization catalyst, process for preparing, and use for ethylene polymerization. US4293673, Union Carbide.

[33] Copéret, C.; Comas-Vives, A.; Conley, M. P.; Estes, D. P.; Fedorov, A.; Mougel, V.; Nagae, H.; Núñez-Zarur, F.; Zhizhko, P. A. Surface Organometallic and Coordination Chemistry toward Single-Site Heterogeneous Catalysts: Strategies, Methods, Structures, and Activities. *Chem. Rev.* **2016**, *116*, 323–421.

[34] Copéret, C.; Chabanas, M.; Petroff Saint-Arroman, R.; Basset, J.-M. Homogeneous and heterogeneous catalysis: bridging the gap through surface organometallic chemistry. *Angew. Chem. Int. Ed.* **2003**, *42*, 156–181.

[35] Resconi, L.; Cavallo, L.; Fait, A.; Piemontesi, F. Selectivity in propene polymerization with metallocene catalysts. *Chem. Rev.* **2000**, *100*, 1253–1346.

[36] Brintzinger, H. H.; Fischer, D.; Mülhaupt, R.; Rieger, B.; Waymouth, R. M. Stereospecific Olefin Polymerization with Chiral Metallocene Catalysts. *Angew. Chem. Int. Ed.* **1995**, *34*, 1143–1170.

[37] Coates, G. W. Precise control of polyolefin stereochemistry using single-site metal catalysts. *Chem. Rev.* **2000**, *100*, 1223–1252.

[38] Barbé, P. C.; Cecchin, G.; Noristi, L. The catalytic system Ti-complex/$MgCl_2$. *Catalytical and radical polymerization (Advances in Polymer Science)*; Springer: Berlin, Heidelberg, 1986.

[39] Grau, E.; Lesage, A.; Norsic, S.; Copéret, C.; Monteil, V.; Sautet, P. Tetrahydrofuran in $TiCl_4$ /THF/$MgCl_2$: a Non-Innocent Ligand for Supported Ziegler–Natta Polymerization Catalysts. *ACS Catal.* **2013**, *3*, 52–56.

[40] D'Anna, V.; Norsic, S.; Gajan, D.; Sanders, K.; Pell, A. J.; Lesage, A.; Monteil, V.; Copéret, C.; Pintacuda, G.; Sautet, P. Structural Characterization of the EtOH–$TiCl_4$–$MgCl_2$ Ziegler–Natta Precatalyst. *J. Phys. Chem. C* **2016**, *120*, 18075–18087.

[41] Copéret, C.; Allouche, F.; Chan, K. W.; Conley, M. P.; Delley, M. F.; Fedorov, A.; Moroz, I. B.; Mougel, V.; Pucino, M.; Searles, K.; Yamamoto, K.; Zhizhko, P. A. Bridging the Gap between Industrial and Well-Defined Supported Catalysts. *Angew. Chem. Int. Ed.* **2018**, *57*, 6398–6440.

[42] Cossee, P. On the mechanism of cis-ligand insertion. *Recl. Trav. Chim. Pays-Bas* **1966**, *85*, 1151–1160.

[43] Arlman, E.; Cossee, P. Ziegler-Natta catalysis III. Stereospecific polymerization of propene with the catalyst system $TiCl_3$-$AlEt_3$. *J. Catal.* **1964**, *3*, 99–104.

[44] Cossee, P. Ziegler-Natta catalysis I. Mechanism of polymerization α-olefins with Ziegler-Natta catalysts. *J. Catal.* **1964**, *3*, 80–88.

[45] Gibson, V. C.; Spitzmesser, S. K. Advances in Non-Metallocene Olefin Polymerization Catalysis. *Chem. Rev.* **2003**, *103*, 283–316.

[46] Britovsek, G. J. P.; Gibson, V. C.; Wass, D. F. The Search for New-Generation Olefin Polymerization Catalysts: Life beyond Metallocenes. *Angew. Chem. Int. Ed.* **1999**, *38*, 428–447.

[47] Mecking, S. Olefin Polymerization by Late Transition Metal Complexes—A Root of Ziegler Catalysts Gains New Ground. *Angew. Chem. Int. Ed.* **2001**, *40*, 534–540.

[48] Camacho, D. H.; Guan, Z. Designing late-transition metal catalysts for olefin insertion polymerization and copolymerization. *Chem. Commun.* **2010**, *46*, 7879–7893.

[49] Chen, C. Designing catalysts for olefin polymerization and copolymerization: beyond electronic and steric tuning. *Nat. Rev. Chem.* **2018**, *2*, 6–14.

[50] Budzelaar, P. H. M. Mechanisms of branch formation in metal-catalyzed ethene polymerization. *Wiley Interdiscip. Rev.: Comput. Mol. Sci.* **2012**, *2*, 221–241.

[51] Xu, H.; Hu, C. T.; Wang, X.; Diao, T. Structural Characterization of β-Agostic Bonds in Pd-Catalyzed Polymerization. *Organometallics* **2017**, *36*, 4099–4102.

[52] Heyndrickx, W.; Occhipinti, G.; Jensen, V. R. Neutral nickel ethylene oligo- and polymerization catalysts: towards computational catalyst prediction and design. *Chem. Eur. J.* **2014**, *20*, 7962–7978.

[53] Falivene, L.; Wiedemann, T.; Göttker-Schnetmann, I.; Caporaso, L.; Cavallo, L.; Mecking, S. Control of Chain Walking by Weak Neighboring Group Interactions in Unsymmetrical Catalysts. *J. Am. Chem. Soc.* **2018**, *140*, 1305–1312.

[54] Chan, M. S.; Deng, L. Q.; Ziegler, T. Density functional study of neutral salicylaldiminato nickel(II) complexes as olefin polymerization catalysts. *Organometallics* **2000**, *19*, 2741–2750.

[55] Johnson, L. K.; Killian, C. M.; Brookhart, M. New Pd(II)- and Ni(II)-Based Catalysts for Polymerization of Ethylene and α-Olefins. *J. Am. Chem. Soc.* **1995**, *117*, 6414–6415.

[56] Deng, L.; Margl, P.; Ziegler, T. A Density Functional Study of Nickel(II) Diimide Catalyzed Polymerization of Ethylene. *J. Am. Chem. Soc.* **1997**, *119*, 1094–1100.

[57] Keim, W. Oligomerization of ethylene to α-olefins: discovery and development of the shell higher olefin process (SHOP). *Angew. Chem. Int. Ed.* **2013**, *52*, 12492–12496.

[58] Keim, W.; Kowaldt, F. H.; Goddard, R.; Krüger, C. Novel Coordination of (Benzoylmethylene)triphenylphosphorane in a Nickel Oligomerization Catalyst. *Angew. Chem. Int. Ed.* **1978**, *17*, 466–467.

[59] Vogt, D. Nonaqueous Organic/Organic Separation (SHOP Process). *Aqueous-Phase Organometallic Catalysis (Ed.: Cornils, Boy; Herrmann, W. A.)*; Wiley-VCH: Weinheim, 2004.

[60] Müller, U.; Keim, W.; Krüger, C.; Betz, P. [{$Ph_2PCH_2C(CF_3)_2O$}NiH(PCy_3)]: Support for a Nickel Hydride Mechanism in Ethene Oligomerization. *Angew. Chem. Int. Ed.* **1989**, *28*, 1011–1013.

[61] Young, C. T.; Goetze, R. von; Tomov, A. K.; Zaccaria, F.; Britovsek, G. J. P. The Mathematics of Ethylene Oligomerisation and Polymerisation. *Top. Catal.* **2020**, *63*, 294–318.

[62] Klabunde, U.; Mülhaupt, R.; Herskovitz, T.; Janowicz, A. H.; Calabrese, J.; Ittel, S. D. Ethylene homopolymerization with P, O-chelated nickel catalysts. *J. Polym. Sci., Part A: Polym. Chem.* **1987**, *25*, 1989–2003.

[63] Ostoja-Starzewski, K. A.; Witte, J. Control of the Molecular Weight of Polyethene in Syntheses with Bis(ylide)nickel Catalysts. *Angew. Chem. Int. Ed.* **1987**, *26*, 63–64.

[64] Ostoja-Starzewski, K. A.; Witte, J. Highly Active Ylide-Nickel Catalysts for the Polymerization of Ethylene. *Angew. Chem. Int. Ed.* **1985**, *24*, 599–601.

[65] Mülhaupt, R. Catalytic Polymerization and Post Polymerization Catalysis Fifty Years After the Discovery of Ziegler's Catalysts. *Macromol. Chem. Phys.* **2003**, *204*, 289–327.

[66] Wang, F.; Chen, C. A continuing legend: the Brookhart-type α-diimine nickel and palladium catalysts. *Polym. Chem.* **2019**, *10*, 2354–2369.

[67] Guo, L.; Dai, S.; Sui, X.; Chen, C. Palladium and Nickel Catalyzed Chain Walking Olefin Polymerization and Copolymerization. *ACS Catal.* **2016**, *6*, 428–441.

[68] Brookhart, M.; Grant, B.; Volpe, A. F. [$(3,5\text{-}(CF_3)_2C_6H_3)_4$B]-[$H(OEt_2)_2$]$^+$: a convenient reagent for generation and stabilization of cationic, highly electrophilic organometallic complexes. *Organometallics* **1992**, *11*, 3920–3922.

[69] Gates, D. P.; Svejda, S. A.; Oñate, E.; Killian, C. M.; Johnson, L. K.; White, P. S.; Brookhart, M. Synthesis of Branched Polyethylene Using (α-Diimine)nickel(II) Catalysts: Influence of Temperature, Ethylene Pressure, and Ligand Structure on Polymer Properties. *Macromolecules* **2000**, *33*, 2320–2334.

[70] Dai, S.; Zhou, S.; Zhang, W.; Chen, C. Systematic Investigations of Ligand Steric Effects on α-Diimine Palladium Catalyzed Olefin Polymerization and Copolymerization. *Macromolecules* **2016**, *49*, 8855–8862.

[71] Wang, B.; Daugulis, O.; Brookhart, M. Ethylene Polymerization with Ni(II) Diimine Complexes Generated from 8-Halo-1-naphthylamines: The Role of Equilibrating Syn / Anti Diastereomers in Determining Polymer Properties. *Organometallics* **2019**, *38*, 4658–4668.

[72] Ittel, S. D.; Johnson, L. K.; Brookhart, M. Late-Metal Catalysts for Ethylene Homo- and Copolymerization. *Chem. Rev.* **2000**, *100*, 1169–1204.

[73] Johnson, L. K.; Mecking, S.; Brookhart, M. Copolymerization of Ethylene and Propylene with Functionalized Vinyl Monomers by Palladium(II) Catalysts. *J. Am. Chem. Soc.* **1996**, *118*, 267–268.

[74] Nakamura, A.; Ito, S.; Nozaki, K. Coordination–Insertion Copolymerization of Fundamental Polar Monomers. *Chem. Rev.* **2009**, *109*, 5215–5244.

[75] Mecking, S.; Johnson, L. K.; Wang, L.; Brookhart, M. Mechanistic Studies of the Palladium-Catalyzed Copolymerization of Ethylene and α-Olefins with Methyl Acrylate. *J. Am. Chem. Soc.* **1998**, *120*, 888–899.

[76] Zou, W.; Chen, C. Influence of Backbone Substituents on the Ethylene (Co)polymerization Properties of α-diimine Pd(II) and Ni(II) Catalysts. *Organometallics* **2016**, *35*, 1794–1801.

[77] Chen, Z.; Leatherman, M. D.; Daugulis, O.; Brookhart, M. Nickel-Catalyzed Copolymerization of Ethylene and Vinyltrialkoxysilanes: Catalytic Production of Cross-Linkable Polyethylene and

Elucidation of the Chain-Growth Mechanism: Catalytic Production of Cross-Linkable Polyethylene and Elucidation of the Chain-Growth Mechanism. *J. Am. Chem. Soc.* **2017**, *139*, 16013–16022.

[78] Dai, S.; Sui, X.; Chen, C. Highly Robust Palladium(II) α-Diimine Catalysts for Slow-Chain-Walking Polymerization of Ethylene and Copolymerization with Methyl Acrylate. *Angew. Chem. Int. Ed.* **2015**, *54*, 9948–9953.

[79] Chen, Z.; Brookhart, M. Exploring Ethylene/Polar Vinyl Monomer Copolymerizations Using Ni and Pd α-Diimine Catalysts. *Acc. Chem. Res.* **2018**, *51*, 1831–1839.

[80] Gottfried, A. C.; Brookhart, M. Living Polymerization of Ethylene Using Pd(II) α-Diimine Catalysts. *Macromolecules* **2001**, *34*, 1140–1142.

[81] Domski, G. J.; Rose, J. M.; Coates, G. W.; Bolig, A. D.; Brookhart, M. Living alkene polymerization: New methods for the precision synthesis of polyolefins. *Prog. Polym. Sci.* **2007**, *32*, 30–92.

[82] Allen, K. E.; Campos, J.; Daugulis, O.; Brookhart, M. Living Polymerization of Ethylene and Copolymerization of Ethylene/Methyl Acrylate Using "Sandwich" Diimine Palladium Catalysts. *ACS Catal.* **2015**, *5*, 456–464.

[83] Stadler, S. M.; Göttker-Schnetmann, I.; Fuchs, A. S.; Fischer, S. R. R.; Mecking, S. Catalytic Chain Transfer Polymerization to Functional Reactive End Groups for Controlled Free Radical Growth. *Macromolecules* **2020**, *53*, 2362–2368.

[84] Hyatt, M. G.; Guironnet, D. Silane as Chain Transfer Agent for the Polymerization of Ethylene Catalyzed by a Palladium(II) Diimine Catalyst. *ACS Catal.* **2017**, *7*, 5717–5720.

[85] Zhang, D.; Nadres, E. T.; Brookhart, M.; Daugulis, O. Synthesis of Highly Branched Polyethylene Using "Sandwich" (8-*p*-Tolyl naphthyl α-diimine)nickel(II) Catalysts. *Organometallics* **2013**, *32*, 5136–5143.

[86] Dai, S.; Chen, C. Direct Synthesis of Functionalized High-Molecular-Weight Polyethylene by Copolymerization of Ethylene with Polar Monomers. *Angew. Chem. Int. Ed.* **2016**, *55*, 13281–13285.

[87] Mahmood, Q.; Zeng, Y.; Yue, E.; Solan, G. A.; Liang, T.; Sun, W.-H. Ultra-high molecular weight elastomeric polyethylene using an electronically and sterically enhanced nickel catalyst. *Polym. Chem.* **2017**, *8*, 6416–6430.

[88] Rose, J. M.; Cherian, A. E.; Coates, G. W. Living polymerization of alpha-olefins with an alpha-diimine Ni(II) catalyst: formation of well-defined ethylene-propylene copolymers through controlled chain-walking. *J. Am. Chem. Soc.* **2006**, *128*, 4186–4187.

[89] O'Connor, K. S.; Lamb, J. R.; Vaidya, T.; Keresztes, I.; Klimovica, K.; LaPointe, A. M.; Daugulis, O.; Coates, G. W. Understanding the Insertion Pathways and Chain Walking Mechanisms of α-Diimine Nickel Catalysts for α-Olefin Polymerization: A ^{13}C NMR Spectroscopic Investigation. *Macromolecules* **2017**, *50*, 7010–7027.

[90] Takeuchi, D.; Osakada, K. Controlled isomerization polymerization of olefins, cycloolefins, and dienes. *Polymer* **2016**, *82*, 392–405.

[91] Milano, G.; Guerra, G.; Mazzeo, M.; Pellecchia, C.; Cavallo, L. (E)–(Z) Selectivity in the Polymerization of 2-Butene Promoted by Ni(II) Brookhart-Type Catalysts. *Macromolecules* **2005**, *38*, 2072–2075.

[92] Leatherman, M. D.; Brookhart, M. Ni(II)-Catalyzed Polymerization of trans-2-Butene. *Macromolecules* **2001**, *34*, 2748–2750.

[93] Wang, C.; Friedrich, S.; Younkin, T. R.; Li, R. T.; Grubbs, R. H.; Bansleben, D. A.; Day, M. W. Neutral Nickel(II)-Based Catalysts for Ethylene Polymerization. *Organometallics* **1998**, *17*, 3149–3151.

[94] Younkin, T. R.; Conner, E. F.; Henderson, J. I.; Friedrich, S. K.; Grubbs, R. H.; Bansleben, D. A. Neutral, single-component nickel (II) polyolefin catalysts that tolerate heteroatoms. *Science* **2000**, *287*, 460–462.

[95] Johnson, L. K.; Bennett, A. M. A.; Wang, L.; Parthasarath, A.; Hauptman, E.; Simpson, R. D.; Feldman, J.; Coughlin, E. B.; Ittel, S. D. Polymerization of Olefins. WO1998030609, DuPont (USA).

[96] Connor, E. F.; Younkin, T. R.; Henderson, J. I.; Waltman, A. W.; Grubbs, R. H. Synthesis of neutral nickel catalysts for ethylene polymerization - the influence of ligand size on catalyst stability. *Chem. Commun.* **2003**, 2272–2273.

[97] Sun, W.-H.; Yang, H.; Li, Z.; Li, Y. Vinyl Polymerization of Norbornene with Neutral Salicylaldiminato Nickel(II) Complexes. *Organometallics* **2003**, *22*, 3678–3683.

[98] Sun, J.; Shan, Y.; Xu, Y.; Cui, Y.; Schumann, H.; Hummert, M. Novel cyclohexyl-substituted salicylaldiminato-nickel(II) complex as a catalyst for ethylene homopolymerization and copolymerization. *J. Polym. Sci., Part A: Polym. Chem.* **2004**, *42*, 6071–6080.

[99] Connor, E. F.; Younkin, T. R.; Henderson, J. I.; Hwang, S.; Grubbs, R. H.; Roberts, W. P.; Litzau, J. J. Linear functionalized polyethylene prepared with highly active neutral Ni(II) complexes. *J. Polym. Sci., Part A: Polym. Chem.* **2002**, *40*, 2842–2854.

[100] Wang, W.-H.; Jin, G.-X. Synthesis, molecular structures and norbornene addition polymerization activity of the neutral nickel catalysts supported by N-naphthyl-salicylaldiminato ligands. *Inorg. Chem. Commun.* **2005**, *8*, 109–112.

[101] Waltman, A. W.; Younkin, T. R.; Grubbs, R. H. Insights into the Deactivation of Neutral Nickel Ethylene Polymerization Catalysts in the Presence of Functionalized Olefins. *Organometallics* **2004**, *23*, 5121–5123.

[102] Berkefeld, A.; Drexler, M.; Möller, H. M.; Mecking, S. Mechanistic insights on the copolymerization of polar vinyl monomers with neutral Ni(II) catalysts. *J. Am. Chem. Soc.* **2009**, *131*, 12613–12622.

[103] Ölscher, F.; Göttker-Schnetmann, I.; Monteil, V.; Mecking, S. Role of Radical Species in Salicylaldiminato Ni(II) Mediated Polymer Chain Growth: A Case Study for the Migratory Insertion Polymerization of Ethylene in the Presence of Methyl Methacrylate. *J. Am. Chem. Soc.* **2015**, *137*, 14819–14828.

[104] Leblanc, A.; Grau, E.; Broyer, J.-P.; Boisson, C.; Spitz, R.; Monteil, V. Homo- and Copolymerizations of (Meth)Acrylates with Olefins (Styrene, Ethylene) Using Neutral Nickel Complexes: A Dual Radical/Catalytic Pathway. *Macromolecules* **2011**, *44*, 3293–3301.

[105] Stadler, S. M.; Göttker-Schnetmann, I.; Mecking, S. Incorporation of Radicals during Ni(II)-Catalyzed Ethylene Insertion Polymerization. *ACS Catal.* **2019**, *9*, 2760–2767.

[106] Zhang, T.; Guo, D.; Jie, S.; Sun, W.-H.; Li, T.; Yang, X. Influence of electronic effect on catalytic activity of salicylaldiminato nickel(II) complexes. *J. Polym. Sci., Part A: Polym. Chem.* **2004**, *42*, 4765–4774.

[107] Zuideveld, M. A.; Wehrmann, P.; Röhr, C.; Mecking, S. Remote substituents controlling catalytic polymerization by very active and robust neutral nickel(II) complexes. *Angew. Chem. Int. Ed.* **2004**, *43*, 869–873.

[108] Göttker-Schnetmann, I.; Wehrmann, P.; Röhr, C.; Mecking, S. Substituent Effects in (κ^2-N,O)-Salicylaldiminato Nickel(II)–Methyl Pyridine Polymerization Catalysts: Terphenyls Controlling Polyethylene Microstructures. *Organometallics* **2007**, *26*, 2348–2362.

[109] Wiedemann, T.; Voit, G.; Tchernook, A.; Roesle, P.; Göttker-Schnetmann, I.; Mecking, S. Monofunctional hyperbranched ethylene oligomers. *J. Am. Chem. Soc.* **2014**, *136*, 2078–2085.

[110] Osichow, A.; Göttker-Schnetmann, I.; Mecking, S. Role of Electron-Withdrawing Remote Substituents in Neutral Nickel(II) Polymerization Catalysts. *Organometallics* **2013**, *32*, 5239–5242.

[111] Kenyon, P.; Mecking, S. Pentafluorosulfanyl Substituents in Polymerization Catalysis. *J. Am. Chem. Soc.* **2017**, *139*, 13786–13790.

[112] Wang, J.; Yao, E.; Chen, Z.; Ma, Y. Fluorinated Nickel(II) Phenoxyiminato Catalysts: Exploring the Role of Fluorine Atoms in Controlling Polyethylene Productivities and Microstructures. *Macromolecules* **2015**, *48*, 5504–5510.

[113] Di Xu; Zhao, X.-X.; Chen, Z.-T.; Ma, Y.-G. Synergistic effect and fluorination effect in ethylene polymerization by nickel phenoxyiminato catalysts. *Chin. J. Polym. Sci.* **2018**, *36*, 244–251.

[114] Weberski, M. P.; Chen, C.; Delferro, M.; Zuccaccia, C.; Macchioni, A.; Marks, T. J. Suppression of β-Hydride Chain Transfer in Nickel(II)-Catalyzed Ethylene Polymerization via Weak Fluorocarbon Ligand–Product Interactions. *Organometallics* **2012**, *31*, 3773–3789.

[115] Mitani, M.; Nakano, T.; Fujita, T. Unprecedented living olefin polymerization derived from an attractive interaction between a ligand and a growing polymer chain. *Chem. Eur. J.* **2003**, *9*, 2396–2403.

[116] Moeller, H. M.; Baier, M. C.; Mecking, S.; Talsi, E. P.; Bryliakov, K. P. The Origin of Living Polymerization with an o-Fluorinated Catalyst: NMR Spectroscopic Characterization of Chain-Carrying Species. *Chem. Eur. J.* **2012**, *18*, 848–856.

[117] Iwashita, A.; Chan, M. C. W.; Makio, H.; Fujita, T. Attractive interactions in olefin polymerization mediated by post-metallocene catalysts with fluorine-containing ancillary ligands. *Catal. Sci. Technol.* **2014**, *4*, 599–610.

[118] Li, S.; Xu, G.; Dai, S. A remote nonconjugated electron effect in insertion polymerization with α-diimine nickel and palladium species. *Polym. Chem.* **2020**, *11*, 2692–2699.

[119] Zou, C.; Tan, C.; Pang, W.; Chen, C. Amidine/Phosphine-Oxide-Based Nickel Catalysts for Ethylene Polymerization and Copolymerization. *ChemCatChem* **2019**, *11*, 5339–5344.

[120] Schiebel, E.; Santacroce, S.; Falivene, L.; Göttker-Schnetmann, I.; Caporaso, L.; Mecking, S. Tailored Strength Neighboring Group Interactions Switch Polymerization to Dimerization Catalysis. *ACS Catal.* **2019**, *9*, 3888–3894.

[121] Behzadi, S.; Chi, M.; Pang, W.; Liang, T.; Tan, C. Camphor-based phosphine-carbonyl ligands for Ni catalyzed ethylene oligomerization. *New J. Chem.* **2020**, *44*, 1076–1081.

[122] Tan, C.; Qasim, M.; Pang, W.; Chen, C. Ligand–metal secondary interactions in phosphine–sulfonate palladium and nickel catalyzed ethylene (co)polymerization. *Polym. Chem.* **2020**, *11*, 411–416.

[123] Liang, T.; Chen, C. Position Makes the Difference: Electronic Effects in Nickel-Catalyzed Ethylene Polymerizations and Copolymerizations. *Inorg. Chem.* **2018**, *57*, 14913–14919.

[124] Zhang, Y.; Mu, H.; Wang, X.; Pan, L.; Li, Y. Elaborate Tuning in Ligand Makes a Big Difference in Catalytic Performance: Bulky Nickel Catalysts for (Co)polymerization of Ethylene with Promising Vinyl Polar Monomers. *ChemCatChem* **2019**, *11*, 2329–2340.

[125] Kenyon, P.; Wörner, M.; Mecking, S. Controlled Polymerization in Polar Solvents to Ultrahigh Molecular Weight Polyethylene. *J. Am. Chem. Soc.* **2018**, *140*, 6685–6689.

[126] Chen, Z.; Mesgar, M.; White, P. S.; Daugulis, O.; Brookhart, M. Synthesis of Branched Ultrahigh-Molecular-Weight Polyethylene Using Highly Active Neutral, Single-Component Ni(II) Catalysts. *ACS Catal.* **2015**, *5*, 631–636.

[127] Tran, Q. H.; Brookhart, M.; Daugulis, O. New Neutral Nickel and Palladium Sandwich Catalysts: Synthesis of Ultra-High Molecular Weight Polyethylene (UHMWPE) via Highly Controlled Polymerization and Mechanistic Studies of Chain Propagation. *J. Am. Chem. Soc.* **2020**, *142*, 7198–7206.

[128] Wehrmann, P.; Mecking, S. Highly Active Binuclear Neutral Nickel(II) Catalysts Affording High Molecular Weight Polyethylene. *Organometallics* **2008**, *27*, 1399–1408.

[129] Berkefeld, A.; Möller, H. M.; Mecking, S. Unusual Reactivity of N,N,N′,N′-Tetramethylethylenediamine-Coordinated Neutral Nickel(II) Polymerization Catalysts. *Organometallics* **2009**, *28*, 4048–4055.

[130] Kenyon, P. Minimally Entangled (Ultra-)High Molecular Weight Polyethylene by Ni(II)-catalysed Polymerisation in Compartmentalised Systems. *Dissertation, University of Konstanz* **2018**.

[131] Kenyon, P.; Falivene, L.; Caporaso, L.; Mecking, S. Ancillary Ligands Impact Branching Microstructure in Late-Transition-Metal Polymerization Catalysis. *ACS Catal.* **2019**, *9*, 11552–11556.

[132] Drent, E.; van Dijk, R.; van Ginkel, R.; van Oort, B.; Pugh, R. I. Palladium catalysed copolymerisation of ethene with alkylacrylates: polar comonomer built into the linear polymer chain. *Chem. Commun.* **2002**, 744–745.

[133] Tan, C.; Chen, C. Emerging Palladium and Nickel Catalysts for Copolymerization of Olefins with Polar Monomers. *Angew. Chem. Int. Ed.* **2019**, *58*, 7192–7200.

[134] Carrow, B. P.; Nozaki, K. Transition-Metal-Catalyzed Functional Polyolefin Synthesis: Effecting Control through Chelating Ancillary Ligand Design and Mechanistic Insights. *Macromolecules* **2014**, *47*, 2541–2555.

[135] Hicks, F. A.; Jenkins, J. C.; Brookhart, M. Synthesis and Ethylene Polymerization Activity of a Series of 2-Anilinotropone-Based Neutral Nickel(II) Catalysts. *Organometallics* **2003**, *22*, 3533–3545.

[136] Hicks, F. A.; Brookhart, M. A Highly Active Anilinotropone-Based Neutral Nickel(II) Catalyst for Ethylene Polymerization. *Organometallics* **2001**, *20*, 3217–3219.

[137] Li, W.; Guo, L.; Li, W. Anilinotropone nickel catalyzed tandem ethylene oligomerization and Friedel-Crafts addition to toluene. *Molecular Catalysis* **2017**, *433*, 122–127.

[138] Cheng, H.; Cai, Z. (Anilino)anthraquinone Nickel-Catalyzed Random Copolymerization of Norbornene and Ethylene. *ChemCatChem* **2018**, *10*, 497–500.

[139] Delferro, M.; Marks, T. J. Multinuclear olefin polymerization catalysts. *Chem. Rev.* **2011**, *111*, 2450–2485.

[140] Xiao, D.; Do, L. H. In Situ Generated Heterometallic Nickel–Zinc Catalysts for Ethylene Polymerization. *Organometallics* **2018**, *37*, 3079–3085.

[141] Chiu, H.-C.; Koley, A.; Dunn, P. L.; Hue, R. J.; Tonks, I. A. Ethylene polymerization catalyzed by bridging Ni/Zn heterobimetallics. *Dalton Trans.* **2017**, *46*, 5513–5517.

[142] Smith, A. J.; Kalkman, E. D.; Gilbert, Z. W.; Tonks, I. A. $ZnCl_2$ Capture Promotes Ethylene Polymerization by a Salicylaldiminato Ni Complex Bearing a Pendent 2,2′-Bipyridine Group. *Organometallics* **2016**, *35*, 2429–2432.

[143] Cai, Z.; Do, L. H. Customizing Polyolefin Morphology by Selective Pairing of Alkali Ions with Nickel Phenoxyimine-Polyethylene Glycol Catalysts. *Organometallics* **2017**, *36*, 4691–4698.

[144] Chen, Z.; Zhao, X.; Gong, X.; Di Xu; Ma, Y. Macrocyclic Trinuclear Nickel Phenoxyimine Catalysts for High-Temperature Polymerization of Ethylene and Isospecific Polymerization of Propylene. *Macromolecules* **2017**, *50*, 6561–6568.

[145] Li, W.-W.; Mu, H.-L.; Liu, J.-Y.; Li, Y.-S. 9,9-Dimethylxanthene-based binuclear phenoxy-imine neutral nickel(II) catalysts for ethylene homo- and copolymerization. *J. Organomet. Chem.* **2017**, *836–837*, 34–43.

[146] Shu, D.; Mouat, A. R.; Stephenson, C. J.; Invergo, A. M.; Delferro, M.; Marks, T. J. Ligand-Unsymmetrical Phenoxyiminato Dinickel Catalyst for High Molecular Weight Long-Chain Branched Polyethylenes. *ACS Macro Lett.* **2015**, *4*, 1297–1301.

[147] Cheng, H.; Wang, H.; Li, Y.; Hu, Y.; Zhang, X.; Cai, Z. Structurally simple dinuclear nickel catalyzed olefin copolymerization with polar monomers. *J. Catal.* **2018**, *368*, 291–297.

[148] Kocen, A. L.; Brookhart, M.; Daugulis, O. A highly active Ni(II)-triadamantylphosphine catalyst for ultrahigh-molecular-weight polyethylene synthesis. *Nat. Commun.* **2019**, *10*, 438.

[149] Zou, C.; Dai, S.; Chen, C. Ethylene Polymerization and Copolymerization Using Nickel 2-Iminopyridine-*N*-oxide Catalysts: Modulation of Polymer Molecular Weights and Molecular-Weight Distributions. *Macromolecules* **2018**, *51*, 49–56.

[150] Liang, T.; Goudari, S. B.; Chen, C. A simple and versatile nickel platform for the generation of branched high molecular weight polyolefins. *Nat. Commun.* **2020**, *11*, 372.

[151] Tan, C.; Chen, C. Nickel catalysts for the synthesis of ultra-high molecular weight polyethylene. *Sci. Bull.* **2020**, *65*, 1137–1138.

[152] Wei, W.; Keh, C. C. K.; Li, C.-J.; Varma, R. S. Water as a reaction medium for clean chemical processes. *Clean Technol. Environ. Policy* **2004**, *6*, 250–257.

[153] Cornils, B. Industrial Aqueous Biphasic Catalysis: Status and Directions. *Org. Process Res. Dev.* **1998**, *2*, 121–127.

[154] Cornils, B.; Herrmann, W. A.; Eckl, R. W. Industrial aspects of aqueous catalysis. *J. Mol. Catal. A: Chem.* **1997**, *116*, 27–33.

[155] Behr, A.; Urschey, M.; Brehme, V. A. Aqueous biphasic catalysis as a powerful tool for catalyst recycling in telomerization and hydrogenation chemistry. *Green Chem.* **2003**, *5*, 198–204.

[156] Cornils, B.; Herrmann, W. A.; Horváth, I. T.; Leitner, W.; Mecking, S.; Olivier-Bourbigou, H.; Vogt, D.; Cornils, B. *Multiphase homogeneous catalysis*; Wiley-VCH: Weinheim, 2005.

[157] Mecking, S.; Held, A.; Bauers, F. M. Aqueous Catalytic Polymerization of Olefins. *Angew. Chem. Int. Ed.* **2002**, *41*, 544–561.

[158] Claverie, J. P.; Soula, R. Catalytic polymerizations in aqueous medium. *Prog. Polym. Sci.* **2003**, *28*, 619–662.

[159] Held, A.; Mecking, S. Coordination Polymerization in Water Affording Amorphous Polyethylenes. *Chemistry – A European Journal* **2000**, *6*, 4623–4629.

[160] Held, A.; Bauers, F. M.; Mecking, S. Coordination polymerization of ethylene in water by Pd(II) and Ni(II) catalysts. *Chem. Commun.* **2000**, 301–302.

[161] Berkefeld, A.; Mecking, S. Mechanistic studies of catalytic polyethylene chain growth in the presence of water. *Angew. Chem. Int. Ed.* **2006**, *45*, 6044–6046.

[162] Bauers, F. M.; Mecking, S. Aqueous Homo- and Copolymerization of Ethylene by Neutral Nickel(II) Complexes. *Macromolecules* **2001**, *34*, 1165–1171.

[163] Soula, R.; Novat, C.; Tomov, A.; Spitz, R.; Claverie, J.; Drujon, X.; Malinge, J.; Saudemont, T. Catalytic Polymerization of Ethylene in Emulsion. *Macromolecules* **2001**, *34*, 2022–2026.

[164] Bastero, A.; Franciò, G.; Leitner, W.; Mecking, S. Catalytic Ethylene Polymerisation in Carbon Dioxide as a Reaction Medium with Soluble Nickel(II) Catalysts. *Chem. Eur. J.* **2006**, *12*, 6110–6116.

[165] Guironnet, D.; Friedberger, T.; Mecking, S. Ethylene polymerization in supercritical carbon dioxide with binuclear nickel(II) catalysts. *Dalton Trans.* **2009**, 8929–8934.

[166] Bauers, F. M.; Mecking, S. High Molecular Mass Polyethylene Aqueous Latexes by Catalytic Polymerization. *Angew. Chem. Int. Ed.* **2001**, *40*, 3020–3022.

[167] Bauers, F. M.; Thomann, R.; Mecking, S. Submicron polyethylene particles from catalytic emulsion polymerization. *J. Am. Chem. Soc.* **2003**, *125*, 8838–8840.

[168] Wehrmann, P.; Zuideveld, M.; Thomann, R.; Mecking, S. Copolymerization of Ethylene with 1-Butene and Norbornene to Higher Molecular Weight Copolymers in Aqueous Emulsion. *Macromolecules* **2006**, *39*, 5995–6002.

[169] Wehrmann, P.; Mecking, S. Aqueous Dispersions of Polypropylene and Poly(1-butene) with Variable Microstructures Formed with Neutral Nickel(II) Complexes. *Macromolecules* **2006**, *39*, 5963–5964.

[170] Kolb, L.; Thomann, R.; Mecking, S. Multiphase Polymer Dispersions and Nanocomposites by Catalytic/Free Radical Emulsion Polymerization. *Macromol. Rapid Commun.* **2004**, *25*, 1824–1828.

[171] Monteil, V.; Stumbaum, J.; Thomann, R.; Mecking, S. Silica/Polyethylene Nanocomposite Particles from Catalytic Emulsion Polymerization. *Macromolecules* **2006**, *39*, 2056–2062.

[172] Jung, C.; Roo, T. de; Mecking, S. Conjugated polymer composite nanoparticles by rapid mixing. *Macromol. Rapid Commun.* **2014**, *35*, 2038–2042.

[173] Liu, Y.; Cheng, C.; Prud'homme, R. K.; Fox, R. O. Mixing in a multi-inlet vortex mixer (MIVM) for flash nano-precipitation. *Chem. Eng. Sci.* **2008**, *63*, 2829–2842.

[174] Monteil, V.; Wehrmann, P.; Mecking, S. A general route to very small polymer particles with controlled microstructures. *J. Am. Chem. Soc.* **2005**, *127*, 14568–14569.

[175] Kolb, L.; Monteil, V.; Thomann, R.; Mecking, S. Aqueous Dispersions of Extraordinarily Small Polyethylene Nanoparticles. *Angew. Chem. Int. Ed.* **2005**, *44*, 429–432.

[176] Korthals, B.; Göttker-Schnetmann, I.; Mecking, S. Nickel(II)–Methyl Complexes with Water-Soluble Ligands L [(salicylaldiminato-κ^2*N,O*)NiMe(L)] and Their Catalytic Properties in Disperse Aqueous Systems. *Organometallics* **2007**, *26*, 1311–1316.

[177] Göttker-Schnetmann, I.; Korthals, B.; Mecking, S. Water-soluble salicylaldiminato Ni(II)-methyl complexes: enhanced dissociative activation for ethylene polymerization with unprecedented nanoparticle formation. *J. Am. Chem. Soc.* **2006**, *128*, 7708–7709.

[178] Osichow, A.; Rabe, C.; Vogtt, K.; Narayanan, T.; Harnau, L.; Drechsler, M.; Ballauff, M.; Mecking, S. Ideal polyethylene nanocrystals. *J. Am. Chem. Soc.* **2013**, *135*, 11645–11650.

[179] Godin, A.; Göttker-Schnetmann, I.; Mecking, S. Nanocrystal Formation in Aqueous Insertion Polymerization. *Macromolecules* **2016**, *49*, 8825–8837.

[180] Weber, C. H.; Chiche, A.; Krausch, G.; Rosenfeldt, S.; Ballauff, M.; Harnau, L.; Göttker-Schnetmann, I.; Tong, Q.; Mecking, S. Single lamella nanoparticles of polyethylene. *Nano Lett.* **2007**, *7*, 2024–2029.

[181] Hristov, I. H.; Dekock, R. L.; Anderson, G. D. W.; Göttker-Schnetmann, I.; Mecking, S.; Ziegler, T. Possible side reactions due to water in emulsion polymerization by late transition metal complexes. 1. Water complexation and hydrolysis of the growing chain. *Inorg. Chem.* **2005**, *44*, 7806–7818.

[182] Berkefeld, A.; Mecking, S. Deactivation Pathways of Neutral Ni(II) Polymerization Catalysts. *J. Am. Chem. Soc.* **2009**, *131*, 1565–1574.

[183] Boucher-Jacobs, C.; Li, B.; Schroeder, C. M.; Guironnet, D. Solubility and activity of a phosphinosulfonate palladium catalyst in water with different surfactants. *Polym. Chem.* **2019**, *10*, 1988–1992.

[184] Zhang, D.; Guironnet, D.; Göttker-Schnetmann, I.; Mecking, S. Water-Soluble Complexes [(κ^2-P,O-Phosphinesulfonato)PdMe(L)] and Their Catalytic Properties. *Organometallics* **2009**, *28*, 4072–4078.

[185] Boucher-Jacobs, C.; Rabnawaz, M.; Katz, J. S.; Even, R.; Guironnet, D. Encapsulation of catalyst in block copolymer micelles for the polymerization of ethylene in aqueous medium. *Nat. Commun.* **2018**, *9*, 841.

[186] Godin, A.; Mecking, S. Aqueous Dispersions of Multiphase Polyolefin Particles. *Macromolecules* **2016**, *49*, 8296–8305.

[187] Tchernook, A.; Krumova, M.; Tölle, F. J.; Mülhaupt, R.; Mecking, S. Composites from Aqueous Polyethylene Nanocrystal/Graphene Dispersions. *Macromolecules* **2014**, *47*, 3017–3021.

[188] Tong, Q.; Schmidt, M. S.; Wittmann, V.; Mecking, S. Multivalent Carbohydrate-Functionalized Polymer Nanocrystals. *Biomacromolecules* **2019**, *20*, 294–304.

[189] Edidin, A. A.; Kurtz, S. M. Influence of mechanical behavior on the wear of 4 clinically relevant polymeric biomaterials in a hip simulator. *J. Arthroplasty* **2000**, *15*, 321–331.

[190] Kurtz, S. M. A Primer on UHMWPE. *UHMWPE biomaterials handbook*, 3rd ed.; Elsevier: Amsterdam, Boston, 2016.

[191] Firouzi, D.; Foucher, D. A.; Bougherara, H. Nylon-coated ultra high molecular weight polyethylene fabric for enhanced penetration resistance. *J. Appl. Polym. Sci.* **2014**, *131*, 40350.

[192] Brach Del Prever, E. M.; Bistolfi, A.; Bracco, P.; Costa, L. UHMWPE for arthroplasty: past or future? *J. Orthop. Traumatol.* **2009**, *10*, 1–8.

[193] Siskey, R.; Smelt, H.; Boon-Ceelen, K.; Persson, M. UHMWPE Homocomposites and Fibers. *UHMWPE Biomaterials Handbook*, 3er ed.; Elsevier: Amsterdam, 2016.

[194] Li, S.; Burstein, A. H. Ultra-high molecular weight polyethylene. The material and its use in total joint implants. *J. Bone Joint Surg. Am* **1994**, *76*, 1080–1090.

[195] Kurtz, S. M. From Ethylene Gas to UHMWPE Component: The Process of Producing Orthopedic Implants. *UHMWPE Biomaterials Handbook*, 3rd ed.; Elsevier: Amsterdam, 2016.

[196] Vega, J. F.; Rastogi, S.; Peters, G. W. M.; Meijer, H. E. H. Rheology and reptation of linear polymers. Ultrahigh molecular weight chain dynamics in the melt. *J. Rheol.* **2004**, *48*, 663–678.

[197] Pokrovskii, V. N. Dynamics of a Macromolecule in an Entangled System. *The Mesoscopic Theory of Polymer Dynamics*; Springer Netherlands: Dordrecht, 2010.

[198] Watanabe, H. Viscoelasticity and dynamics of entangled polymers. *Prog. Polym. Sci.* **1999**, *24*, 1253–1403.

[199] Forte, G.; Ronca, S. Synthesis of Disentangled Ultra-High Molecular Weight Polyethylene: Influence of Reaction Medium on Material Properties. *Int. J. Polym. Sci.* **2017**, 7431419.

[200] Huang, Y.-F.; Xu, J.-Z.; Zhang, Z.-C.; Xu, L.; Li, L.-B.; Li, J.-F.; Li, Z.-M. Melt processing and structural manipulation of highly linear disentangled ultrahigh molecular weight polyethylene. *Chem. Eng. J.* **2017**, *315*, 132–141.

[201] Bowden, A. E.; Bergström, J. Computer Modeling and Simulation of UHMWPE. *UHMWPE Biomaterials Handbook*, 3rd ed.; Elsevier: Amsterdam, 2016.

[202] Avanzini, A. Mechanical characterization and finite element modelling of cyclic stress–strain behaviour of ultra high molecular weight polyethylene. *Mater. Des.* **2008**, *29*, 330–343.

[203] Coates, G. W.; Hustad, P. D.; Reinartz, S. Catalysts for the Living Insertion Polymerization of Alkenes: Access to New Polyolefin Architectures Using Ziegler–Natta Chemistry. *Angew. Chem. Int. Ed.* **2002**, *41*, 2236–2257.

[204] Padmanabhan, S.; Sarma, K. R.; Rupak, K.; Sharma, S. Synthesis of ultra high molecular weight polyethylene: A differentiate material for specialty applications. *Mater. Sci. Eng., B* **2010**, *168*, 132–135.

[205] Makio, H.; Fujita, T. Development and application of FI catalysts for olefin polymerization: unique catalysis and distinctive polymer formation. *Acc. Chem. Res.* **2009**, *42*, 1532–1544.

[206] Matsui, S.; Fujita, T. FI Catalysts: super active new ethylene polymerization catalysts. *Catal. Today* **2001**, *66*, 63–73.

[207] Yu, S.-M.; Mecking, S. Extremely narrow-dispersed high molecular weight polyethylene from living polymerization at elevated temperatures with o-F substituted Ti enolatoimines. *J. Am. Chem. Soc.* **2008**, *130*, 13204–13205.

[208] Padmanabhan, S.; Sarma, K. R.; Sharma, S. Synthesis of Ultrahigh Molecular Weight Polyethylene Using Traditional Heterogeneous Ziegler–Natta Catalyst Systems. *Ind. Eng. Chem. Res.* **2009**, *48*, 4866–4871.

[209] GUR® UHMW-PE by Calanese. https://www.celanese.com/engineered-materials/products/GUR-UHMW-PE (accessed May 15, 2020).

[210] Han, K. S.; Wallace, J. F.; Truss, R. W.; Geil, P. H. Powder compaction, sintering, and rolling of ultra high molecular weight polyethylene and its composites. *J. Macromol. Sci. Phys. B* **1981**, *19*, 313–349.

[211] Halldin, G. W.; Kamel, I. L. Powder processing of ultra-high molecular weight polyethylene I. Powder characterization and compaction. *Polym. Eng. Sci.* **1977**, *17*, 21–26.

[212] Deplancke, T.; Lame, O.; Rousset, F.; Aguili, I.; Seguela, R.; Vigier, G. Diffusion versus Cocrystallization of Very Long Polymer Chains at Interfaces: Experimental Study of Sintering of UHMWPE Nascent Powder. *Macromolecules* **2014**, *47*, 197–207.

[213] Olley, R.; Hosier, I.; Bassett, D.; Smith, N. On morphology of consolidated UHMWPE resin in hip cups. *Biomaterials* **1999**, *20*, 2037–2046.

[214] Bastiaansena, C.; Meyer, H.; Lemstra, P. Memory effects in polyethylenes: influence of processing and crystallization history. *Polymer* **1990**, *31*, 1435–1440.

[215] Kurtz, S. M.; Zagorski, M. Packaging and Sterilization of UHMWPE. *UHMWPE Biomaterials Handbook*, 3rd ed.; Elsevier: Amsterdam, 2016.

[216] Bellare, A.; Kurtz, S. M. UHMWPE Biomaterials Handbook. *High Pressure Crystallized UHMWPEs*, 3rd ed.; Elsevier: Amsterdam, 2016.

[217] Geil, P. H.; Anderson, F. R.; Wunderlich, B.; Arakawa, T. Morphology of polyethylene crystallized from the melt under pressure. *J. Polym. Sci. A* **1964**, *2*, 3707–3720.

[218] Wunderlich, B.; Arakawa, T. Polyethylene crystallized from the melt under elevated pressure. *J. Polym. Sci. A* **1964**, *2*, 3697–3706.

[219] Wang, X.-Y.; Li, S.-Y.; Salovey, R. Processing of ultrahigh molecular weight polyethylene. *J. Appl. Polym. Sci.* **1988**, *35*, 2165–2171.

[220] Suh, N. P.; Mosleh, M.; Arinez, J. Tribology of polyethylene homocomposites. *Wear* **1998**, *214*, 231–236.

[221] DSM. Dyneema® Fiber. https://www.dsm.com/dyneema/en_GB/our-products/dyneema-fiber.html (accessed May 14, 2020).

[222] Honeywell. Spectra®. https://www.packagingcomposites-honeywell.com/spectra/ (accessed May 14, 2020).

[223] Vlasblom, M. P.; van Dingenen, J. The manufacture, properties and applications of high strength, high modulus polyethylene fibers. *Handbook of tensile properties of textile and technical fibres*; Woodhead Publishing: Oxford, 2009.

[224] Hine, P. J.; Ward, I. M.; Olley, R. H.; Bassett, D. C. The hot compaction of high modulus melt-spun polyethylene fibres. *J. Mater. Sci.* **1993**, *28*, 316–324.

[225] Cohen, Y.; Rein, D. M.; Vaykhansky, L. A novel composite based on ultra-high-molecular-weight polyethylene. *Compos. Sci. Technol.* **1997**, *57*, 1149–1154.

[226] Deng, M.; Shalaby, S. W. Properties of self-reinforced ultra-high-molecular-weight polyethylene composites. *Biomaterials* **1997**, *18*, 645–655.

[227] Puértolas, J. A.; Kurtz, S. M. UHMWPE Matrix Composites. *UHMWPE Biomaterials Handbook*, 3rd ed.; Elsevier, 2016.

[228] Wright, T. M.; Astion, D. J.; Bansal, M.; Rimnac, C. M.; Green, T.; Insall, J. N.; Robinson, R. P. Failure of carbon fiber-reinforced polyethylene total knee-replacement components. A report of two cases. *J. Bone Joint Surg. Am.* **1988**, *70*, 926–932.

[229] Puértolas, J. A.; Kurtz, S. M. Evaluation of carbon nanotubes and graphene as reinforcements for UHMWPE-based composites in arthroplastic applications: A review. *J. Mech. Behav. Biomed. Mater.* **2014**, *39*, 129–145.

[230] Maksimkin, A. V.; Kaloshkin, S. D.; Kaloshkina, M. S.; Gorshenkov, M. V.; Tcherdyntsev, V. V.; Ergin, K. S.; Shchetinin, I. V. Ultra-high molecular weight polyethylene reinforced with multi-walled carbon nanotubes: Fabrication method and properties. *J. Alloys Compd.* **2012**, *536*, 538-554.

[231] Kanagaraj, S.; Varanda, F. R.; Zhil'tsova, T. V.; Oliveira, M. S.; Simões, J. A. Mechanical properties of high density polyethylene/carbon nanotube composites. *Compos. Sci. Technol.* **2007**, *67*, 3071–3077.

[232] Lahiri, D.; Dua, R.; Zhang, C.; Socarraz-Novoa, I. de; Bhat, A.; Ramaswamy, S.; Agarwal, A. Graphene nanoplatelet-induced strengthening of ultrahigh molecular weight polyethylene and biocompatibility in vitro. *ACS Appl. Mater. Interfaces* **2012**, *4*, 2234–2241.

[233] Hu, H.; Zhang, G.; Xiao, L.; Wang, H.; Zhang, Q.; Zhao, Z. Preparation and electrical conductivity of graphene/ultrahigh molecular weight polyethylene composites with a segregated structure. *Carbon* **2012**, *50*, 4596–4599.

[234] Fang, L.; Gao, P.; Leng, Y. High strength and bioactive hydroxyapatite nano-particles reinforced ultrahigh molecular weight polyethylene. *Compos. Part B Eng.* **2007**, *38*, 345–351.

[235] Kang, X.; Zhang, W.; Yang, C. Mechanical properties study of micro- and nano-hydroxyapatite reinforced ultrahigh molecular weight polyethylene composites. *J. Appl. Polym. Sci.* **2016**, *133*, 42869.

[236] Muratoglu, O. K.; Bragdon, C. R.; O'Connor, D. O.; Jasty, M.; Harris, W. H.; Gul, R.; McGarry, F. Unified wear model for highly crosslinked ultra-high molecular weight polyethylenes (UHMWPE). *Biomaterials* **1999**, *20*, 1463–1470.

[237] Horii, F.; Zhu, Q.; Kitamaru, R.; Yamaoka, H. ^{13}C NMR study of radiation-induced crosslinking of linear polyethylene. *Macromolecules* **1990**, *23*, 977–981.

[238] Manley, M. T. Highly Cross-Linked and Annealed UHMWPE. *UHMWPE Biomaterials Handbook*, 3rd ed.; Elsevier: Amsterdam, 2016.

[239] Muratoglu, O. K.; Bragdon, C. R. Highly Cross-Linked and Melted UHMWPE. *UHMWPE Biomaterials Handbook*, 3rd ed.; Elsevier: Amsterdam, 2016.

[240] Rastogi, S.; Yao, Y.; Ronca, S.; Bos, J.; van der Eem, J. Unprecedented High-Modulus High-Strength Tapes and Films of Ultrahigh Molecular Weight Polyethylene via Solvent-Free Route. *Macromolecules* **2011**, *44*, 5558–5568.

[241] Schaller, R.; Feldman, K.; Smith, P.; Tervoort, T. A. High-Performance Polyethylene Fibers "Al Dente": Improved Gel-Spinning of Ultrahigh Molecular Weight Polyethylene Using Vegetable Oils. *Macromolecules* **2015**, *48*, 8877–8884.

[242] Smith, P.; Lemstra, P. J.; Booij, H. C. Ultradrawing of high-molecular-weight polyethylene cast from solution. II. Influence of initial polymer concentration. *J. Polym. Sci. Polym. Phys. Ed.* **1981**, *19*, 877–888.

[243] Smith, P.; Chanzy, H. D.; Rotzinger, B. P. Drawing of virgin ultrahigh molecular weight polyethylene: An alternative route to high strength/high modulus materials. *J. Mater. Sci.* **1987**, *22*, 523–531.

[244] Lippits, D. R.; Rastogi, S.; Höhne, G. W. H. Melting kinetics in polymers. *Phys. Rev. Lett.* **2006**, *96*, 218303.

[245] Smith, P. Entanglement concepts and drawing of polyethylene. *Macromolecules* **1983**, *16*, 1802–1803.

[246] Irvine, P. A.; Smith, P. Development of the axial Young's modulus with draw ratio of flexible-chain polymers. *Macromolecules* **1986**, *19*, 240–242.

[247] Smith, P.; Lemstra, P. J.; Pijpers, J. P. L. Tensile strength of highly oriented polyethylene. II. Effect of molecular weight distribution. *J. Polym. Sci. Polym. Phys. Ed.* **1982**, *20*, 2229–2241.

[248] Lemstra, P. J.; van Aerle, N. A. J. M.; Bastiaansen, C. W. M. Chain-Extended Polyethylene. *Polym. J.* **1987**, *19*, 85–98.

[249] Rastogi, S.; Spoelstra, A. B.; Goossens, J. G. P.; Lemstra, P. J. Chain Mobility in Polymer Systems: on the Borderline between Solid and Melt. 1. Lamellar Doubling during Annealing of Polyethylene. *Macromolecules* **1997**, *30*, 7880–7889.

[250] Smith, P.; Lemstra, P.; Kalb, B.; Pennings, A. Ultrahigh-strength polyethylene filaments by solution spinning and hot drawing. *Polym. Bull.* **1979**, *1*, 733–736.

[251] Romano, D.; Ronca, S.; Rastogi, S. A hemi-metallocene chromium catalyst with trimethylaluminum-free methylaluminoxane for the synthesis of disentangled ultra-high molecular weight polyethylene. *Macromol. Rapid Commun.* **2015**, *36*, 327–331.

[252] Rastogi, S.; Lippits, D. R.; Peters, G. W. M.; Graf, R.; Yao, Y.; Spiess, H. W. Heterogeneity in polymer melts from melting of polymer crystals. *Nat. Mater.* **2005**, *4*, 635–641.

[253] Pandey, A.; Champouret, Y.; Rastogi, S. Heterogeneity in the Distribution of Entanglement Density during Polymerization in Disentangled Ultrahigh Molecular Weight Polyethylene. *Macromolecules* **2011**, *44*, 4952–4960.

[254] Lippits, D. R.; Rastogi, S.; Talebi, S.; Bailly, C. Formation of Entanglements in Initially Disentangled Polymer Melts. *Macromolecules* **2006**, *39*, 8882–8885.

[255] Rastogi, S.; R. Lippits, D.; W. H. Höhne, G.; Mezari, B.; C. M. M. Magusin, P. The role of the amorphous phase in melting of linear UHMW-PE; implications for chain dynamics. *J. Phys.: Condens. Matter* **2007**, *19*, 205122.

[256] Ronca, S.; Forte, G.; Ailianou, A.; Kornfield, J. A.; Rastogi, S. Direct Route to Colloidal UHMWPE by Including LLDPE in Solution during Homogeneous Polymerization of Ethylene. *ACS Macro Lett.* **2012**, *1*, 1116–1120.

[257] Tervoort, T. A.; Visjager, J.; Smith, P. On Abrasive Wear of Polyethylene. *Macromolecules* **2002**, *35*, 8467–8471.

[258] Barham, P. J. Crystallization and Morphology of Semicrystalline Polymers. *Materials science and technology (Cahn, R. W.; ed.)*; Wiley-VCH: Weinheim, 2006.

[259] Mandelkern, L. The Relation between Structure and Properties of Crystalline Polymers. *Polym. J.* **1985**, *17*, 337–350.

[260] Burkhardt, G.; Hüsgen, U.; Kalwa, M.; Pötsch, G.; Schwenzer, C. Plastics Processing, 1. Processing of Thermoplastics. *Ullmann's Encyclopedia of Industrial Chemistry*; Wiley-VCH: Weinheim, 2001.

[261] Banks, W.; Hay, J. N.; Sharples, A.; Thomson, G. The crystallization of polyethylene II. *Polymer* **1964**, *5*, 163–175.

[262] Banks, W.; Gordon, M.; roe, R.-J.; Sharples, A. The crystallization of polyethylene I. *Polymer* **1963**, *4*, 61–74.

[263] Reiter, G.; Strobl, G. R. Progress in Understanding of Polymer Crystallization; Springer: Berlin, Heidelberg, 2007.

[264] Keller, A. A note on single crystals in polymers: Evidence for a folded chain configuration. *Philos. Mag.* **1957**, *2*, 1171–1175.

[265] Ungar, G.; Stejny, J.; Keller, A.; Bidd, I.; Whiting, M. C. The crystallization of ultralong normal paraffins: the onset of chain folding. *Science* **1985**, *229*, 386–389.

[266] Muthukumar, M. Shifting Paradigms in Polymer Crystallization. *Progress in Understanding of Polymer Crystallization*; Springer: Berlin, Heidelberg, 2007.

[267] Damasceno, P. F.; Engel, M.; Glotzer, S. C. Predictive self-assembly of polyhedra into complex structures. *Science* **2012**, *337*, 453–457.

[268] Yoreo, J. de Crystal nucleation: more than one pathway. *Nat. Mater.* **2013**, *12*, 284–285.

[269] Ortmann, P.; Trzaskowski, J.; Krumova, M.; Mecking, S. Precise Microstructure Self-Stabilized Polymer Nanocrystals. *ACS Macro Lett.* **2013**, *2*, 125–127.

[270] Scheinhardt, B.; Trzaskowski, J.; Baier, M. C.; Stempfle, B.; Oppermann, A.; Wöll, D.; Mecking, S. Anisotropic Polyethylene Nanocrystals Labeled with a Single Fluorescent Dye Molecule: Toward Monitoring of Nanoparticle Orientation. *Macromolecules* **2013**, *46*, 7902–7910.

[271] Yan, L.; Rank, C.; Mecking, S.; Winey, K. I. Gyroid and Other Ordered Morphologies in Single-Ion Conducting Polymers and Their Impact on Ion Conductivity. *J. Am. Chem. Soc.* **2020**, *142*, 857–866.

[272] Rank, C.; Yan, L.; Mecking, S.; Winey, K. I. Periodic Polyethylene Sulfonates from Polyesterification: Bulk and Nanoparticle Morphologies and Ionic Conductivities. *Macromolecules* **2019**, 52, 8466–8475.

[273] Kryuchkov, V. A.; Daigle, J.-C.; Skupov, K. M.; Claverie, J. P.; Winnik, F. M. Amphiphilic Polyethylenes Leading to Surfactant-Free Thermoresponsive Nanoparticles. *J. Am. Chem. Soc.* **2010**, *132*, 15573–15579.

[274] Pitet, L. M.; Hillmyer, M. A. Carboxy-Telechelic Polyolefins by ROMP Using Maleic Acid as a Chain Transfer Agent. *Macromolecules* **2011**, *44*, 2378–2381.

[275] German, I.; Kelhifi, W.; Norsic, S.; Boisson, C.; D'Agosto, F. Telechelic polyethylene from catalyzed chain-growth polymerization. *Angew. Chem. Int. Ed.* **2013**, *52*, 3438–3441.

[276] Jian, Z.; Falivene, L.; Boffa, G.; Sánchez, S. O.; Caporaso, L.; Grassi, A.; Mecking, S. Direct Synthesis of Telechelic Polyethylene by Selective Insertion Polymerization. *Angew. Chem. Int. Ed.* **2016**, *55*, 14378–14383.

[277] Witt, T.; Häußler, M.; Kulpa, S.; Mecking, S. Chain Multiplication of Fatty Acids to Precise Telechelic Polyethylene. *Angew. Chem. Int. Ed.* **2017**, *56*, 7589–7594.

[278] Rank, C.; Häußler, M.; Rathenow, P.; King, M.; Globisch, C.; Peter, C.; Mecking, S. Anisotropic Extended-Chain Polymer Nanocrystals. *Macromolecules* **2019**, *52*, 6142–6148.

[279] Ruiz de Ballesteros, O.; Auriemma, F.; Guerra, G.; Corradini, P. Molecular Organization in the Pseudo-hexagonal Crystalline Phase of Ethylene–Propylene Copolymers. *Macromolecules* **1996**, *29*, 7141–7148.

[280] Inci, B.; Lieberwirth, I.; Steffen, W.; Mezger, M.; Graf, R.; Landfester, K.; Wagener, K. B. Decreasing the Alkyl Branch Frequency in Precision Polyethylene: Effect of Alkyl Branch Size on Nanoscale Morphology. *Macromolecules* **2012**, *45*, 3367–3376.

[281] Bärenwald, R.; Goerlitz, S.; Godehardt, R.; Osichow, A.; Tong, Q.; Krumova, M.; Mecking, S.; Saalwächter, K. Local Flips and Chain Motion in Polyethylene Crystallites: A Comparison of Melt-Crystallized Samples, Reactor Powders, and Nanocrystals. *Macromolecules* **2014**, *47*, 5163–5173.

[282] Rochette, C. N.; Rosenfeldt, S.; Henzler, K.; Polzer, F.; Ballauff, M.; Tong, Q.; Mecking, S.; Drechsler, M.; Narayanan, T.; Harnau, L. Annealing of Single Lamella Nanoparticles of Polyethylene. *Macromolecules* **2011**, *44*, 4845–4851.

[283] Basu, N.; Osichow, A.; Mecking, S.; Reiter, G. Morphological changes during annealing of polyethylene nanocrystals. *Eur. Phys. J. E* **2012**, *35*, 1–12.

[284] Tong, Q.; Mecking, S. Submicron films prepared from aqueous dispersions of nanoscale polymer crystals. *J. Polym. Sci., Part A: Polym. Chem.* **2009**, *47*, 6420–6432.

[285] Organ, S. J.; Keller, A. Solution crystallization of polyethylene at high temperatures. *J. Mater. Sci.* **1985**, *20*, 1571–1585.

[286] Keller, A. Polymer crystals. *Rep. Prog. Phys.* **1968**, *31*, 623–704.

[287] Bassett, D. C.; Keller, A. On the habits of polyethylene crystals. *Philos. Mag.* **1962**, *7*, 1553–1584.

[288] Toda, A. Growth mode and curved lateral habits of polyethylene single crystals. *Faraday Disc.* **1993**, *95*, 129.

[289] Ungar, G.; Putra, E. G. R.; Silva, D. S. M. de; Shcherbina, M. A.; Waddon, A. J. The Effect of Self-Poisoning on Crystal Morphology and Growth Rates. *Advances in Polymer Science*; Springer: Berlin, Heidelberg, 2005.

[290] Barham, P. J.; Chivers, R. A.; Keller, A.; Martinez-Salazar, J.; Organ, S. J. The supercooling dependence of the initial fold length of polyethylene crystallized from the melt: unification of melt and solution crystallization. *J. Mater. Sci.* **1985**, *20*, 1625–1630.

[291] Martinez-Salazar, J.; Barham, P. J.; Keller, A. Studies on polyethylene crystallized at unusually high supercoolings: Fold length, habit, growth rate, epitaxy. *J. Polym. Sci. Polym. Phys. Ed.* **1984**, *22*, 1085–1096.

[292] Jones, R. L.; Kumar, S. K.; Ho, D. L.; Briber, R. M.; Russell, T. P. Chain conformation in ultrathin polymer films. *Nature* **1999**, *400*, 146–149.

[293] Frank; Rao; Despotopoulou; Pease; Hinsberg; Miller; Rabolt Structure in Thin and Ultrathin Spin-Cast Polymer Films. *Science* **1996**, *273*, 912–915.

[294] Tong, Q.; Krumova, M.; Mecking, S. Crystalline Polymer Ultrathin Films from Mesoscopic Precursors. *Angew. Chem. Int. Ed.* **2008**, *47*, 4509–4511.

[295] Myers, D. *Surfactant science and technology*, 3rd ed.; Wiley-Interscience: Hoboken, NJ, 2006.

[296] Miszta, K.; Graaf, J. de; Bertoni, G.; Dorfs, D.; Brescia, R.; Marras, S.; Ceseracciu, L.; Cingolani, R.; van Roij, R.; Dijkstra, M.; Manna, L. Hierarchical self-assembly of suspended branched colloidal nanocrystals into superlattice structures. *Nat. Mater.* **2011**, *10*, 872–876.

[297] Wang, T.; Zhuang, J.; Lynch, J.; Chen, O.; Wang, Z.; Wang, X.; LaMontagne, D.; Wu, H.; Wang, Z.; Cao, Y. C. Self-assembled colloidal superparticles from nanorods. *Science* **2012**, *338*, 358–363.

[298] Qiu, H.; Hudson, Z. M.; Winnik, M. A.; Manners, I. Micelle assembly. Multidimensional hierarchical self-assembly of amphiphilic cylindrical block comicelles. *Science* **2015**, *347*, 1329–1332.

[299] Wang, X.; Guerin, G.; Wang, H.; Wang, Y.; Manners, I.; Winnik, M. A. Cylindrical block copolymer micelles and co-micelles of controlled length and architecture. *Science* **2007**, *317*, 644–647.

[300] Gilroy, J. B.; Gädt, T.; Whittell, G. R.; Chabanne, L.; Mitchels, J. M.; Richardson, R. M.; Winnik, M. A.; Manners, I. Monodisperse cylindrical micelles by crystallization-driven living self-assembly. *Nat. Chem.* **2010**, *2*, 566–570.

[301] Qiu, H.; Gao, Y.; Boott, C. E.; Gould, O. E. C.; Harniman, R. L.; Miles, M. J.; Webb, S. E. D.; Winnik, M. A.; Manners, I. Uniform patchy and hollow rectangular platelet micelles from crystallizable polymer blends. *Science* **2016**, *352*, 697–701.

[302] He, X.; Hsiao, M.-S.; Boott, C. E.; Harniman, R. L.; Nazemi, A.; Li, X.; Winnik, M. A.; Manners, I. Two-dimensional assemblies from crystallizable homopolymers with charged termini. *Nat. Mater.* **2017**, *16*, 481–488.

[303] Warren, N. J.; Armes, S. P. Polymerization-induced self-assembly of block copolymer nano-objects via RAFT aqueous dispersion polymerization. *J. Am. Chem. Soc.* **2014**, *136*, 10174–10185.

[304] Boott, C. E.; Gwyther, J.; Harniman, R. L.; Hayward, D. W.; Manners, I. Scalable and uniform 1D nanoparticles by synchronous polymerization, crystallization and self-assembly. *Nat. Chem.* **2017**, *9*, 785–792.

[305] Dou, H.; Li, M.; Qiao, Y.; Harniman, R.; Li, X.; Boott, C. E.; Mann, S.; Manners, I. Higher-order assembly of crystalline cylindrical micelles into membrane-extendable colloidosomes. *Nat. Commun.* **2017**, *8*, 426.

[306] Thompson, K. L.; Williams, M.; Armes, S. P. Colloidosomes: synthesis, properties and applications. *J. Colloid Interface Sci.* **2015**, *447*, 217–228.

[307] Finnegan, J. R.; He, X.; Street, S. T. G.; Garcia-Hernandez, J. D.; Hayward, D. W.; Harniman, R. L.; Richardson, R. M.; Whittell, G. R.; Manners, I. Extending the Scope of "Living" Crystallization-Driven Self-Assembly: Well-Defined 1D Micelles and Block Comicelles from Crystallizable Polycarbonate Block Copolymers. *J. Am. Chem. Soc.* **2018**, *140*, 17127–17140.

[308] He, Y.; Eloi, J.-C.; Harniman, R. L.; Richardson, R. M.; Whittell, G. R.; Mathers, R. T.; Dove, A. P.; O'Reilly, R. K.; Manners, I. Uniform Biodegradable Fiber-Like Micelles and Block Comicelles via "Living" Crystallization-Driven Self-Assembly of Poly(l-lactide) Block Copolymers: The Importance of Reducing Unimer Self-Nucleation via Hydrogen Bond Disruption. *J. Am. Chem. Soc.* **2019**, *141*, 19088–19098.

[309] Schmelz, J.; Schedl, A. E.; Steinlein, C.; Manners, I.; Schmalz, H. Length control and block-type architectures in worm-like micelles with polyethylene cores. *J. Am. Chem. Soc.* **2012**, *134*, 14217–14225.

[310] Jin, X.-H.; Price, M. B.; Finnegan, J. R.; Boott, C. E.; Richter, J. M.; Rao, A.; Menke, S. M.; Friend, R. H.; Whittell, G. R.; Manners, I. Long-range exciton transport in conjugated polymer nanofibers prepared by seeded growth. *Science* **2018**, *360*, 897–900.

[311] Schmalz, H.; Schmelz, J.; Drechsler, M.; Yuan, J.; Walther, A.; Schweimer, K.; Mihut, A. M. Thermo-Reversible Formation of Wormlike Micelles with a Microphase-Separated Corona from a Semicrystalline Triblock Terpolymer. *Macromolecules* **2008**, *41*, 3235–3242.

[312] Schmelz, J.; Karg, M.; Hellweg, T.; Schmalz, H. General pathway toward crystalline-core micelles with tunable morphology and corona segregation. *ACS Nano* **2011**, 5, 9523–9534.

[313] Gröschel, A. H.; Walther, A.; Löbling, T. I.; Schacher, F. H.; Schmalz, H.; Müller, A. H. E. Guided hierarchical co-assembly of soft patchy nanoparticles. *Nature* **2013**, *503*, 247–251.

[314] Li, X.; Wolanin, P. J.; MacFarlane, L. R.; Harniman, R. L.; Qian, J.; Gould, O. E. C.; Dane, T. G.; Rudin, J.; Cryan, M. J.; Schmaltz, T.; Frauenrath, H.; Winnik, M. A.; Faul, C. F. J.; Manners, I. Uniform electroactive fibre-like micelle nanowires for organic electronics. *Nat. Commun.* **2017**, *8*, 15909.

[315] Tao, D.; Feng, C.; Cui, Y.; Yang, X.; Manners, I.; Winnik, M. A.; Huang, X. Monodisperse Fiber-like Micelles of Controlled Length and Composition with an Oligo(p-phenylenevinylene) Core via "Living" Crystallization-Driven Self-Assembly. *J. Am. Chem. Soc.* **2017**, *139*, 7136–7139.

[316] Shin, S.; Menk, F.; Kim, Y.; Lim, J.; Char, K.; Zentel, R.; Choi, T.-L. Living Light-Induced Crystallization-Driven Self-Assembly for Rapid Preparation of Semiconducting Nanofibers. *J. Am. Chem. Soc.* **2018**, *140*, 6088–6094.

[317] Tao, D.; Wang, Z.; Huang, X.; Tian, M.; Lu, G.; Manners, I.; Winnik, M. A.; Feng, C. Continuous and Segmented Semiconducting Fiber-like Nanostructures with Spatially Selective Functionalization by Living Crystallization-Driven Self-Assembly. *Angew. Chem. Int. Ed.* **2020**, *59*, 8232–8239.

[318] Morin, J.-F.; Leclerc, M. *Design and synthesis of conjugated polymers*; Wiley-VCH: Weinheim, 2010.

[319] Haider, T. P.; Völker, C.; Kramm, J.; Landfester, K.; Wurm, F. R. Plastics of the Future? The Impact of Biodegradable Polymers on the Environment and on Society. *Angew. Chem. Int. Ed.* **2019**, *58*, 50–62.

[320] Vroman, I.; Tighzert, L. Biodegradable Polymers. *Materials* **2009**, *2*, 307–344.

[321] Blanazs, A.; Armes, S. P.; Ryan, A. J. Self-Assembled Block Copolymer Aggregates: From Micelles to Vesicles and their Biological Applications. *Macromol. Rapid Commun.* **2009**, *30*, 267–277.

[322] Schacher, F. H.; Rupar, P. A.; Manners, I. Functional block copolymers: nanostructured materials with emerging applications. *Angew. Chem. Int. Ed.* **2012**, *51*, 7898–7921.

[323] Gröschel, A. H.; Müller, A. H. E. Self-assembly concepts for multicompartment nanostructures. *Nanoscale* **2015**, *7*, 11841–11876.

[324] Lu, W.; Lieber, C. M. Nanoelectronics from the bottom up. *Nat. Mater.* **2007**, *6*, 841–850.

[325] Dreyer, A.; Feld, A.; Kornowski, A.; Yilmaz, E. D.; Noei, H.; Meyer, A.; Krekeler, T.; Jiao, C.; Stierle, A.; Abetz, V.; Weller, H.; Schneider, G. A. Organically linked iron oxide nanoparticle supercrystals with exceptional isotropic mechanical properties. *Nat. Mater.* **2016**, *15*, 522–528.

[326] Zhou, S.; Huo, D.; Goines, S.; Yang, T. H.; Lyu, Z.; Zhao, M.; Gilroy, K. D.; Wu, Y.; Hood, Z. D.; Xie, M.; Xia, Y. Enabling Complete Ligand Exchange on the Surface of Gold Nanocrystals through the Deposition and Then Etching of Silver. *J. Am. Chem. Soc.* **2018**, *140*, 11898–11901.

[327] Natalio, F.; Corrales, T. P.; Panthofer, M.; Schollmeyer, D.; Lieberwirth, I.; Muller, W. E.; Kappl, M.; Butt, H. J.; Tremel, W. Flexible minerals: self-assembled calcite spicules with extreme bending strength. *Science* **2013**, *339*, 1298–1302.

[328] Nie, Z.; Petukhova, A.; Kumacheva, E. Properties and emerging applications of self-assembled structures made from inorganic nanoparticles. *Nat. Nanotechnol.* **2010**, 5, 15–25.

[329] Grzelczak, M.; Vermant, J.; Furst, E. M.; Liz-Marzan, L. M. Directed self-assembly of nanoparticles. *ACS Nano* **2010**, *4*, 3591–3605.

[330] Trepka, B.; Erler, P.; Selzer, S.; Kollek, T.; Boldt, K.; Fonin, M.; Nowak, U.; Wolf, D.; Lubk, A.; Polarz, S. Nanomorphology Effects in Semiconductors with Native Ferromagnetism: Hierarchical Europium (II) Oxide Tubes Prepared via a Topotactic Nanostructure Transition. *Adv. Mater.* **2018**, *30*, 1703612.

[331] Whittell, G. R.; Hager, M. D.; Schubert, U. S.; Manners, I. Functional soft materials from metallopolymers and metallosupramolecular polymers. *Nat. Mater.* **2011**, *10*, 176–188.

[332] Rothfuss, H.; Knöfel, N. D.; Roesky, P. W.; Barner-Kowollik, C. Single-Chain Nanoparticles as Catalytic Nanoreactors. *J. Am. Chem. Soc.* **2018**, *140*, 5875–5881.

[333] Ouchi, M.; Badi, N.; Lutz, J. F.; Sawamoto, M. Single-chain technology using discrete synthetic macromolecules. *Nat. Chem.* **2011**, *3*, 917–924.

[334] Lyon, C. K.; Prasher, A.; Hanlon, A. M.; Tuten, B. T.; Tooley, C. A.; Frank, P. G.; Berda, E. B. A brief user's guide to single-chain nanoparticles. *Polym. Chem.* **2015**, *6*, 181–197.

[335] Schmidt, B. V. K. J.; Fechler, N.; Falkenhagen, J.; Lutz, J. F. Controlled folding of synthetic polymer chains through the formation of positionable covalent bridges. *Nat. Chem.* **2011**, *3*, 234–238.

[336] Wen, J. G.; Zhang, J.; Zhang, Y.; Yang, Y. F.; Zhao, H. Y. Controlled self-assembly of amphiphilic monotailed single-chain nanoparticles. *Polym. Chem.* **2014**, *5*, 4032–4038.

[337] Hanlon, A. M.; Lyon, C. K.; Berda, E. B. What Is Next in Single-Chain Nanoparticles? *Macromolecules* **2016**, *49*, 2–14.

[338] Altintas, O.; Barner-Kowollik, C. Single-Chain Folding of Synthetic Polymers: A Critical Update. *Macromol. Rapid Commun.* **2016**, *37*, 29–46.

[339] Frisch, H.; Tuten, B. T.; Barner-Kowollik, C. Macromolecular Superstructures: A Future Beyond Single Chain Nanoparticles. *Isr. J. Chem.* **2020**, *60*, 86–99.

[340] Gladysz, J. A. Ponytails - Structural and Electronic Considerations. *Handbook of Fluorous Chemistry*; John Wiley & Sons: Weinheim, 2004.

[341] Dalvi, V. H.; Rossky, P. J. Molecular origins of fluorocarbon hydrophobicity. *Proc. Natl. Acad. Sci.* **2010**, *107*, 13603–13607.

[342] Frisch, H.; Menzel, J. P.; Bloesser, F. R.; Marschner, D. E.; Mundsinger, K.; Barner-Kowollik, C. Photochemistry in Confined Environments for Single-Chain Nanoparticle Design. *J. Am. Chem. Soc.* **2018**, *140*, 9551–9557.

[343] Hanlon, A. M.; Chen, R.; Rodriguez, K. J.; Willis, C.; Dickinson, J. G.; Cashman, M.; Berda, E. B. Scalable Synthesis of Single-Chain Nanoparticles under Mild Conditions. *Macromolecules* **2017**, *50*, 2996–3003.

[344] Vigderman, L.; Khanal, B. P.; Zubarev, E. R. Functional gold nanorods: synthesis, self-assembly, and sensing applications. *Adv. Mater.* **2012**, *24*, 4811-41, 5014.

[345] Udayabhaskararao, T.; Altantzis, T.; Houben, L.; Coronado-Puchau, M.; Langer, J.; Popovitz-Biro, R.; Liz-Marzan, L. M.; Vukovic, L.; Kral, P.; Bals, S.; Klajn, R. Tunable porous nanoallotropes prepared by post-assembly etching of binary nanoparticle superlattices. *Science* **2017**, *358*, 514–518.

[346] Jana, N. R. Shape effect in nanoparticle self-assembly. *Angew. Chem. Int. Ed.* **2004**, *43*, 1536–1540.

[347] Ye, X.; Jin, L.; Caglayan, H.; Chen, J.; Xing, G.; Zheng, C.; Doan-Nguyen, V.; Kang, Y.; Engheta, N.; Kagan, C. R.; Murray, C. B. Improved Size-Tunable Synthesis of Monodisperse Gold Nanorods through the Use of Aromatic Additives. *ACS Nano* **2012**, *6*, 2804–2817.

[348] Walsh, D. J.; Guironnet, D. Macromolecules with programmable shape, size, and chemistry. *Proc. Natl. Acad. Sci.* **2019**, *116*, 1538–1542.

[349] Göttker-Schnetmann, I.; Mecking, S. A Practical Synthesis of [(tmeda)Ni(CH_3)$_2$], Isotopically Labeled [(tmeda)Ni($^{13}CH_3$)$_2$], and Neutral Chelated-Nickel Methyl Complexes. *Organometallics* **2020**, *39*, 3433–3440.

[350] Herde, J. L.; Lambert, J. C.; Senoff, C. V.; Cushing, M. A. Cyclooctene and 1,5-Cyclooctadiene Complexes of Iridium(I). *Inorg. Synth.* **1974**, *15*, 18–20.

[351] Schindelin, J.; Arganda-Carreras, I.; Frise, E.; Kaynig, V.; Longair, M.; Pietzsch, T.; Preibisch, S.; Rueden, C.; Saalfeld, S.; Schmid, B.; Tinevez, J.-Y.; White, D. J.; Hartenstein, V.; Eliceiri, K.; Tomancak, P.; Cardona, A. Fiji: an open-source platform for biological-image analysis. *Nat. Methods* **2012**, *9*, 676.

[352] Schneider, C. A.; Rasband, W. S.; Eliceiri, K. W. NIH Image to ImageJ: 25 years of image analysis. *Nat. Methods* **2012**, *9*, 671.

[353] Rueden, C. T.; Schindelin, J.; Hiner, M. C.; DeZonia, B. E.; Walter, A. E.; Arena, E. T.; Eliceiri, K. W. ImageJ2: ImageJ for the next generation of scientific image data. *BMC Bioinf.* **2017**, *18*, 529.

[354] Ghosh, S. K.; Ojeda, A. S.; Guerrero-Leal, J.; Bhuvanesh, N.; Gladysz, J. A. New media for classical coordination chemistry: phase transfer of Werner and related polycations into highly nonpolar fluorous solvents. *Inorg. Chem.* **2013**, *52*, 9369–9378.

[355] Ishiyama, T.; Takagi, J.; Ishida, K.; Miyaura, N.; Anastasi, N. R.; Hartwig, J. F. Mild Iridium-Catalyzed Borylation of Arenes. High Turnover Numbers, Room Temperature Reactions, and Isolation of a Potential Intermediate. *J. Am. Chem. Soc.* **2002**, *124*, 390–391.

[356] Spek, A. L. PLATON SQUEEZE: a tool for the calculation of the disordered solvent contribution to the calculated structure factors. *Acta Crystallogr., Sect. C: Cryst. Struct. Commun.* **2015**, *71*, 9–18.

[357] Sheldrick, G. M. SHELXT - integrated space-group and crystal-structure determination. *Acta Crystallogr., Sect. A: Found. Crystallogr.* **2015**, *71*, 3–8.

[358] Dolomanov, O. V.; Bourhis, L. J.; Gildea, R. J.; Howard, J. A. K.; Puschmann, H. OLEX2: a complete structure solution, refinement and analysis program. *J. Appl. Crystallogr.* **2009**, *42*, 339–341.

[359] Sheldrick, G. M. Crystal structure refinement with SHELXL. *Acta Crystallogr., Sect. C: Cryst. Struct. Commun.* **2015**, *71*, 3–8.

[360] Rees, B.; Jenner, L.; Yusupov, M. Bulk-solvent correction in large macromolecular structures. *Acta Crystallogr., Sect. D: Biol. Crystallogr.* **2005**, *61*, 1299–1301.

[361] Farrugia, L. J. ORTEP-3 for Windows - a version of ORTEP-III with a Graphical User Interface (GUI). *J. Appl. Crystallogr.* **1997**, *30*, 565.

[362] Whiteley, K. S. Polyethylene. *Ullmann's Encyclopedia of Industrial Chemistry*; Wiley-VCH: Weinheim, 2012.

[363] Kainz, S.; Koch, D.; Leitner, W.; Baumann, W. Perfluoroalkyl-Substituted Arylphosphanes as Ligands for Homogenous Catalysis in Supercritical Carbon Dioxide. *Angew. Chem. Int. Ed.* **1997**, *36*, 1628–1630.

[364] Hu, Y.; Chen, W.; Osuna, A. M. B.; Xiao, J.; Stuart, A. M.; Hope, E. G. Rapid hydroformylation of alkyl acrylates in supercritical CO2. *Chem. Commun.* **2001**, 725–726.

[365] Gladysz, J. A.; Corrêa da Costa, R. Strategies for the Recovery of Fluorous Catalysts and Reagents - Design and Evaluation. *Handbook of Fluorous Chemistry*; Wiley-VCH: Weinheim, 2004.

[366] Morton, D.; Leach, S.; Cordier, C.; Warriner, S.; Nelson, A. Synthesis of natural-product-like molecules with over eighty distinct scaffolds. *Angew. Chem. Int. Ed.* **2009**, *48*, 104–109.

[367] Leach, S. G.; Cordier, C. J.; Morton, D.; McKiernan, G. J.; Warriner, S.; Nelson, A. A fluorous-tagged linker from which small molecules are released by ring-closing metathesis. *J. Org. Chem.* **2008**, *73*, 2753–2759.

[368] Lim, J.; Lee, S. S.; Ying, J. Y. Silica-supported catalysts for ring-closing metathesis: effects of linker group and microenvironment on recyclability. *Chem. Commun.* **2008**, 4312–4314.

[369] Dinh, L. V.; Gladysz, J. A. "Catalyst-on-a-tape"-Teflon: a new delivery and recovery method for homogeneous fluorous catalysts. *Angew. Chem. Int. Ed.* **2005**, *44*, 4095–4097.

[370] Xi, Z.; Bazzi, H. S.; Gladysz, J. A. Activation of Single-Component Nickel(II) Polyethylene Catalysts via Phase Transfer of Fluorous Phosphine Ligands. *J. Am. Chem. Soc.* **2015**, *137*, 10930–10933.

[371] Ravishankara, A. R.; Solomon, S.; Turnipseed, A. A.; Warren, R. F. Atmospheric lifetimes of long-lived halogenated species. *Science* **1993**, *259*, 194–199.

[372] Tzschucke, C. C.; Markert, C.; Glatz, H.; Bannwarth, W. Fluorous biphasic catalysis without perfluorinated solvents: application to Pd-mediated Suzuki and Sonogashira couplings. *Angew. Chem. Int. Ed.* **2002**, *41*, 4500–4503.

[373] Wende, M.; Meier, R.; Gladysz, J. A. Fluorous catalysis without fluorous solvents: a friendlier catalyst recovery/recycling protocol based upon thermomorphic properties and liquid/solid phase separation. *J. Am. Chem. Soc.* **2001**, *123*, 11490–11491.

[374] Solyntjes, S.; Neumann, B.; Stammler, H.-G.; Ignat'ev, N.; Hoge, B. Bismuth Perfluoroalkylphosphinates: New Catalysts for Application in Organic Syntheses. *Chem. Eur. J.* **2017**, *23*, 1568–1575.

[375] Mundil, R.; Sokolohorskyj, A.; Hošek, J.; Cvačka, J.; Císařová, I.; Kvíčala, J.; Merna, J. Nickel and palladium complexes with fluorinated alkyl substituted α-diimine ligands for living/controlled olefin polymerization. *Polym. Chem.* **2018**, *9*, 1234–1248.

[376] Jiao, H.; Le Stang, S.; Soós, T.; Meier, R.; Kowski, K.; Rademacher, P.; Jafarpour, L.; Hamard, J.-B.; Nolan, S. P.; Gladysz, J. A. How to insulate a reactive site from a perfluoroalkyl group: photoelectron spectroscopy, calorimetric, and computational studies of long-range electronic effects in fluorous phosphines $P((CH_2)_m(CF_2)_7CF_3)_3$. *J. Am. Chem. Soc.* **2002**, *124*, 1516–1523.

[377] Mu, H.; Pan, L.; Song, D.; Li, Y. Neutral Nickel Catalysts for Olefin Homo- and Copolymerization: Relationships between Catalyst Structures and Catalytic Properties. *Chem. Rev.* **2015**, *115*, 12091–12137.

[378] Radlauer, M. R.; Buckley, A. K.; Henling, L. M.; Agapie, T. Bimetallic Coordination Insertion Polymerization of Unprotected Polar Monomers: Copolymerization of Amino Olefins and Ethylene by Dinickel Bisphenoxyiminato Catalysts. *J. Am. Chem. Soc.* **2013**, *135*, 3784–3787.

[379] Hansch, C.; Leo, A.; Taft, R. W. A Survey of Hammett Substituent Constants and Resonance and Field Parameters. *Chem. Rev.* **1991**, *91*, 165–195.

[380] Vaidya, T.; Klimovica, K.; LaPointe, A. M.; Keresztes, I.; Lobkovsky, E. B.; Daugulis, O.; Coates, G. W. Secondary Alkene Insertion and Precision Chain-Walking: A New Route to Semicrystalline "Polyethylene" from α-Olefins by Combining Two Rare Catalytic Events. *J. Am. Chem. Soc.* **2014**, *136*, 7213–7216.

[381] Osichow, A. Katalysatoren für die Erzeugung idealer Polyethylen-Nanokristalle. *Dissertation, University of Konstanz* **2014**.

[382] Ortin, A.; del Hierro, P. Analysis of Ultra-High Molecular Weight Polyethylene (UHMWPE) by GPC-IR and Viscometry. *GPC Conference*; Washington D.C., USA, 2015.

[383] Frijns-Bruls, T.; Ortin, A.; Weusten, J.; Geladé, E. Studies on the Application of Filter-Based IR Detector for Polyolefin Characterization with HT-SEC. *Macromol. Symp.* **2015**, *356*, 87–94.

[384] Frijns-Bruls, T.; Ortin, A.; Weusten, J.; Geladé, E. Studies on the use of filter-based IR detector for short-chain branching characterization of polyolefin copolymers with HT-SEC. *7th International Conference on Polyolefin Characterization (ICPC)*; Houston, USA, 2018.

[385] Ortín, A.; Montesinos, J.; López, E.; del Hierro, P.; Monrabal, B.; Torres-Lapasió, J. R.; García-Álvarez-Coque, M. C. Characterization of Chemical Composition along the Molar Mass Distribution in Polyolefin Copolymers by GPC Using a Modern Filter-Based IR Detector. *Macromol. Symp.* **2013**, *330*, 63–80.

[386] Sheppard, W. A.; Sharts, C. M. *Organic fluorine chemistry*; Benjamin: New York, 1969.

[387] Pavlath, A. E.; Leffler, A. J. *Aromatic fluorine compounds*; Reinhold: New York, 1962.
[388] Clark, J. H. *Aromatic Fluorination*, 1st ed.; CRC Press: Milton, 2018.
[389] Reddy, M. L. N.; Wiles, M. R.; Massey, A. G. Ligands containing Fluoroaromatic Groups. *Nature* **1968**, *217*, 740.
[390] Sheppard, W. A. Pentafluorophenyl group. Electronic effect as a substituent. *J. Am. Chem. Soc.* **1970**, *92*, 5419–5422.
[391] Hogben, M. G.; Graham, W. A. G. Chemical shifts and coupling constants in pentafluorophenyl derivatives. I. Correlations of chemical shifts, coupling constants, and π-electronic interactions. *J. Am. Chem. Soc.* **1969**, *91*, 283–291.
[392] Giese, M.; Albrecht, M.; Rissanen, K. Anion-π Interactions with Fluoroarenes. *Chem. Rev.* **2015**, *115*, 8867–8895.
[393] Neel, A. J.; Hilton, M. J.; Sigman, M. S.; Toste, F. D. Exploiting non-covalent π interactions for catalyst design. *Nature* **2017**, *543*, 637–646.
[394] Patrick, C. R.; Prosser, G. S. A Molecular Complex of Benzene and Hexafluorobenzene. *Nature* **1960**, *187*, 1021.
[395] Sharber, S. A.; Baral, R. N.; Frausto, F.; Haas, T. E.; Müller, P.; Thomas Iii, S. W. Substituent Effects That Control Conjugated Oligomer Conformation through Non-covalent Interactions. *J. Am. Chem. Soc.* **2017**, *139*, 5164–5174.
[396] Coates, G. W.; Dunn, A. R.; Henling, L. M.; Ziller, J. W.; Lobkovsky, E. B.; Grubbs, R. H. Phenyl–Perfluorophenyl Stacking Interactions: Topochemical [2+2] Photodimerization and Photopolymerization of Olefinic Compounds. *J. Am. Chem. Soc.* **1998**, *120*, 3641–3649.
[397] Das, A.; Theato, P. Activated Ester Containing Polymers: Opportunities and Challenges for the Design of Functional Macromolecules. *Chem. Rev.* **2016**, *116*, 1434–1495.
[398] Gaballa, H.; Shang, J.; Meier, S.; Theato, P. The glucose-responsive behavior of a block copolymer featuring boronic acid and glycine. *J. Polym. Sci., Part A: Polym. Chem.* **2019**, *57*, 422–431.
[399] Jo, H.; Haberkorn, N.; Pan, J.-A.; Vakili, M.; Nielsch, K.; Theato, P. Fabrication of Chemically Tunable, Hierarchically Branched Polymeric Nanostructures by Multi-branched Anodic Aluminum Oxide Templates. *Langmuir* **2016**, *32*, 6437–6444.
[400] Piers, W. E.; Chivers, T. Pentafluorophenylboranes: from obscurity to applications. *Chem. Soc. Rev.* **1997**, *26*, 345–354.
[401] Erker, G. Tris(pentafluorophenyl)borane: a special boron Lewis acid for special reactions. *Dalton Trans.* **2005**, 1883–1890.
[402] Mkhalid, I. A. I.; Barnard, J. H.; Marder, T. B.; Murphy, J. M.; Hartwig, J. F. C-H Activation for the Construction of C-B Bonds. *Chem. Rev.* **2010**, *110*, 890–931.
[403] Yang, X.; Stern, C. L.; Marks, T. J. Cationic Zirconocene Olefin Polymerization Catalysts Based on the Organo-Lewis Acid Tris(pentafluorophenyl)borane. A Synthetic, Structural, Solution Dynamic, and Polymerization Catalytic Study. *J. Am. Chem. Soc.* **1994**, *116*, 10015–10031.
[404] Welch, G. C.; Juan, R. R. S.; Masuda, J. D.; Stephan, D. W. Reversible, metal-free hydrogen activation. *Science* **2006**, *314*, 1124–1126.
[405] Berkefeld, A.; Piers, W. E.; Parvez, M. Tandem frustrated Lewis pair/tris(pentafluorophenyl)borane-catalyzed deoxygenative hydrosilylation of carbon dioxide. *J. Am. Chem. Soc.* **2010**, *132*, 10660–10661.
[406] Stephan, D. W.; Erker, G. Frustrated Lewis pairs: metal-free hydrogen activation and more. *Angew. Chem. Int. Ed.* **2010**, *49*, 46–76.
[407] Chernichenko, K.; Madarász, Á.; Pápai, I.; Nieger, M.; Leskelä, M.; Repo, T. A frustrated-Lewis-pair approach to catalytic reduction of alkynes to cis-alkenes. *Nat. Chem.* **2013**, *5*, 718-723.

[408] Houghton, A. Y.; Hurmalainen, J.; Mansikkamäki, A.; Piers, W. E.; Tuononen, H. M. Direct observation of a borane–silane complex involved in frustrated Lewis-pair-mediated hydrosilylations. *Nat. Chem.* **2014**, *6*, 983-988.

[409] Chan, K. W.; Mance, D.; Safonova, O. V.; Copéret, C. Well-defined Silica-supported Tungsten(IV)-oxo Complex: Olefin Metathesis Activity, Initiation and Role of Brønsted Acid Sites. *J. Am. Chem. Soc.* **2019**, *141*, 18286-18292.

[410] Krossing, I.; Raabe, I. Noncoordinating Anions—Fact or Fiction? A Survey of Likely Candidates. *Angew. Chem. Int. Ed.* **2004**, *43*, 2066–2090.

[411] Jutzi, P.; Müller, C.; Stammler, A.; Stammler, H.-G. Synthesis, Crystal Structure, and Application of the Oxonium Acid $[H(OEt_2)_2]^+$ $[B(C_6F_5)_4]^-$. *Organometallics* **2000**, *19*, 1442–1444.

[412] Zhou, J.; Lancaster, S. J.; Walker, D. A.; Beck, S.; Thornton-Pett, M.; Bochmann, M. Synthesis, structures, and reactivity of weakly coordinating anions with delocalized borate structure: the assessment of anion effects in metallocene polymerization catalysts. *J. Am. Chem. Soc.* **2001**, *123*, 223–237.

[413] Mason, A. F.; Coates, G. W. New phenoxyketimine titanium complexes: combining isotacticity and living behavior in propylene polymerization. *J. Am. Chem. Soc.* **2004**, *126*, 16326–16327.

[414] Edson, J. B.; Wang, Z.; Kramer, E. J.; Coates, G. W. Fluorinated bis(phenoxyketimine)titanium complexes for the living, isoselective polymerization of propylene: multiblock isotactic polypropylene copolymers via sequential monomer addition. *J. Am. Chem. Soc.* **2008**, *130*, 4968–4977.

[415] Saito, J.; Mitani, M.; Mohri, J.; Yoshida, Y.; Matsui, S.; Ishii, S.; Kojoh, S.; Kashiwa, N.; Fujita, T. Living Polymerization of Ethylene with a Titanium Complex Containing Two Phenoxy-Imine Chelate Ligands. *Angew. Chem. Int. Ed.* **2001**, *40*, 2918–2920.

[416] Talarico, G.; Busico, V.; Cavallo, L. "Living" Propene Polymerization with Bis(phenoxyimine) Group 4 Metal Catalysts: New Strategies and Old Concepts. *Organometallics* **2004**, *23*, 5989–5993.

[417] Bryliakov, K. P.; Talsi, E. P.; Möller, H. M.; Baier, M. C.; Mecking, S. Noncovalent Interactions in o-Fluorinated Post-titanocene Living Ethylene Polymerization Catalyst. *Organometallics* **2010**, *29*, 4428–4430.

[418] Lafrance, M.; Rowley, C. N.; Woo, T. K.; Fagnou, K. Catalytic intermolecular direct arylation of perfluorobenzenes. *J. Am. Chem. Soc.* **2006**, *128*, 8754–8756.

[419] Walsh, D. J.; Hyatt, M. G.; Miller, S. A.; Guironnet, D. Recent Trends in Catalytic Polymerizations. *ACS Catal.* **2019**, *9*, 11153–11188.

[420] Tong, Q.; Krumova, M.; Göttker-Schnetmann, I.; Mecking, S. Crystallization as a means for the switching of nanoscale containers. *Langmuir* **2008**, *24*, 2341–2347.

[421] Mun, T. C. Production of Polyethylene Using Gas Fluidized Bed Reactor. *Conference Proceedings* **2004**, https://pdfs.semanticscholar.org/eaa8/47ce6cbad3a55f6e6fa7d9e9307181d1b54b.pdf (accessed June 9, 2020).

[422] Davis, S. S.; Smith, A. The Influence of the Disperse Phase on the Stability of Oil-in-Water Emulsions. *Theory and practice of emulsion technology*; Academic Press: London, 1976.

[423] Sloan, E. D.; Koh, C. A. *Clathrate hydrates of natural gases*, 3rd ed.; CRC Press: Boca Raton, Fla., 2008.

[424] Luo, H.; Sun, C.-Y.; Peng, B.-Z.; Chen, G.-J. Solubility of ethylene in aqueous solution of sodium dodecyl sulfate at ambient temperature and near the hydrate formation region. *J. Colloid Interface Sci.* **2006**, *298*, 952–956.

[425] Kumar, A.; Bhattacharjee, G.; Kulkarni, B. D.; Kumar, R. Role of Surfactants in Promoting Gas Hydrate Formation. *Ind. Eng. Chem. Res.* **2015**, *54*, 12217–12232.

[426] Holmberg, K. Surfactants. *Ullmann's Encyclopedia of Industrial Chemistry*; Wiley-VCH: Weinheim, 2019.

[427] Reynolds, J. A.; Tanford, C. Binding of dodecyl sulfate to proteins at high binding ratios. Possible implications for the state of proteins in biological membranes. *Proc. Natl. Acad. Sci.* **1970**, *66*, 1002–1007.

[428] Smulders, E.; Rybinski, W. von; Sung, E.; Rähse, W.; Steber, J.; Wiebel, F.; Nordskog, A. Laundry Detergents. *Ullmann's Encyclopedia of Industrial Chemistry*; Wiley-VCH: Weinheim, 2007.

[429] Pederson, T. Turning a PAGE: the overnight sensation of SDS-polyacrylamide gel electrophoresis. *FASEB J.* **2008**, *22*, 949–953.

[430] Nakagaki, M.; Yokoyama, S. Acid-Catalyzed Hydrolysis of Sodium Dodecyl Sulfate. *J. Pharm. Sci.* **1985**, *74*, 1047–1052.

[431] Smith, D. K.; Korgel, B. A. The importance of the CTAB surfactant on the colloidal seed-mediated synthesis of gold nanorods. *Langmuir* **2008**, *24*, 644–649.

[432] Bogardus, J. B.; Higuchi, T. Kinetics and Mechanism of Hydrolysis of Labile Quaternary Ammonium Derivatives of Tertiary Amines. *J. Pharm. Sci.* **1982**, *71*, 729–735.

[433] Bücker, D.; Sickinger, A.; Ruiz Perez, J. D.; Oestringer, M.; Mecking, S.; Drescher, M. Direct Observation of Chain Lengths and Conformations in Oligofluorene Distributions from Controlled Polymerization by Double Electron-Electron Resonance. *J. Am. Chem. Soc.* **2020**, *142*, 1952–1956.

[434] Ruiz Perez, J. D.; Mecking, S. Anisotropic Polymer Nanoparticles with Tunable Emission Wavelengths by Intersegmental Chain Packing. *Angew. Chem. Int. Ed.* **2017**, *56*, 6147–6151.

[435] Wimmer, F. P. Functional Group Tolerance of Ni(II)-Insertion Catalysts towards Cell Environments. *Master Thesis, University of Konstanz* **2017**.

[436] Joshi, J. V.; Aswal, V. K.; Goyal, P. S. Combined SANS and SAXS studies on alkali metal dodecyl sulphate micelles. *J. Phys.: Condens. Matter* **2007**, *19*, 196219.

[437] Rakitin, A. R.; Pack, G. R. Molecular Dynamics Simulations of Ionic Interactions with Dodecyl Sulfate Micelles. *J. Phys. Chem. B* **2004**, *108*, 2712–2716.

[438] Jones, R. R. M.; Maldonado, R.; Szajdzinska-Pietek, E.; Kevan, L. Electron spin echo modulation of doxylstearic acid probes of the surface and internal structure of lithium dodecyl sulfate micelles: comparison with sodium dodecyl sulfate and tetramethylammonium dodecyl sulfate micelles. *J. Phys. Chem.* **1986**, *90*, 1126–1129.

[439] Sheu, E. Y.; Wu, C. F.; Chen, S. H. Effects of ion sizes on the aggregation and surface charge of ionic micelles in 1:1 electrolyte solutions. *J. Phys. Chem.* **1986**, *90*, 4179–4187.

[440] Missel, P. J.; Mazer, N. A.; Carey, M. C.; Benedek, G. B. Influence of alkali-metal counterion identity on the sphere-to-rod transition in alkyl sulfate micelles. *J. Phys. Chem.* **1989**, *93*, 8354–8366.

[441] Benrraou, M.; Bales, B. L.; Zana, R. Effect of the Nature of the Counterion on the Properties of Anionic Surfactants. 1. Cmc, Ionization Degree at the Cmc and Aggregation Number of Micelles of Sodium, Cesium, Tetramethylammonium, Tetraethylammonium, Tetrapropylammonium, and Tetrabutylammonium Dodecyl Sulfates. *J. Phys. Chem. B* **2003**, *107*, 13432–13440.

[442] Lee, H. S.; Adhimoolam Arunagirinathan, M.; Vagias, A.; Lee, S.; Bellare, J. R.; Davis, H. T.; Kaler, E. W.; McCormick, A. V.; Bates, F. S. Almost Fooled Again: New Insights into Cesium Dodecyl Sulfate Micelle Structures. *Langmuir* **2014**, *30*, 12743–12747.

[443] Cha, M.; Shin, K.; Kim, J.; Chang, D.; Seo, Y.; Lee, H.; Kang, S.-P. Thermodynamic and kinetic hydrate inhibition performance of aqueous ethylene glycol solutions for natural gas. *Chem. Eng. Sci.* **2013**, *99*, 184–190.

[444] Lingelem, M. N.; Majeed A. I.; Stange, E. Industrial Experience in Evaluation of Hydrate Formation, Inhibition, and Dissociation in Pipeline Design and Operation. *Ann. N.Y. Acad. Sci.* **1994**, *715*, 75–93.

[445] Jeevanandam, J.; Barhoum, A.; Chan, Y. S.; Dufresne, A.; Danquah, M. K. Review on nanoparticles and nanostructured materials: history, sources, toxicity and regulations. *Beilstein J. Nanotechnol.* **2018**, *9*, 1050–1074.

[446] Alivisatos, A. P. Semiconductor Clusters, Nanocrystals, and Quantum Dots. *Science* **1996**, *271*, 933–937.

[447] Yoreo, J. J. de; Gilbert, Pupa U. P. A.; Sommerdijk, Nico A. J. M.; Penn, R. L.; Whitelam, S.; Joester, D.; Zhang, H.; Rimer, J. D.; Navrotsky, A.; Banfield, J. F.; Wallace, A. F.; Michel, F. M.; Meldrum, F. C.; Cölfen, H.; Dove, P. M. Crystallization by particle attachment in synthetic, biogenic, and geologic environments. *Science* **2015**, *349*, aaa6760.

[448] Anu Mary Ealia, S.; Saravanakumar, M. P. A review on the classification, characterisation, synthesis of nanoparticles and their application. *IOP Conf. Ser.: Mater. Sci. Eng.* **2017**, *263*, 32019.

[449] Li, M.; Schnablegger, H.; Mann, S. Coupled synthesis and self-assembly of nanoparticles to give structures with controlled organization. *Nature* **1999**, *402*, 393–395.

[450] Whitesides, G. M.; Grzybowski, B. Self-assembly at all scales. *Science* **2002**, *295*, 2418–2421.

[451] Midya, J.; Cang, Y.; Egorov, S. A.; Matyjaszewski, K.; Bockstaller, M. R.; Nikoubashman, A.; Fytas, G. Disentangling the Role of Chain Conformation on the Mechanics of Polymer Tethered Particle Materials. *Nano Lett.* **2019**, *19*, 2715–2722.

[452] Yang, L.; Wang, Z.; Ji, Y.; Wang, J.; Xue, G. Highly Ordered 3D Graphene-Based Polymer Composite Materials Fabricated by "Particle-Constructing" Method and Their Outstanding Conductivity. *Macromolecules* **2014**, *47*, 1749–1756.

[453] Mann, S. The Chemistry of Form. *Angew. Chem. Int. Ed.* **2000**, *39*, 3392–3406.

[454] Garcia-Tunon, E.; Barg, S.; Bell, R.; Weaver, J. V. M.; Walter, C.; Goyos, L.; Saiz, E. Designing smart particles for the assembly of complex macroscopic structures. *Angew. Chem. Int. Ed.* **2013**, *52*, 7805–7808.

[455] Henzie, J.; Grünwald, M.; Widmer-Cooper, A.; Geissler, P. L.; Yang, P. Self-assembly of uniform polyhedral silver nanocrystals into densest packings and exotic superlattices. *Nat. Mater.* **2011**, *11*, 131–137.

[456] Sturm Née Rosseeva, E. V.; Cölfen, H. Mesocrystals: structural and morphogenetic aspects. *Chem. Soc. Rev.* **2016**, *45*, 5821–5833.

[457] Cheng, M.-J.; Zhang, Q.; Shi, F. Macroscopic Supramolecular Assembly and Its Applications. *Chin. J. Polym. Sci.* **2018**, *36*, 306–321.

[458] Wang, J.-T.; Wang, J.; Han, J.-J. Fabrication of advanced particles and particle-based materials assisted by droplet-based microfluidics. *Small* **2011**, *7*, 1728–1754.

[459] Zhu, E.; Wang, S.; Yan, X.; Sobani, M.; Ruan, L.; Wang, C.; Liu, Y.; Duan, X.; Heinz, H.; Huang, Y. Long-Range Hierarchical Nanocrystal Assembly Driven by Molecular Structural Transformation. *J. Am. Chem. Soc.* **2019**, *141*, 1498–1505.

[460] Dobler, F.; Pith, T.; Lambla, M.; Holl, Y. Coalescence mechanisms of polymer colloids. *J. Colloid Interface Sci.* **1992**, *152*, 12–21.

[461] Zastrow, M. 3D printing gets bigger, faster and stronger. *Nature* **2020**, *578*, 20–23.

[462] Jones, N. Science in three dimensions: the print revolution. *Nature* **2012**, *487*, 22–23.

[463] Truby, R. L.; Lewis, J. A. Printing soft matter in three dimensions. *Nature* **2016**, *540*, 371–378.

[464] Ligon, S. C.; Liska, R.; Stampfl, J.; Gurr, M.; Mülhaupt, R. Polymers for 3D Printing and Customized Additive Manufacturing. *Chem. Rev.* **2017**, *117*, 10212–10290.

[465] Wang, Y. M.; Voisin, T.; McKeown, J. T.; Ye, J.; Calta, N. P.; Li, Z.; Zeng, Z.; Zhang, Y.; Chen, W.; Roehling, T. T.; Ott, R. T.; Santala, M. K.; Depond, P. J.; Matthews, M. J.; Hamza, A. V.; Zhu, T. Additively manufactured hierarchical stainless steels with high strength and ductility. *Nat. Mater.* **2018**, *17*, 63–71.

[466] Zhang, D.; Qiu, D.; Gibson, M. A.; Zheng, Y.; Fraser, H. L.; StJohn, D. H.; Easton, M. A. Additive manufacturing of ultrafine-grained high-strength titanium alloys. *Nature* **2019**, *576*, 91–95.

[467] Kotz, F.; Arnold, K.; Bauer, W.; Schild, D.; Keller, N.; Sachsenheimer, K.; Nargang, T. M.; Richter, C.; Helmer, D.; Rapp, B. E. Three-dimensional printing of transparent fused silica glass. *Nature* **2017**, *544*, 337–339.

[468] Masood, S. H. Advances in Fused Deposition Modeling. *Comprehensive materials processing*; Elsevier Ltd.: London, 2014.

[469] Baumann, F.; Bugdayci, H.; Grunert, J.; Keller, F.; Roller, D. Influence of slicing tools on quality of 3D printed parts. *Comput.-Aided Des. Applic.* **2016**, *13*, 14–31.

[470] Šljivic, M.; Pavlovic, A.; Kraišnik, M.; Ilić, J. Comparing the accuracy of 3D slicer software in printed enduse parts. *IOP Conf. Ser.: Mater. Sci. Eng.* **2019**, *659*, 12082.

[471] Schirmeister, C. G.; Hees, T.; Licht, E. H.; Mülhaupt, R. 3D printing of high density polyethylene by fused filament fabrication. *Addit. Manuf.* **2019**, *28*, 152–159.

[472] Fischer, J. *Handbook of molded part shrinkage and warpage*, 2nd ed.; William Andrew: Oxford, 2012.

[473] Hofmann, D.; Kurek, A.; Thomann, R.; Schwabe, J.; Mark, S.; Enders, M.; Hees, T.; Mülhaupt, R. Tailored Nanostructured HDPE Wax/UHMWPE Reactor Blends as Additives for Melt-Processable All-Polyethylene Composites and in Situ UHMWPE Fiber Reinforcement. *Macromolecules* **2017**, *50*, 8129–8139.

[474] Ramli, M. S.; Wahab, M. S.; Ahmad, M.; Bala, A. S. FDM preparation of bio-compatible UHMWPE polymer for artificial implant. *J. Eng. Appl. Sci.* **2016**, *11*, 5474–5480.

[475] Ahmad, M.; Wahit, M. U.; Kadir, M. R. A.; Dahlan, K. Z. M.; Jawaid, M. Thermal and mechanical properties of ultrahigh molecular weight polyethylene/high-density polyethylene/polyethylene glycol blends. *J. Polym. Eng.* **2013**, *33*, 599–614.

[476] Araujo Borges, R.; Choudhury, D.; Zou, M. 3D printed PCU/UHMWPE polymeric blend for artificial knee meniscus. *Tribol. Int.* **2018**, *122*, 1–7.

[477] Rocha, C. R.; Torrado Perez, A. R.; Roberson, D. A.; Shemelya, C. M.; MacDonald, E.; Wicker, R. B. Novel ABS-based binary and ternary polymer blends for material extrusion 3D printing. *J. Mater. Res.* **2014**, *29*, 1859–1866.

[478] Goodridge, R. D.; Hague, R. J.; Tuck, C. J. An empirical study into laser sintering of ultra-high molecular weight polyethylene (UHMWPE). *J. Mater. Process. Technol.* **2010**, *210*, 72–80.

[479] Deplancke, T.; Lame, O.; Rousset, F.; Seguela, R.; Vigier, G. Mechanisms of Chain Reentanglement during the Sintering of UHMWPE Nascent Powder: Effect of Molecular Weight. *Macromolecules* **2015**, *48*, 5328–5338.

[480] Boyle, B. M.; Xiong, P. T.; Mensch, T. E.; Werder, T. J.; Miyake, G. M. 3D printing using powder melt extrusion. *Addit. Manuf.* **2019**, *29*, 100811.

[481] Xue, Y.-Q.; Tervoort, T. A.; Lemstra, P. J. Welding Behavior of Semicrystalline Polymers. 1. The Effect of Nonequilibrium Chain Conformations on Autoadhesion of UHMWPE. *Macromolecules* **1998**, *31*, 3075–3080.

[482] Barham, P. J.; Sadler, D. M. A neutron scattering study of the melting behaviour of polyethylene single crystals. *Polymer* **1991**, *32*, 393–395.

[483] Häußler, M.; Schnitte, M.; Mecking, S. *unpublished results* **2020**.

[484] Schultze-Gebhardt, F.; Herlinger, K.-H. Fibers (1. Survey). *Ullmann's Encyclopedia of Industrial Chemistry*; Wiley-VCH: Weinheim, 2005.

[485] Carothers, W. H.; Hill, J. W. Studies of Polymerization and Ring Formation. XV. Artificial fibers from synthetic linear condensation superpolymers. *J. Am. Chem. Soc.* **1932**, *54*, 1579–1587.

[486] Staudinger, H.; Johner, H.; Signer, R.; Mie, G.; Hengstenberg, J. Der polymere Formaldehyd, ein Modell der Zellulose. *Z. Phys. Chem.* **1927**, *126*, 425–448.

[487] Staudinger, H.; Lüthy, M. Hochpolymere Verbindungen. 3. Mitteilung. Über die Konstitution der Poly-oxymethylene. *Helv. Chim. Acta* **1925**, *8*, 41–64.

[488] Estes, L. L.; Sattler, H.; Berg, H.; Wolf, K.-H.; Kausch, M.; Schröer, H.; Pellegrini, A.; Olivieri, P.; Schoene, W.; Nogaj, A.; Süling, C.; Menault, J.; Osugi, T.; Morimoto, O.; Frankenburg, P. E. Fibers (4. Synthetic Organic). *Ullmann's Encyclopedia of Industrial Chemistry*; Wiley-VCH: Weinheim, 2005.

[489] van der Werff, H.; Heisserer, U. High-performance ballistic fibers. *Advanced fibrous composite materials for ballistic protection*; Elsevier Ltd: London, 2016.

[490] Wang, J.; Smith, K. J. The breaking strength of ultra-high molecular weight polyethylene fibers. *Polymer* **1999**, *40*, 7261–7274.

[491] Smith, P.; Lemstra, P. J. Ultra-high-strength polyethylene filaments by solution spinning/drawing. *J. Mater. Sci.* **1980**, *15*, 505–514.

[492] Kalb, B.; Pennings, A. J. Spinning of high molecular weight polyethylene solution and subsequent drawing in a temperature gradient. *Polym. Bull.* **1979**, *1*, 871–876.

[493] Dees, J. R.; Spruiell, J. E. Structure development during melt spinning of linear polyethylene fibers. *J. Appl. Polym. Sci.* **1974**, *18*, 1053–1078.

[494] Shen, S.; Henry, A.; Tong, J.; Zheng, R.; Chen, G. Polyethylene nanofibres with very high thermal conductivities. *Nat. Nanotechnol.* **2010**, *5*, 251–255.

[495] Choy, C. L.; Wong, Y. W.; Yang, G. W.; Kanamoto, T. Elastic modulus and thermal conductivity of ultradrawn polyethylene. *J. Polym. Sci., Part B: Polym. Phys.* **1999**, *37*, 3359–3367.

[496] Wang, Z.; Carter, J. A.; Lagutchev, A.; Koh, Y. K.; Seong, N.-H.; Cahill, D. G.; Dlott, D. D. Ultrafast flash thermal conductance of molecular chains. *Science* **2007**, *317*, 787–790.

[497] Rein, D. M.; Shavit-Hadar, L.; Khalfin, R. L.; Cohen, Y.; Shuster, K.; Zussman, E. Electrospinning of ultrahigh-molecular-weight polyethylene nanofibers. *J. Polym. Sci., Part B: Polym. Phys.* **2007**, *45*, 766–773.

[498] Ward, I. M.; Lemstra, P. J. Production and properties of high-modulus and high-strength polyethylene fibres. *Handbook of textile fibre structure*; Woodhead Publishing: Cambridge, 2009.

[499] Bousmina, M.; Qiu, H.; Grmela, M.; Klemberg-Sapieha, J. E. Diffusion at Polymer/Polymer Interfaces Probed by Rheological Tools. *Macromolecules* **1998**, *31*, 8273–8280.

[500] Liaw, C.-Y.; Guvendiren, M. Current and emerging applications of 3D printing in medicine. *Biofabrication* **2017**, *9*, 24102.

[501] Murphy, S. V.; Atala, A. 3D bioprinting of tissues and organs. *Nat. Biotechnol.* **2014**, *32*, 773–785.

[502] Godoi, F. C. *Fundamentals of 3D food printing and applications*; Elsevier: London, 2018.

[503] Sultan, S.; Abdelhamid, H. N.; Zou, X.; Mathew, A. P. CelloMOF: Nanocellulose Enabled 3D Printing of Metal-Organic Frameworks. *Adv. Funct. Mater.* **2019**, *29*, 1805372.

[504] Chen, Q.; Cao, P.-F.; Advincula, R. C. Mechanically Robust, Ultraelastic Hierarchical Foam with Tunable Properties via 3D Printing. *Adv. Funct. Mater.* **2018**, *28*, 1800631.

[505] Schroeder, T. B. H.; Guha, A.; Lamoureux, A.; VanRenterghem, G.; Sept, D.; Shtein, M.; Yang, J.; Mayer, M. An electric-eel-inspired soft power source from stacked hydrogels. *Nature* **2017**, *552*, 214–218.

[506] Kenel, C.; Casati, N. P. M.; Dunand, D. C. 3D ink-extrusion additive manufacturing of CoCrFeNi high-entropy alloy micro-lattices. *Nat. Commun.*, *10*, 1–8.

[507] Peng, J.; Witting, I.; Geisendorfer, N.; Wang, M.; Chang, M.; Jakus, A.; Kenel, C.; Yan, X.; Shah, R.; Snyder, G. J.; Grayson, M. 3D extruded composite thermoelectric threads for flexible energy harvesting. *Nat. Commun.*, *10*, 1–8.

[508] Schaffner, M.; Faber, J. A.; Pianegonda, L.; Rühs, P. A.; Coulter, F.; Studart, A. R. 3D printing of robotic soft actuators with programmable bioinspired architectures. *Nat. Commun.* **2018**, *9*, 878.

[509] Ntagios, M.; Nassar, H.; Pullanchiyodan, A.; Navaraj, W. T.; Dahiya, R. Robotic Hands with Intrinsic Tactile Sensing via 3D Printed Soft Pressure Sensors. *Adv. Intell. Syst.* **2019**, *521*, 1900080.

[510] Muth, J. T.; Vogt, D. M.; Truby, R. L.; Mengüç, Y.; Kolesky, D. B.; Wood, R. J.; Lewis, J. A. Embedded 3D printing of strain sensors within highly stretchable elastomers. *Adv. Mater.* **2014**, *26*, 6307–6312.

[511] Wu, A. S.; Small Iv, W.; Bryson, T. M.; Cheng, E.; Metz, T. R.; Schulze, S. E.; Duoss, E. B.; Wilson, T. S. 3D Printed Silicones with Shape Memory. *Sci. Rep.* **2017**, *7*, 4664.

[512] Unversity of Konstanz. The University of Konstanz Logo. https://www.uni-konstanz.de/en/university/news-and-media/create-online-and-print-media/corporate-design/the-university-of-konstanz-logo/ (accessed March 12, 2020).

[513] Thingiverse.com. Starwars Holocom (3DPapst). https://www.thingiverse.com/thing:4219281 (accessed March 13, 2020).

[514] Guyot, A.; Chu, F.; Schneider, M.; Graillat, C.; McKenna, T. F. High solid content latexes. *Prog. Polym. Sci.* **2002**, *27*, 1573–1615.

[515] Schneider, M.; Claverie, J.; Graillat, C.; McKenna, T. F. High solids content emulsions. I. A study of the influence of the particle size distribution and polymer concentration on viscosity. *J. Appl. Polym. Sci.* **2002**, *84*, 1878–1896.

[516] Flörke, O. W.; Graetsch, H. A.; Brunk, F.; Benda, L.; Paschen, S.; Bergna, H. E.; Roberts, W. O.; Welsh, W. A.; Libanati, C.; Ettlinger, M.; Kerner, D.; Maier, M.; Meon, W.; Schmoll, R.; Gies, H.; Schiffmann, D. Silica. *Ullmann's encyclopedia of industrial chemistry*, 7th ed.; Wiley-VCH: Weinheim, 2008.

[517] Evonik Resource Efficiency GmbH. Aerosil® - Fumed Silica (Technical Overview). https://www.aerosil.com/sites/lists/RE/DocumentsSI/Technical-Overview-AEROSIL-Fumed-Silica-EN.pdf (accessed March 24, 2020).

[518] Evonik Resource Efficiency GmbH. Aerosil® and Aeroixde® for 3D Printing Applications/Additive Manufacturing (Technical Information 1428). https://3d-printing.evonik.com/product/additive-manufacturing/downloads/aerosil-and-aeroxide-for-3d-printing-applications.pdf (accessed March 24, 2020).

[519] Evonik Industries. AEROSIL® 200. https://products-re.evonik.com/www2/uploads/productfinder/AEROSIL-200-EN.pdf (accessed March 25, 2020).

[520] Marlin Firmware. https://marlinfw.org/ (accessed March 17, 2020).

[521] OctoPrint. https://github.com/foosel/OctoPrint (accessed March 17, 2020).

[522] OctoPi. https://github.com/guysoft/OctoPi (accessed April 3, 2020).

[523] OctoPrint-EEPROM-Marlin (ambsr). https://github.com/amsbr/OctoPrint-EEPROM-Marlin (accessed April 3, 2020).

[524] Slic3r. https://github.com/slic3r/Slic3r (accessed April 3, 2020).

[525] Prusa3D. PrusaSlicer. https://github.com/prusa3d/PrusaSlicer (accessed April 3, 2020).

[526] Moore, D. M. *Instant Slic3r - Unravel the mysteries behind taking a virtual model and turning it into a physical object*; Packt Pub: Birmingham, 2013.

[527] Thingiverse.com. Calibration tests parts (LothanStar). https://www.thingiverse.com/thing:335243 (accessed April 8, 2020).

[528] Tinkercad | Create 3D digital designs with online CAD. https://www.tinkercad.com/ (accessed March 10, 2020).